SENSORDEVICES 2011

The Second International Conference on Sensor Device Technologies and Applications

WISH 2011

The First International Workshop on Intelligent Sensor Hub

ISBN: 978-1-61208-145-8

August 21-27, 2011

Nice/Saint Laurent du Var, France

SENSORCOMM 2011 Editors

Sergey Yurish, IFSA - Barcelona, Spain

Thomas Herzog, Fraunhofer Institute for Non-Destructive Testing IZFP - Dresden, Germany

Henning Heuer, Fraunhofer Institute for Non-Destructive Testing IZFP - Dresden, Germany

Vítor Carvalho, Minho University, Portugal

SENSORDEVICES 2011

Foreword

The Second International Conference on Sensor Device Technologies and Applications (SENSORDEVICES 2011),held between August 21-27, 2011 in Nice/Saint Laurent du Var, France, was a multi-track event covering topics related to sensing device technologies: ultrasonic, piezo, infrared, medical, etc .

Most of the sensor-oriented research and industry initiatives are focusing on sensor networks, data security, exchange protocols, energy optimization, and features related to intermittent connections. Recently, the concept of Internet-of-things gathers attention, especially when integrating IPv4 and IIPv6 networks. The followup and complementing event SENSORDEVICES 2011, The Second International Conference on Sensor Device Technologies and Applications, initiates a series of events focusing on sensor devices themselves, the technology-capturing style of sensors, special technologies, signal control and interfaces, and particularly sensors-oriented applications. The evolution of the nano-and microtechnologies, nanomaterials, and the new business services make the sensor device industry and research on sensor-themselves very challenging.

SENSORDEVICES 2011 also included:

- WISH 2011, The First International Workshop on Intelligent Sensor Hub

We take here the opportunity to warmly thank all the members of the SENSORDEVICES 2011 Technical Program Committee, as well as the numerous reviewers. The creation of such a broad and high quality conference program would not have been possible without their involvement. We also kindly thank all the authors who dedicated much of their time and efforts to contribute to SENSORDEVICES 2010. We truly believe that, thanks to all these efforts, the final conference program consisted of top quality contributions.

Also, this event could not have been a reality without the support of many individuals, organizations, and sponsors. We are grateful to the members of the SENSORDEVICES 2011 organizing committee for their help in handling the logistics and for their work to make this professional meeting a success. We hope that SENSORDEVICES 2011 was a successful international forum for the exchange of ideas and results between academia and industry and for the promotion of progress in the area of sensor devices and their applications.

We hope Côte d'Azur provided a pleasant environment during the conference and everyone saved some time for exploring the Mediterranean Coast.

SENSORDEVICES 2011 Chairs

Advisory Chairs
Sergey Yurish, IFSA - Barcelona, Spain
Petre Dini, Concordia University, Canada / China Space Agency Center, China
Elena Gaura, Coventry University, UK
Vittorio Ferrari, Università di Brescia, Italy

Research/Industry Chairs
Raluca - Ioana Stefan-van Staden, National Institute of Research for Electrochemistry and Condensed Matter, Bucharest, Romania
Alberto Yúfera, Centro Nacional de Microelectronica (CNM-CSIC) - Sevilla, Spain

Special Area Chairs

Ultrasonic and piezoelectric sensors
Thomas Herzog, Fraunhofer Institute for Non-Destructive Testing IZFP - Dresden, Germany
Henning Heuer, Fraunhofer Institute for Non-Destructive Testing IZFP - Dresden, Germany

Optical sensors
Vítor Carvalho, Minho University, Portugal
Irinela Chilibon, National Institute of Research and Development for Optoelectronics - Bucharest, Romania

Gas sensors
Dongfang Yang, National Research Council Canada - London, Canada

Nanosensors
Marco Tartagni, University of Bologna - Cesena, Italy

Testing and validation
Ksenia V. Sapozshnikova D.I. Mendeleyev Institute for Metrology - St. Petersburg, Russia

Vibration sensors
Subodh Kumar Singhal, National Physical Laboratory, New Delhi, India

WISH Chair
Stephane Gervais-Ducouret, Freescale Semiconductor, Inc., France

SENSORDEVICES 2011

Committee

SENSORDEVICES Advisory Chairs

Sergey Yurish, IFSA - Barcelona, Spain
Petre Dini, Concordia University, Canada / China Space Agency Center, China
Elena Gaura, Coventry University, UK
Vittorio Ferrari, Università di Brescia, Italy

SENSORDEVICES 2011 Research/Industry Chairs

Raluca - Ioana Stefan-van Staden, National Institute of Research for Electrochemistry and Condensed Matter, Bucharest, Romania
Alberto Yúfera, Centro Nacional de Microelectronica (CNM-CSIC) - Sevilla, Spain

SENSORDEVICES Special Area Chairs

Ultrasonic and piezoelectric sensors
Thomas Herzog, Fraunhofer Institute for Non-Destructive Testing IZFP - Dresden, Germany
Henning Heuer, Fraunhofer Institute for Non-Destructive Testing IZFP - Dresden, Germany

Optical sensors
Vítor Carvalho, Minho University, Portugal
Irinela Chilibon, National Institute of Research and Development for Optoelectronics - Bucharest, Romania

Gas sensors
Dongfang Yang, National Research Council Canada - London, Canada

Nanosensors
Marco Tartagni, University of Bologna - Cesena, Italy

Testing and validation
Ksenia V. Sapozshnikova D.I. Mendeleyev Institute for Metrology - St. Petersburg, Russia

Vibration sensors
Subodh Kumar Singhal, National Physical Laboratory, New Delhi, India

SENSORDEVICES 2011 Technical Program Committee

Francisco Javier Arcega Solsona, University of Zaragoza, Spain
Selcuk Atalay, Inonu University - Malatya, Turkey
Faruk Bagci, German University Cairo, Egypt
Sukumar Basu, Jadavpur University - Kolkata, India
Partha Bhattacharyya, Bengal Engineering and Science University, West Bengal, India

Vittorio M.N. Passaro, Politecnico di Bari, Italy
Alexei Nabok, Sheffield Hallam University, UK
Konandur Rajanna, Indian Institute of Science - Bangalore, India
Càndid Reig, University of Valencia, Spain
Teresa Restivo, University of Porto, Portugal
Mounir Bousbia Salah, University of Annaba, Algeria
Ksenia V. Sapozshnikova, D.I. Mendeleyev Institute for Metrology - St. Petersburg, Russia
Renshi Sawada, Kyushu University - Fukuoka, Japan
Yuriy Shmaliy, Guanajuato University, Mexico
Arvind K. Srivastava, NanoSonix Inc. - Skokie, USA
S. K. Singhal, National Physical Laboratory, New Delhi, India
Junho Song, Sunnybrook Health Science Centre - Toronto, Canada
Nickolaj Starodub, National University of Life and Environmental Sciences of Ukraine, / T. Shevchenko Kiev State University of Ukraine, Ukraine
Raluca - Ioana Stefan-van Staden, National Institute of Research for Electrochemistry and Condensed Matter, Bucharest, Romania
Arndt Steinke, CiS Forschungsinstitut für Mikrosensorik und Photovoltaik GmbH - Erfurt, Germany
Guo-Dung Su, National Taiwan University, Taiwan
Chelakara S. Subramanian, Florida Institute of Technology - Melbourne, USA
Roman Szewczyk, Warsaw University of Technology, Poland
Yen Kheng Tan, Nanyang Technological University, Singapore
Jaw-Luen Tang, National Chung Cheng University - Chia-Yi, Taiwan
Marco Tartagni, University of Bologna - Cesena, Italy
Roald Taymanov, D.I.Mendeleyev Institute for Metrology, Russia
Gui Yun Tian, Newcastle University, UK
Antonio Valente, University of Trás-os-Montes and Alto Douro (UTAD) - Vila Real, Portugal
Igone Velez, CEIT & Universidad de Navarra, Spain
Manuela Vieira, ISEL, Portugal
Dongfang Yang, National Research Council Canada - London, Canada
Xiaoling Yang, University of Illinois at Urbana-Champaign, USA
Alberto Yufera, Instituto de Microelectrónica de Sevilla (IMSE), Spain
Sergey Y. Yurish, IFSA - Barcelona, Spain
Boris Zaitsev Davydovich, Russian Academy of Sciences - Saratov Branch, Russia
Cyrus Zamani from University of Barcelona, Spain
Guigen Zhang, Clemson University, USA
Weiping Zhang, Shanghai Jiao Tong University, P. R. China
Qitao Zhao, The University of Texas at Arlington, USA
Ya-Pu Zhao, Chinese Academy of Sciences - Beijing, China

WISH Chair

Stephane Gervais-Ducouret, Freescale Semiconductor, Inc., France

WISH 2011 Technical Program Committee

Bruno Flament, Movea, France
Mathieu Forget, Freescale Semiconductor, Inc., USA
Stefano Frattesi, Indesit, Italy

Levent Gürgen, CEA, France
Mark Pedley, Freescale Semiconductor, Inc., USA
Laurent Perroton, ESIEE, France
Mike Stanley, Freescale Semiconductor, Inc., USA
Gervais-Ducouret Stephane, Freescale Semiconductor, Inc., France
Jacques Trichet, Freescale Semiconductor, Inc., USA
Francois Villeneuve, Freescale Semiconductor, Inc., USA
Jeannette Wilson, Freescale Semiconductor, Inc. USA

Copyright Information

For your reference, this is the text governing the copyright release for material published by IARIA.

The copyright release is a transfer of publication rights, which allows IARIA and its partners to drive the dissemination of the published material. This allows IARIA to give articles increased visibility via distribution, inclusion in libraries, and arrangements for submission to indexes.

I, the undersigned, declare that the article is original, and that I represent the authors of this article in the copyright release matters. If this work has been done as work-for-hire, I have obtained all necessary clearances to execute a copyright release. I hereby irrevocably transfer exclusive copyright for this material to IARIA. I give IARIA permission or reproduce the work in any media format such as, but not limited to, print, digital, or electronic. I give IARIA permission to distribute the materials without restriction to any institutions or individuals. I give IARIA permission to submit the work for inclusion in article repositories as IARIA sees fit.

I, the undersigned, declare that to the best of my knowledge, the article is does not contain libelous or otherwise unlawful contents or invading the right of privacy or infringing on a proprietary right.

Following the copyright release, any circulated version of the article must bear the copyright notice and any header and footer information that IARIA applies to the published article.

IARIA grants royalty-free permission to the authors to disseminate the work, under the above provisions, for any academic, commercial, or industrial use. IARIA grants royalty-free permission to any individuals or institutions to make the article available electronically, online, or in print.

IARIA acknowledges that rights to any algorithm, process, procedure, apparatus, or articles of manufacture remain with the authors and their employers.

I, the undersigned, understand that IARIA will not be liable, in contract, tort (including, without limitation, negligence), pre-contract or other representations (other than fraudulent misrepresentations) or otherwise in connection with the publication of my work.

Exception to the above is made for work-for-hire performed while employed by the government. In that case, copyright to the material remains with the said government. The rightful owners (authors and government entity) grant unlimited and unrestricted permission to IARIA, IARIA's contractors, and IARIA's partners to further distribute the work.

Table of Contents

Microcondensation sensors for field tests and for simulation of environment in climat chambers 1
Thomas Frank, Michael Hintz, Barbara March, and Arndt Steinke

Silver Gate Field Effect Transistor for Oxygen Gas Sensor 5
Keiji Tsukada, Daisuke Kiriake, Kenji Sakai, and Toshihiko Kiwa

Dynamic calibration of force sensors using sinusoidal excitations 8
Christian Schlegel, Gabriela Kieckenap, Bernd Glockner, and Rolf Kumme

Detection of Ice Formation over a Road Surface 14
Amedeo Troiano, Eros Pasero, and Luca Mesin

An Overview Over Yarn Mass Parameterization Methods 18
Vitor Carvalho, Nuno Goncpalves, Filomena Soares, Michael Belsley, and Rosa Vasconcelos

Embedded Sensor for Solid-State Hydrogen Storage Devices 25
Denis Marcotte and Frederic Domingue

Analytical technique of spectroscopic ellipsometry 29
Alexei Nabok, Verena Kriechbaumer, Mohd Kamarulzaki Mustafa, Benjamin Abell, David Smith, and Anna Tsargorodskaya

Optimized Mini Search Coil Magnetometer Suited To Large Bandwidth Applications 34
Maria Timofeeva, Gilles Allegre, Didier Robbes, Julien Gasnier, and Stephane Flament

Smart and Intelligent Optoelectronic Sensor Systems: OEM Design Approach 38
Sergey Y. Yurish

Energy Efficient Embedded Wireless System Used For Localisation In Indoor Environments 44
Nicolas Fourty, Yoann Charlon, and Eric Campo

Multimodal Water Content and Nutrient Concentration Sensor for On-Site Soil Monitoring 50
Masato Futagawa, MD. Iqramul Hussain, Keita Kamado, Fumihiro Dasai, Makoto Ishida, and Kazuaki Sawada

Love Wave Sensors Functionalized with Cobalt Corroles or Metalloporphyrines Applied to the Detection of Carbon Monoxide 54
Meddy Vanotti, Virginie Blondeau-Patissier, and Sylvain Ballandras

Distributed Chemical Sensor Networks for Environmental Sensing 58
Fiachra Collins, Dylan Orpen, Damien Maher, John Cleary, Cormac Fay, and Dermot Diamond

Potentialities of LSMO thin films for room temperature magnetic and temperature sensors 63
Sheng Wu, Dalal Fadil, Shuang Liu, Ammar Aryan, Benoit Renault, Jean-Marc Routoure, Bruno Guillet, Stephane Flament, and Laurence Mechin

MEMS-based Ethanol Sensor Using Zinc Oxide Nanostructured Films 69
Hardik Pandya, Sudhir Chandra, and Anoop Vyas

Towards Flexible Biocompatible Pressure Sensors: Covering Polymeric Films with a Highly Piezoresistive Organic Molecular Metal 75
Elena Laukhina, Vladimir Laukhin, Victor Lebedev, Concepcio Rovira, and Jaume Veciana

Development and Application of Nanoscale Polymeric Platforms for Advanced Protein Sensors 81
Jong-in Hahm and Sheng Song

A Rapid Modeling and Prototyping Technique for Piezoelectric Energy Harvesting Systems 86
Aldo Romani, Rudi Paolo Paganelli, Enrico Sangiorgi, and Marco Tartagni

Standard VHDL Modeling and Top-Simulation for the Development of an Integrated Smart-Bolometer 91
Matthieu Denoual and Patrick Attia

Detection of Infrared Radiation by Position-sensitive Superconducting Bolometer 95
Francesco Laviano, Luca Mesin, Roberto Gerbaldo, Gianluca Ghigo, Laura Gozzelino, Enrica Mezzetti, and Alberto Rovelli

PIR Sensor Array for Hand Motion Recognition 99
Piotr Wojtczuk, Alistair Armitage, T. David Binnie, and Tim Chamberlain

Group IV Photonic Slot Structures for Highly Efficient Gas Sensing in mid-IR 103
Vittorio Passaro, Benedetto Troia, and Francesco De Leonardis

Statistical Analysis of Dark Current in Silicon Photomultipliers 109
Giuseppina Valvo, Alfio Russo, Delfo Sanfilippo, Giovanni Condorelli, Clarice Di Martino, Beatrice Carbone, Piergiorgio Fallica, Roberto Pagano, Sebania Libertino, and Salvatore Lombardo

Nanoparticles with Conductive Polymer as Photosensing Applications 113
Si-Han Zeng, Shin-Hung Tsai, and Guo-Dung Su

Effect of the Optical Bias on the a-Si:H Optical Demultiplexer Device 118
Miguel Fernandes, Manuela Vieira, Manuel Vieira, and Paula Louro

Acoustic Emission Sensing of Structures 123
Irinela Chilibon, Marian Mogildea, and George Mogildea

Investigations on aluminum nitride thin film properties and design considerations for smart high frequency ultrasound sensors 129
Thomas Herzog, Susan Walter, and Henning Heuer

Reactive pulse magnetron sputtering for deposition of piezoelectric AlN layers 135
Daniel Gloss, Hagen Bartzsch, Matthias Gittner, Peter Frach, Thomas Herzog, Susan Walter, and Hennig Heuer

New Ultrasonic Sensor for a Simultaneous Mechanical and Electrical Characterization for the Contact Quality of a Mechanically Loaded Interface 139
Naima Alaoui-Ismaili, Franck Augereau, and Gilles Despaux

A Microelectrode-Cell Sensor Model for Real Time Monitoring 143
Alberto Yufera, Daniel Canete, and Paula Daza

Cell chip to analyze cell lines and cell cycle stages based on electrochemical method 147
Md. Abdul Kafi, Tae-Hyung Kim, and Jeong-Woo Choi

Flexible All-organic Highly Tenzo-resistive bi Layer Films as Weightless Strain and Pressure Sensors for Medical Devices 151
Vladimir Laukhin, Elena Laukhina, Victor Labedev, Raphael Pfattner, Concepcio Rovira, and Jaume Veciana

Building a Prototype for a Magnetic Nanoparticle Bead Based Biosensing Device 155
Wen Yaw Chung, Kimberly Jane Uy, Yi Ying Yeh, Ting Ya Yang, Hao Chun Yang, and Hsi Wen Li

An Automatic System for Bilayer Lipid Membrane Formation and Monitoring 160
Michele Rossi, Federico Thei, and Marco Tartagni

Smart Sensor Magnetometer Based Virtual Gyroscope 165
Baptiste Delporte, Laurent Perroton, Thierry Grandpierre, and Jacques Trichet

Consistency and Distributed Sensor Data Processing 171
Francois Pacull, Laurent-Frederic Ducreux, Suzanne Lesecq, and Stephanie Riche

Microcondensation Sensors for Field Tests and for Simulation of Environments in Climate Chambers

Thomas Frank, Michael Hintz, Barbara March, and Arndt Steinke
CiS Forschungsinstitut für Mikrosensorik und Photovoltaik GmbH
99099 Erfurt, Germany
e-mail: tfrank@cismst.de; mhintz@cismst.de; bmarch@cismst.de; asteinke@cismst.de

***Abstract* - Condensation associated with the risk of electrochemical and chemical migration plays an increasing significance in the field of reliability of electronic components. The trends towards challenging electronic assembly technologies such as minimization of conductive track widths and spacing, and higher density in electric elements are increasingly faced with the negative influences of micro-condensation. The condensation occurs as a result of the thermodynamic conditions in the environment of the electronic board. The condensed water is in equilibrium of condensation and evaporation, not in a static state. Due to this fact, there is a demand for sensors to record the real state permanently. Due to its miniaturized packaging, a new generation of micro-condensation sensors allows placement on different parts of electronic devices. Results of field tests in different automobiles and in climate chambers are presented.**

Keywords – condensation, humidity, migration, corrosion.

I. INTRODUCTION

In recent years, humidity sensors have found an extended range of application. Increasing demand for improvements of quality, reliability and energy control of technical and non-technical processes lead to new relative and absolute measurement humidity sensors [1]. The common type of sensors, the polymer sensors, is fabricated from a hygroscopic material. The electrical properties change as it absorbs water molecules. For measurement of absolute humidity dew point hygrometers are offered. The gas is cooling down until condensation appears on a small mirror. The temperature at which this happens is measured and is defined as the dew point temperature. The onset of condensation is sensed optically [2].

Failures of electronic components due to corrosion as a result of condensate ion can be studied only to a limited extent with the above mentioned instruments [3]. For monitoring by measurements of condensation processes in field tests or laboratory conditions, new measuring systems are required.

The presented microcondensation sensors measure the condensation directly. The basic principle consists of a stray field capacitor where the electric flux lines intersect the condensed water drops [4].

The miniaturization of the stray field interdigital capacitor in combination with a signal preprocessing close to this transducer, allows the measurement of water mass in the range up to 30 µg/mm^2. Depending on the comb pattern of specifically designed stray field capacity in combination with a water drops sensitive detection system, a change of the capacity with increasing water mass is fact. By varying the comb pattern, the sensitivity to the measured water mass can be adjusted (water drops in the range of 5 - 15 or 5 - 30 µg/mm²).

II. INFLUENCE OF CONDENSATION ON CORROSION

In the last years, an increasing number of papers were published dealing with any kind of corrosion of printed circuit electronic boards [5, 6]. Most of these are related to failures concerning the electronic reliability. Some authors reduce the failure to electrochemical or chemical corrosion [7, 8, 9]. Adding the growth of dendrites, the problem is becoming worse. Figure 1 presents a selection of typical failures.

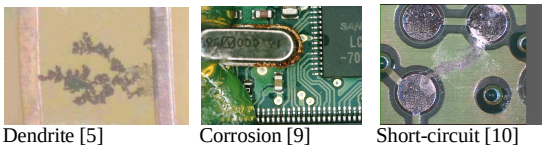

Dendrite [5] Corrosion [9] Short-circuit [10]

Figure 1. Different kinds of failure

What do all these examples of corrosion have in common? An essential role for the initiation of corrosion plays the presence of moisture. The presence of moisture causes electrolysis processes. These cause uncontrolled currents (leakage). The corrosion occurs by dissolution of the metal due to anodic oxidation. Electrolysis processes are already initiated significantly at relative humidities below dewing. Very thin films of water are formed already at 40 % relative humidity. At relative humidity of 60 %, water films are formed with a thickness up to 4 molecular layers. This water film can already interact with hygroscopic impurities on the board. At relative humidity of 80 %, water films are formed with a thickness up to 10 molecular layers [10]. These act similar to "normal water". Solution processes of salts on the surface can start and ionic processes run subsequently. In combination with higher temperatures these corrosion and migration processes are accelerated.

Electronic boards are more exposed to changing climatic conditions. This is a growing risk of condensation of water

 ISBN: 978-1-61208-145-8

vapor on the materials and components of electronic devices and consequently the risk of corrosion.

The processes could not only be described by the real climatic conditions. Rather, knowledge of the processes near the surface is required. Quantitative data of surface temperature, of humidity in the boundary layer, and, in particular, of the real condensation are necessary. Using microcondensation sensors, these data can be obtained.

III. MICROSYSTEM

Based on the increasing interest in direct condensation testing, different principles exist (e.g. optical [11], optoelectronical [12], and capacity [13] transducers).

We introduce an impedimetric principle and prefer such a solution for reasons of better miniaturization, better integration of condensation and temperature sensor, and to create smart systems with lower power consumption.

Because the customer is mainly interested in a calibrated sensor signal, the complete micro sensor system must be integrated. Starting with the detection system, transducer and signal pre-processing, the system has to be completed by the signal processing (linearization, error compensation, calibration, programming) and interface.

A. *Detection system*

The detection system consists of a PE CVD Si3N4 layer, typically approximately 500 nm in thickness. This system has to guarantee a high and long term stability and reproducibility (see Figure 2) of condensation. A second task of this layer is the protection of the metal layer underneath against corrosion.

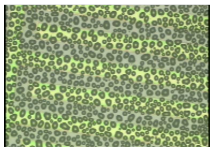

Figure 2. Condensation on sensor surface

B. *Transducer*

Two transducers are necessary, one for the measurement of temperature of the condensate and one for water mass measurement. The temperature transducer has been realized with a typical monolithic pn - junction. The water mass transducer has been designed as stray field capacity with interdigital structures (Figure 3). With a gap/line ratio of 25/33 (Figure 4), water mass measurements are possible between 5 and 25 µg/mm2.

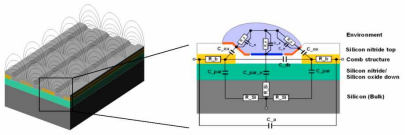

Figure 3. Model of stray field capacity

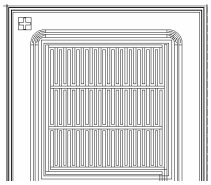

Figure 4. Design of interdigital electrodes

C. *Signal pre-processing*

With the demand regarding III, the signal pre-processing has been reduced to a capacity-frequency converter. This converter allows a distance from the sensor element to the signal processing of about 1 - 2 meter. The temperature sensor does not need signal pre-processing. The change of temperature related flow voltage (2 mV/K) can be prepared for the electronic via the same signal line.

The detection system, transducer, and signal pre-processing are hybrid integrated components (figure 5).

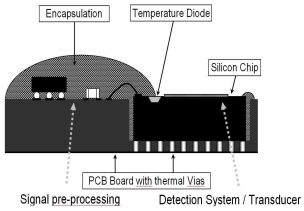

Figure 5. Draft of a cross section of a sensor element (detection system, transducer, signal pre-processing)

D. *Signal processing/Interface*

To obtain calibrated output signals for temperature and water mass, the primary signals from the sensor element have to be reworked. Therefore, the electronic part contains the appropriate parameters for linearization, temperature compensation, and programming. Tests for radio interference emission and immunity to electromagnetic fields were carried out and the results confirm that the sensor system (figure 6) meets the requirements of the automobile industry.

Figure 6. Complete sensor system

 ISBN: 978-1-61208-145-8

IV. RESULTS

A. *Calibrated output signal*

The sensor system provides calibrated analog or digital output signals for temperature and water mass.

The calibration of the water mass is realized by taking pictures of the sensor surface at different stages of dewing and simultaneous measurement of the output signal of the sensor. By means of image processing, knowing the contact angle of water at the sensor surface, and mathematical models, a correlation between the determined water mass and the output signal was fixed. An external processor processes the signals to an analog (0-1V) or digital (I^2C) output signal (Figure 7).

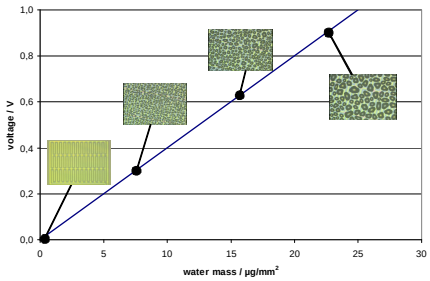

Figure 7. Calibration curve

The calibration of temperature is realised by comparison with resistance thermometer as reference in thermostat bath in dipping process.

B. *Test results in automobiles*

Different automobile suppliers have measured the condensation on different printed circuit boards at several places in an automobile and under different climatic conditions by means of the condensation sensor.

Figure 8. Sensor module on HIFI control unit (picture courtesy of BMW Group München)

One of the last tests was carried out at BMW, for example. Mounting places chosen were the battery in the right-side tray, the transmission tunnel on the airbag sensor, the fuse box on the passenger side, the vehicle battery, the data acquisition, and the HIFI control unit in the rear trunk. Sensor modules are used to measure condensation and temperature as well as relative humidity and temperature. Figure 8 shows the sensor modules placed on the HIFI control unit.

C. *Tests in climate chambers*

Based on the results in the automobile, comparable conditions were simulated in climate test chambers. With the standard ISO/DIS 16750-4 a temperature and humidity profile was defined to generate a dewing effect such as in an automobile environment (Figure 9) [14].

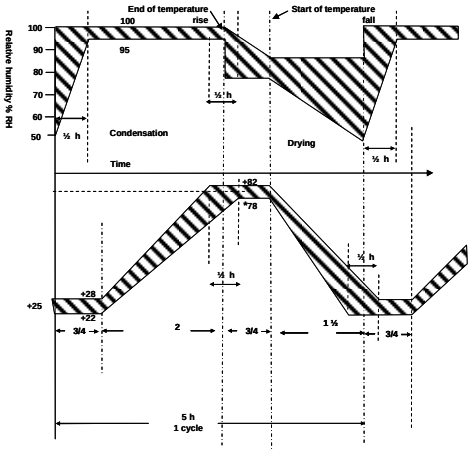

Figure 9. Dewing test cycle according to ISO/DIS 16750-4

With the condensation sensor mounted on the surface to be detected, statements can be taken about the real micro climate at the boundary layer during the test cycle (Figure 10).

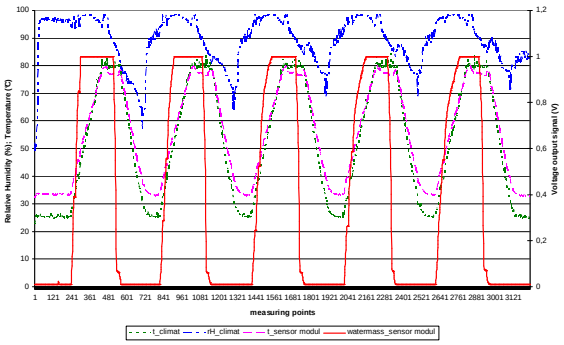

Figure 10. Measurement of condensation (watermass_sensor modul) and temperature (t_sensor modul) during the dewing test cycle in climate chamber (t_climate, rH_ climate)

The measured values in Figure 10 confirm that during the cycle time of 3 h the surface temperature has increased from 25 °C up to 80 °C and a condensate of 15 µg/mm2 has formed on the board.

 ISBN: 978-1-61208-145-8

V. CONCLUSION

In the paper a miniaturized sensor system has been described. The sensor system allows first time quantitative measurement of condensate mass and temperature with calibrated output signals. The system is suitable for field measurement. Tests in climate chambers and in automobiles are presented.

This sensor system is a tool for reliability tests and to support R&D and production of highly integrated printed circuit boards.

REFERENCES

[1] AMA-Studie Sensor-Trends 2014, AMA Fachverband für Sensorik e.V., Berlin, April 2010

[2] Roland Wernecke, Industrielle Feuchtemesstechnik, Wiley-VCH Verlag

[3] Steinke, A. et al.: Improved Reliability Tests for Electric Components by Innovative Micro Condensation Sensors. In Gessner T. (HRSG.): SMART SYSTEMS INTEGRATION 2007, Berlin Offenbach: VDE Verlag, 2007, S. 329-332.

[4] Suppa, M.: Prüf- und Teststrategie Schutzlacke und Lötpasten und Prozesse, 4. DVS/GMM-Fachtagung, 13.-14.02.2008, Fellbach

[5] Schimpf, C.; Feldmann, K.; Matzner, C.; and Steinke, A.: Failure of Electronic Devices due to Condensation, MicroNanoReliability 2007, September 2nd-5th, 2007, Berlin

[6] Scherl, R.: Klimasicheres Design elektrischer und elektronischer Baugruppen; GfKORR- Jahrestagung "Beschichtungssysteme zum Schutz elektronischer Baugruppen; 9.-10.11.2010

[7] Franke, J.; and Matzner, C.: Einfluss von Schadgasen auf die Klimabeständigkeit elektronischer Baugruppen; 2. Landshuter Symposium Mikrosystemtechnik, 18.02.2010

[8] ESPEC Technology Report 1997, No. 4

[9] March, B.; Matzner, C.; Schimpf, C.; and Steinke, A.: Ausfallverhalten elektronischer Baugruppen unter Betauungseinfluss; EBL 2008, Fachtagung: Elektronische Baugruppen und Leiterplatten; 13.–14. 02.2008, Fellbach

[10] Thierauf, J.: Klima- und Betauungstests in der BMW Group für Baugruppen; Tagungsband Kongress SMT & Hybrid 2008, Nürnberg

[11] Technology offer; aFoBt Sensor; PROvendis GmbH, Mühlheim/Ruhr, www.provendis.info

[12] Wieduwilt, T.; Schwotzer, G.; and Böhm, A.: Neuartiger optischer Taupunktsensor, DGaO-Proceedings 2007-ISSN:1614-8436

[13] Cäsar, J.: Betauungssensoren Theorie und praktische Erfahrungen; 32. Jahrestagung der GUS, 26.-28.03.2003, Pfinztal

[14] DIN ISO/DIS 16750-4

 ISBN: 978-1-61208-145-8

Silver Gate Field Effect Transistor for Oxygen Gas Sensor

Keiji Tsukada, Daisuke Kiriake, Kenji Sakai, Toshihiko Kiwa
Graduate School of Natural Science and Technology, Okayama University
Okayama, Japan
tsukada@cc.okayama-u.ac.jp

***Abstract*— A silver gate field effect transistor (FET) integrated thermal controller was developed for a new type of oxygen gas sensor. It showed a threshold voltage change at a temperature as low as 80˚C. Oxygen response characteristics of the FET prepared with different productions of silver materials using a vacuum-evaporated membrane, printed material using silver-nanoparticles and silver epoxy were compared. The FET with a gate of silver epoxy showed the largest sensitivity of 135 mV/decade in the oxygen concentration range from 5% to 40% at 120˚C.**

Keywords-FET; oxygen gas; silver gate

I. INTRODUCTION

The oxygen gas sensor is one of the most commonly used chemical sensors. There are many types of sensor such as potentiometric, resistive, amperometric and optic sensors. Miniaturization and mass-production are desired for sensor devices, especially in multipoint measurement such as in sensor networks. A solid-state sensor is suitable for such demands. At present, oxygen sensors based on yttria-stabilized zirconia (YSZ) electrolytes as solid-state are being successfully utilized for automobile and industry monitoring. An oxygen sensor with YSZ is suitable for high temperature conditions such as in automobile exhausts and furnaces. On the other hand, it is limited to low temperature operation lower than 500˚C because the resistivity of YSZ is too high at low temperatures. Recently, solid-state oxygen sensors operable at low temperature have been reported. For example, a ZnO nanowire-based sensor [1] and platinum-doped In_2O_3 nanocrystals [2] operable at room temperature showed resistance change to oxygen. One of the authors reported a field effect transistor (FET) type oxygen sensor operable at room temperature, and the FET-type sensor showed a sensitivity of 6 mV/decade to oxygen partial pressure [3]. The FET-type sensor has a gate of about 10-nm-thick platinum/ YSZ layer deposited on the gate insulator of FET. The interface between the YSZ layer and the Pt layer was an active site for oxygen dissociation. However, it was very difficult to optimize the gate structure because the interface of gas-Pt-YSZ had to exist on the gate surface. Silver is an oxygen selective material and acts as a catalyst to oxygen; therefore gas diffusion electrodes with silver catalysts have been investigated for fuel cells, batteries, etc [4]. In this study, we applied silver as the gate material for the FET-type gas sensor.

II. EXPERIMENTAL

The developed FET has a gate structure of upper silver material as the oxygen sensitive layer, and double insulator layers of a 125-nm-thick Si_3N_4 and a 43-nm-thick SiO_2 (Fig. 1), which are based on a similar structure to that of the previous reported hydrogen sensor [5]. The FET is an n-channel type FET with a channel 40 μm long and 390 μm wide. To investigate the optimization of the silver gate, three types of fabrication method were compared. One is a thin film that was fabricated by vacuum evaporation. The second material was fabricated using silver-nanoparticles. The FET insulator gate was coated with the silver-nanoparticles ink (nanometal ink L-Ag, ULVAC), and then baked at 120˚C. The third material was silver epoxy (CircuitWorks®), which was fabricated by a printing mixture of epoxy and hardener, and then cured at room temperature. To control the temperature of the Ag-gate FET sensor, a temperature sensor using a p-n junction diode and a heater using Ti/Ni/Au resistance were integrated into the same chip. To measure the oxygen response, voltage follower circuits were used to determine the threshold voltage change of the FET. The voltage follower circuits worked to maintain the constant drain-source voltage and current of the FET. To maintain the constant gate voltage, the Ag-gate was connected to the electrode. This circuit configuration operated such that the output voltage change of the circuit was the same as the work-function change of the silver. The work-function change was equal to the threshold voltage change of the FET. Sample gases with different oxygen concentration were prepared by a gas mixture using oxygen and nitrogen gases. The gas sensor was installed in a flow-through cell, and sample gas was flowed into the cell at a flow rate of 0.5 l/min.

III. RESULTS AND DISCUSSION

The oxygen gas response of the developed sensor was evaluated by the gas flow system. To control oxygen concentrations, pure oxygen and nitrogen gas were mixed. First, the sensor reproducibility as a function of oxygen concentration ranging from 10% to 20% was studied at 100˚C (Fig. 2). The oxygen sensor with silver epoxy showed the largest sensitivity and best stability. In contrast, the sensor with silver nanoparticles showed poor response. The sensitivity of the FET with silver epoxy was 50 mV/decade, and it was larger than the Nernstian response

 ISBN: 978-1-61208-145-8

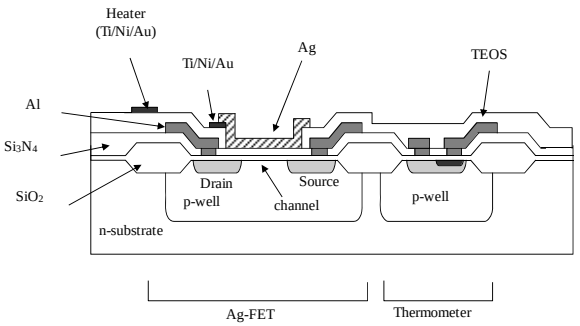

Figure 1. Schematic diagram of the structure of the integrated silver-gate FET with thermal control.

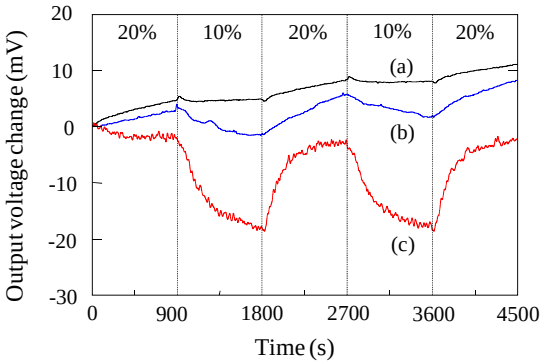

Figure 2. Comparison of oxygen response characteristics of the FET-type sensor using different silver membranes at 100˚C: (a) silver nanoparticle membrane, (b) silver vacuum evaporation membrane, (c) silver epoxy membrane.

sensitivity (19 mV/decade at 100˚C) based on the equilibrium reaction as below.

$$\frac{1}{2}O_2 + 2e^- \leftrightarrow O^{2-} \quad (1)$$

If the reaction occurs at the membrane surface, the silver membrane potential changes according to the Nernst equation below:

$$\emptyset_m = \text{const} - \left(\frac{RT}{4F}\right) \ln P_{O_2} \quad (2)$$

where ϕ_m is the membrane potential, F is Faraday's constant, R is the gas constant, T is absolute temperature, and P_{O2} is the partial pressure of oxygen. The sensitivity of the sensor with the silver vacuum evaporation was 20 mV/decade, and it was nearly equal to the Nernstian response.

To investigate the response difference, membrane structures were observed by scanning electron microscopy (Fig. 3). The silver vacuum evaporation membrane showed a very smooth surface whereas the silver nanoparticle membrane showed a crushed surface. This was due to the poor adherence to the Si3N4 gate insulator, and therefore it showed the lowest response. The silver epoxy membrane showed a porous and rough surface. This created the largest surface, so active sites of the silver membrane were considered to be rich. The silver vacuum evaporation membrane had a very smooth surface, where it was assumed that the smooth surface created the monolayer reaction at the activated site on the membrane, and then the membrane potential was described by the Nernst equation. On the other hand, the sensor with the silver epoxy had a porous and rough surface, and it created the multilayer of the dissociated oxygen inside the gate membrane. The higher sensitivity was considered due to the dissociated oxygen diffusion inside the silver gate.

The oxygen response was obtained over 80˚C, and sensitivity was increased according to the temperature increment (Fig.4). It was not linear. According to the temperature increment, activation energy increased and then oxygen dissociation reaction was accelerated. The oxygen response to a wider oxygen range from 5% to 40% was investigated. The sensor showed a linear response to

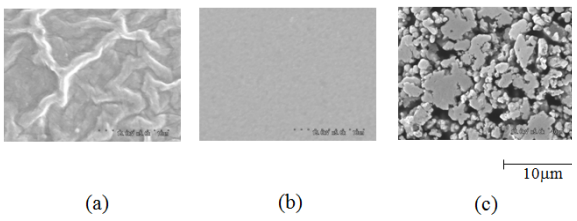

Figure 3. SEM images of the silver membrane: (a) silver nanoparticle membrane, (b) silver vacuum evaporation membrane, (c) silver epoxy membrane.

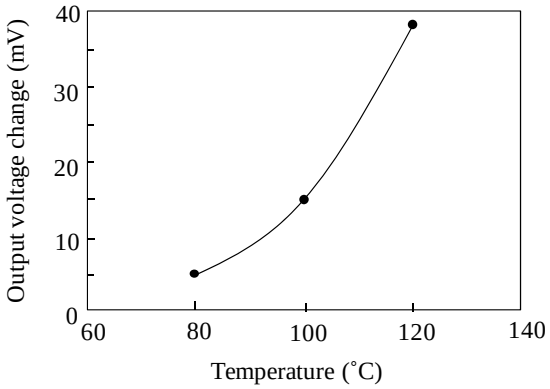

Figure 4. Temperature dependence of the sensitivity of FET-type oxygen sensor with silver epoxy gate.

 ISBN: 978-1-61208-145-8

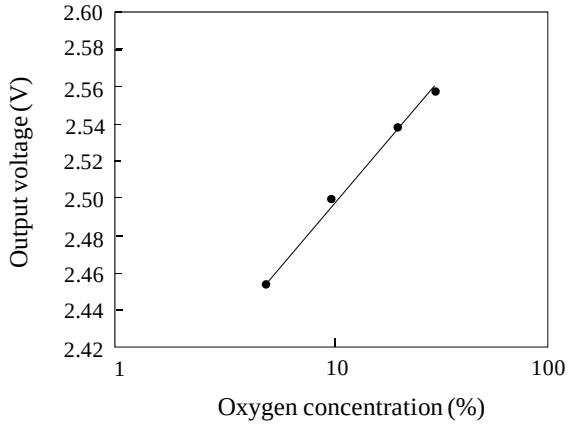

Figure 5. Calibration curve of the FET-type oxygen sensor at 120˚C.

logarithmic oxygen concentration, and it was 135 mV/decade at 120˚C (Fig. 5).

In this study, we proposed a new oxygen sensor for the silver-gate FET. The silver-gate FET using silver epoxy showed the largest sensitivity compared with other silver membranes. This was considered due to the sterically-congested dissociated oxygen at the silver membrane.

REFERENCES

[1] C. Lu, S. Chang, S. Chang, et al., “ZnO nanowire-based oxygen gas sensor”, IEEE Sensors Journal, vol. 9, pp. 485-489, 2009

[2] G. Neri, A. Bonavita, G. Micali et al., “A highly sensitive oxygen sensor operating at room temperature based on platinum-doped In2O3 nanocrystals”, Chemical Communications, pp.6032-6034, 2005

[3] Y. Miyahara, K. Tsukada, H. Miyagi, “Field-effect transistor using a solid electrolyte as a new oxygen sensor”, Journal of Applied Physics, vol. 63, pp. 2431-2434, 1988

[4] E. Gulzow, N. Wagner, M. Schulze, “Preparation of gas diffusion electrodes with silver catalysts for alkaline fuel cells”, Fuel Cells, vol. 3, pp. 67-72, 2003

[5] K. Tsukada, Masatoshi Kariya, Tomiharu Yamaguchi, et al., “Dual-gate field-effect transistor hydrogen gas sensor with thermal compensation”, Japanese Journal of Applied Physics, vol. 49, pp. 024206-024206-5, 2010.

 ISBN: 978-1-61208-145-8

Dynamic Calibration of Force Transducers Using Sinusoidal Excitations

Christian Schlegel, Gabriela Kiekenap, Bernd Glöckner, Rolf Kumme
Physikalisch-Technische Bundesanstalt, Bundesallee 100
D-38116 Braunschweig, Germany
e-mail: Christian.Schlegel@ptb.de
Gabriela.Kiekenap@ptb.de
Bernd.Gloeckner@ptb.de
Rolf.Kumme@ptb.de

Abstract— **The primary calibration of force transducers using sinusoidal excitations with electrodynamic shaker systems will be described. First a view comment concerning the importance of dynamic force measurements will be given. That will be followed by a mathematical description of the basics of dynamic measurements based on linear differential equations. Some useful approximations are given to average measured data. The technical equipment will be introduced together with a discussion concerning the traceability as well as the uncertainty consideration. Finally an exemplary calibration performed on a strain gage transducer will be presented.**

Keywords: dynamic force, force calibration, laser vibrometer, acceleration measurement

I. INTRODUCTION

In the last few decades very precise static force measurements were developed and are now routinely used for calibration services in many national metrology institutes (NMI's) around the world. The force scale which is covered nowadays reaches from µN-MN [1-2]. Thereby, relative measurement uncertainties down to $2 \cdot 10^{-5}$ are obtained using deadweight machines, which are the best standard to realize a traceable force. The force, F, is just the product of the SI base unit mass, m, and the gravitational acceleration, g, following Newton's law, $F=m \cdot a$, with the acceleration, $a=g$.

Besides the precise realization of a force in a standard machine, there must be selected force transducer available which can be used as a transfer standard to give the primary calibration to the secondarily calibration laboratories and industry. The crucial fact is now that often these static calibrated force transducers are used in dynamic applications. That is the reason why more and more NMI's have established procedures for a dynamic calibration of force transducers and also other sensors.

Currently in the European Metrology Research Programme (EMRP) one promoted research topic is the: "Traceable Dynamic Measurement of Mechanical Quantities", which includes, apart from a work package about dynamic force, also work packages about dynamic pressure, dynamic torque, the electrical characterization of measuring amplifiers and mathematical and statistical methods and modelling [3].

Similar to the static calibration philosophy primary calibrations have to be provided which guarantee traceability to the SI base units and also transfer transducers (reference standards) to transfer these calibrations e.g. to an industrial application. This transfer turned out to be the most complicated task because of the crucial influence of environmental conditions present in certain applications. Mostly the transducers are clamped from both sides which lead to sensitivity losses due to the dynamics of these connections which are more or less not infinitely stiff. On the other hand the resonant frequency often shifts down to lower frequencies which can also drastically change the sensitivity. The problem can be solved to a certain extent by modelling the whole construction including all relevant parameters. For that reason it is also important to determine the force transducer parameters like stiffness and damping which can be obtained during a dynamic calibration. This article describes one possibility for a primary dynamic force calibration using sinusoidal excitations. The whole procedure as well as most of the set-ups where developed over two decades and are extensively described in [4]. Other methods as well as analysis procedures for dynamic force calibration are described in [5-9].

 ISBN: 978-1-61208-145-8

II. MATHEMATICAL DESCRIPTION

To obtain an analytical "handle" for the description of the dynamic behaviour of a dynamically excited force transducer, the well-known spring-mass-damper model can be applied. In figure 1 one can see a simplified picture of a force transducer which is equipped with a test mass, m_t. The connection of that mass to the transducer is modelled by a certain stiffness, k_c, and a damping constant, b_c. The transducer itself consists of a bottom mass, m_b, and a head mass, m_i. Both masses are also connected by a spring with stiffness, k_f, and a corresponding dumping constant, b_f. The coordinates in space of all three masses are then given by the vector (x_t, x_i, x_b), if only a vertical movement is considered. A periodical force acts from the bottom on the mass, m_b, (see Fig.1). This force is generated by an electrodynamic shaker system. The acceleration of the top mass, $\ddot{x}_t$, the acceleration on the shaker table, $\ddot{x}_b$, and the force transducer electrical signal are measured during the calibration procedure. This transducer signal is directly proportional to the material tension/compression and can be described in the model by the difference of the spring coordinates x_i-x_b .

The system depicted in figure 1 can be finally modelled by the following system of linear differential equations with constant coefficients:

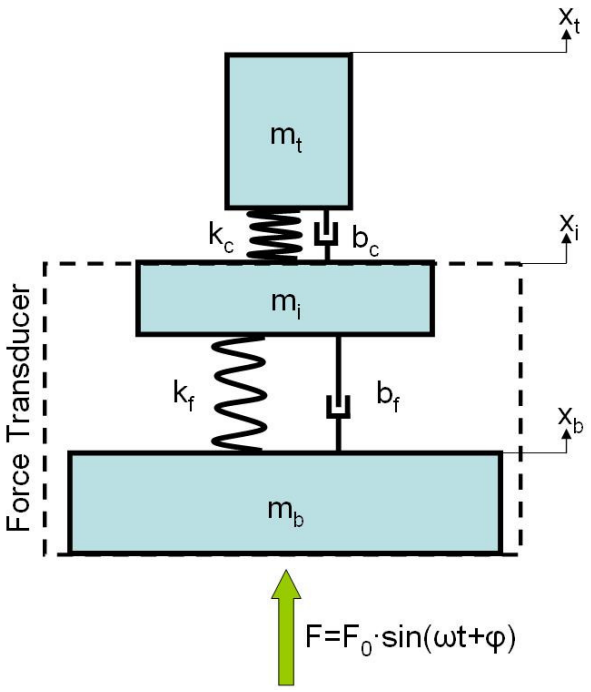

Figure 1. Schematic model of a force transducer equipped with a top mass. The transducer itself can be seen as a spring-mass-damper, which consists of two masses connected by a spring. The adaptation of the test mass is also modelled by a damped spring, whose stiffness is mostly much stronger than that of the transducer.

$$\begin{aligned} m_t\ddot{x}_t &= -k_c(x_t - x_i) - b_c(\dot{x}_t - \dot{x}_i) \\ m_i\ddot{x}_i &= k_c(x_t - x_i) + b_c(\dot{x}_t - \dot{x}_i) - k_f(x_i - x_b) - b_f(\dot{x}_i - \dot{x}_b) \\ m_b\ddot{x}_b &= k_f(x_i - x_b) + b_f(\dot{x}_i - \dot{x}_b) + F \end{aligned} \tag{1}$$

It should be noted that the system can be simplified if the coupling of the top mass has practically no influence on the dynamic process. This would correspond to the special case, $k_c \rightarrow \infty$, $b_c \rightarrow 0$, and the top mass as well as the head mass of the transducer can be summarized as one mass body. In the calibration process the dynamic sensitivity, which is the ratio between the measured force transducer signal and the acting dynamic force, is measured as follows.

$$\left|\frac{x_i - x_b}{x_t}\right| = \frac{m_t + m_i}{k_f} \cdot \sqrt{\frac{1 - 2\omega^2 \frac{\mu}{k_c}\left(1 - \frac{b_c^2}{2\mu k_c}\right) + \left(\omega^2 \frac{\mu}{k_c}\right)}{\left(1 + \left(\omega\frac{b_f}{k_f}\right)^2\right) \cdot \left(1 + \left(\omega\frac{b_c}{k_c}\right)^2\right)^2}} \tag{2}$$

In equation 2 the reduced mass $\mu=(m_t \cdot m_i)/(m_t+m_i)$ was introduced. This equation can be drastically simplified if the top mass coupling is neglected and one applies a Taylor series development of the second order for the frequency ω:

$$\left|\frac{x_i - x_b}{x_t}\right| \approx \frac{m_t + m_i}{k_f} \cdot \left(1 - \frac{b_f}{k_f}\omega^2\right) = p_1 \cdot \left(1 - p_2 \cdot \omega^2\right) \tag{3}$$

This equation is very convenient for fitting purposes to approximate the measured sensitivities just by the two parameters, p_1 and p_2.

The measured sensitivity is calculated from the ratio of the transducer signal, U_f, and the acting dynamic force:

$$S_f = \frac{U_f}{(m_t + m_i) \cdot \ddot{x}_t \cdot K_{corr}} \approx S_{f0} \cdot (1 - p\omega^2) \tag{4}$$

The parameter, K_{corr}, takes into account the vertical acceleration gradient over the mass body. Finite element simulations have shown that the individual mass points of the mass body have slightly different accelerations in the vertical direction [4]. This correction factor can be neglected, if quite small masses are used (only a few

 ISBN: 978-1-61208-145-8

centimetres in height). The factor S_{f0} is the static sensitivity obtained for the limiting case ω=0, whereby p=p_1. As one can see from approximation (4), the sensitivity drops down quadratically with increasing the frequency ω.

Besides the amplitude of the sensitivity according to equation (4), also the phase shift between the acceleration x_t and the force signal U_f can be derived by the model:

$$\varphi(\omega) = \tan^{-1}\left[-\frac{b_f}{k_f}\omega\cdot\left(\frac{1+\omega^2\cdot f_1(1/k_c, b_f, \mu)}{1+\omega^4\cdot f_2(1/k_c, b_f, \mu)+\omega^2\cdot f_3(1/k_c, b_f, \mu)}\right)\right]$$

$$\varphi(\omega) \approx \tan^{-1}\left(-\frac{b_f}{k_f}\omega\right) \approx -\frac{b_f}{k_f}\omega \qquad (5)$$

The quite complicated equation (5) contains functions f_1-f_3 which are all proportional to $1/k_c$, so that these terms can be neglected for the limiting case of infinite coupling stiffness of the top mass. In addition the arcus-tangent function can be approximated by a Taylor series of the first order for the frequency ω, which leads to a linear phase shift between the acceleration- and force transducer signal.

III. MEASUREMENT SET-UP

The essential prerequisites for a primary sinusoidal force calibration are seen in figure 2. First of all one needs an exciter. At PTB we have three electromagnetic shaker systems, a small one for forces up to 100 N and 10 Hz until 2 kHz, a medium one up to 800 N for 10 Hz till 3 kHz and a large shaker up to forces of 10 kN and frequencies of 10 Hz to 2 kHz. The shakers consist of two parts, the vibration exciter itself and a power amplifier. The kind of excitation is determined by the chosen signal created by a function generator. This signal directly modulates the current signal which drives the coil of the shaker armature.The acceleration of the top mass can be measured principally in two different ways, either by a primary method using a laser Doppler vibrometer or by accelerometers.

Usually the vibrometer is used, which consists of a laser head providing a 632.8 nm red laser beam and a certain controller. There are two kinds of laser heads, one with a fixed beam and the other one with a scanning opportunity. The scanning vibrometer is able to scan surfaces in an angle region of ±25° in the x- and y- directions. This offers the

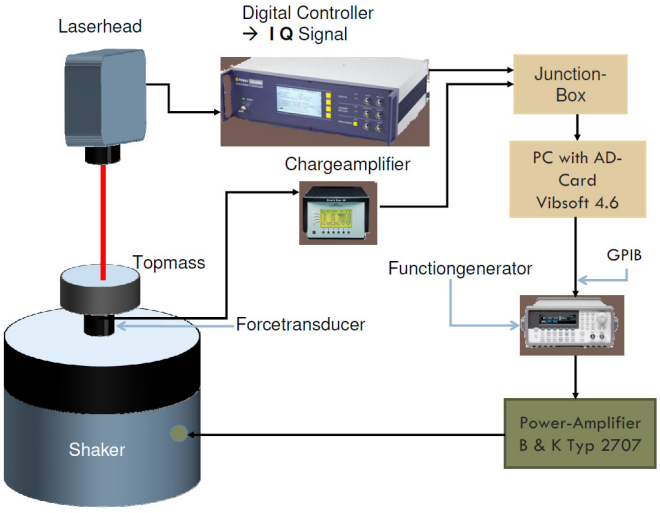

Figure 2. Schematic measurement set-up for the sinusoidal force calibration

possibility to investigate surface vibrations. The modular controller consists of different digital processing units, two velocity decoders, a displacement decoder and a digital quadrature decoder. In summary a frequency range from 0-2.5 MHz with a maximum velocity of 10 m/s and a resolution of 0.02 µm/s can be realized. The signal processing inside the decoders is fully digital, the output is provided as an analogue signal. For precise calibrations the digital quadrature encoder is used in connection with certain software which calculates the displacement according to the arcus-tangent procedure. The analogue IQ output signals are bundled together with the transducer output signal and the acceleration signal from the shaker armature in a junction box which is then cabled to a 5 MHz PC sampling card.

IV. TRACEABILITY AND UNCERTAINTY CONSIDERATION

The sinusoidal calibration of force transducers is a primary calibration method which means that all measured quantities are traceable to the SI base units and all measuring equipment used is calibrated using certain standards, which are well established procedures. The calibration of the weights used as top masses is done according to the international recommendation OIML R 111-1 [10]. According to this document the top masses can be classified at least as Class M_1, which leads to a maximum error for a 1 kg weight of 50 mg or a relative standard measurement uncertainty of $5\cdot10^{-5}$. Apart from the mass determination, the acceleration measurement is the most important part of the calibration. In figure 3 the traceability chains are shown for different ways

 ISBN: 978-1-61208-145-8

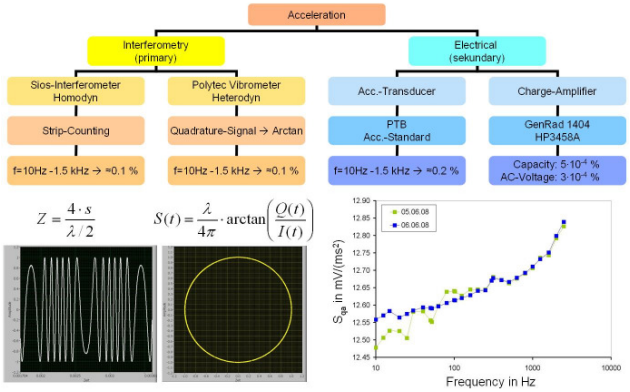

Figure 3. The traceability chains of the acceleration measurement are shown for a primary and secondary method. Left hand side shows the primary method using laser interferometers/vibrometers, the right hand side show the traceability using accelerometers with certain conditioning amplifiers.

of acceleration measurement. There are, in principle, two ways, the primary method using interferometers/vibrometers and the secondary method based on a certain electrical chain. The vibrometer measurement can differ according to the involved overlap of certain laser beams in the homodyne or heterodyne interferometers. Both instruments are based on modified Mach-Zehnder interferometers. In the heterodyne interferometer, the measuring laser beam is spitted whereby one part is additionally mixed with a high frequency using a Bragg cell, usually 40 MHz, to provide the Doppler encoding. The homodyne interferometers are used for larger displacements which can be determined by counting the interference maxima, which is also known as the fringe counting method. The displacement is, thereby, only a function of the laser wave length and the number of fringes. Fringe counting can be performed with very precise instruments, like the high performance counter Fluke PM6681. According to the fringe counting equation, see figure 3, the uncertainty is very small. The relative counting error of the Fluke counter is at 1 kHz, ΔCounts/Counts $\approx 5 \cdot 10^{-8}$ and the relative wavelength error is in the order of $\Delta\lambda/\lambda \approx 10^{-6}$. The main error is made if the displacement comes in the order of $\lambda/2$, because this is the resolution limit of the fringe counting. Keeping in mind a lower limit for the displacement of 400 µm, one can obtain uncertainties of 0.1% in the range from 10 Hz to 1.5 kHz.

As mentioned above, the heterodyne technique is based on the arcus-tangent calculation of the quadrature signal. If one plots the IQ measuring points in a 2 dimensional grid, as seen in figure 3, one obtains a circle in the most perfect case. The fully digital quadrature encoding avoids all errors made in former times by analogue filters and mixing devices. By default the whole electrical chain of the vibrometer controller is calibrated by the manufacturer through coupling of very precise known artificial displacement signals directly in the controller. These measurements result in uncertainties which are below 0.1% [11]. On the other hand, the vibrometer used for the sinusoidal force calibration was calibrated against the national acceleration standard. Thereby, the acceleration values obtained by the measuring program had deviations from the standard set-up of 0.02-0.04%. With a clear conscience one can obtain an uncertainty at least of 0.1% for the frequency range of 10Hz-1.5 kHz with the heterodyne method.

The right-hand side of figure 3 shows the conventional method of acceleration measurement using accelerometers in combination with certain conditioning amplifiers. Normally a charge amplifier is used which can be calibrated with a very precise reference capacity and a high accurate voltmeter. The relative standard measurement uncertainty of both devices is a few 10^{-4} % according to the calibration certificate which was obtained by a standard calibration procedure at PTB. For the use in a calibration set-up, one has to consider the whole measuring chain consisting of the accelerometer and its conditioning amplifier. The measuring chain can be included by a calibrated sensitivity factor, S_{qa}, which commonly has an uncertainty around 0.2 %, as illustrated by example in figure 3. According to the charge amplifier calibration for the accelerometer measuring chain also the force transducer can be handled, if a piezoelectric transducer is used.

For the case of transducers based on the strain gage technique, a special calibration device, also called bridge standard, was developed [4]. The bridge standard simulates, in principle, a force transducer and is based on a Wheatstone bridge whose bridge voltage is, as in the real case, provided by the amplifier. In place of a force transducer the bridge standard is connected to the conditioning amplifier. The output to the amplifier is a dynamic bridge detuning which can be steered through an analogue input signal from an arbitrary function generator with voltage amplitudes. Inside the device the input signal is transformed to a mV voltage. The signal which is seen from the amplifier can be measured in addition on an auxiliary output channel.

The total (combined) measurement uncertainty, u_c, of the sinusoidal calibration can then be separated into two main parts, a set-up dependent part, u_s and a part which is obtained by the actual calibration measurement, u_m:

$$u_c = \sqrt{u_s^2 + u_m^2} \cdot$$

The part, u_s, is, in principle, a constant given for a certain set up and reflects the smallest achievable measurement uncertainty. This part depends - according to equation 4 on three parts, the uncertainty of the acceleration measurement, the uncertainty of the conditioning amplifier calibration and the uncertainty of the mass determination. Note that the

 ISBN: 978-1-61208-145-8

Modell Equation:

$S = (U/V)/(m \cdot a)$

S: Sensitivity, *U:* Conditioning amplifier voltage, *V:* Amplification factor, *m:* Topmass, *a:* Acceleration

Uncertainty-Budget:

Quantity	Value	Standard measurment uncertainty	Degree of freedom	Sensitivity coefficient	Uncertainty contribution	Index
U	205.0 mV	0.00488 %	50	$400 \cdot 10^{-9}$	$4.0 \cdot 10^{-9}$ mV/N	0.3 %
V	2500.0	$8.00 \cdot 10^{-6}$ %	50	$-33 \cdot 10^{-9}$	$-6.6 \cdot 10^{-12}$ mV/N	0.0 %
M	10.0 kg	0.0500 %	50	$-8.2 \cdot 10^{-6}$	$-41 \cdot 10^{-9}$ mV/N	30.7 %
a	100.0 m/s²	0.0750 %	50	$-820 \cdot 10^{-9}$	$-62 \cdot 10^{-9}$ mV/N	69.0 %
S	$82.0 \cdot 10^{-6}$ mV/N	0.0903 %	87			

Result:

Sensitivity-Value: $82.00 \cdot 10^{-6}$ mV/N
Relative expanded measurement uncertainty: ±0.18 %
Expansion Factor: 2.0
Coverage: t-Table 95%

Figure 4. There is shown an example of the standard uncertainty evaluation, u_s, of the dynamic sensitivity at a frequency of 400 Hz. The calculation was done according the "Guide to the expression of uncertainty in measurement", GUM [12].

uncertainty of the head mass, m_i, of the transducer is not included in this part, because this mass has to be determined with the aid of the actual measurement. According to the numbers for the certain uncertainties given above, this part results in an uncertainty contribution of 0.1-0.25 %. Figure 4 shows as an example the uncertainty evaluation for u_s which is obtained at 400 Hz.

The part, u_m, includes the uncertainty of the internal mass determination and depends further mainly on the standard deviations of the performed measured sensitivity points. By using the scanning vibrometer for the acceleration measurement on the top mass one can measure up to 100 points, depending on the actual geometry of the weight. Through this opportunity special disturbing influences like rocking modes or mechanical adaptation influences of the transducer can be taken into account. It should be noted that these influences contribute more than other errors made, by e.g., the sine approximation of the measured data or the uncertainties caused by special filter techniques applied in the analysis procedure.

Experience has shown that the uncertainty part, u_m, is on average below 1 kHz between 0.4-1% and above 1 kHz around 1-2%.

V. MEASUREMENT EXAMPLE

Figure 5 illustrates the output of a special calibration. In this case a 25 kN force transducer based on the strain gage technique was measured with five top masses as seen in the upper panel of figure 4. As seen from the sensitivity plot, all masses are in good agreement below a frequency of 1 kHz.

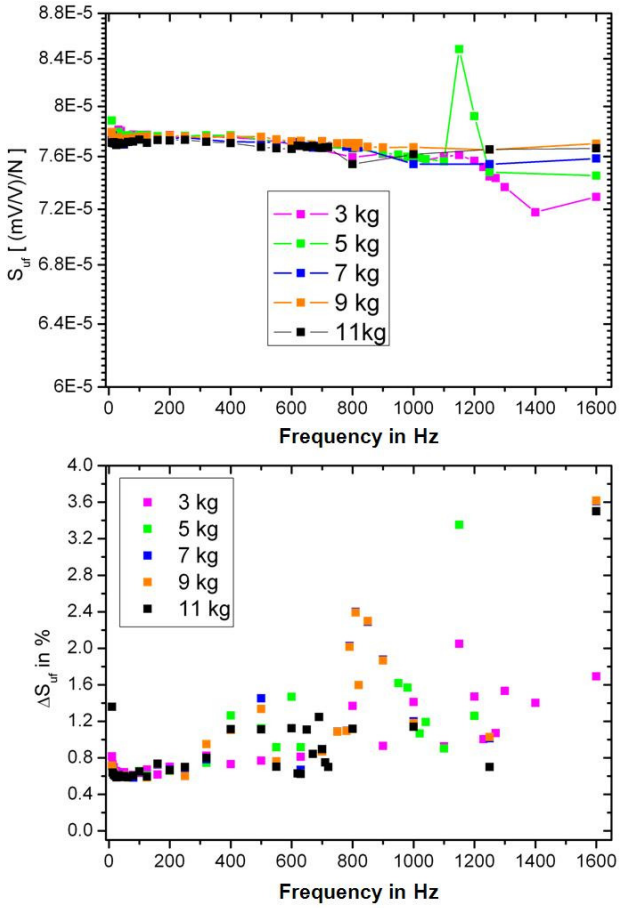

Figure 5: Dynamic sensitivity, upper panel, of a 25 kN strain gage force transducer measured by five top masses. The lower panel shows the uncertainties of the individual measuring points.

This is also confirmed by the combined relative standard measurement uncertainty, given in %, which can be seen in the the lower panel of figure 5. The different top masses cause different resonance frequencies which lay in the range of 700-1400 Hz. Measuring points near the resonance and also beyond naturally have a bigger uncertainty.

To acquire a figure of merit, all the sensitivity curves obtained with the different top masses can be fitted with a function according to equation 4 and the mean value for the obtained parameters can be calculated. Including the uncertainties of the individual points in the fit procedure moreover, leads to a realistic error also for the fit parameters. The averaged fit results, together with the obtained uncertainty range are shown in figure 6. The sensitivity at frequency, f=0, was scaled to 100 % to illustrate the sensitivity drop as a function of frequency in an easy readable way. Thus, it can immediately be seen, that the transducer shows only 96% of its sensitivity at 1.6 kHz.

 ISBN: 978-1-61208-145-8

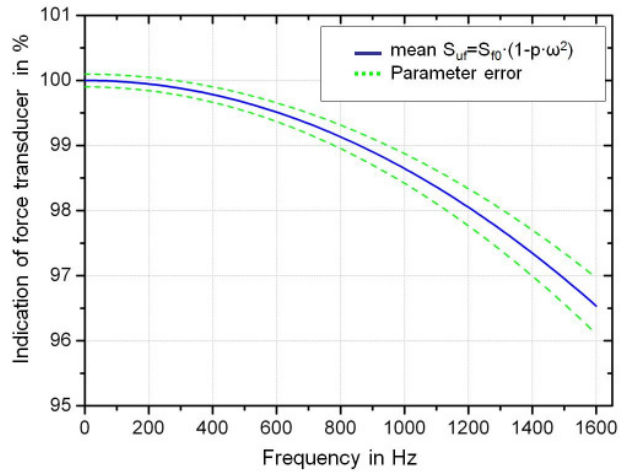

Figure 6: Averaged sensitivity according to the described fit procedure normalized at an indication of 100% given by the transducer at f=0 Hz.

VI. CONCLUSION

The traceable sinusoidal calibration of force transducers was demonstrated. The calibration mainly depends on the acceleration measurement and the calibration of the electrical chain of the conditioning amplifiers used. For the most accurate acceleration measurement, laser Doppler vibrometers can be used which are traced back to the laser wavelength. In the case of piezoelectric force transducers the charge amplifiers can be very precisely calibrated using a reference capacity and a primary calibrated multimeter. For strain gage transducers, a special calibration bridge standard was developed to dynamically calibrate voltage ratios.

In chapter IV it was shown that one can perform the calibration depending on the involved top masses with relative standard measurement uncertainties of ≈0.4-2.0%. The main uncertainty contributions are not caused by the set-up but rather by the mechanical influences like adaptations and the rocking modes of the transducer. These disturbing influences can be detected during a calibration measurement by applying additional sensors like, e.g., triaxial accelerometers. If a certain threshold of transverse acceleration is exceeded, e.g., caused by rocking modes or side resonances of the transducer, the corresponding data will be no further considered. In addition special adapters can be developed to suppress these effects.

REFERENCES

[1] F. Tegtmeier, R. Kumme, M. Seidel, “Improvement of the realization of forces between 2 MN and 5 MN at PTB – the new 5 MN force standard machine”, *XIX IMEKO World Congress*, pp. 186-191, Lisbon, 2009.

[2] Ch. Schlegel, O. Slanina, G. Haucke, R. Kumme, “Construction of a Standard Force Machine for the range of 100 µN – 200 mN”, IMEKO 2010, TC3, pp. 33-36, Pattaya, 2010.

[3] European Metrology Research Programme (EMRP), http://www.emrponline.eu, last access 23.05.2011.

[4] R. Kumme, “Investigation of a primary method for a dynamic calibration of force measuring instruments: a contribution to reduce the measuring uncertainty”, doctoral thesis (in German) , PTB, 1996.

[5] S. Eichstädt, C. Elster, T. J. Esward and J. P. Hessling, Deconvolution filters for the analysis of dynamic measurement processes: a tutorial, 2010, Metrologia, 47, 522-533.

[6] G. Wegener and Th. Bruns, Traceability of torque transducers under rotating and dynamic operating conditions, 2009, Measurement, 42, 1448-1453.

[7] M. Kobusch, Th. Bruns and E. Franke, Challenges in Practical Dynamic Calibration, 2009, Advanced mathematical and computational tools in metrology and testing: AMCTM VIII (2008 Paris France), edited by Franco Pavese, Series on Advances in Mathematics for Applied Sciences - Vol. 78, pp. 204-212, World Scientific Publishing, Singapore.

[8] C. Elster and A. Link, Uncertainty evaluation for dynamic measurements modelled by a linear time-invariant system, 2008, Metrologia, 45, 464-473.

[9] M. Kobusch, “The 250 kN primary shock force calibration device at PTB”, IMEKO 2010, Thailand, Pattaya, November 2010.

[10] International Recommendation, OIML R 111-1, International Organization of Legal Metrology, 2004.

[11] G. Siegmund, “Sources of Measurement Error in Laser Doppler Vibrometers and Proposal for Unified Specifications”, 8th. Int. Conf. on Vibration Measurements by Laser Techniques, Proc. of SPIE Vol. 70980Y, 2008.

[12] ISO/IEC Guide 98-3:2008: Uncertainty of measurement – Part3: Guide to the expression of uncertainty in measurement. ISO, Genf 2008, ISBN92-67-10188-9.

 ISBN: 978-1-61208-145-8

Detection of Ice Formation over a Road Surface

Amedeo Troiano
dept. Electronics
Politecnico di Torino
Torino, Italy
Email: amedeo.troiano@polito.it

Eros Pasero
dept. Electronics
Politecnico di Torino
Torino, Italy
Email: eros.pasero@polito.it

Luca Mesin
dept. Electronics
Politecnico di Torino
Torino, Italy
Email: luca.mesin@polito.it

***Abstract*—The reliable detection of ice over road surfaces is an important issue for reducing maintenance costs and improving traffic safety. An innovative capacitive sensor was developed to detect the presence of ice on its surface, and its repeatability, stability and reliability were assessed in simulations and experiments described in previous papers. The indications of the sensor are compared in this paper with the objective identification of ice formation or melting over a road surface in laboratory, under dynamic or stationary conditions. The sensor provides indications which are in line with the condition of the road surface, with a mean error in the identification of the time instants of ice-wet and wet-ice transitions lower than about 10 minutes, both under different temperature gradients or in stable conditions.**

***Keywords*-Capacitive sensor; ice detection; road and runway information system.**

I. INTRODUCTION

Detection of ice formation found important applications in different fields. For instance, an adequate assessment of the conditions of road surfaces may enhance traffic safety [1]; detection of ice on the surface of the runway of airports can improve safety during take off and landing of the aircrafts [2]; finally, the detection of presence of ice on walkways may prevent people falls.

Different technologies were developed to detect ice, depending on the application. Some techniques put directly the sensor in contact with the surface over which ice may form, others allow for a remote sensing. Different sensors were developed exploiting different physical principles, e.g. concerning vibration [3], electro-optics [4], fiber-optics [5], radio frequency [6], micro-mechanics [7], ultrasounds [8], and inductive [9] effects.

In order to detect ice formation on the surface of a road or a runway, embedding the sensors directly on the pavements is preferable. However, the previously indicated methods are not feasible for this application since they are not enough robust or they are based on indirect measurements. Thus, an innovative, low cost ice sensor was introduced in [10] to detect water and ice on exposed surfaces, based on a capacitance measurement. The sensor was investigated by simulations and experiments, both in laboratory [11] and in the field [12] [13].

Reliability and repeatability of the estimates were investigated in laboratory conditions by comparing the instants in which ice formation and melting were identified by different sensors [10]. The sensors provided indications close to each other, with a spread of the time instants in which a state transition was identified in the order of a few minutes. However, the surface of the sensor is flat and very different from that of the road, which is a rough surface due to the bitumen. Moreover, the sensor blocks percolation of water, which is very important in determining the road surface conditions. Thus, the icing and melting processes on the sensor and on the surface of a road may have a deviation, which is difficult to predict. In order to address this issue, some sensors were embedded in a road, with bitumen covering some of them [10] [12]. Nevertheless, the icing process over a bituminized sensor may be different from that of a road even if the two surfaces are the same, since percolation under them is different. Moreover, the indication of a bituminized sensor is still mediated by the sensor, so that it cannot be considered as an external reference. The METAR (METeorological Aerodrome Report) message of the Turin Airport was considered in [12] as an external, objective indication. Data were acquired for 10 months. Rain, fog, and snowfall events were highly correlated with the output of the sensors, but correlation with ice could not be assessed. In the same paper, the indications of the sensor were compared to those of a mathematical model of indirect ice prediction from meteorological data. Correlation was low and, trusting on the sensor indications, it was suggested that a precise prediction of ice formation should require an adaptive model which fits local weather data and ice formation on the specific road under consideration, instead of a simple general law. Thus, also the mathematical models proposed in the literature to relate meteorological variables to ice formation are not considered as reliable independent references to test the sensor.

This work is devoted to the objective of test our sensor: its indications are compared with the ice formation and melting over a road model identified by direct inspection.

 ISBN: 978-1-61208-145-8

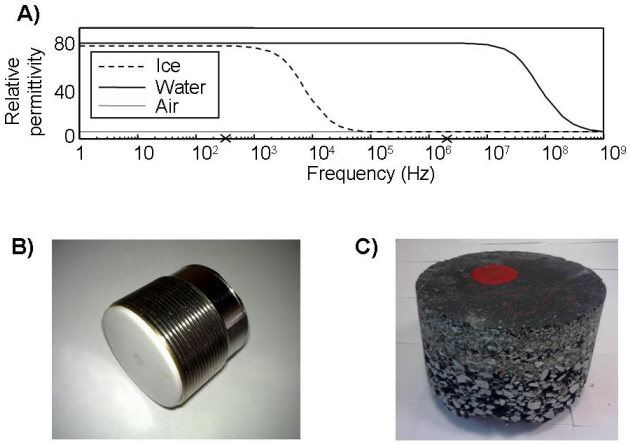

Figure 1. (A) Relative permittivity of air, water (at 25°C), and ice (at -10°C) as a function of frequency. (B) Picture of the ice sensor. (C) Picture of the road core.

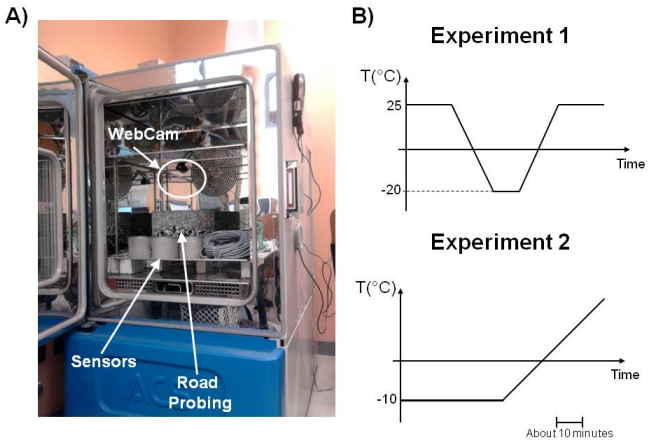

Figure 2. (A) Picture of the experimental setup. Sensors and road core placed in the climatic chamber, together with an USB webcam to acquire images. (B) Representation of the two experiments.

II. METHODS

The sensor described in [10] consists of a multi-frequency capacitance measurement system. The capacitance is related to the relative permittivity of the material placed over the sensor, which depends on temperature and measurement frequency [14]. On the other hand, it is worth noticing that it is not affected by contaminants (e.g. salt) present over the road [12]. Figure 1A shows the relation between the relative permittivity of air, water and ice, and the measurement frequency for specific values of temperature. Due to the variations of relative permittivity with frequency, it is possible to distinguish between water, ice and air by two capacitive measurements, at low (200Hz) and high (20MHz) frequency [10]. The capacitance is measured using a transfer charge circuit. The sensor is shown in Figure 1B.

The road model was obtained using a road core with diameter of 30 cm and thickness of 20 cm, shown in Figure 1C. It does not contain the sensor and is constituted by three layers, with asphalt and concrete with different granularity, allowing a good distribution of loads and a proper drain and filtration. The road core is a representation of the asphalt of the runways of the Turin-Caselle airport.

In order to compare the indication of presence of ice provided by the sensor with the ice formation and melting over a road, experimental tests were performed applying the same environmental conditions to three sensors and to the road core, and evaluating the dispersion of the time instants in which phase changes were detected. Experimental tests were executed inserting the sensors and the road core in a climatic chamber (Angelantoni - Challenge 250; temperature range for climatic test from -40°C to +180°C), as shown in Figure 2A. Sensors were connected to a data acquisition system via the RS485 communication protocol, for the collection of the data. At the top of the climatic chamber, an USB webcam (Logitech - QuickCam Pro 9000; operative temperature range from -20°C to +60°C) was inserted to acquire images from the road core in order to detect the formation of the ice over it. A PC was used to store images from the USB webcam and sensory data from the acquisition system using the RS232 protocol. Images and data were simultaneously acquired using a sampling frequency of 1 sample per minute.

Two different experimental tests were performed, the first imposing a linear gradient of temperature, the second leaving the climatic camber in static condition. Specifically, in the first test, the sensors and the road core were first introduced into the climatic chamber with a temperature of 25°C, for approximately 10 minutes in order to wait that the indications of the sensor became stationary. Then, 1 mm of tap water was placed over each sensor and at the center of the road core. Different temperature gradients were applied and the time instants in which the sensors identified ice formation and the road core surface froze were investigated. Specifically, the climatic chamber was arranged to reach -20°C with different temperature gradients equal to -0.25°C/min, -0.5°C/min, and -0.75°C/min. During this period, the water froze. Once reached the minimum temperature of -20°C, the climatic chamber kept stable conditions for approximately 10 minutes, and then it was arranged to reach 25°C with opposite temperature gradient. During this period, the ice melted. The climatic chamber kept the temperature of 25°C for approximately 10 minutes. Then, sensors and the road core were dried.

In the second test, sensors and road core were first placed in the climatic chamber. Then, the chamber was arranged to reach -10°C with a temperature gradient of -1°C/min. Once

 ISBN: 978-1-61208-145-8

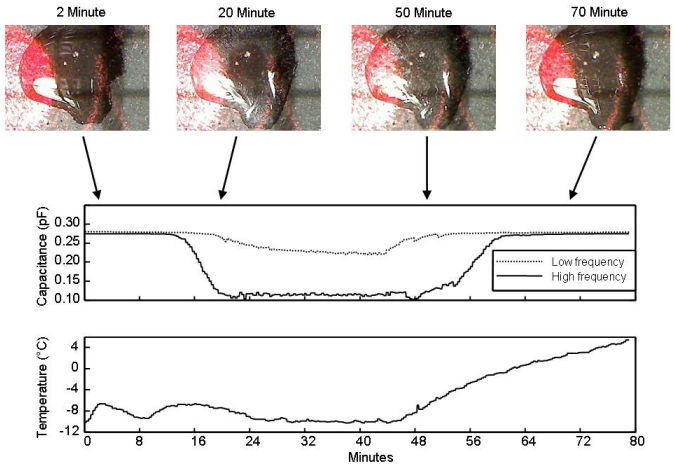

Figure 3. Example of data processing during the second type of experiment. Images captured by the camera are shown on the top. On the bottom, the values of sensor capacitance and the temperature of the climatic chamber are depicted.

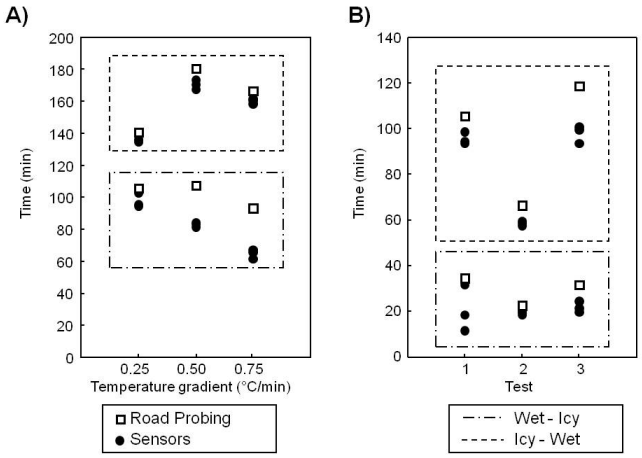

Figure 4. Time instants in which ice formed or melted over the road core compared to the indications of the sensors. A) First experiments, in which different gradients of temperature are applied. B) Second experiments, in which stable conditions at -10°C were maintained by the chamber till water froze and then it was switch off and the door was opened till the ice melted.

reached the temperature of -10°C, the climatic chamber was arranged to keep stable conditions. One mm of tap water was placed over each sensor and at the center of the road core. After closing the chamber, the water placed over the sensors and the road core froze. Then, the climatic chamber was open at ambient conditions and the ice melted. Finally, sensors and the road core were dried. This experiment was repeated in three different days in order to investigate the repeatability of the data.

A representation of the two experiments is shown in Figure 2B.

III. Results

An example of data processing is shown in Figure 3. The images captured by the camera allowed for the identification of the time instants in which water over the road core started to ice, or when ice started to melt. A synchronous detection of the sensor capacitance (one example is shown in the figure) indicates the formation or melting of ice over the sensor. Data from the camera and from the sensors were compared in terms of the time instants in which ice was formed or melted over the road core and those in which state transitions were identified by the sensors.

The general results of the experiments are shown in Figure 4. The time intants of formation and melting of ice are shown for the sensors and compared to those in which the same happened over the road model. The indication of the sensors are repeatable: in the first experiment, the standard deviation (STD) of identified transition instants is about 3 and 2 minutes for the wet-icy and icy-wet transition, respectively; for the second experiment, STD of the identified transition instants is about 4.5 and 2.5 minutes for the wet-icy and icy-wet transition, respectively. Moreover, their indications are in line with the formation or melting of ice over the road core: mean difference between the mean transition instants identified by the sensors and the actual time of state change of water over the road model was about 11 and 2.5 minutes, for the wet-icy and icy-wet transition, respectively, during the first experiment; for the second experiment, the mean difference was about 5 and 7 minutes for the wet-icy and icy-wet transition, respectively. There was always a negative bias between the indication of the sensors and the conditions of the road.

IV. Conclusions

Repeatability and reliability of the estimates provided by the ice sensor are investigated comparing the time instants in which water state transitions occurred over a road core and those indicated by the sensor. Controlling the surface of a road model placed in the same environmental conditions of a sensor is an objective way to get an external validation of its indication.

Repeatability was satisfied, as different sensors provided the same indication with time delay of a few minutes (in line with [10]). Spread of the wet-icy transitions was larger than in the case of icy-wet transition (see [10] for discussion about this result). The reliability of the estimates was also satisfied, as the delay between the state changes identified by the sensors and those obtained over the road were reasonably low (lower than about 10 minutes in all experiments considered).

It is worth noticing that there is a deviation between the indications of the sensor and what happens over the road core, as the indications of the sensor anticipate the road

 ISBN: 978-1-61208-145-8

conditions (of a few minutes, as stated before). Ice forms before over the sensor, due to the smooth surface of the sensor, which facilitates the formation of ice crystals on it than over the road. Moreover, ice melts before over the sensor than over the road core: this is probably due to the low power consumption of the electronics, which warms the surface of the sensor. Caution is recommended before exploiting this deviation in order to predict road surface conditions, as the time delay surely depends on the specific weather conditions. Nevertheless, the precision of the indications of the sensor indicates its feasibility for different applications, such as ice forecasting or identification of different liquid solutions.

ACKNOWLEDGMENT

This work was sponsored by the national project AWIS (Airport Winter Information System), funded by Piedmont Authority, Italy.

REFERENCES

[1] N. S. T. Lee, H. A. Karimi, and E. J. Krakiwsky, *Road information systems: impact of geographic information systems technology to automatic vehicle navigation and guidance,* Toronto, Canada: VNIS, 1989.

[2] E. Pasero, W. Moniaci, and G. Raimondo, *AWIS: an Airport Winter Information System,* Prague, Czech Republic: SIRWEC, 2008.

[3] C. Barre, D. Lapeyronnie, and G. Salaun, *Ice detection assembly installed on an aircraft,* U. S. Patent 7000871, Feb. 21, 2006.

[4] M. Anderson, *Electro-optic ice detection device,* U.S. Patent 6425286, Jul. 30, 2002.

[5] W. Li, J. Zhang, L. Ye, and H. Zhang, *A Fiber-Optic Solution to Aircraft Icing Detection and Measurement Problem,* Kiev, Ukraine: ITCS, 2009.

[6] J. T. Abaunza, *Aircraft icing sensors,* U. S. Patent 5772153, Jul. 30, 1998.

[7] R. DeAnna, *Ice detection sensor,* U.S. Patent 5886256, Mar. 23, 1999.

[8] H. Gao and J. L. Rose, *Ice detection and classification on an aircraft wing with ultrasonic shear horizontal guided waves,* IEEE Transactions on Ultrasonics, Ferroelectrics and Frequency Control, vol. 56(2), pp. 334-344, 2009.

[9] H. Lee and B. Seegmiller, *Ice detector and deicing fluid effectiveness monitoring system,* U.S. Patent 5523959, Jun. 4, 1996.

[10] A. Troiano, E. Pasero, and L. Mesin, *New System for Detecting Road Ice Formation,* IEEE Transactions on Instrumentation and Measurement, vol. 60(3), pp. 1091-1101, 2011.

[11] A. Troiano, E. Pasero, and L. Mesin, *An innovative water and ice detection system for road and runway surfaces monitoring,* Berlin, Germany: PRIME, 2010.

[12] A. Troiano, E. Pasero, and L. Mesin, *In the Field Application of a New Sensor for Monitoring Road and Runway Surfaces,* Sensors & Transducers, vol. 10, pp. 71-83, 2011.

[13] L. Mesin, A. Troiano, and E. Pasero, *In Field Application of an Innovative Sensor for Monitoring Road and Runway Surfaces,* Venice, Italy: SENSORDEVICES, 2010.

[14] A. Von Hippel, *The dielectric relaxation spectra of water, ice, and aqueous solutions, and their interpretation: critical survey of the status-quo for water,* IEEE Transactions on Electrical Insulation, vol. 23(5), pp. 801-840, 1988.

 ISBN: 978-1-61208-145-8

An Overview Over Yarn Mass Parameterization Methods

Vítor Carvalho, Nuno Gonçalves and Filomena Soares
Dept. industrial electronics
Minho university
Guimarães, Portugal
vcarvalho@dei.uminho.pt, a42109@alunos.uminho.pt, fsoares@dei.uminho.pt

Michael Belsley[1] and Rosa Vasconcelos[2]
[1]Dept. physics , [2]Dept. textile engineering
Minho university
[1]Braga, [2]Guimarães, Portugal
[1]belsley@fisica.uminho.pt, [2]rosa@det.uminho.pt

***Abstract*—This paper presents a description of two different approaches to determine and measure the yarn mass parameters. The first approach (YSQ) is based on: a capacitive sensor to determine yarn mass and on optical sensors with Fourier optics to determine yarn hairiness and diameter. The second approach determines all yarn mass parameters using image processing techniques. Both approaches present innovative, low cost, portable and high-precision yarn evaluation testers, for quality control of yarn characteristics under laboratory conditions. It is believed that the solution based on image processing techniques allows a high level of advantages, among others, reduced hardware and maintenance necessities with a very high resolution. The software was developed in LabVIEW, using the toolbox IMAQ Vision for image processing.**

Keywords-yarn mass parameters; optical signal processing; yarn hairiness; yarn diameter;capacitive sensors; optival sensors; image processing.

I. INTRODUCTION

The correct and accurate evaluation of yarns is a subject of major importance to the Textile Industry, as the final fabric quality depends directly on the yarn quality. To undertake these yarn tests several companies have developed specific equipment. The Tester 5 from *Uster* [1] is important for its relevant contribution to the development of quantitative yarn characterization.

However, these yarn testers have a significant cost, require a considerable area for their installation and present limited resolution and precision in the evaluation of certain yarn parameters.

As a result, many yarn producers do not have their own yarn testers and, instead, choose to subcontract dedicated testing laboratories for yarn quality determination. This process is time consuming and eliminates the possibility of acting in useful time during yarn production, reducing efficiency.

To overcome these drawbacks, we have developed new equipment, entitled YSQ (Yarn System Quality) [2]. The YSQ measures the yarn diameter, the yarn hairiness and the yarn irregularity based on optical and capacitive sensors. Moreover, it integrates an external module to obtain yarn production characteristics, based on image processing (IP). At present, in the Textile Industry there are no available commercial equipment or known prototypes to obtain these characteristics automatically. Instead, they are obtained manually by human ocular inspection or by using an analogue microscope, being the results susceptible to errors [3, 4].

The high precision levels of parameterization performed by the YSQ, together with its low cost and high portability make it a reliable and efficient solution for the Industry.

Furthermore, and after studying the image processing possibilities in the production characteristics module of the YSQ, we started considering to specify the traditional yarn mass parameters as technological solutions based on IP, as they are characterized by high reliability and efficiency and can present some advantages over the traditional methods (very low cost, small size and weight, reduced hardware, reliability and possibility of very high resolution).

IP based applications have been used in the textile field since 1964 [5], although they have not yet been converted to viable quality control methods [6].

Due to its influence on the quality of textiles, yarn hairiness is considered to be one of the most significant parameters. In textile industry the equipment used to measure the hairiness are based on photoelectric methods, like the Shirley's apparatus and the Uster Tester 3 devices [7]. Several algorithms are currently under development to characterize the yarn hairiness with IP. The method proposed by [8], measures the real length of the protruding fibers from the yarn core, as well as, their number in order to quantify hairiness. Reference [9] introduced a new method to measure hairiness, based on the assumption that the hairs close and parallel to the yarn core would be a better indicator of hairiness, proposing then a new parameter: Hair Area Index. This concept measures the area covered by hairs and is divided by the area of the yarn core to obtain a dimensionless quantity. Nevertheless, it is still necessary to develop algorithms to detect and characterize loop fibers length and to clearly distinguish between protruding fibers and loop fibers when they are interlaced.

Another important parameter is the yarn diameter, since it

 ISBN: 978-1-61208-145-8

is used to predict fabric structural parameters such as width, cover factor, porosity and fabric comfort [10]. The characterization of yarn diameter with IP can also be achieved with algorithms already applied to the extraction of yarn core [11, 12]. But, algorithms to measure the exact length of yarn irregularities (thin places, thick places and neps) [13] need to be developed. The characterization of yarn mass can be inferred from the yarn diameter, depending, among other parameters, on the yarn fiber density and porosity [14, 15].

Besides the YSQ, this paper also presents a new solution to automatically characterize the mass parameters of yarn and a preliminary study to identify and quantify the loop and protruding fibers (hairiness) based on IP.

This paper considers the following organization: Section I – Introduction, presents an overview over the traditional methods of yarn parameterization as well as describes the evolutions obtained with the solutions presented in this work; Section II – Textile Parameters Theoretical Considerations, describes the theoretical concepts of the yarn parameters quantified; Section III – YSQ Sensors System, presents the electronic and optical hardware used as well its configurations over the technical solutions of this work; Section IV – Yarn Mass Parameterization Using Image Processing, describes the image processing algorithms used to quantify the yarn parameters measured in this work; Section V – Conclusions and Future Work, presents the final remarks and the project following steps.

II. TEXTILE PARAMETERS THEORECTICAL CONSIDERATIONS

This section describes the typical configuration of a yarn, the definition of faults, hairiness and the most important yarn production characteristics [3, 4, 16-18].

A. Yarn Configuration, Faults and Hairiness

The most important parameters used to specify yarn quality are linear density, structural features and fibre content. An example of yarn configuration is shown in Figure 1.

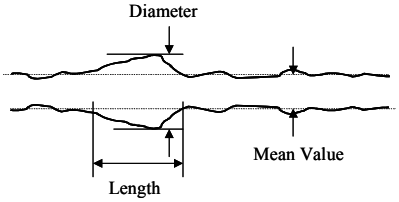

Figure 1. Yarn configuration example

As Figure 1 suggests there is a direct relationship between the variation of yarn mass and the yarn diameter. Thus the calculation of the diameter can be obtained by d(mm) = 0.037sqrt(Tex) , where Tex is the mass of the yarn in one kilometer of length (g/km) – yarn linear mass. This relation allows the possibility of determining yarn irregularity based on yarn diameter measurements.

The number of yarn faults and yarn mass measurements enables a quality rating of the products tested. There are three kinds of yarn faults, classified as (Figure 2): thin places - a decrease in the mass during a short length (4 mm); thick places - an increase in the mass, usually less than 100 % of the sensitivity, and lasting more than 4 mm; neps - huge amount of yarn mass (equal or superior to 100 % of sensitivity) in a short length (typically from 1 mm to 4 mm).

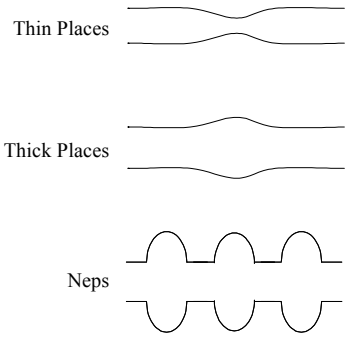

Figure 2. Types of yarn faults

Apart from faults, another important feature which greatly influences the appearance of fabrics is the level of yarn hairiness. Hairiness is the result of released fibres over the strand. Figure 3 presents an example of hairiness [3, 17, 19-21].

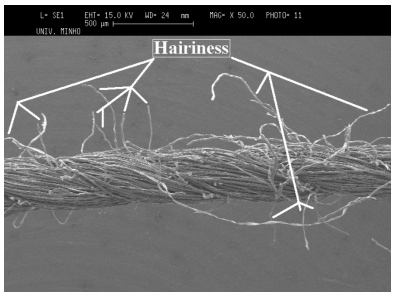

Figure 3. Identification of yarn hairiness in an electron microscope picture

The hairiness coefficient (H) specifies the length of hairs in a meter of yarn.

Measurements of the yarn hairiness, mass and diameter, allow the determination of several statistical parameters which are relevant when characterizing yarn quality and, subsequently, the fabrics.

B. Yarn Production Characteristics

Four important production characteristics of commercial yarns are the fiber's twist orientation, the number of cables (folded yarns and non-folded yarns), the folded yarn twist step and the folded yarn twist orientation [3, 4]. The two final production characteristics mentioned are only obtained when dealing with folded yarns. Figure 4 identifies the four

 ISBN: 978-1-61208-145-8

described production characteristics using as an example an electron microscope image of a 4.2 g/km cotton yarn. It is a folded yarn as two separate cables are clearly visible. The folded yarn twist step (d) is 0.3334 mm, with an orientation clockwise and a fiber twist orientation opposite (anti-clockwise) to the folded yarn direction.

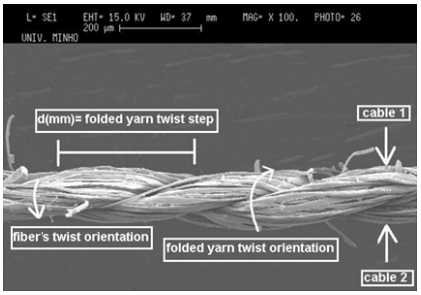

Figure 4. Identification of the yarn production characteristics in an electron microscope picture

III. YSQ SENSORS SYSTEM

This section describes the optical and electronic setups used to obtain the measurements of yarn hairiness, yarn diameter and mass variation in the YSQ [22-24]. Moreover, it also describes the hardware of the external YSQ module, employed to obtain the yarn production characteristics.

A. Three Directions Optical Configuration – Main Module

In order to reduce YSQ volume and cost, one diode laser source was employed (Eudyna FLD6A2TK [18]) to establish three different beams. This single source (Src) was divided in three beams using two beam splitters (S1, first beam splitter division 50 % / 50 % of full signal for each resultant direction, S2, second beam splitter division ≈ 2 % / 48% of full signal for each resultant direction), as presented in Figure 5.

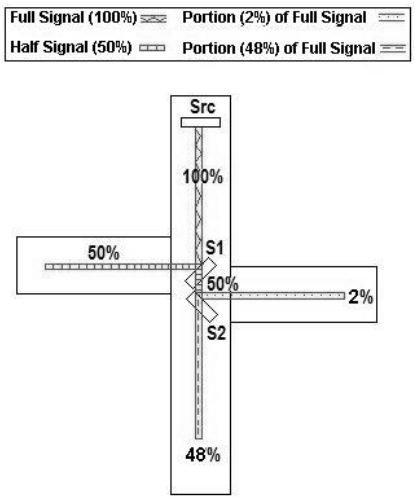

Figure 5. Light signal source intensity beam division

Figure 6 presents the YSQ optical setup employed where, Src is the diode laser source that emits light at 685 ± 10 nm in both a single transverse and a single longitudinal mode, with a low aspect ratio of 1.3, the two HPF represent a high-pass spatial filter, LPF is a low-pass spatial filter, FL is the Fourier lens, S1 is the first beam splitter, S2 is the second beam splitter and L1 to L4 are plano-convex lenses.

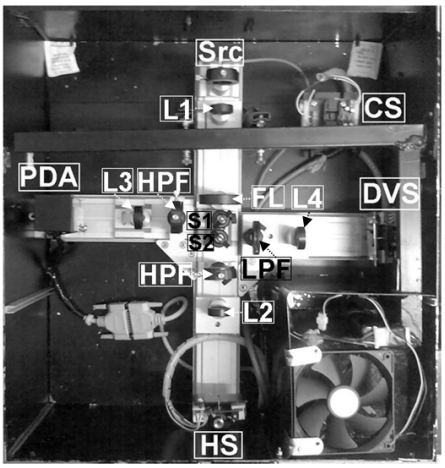

Figure 6. YSQ optical configuration

Observing Figure 6 one can see that the beam splitters were placed immediately after the Fourier lens. As in this case there are two different types of spatial filters (high-pass filters, HPF and low-pass filters, LPF), the beam division should be performed before the signal filtering to allow the application of different filters. Figure 7 presents an image obtained in the image plane of lenses L2 (HS-Hairiness Sensor) and L3 (PDA-Photodiode Array), where only the yarn contours and hairiness are highlighted by the high-pass spatial filter (the yarn core and light which is not blocked by the yarn were eliminated).

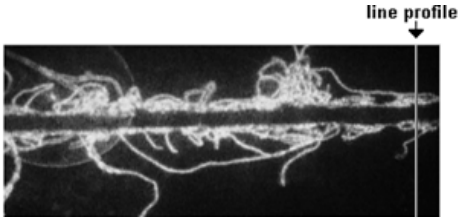

Figure 7. Image plane of lenses L2 and L3

Figure 8 presents an image obtained in the image plane of lens L4 (DVS-Diameter Variation Sensor), where only a shadow of the yarn core and light which is not blocked by the yarn are transmitted by a low-pass spatial filter (the yarn contours and hairiness were eliminated).

 ISBN: 978-1-61208-145-8

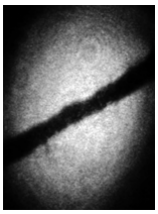

Figure 8. Image plane of lens L4

B. *Electronics Configuration – Main Module*

The images obtained in the image plane of lenses L2 (HS) and L4 (DVS) are aquired by two equal configurations of the developed electronic yarn measurement hardware shown in Figure 9 [22, 23].

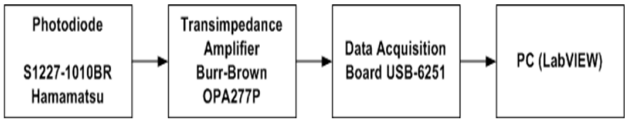

Figure 9. Custom developed electronic yarn measurement hardware for the HS and DVS

The measurement of precise yarn diameter (PDA) was based on line profile analysis [24]. Figure 10 presents the line profile analysis indicated in Figure 7 for 512 pixels, where the red plane intensity line profile signal, is proportional to the voltage signal resulting from the hairiness distribution image of the linear array photodiodes.

Considering the typical hairiness distribution profile (Figure 10), starting from the yarn core signal (reduced signal intensity of between the two main distribution peaks), in the right and left directions, respectively, the first signal peak intensity is obtained for the yarn contours.

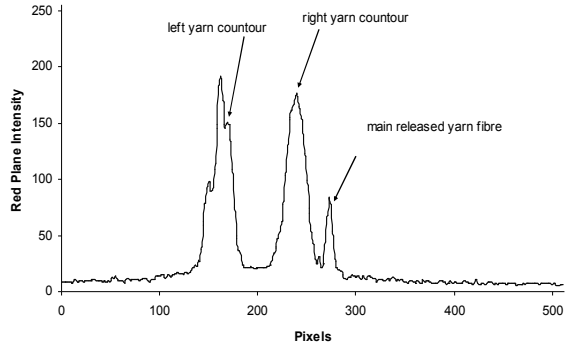

Figure 10. Line profile analysis example

The yarn diameter characterization can be determined considering the number of pixels between the left and right yarn contour pixels, the optical amplification (0.37) and the pixels pitch.

The experimental setup was developed based on the S8378-256Q CMOS line array and the C9001 Driver Circuit, both from Hamamatsu [25].

The yarn mass variation system considers a 1 mm parallel plate capacitive sensor based on the integrated circuit MS3110 from Irvine Sensors [16, 26, 27], allowing direct yarn mass measurements in samples of 1 mm. The sensor adopts a differential configuration to assure a higher robustness to variations in temperature, air humidity and pressure. It integrates transducer amplification and signal conditioning as shown in Figure 11.

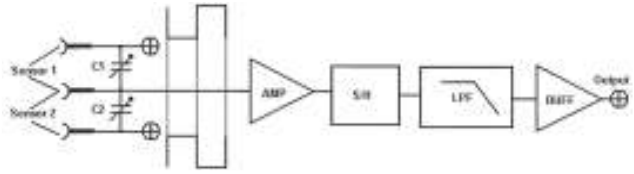

Figure 11. Capacitive sensor configuration [C1,C2 – Adjustable capacitors to calibrate the sensors, AMP – Capacity to voltage converter and amplifier, S/H – Sample and hold, LPF – Two pole low pass filter, and BUFF – Output buffer]

The software to acquire and process the data was developed in LabVIEW from National Instruments [28].

C. *Yarn Productions Characteristics ExternalModule Hadware Design – Optics and Electronics*

In order to keep the total system price at an acceptable level, a low cost analogue microscope coupled to a web CMOS camera was used. The microscope provides sufficient amplification and image detail, while there are no special requirements regarding the camera resolution. Figure 12 shows the flowchart of the designed system.

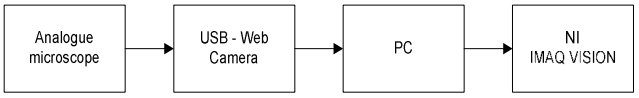

Figure 12. Yarn Image Acquisition Flowchart

The analogue microscope employed is the Biolux Al from Bresser [29] and the USB Web Camera used is the Deluxe from Hercules [30]. The web camera was placed at the exit plane of the microscope ocular, capturing the analogue image produced by the microscope. With an optical amplification of 40X, it was found that a sensor resolution of 640x480 pixels is adequate to correctly evaluate the yarn production characteristics.

In order to obtain higher contrasts for the yarn geometry relief, the illuminated yarn surface must be as close as possible to a monochromatic light source. As the white led illumination available on the microscope emits a wide range of wavelengths, an external yellow light source was used, which is somewhat closer to an ideal monochromatic light source. Figure 13 presents an example of a picture of a 22 g/km linear mass yarn obtained using the described setup.

 ISBN: 978-1-61208-145-8

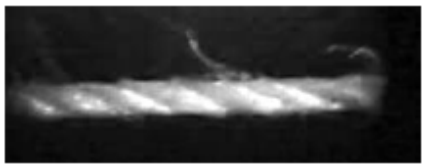

Figure 13. Picture of a 22 g/km yarn

Therefore, considering the clear contrast between the yarn zones with higher relief, corresponding to the most accentuated twist areas or yarn areas which are closer to the light source (as seen in Figure 13), a tool was developed using the IMAQ Vision software [31-33] for LabVIEW®, to determine the yarn production characteristics. Then it was possible to classify the yarn production characteristics by the following:

- Folded (multiple cable) yarn twist step: obtained by the average of the horizontal pixel distance between particles;
- Folded yarn twist orientation: determined by the orientation angle for each particle, under the following conditions: If the orientation angle lies between 90º and 180º, then the twist orientation is anti-clockwise; if the orientation angle lies between 0º and 90º, than the twist orientation is in the clockwise direction.
- Number of cables (folded or non-folded (single) yarn): If only one particle is identified - single cable (non-folded yarn); if the number of particles is greater than one - multiple cables (folded yarn).
- Fibers twist orientation: in folded yarns, the fibers twist orientation is opposite to the twist orientation. This is a general fact in Textile Industry to avoid the fibers untwist over the yarns [3, 4].

IV. YARN MASS PARAMETERIZATION USING IMAGE PROCESSING

This section describes the methodology used for measuring the diameter, for calculating of the hairiness coefficient and the detection of imperfections in the yarn, through image processing techniques. Furthermore a preliminary study for the detection and differentiation between protruding and loop fibers is also presented.

A. Diameter Determination

Figure 14 represents the block diagram of the algorithm used to determine the diameter by image processing techniques.

The algorithm summarizes the application of various techniques of image processing that allows obtaining, as final result, the contours of the yarn core, excluding, all hairiness around the core. The diameter calculation is made through the detection of all the edges along a set of parallel searching lines. Once all edges are detected, the distance is calculated between the pairs of edges detected by all the search lines. The diameter is obtained by, the average of all the distances calculated. Once calculated the diameter, the yarn mass is easily obtained through the theoretical correlation between mass and diameter, presented in section II-A.

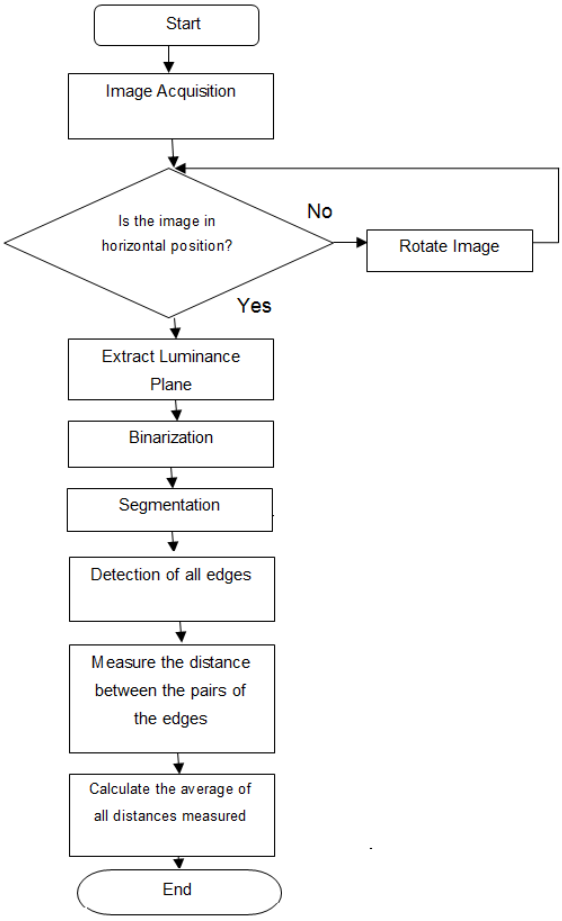

Figure 14. Diameter determination block diagram

Figure 15 presents the image-based sample of the yarn captured by the image acquisition system and Figure 16, the result after the application of the sequence of functions presented in Figure 14.

Figure 15. Original sample image acquired

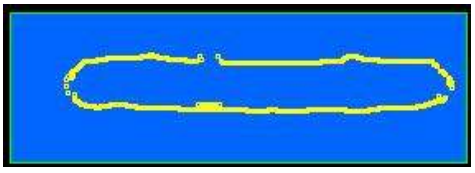

Figure 16. Image resultant from the aplication of the Figure 14 functions to Figure 15.

B. *Determination of yarn faults (Thin and Thick places)*

With the yarn diameter and due to the correlation between the mass and the diameter, thick and thin places can be analyzed by comparing the distances measured along the yarn with the average diameter at several levels of analysis. Figure 17 shows the algorithm applied.

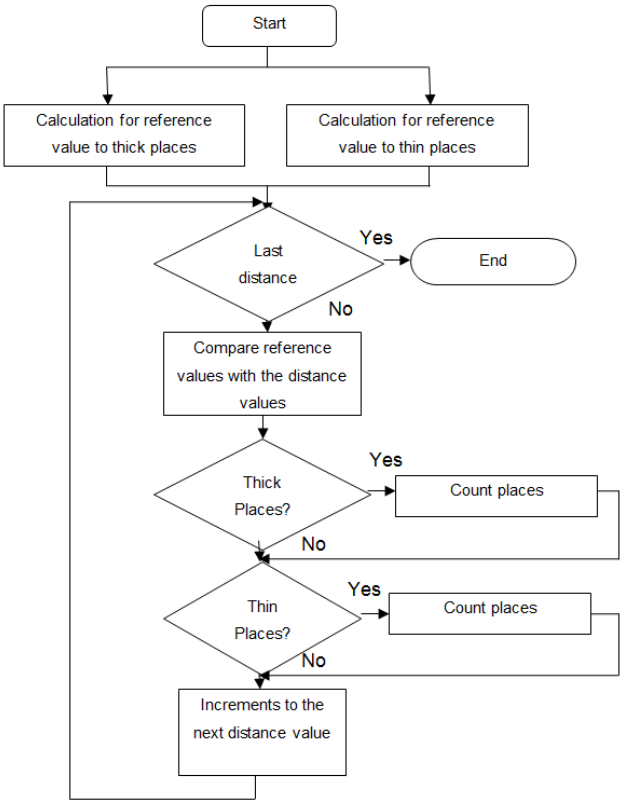

Figure 17. Algorithm used to detect yarn faults

C. *Yarn Hairiness Determination*

In this study, spatial pre-processing techniques, as well as segmentation and spatial filtering techniques were used to isolate the yarn core and to highlight and quantify the protruding and loop fibers from the original image. In order to isolate the protruding and loop fibers from the yarn, logical operators were used between the image with the highlight fibers and the yarn core. Figure 18 presents the algorithm implemented.

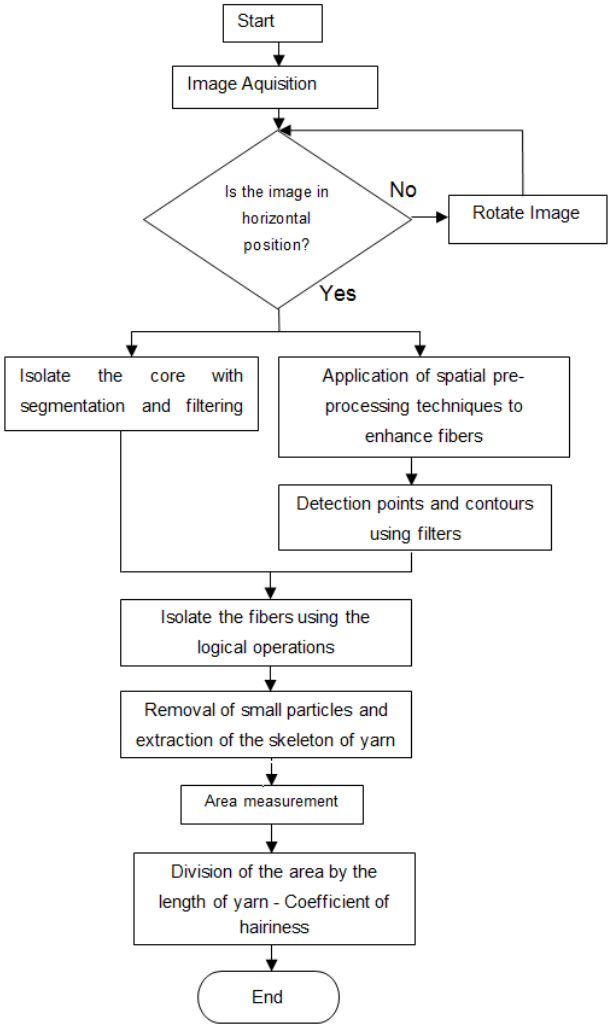

Figure 18. Algorithm used to measure the yarn hairiness index

Figure 19 shows the sample base yarn image where the image processing techniques were applied and Figure 20, its result.

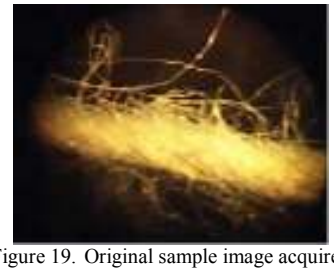

Figure 19. Original sample image acquired

 ISBN: 978-1-61208-145-8

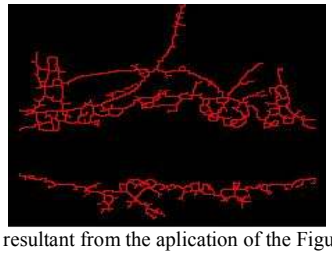

Figure 20. Image resultant from the aplication of the Figure 18 functions to Figure 19.

V. CONCLUSIONS AND FUTURE WORK

This paper presents two different approaches to quantify the yarn mass parameters, namely, based on capacitive and optical sensors and based on image processing techniques.

To perform the measurements of the first approach, the equipment YSQ was built. A capacitive sensor is used to measure yarn mass, and optical sensors, with optical signal processing are used to quantify yarn hairiness and diameter. An additional module of yarn production characteristics was developed using image processing. This equipment presents several advantages when compared to the commercial available equipment, like low cost, high portability and superior resolution (all the analysis is performed in steps of yarn length of 1mm or inferior).

Considering the computational power evolution of computers, a solution to measure the yarn mass parameters (diameter, hairiness and mass) with image processing was developed. This solution presents even more advantages to the traditional equipment, as low cost, equipment hardware, maintenance, dimension and high resolution.

Future work will consider a comparison of results between both approaches. Furthermore, the optimization of the algorithms of image processing applied in the second approach is still under work.

ACKNOWLEDGMENT

The authors are grateful to the Portuguese Foundation (FCT) for funding through the scholarship (BD/ 19028/ 2004) and to the Portuguese Research Centers Algoritmi and 2C2T for financial support of the project.

REFERENCES

[1] www.uster.com (access in May 2011)

[2] V. Carvalho, M. Besley, R. Vasconcelos and F. Soares, "Automatic Yarn Characterization System", IEEE Sensors 2008, 26-29 October, Lecce, Italy.

[3] B. Goswami, J. Martindale and F. Scardino, "Textile Yarns: Technology, Structure and Applications", 2nd Edition, John Wiley & Sons, New York, 1977.

[4] M. Castro and M. Araújo, "Manual de Engenharia Têxtil - Vol. II", Gulbenkian, Lisbon, 1986.

[5] Shiloh, M., "A computer for the evaluation of the crimp diameter of textile fibers" Textile Research Journal, 1964, 34(5): p. 430-434.

[6] S. Jaganathan, "Characterization Methods and Physical Properties of Novelty Yarn" , MSc Thesis, North Carolina State University, Raleigh, 2005.

[7] Anirban Guha, C. Amarenath, S. Pateria and R, "Measurement of yarn hairiness by digital image processing" The journal of the Textile Institute, Vol. 101, Issue 3, March 2010, pp. 214-222.

[8] M. Kuzanski and L. Jackowska-Strumillo, "Yarn Hairiness Determination – The algorithms of computer measurement methods", MEMSTECH'2007, May 23-26, Lviv-Polyana, Ukraine, p.154-157.

[9] http://www.indiantextilejournal.com/articles/FAdetails.asp?id=552 (access in May 2011).

[10] M. Kuzanski, "The Algorithms of the Yarn Shape Detection and Calculation of the Protruding Fibres Length", MEMSTECH'2008, May 21-24, Lviv-Polyana, Ukraine, p.98-100.

[11] W. Jian and Y. Li, "Evaluation of Yarn Regularity Using Computer Vision", 9th International Conference on Pattern Recognition, Vol. 2, November 14-17, p.854-856.

[12] V. Carvalho, "Automatic Yarn Characterization System", PhD Thesis, Minho University, Braga, 2008.

[13] B.C. Goswami, J.G. Martindale and F.L. Scardino, Textile Yarns: Technology, Structure and Applications, 2nd Edition, John Wiley & Sons, New York, 1977.

[14] A. Cay, S. Vassiliadis, M. Rangoussi and I. Tarakçioglu, "On the Use of Image Processing Techniques for the Estimation of the Porosity of Textile Fabrics", Proceedings of World Academy of Science, Engineering and Technology – PWASET, Vol. 2, January 2005, p.73-76.

[15] J.G. Pinto, R. Vasconcelos, F.O. Soares and J. L. Monteiro, "A new system for direct measurement of yarn mass with 1mm accuracy", IEEE International Conference on Industrial Technology, Bangkok, Dezembro, 2002, pp. 1158 1163.

[16] V. Carvalho, "Parametrização de Fio Têxtil Baseada na Análise de Massa", Msc Thesis, Minho University, Guimarães, 2004.

[17] J. Neves, "A Irregularidade dos Fios Têxteis, Sua Origem, Medição e Análise", Oporto, 1968.

[18] R. Furter, "Evenness Testing in Yarn Production: part I", The Textile Institute and Zellweger Uster AG, Manchester, 1982.

[19] A. Anand, V. Chhaniwasl and C. Narayanamurthy, "Hairiness Measurement of Textile Yarns Using Crossed Polarizers", Review of Scientific Instruments, 2005, 76.

[20] A. Barella, "Yarn Hairiness", Textile Progress, 1981, 13, p.1.

[21] A. Barella, "The Hairiness of Yarns", Textile Progress, 1992, 24, p.3.

[22] V. Carvalho, P. Cardoso, M. Belsley, R. Vasconcelos and F. Soares, "Yarn Hairiness Parameterization Using a Coherent Signal Processing Technique", Sensors and Actuators A: Physical, Volume 145, Issue 1, p217-224.

[23] V. Carvalho, P. Cardoso, M. Belsley, R. Vasconcelos, F. O. Soares, "Yarn Diameter Measurements Using Coherent Optical Signal Processing", IEEE Sensors Journal, Vol. 8, Issue 11, November 2008, pp.1785-1793.

[24] V. Carvalho, P. Cardoso, M. Belsley, R. Vasconcelos, F. O. Soares, "Yarn Hairiness Characterization Using Two Orthogonal Directions", IEEE Transactions on Instrumentation and Measurement, 2009, in press, doi: 10.1109/TIM.2008.2005082.

[25] www.hamamatsu.co.jp (access in May 2011)

[26] V. Carvalho, J. Pinto, J. Monteiro, R. Vasconcelos and F. Soares, "Yarn Parameterization Based on Mass Analysis", Sensors and Actuators A: Physical, Vol. 115, Issues 2-3, September 2004, p.540-548.

[27] www.irvine-sensors.com (access in May 2011)

[28] www.ni.com (access in May 2011)

[29] http://www.bresseroptics.co.uk (access in May 2011)

[30] http://www.hercules.com (access in May 2011)

[31] IMAQ, IMAQ Vision Concepts Manual, National Instruments, Austin, 2004.

[32] T. Klinger, "Image Processing with LabVIEW and IMAQ Vision", Prentice Hall, New Jersey, 2003.

[33] C.G. Relf, "Image Acquisition and Processing with LabVIEW" CRC, Boca Raton, 2003.

 ISBN: 978-1-61208-145-8

Embedded Sensor for Solid-State Hydrogen Storage Devices

Denis Marcotte and Frédéric Domingue
Institut de recherche sur l'hydrogène
Université du Québec à Trois-Rivières
Trois-Rivières, Canada
E-mail: denis.marcotte@uqtr.ca , frederic.domingue@uqtr.ca

***Abstract*— In this paper, we present two potential sensors used to monitor the state of charge of a solid-state hydrogen storage device. The embedded sensors are based on the variation of the electrical properties of the storage material related to the hydrogen content. Specifically, the proposed sensors are based on variation of the resistivity and the magnetic properties. We present the preliminary results. The measured results confirm the possibility to determine the state of charge of the $LaNi_5$ hydrogen storage devices using the variation of the resistivity while the study of the magnetic properties is under progress.**

Keywords: Embeded sensor; hydrogen monitoring; metal hydride; solid-state hydrogen storage device

I. INTRODUCTION

The continuously growing demand in energy motivated the development of renewable energy sources. An interesting solution is hydrogen, an excellent energy carrier. Its use reduces pollution that traditional fuels emit [1]. There are several products on the market using this energy vector such as cars, buses, power generators, electronic devices and appliances. The hydrogen storage devices are clearly one of the important components in the portable hydrogen energy systems. The hydrogen can be stored in various forms such as pressurized gas, cryogenic liquid, solid fuel as chemical or metal hydride compounds. Metal hydrides provide safety advantages over high pressure, compressed storage or low temperature, cryogenic storage, as the hydrogen is stored in a solid metal matrix at a low pressure with a slow release rate. These metal hydrides are promising mediums for portable hydrogen-powered generators. However, an important challenge with the metal hydride storage devices concerns the hydrogen metering techniques. The current approach consists in estimating the remaining hydrogen in the storage device based on electrical energy consumption. This solution is not precise and needs to be replaced by a specific sensor. The commercial products need low cost and compact sensors embedded into the metal hydride devices for the hydrogen metering.

This paper presents two approaches for the development of sensors embedded in the solid-state hydrogen storage devices to evaluate the state of charge. In this work, the storage material is the lanthanum nickel hydride (LaNi5). As opposed to the gaseous form, the pressure measurement cannot be used to determine the hydrogen content. Indeed, we propose to monitor the hydrogen content through the variation of the electrical properties of the storage material (LaNi5). Specifically, the proposed sensors are based on variation of the resistivity and the magnetic properties. The theoretical approach and the preliminary results are presented.

II. THEORY

The metal hydrides have phases that are named the α phase, where the metal begins to absorb hydrogen, and the β phase, where the metal is returned to its absorption maximum. These phases change depending on the substance used. Fig. 1 illustrates the variation of the pressure during the hydrogen absorption and desorption. Clearly, the pressure remains constant even if the amount of hydrogen changes.

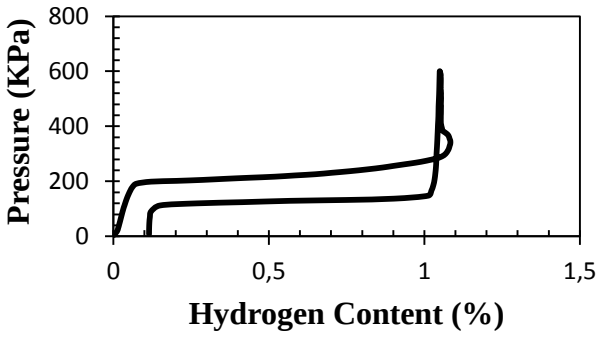

Figure 1. Typical PCT curve for LaNi5.

Several studies have focused on the characterization of intermetallic compounds. The electrical resistivity for various hydride compounds, such as the $MmTm_3$, the $MmNi_{4.5}Al_{0.5}$ and the $LaNi_5$, has been characterized [2-6]. The studies illustrate that the resistivity varies with hydrogen. Especially, the resistivity of the $LaNi_5$ decreases during the absorption of hydrogen. In other hand, the magnetic properties vary also with the hydrogen content. The susceptibility of the $LaNi_5$ is affected by the concentration of hydrogen absorbed by the compound, as discussed in several researches [7-9].

A. Proposed Sensing Principles

The recent technologies of micromachining make it possible to manufacture compact and low cost sensors

 ISBN: 978-1-61208-145-8

suitable for embedment in the hydrogen storage device. The mass production of these technologies helps to reduce the estimated cost of the sensors and measuring circuits to less than a few dollars per unit. The variation of the electrical properties of the hydrogen storage material, in this case LaNi5, will affect the output of the sensor.

B. Resistivity

The resistance of the LaNi5 changes with the concentration of hydrogen. The measurement device is based on two conductive electrodes in contact with the LaNi5. The state of charge is thus estimated by measuring the resistance between the electrodes.

C. Susceptibility

The susceptibility of the LaNi5 changes with the concentration of hydrogen. The state of charge is estimated by measuring an inductance embedded in the $LaNi_5$ storage device. The susceptibility variation modifies the inductance value. Fig 2b presents both sensing approaches.

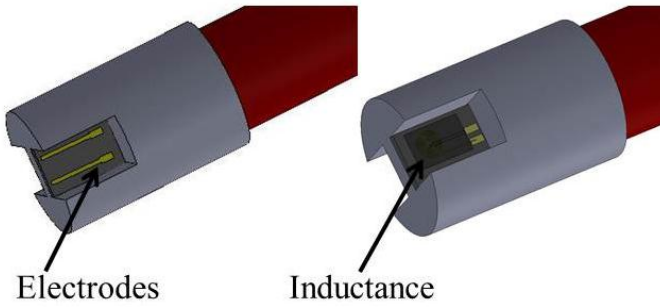

Figure 2. The proposed sensor device :
a) resistive sensor and b) inductive sensor.

III. SIMULATED RESULTS

The simulations, using a finite element simulator, were performed with the parameters and the data presented in Table I. While the $LaNi_5$ powder is presenting large grains, the parameters for the bulk material have been used. The simulated model includes the variation of the electrical properties of the LaNi5 according to the hydrogen content.

TABLE I
PARAMETERS USED FOR THE SIMULATIONS

H_2 State	Parameter	Unit	Value
Charged	Resistivity [5]	μΩm	430
	Susceptibility [9]	m^3/Kg	$16,3 \times 10^{-9}$
Empty	Resistivity [5]	μΩm	10
	Susceptibility [9]	m^3/Kg	$57,8 \times 10^{-9}$

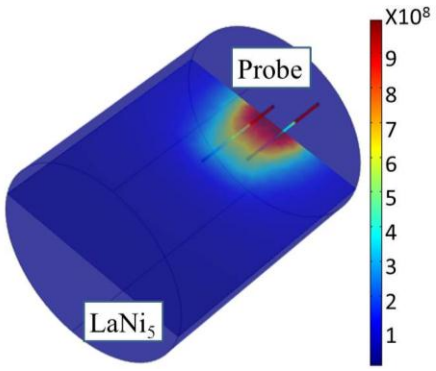

Figure 3. Simulated Current Density (A/m^2) .

TABLE II
SIMULATED RESULTS USING A FINITE ELEMENT SIMULATOR

H_2 State	Parameters	Unit	Value
Charged	Resistance	Ω	0,018530
Empty	Resistance	Ω	0,001307

The resistance variation is 1,72% between the charged and the empty states. However, Fig. 2 shows the current distribution in the material. While the electrodes' spacing is quite small compared to the LaNi5 volume, the current distribution is present only in a local region. Additional characterization are required to determine if longer electrodes are needed.

IV. EXPERIMENTAL RESULTS

A. Proposed Test Bench

The PCT (Pressure, Composition and Temperature) test bench enables the absorption and desorption of hydrogen by controlling its pressure and temperature. We have set a Labview platform that captures the data with external equipment. The test devices are: a multimeter, an LCR meter, an oscilloscope and a function generator. This allows monitoring in real time of the sensor and observes its evolution in relation to the change of hydrogen.

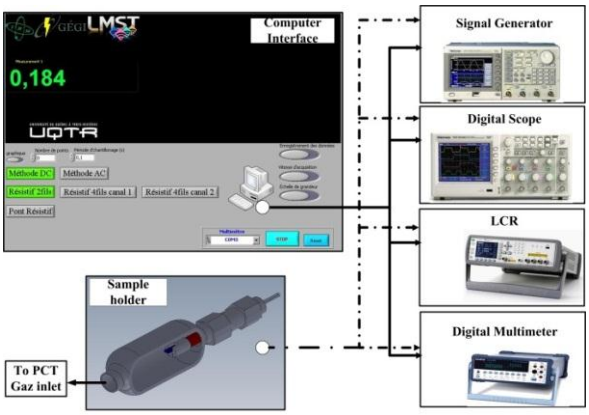

Figure 4. Automated Test Bench for Electrical Characterization during the absorption and desorbtion of hydrogen

B. Resistivity Measurement

The experiment was conducted on a sample of 254 grams of $LaNi_5$, with a temperature controlled chamber of 23°C. The procedure of charging the metal hydride with hydrogen was to: first fill an adjacent tank, then monitor the hydrogen pressure of the reservoir and that of the sample, and when the storage tank was filled to capacity and we had a pressure of 2800kPa, close the valve of hydrogen and open the valve of the sample so that the metal hydride would charge. The changing value of the resistance was collected through an automated test bench. Here are the data stored.

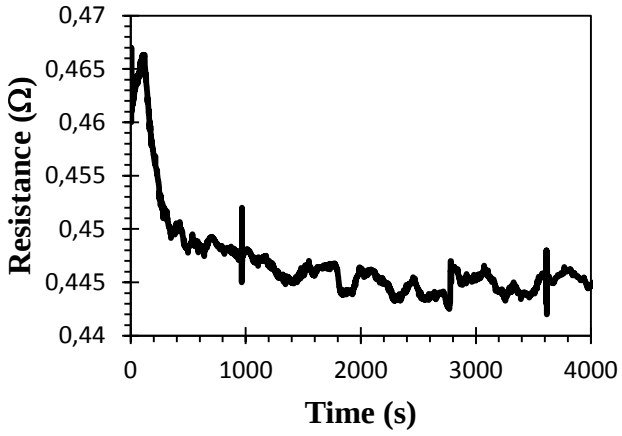

Figure 5. Variation of resistance during hydrogen absorption

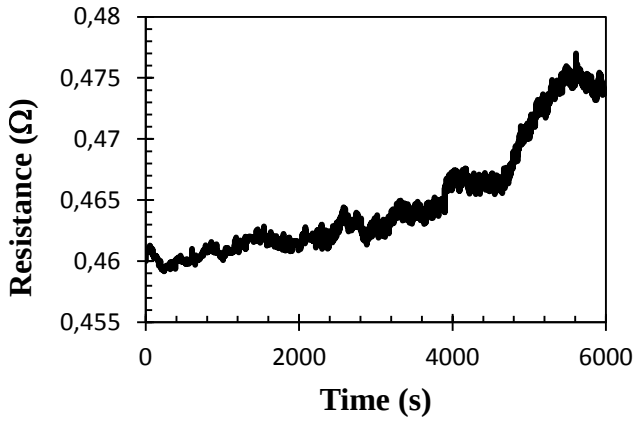

Figure 6. Variation of resistance during hydrogen desorbtion

The simulations illustrate a perfect contact between the block of metal and the electrodes. The resistance of the wire and the contact with the $LaNi_5$ must be taken into account. The measured resistance of the wire used in the test bench is 0.325Ω while the contact resistance is estimated at 0.125Ω. Table II presents the measured results and the simulated results including the correction for the wire and the contact.

TABLE III
COMPARISON BETWEEN EXPERIMENTAL AND SIMULATED RESULTS

H_2 State	Parameters	Unit	Value
Charged	Simulated Resistance with corrections	Ω	0,4513
	Measured Resistance	Ω	0,445
Empty	Simulated Resistance with corrections	Ω	0,4685
	Measured Resistance	Ω	0,464

Further experimentation is necessary to determine if the resistive sensors are suitable for this application. The effects of the temperature have to be investigated.

C. Developped Sample Holder

The sample-holder that contains the sensor was assembled by stereolithography. The fabrication was done at the University du Québec à Trois-Rivières. In our case, we used polymer to achieve the coveted results. The circuit was glued with epoxy. An electrical feedthrough allowed the connection of the embedded sensor to the automated test bench.

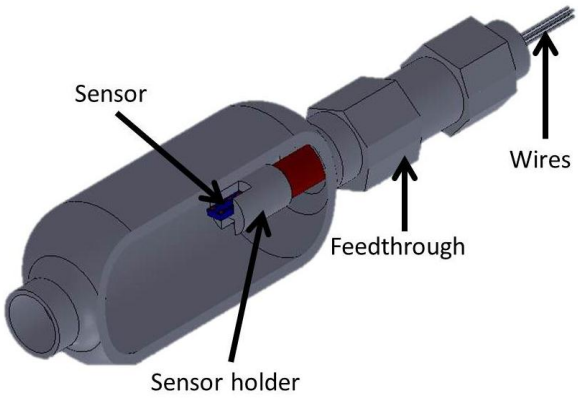

Figure 7. Developped Sample Holder Used in the Projet

V. FUTURE WORK

A. Theory of Magnetic Properties

Alternatively, we begin to study another phenomenon, which will reveal the hydrogen content in the sample. The other feature is the variation of the magnetic powder which is influenced by the presence of hydrogen. What will be revealed is the concentration of the entire surface of the cylinder and not just of a specific place. Studies clearly show the variation in susceptibility of $LaNi_5$ by presence or absence of hydrogen [8, 9].

We will discuss this feature by using inductance directly in the sample. The inductance is not required to be in contact with the powder as opposed to resistivity.

 ISBN: 978-1-61208-145-8

We calculate the inductance of the magnetic field in relation to the surface. This relationship has a direct effect on the value of the inductor, because it is the latter, which is multiplied by the number of turns of the coil and everything is divided by the current, see equation 1[10].

$$L = \frac{N \oint B ds}{I} \quad (1)$$

where L represents the inductance, N is the number of turns of the inductance, B is the magnetic field, ds is the variation of the surface and finally I is the effective current.

B. Developped Magnetic Sensor

We propose to fabricate the inductive sensor on an alumina substrate. The proposed inductive sensors will be fabricated using a three-mask process. First, a 40 nm layer of evaporated chromium and a 1 µm layer of gold are defined using a typical bi-layer lift-off technique. Next, a 30 nm TiW adhesion layer and a 0.7 µm PECVD silicon oxide layer is deposited and dry-etched in a reactive ion etching chamber in the second photolithography step. This oxide layer is used as the insulator between the inductance and the LaNi5. Finally, the bridge is formed using a 1.0µm thick electroplated gold on a 100 nm Au seed layer. Fig. 8 shows the proposed inductive sensor.

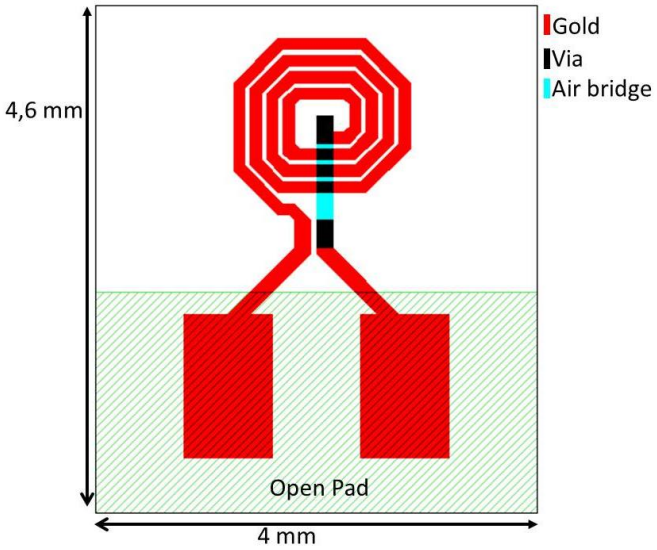

Figure 8. Inductance Sensor

VI. CONCLUSION

In this article, we presented the development of an embedded sensor in a solid-state hydrogen storage device. Two approaches are currently studied based on the variation of the electrical properties of the storage material. The resistive solution has been validated with experimental measurements. While the resistance decreases in the presence of hydrogen. Further experimentation is necessary to determine if the resistive sensors are adaptable to other metal hydride such as magnesium. On the other hand, the variation of the magnetic properties seems a good alternative. An inductive sensor is currently under development.

ACKNOWLEDGMENT

This research was supported by the NSERC Hydrogen Canada (H2CAN) Strategic Research Network. The authors also gratefully acknowledge Palcan Energy Corporation for the financial contribution. The authors are thankful to Dr. Jacques Huot and his team for their support.

REFERENCES

[1] U. D. of Energy, "hydrogen from coal program research, development, and demonstration plan for the period 2009 through 2016," D. o. Energy, Ed., ed, 2009.

[2] A. L. Mohana Reddy, G. Srinivas and S. Ramaprabhu, "Hydriding and electrical resistivity properties of MmTM3-hydrogen (TM=Fe, Co and Ni) system," *International Journal of Hydrogen Energy*, vol. 32, pp. 3356-3362, 2007.

[3] I. P. Jain, Y. K. Vijay and M.I.S. Dakka, "Electrical resistance variations with content of hydrogen in bulk MmNi4.5Al0.5," *International Journal of Hydrogen Energy*, vol. 27, pp. 85-90, 2002.

[4] A. Vashistha, P. Sharma, G. Agarwal and I.P. Jain, "Hydrogen absorption mechanism in obliquely deposited MmNi(4.5)Al(0.5) thin film," *International Journal of Hydrogen Energy*, vol. 33, pp. 404-407, Jan 2008.

[5] F. Ishikawa,H. Tega, I. Yamamoto and M. Yamaguchi, "Relationships between the electrical resistivity and the metal hydride phases," *Journal of Alloys and Compounds*, vol. 231, pp. 182-187, Dec 1995.

[6] G. Adachi,K. Niki and J. Shiokawa, "The effect of hydrogen absorption on the electrical resistivities of LaNi5 and MmNi4.5Mn0.5 films (Mm [triple bond; length as m-dash] misch metal)," *Journal of the Less Common Metals*, vol. 88, pp. 213-216, 1982.

[7] L. T. Tai, B.T. Hang, N.P.Thuy and T.D. Hien, "Magnetic properties of LaNi5-based compounds," *Journal of Magnetism and Magnetic Materials*, vol. 262, pp. 485-489, Jun 2003.

[8] T. P. Blach and E. M. Gray, "Magnetic properties of the LaNi5-H system," *Journal of Alloys and Compounds*, vol. 253, pp. 336-338, May 1997.

[9] L. Schlapbach, "Magnetic-properties of LANI5 and their variation with hydrogen absorption and desorption," *Journal of Physics F-Metal Physics*, vol. 10, pp. 2477-2490, 1980.

[10] M. N. O. Sadiku, Ed., "*Elements of electtromagnetics*," New York: Saunders college 1989, p.357

 ISBN: 978-1-61208-145-8

Analytical Technique of Spectroscopic Ellipsometry for Studying Protein-Protein Interaction

A. Nabok[1], V. Kriechbaumer[2], M.K. Mustafa[1], B.Abell[2], D.Smith[2], A.Tsargorodskaya[1]
[1] Materials and Engineering Research Institute,
[2] Biomedical Research Centre,
Sheffield Hallam University, Sheffield, S1 1WB, UK,
e-mail: a.nabok@shu.ac.uk

Abstract—**The method of total spectroscopic ellipsometry in its total internal reflection (TIRE) mode was utilized in this work for the study of protein-protein interaction. Two different systems were studied here: (i) the interaction of chaperones, such as heat shock proteins Hsp70 and Hsp81 with different chaperone receptors including the new one OEP61-TM; (ii) the aggregation of alpha-synuclein monomers and oligomers (involved in Parkinson's diseases) in phospholipid membranes. The method of TIRE provides unique quantified information on such protein interaction. Changes in the effective thickness of adsorbed molecular layer obtained by fitting the single TIRE spectra allows us to quantify the process of binding of chaperons to receptors or aggregation of alpha-synuclein in the lipid membrane. TIRE dynamic measurements allow monitoring protein interaction in-situ and evaluate the association (affinity) constants of such interaction. TIRE study revealed a clear separation between specific and non-specific interaction of proteins; such data were reported for the first time. A complementary method of atomic force microscopy (AFM) was used in this work to visualize the protein build-up on the surface.**

Keywords- ***chaperone, receptors, alpha-synuclein, spectroscopic ellipsometry, total internal reflection ellipsometry, electrostatic layer-by-layer deposition; AFM***

I. INTRODUCTION

This work is dedicated to the study protein-protein interaction, a problem which is far from being extensively studied and fully understood, as compared to more established fields of immune and enzyme reactions. Two examples are studied in our work: first, the interaction of chaperone proteins with respective receptors extracted from plants, and second, the study of aggregation of α-synuclein, a peptide involved in Parkinson's disease.

Chaperone proteins play an important role in cells protecting proteins from high temperatures and other cellular stresses, stabilizing protein structure and preventing them from aggregation and degradation. It was recently suggested that molecular chaperones, such as heat shock proteins Hsp70 and Hsp81, can form complexes with freshly translated proteins and thus prevent their aggregation [1]. Furthermore, the recent finding of chaperone receptors in plants [2] indicates more specific involvement of molecular chaperones in protein targeting. The study of the mechanisms of protein targeting may have a substantial impact in a number of applications including the origin of neurological diseases.

The problem of aggregation of α-synuclein in lipid membranes was identified as the main mechanism of Parkinson's disease development. These α-synuclein oligomers are thought to be the toxic entities responsible for bring about cell death, and similar oligomers have also been implicated in a range of other disease states. One of the possible mechanisms of α-synuclein build-up is the penetration of oligomeric α-synuclein into the membrane as opposed to resting on the surface. This is a novel mechanism that indicates cellular toxicity can be caused by punching holes through the membrane.

Physical methods such as total internal reflection ellipsometry (TIRE) can compliment traditional biological methods of studying protein-protein interaction and provide necessary quantification of such interactions. The method of (TIRE) was selected here because of its high sensitivity to molecular adsorption [3] and its recent successful applications in bio-sensing [4-6]. The results of TIRE study of interaction of chaperones (Hsp70 and Hsp81) with the novel plant chaperone receptor OEP61 are presented here for the first time. The method of atomic force microscopy was exploited in this work as a complimentary technique of visualizing protein aggregates on the surface; it was successfully implemented here for direct observation of α-synuclein oligomers in lipid membranes.

II. TEXPERIMENTAL METHODS AND SAMPLES PREPARATION

The experimental set-up for total internal reflection ellipsometry (TIRE), schematically shown in Fig. 1a, is based upon commercial M2000 J.A. Woollam spectroscopic ellipsometer with the addition of a 68^0 glass prism which provides the coupling of light into a thin metal (gold) film [3,4]. By its geometry, the method of TIRE closely resembles the technique of surface plasmon resonance (SPR) with one crucial difference of detecting two parameters of Ψ and Δ in comparison to only one parameter of reflected light

 ISBN: 978-1-61208-145-8

intensity in SPR. Parameters of Ψ and Δ can be defined, respectively, as the ratio of amplitudes and the phase shift between p- and s- components of polarized light:

$$tn\Psi = \frac{A_p}{A_s}, \ \Delta = \varphi_p - \varphi_s \qquad (1)$$

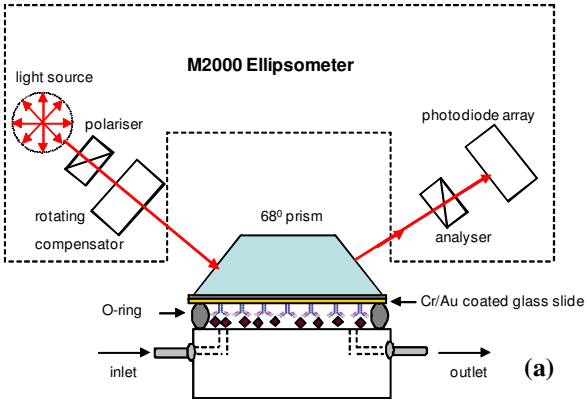

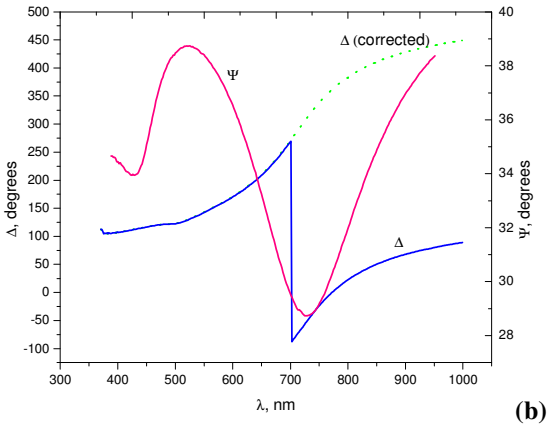

Fig. 1. (a) TIRE experimental set-up. (b) Typical TIRE spectra of Ψ and Δ measured on bare surface of gold. Dotted line shows corrected (by adding 360° to negative values) of Δ(λ) spectrum.

Fig. 1b shows typical spectra of Ψ and Δ; the spectrum of Ψ is very much similar to a traditional SPR curve, while the spectrum of Δ provides a new phase related quantity not available in the SPR method. The method of TIRE often called as "phase SPR" was proved to be much more (at least 10 times) more sensitive than traditional SPR [3].

Two types of TIRE measurements were performed: (i) Single spectroscopic scans which were carried out in the same Trizma-HCl buffer solution (pH 7.5) after completion every adsorption (binding) steps. These measurements were followed by fitting of TIRE spectra to the four-layer model and evaluation of the thickness of the molecular layer adsorbed on the surface of gold. The details and limitations of the fitting procedure were outlined in detail in our early publications, for example [3]; (ii) Dynamic spectral measurements during in which a number of Ψ and Δ spectra were recorded *in-situ* during all adsorption (or binding) stages after a certain time interval; then the time dependences of Ψ and Δ at a selected wavelength were presented and further analyzed for the purpose of studying the kinetics of adsorption and binding processes. Following the procedure outlined in detail in [4-6] the rates of adsorption r_a and de-sorption r_d were found, and the association K_A and affinity K_D constants were found as their ratio:

$$K_A(l/mol) = \frac{k_a}{k_d}, \ K_D(mol/l) = \frac{1}{K_A} = \frac{k_d}{k_a} \qquad (2)$$

The method of atomic force microscopy (AFM) in tapping mode was utilized here for the study of morphology of adsorbed molecular layers and evaluation of the surface roughness of the surface. Nanoscope IIIa instrument (from Digital Technology) was used in a tapping mode with the mean oscillation frequency of 300 kHz, and scanning rate of 1s. The radius of silicon "super sharp" tips (from Veeco) was about 2 nm.

The substrates for TIRE measurements were prepared by thermal evaporation of a Cr layer (3 nm) on microscopic glass slides followed by a Au layer of (25-27nm in thickness) without breaking the vacuum of about 10^{-6} Torr using BOC Edwards Auto-360 vacuum system. The presence of thin Cr layer improves the adhesion of gold to the glass. Depending on the application, Cr/Au coated slides were treated differently to achieve the best adhesion properties for deposition of different molecular layers.

For immobilization of chaperones receptors the technology of electrostatic layer-by-layer deposition [7] was utilized. In this case, in order to increase the negative surface charge on the surface, the gold layer was treated overnight in the 0.1 M solution of mercaptoethyl sodium sulfonate in methanol. Then the layer of polycations (polyallylamine hydrochloride or PAH) was adsorbed on the surface providing a positive charge required for electrostatic adsorption of chaperone receptors such as OEP61.

For deposition of natural chloroplast membranes containing chaperone receptors the method of Langmuir-Schaefer was used. The monolayers of chloroplast were formed on the water surface in the Langmuir trough (NIMA mini trough) and then compressing it to a surface pressure of 20mN/m. The layer of chloroplast was transferred onto silion and gold coated sample by touching the surface with a sample (method of horizontal lifting or Langmuir-Schaefer).

Finally, the samples for deposition of lipid membranes were prepared by treating gold coated samples in cystamine hydrochloride solution (0.1 M solution in methanol, overnight treatment) to increase the positive surface change.

The samples (solutions) of chaperone receptors (OEP61, HOP, HOP2A, TOC64 , chaperones (Hsp70 and Hsp81), α-synuclein in both monomer and oligomer forms, chloroplast membranes, and phospholipids were supplied by our collaborators from Biomedical Research Centre. The methodology of protein preparation was described earlier in detail.

 ISBN: 978-1-61208-145-8

III. RESULTS AND DISCUSSON

A. *Interaction of chaperons with receptors immobilized electrostatically*

Typical results of TIRE single scans (e.g. Δ spectra) taken after each step of adsorption (binding) are shown in Fig. 2a. The calibration curve, e.g. the dependence of the thickness of adsorbed layer vs. the concentration of chaperones, which was obtained by fitting the Δ spectra are given Fig. 2b.

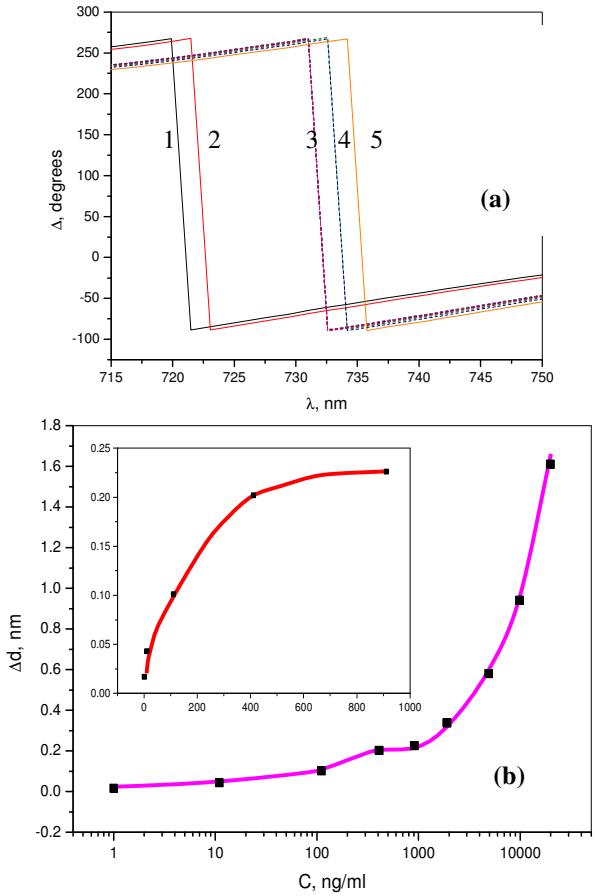

Fig. 2. (a) Typical set of Δ spectra for bare gold surface (1), after adsorption of PAH (2), OEP61 receptors (3) and binding of Hsp70 chaperones of different concentrations: 300 ng/ml (4), and 10μg/ml (5); (b) Time dependence of the thickness increment on the concentration of Hsp70 in solution. Zoomed-in section of the calibration curve at low concentration is given as inset in a linear scale.

The spectral shift in Fig. 2a corresponds to adsorption (or binding) of different molecular layers. Due to a limited resolution of the original Δ spectra, only spectra of two concentrations 300 ng/ml and 10μg/ml of Hsp70 are shown. The correction of Δ spectra allows increasing the resolution; the same effect can be achieved by TIRE data fitting. Typical calibration curve for binding Hsp70 chaperones to OEP61 specific receptors is given in Fig. 2b. As one can see, the effective thickness of adsorbed molecular layer increases and reaches saturation upon binding the chaperones in low concentrations (up to 1 μg/ml) to respective receptors. The maximal values of the response, summarized in Table 1, depend on the type of receptors and chaperones used. It is clear, that OEP61 receptor binds specifically Hsp70 but does not bind non-complementary chaperone Hsp81. At the same time the receptors HOP2A and TOC64 known to be specific to Hsp81 demonstrate binding behavior. However at large concentrations of chaperones exciding 1:1 ratio, a sharp increase of the response is observed for all receptor-chaperone pairs and is most likely caused by non- specific binding.

Table 1. The thickness increment (at saturation) and affinity constants for different pairs of chaperone-receptor.

Receptor	Chaperone	Low concentration		High concentrat.
		δd_{max} (nm)	K_A (l/Mol)	K_A (l/Mol)
OEP61	Hsp70	0.23	$(1.03\pm0.18) \times 10^9$	$(2.08 \pm 0.03) \times 10^6$
	Hsp81	0	n.a.	$(9.47 \pm 1.27) \times 10^4$
HOP2A	Hsp81	0.63	$(4.9 \pm 0.54) \times 10^8$	$(2.46 \pm 0.43) \times 10^4$
TOC64	Hsp81	0.45	$(7.56\pm1.86) \times 10^8$	$(8.34 \pm 0.95) \times 10^5$

The study of binding kinetics using dynamic TIRE measurements allowed the evaluation of the association constant K_A (see an example in Fig. 3). The values of K_A summarized in Table 1 for different receptor-chaperone pairs are typically in the range of 10^8-10^9 (l/mol) which is characteristic for specific receptor-chaperone interaction at low concentrations of chaperones.

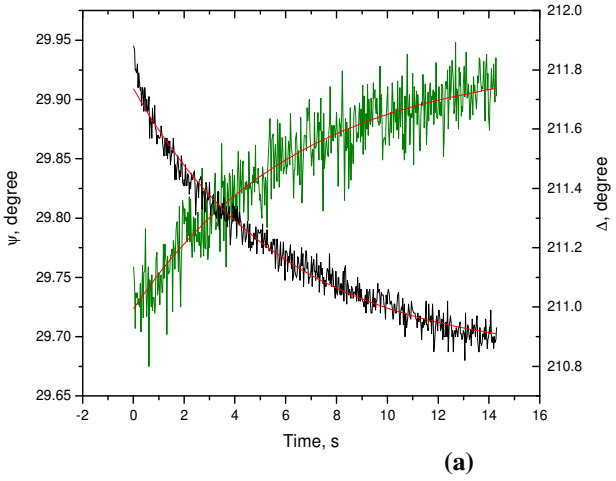

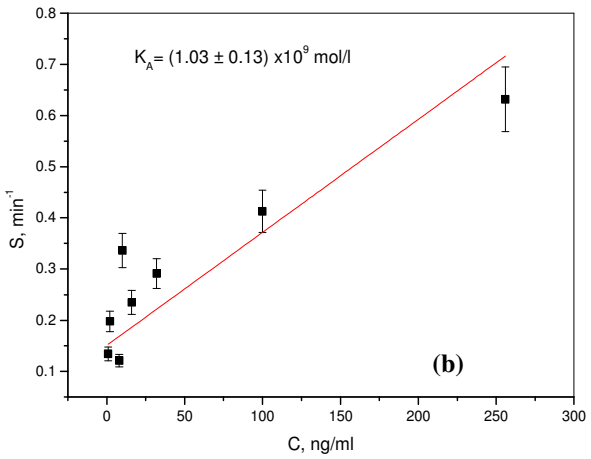

Fig. 3: (a) Typical time dependencies of Ψ and Δ during binding Hsp70 chaperone to OEP61 receptor; (b) Evaluation of the association constant (K_A)

At large concentrations of chaperones, however, much lower values of K_A in the range of 10^4-10^6 (l/mol) were found confirming the earlier suggestion of non-specific interaction. The above quantitative analysis demonstrates a clear separation of specific and non-specific binding.

B. Interaction of chaperones with receptors naturally present in chloroplast membranes

Similar type of TIRE measurements and data analysis were performed for binding chaperones to OEP61 receptors present in natural samples of chloroplast membranes. The results obtained are in line with those presented in the previous section. Binding of Hsp70 at low concentrations from 1ng/ml up to 1μg/ml yields the thickness increase reaching saturation at the level of 0.35 to 0.47nm. At larger concentrations (from 5 to 500 μg/ml) however, the thickness increases sharply again which indicate non-specific binding of chaperones. The study of TIRE kinetics also revealed a huge difference in K_A values (from $8.5 \cdot 10^8$ to 10^9 (l/mol) at low concentrations of chaperones and those in the range of 10^5 to $3 \cdot 10^5$ (l/mol) at high concentrations. Such 4 orders of magnitude difference gives clear separation between specific and non-specific binding of Hsp70 chaperons to OEP61 receptors in chloroplast membranes.

It is interesting that to note that blocking OEP61 receptors with specific antibodies diminish binding of low concentrations of Hsp70 chaperones to almost zero values; the association constant can not be calculated in this case. However, at high concentrations of Hsp70 chaperones non-specific binding appeared again yielding the K_A values of about $8.5 \cdot 10^4$ (l/mol) typical for such processes.

Typical AFM image of a sample of chloroplast membrane after binding Hsp70 chaperones in Fig. 4 shows clearly the aggregates with the height of about 6 nm and horizontal dimensions of about 25 nm. At the same time, AFM images of bare chloroplast membranes revealed rather flat and mostly featureless surface with the mean roughness of about 0.5nm. Considering the enlargement of horizontal features due to a finite tip radius of 2-4 nm, these aggregates could correspond to chaperone molecules of on the surface of a sample.

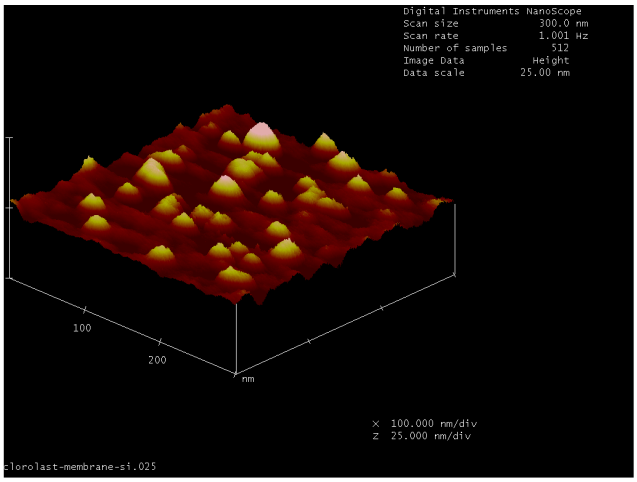

Fig. 4. Typical AFM tapping mode image of chloroplast membrane on silicon surface after adsorption of Hsp70 chaperones.

C. The study of aggregation of α-synuclein in lipid membranes.

Preliminary study of the surface morphology of α-synuclein oligomers adsorbed on the surface of lipid membranes deposited on mica was carried out using AFM. Fig. 5 shows typical AFM images of a lipid layer containing α-synuclein. The features with the horizontal dimensions of 20-30nm may correspond to α-synuclein aggregates or oligomers containing 5 to 6 monomer molecules.

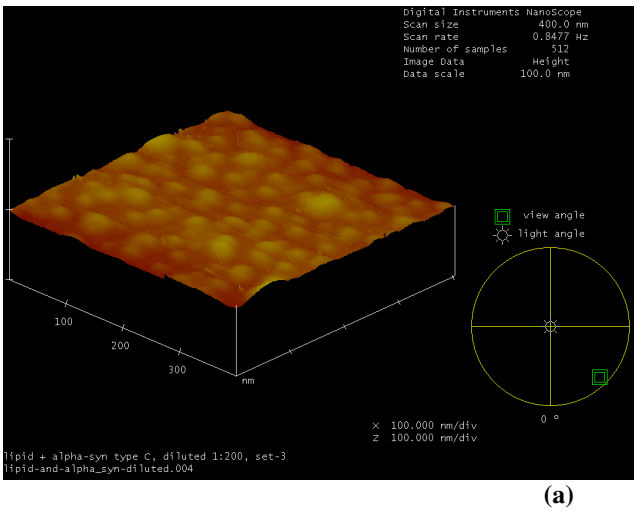

(a)

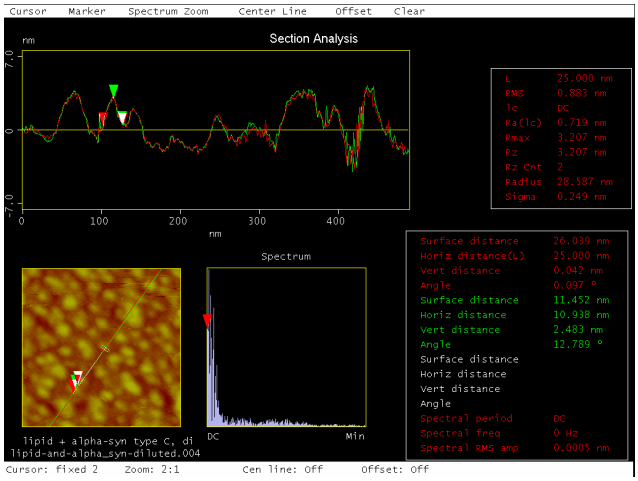

(b)

Fig. 5. Tapping mode AFM images of a lipid layer containing α-synuclein oligomers on mica support: (a) pseudo-3D image; (b) section analysis showing horizontal and vertical dimensions of features along the selected line.

Since the height of these features is in the range of 2 to 3 nm, it can be concluded that α-synuclein oligomers are embedded in the lipid membrane. The roughness analysis of AFM images confirms the above conclusions. It showed that the surface of mica substrates is very flat with the mean roughness of 0.150nm. After deposition of a lipid layer mean roughness has increased to 0.224 nm; the presence of α-synuclein oligomers has resulted in further roughness increase to 1.266 nm.

Further study of α- synuclein monomers and oligomers on the surface of lipids using the methods of AFM and TIRE is currently underway.

IV. CONCLUSIONS AND FUTURE WORK

The optical analytical technique of total internal reflection ellipsometry has found another useful application in the study of protein-protein interaction. The obtained quantified information on the thickness of adsorbed molecular layers and the association constant of binding allows detailed characterization of a novel chaperone receptor extracted from plants in its abilityto bind specifically Hsp70 chaperone. The binding abilities of OEP61 receptors electrostaically adsorbed on the surface and those present naturally in chloroplast membranes were accessed and found to be similar. This confirms one more time that the method of electrostatic layer-by-layer deposition can be successfully used for immobilization of proteins, and elecrostatically immobilized proteins (chaperones this time) retain their functionality. A clear separation of specific and non-specific interactions of proteins was demonstrated in the work for the first time.

A complementary AFM study revealed the presence of proteins (chaperones) on the surface. An important finding of embedding of α-synuclein oligomers into the lipid membrane was confirmed with AFM. Further study of the mechanism of α-synuclein aggregation in lipid membranes using methods of AFM and TIRE is currently underway. This work may shed light into the origin of Parkinson's other neurological diseases.

ACKNOWLEDGMENT

The authors would like to thank EPSRC program "Engineering for Life" for partial financial support of this work.

REFERENCES

[1] W. Wickner, R. Fau- Scheckman, R. Schekman, "Protein translocation across biological membranes". Science, vol. 310 2005, pp. 1452-1456.

[2] S. Qbadou, T. Becker, O. Mirus, I.Tews, J. Soll, E Schleiff, "The molecular chaperone Hsp90 delivers precursor proteins to the chloroplast import receptor Toc64". EMBO J., vol. 25, 2006, pp. 1836-1847.

[3] A. Nabok, A.Tsargorodskaya, "The method of total internal reflection ellipsometry for thin film characterisation and sensing", Thin Solid Films, vol. 516, 2008, pp. 8993-9001.

[4] A. Nabok , A. Tsargorodskaya, A. Holloway, N.F. Starodub, A. Demchenko, "Specific binding of large aggregates of amphiphilic molecules to respective antibodies", Langmuir, vol. 23, 2007, pp. 8485-8490.

[5] A. Nabok , A. Tsargorodskaya, A. Holloway, N.F. Starodub, O. Gojster, "Registration of T-2 mycotoxin with total internal reflection ellipsometry and QCM impedance methods", Biosensors & Bioelectron., vol. 22, 2007, pp. 885-890.

[6] A. Nabok, A. Tsargorodskaya, M.K. Mustafa, I. Szekacs, N.F.Starodub, A.Szekacs, "Detection of low molecular weight toxins using optical phase detection techniques, Sensors and Actuators B, Chemical , 2010 (in press).

[7] "Protein Architecture. Interfacing Molecular Assemblies and Immobilization Biotechnology", Y. Lvov and H. Mohwald (eds.), Marcel Dekker Inc., 2000, p.167.

 ISBN: 978-1-61208-145-8

Optimized Mini Search Coil Magnetometer Suited To Large Bandwidth Applications

M. Timofeeva[1], G. Allegre[1], D. Robbes[1], J. Gasnier[1], S. Flament[2]
GREYC UMRS 6072,
Université de Caen[1] & ENSICAEN[2],
6, Bd Marechal Juin, 14050 CAEN Cedex,
France
sflament@ensicaen.fr

***Abstract*— In the framework of a collaborative work with industry aiming at the development of a robust small size (1 cm^3) large bandwidth magnetometer, a theoretical and experimental comparison of optimized search coils based magnetometers, operating either in the Flux mode or in the classical Lenz-Faraday mode, is presented. The improvements provided by the Flux mode in terms of bandwidth and measuring range of the sensor are detailed.**
A compact original flux mode differential magnetometer is presented and detailed in terms of measurement range, bandwidth and transfer. Theory, SPICE model and measurements are in perfect agreement.

Keywords-search coil sensor; differential magnetometer; transimpedance amplifier; biomedical and geomagnetic measurements; non destructive evaluation

I. INTRODUCTION

This research work takes place in the context of an industrial contract aiming at developing a robust small size (1 cm^3) large bandwidth magnetometer. We investigated benefits provided by using search coils operating in the flux mode, instead of the classical Lenz-Faraday mode. This paper consists in a theoretical and experimental comparative study of sensors specifications (bandwidth, sensitivity, measuring range) depending on the operating mode. To meet the industrial constraints, we fixed a budget (ie we selected a search coil and a low noise differential instrumentation amplifier). The obtained results are providing new solutions for applications requiring large bandwidth like pulsed eddy current non destructive evaluation [1], biomedical or geomagnetic measurements in the [1Hz-1MHz] bandwidth, for which Lenz mode magnetometers are not well adapted.

We present in the Section II the main characteristics of the sensors for the two operating mode. In Section III, we discuss how to optimize the signal conditioning so as to obtain low noise and large bandwidth magnetic field sensors. We show that using search coils in a Flux mode enables a large enhancement of both bandwidth and measuring range of the sensor without reduction of its sensitivity. Section IV is devoted to the study of a coupled search coils sensor in Flux mode and the design of a small size differential magnetometer.

II. SENSORS CHARACTERISTICS AND ELECTRICAL EQUIVALENT MODEL IN FLUX MODE AND LENZ MODE

In the Lenz mode, the search coil generates a voltage signal proportional to the flux time derivative not to the field density B and is connected to a voltage instrumentation amplifier. In the flux mode, the short circuit current, proportional to the field density, is measured. In that case the coil has to be connected to an infinite input admittance transimpedance amplifier [2]. Thus, search coils sensor can be considered as voltage or current source depending of the mode they are being operated. Their Thevenin equivalent voltage generator E_{Th}, Thevenin impedance Z_{Th}, Norton equivalent current generator I_N and Norton equivalent admittance Y_N (Fig. 1) can be calculated as a function of both the flux density B_e to measure and the coil features: inductance L_b, noisy resistance R_b, parasitic capacity C_b and flux equivalent surface S_{eq}, which is defined as the ratio of the collected flux to the flux density and experimentally determined. One gets:

$$E_{Th} = \frac{e_{nRb} - j\omega B_e S_{eq}}{(1 - L_b C_b \omega^2) + j\omega R_b C_b}$$

$$Z_{Th} = \frac{R_b + j\omega L_b}{(1 - L_b C_b \omega^2) + j\omega R_b C_b}$$

$$I_N = \frac{e_{nRb} - j\omega B_e S_{eq}}{R_b + j\omega L_b} \quad \text{and} \quad Y_N = \frac{1}{Z_{th}},$$

where e_{nRb} stands for the Johnson voltage noise source of R_b.

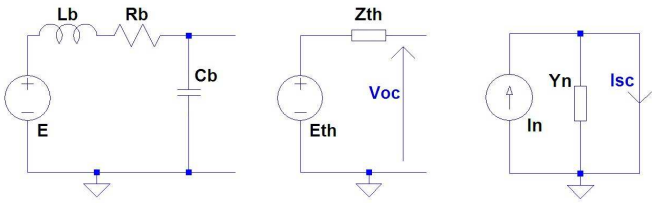

Figure 1: Electrical equivalent circuit of a search coil (a) operating in Lenz mode (b) or Flux mode (c). In Lenz mode the magnetic flux is related to the open circuit voltage Voc whereas in Flux mode, the flux density is related to the short circuit current Isc.

 ISBN: 978-1-61208-145-8

The transfer functions $T_V = \frac{\partial E_{Th}}{\partial B_e}$ and $T_I = \frac{\partial I_N}{\partial B_e}$ and the intrinsic magnetic noise sensitivity, defined as the input noise flux density ($T/\sqrt{Hz}$) that produces a voltage (or current) equal to the contribution of the Johnson noise of the resistance R_b, are plot as a function of the frequency in Fig. 2. One deduces from these figures that in the Lenz mode the bandwidth is intrinsically upper limited by the coil resonant frequency and that the measuring range is inversely proportional to the frequency, whereas in the flux mode the bandwidth is larger, since not affected by the coil resonant frequency, and the measuring range is constant above a low cut off frequency equal to $\frac{R_b}{2\pi L_b}$ [3]. The magnetic sensitivity in the Lenz mode decreases as the frequency and is thus better at high frequency than in the flux mode. In this latter case, the sensitivity is constant over the bandwidth sensor.

As a brief conclusion, intrinsically, the flux mode sensor is well suited to applications requiring a large bandwidth and frequency independent measuring range whereas the Lenz mode magnetometer is rather adapted to applications in limited frequency range and provides in that case a better sensitivity than the Flux mode magnetometer.

Signal amplification is different depending on the operation mode of the search coil. The signal has to be amplified for the Lenz mode by a voltage amplifier, with as high as possible input impedance Z_i, and for the Flux mode Lenz mode by a transimpedance amplifier, with as large as possible input admittance Y_i. These amplifiers can be replaced by their equivalent noisy quadripolar model as shown on Fig. 3 and 4. Such models are very useful for calculating the effective sensitivity of the sensor taking into account the noise due to the amplifier stage and more generally to state the required characteristics of both search coils and amplifier for given sensor specifications in terms of bandwidth and sensitivity.

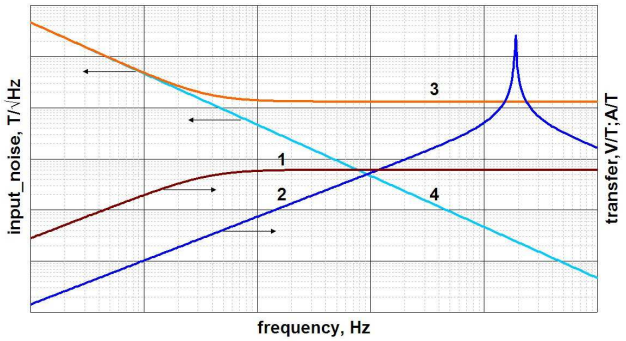

Figure 2: Transfer function and intrinsic sensitivity of search coil magnetometer in Lenz mode (2 & 4) and Flux mode (1 & 3) as a function of the frequency.

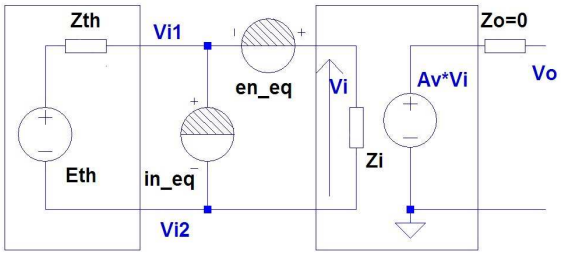

Figure 3: Equivalent electrical model of the Lenz mode magnetometer. Av is the voltage Gain and Z_i the input impedance, which has to be as large as possible.

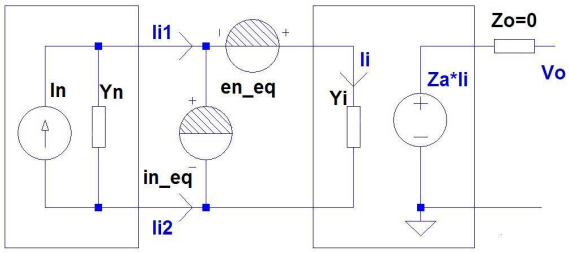

Figure 4: Equivalent electrical model of the Flux mode magnetometer. Za is the amplifier transimpedance and Y_i is the input admittance, which has to be as large as possible.

For signal conditioning, we selected an instrumentation amplifier structure (like the one included in the INA 163 integrated circuit) that we configurated so as to operate either as a voltage amplifier (for the Lenz mode) or as a transimpedance amplifier (for the Flux mode), as shown on Fig. 5 and 6.

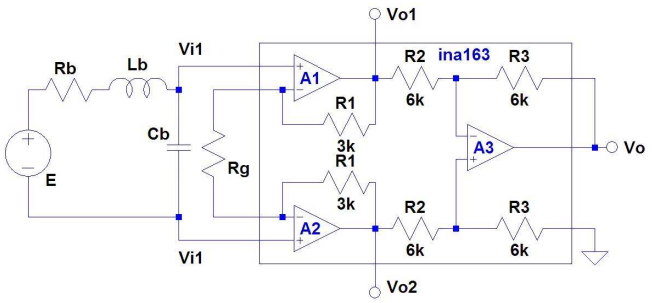

Figure 5: Signal conditioning for Lenz mode magnetometer. Rg is the gain-set resistor.

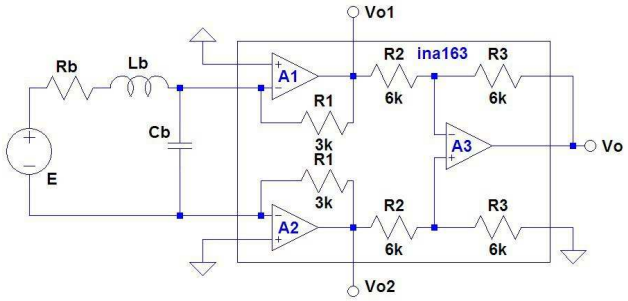

Figure 6: Signal conditioning for Flux mode magnetometer

III. SEARCH COILS SENSORS OPTIMIZATION

The classical Lenz mode magnetometer, which is rather a magnetic flux derivative meter, can be converted into a B field meter by using an integrator output stage [4]. We designed a solution with the integrator embedded inside the amplifier (Fig. 7). The transfer function T_{Lenz} of this Lenz mode B field meter is in that case given by:

$$T_{Lenz} = \frac{\partial V_o}{\partial B_e} = \frac{j\omega S_{eq}}{1 - L_b C_b \omega^2 + j\omega R_b C_b}\left(1 + \frac{2R_1}{Z_g}\right)$$

$$\text{where } Z_g = \frac{R_{g1}R_{g2}}{R_{g1}+R_{g2}} \cdot \frac{1 + j\omega\tau_{g1}}{1 + j\omega\tau_{g2}}$$

$$\text{and } \tau_{g1} = \frac{L_g}{R_{g1}}, \qquad \tau_{g2} = \frac{L_g}{R_{g1}+R_{g2}}$$

The magnetometer low cut off frequency can be adjusted by proper choice of integrator parameters. Nevertheless, the magnetometer bandwidth is still limited by the search coils resonance and the measuring range is not enlarged by the integrator stage.

For the standard Flux mode magnetometer, the low cut off frequency is fixed by the search coil parameter. This low cut off frequency can be significantly reduced by including a compensation stage in the transimpedance amplifier as described in Fig. 8.

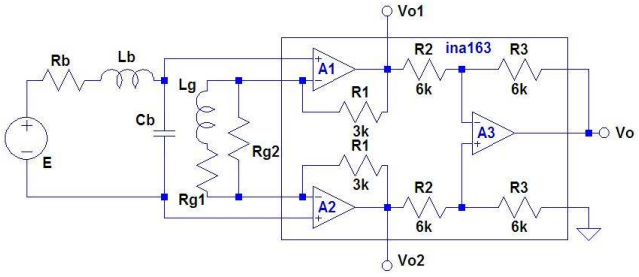

Figure 7: Lenz mode B field meter with embedded integrator stage (Lg, Rg1 and Rg2), which replaces the gain-set resistor Rg in Fig. 5.

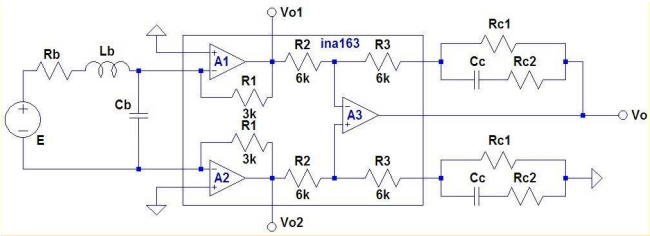

Figure 8: Flux mode magnetometer with compensation stage (Rc1, Rc2 and Cc) for bandwidth enhancement at low frequency.

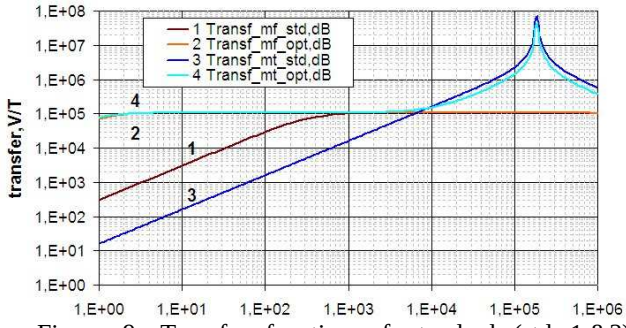

Figure 9: Transfer function of standard (std 1 &3) magnetometer and optimized (opt 2 & 4) magnetometer.

The function transfer T_{Flux} writes:

$$T_{Flux} = \frac{\partial V_o}{\partial B_e} = \frac{j\omega S_{eq}}{R_b(1 + j\omega\tau_b)} \cdot \frac{R_1}{R_2} \cdot \left(R_3 + \frac{R_{c1}(1 + j\omega\tau_{c2})}{(1 + j\omega\tau_{c1})}\right)$$

$$\text{where } \tau_b = L_b/R_b, \quad \tau_{c1} = C_c(R_{c1}+R_{c2}), \quad \tau_{c2} = C_c R_{c2}$$

Using the compensation stages described ahead, whatever is the mode of the magnetometer, one can obtained the same cut off low frequency and the same transfer value in the magnetometer bandwidth. The Lenz mode magnetometer bandwidth stays nevertheless limited by the search coil resonant frequency.

IV. DIFFERENTIAL MAGNETOMETER BASED ON COUPLED SEARCH COILS

A significant reduction of common mode signals as well as parasitic signals sensed in connecting wires is usually achieved by the use of a differential structure. An original flux mode differential magnetometer is presented in Fig. 10. The Norton equivalent model and the transfer function of this magnetometer can be calculated as follows:

$$I_N = \frac{(e_{nRb1} + e_{nRb2}) - 2j\omega B_e S_{eq}}{2(R_b + j\omega(L_b + M))}$$

$$\frac{1}{Y_N} = \frac{2(R_b + j\omega(L_b + M))}{(1 - (L_b + M)C_b\omega^2) + j\omega R_b C_b}$$

$$T_{Diff} = \frac{\partial V_s}{\partial B_e} = \frac{2R_1R_3}{R_b R_2} \cdot \frac{pS_{eq}}{1 + \tau_{bd}p}$$

$$\text{where } \tau_{bd} = \frac{L_b + M}{R_b} \text{ and } M = k\sqrt{L_{b1}L_{b2}}$$

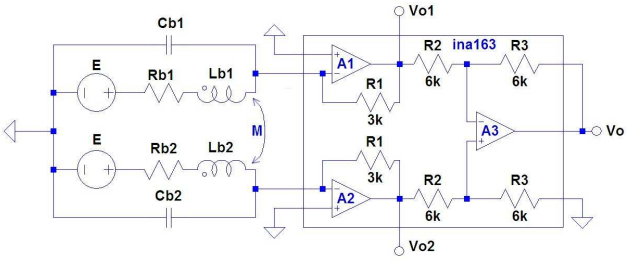

Figure 10: Flux mode differential magnetometer structure

The low cut off frequency can be significantly reduced by including the compensation stage described in Section III. The theoretical study was compared to experimental measurements and calculations using a SPICE simulator. All results are in very good agreement as shown on Fig. 11.

The search coils coupling leads to correlation of the voltage noise sources of the two input amplifiers A_1 and A_2 of the instrumentation amplifier and thus to noise reduction of the sensor [5]. The coupling allows also a significant size reduction of the magnetometer since the coils can be wounded together on the same magnetic coil. In order to check the validity of the theoretical study, experimental measurements and calculations using a SPICE simulator were performed. All results fits very well as shown on Fig. 12.

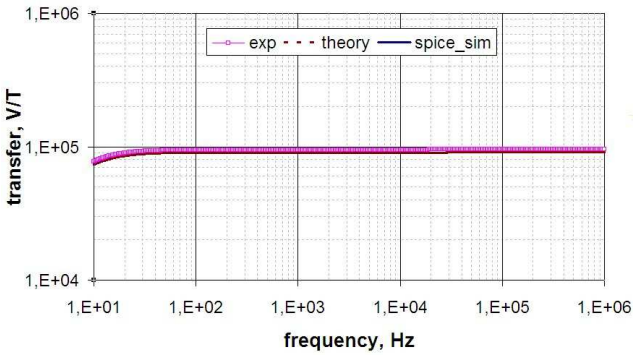

Figure 11: Transfer function of the differential Flux mode magnetometer. Theoretical, experimental and SPICE simulation curves are in very good agreement. Search coils features are: $R_{b1} = R_{b2} = 45$ohms, $L_{b1} = L_{b2} = 4.7$mH, $Cb_1 = Cb_2 = 60$pF, $S_{eq} = 0.152 m^2$, Volume = 0.83 cm^3, intrinsic search coil transfer equal to 28A/T and search coil low cut off frequency equal to 1,5kHz. The compensation stage of the magnetometer (see Section III) was designed so as to obtain an 8 Hz low cut off frequency.

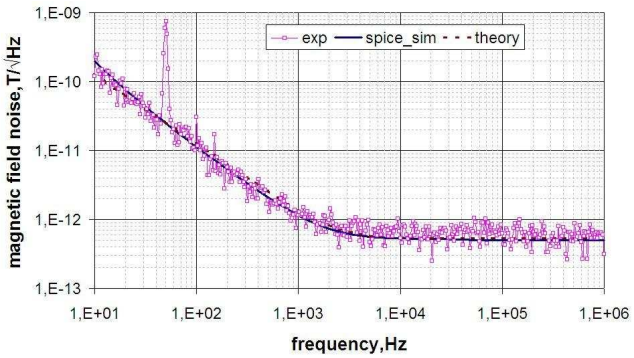

Figure 12: Flux noise sensitivity of the differential Flux mode magnetometer. Theoretical, experimental and SPICE simulation curves are in very good agreement. Search coils features are the same as in Fig. 11.

V. CONCLUSIONS AND PERSPECTIVES

A detailed comparison of transfer function and noise sensitivity of search coils magnetometer operating either in Lenz mode of Flux mode was presented. We explained how to optimize both magnetometers and showed that the Flux mode provides a transfer function, which can be set constant over a bandwidth ranging from 1 Hz to 1 MHz, larger than what can be achieved in Lenz mode. The Flux mode also provides a constant measuring range over the full bandwidth, which is not the case for Lenz mode magnetometer. Such features are very interesting for applications requiring a large bandwidth and a good sensitivity over the whole bandwidth. An original differential flux mode magnetometer, which is much more compact than classical Lenz mode search coil differential magnetometer, was proposed and studied in details, namely in terms of transfer function and noise. Theoretical analysis, SPICE simulations and experimental measurements are in very good agreement.

REFERENCES

[1] C. Dolabdjian, L. Perez, V. O . De Haan and P. A. De Jong, ''Performance of Magnetic Pulsed-Eddy-Current System Using High Dynamic and High Linearity Improved Giant MagnetoResistance Magnetometer'', IEEE Sensors Journal, vol 6, N°6, pp. 1511-1517 (2006)

[2] M. Timofeeva, G. Allègre, S. Flament and D. Robbes, ''Des lois de l'induction aux théorèmes de thévenin et Norton'', CETSIS 2010

[3] R. J. Prance, T. D. Clarke and H. Prance, ''Compact broadband gradiometric induction magnetometer system'', Sensors and actuators **76** (1999), pp. 117-121

[4] S. Tumanski, "Induction coil sensors-a review", Measurement Science and Technology, **18** (2007), pp. R31-R46

[5] M. Timofeeva, G. Allegre, D. Robbes, J. Gasnier and S. Flament, "Input noise model of differential amplification structure and application to magnetic sensitivity evaluation of search coils magnetometers", submitted to IEEE sensors 2011.

 ISBN: 978-1-61208-145-8

Smart and Intelligent Optoelectronic Sensor Systems: OEM Design Approach

Sergey Y. Yurish[1, 2]
[1]Technology Assistance BCNA 2010, S. L.
[2]International Frequency Sensor Association (IFSA)
Barcelona, Spain
e-mail: SYurish@sensorsportal.com

***Abstract*—Light-to-frequency converters are widely used in various optoelectronic sensor systems. However, a further frequency-to-digital conversion is a bottleneck in such systems due to a broad frequency range of light-to-frequency converters. This paper describes an effective OEM design approach, which can be used for smart and intelligent sensor systems design. The design is based on novel, multifunctional integrated circuit of Universal Sensors & Transducers Interface especially designed for such sensor applications. Experimental results have confirmed an efficiency of this approach and high metrological performances.**

Keywords-optical sensor; smart sensor system, light-to-frequency converter, USTI, intelligent sensor system, IEEE 1451

I. INTRODUCTION

Optoelectronic sensors are widely used in various applications such as medical, automobile, environmental, bio-chemical, etc. Many of them are based on integrated light-to-frequency converters, which convert a light intensity to quasi-digital (frequency or duty-cycle) format for direct connection to a microcontroller, DSP or interfacing with a PC. In comparison with analog output (voltage or current), the frequency signal as an informative parameter of sensor's output has a lot of advantages, namely: a high noise immunity, high reference accuracy, wide dynamic range, multiparametricity, simplicity of coding, multiplexing, interfacing and integration, etc.

Modern light-to-frequency converters [1] have a broad frequency range: from part of Hz to 1.6 MHz (Table 1). Nevertheless a simple frequency-to-digital conversion (based on classical methods for frequency measurements) can be performed by any low-cost microcontroller, a wide dynamic frequency range of such converters brings as usually, many design problems. In order to get reasonable or high metrological performances of designed optical sensor systems, the frequency-to-digital conversion should be based on advanced methods for frequency measurements. Such methods must have a constant quantization relative error in a whole broad frequency range, scalable resolution, non-redundant conversion time and a possibility to measure frequency, which exceeds a reference frequency: $f_x > f_0$ in order to design a sensor systems with a reasonable power consumption.

Existing on the modern sensor market digital light sensors with embedded ADCs as usually have a slow conversion time, for example, the embedded 16-bit ADC of light sensor from Intersil (ISL29015) has the integration time 45-90 ms [2]; the ADC from Maxim MAX9635 has the conversion time 97-107 ms [3]. Such sensors can be used for proximity or ambient light applications, but it can not be used for light sensing applications, in which a conversion speed is a critical parameter.

TABLE I. LIGHT-TO-FREQUENCY CONVERTERS' PERFORMANCES

Sensor (LFC)	Performances		
	Output Frequency Range	*Spectral Response, nm*	*Non-linear FS Error, %*
TAOS (USA)			
TSL230	0.4 Hz … 1.1 MHz	350…1000	0.2
TSL235	0.4 Hz … 500 kHz	350…1000	0.2
TSL237	2 Hz … 600 kHz	350…1000	1
TSL245	0.4 Hz … 500 kHz	850…1000	0.2
Hamamatsu (Japan)			
S9705	0 Hz … 1 MHz	300…1000	3
Melexis (Belgium)			
MLX75304	1 Hz … 1.6 MHz	500…1000	N/a

N/a – not available.

The main aim of these research and development was to propose a universal design solution for all existing light-to-frequency converters in order to eliminate all mentioned above design problems, and introduce intelligent and smart features for various sensor systems, which can be realized in different technologies: hybrid, standard CMOS technology, System-on-Chip (SoC) or/and System-in-Package (SiP).

This paper is divided into four main parts. The first part describes a design approach for various optical sensor systems based on a light-to-frequency converter (LFC) and Universal Sensors and Transducers Interface circuit (USTI). The description includes the system design in term of OEM hardware and software. The second part devotes to experimental investigation of designed optoelectronic sensor system prototype based on the light-to-frequency converter S9705 from Hamamatsu [4]. The third part includes an experimental determination of main metrological performances of designed sensor system. The last part of the paper provides conclusions and future research directions.

 ISBN: 978-1-61208-145-8

II. SMART SENSOR SYSTEM DESIGN

A. *Universal Sensors and Transducers Interface*

The proposed solution is based on the developed by the author USTI integrated circuit. In comparison with the developed earlier and introduced on the modern market in 2004 and 2007 Series of Universal Frequency-to-Digital Converters UFDC-1 and UFDC-1M-16 respectively [5, 6] this new IC has extended frequency range up to 9 MHz without prescaling and 144 MHz with prescaling, reduced relative error up to ±0.0005 %, increased functionality and decreased conversion time. It is based on the patented modified method of the dependent count for quick and precision measurement of frequency and period of electrical signals [7]. This 2-channel IC has three popular serial interfaces: RS232, I^2C and SPI, which are widely used in various sensor systems. It contains of three main blocks: measuring unit, communication unit and time-to-digital converter (TDC). Only one external component – a 20 MHz quartz crystal oscillator should be used as a reference. The measuring unit releases 2-channel measurements of various frequency-time parameters of electrical signals with programmable relative error form 1 % to 0.0005 %: frequency, period, duty-cycle, phase shift, time intervals, duty-off factor, pulse number, frequency (period) deviation, frequencies or periods ratios and differences, etc. The communication unit supports three popular serial interfaces, such as RS232 (master and slave communication modes with programmable baud rate), SPI and I^2C (slave communication mode). The TDC is used in parameter-to-digital converter for a direct interfacing of capacitive, resistive and bridge sensing elements to USTI.

The USTI can work in RS232 master communication mode. In this mode, neither microcontroller nor PC or DAQ system are necessary to control this IC. It will continuously generate measuring results on its output.

B. *Sensing Element*

The S9705 is a CMOS photo IC combining a current-to-frequency converter and photodiode and outputs an oscillating frequency (duty ratio 50 %) proportional to input light intensity incident in the photodiode [4].

The CMOS level digital output allows direct connection to the USTI. The sensing element has a wide dynamic range, spectral response (see Table 1), and light intensity can be easy measured by the USTI. The light-to-frequency converter S9705 and USTI are shown in Figure 1, and circuit diagram of optoelectronic sensor system example based on these components is shown in Figure 2.

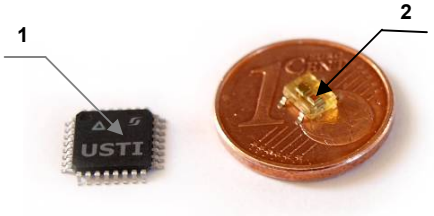

Figure 1. USTI (1), and light-to-digital converter S9705 (2).

Other optical sensors, for example, colour sensor TCS230 from TAOS (USA) [1] or reflective colour sensor OPB780 from OPTEK Technology [8] can also be interfaced by the same manner. Two frequency output sensors can be connected to the USTI at the same time.

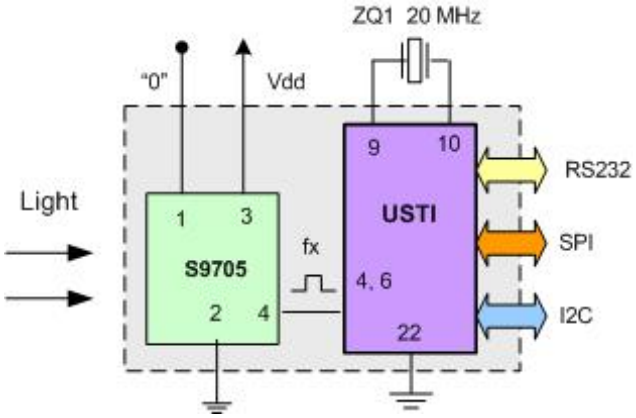

Figure 2. Circuit diagram of optoelectronic sensor system.

A software example for the RS232 interfacing slave connection mode for two optical sensors (light sensor S9705 and colour sensor OPB780) is shown in Figure 3.

```
>A02      ;Set the relative error 0.25 %
>M00      ;Set up a frequency measurement mode in the 1st channel
>S        ;Start a frequency measurement (light sensor)
>C        ;Check the measurement status ('r'-ready, 'b' -in progress
>R        ;Read a result of frequency measurement in Hz
>462987.345

>M0E      ;Set  up a frequency measurement mode in the 2nd channel
>S        ;Start a frequency measurement (colour sensor)
>C        ;Check the measurement status ('r' -ready, 'b'-in progress
>R        ;Read a result of frequency measurement in Hz
>37005.0119
```

Figure 3. Commands for RS232 communication mode at light and colour measurements by the USTI.

The command 'A02' sets the relative error for frequency-to-digital conversion [9] and should be use only once. The relative error must be in ten times less (or at the least, in 5 times less) than the sensor's error in order to be neglected. Appropriate command 'M' sets the frequency measurement mode in the 1st and 2nd channels. The command 'S' starts measurement in appropriate channel. The command 'C' checks the measurements status and returns the value 'b' if the measurement in progress or the value 'r' if the measuring results is ready. The last command 'R' reads results. The use of 'C' command is very important at low frequencies measurements. In opposite side, there is a risk to get a previous result instead of the new one.

Any terminal software can be used with the USTI in RS232 slave communication mode (for example, Terminal V1.9b Window [10]). The following options should be selected for this software: appropriate number of serial port, baud rate – 2400; data bits – 8; Parity – none; Stop Bits – 1; Handshaking- none. For data acquisition, the LabView software or similar can be easily used.

 ISBN: 978-1-61208-145-8

C. Conversion Time

The conversion rate of USTI is determined by the method of frequency measurement [7] and can be calculated according the following equation:

$$\begin{cases} t_{conv} = \dfrac{1}{f_x} \quad if \quad \dfrac{N_\delta}{625\ kHz} \prec T_x \\ t_{conv} = \dfrac{N_\delta}{625\ kHz} + (0 \div T_x) \quad if \quad \dfrac{N_\delta}{625\ kHz} \geq T_x \end{cases}, \qquad (1)$$

where $N_\delta = 1/\delta$ is the number proportional to the required programmable relative error δ; $T_x = 1/f_x$ is the period of converted frequency, f_0=625 kHz is the internal reference frequency of USTI.

A measurement time T_{meas} for the USTI includes three main components: conversion rate (t_{conv}), communication (t_{comm}) time and calculations (t_{calc}) time:

$$T_{meas} = t_{conv} + t_{comm} + t_{calc} \qquad (2)$$

All these components can be calculated by the same way as was described in [6]. For example, the communication time for a slave communication mode (RS232 interface) can be calculated according to the following equation:

$$t_{comm} = 10 \cdot n \cdot t_{bit}, \qquad (3)$$

where t_{bit} is the time for one bit transmitting; n is the number of bytes (n=13…24 for ASCII format).

The communication time for SPI interface should be calculated as:

$$t_{comm} = 8 \cdot n \cdot \frac{1}{f_{SCLK}}, \qquad (4)$$

where f_{SCLK} is the serial clock frequency, which should be chosen for the USTI in the range from 100 to 500 kHz; n=12…13 is the number of bytes. The number n is dependent on measurement result format: BCD (n=13) or binary (n=12). The communication standard mode's speed for the I^2C interface can be determined according to the same equation (4), where instead of f_{SCLK} the serial clock frequency f_{SC} should be used, which equals to 100 kHz for the USTI; n=12…13 is the number of bytes for measurement result: BCD (n=13) or binary (n=12).

The calculation time depends on operands and is as usually t_{calc} ~ 3.6 ms.

Due to non-redundant conversion time for the modified method of the dependent count [7] it is possible to obtain the conversion time, less than in digital output optical sensors mentioned above. The same is also true for the design approach, when analog light sensor (with voltage output), voltage-to-frequency converter and USTI are used to build a sensor system. The conversion time can be decreased in 3-10 times in comparison with existing standard integrated digital sensors, mentioned above [2, 3].

D. Intelligent Features

One of the intelligent functions of modern sensor system is so-called self-identification. The USTI can contain a Transducer Electronic Data Sheet (TEDS) according to the IEEE 1451 standard in its memory. A possible TEDS for optical sensor system is shown in Table 2. This TEDS must also contain a value of programmable relative error for the frequency-to-digital conversion (USTI relative error).

TABLE II. TEDS FOR OPTICAL FREQUENCY OUTPUT SENSOR

TEDS Structure	Example of Light-to-Frequency Converters	
Basic TEDS	Manufacturer ID	19
	Model ID	9705
	Version letter	S
	Serial number	00639F
Standard and Extended TEDS (fields will vary according to transducer type)	Calibration date	21 September 2010
	Spectral Response	300-1000 nm
	Frequency output minimal	0.1 Hz
	Frequency output maximal	1 MHz
	Linearity	±3 %
	USTI's relative error	±0.25 %
User Area	Sensor location	A18-2
	Calibration due date	21 September 2011

The USTI supports three functions of smart transducers: high accurate frequency (time)-to-digital conversion, TEDS storage in the flash memory and communications.

III. EXPERIMENTAL RESULTS

The aim of experimental investigation was to determine main metrological performances of the designed optical sensor system based on the light-to-frequency converter S9705 (Hamamatsu, Japan) and USTI IC. The measuring set-up is shown in Figure 4.

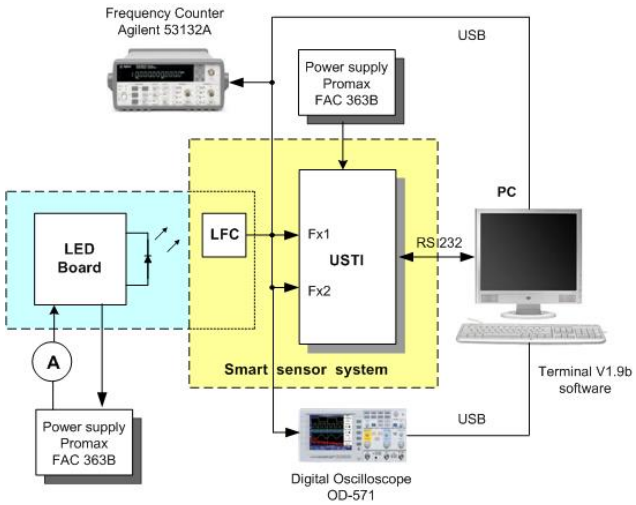

Figure 4. Measuring set-up.

Preliminarily, the USTI has been calibrated at laboratory temperature range (+25.3 ^{0}C to +26.4 ^{0}C) in order to eliminate additional systematic error due to quartz oscillator trimming inaccuracy (calibration tolerance) and a short term temperature instability [11]. The USTI has been connected to a PC, where terminal software Terminal v1.9b was running.

The light-to-frequency converter S9705 has mounted on a LED evaluation board together with a white light diode, the light intensity of which was set-up with the help of current source (Promax FAC 363B) and changing by a potentiometer with 25 μA step. The current through this diode was measuring by an amperemeter (Figure 4).

The circuit diagram and photo of the LED evaluation board are shown in Figures 5 and 6 respectively.

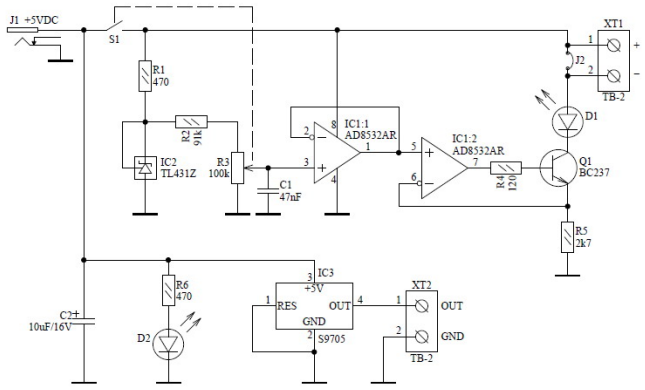

Figure 5. Circuit diagram of LED evaluation board.

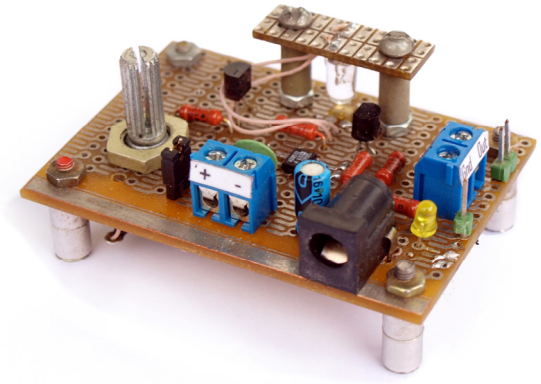

Figure 6. LED evaluation board.

The output of LFC was directly connected to the USCI. The frequency counter Agilent 53132A was used for frequency measurements in parallel with the USTI, and digital oscilloscope - for wave form visualization at LFC's output/USTI input. The frequency measurements have made for minimal and maximal possible frequencies of LED evaluation board: 5 Hz and 462 kHz respectively for both cases: without and with Schmidt trigger (74HC14D). Oscillograms of investigated sensor's output signals are shown in Figures 7-12.

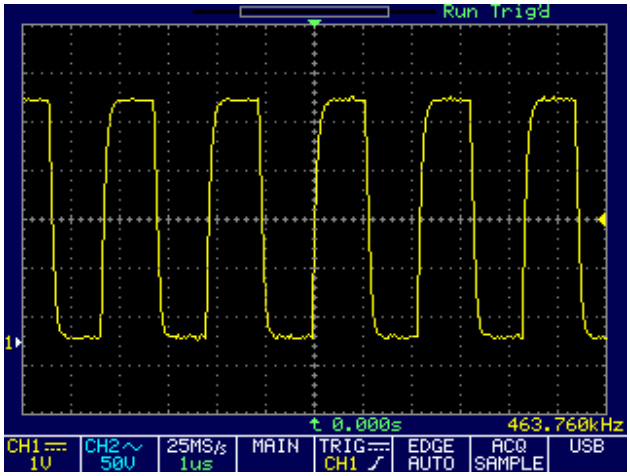

Figure 7. Oscillograms of maximal frequency signal (~ 463 Hz).

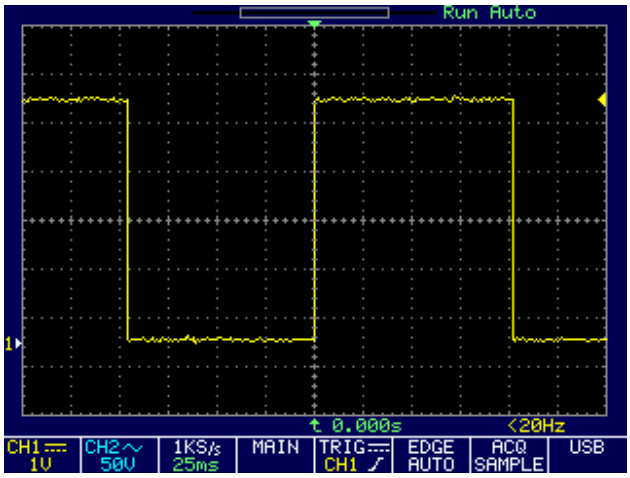

Figure 8. Oscillograms of minimal frequency signal (~ 5 Hz).

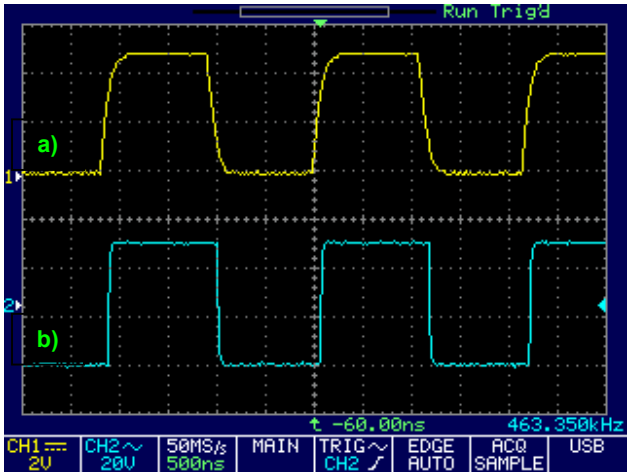

Figure 9. Oscillograms at USTI input for frequency signal ~463 Hz: without Schmidt trigger (a) and with Schmidt trigger (b).

 ISBN: 978-1-61208-145-8

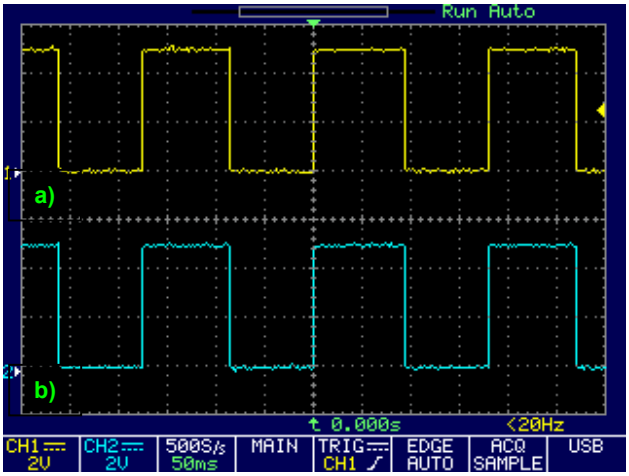

Figure 10. Oscillograms at USTI input for frequency signal ~5 Hz: without Schmidt trigger (a) and with Schmidt trigger (b).

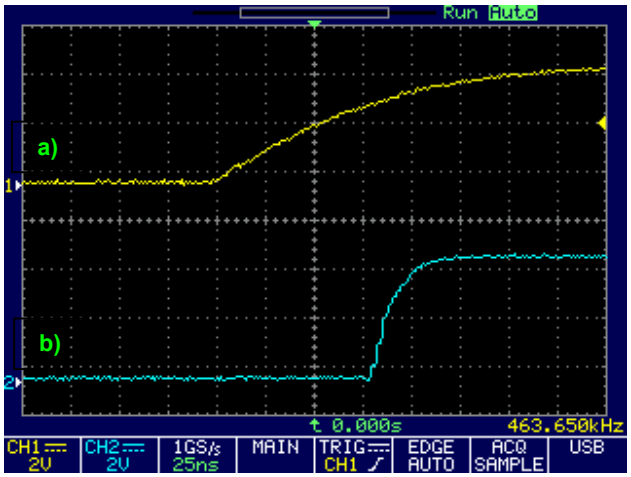

Figure 11. Front of 463 Hz input pulse signal: without Schmidt trigger, rise time 110 ns (a) and with Schmidt trigger, rise time 24 ns (b).

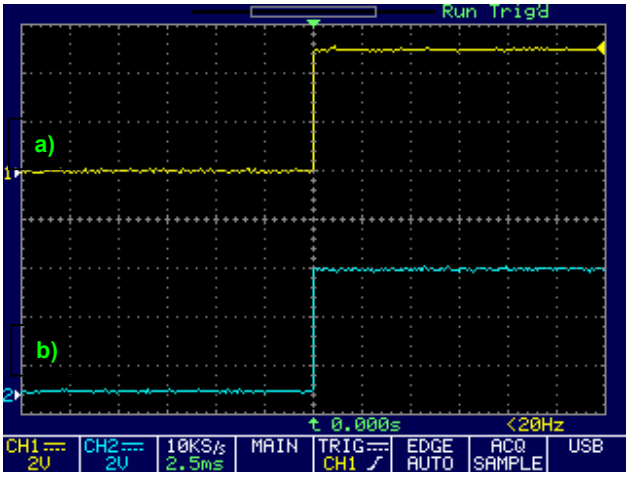

Figure 12. Front of 5 Hz input pulse signal: without Schmidt trigger, rise time 80 µs (a), and with Schmidt trigger, rise time 70.7 µs (b).

The dependence of LFC's output frequency on current through the white light diode on the LED evaluation board is shown in Figure 13.

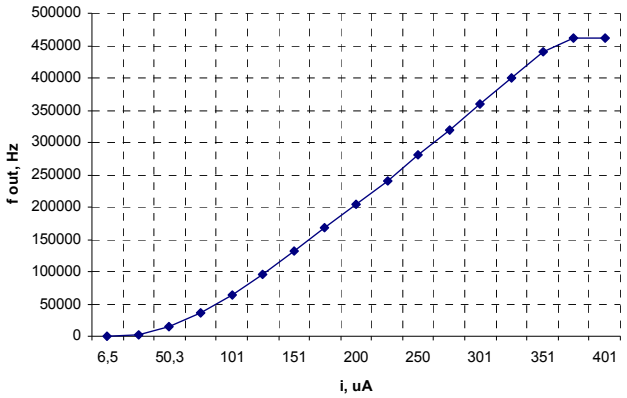

Figure 13. Output frequency vs. current through a white light diode.

Each of investigated frequencies where measured 60 times and classical statistics was used for results processing. Measuring results for maximal and minimal frequencies for both: without and with Schmidt trigger are shown in Figure 14 and 15.

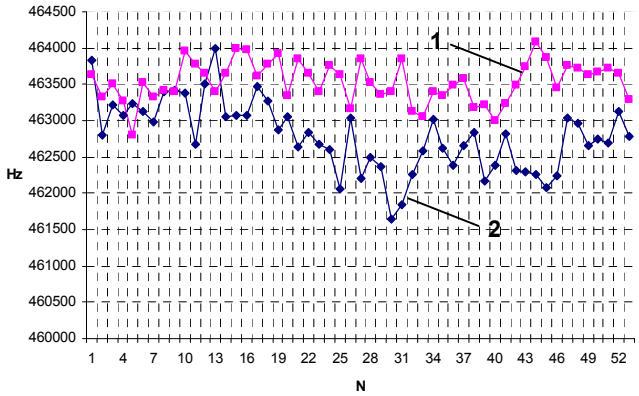

Figure 14. Measuring results for maximal frequency ~ 463 Hz: with Schmidt trigger (1), without Schmidt trigger (2).

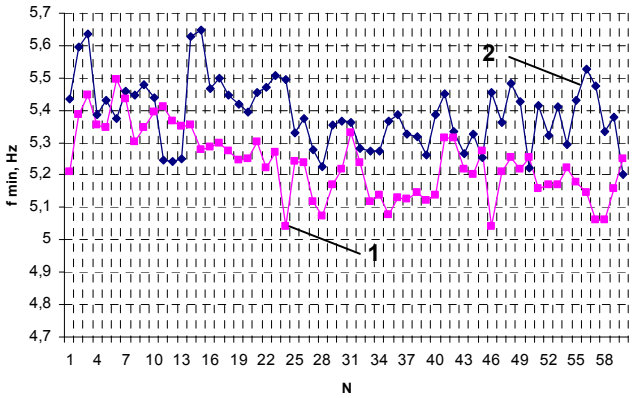

Figure 15. Measuring results for minimal frequency ~ 5 Hz: with Schmidt trigger (1) and without Schmidt trigger (2).

 ISBN: 978-1-61208-145-8

The χ^2 test for goodness of fit test was applied to investigate the significance of the differences between observed data in the histograms and the theoretical frequency distribution for data from the Gaussian distribution law.

The number of equidistant classes was calculated according to the following equation:

$$k = 1.9 \times N^{0.4}, \quad (5)$$

where N is the number of measurements.

At probability P = 97 %, and 6 equidistant classes k=6, the hypothesis of Gaussian distribution law can be accepted for all sets of measurement data. The statistical characteristics are adduced in Table 3 and 4.

TABLE III. STATISTICAL CHARACTERISTICS (AT 463 KHZ FREQUENCY MEASUREMENT)

Parameter	463 kHz	
	Without Schmidt trigger	**With Schmidt trigger**
Number of measurements, N	53	60
Minimum f_x (min)	461653.265	464151.555
Maximum f_x (max)	463991.336	0.0062
Sampling Range, f_x (max) - f_x (min)	2338.0705	1354.2603
Arithmetic Mean	462788.685	463572.681
Variance	234229.738	6.6E-0009
Standard Deviation	483.9729	283.4972
Coefficient of Variation	956.2286	1635.1932
Confidence interval for arithmetic mean at P=97 %	462644.42< f_x < 462932.95	463493.257 < f_x < 463652.105
Relative error, %	0.014	0.16
χ^2 – test (S) at: k=6; P = 97 % χ^2_{max} = 8.9	1.7272	2.5423
Hypothesis about Gaussian distribution	Accepted	Accepted

As it is shown from the tables, the Schmidt trigger does not increased accuracy of frequency-to-digital conversion.

IV. CONCLUSIONS

The proposed design approach for optoelectronic sensor systems based on the USTI IC gives a unique opportunity to create various OEM sensor systems with high metrological performances including intelligent feature such as self-identification. Taking into account, that many semiconductor sensors and the USTI IC are made according to CMOS standard technological processes, different sensor systems and digital sensors can be realized in various existing technologies: hybrid, system-in-chip and system-in-package.

Since 2011 the USTI is available on the modern market from Technology Assistance BCNA 2010 S. L., Spain [12].

ACKNOWLEDGMENT

This research and development was funded by the European Commission in the frame of Marie Curie Chairs Excellence (EXC) project MEXT-CT-2005-023991 Smart Sensors Systems Design (SMARTSES) and supported by International Frequency Sensor Association (IFSA).

TABLE IV. STATISTICAL CHARACTERISTICS (AT 5 HZ FREQUENCY MEASUREMENT)

Parameter	5 Hz	
	Without Schmidt trigger	**With Schmidt trigger**
Number of measurements, N	60	60
Minimum f_x (min)	5.2014	5.041
Maximum f_x (max)	5.6466	5.4959
Sampling Range, f_x (max) - f_x (min)	0.4452	0.454
Arithmetic Mean	5.3899	5.236
Variance	0.0109	0.1071
Standard Deviation	0.1045	0.0001
Coefficient of Variation	51.577	48.907
Confidence interval for arithmetic mean at P=97 %	5.3606 < f_x < 5.4192	5.206 < f_x < 5.266
Relative error, %	0.54	0.57
χ^2 – test (S) at: k=6; P = 97 % χ^2_{max} = 8.9	6.6726	1.8498
Hypothesis about Gaussian distribution	Accepted	Accepted

REFERENCES

[1] List of Optical Sensors Manufacturers at Sensors Web Portal: http://www.sensorsportal.com/HTMLL/SENSORS/OptoSens_Manufacturers.htm

[2] Integrated Digital Ambient Light Sensor and Proximity Sensor ISL29015, Datasheet, Intersil, 2008.

[3] Industry's Lowest-Power Ambient Light Sensor with ADC, MAX9635, Maxim, 2010.

[4] Light-to-frequency Converter Photo IC S9705, Hamamatsu, 2007.

[5] S. Y. Yurish, N. V. Kirianaki and R. Pallas-Areny, "Universal Frequency-to-Digital Converter for Quasi-digital and Smart Sensors: Specifications and Applications", Sensor Review, vol. 25, No.2, April 2005, pp.92-99.

[6] S.Y.Yurish, "High-Speed Universal Frequency-to-Digital Converter for Quasi-Digital Sensors and Transducers", Sensors & Transducers, vol. 80, issue 6, June 2007, pp. 1225-1229.

[7] S.Y. Yurish, "Novel Modified Method of the Dependent Count for High Precision and Fast Measure-ments of Frequency-Time Parameters of Electric Signals", Proc. of 2008 IEEE International Instru-mentation & Measurement Technology Conference - I²MTC, Victoria, Vancouver Island, British Co-lumbia, Canada, 12-15 May 2008, pp. 876-881.

[8] Reflective Colour Sensor Assembly OPB780Z, Optec Technology, Inc., USA, 2009.

[9] Universal Sensors and Transducers Interface (USTI). Specification and Application Note, Technology Assistance BCNA, 2010, S.L., Spain, 2011.

[10] Terminal V1.9b software for Windows: http://www.sensorsportal.com/DOWNLOADS/Terminal.exe

[11] S. Y. Yurish, "Advanced automated calibration technique for Universal Sensors and Transducers Interface IC", Proc. IEEE International Instrumentation and Measurement Technology Conference (I²MTC 2009), May 2009, pp.402-405.

[12] http://www.techassist2010.com/

 ISBN: 978-1-61208-145-8

Energy Efficient Embedded Wireless System Used For Localisation In Indoor Environments

Nicolas Fourty
LCIS, Université de Grenoble 2
IUT de Valence ; F-26901 Valence, France
nicolas.fourty@iut-valence.fr

Yoann Charlon, Eric Campo
CNRS ; LAAS ; 7 avenue du Colonel Roche, F-31077 Toulouse Cedex 4, France
Université de Toulouse ; UPS, INSA, INP, ISAE, UT1, UTM, LAAS ; F-31077 Toulouse Cedex 4, France
charlon@laas.fr, campo@laas.fr

***Abstract*—The paper presents an embedded telemetry system used in combination of localisation algorithm for a precise indoor pedestrian localisation. The system is based on the association of two wireless technologies: ultrasonic and 802.15.4. The novelty is the use of 802.15.4 RF signal to give the reference starting time of the ultrasonic emission. A ToA (Time of Arrival) measurement provides the distance between two mobiles or a mobile and a fixed beacon with a few centimeters accuracy. A material prototype implementing this method was performed and a first evaluation was conducted.**

Keywords- wireless sensors; telemetry; low power; ultrasonic; localization; 802.15.4; indoor environment.

I. INTRODUCTION

Many localization techniques could be used to track people or device in indoor or outdoor environment. In indoor, infrared, ultrasound, narrowband radio, WiFi, or UWB location systems are the most common [1-3]. In outdoor, we find essentially systems based on GPS location. The main problem is that these systems require heavy and cost infrastructure with a not easy deployment. In this context, this paper, which is part of a research project funded by the French National Research Agency (ANR) aims to define a new indoor localisation system in continuation of outdoor localisation system such as GPS [4]. The project is trying to address two specific problems:

- Helping people to locate themselves inside complex buildings.
- Helping to locate someone moving in a complex building.

Applications may be various: security, technical management, health… The system must enable the user to locate or to be located in the building with a good accuracy (centimeters) [5]. We could also consider for mobile robot applications the improvement to one cm accuracy or more using data harvesting from other sensors. Although the project is intended to compute the location from different sensors and location prediction algorithm, this paper is focused on the distance evaluation to fixed points inside buildings.

Several localisation algorithms are used to compute the exact location and to enhance the resolution [6,7]. The system presented here is a precise telemetry system composed of three nodes: a first node, which is an energy efficient mobile device and worn by an instrumented person, a second node, which is fixed (called “Beacons”). These nodes help the mobile device to locate precisely. A last node (a remote gateway) saves localisation information of all mobile devices.

In this paper, we first present the basic principles of the proposed system, then hardware and software development are described. Finally, characterization results of the system are presented. A conclusion ends the paper.

II. OPERATING PRINCIPLES

The system has two main functionalities. The first one is to estimate the distance between a user, typically a pedestrian in a building, and a fixed reference, and the second one is to send distance data to a collecting point using radio communications.

For this last function two operating modes are possible:

- The first one is called “autonomous mode”. In this mode the system collects and stores data in a flash memory. Data is harvested through the serial link when desired.
- The second mode is “normal mode”. In this mode, distance data isn’t stored in the system but immediately sent to the collecting point using radio communications. This mode will be used in the rest of the paper. Fig. 1 shows the system architecture in the two modes.

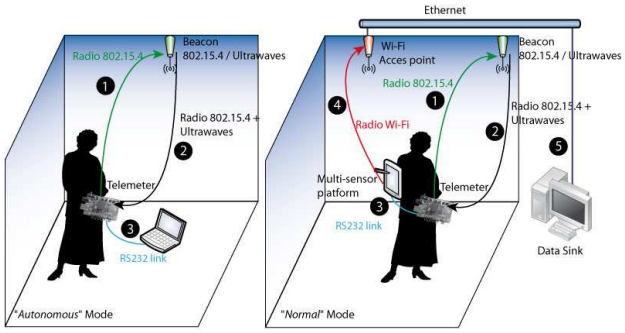

Figure 1. System architecture and two possible modes.

Depending on the mode remote data collection involves several stages:

- Stage 1: the telemeter sends a request radio frame to the beacon using its 802.15.4 interface [8]. The frame will be presented in the next section.

 ISBN: 978-1-61208-145-8

- Stage 2: The beacon receives the request from the telemeter and replies to the telemeter by sending simultaneously an RF response and an ultrasonic pulse.
- Stage 3: When the telemeter receives the response frame from the beacon, the telemeter starts a timer, which is going to measure the flight time of the ultrasonic pulse (ToA method [9]). When the ultrasonic pulse reaches the telemeter an interrupt is generated and the distance is computed. In autonomous mode, data (distance, beacon address) are stored on the telemeter or are immediately sent to a collecting PC using a serial RS232 link. It is the end of operations in this mode.

For normal mode, data are sent to a multi-sensor platform, which performs data aggregation from other sensors. In order to keep the free positioning of all the sensors on the person data are sent using Bluetooth protocol (not represented in Fig. 1).

- Stage 4: Data are received from the Bluetooth interface of the platform and are processed. Then, the platform checks all sensor parameters and transmits the status of the person using its WiFi interface.
- Stage 5: Data received by a WiFi access point is sent through the Ethernet network to the data sink.

III. HARDWARE PRESENTATION

The telemeter system is constituted of two parts separated in two specific boards connected through dedicated Programmable Input/Output (PIO). The first board contains the processor and radio modem, while the second board is dedicated to the ultrasonic pulses emission/reception.

A. Processor and radio board

The main component of the device is the 13213 from Freescale Semiconductors [10]. This component is a System In Package (SIP) including a processor and a 802.15.4 compliant transceiver. Our design is inspired from 13213-ICB reference design from Freescale, and all necessary interfaces have been integrated on the board to configure and to debug our telemeter. The block diagram of the system is presented in Fig. 2.

The 13213 processor is responsible for both functionalities: handling the transceiver and commanding the application. This characteristic limits the application code size (60kBytes) but enables to decrease the delay due to Physical layer (decoding demodulation). Indeed as soon as a frame is received a software interrupt is generated on the processor, which can start a timer on a beacon response (stage 2).

Moreover, the chip handles the serial RS232 link, which enables the system to send data to the multi-sensor platform (stage 3).

At last, several Input/Output and debug ports (BDM) have been placed on the MCU board in order to check the good communication between the boards.

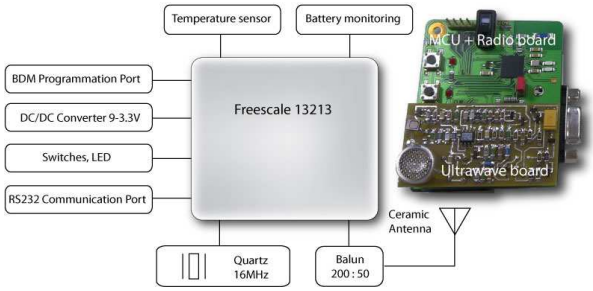

Figure 2. System block diagram.

B. RF and ultrasonic signals

The ultrasonic part aims at computing the flight time of an ultrasonic pulse in the 40kHz frequency range. The system combines the use of one RF electromagnetic wave with one ultrasonic pulse. The propagation speed of the electromagnetic wave being much more important than the sonic pulse speed, the flight time of the RF wave can be considered as instantaneous.

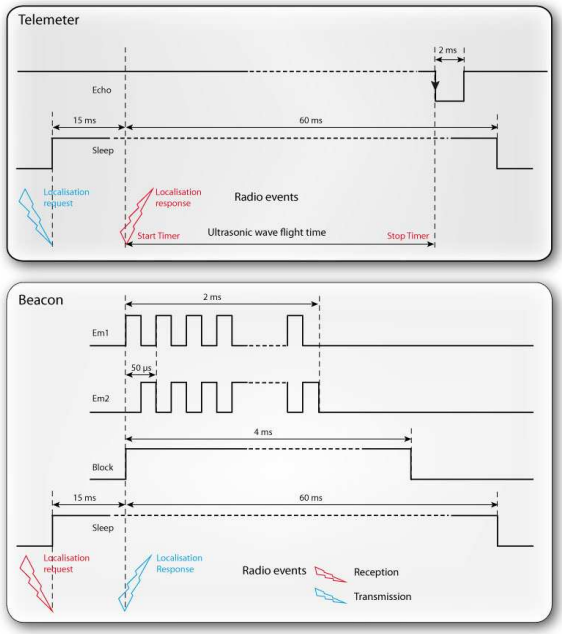

Figure 3. Ultrasonic part management signals.

Thus, the RF beacon response to a localisation request starts a timer of the processor, which timer is stopped when the ultrasonic pulse generated by the beacon node reaches the telemeter. Fig. 3 shows the temporal mode of the operation.

The ultrasonic pulse generation is managed by two programmable outputs of the beacon processor in *push-pull* mode (Em1 and Em2 signals), while on the telemeter the reception of an ultrasonic pulse in the 40kHz frequency band generates an interrupt on an input configured in the *input compare* mode (Echo signal).

Two other outputs of the processor are used for managing the ultrasonic board: the “Block” signal, enabling to block the listening while an ultrasonic pulse is generated, and the “Sleep” signal enabling to put the ultrasonic part in *low power* mode.

 ISBN: 978-1-61208-145-8

The 15ms guard time is due to the charging of the ultrasonic board input capacitor. The ultrasonic pulses have been limited to 2ms in order not to fill the environment of parasitic echoes. If the telemeter doesn't receive the ultrasonic pulse in less than 60ms, the telemeter puts the ultrasonic board in low power mode and goes to sleep mode until the next localisation request.

The localisation request can be either executed periodically from a timer, or requested from the serial link from the multi-sensor platform.

IV. SOFTWARE PRESENTATION

In order to program easily the application Freescale offers several software solutions called Code Bases: a basic solution called SMAC, a more complex 802.15.4 compliant stack and a Zigbee compliant stack [8].

For our system we have chosen the basic SMAC (Simple Media Access Controller) for several reasons. The most important reason is that this code base is completely open source and gives access to very low level primitives enabling maximal energy savings. Moreover this code base is very small and easy to implement. The source code is in standard C language and the development environment is Code Warrior [11].

A. *Application software*

The application code is integrated in a state machine running on the Beacon node and the Telemeter. Localisation requests are done periodically using a timer on the telemeter.

1) Telemeter: The state machine is described in Fig. 4.

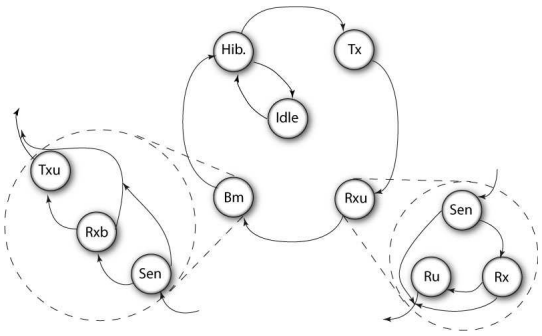

Figure 4. Telemeter state machine.

In order to save energy the system spends the most of its time in a deep sleep mode called *Hibernate mode*. In the *Hibernate mode* both the transceiver and the processor are powered off. Only a crystal is powered allowing the processor to wake up and after to wake up the radio stage.

The system is wake up from *Hibernate mode* (Hib) every 1 second by the real time interrupt timer to manage pending commands (Idle). If the telemeter doesn't receive any command from the multi-sensor platform the telemeter returns to hibernation.

Every 5 seconds, the telemeter wakes up from hibernate and broadcasts a localisation request (Tx).

Then it waits first the Radio localisation response (Rx) and in a second step it waits the ultrasonic pulse (Ru). These two states and the sensing stage constitute the macroscopic reception state (Rxu).

When the pulse is received or after 60ms the telemeter enters the beacon mode macroscopic state (Bm). This mode is used by the system data sink to increase beacon range and the robustness of the architecture. In this mode the telemeter plays the role of a beacon node for another telemeter out of the range. It waits a 3s guard time for localisation request from other telemeters (Rxb). If a request is received the state machine goes to the Txu state where a radio localisation response frame and an ultrasonic pulse are generated. Then, the telemeter enters Hibernate mode. If there is no received localisation request the telemeter directly goes to Hibernate state.

A special attention must be given to the Rxb guard time since radio stage activation consumes more energy.

2) Beacon: The beacon node state machine is a special case of the telemeter state machine since it is the beacon mode macroscopic state. The beacon node is always in reception mode sensing (Sen) localisation request. As soon as the beacon node receives a localisation request (Rxb) the beacon node generates a localisation response and an ultrasonic pulse (Txu) before returning to sensing mode (Sen).

B. *Frame format*

1) Radio frames: The radio frame format uses the 802.15.4 standard header and adds some fields. Frames are between 12 and 14 bytes long and are composed of three parts described in Fig. 5.

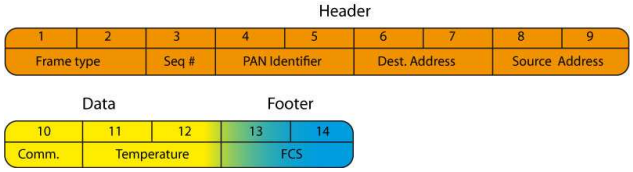

Figure 5. Radio frame format.

For energy savings it is important to note that several fields are useless (Frame type, Sequence number, PAN ID). Moreover the address field are oversized (2 Bytes) and could be limited to 1 Byte. However the 802.15.4 frame header enables to use most of network analyser such as Daintree Network SNA [12] to monitor the radio communications.

The frame is composed of three parts:

- The header field.
- Bytes 1 and 2 define the 802.15.4 frame type (Data, ACK, Beacon…)
- Byte 3 is the sequence number incremented with each emission.
- Bytes 4 and 5 define the network identifier and allow creating several networks.
- Bytes 6 and 7 identify the destination address. 0xFF is used for broadcast (localisation request).
- Bytes 8 and 9 identify the source address. The first one identifies the node type (beacon or telemeter) and the second one gives them a number (short address).

 ISBN: 978-1-61208-145-8

- Data field: Byte 10 identifies the command type. Two commands are implemented: Localisation Request and Localisation Response. Bytes 11 and 12 enable to send the temperature from the beacon node to the telemeter in order to take into account for US wave propagation speed compensation. This field can be used as parameters for other non implemented commands.
- The footer field: Bytes 13 and 14 are generated automatically by the data transmission primitive implemented in the SMAC code base. The FCS enables frame error detection.

2) Serial frames: After the telemeter has received the localisation response from a beacon node, the telemeter activates a 60ms watchdog and a timer enabling the US wave flight time computation. When the US wave reaches the receiver (a MEMS microphone) or when the watchdog expires, a serial data frame is sent to the multi-sensor platform. The format of serial frames is given in Fig. 6.

1	2	3	4	5	6	7	8	9
Start	Flight time		Temperature		Battery level		RSSI	Stop

Figure 6. Serial frame format.

Byte 1 is used as a start frame delimiter in order to limit erroneous frames.

Bytes 2 and 3 transmit the US wave flight time calculated with (1)

$$T_f = field \times 0{,}5\mu s. \quad (1)$$

Bytes 4 and 5 transmit the beacon temperature information to the multi-sensor platform.

Bytes 6 and 7 transmit the battery level from the integrated battery monitoring system.

Byte 8 gives the link quality indicator, which will enable us to compute the Receive Signal Strength Indicator (RSSI) with (2)

$$RSSI = -\frac{field}{2} dBm. \quad (2)$$

Byte 9 is used as a stop frame delimiter in order to limit erroneous frames.

V. SYSTEM CHARACTERIZATION

Electrical and radiofrequency characterization have been performed. Comparison with a well-known system is also made.

A. Electric consumption

In order to characterize electrically the telemeter, we have measured the current going through a serial 50Ω resistor before the 9V to 5V DC/DC converter. Fig. 7 represents a telemeter cycle, which is done every 5 seconds. In the picture, we have simplified the cycle by removing the beacon mode state after the macroscopic receive state (Rxu). Four different stages can be identified:

- The first stage is the wake up period. This stage is fixed by the LED in initialisation and lasts 40ms while current consumption sensed is 5mA.
- The second stage consists of both radio transmission and ultrasonic part powering. This stage lasts 20ms and while the mobile device starts to transmit localisation request the ultrasonic part is enabled in order to compensate analog component delay. The current consumption is about 65mA.
- The third stage is the received period. The device listening and the beacon response consume 35mA. This stage can be divided in two cases, superposed in Fig. 7: In the first case the beacon is in range and the radio data frame is received. After the reception, the waiting for the ultrasonic (US) wave starts and the ultrasonic power is sensed by the analog circuit, the radio and the analog circuit are turned off. If no power is received the max power is reported. In the second case the beacon is not in range. The watchdog expires and the device returns to Hibernate mode.
- The last stage is the going to Hibernate mode. This stage lasts 30ms and is controlled by adjusting the LED on delay indicating the US received.

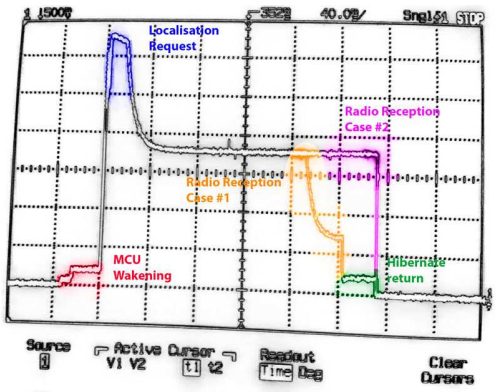

Figure 7. Telemeter current consumption.

B. Ultrasonic characterization

1) Test environment

The analog part characterization has been realized in an empty 9m x 7m lab room. Fig. 8 shows the room configuration and angular tests performed.

The room height is about 3m and the ground and walls are mixed reflective surface (concrete, plaster, bricks…).

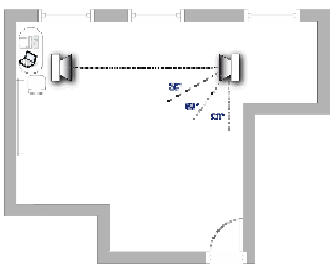

Figure 8. Test room configuration.

2) Distance and polarity impact

This characterization is focused on the distance and polarity impact on measurements. The temperature during these tests is kept around 22°C (+/- 2°C).

The measures presented in Fig. 9 were realized at 1.1 meter from the ground and with constant temperature.

Due to piezoelectric transducer directivity we tried several test pointing positions to compute the directivity effects on measurements. Four test positions were performed: 30, 60 and 90° from the direct view position.

The maximal range of the system is 9m but it can be improved by increasing the US pulse power. However, this modification increases the measurement variance.

The absolute error in all position stays under 8cm and the maximal error is observed when the device is in the 90° from the beacon position.

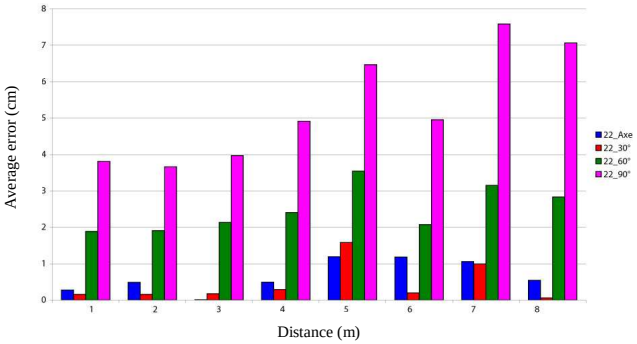

Figure 9. Distance error function of time and position (22°C).

Fig. 10 represents the polarization impact on measurements. For these measures we only made a quarter turn in the board plane to measure the XY directivity of the transducer but we haven't noticed any impact on the flight time measured.

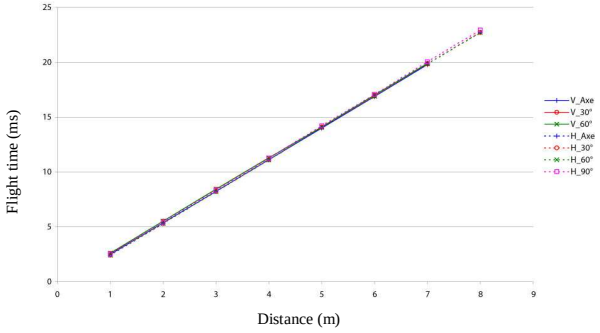

Figure 10. Polarity impact on flight time measures.

3) Temperature impact

For these tests we kept the same color convention for position. Fig. 11 describes the absolute error in function of distance for different positions at 12°C (+-2°C). The error measured is computed without any temperature compensation. We notice that we have the same behaviour as for 22°C. The computed propagation speed is decreased from 344.8m/s to 336.9m/s. The maximal error is obtained for the 90° position. Although the absolute maximal error is increased to 30cm, the relative error stays below 5%.

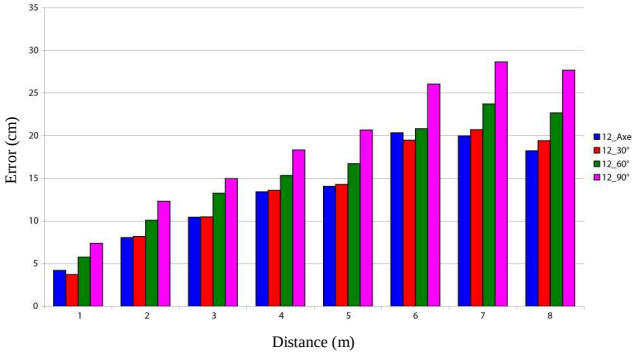

Figure 11. Distance error function of time and position (12°C).

4) Attenuation impact

We covered the mobile device with a piece of cotton tissue and we have measured the absolute error in function of distance and position. The attenuation due to the tissue increases the absolute error and has an important impact on the error when the position is at 90° from the direct view. However, the results are clearly satisfying since the maximal absolute error without any compensation of temperature or attenuation stays below 35cm and the relative error stays below 8%.

5) *Multi-path impact*

Fig. 12 shows the two test scenarios performed to evaluate multipath effects. The first scenario in configuration (a) evaluates the case where the power of the echo is superior to the power of the direct path while the scenario presented in configuration (b) evaluates the impact of a reflective object in parallel at the direct path for different distance (Pdirect > Pecho).

For these scenarios several distances between the reflective elements and devices have been tested but none of them showed an impact on the computed distance. In the case (a) the direct path is always reported.

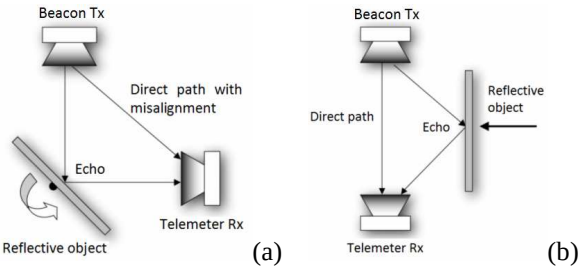

Figure 12. Test configurations for evaluating multipath effects.

6) *Obstacles and acoustic environment impact*

We tried to evaluate the impact of different objects being in the direct path. Several obstacles materials and sizes have been tested (cork, wood, carton, persons). The results have not allowed us to model precisely the behaviour in function of the size or the material but we noticed that for a constant distance position and temperature when the obstacles size increases the flight time increases. The error is superior but the relative error due obstacles is negligible (<1%).

 ISBN: 978-1-61208-145-8

The last tests evaluate the impact of a noisy environment on the measurements. In targeted applications (health) the main noise source is voice that's why we have focused our tests on FM radio noise source, white noise and pink noise (-3dB/octave). The tests have been processed in the same lab room with an ambient audio noise measured of 38dBSPL (Sound Pressure Level). The noise source was placed at 20cm behind the transmitter (worst case) and the noise measures were taken at 20cm perpendicularly to the direct path. The noise source was a speaker whose indicated bandwidth was 50-25000Hz. Four noise levels have been tested 68, 78, 88 and 100dBSPL for the 3 noise sources. Until 88dBSPL, no change in measured flight time has been noticed. But for 100dBSPL the device started to indicate incoherent measurements.

C. System performance comparison

The Cricket system from the MIT laboratory [13] is a compact embedded system for indoor localisation. It is constituted of ultrasonic piezoelectric transducers (40kHz) and a 433MHz Radio frequency transceiver. The distance computation is based on the round-trip flight time. An ultrasonic wave is generated by a transducer and is received by the other on the same board. Then, the distance is transmitted via the RF transceiver. This system has been chosen as the reference level for performance evaluation.

Another difference between our system and the Cricket is that we use omnidirectional transducers whereas the Cricket only has a 40° opening. Even if the cricket datasheet announced a 40° opening all the position tested above 30° have been unreliable and the measurements only have been done in the direct path. Moreover the system has been designed for short range measurements (anti-collision robotic application). Due to the round trip of the ultrasonic wave, the attenuation is important and the maximum range measured is about 7m. Fig. 13 indicates the relative error in function of distance for our telemeter localisation system and the Cricket system.

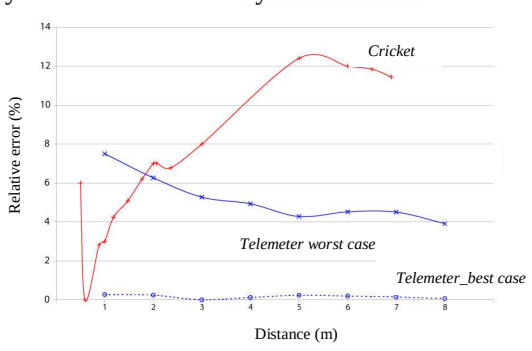

Figure 13. Relative error of systems comparison.

The two extreme cases are presented: the best case is obtained at 22°C in direct path (dashed) and the worst case at 12°C plus attenuation without any compensation in 90° position. The Cricket system stays under 10% of relative error from 30cm to 3m. In this range, the Cricket system is more precise than the worst case of our system however only the direct path was measurable for the Cricket system. Obviously, this comparison would need to be complemented and more detailed for example in energy efficiency.

VI. CONCLUSION

This paper proposed an original telemeter system allowing localisation for pedestrian in indoor environment. The system uses the 802.15.4 RF signal to start the time of an ultrasonic emission. The measure is computed from the flight time of the ultrasonic signal between the telemeter worn by the user and a beacon fixed in the environment. Characterization of ultrasonic performances shows good reliability, linearity and multipath immunity. This system have been tested and compared with the MIT Cricket system and have demonstrated several advantages such as:

- Good accuracy (better from 5% to 10% in the worst case and over 3m).
- Good opening angle (90° from the direct path.
- Good maximal range (up to 10m).
- Energy efficiency: The 802.15.4 low power modes enable up to two weeks with standard alkaline batteries (for a measurement every second).

Now, the system is integrating before deploying in real building.

ACKNOWLEDGMENT

This work has been funded by ANR-Telecom French program.

REFERENCES

[1] J. Hightower and G. Borriello, "Location systems for ubiquitous Computing," *Computer*, 34(8):57-66, August 2001.

[2] P. Bahl and V. Padmanabhan, "RADAR: An In-building RF-based User Location and Tracking System," In Proc. of the IEEE Infocom 2000, pp. 775-784, March 2000.

[3] M. Sugano, T. Kawazoe, Y. Ohta, and M. Murta, "Indoor localization system using RSSI measurement of wireless sensor network based on Zigbee standard," in Proc. of Wireless Sensor Networks (WSN), July 2006.

[4] Y. Oster, D. Kubrak, and J.F. Vidal, "FIL project: a low cost hybrid positioning system for pedestrians – the user's viewpoint," Toulouse Space Show, 6p., Toulouse, France, 8-11 juin, 2010.

[5] O. Woodman and R. Harle, "Pedestrian Localisation for indoor environment," Ubicomp'08, Seoul, Korea, September 2008.

[6] J. Chen, X.J. Wu, P.Z. Wen, F. Ye, and J.W Liu, "A new distributed localization algorithm for ZigBee wireless networks," In Proc. of Control and Decision Conference (CCDC), Guilin, China, pp. 4451-4456, june 2009.

[7] E. Cassano, F. Florio, F. De Rango, S. Marano, "A performance comparison between ROC-RSSI and trilateration localization techniques for WPAN sensor networks in a real outdoor testbed," In Proc. of Wireless Telecommunications Symposium (WTS), Prague,Czech Republic, pp. 1-8, April 2009.

[8] IEEE 802.15.4 WPAN™ Task group 4, IEEE 802.15.4-2006, http://www.ieee802.org/15/pub/TG4.html

[9] M. Ciurana, S. Cugno, and F. Barcel-Arroyo, "WLAN indoor positioning based on TOA with two reference points," In Proc. WPNC'07, 4th workshop on positioning, navigation and communication, pp. 23-28, March 2007.

[10] Freescale:http://www.freescale.com/webapp/sps/site/prod_summary.jsp?code=MC13213

[11] Freescale:http://www.freescale.com/webapp/sps/site/homepage.jsp?code=CW_HOME

[12] Daintree Networks: http://www.daintree.net/sna/sna.php

[13] N. B. Priyantha, A. Chakraborty, and H. Balakrishnan, "The Cricket Location-Support System," Proc. of the Sixth Annual ACM International Conference on Mobile Computing and Networking (MOBICOM), August 2000.

 ISBN: 978-1-61208-145-8

Multimodal Water Content and Nutrient Concentration Sensor for On-Site Soil Monitoring

Masato Futagawa
MD. Iqramul Hussain
Keita Kamado
Fumihiro Dasai
Makoto Ishida
Kazuaki Sawada

Toyohashi University of Technology
Toyohashi, Japan
futagawa@gcoe.tut.ac.jp
hussain-i@int.ee.tut.ac.jp
kamado-k@int.ee.tut.ac.jp
dasai-f@int.ee.tut.ac.jp
ishida@ee.tut.ac.jp
sawada@ee.tut.ac.jp

***Abstract*— We have fabricated a new multimodal sensor chip that is capable of measuring water content and nutrient concentration on-site simultaneously. Heretofore in agriculture, water content sensors, for example the TDR sensor, could not provide water content information correctly, since the results of these sensors are affected by the nutrient concentration in the soil solution. Therefore, tensiometers (shown in Fig. 1 (a)) have generally been used in agriculture. These are large-scale sensors and are not suitable for precision agriculture. Our proposed sensors are the world's first to be able to monitor water content without being influenced by the nutrient concentration, and nutrient concentration without influence from the water content.**

Keywords-water content; ion concentration; phase; electrical conductivity; on-site monitoring; agriculture

I. INTRODUCTION

On-site monitoring to enable precise control is becoming a requirement in agriculture. In particular, accurate determination of the water content in soil and of the nutrient concentration in water is considered to be the most important information for increasing the production of agricultural crops. The water content is the proportion of water by volume with respect to everything else, usually air and soil clod. The nutrient concentration (which has the same meaning as 'ion concentration') [1] in water can generally be observed by electrical conductivity measurements.

Fig. 1 shows how tensiometers can measure water content by utilizing the moisture-holding ability of soils. Because tensiometers have simple mechanisms and are reasonably priced, many farmhouses use them. However, they can't measure the ion concentration and can't be set near the roots of plants because of their large size. Hence, tensiometers are unsuitable for precise on-site monitoring.

In the case of on-site monitoring in soil, it is difficult to separate electrical conductivity information from water content information. For example, when the nutrient ion concentration is 1 S/m and the water content is 0.5 m^3/m^3, the measurement result of electrical conductivity is 0.5 S/m.

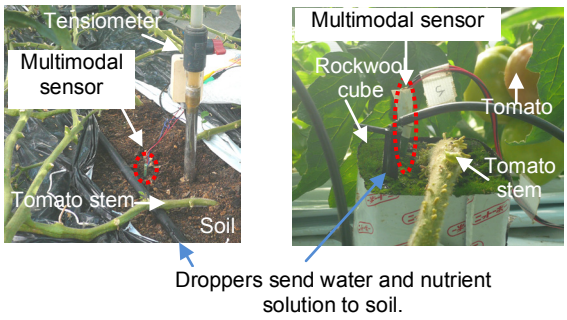

(a) A tomato plant bed, in which soil is used, monitored by a multimodal sensor.

(b) Tomato plant bed, in which Rockwool is used, monitored by a multimodal sensor.

Figure 1. These pictures show how a multimodal sensor is used for on-site monitoring of two kinds of plant beds in precision agriculture.

Therefore, for the measurement of water content and to obtain information about the nutrient concentration in soil, time domain reflectometry (TDR) sensors [2][3] and thermal type sensors [4] have been studied by other groups. These sensors measure water content information and electrical conductivity information separately, and then information about nutrient concentration is elicited by eliminating water content data from the electrical conductivity data. These water content sensors require high frequency (> 1 GHz) operation, or for the soil to be heated in order to measure complete water content values without the effects of nutrient concentration. In addition, the sensor sizes are not small enough (length, width: > 2 cm) to be incorporated with an electronic control system.

We have proposed a new multimodal sensor chip that is capable of measuring water content and nutrient concentration on-site simultaneously. The sensor is small in size and is capable of operating at lower frequency than TDR by employing new calculation methods.

In this paper, after introducing the basic concepts regarding the background and motivation of our research in Section I we formulated the theoretical and mathematical concepts in Section II. In later sections such as in Section III, we described the material structure of the sensor; in Section IV, measurement and results, finally in Section V we

 ISBN: 978-1-61208-145-8

articulated our conclusion based on the results of our research.

II. NEW MEASUREMENT METHODS

A. Ion Concentration Measurement Method using Phase

Measurement methods for water content are gauged against the dielectric constant. The relative permittivity of water, which is about 80, is larger than that of other materials commonly found in soil; for example, the relative permittivity of air is 1, and that of soil is about 5. In order to measure water capacitances and to eliminate the effect of ion concentration, TDR sensors operate at high frequencies of between 100 MHz and 1 GHz. However, the operating circuits that are required for high frequency operation are complex and costly, and the relative permittivity of water is also changed by ion concentration; the relative permittivity is 80 at 7 mS/m ion concentration (tap water) and is 70 at 7 S/m (seawater) [5].

We propose a new measurement method that measures the phase characteristics of water. This method analyzes the ion concentration information and is unaffected by the water content value. Equations 1 through 3 show the water characteristics using a parallel circuit model of resistance and capacitance.

$$Z_{total} = \frac{1}{\frac{1}{R_{water}} + j\omega C_{water}} = \frac{R_{water}(1 - j\omega C_{water} R_{water})}{1 + \omega^2 C_{water}{}^2 R_{water}{}^2} \quad (1)$$

$$R_{water} = \frac{D}{\sigma_{water} LW} \quad , \quad C_{water} = \varepsilon_{water}\varepsilon_o \frac{LW}{D} \quad (2)$$

$$\theta_{total} = \tan^{-1}\left(-\omega C_{water} R_{water}\right) = \tan^{-1}\left(\frac{-\omega\varepsilon_{water}\varepsilon_o}{\sigma_{water}}\right) \quad (3)$$

where, Z_{total} is the combined impedance, R_{water} is the resistance of water, C_{water} is the capacitance of water, D is the distance along the direction of passing current, L and W are the length and width of the section area of the path of the passing current, σ_{water} is the electrical conductivity (which provides information about ion concentration), ε_{water} is the relative permittivity, ε_0 is the permittivity of vacuum, θ_{water} is the phase of Z_{total}.

In the case of 50 % water per unit volume of soil, equation 3 changes to equation 4. In this equation, the phase remains almost unchanged with respect to water content information!

$$\left.\begin{aligned} \theta_{total} &= \tan^{-1}\left\{\frac{-\omega(0.5\varepsilon_{water} + 0.5\varepsilon_{soil})\varepsilon_o}{0.5\sigma_{water} + 0.5\sigma_{soil}}\right\} \approx \tan^{-1}\left(\frac{-\omega\varepsilon_{water}\varepsilon_o}{\sigma_{water}}\right) \\ &\because \varepsilon_{water} \rangle\rangle \varepsilon_{soil} \quad , \quad \sigma_{water} \rangle\rangle \sigma_{soil} \end{aligned}\right\} \quad (4)$$

In the case when the ion concentration changes from 7 mS/m (tap water) to 7 S /m (seawater) in water without including soil, equation 3 changes to equation 5. In this equation, the phase is changed almost exclusively by the ion concentration for smaller relative permittivity changes!

Because the phase at the highest sensitivity is π/4 rad, suitable frequencies for the input signals are between 500 kHz and 10 MHz. Hence the frequencies used in our method are smaller than those used in TDR methods.

$$\left.\begin{aligned} \theta_{total} &= \tan^{-1}\left\{\frac{-\omega\left(\frac{70}{80}\varepsilon_{tapwater}\right)\varepsilon_o}{\frac{7}{7\times10^{-3}}\sigma_{tapwater}}\right\} \approx \tan^{-1}\left(10^{-3} \times \frac{-\omega\varepsilon_{tapwater}\varepsilon_o}{\sigma_{tapwater}}\right) \\ &\because \varepsilon_{tapwater} = 80, \varepsilon_{seawater} = 70, \\ &\sigma_{tapwater} = 7\times10^{-3} S/m, \sigma_{seawater} = 7 S/m \end{aligned}\right\} \quad (5)$$

B. Water Content Calculation Method using Phase and Electrical Conductivity Information

Electrical conductivity sensors have been studied by our group in the past [6]. Since these sensors operate at the low frequency of 10 kHz, equation 1 changes to equation 6. This equation shows that the ion concentration of water without other materials can be measured using electrical conductivity. The value σ_{water} represents exactly the electrical conductivity information.

$$\left.\begin{aligned} Z_{total} &= \frac{1}{\frac{1}{R_{water}} + j\omega C_{water}} \approx R_{water} = \frac{D}{\sigma_{water} LW} \\ &\because \frac{1}{R_{water}} \rangle\rangle \omega C_{water} \end{aligned}\right\} \quad (6)$$

In the case of 50 % water per unit volume of soil, the total electrical conductivity σ_{total} changes to equation 7. The equation shows that electrical conductivity is affected by the volume of water per unit volume, which is the same as being affected by the water content!

$$\left.\begin{aligned} \sigma_{total} &= 0.5\sigma_{water} + 0.5\sigma_{soil} \approx 0.5\sigma_{water} \\ &\because \sigma_{water} \rangle\rangle \sigma_{soil} \end{aligned}\right\} \quad (7)$$

From these equations, the electrical conductivity can be determined by multiplying the water content by the ion concentration, and water content information can be calculated by using equation 8.

$$WC[m^3/m^3] = \frac{EC[S/m]}{IC[S/m]} \quad (8)$$

where WC is the water content information, IC is the ion concentration information shown by equation 5, and EC is the electrical conductivity information shown by 7.

III. STRUCTURE OF A SENSOR DEVICE

We fabricated a multimodal sensor with a Pt electrode area to measure electrical conductivity and a capacitive probe area to measure phase information, as shown in Fig. 2. Because the multimodal sensor is very small and can be fabricated by CMOS process technology, it was possible to insert the sensor into several kinds of plant beds. Images of two kinds of experiments using our multimodal sensor in agricultural applications are shown in Fig. 1.

The Pt electrodes for sensing electrical conductivity had been studied previously [6]. The sensing method is capable of measurement covering a wide range, between 1 mS/m and 10 S/m. The voltage was applied using a 10 kHz sine-wave and was of 250 mV in amplitude. Characteristically, the Pt electrodes can apply an electric current to a solution at low frequency, for example, 10 kHz, since the effects of electrical double layers on the Pt electrodes and of the parasitic capacitance of water can be minimized at this frequency.

In the capacitive probe area, Al electrodes were covered with a thin SiNx film (50 nm thickness) to protect them from the solution and to lower the electrical current. The SiNx parasitic capacitance had to be designed to be larger than the capacitance of water since the SiNx and the parasitic capacitance of water were connected in series. The SiOx parasitic capacitance under the Al electrode-area had to be designed to be smaller than the capacitance of water, because the SiOx and parasitic capacitance of water were connected in parallel.

The SiNx on the top film and the SiOx under the Al electrodes were designed to be 50 nm and 1 µm in thickness respectively. In this experiment, the applied voltage used a 500 kHz sine wave of 250 mV amplitude. Measurement at 500 kHz produced a larger range of phase changes for (θ_{water}) between 0 and -90 degrees.

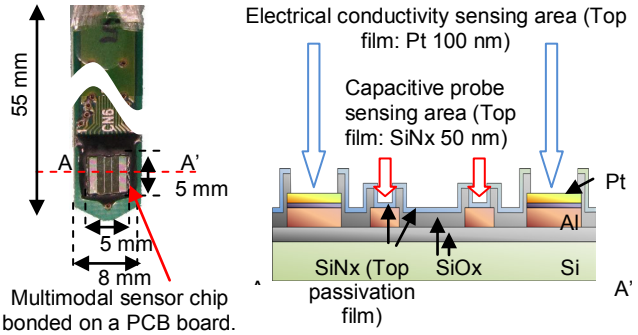

(a) The picture shows a multimodal sensor. The sensor has a small chip size, and is bonded on a PCB board that is inserted into the beds.

(b) A cross-sectional view of picture (a) is shown. A multimodal sensor is integrated with an electrical conductivity sensing area and a capacitive probe sensing area.

Figure 2. These pictures show an image of the sensor format and the structure of the sensor areas.

IV. MEASUREMENT RESULTS AND DISCUSSION

Fig. 3 shows images of an experiment to determine changes in water content (shown in Fig. 3 (a)), and in ion concentration (shown in Fig. 3(b)). A solution of tap water and common salt (NaCl) was used for the ion concentration test. When the water content is 1.0 m^3/m^3, as shown in Fig. 3 (b), then the electrical conductivity and the ion concentration are the same.

The graph in Fig. 4 shows that the results of the phase measurement of the water element are changed due to the ion concentration alone (shown in Fig. 4 (a)), and not by the water content (shown in Fig. 4 (b))! The graph in Fig. 5 shows that electrical conductivity information is composed of the water content (shown in Fig. 5 (a)) and the ion concentration (shown in Fig. 5 (b)). This graph shows that the electrical conductivity information is the water content multiplied by the ion concentration!

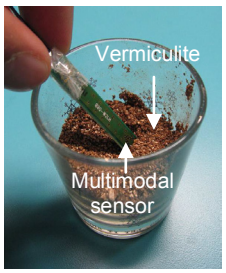

(a) The picture shows a photo of a water content experiment using vermiculite, as shown in Fig. 4 (a) and Fig. 5 (a).

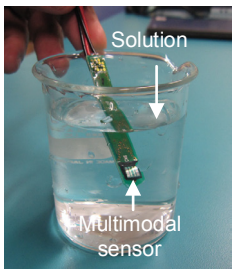

(b) The picture shows an experiment photo of ion concentration of solution. Of course, water content of the solution is 1.0 m^3/m^3! The test results show Fig. 4 (b) and Fig. 5 (b).

Figure 3. These pictures show images of experiments to determine changes in water content and changes in ion concentration.

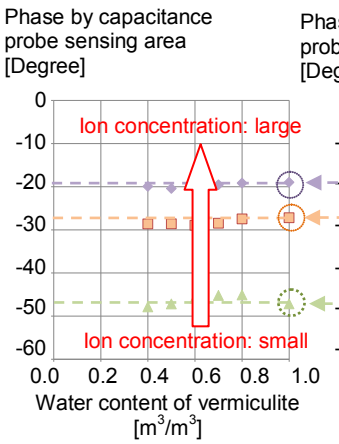

(a) Vermiculites were interfused with three solutions with different ion concentrations. Experiment of the relationship between water content and phase.

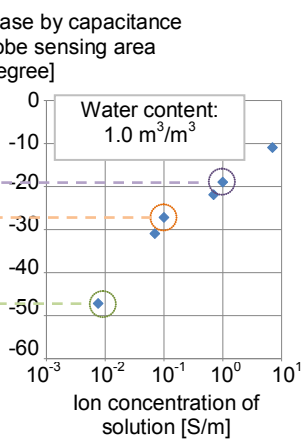

(b) Experiment to determine the relationship between ion concentration and phase.

Figure 4. Vermiculite and a solution are measured using the capacitance probe sensing area operating at 500 kHz. These graphs show that the sensor can monitor only ion concentration, and not water content!

 ISBN: 978-1-61208-145-8

The graph in Fig. 6 shows an image of the derivation of water content from electrical conductivity and ion concentration using equation 8. From these measurement results and from equation 8, information about the water content can be determined!

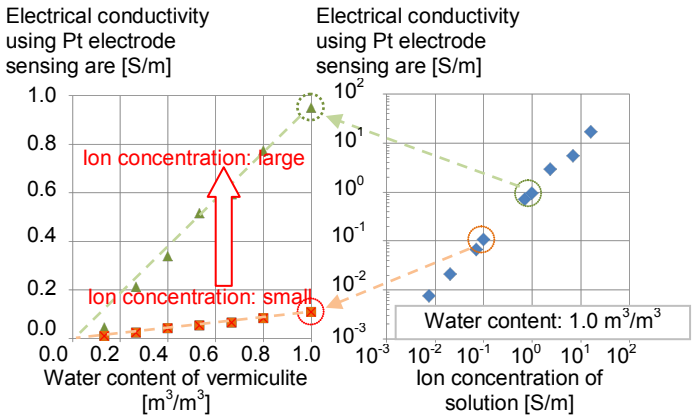

(a) Experimentation to investigate the relationship between water content and electrical conductivity.

(b) Experimentation to determine the relationship between ion concentration and electrical conductivity.

Figure 5. Vermiculite and a solution measured by the Pt electrode sensing area operated at 10 kHz. These graphs show that the sensor can monitor electrical conductivity by multiplying water content by ion concentration!

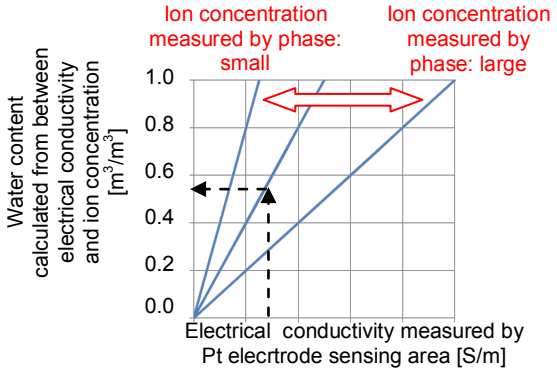

Figure 6. Image of the derivation of water content from the electrical conductivity and the ion concentration using equation 8.

V. CONCLUSION

A small multimodal sensor capable of providing on-site measurement of water content and ion concentration over a small area (for example, near to plant roots) was fabricated using CMOS circuit process technology. We proposed new measurement methods for ion concentration and water content determination, and designed appropriate film thicknesses, materials and so on for novel multimodal sensor devices. From phase information measured using a capacitance probe, ion concentration information that was unaffected by water content information could be gathered over a wide measurement range. When using Pt electrodes, the electrical conductivity could be determined by multiplying water content by ion concentration. We succeeded in measuring the water content without any effect caused by ion concentration (that is, nutrient concentration) and in measuring ion concentration without any effect from water content when using the new multimodal sensor.

REFERENCES

[1] S. P. Friedman, “Soil properties influencing apparent electrical conductivity: a review“, Computers and Electronics in Agriculture, Vol. 46, Issues 1-3, pp. 45-70, 2005.

[2] F. N. Dalton and M. Th. Van Genuchten, “The Time-Domain Reflectometry Method for Measureing Soil Water Content and Salinity”, Geoderma, Vol. 38, pp. 237-250, 1986.

[3] D. A. Robinson, T. J. Kelleners, J. D. Cooper, C. M. K. Gardner, P. Wilson, I. Lebron, and S. Logsdon, “Evaluation of Capacitance Probe Frequency Response Model Accounting for Bulk Electrical Conductivity”, Vadose Zone Journal, Vol. 4, No. 4, pp. 992-1003, 2005.

[4] K. L. Bristow, G. J. Kluitenberg, C. J. Goding, and T. S. Fitzgerald, “A small multi-needle probe for measuring soil thermal properties, water content and electrical conductivity”, Computers and Electronics in Agriculture, Vol.31, pp. 265-280, 2001.

[5] P. Wang and A. Anderko, “Computation of dielectric constants of solvent mixtures and electrolyte solutions”, Fluid Phase Equilibria, Vol. 186, pp. 103-122, 2001.

[6] M.Futagawa, T.Iwasaki, T.Noda, H.Takao, and M. Ishida K.Sawada, “Miniaturization of Electrical Conductivity Sensors for a Multimodal Smart Microchip”, Japanese Journal of Applied Physics, Vol. 48, pp. 04C184-1-4, 2009.

 ISBN: 978-1-61208-145-8

Love Wave Sensors Functionalized with Cobalt Corroles or Metalloporphyrines Applied to the Detection of Carbon Monoxide

Meddy Vanotti, Virginie Blondeau-Patissier,
Sylvain Ballandras
Times and frequency department
FEMTO-ST Institute
Besançon, France
e-mail : meddy.vanotti@femto-st.fr
e-mail : virginie.blondeau@femto-st.fr

Sylvain Ballandras
Senseor
Mougins, France
e-mail : ballandr@femto-st.fr

Abstract - **This article described highly sensitive gas sensors for monitoring low ppm or ppb concentrations of carbon monoxide using phase variations at constant frequency of Love waves generated by a surface acoustic wave device. The sensing material for gas detection employed in this study is a silica layer modified with one of three compounds that assure a selective trapping of CO. The authors demonstrate that surface acoustic wave devices with non-conductive sensing layers as described can be used for molecular recognition such as to detect carbon monoxide molecules. This article reported an interest and original work.**

Keywords- CO detection; SAW device; porphyrine; cobalt corroles.

I. INTRODUCTION

Carbon Monoxide (CO) is produced by incomplete combustion. Because of its intrinsic properties, it is naturally undetectable by human body. His toxicity and undetectability make him a dangerous compound. This observation leads to the necessity of developing a device able to detect the presence of CO in the air.

The strong demand for the development of lab-on-chip analysis devices has pushed to investigate many different approaches in that matter. Among these, the use of surface acoustic waves has received a particular interest during the last decade. Specially, pure shear guided waves in stratified substrates such as amorphous silica on quartz allowing for the use of Love waves appears as an attractive solution to fabricate devices able to operate in water, since shear waves are not radiated in fluids and because of their noticeable sensitivity to gravimetric effects related to surface adsorption. Many devices based on delay line configurations have been built and tested with various successes. However, the use of resonators instead of delay lines is expected to provide better sensing capabilities particularly when monitoring phase shifts at constant frequency due to gravimetric effects. For Surface Acoustic Wave devices (SAW), mass sensitivity is given by the Sauerbrey relation (1).

$$S_m = \frac{\Delta f}{f_0} \cdot \frac{A}{\Delta m} \qquad (1)$$

where f_o is the resonance frequency of the unperturbed SAW sensor, A is the active area, Δm and Δf are mass and frequency variations, respectively. SAW devices working at 125 MHz are used in these developments. The sensibility of these devices is about 250cm²/g.

Besides, a great variety of artificial receptors particularly useful for chemical sensors development have been fabricated, benefiting from progresses of synthetic chemistry methodologies. SAWs (Fig. 1) have allowed for demonstrating the exploitation of CO molecular trapping occurring in non-conductive sensing layers [1]. We propose in this paper to compare the performance of different compounds used as sensing layer. We have monitored phase variations of SAW devices, functionalized with three different sensing layers, when loaded with CO molecules. The three tested compounds are cobalt corroles [5,10,15-Tris(2,6-dichlorophenyl) corrolato]Co(III)] (Fig. 2) [2] and two metalloporphyrines [Fe(II)-(5,10,15,20-tetrakis(3,5-dihydroxyphenyl)porphyrin] [3, 4] referred as porphyrine #5 and [5,10,15,20-tetrakis (3,5-dimethoxyphenyl) porphyrin) Mn(III)] referred as porphyrine #6 (Fig. 4) .

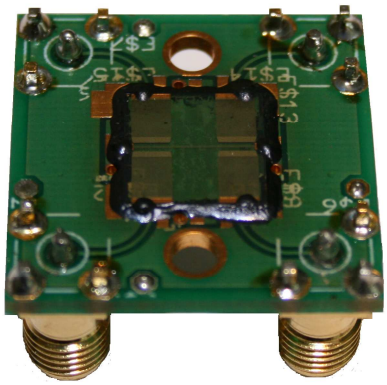

Figure 1. SAW device

 ISBN: 978-1-61208-145-8

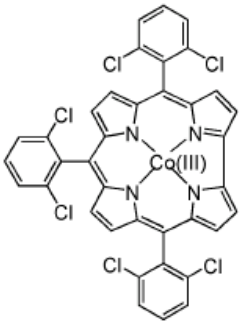

Figure 2. Scheme of a cobalt corrole [5,10,15-Tris(2,6-dichlorophenyl)corrolato]cobalt(III)])

II. EXPERIMENTS

For Love-wave-based sensors, since the acoustic wave generated by the transducers is mainly a surface acoustic wave, it reveals extremely sensitive to perturbations occurring at the surface of the device. Modification of the acoustic wave propagation conditions in the silica guiding layer leads to the modification of the physical characteristics of the wave. During the tests, CO sensors have been exposed to changes of several experimental parameters (temperature, flow, pressure, presence of gas). In order to exclusively extract the information concerning CO adsorption, we used a specific differential setup comprising two SAW devices. In contrast to previous experiments [1][3] the experiments were conducted at atmospheric pressure to more closely simulate sensor application conditions. To this end, a dedicated gas test setup, optimized for CO detection, has been developed.

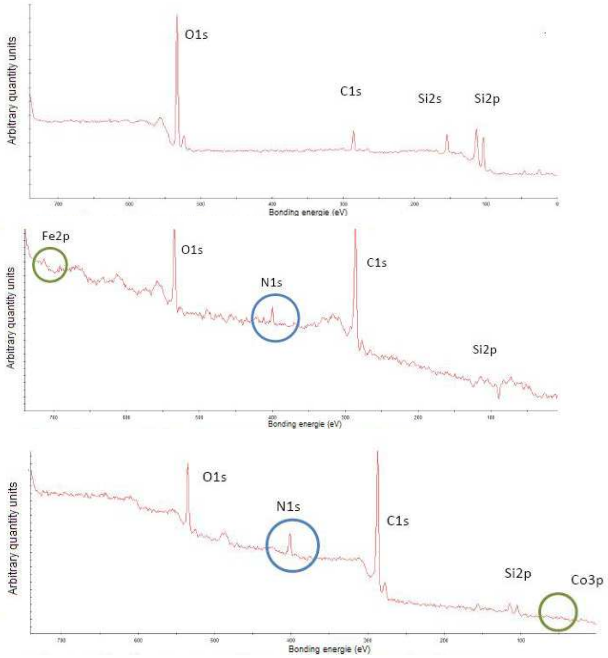

Figure 3. X-ray spectra of SAW devices before functionalization deposition (first); after porphyrines #5 spray coating (second); after cobalt corroles spray coating (third)

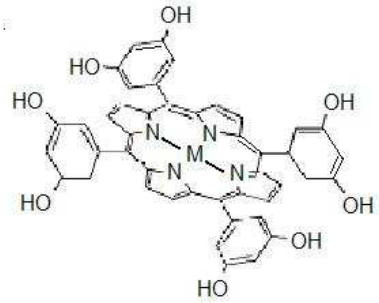

Figure 4. Scheme of an organometallic prophyrin (M: central metal atom) M-(5,10,15,20-tetrakis(3,5-dimethoxyphenyl)porphyrin)

A crucial point of the development of SAW sensor is the functionalization of its active surface with chemical treatment able to assure the selective trapping of CO. Sensing layers were synthesized following literature methods [2][4][5]. Prophyrins and cobalt corroles were dissolved in a proper solvent (10^{-3} M in $CHCl_3$) and deposited by spray coating. Love-wave devices used, consists in delay lines built on (AT, Z) cut of quartz. The wave guidance is achieved by depositing a 2.5 µm thick silica overlay onto the InterDigited Transducers (IDTs) and the propagation path as well. The Love wave is generated and detected using IDTs composed of 50 pairs of 4-finger-per-wavelength electrodes made of 200 nm thick evaporated aluminium.

In order to ensure the presence of the functionalization, we made a XPS (X ray Photon Spectroscopy) analysis of the surface of SAW devices before and after the deposition of cobalt corroles and porphyrines. A few spectra are reported here. The resulting wide scans are presented in Fig. 3. The raising of two peaks characteristic of the presence of silicon (Si2p and Si2s), oxygen (O1s) and the presence of small peaks of carbon due to pollution can be observed on the bare device's spectrum showing the absence of functionalization onto the silica composed surface. After cobalt corroles deposition, we note the augmentation of the carbon peak and the appearance of two peaks showing the presence of nitrogen and cobalt. A decrease of O1s and silicon intensity peaks has been observed. This tends to prove that a thin film has been effectively deposited onto the surface. The apparition of a nitrogen peak also confirms the presence of an overlay onto the silica surface due to four atoms of nitrogen surrounding the organometallic atom. Analyses of devices that have been covered with porphyrines #5 and #6 show Fe and Mn organometallic peaks. The oxygen peak is still higher than in presence of corroles due to –OH groups on both. The XPS analysis has yield evidences of the deposition of the two compounds onto the SAW device's surface. It has also allowed for the chemical characterisation of these functionalizations.

An experimental bench has especially been developed for high sensitivity detection of CO (Fig. 5). In order to proceed to differential acquisition [6] allowing for minimizing the influence of changing experimental parameters preventing

 ISBN: 978-1-61208-145-8

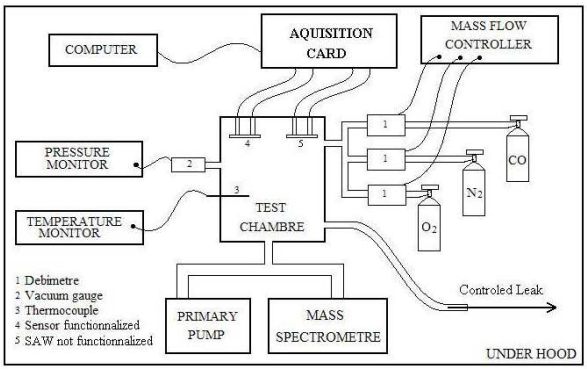

Figure 5. Scheme of our specific cell for toxic gas detection.

the CO detection, two sensors are used. One coated with corroles sensitive to CO [1][2] and the other non-functionalized used as a reference.

The cell is equipped with three mass flow meters driven by a controller allowing the dilution of CO with N_2 and O_2. Moreover, a primary pump provides vacuum conditions that permit a faster regeneration of the sensitive area of the sensors, making it reusable.

III. MOTIVATION AND RESULTS

We report here the results obtained for CO detection using SAW devices functionalized with cobalt corroles and metalloporphyrines, which reversibly interact with gaseous analytes by coordination with the central metal atom. One can see in Fig. 6 the trend of a phase variation due to CO adsorption onto the surface of a device functionalized with cobalt corroles. The experiments have been achieved at least three times to validate the results. We obtained the same trends with devices functionalized with porphyrines, with slightly different slopes. In every case, we confirm reversibility of the adsorption. We have monitored the respective phase shift velocity undergone by the Love wave, propagating within the guiding layer of the devices functionalized with each compounds, versus the CO concentration of the gas injected in the test cell and confirm a linear correlation (Figure 7, 8 and 9).

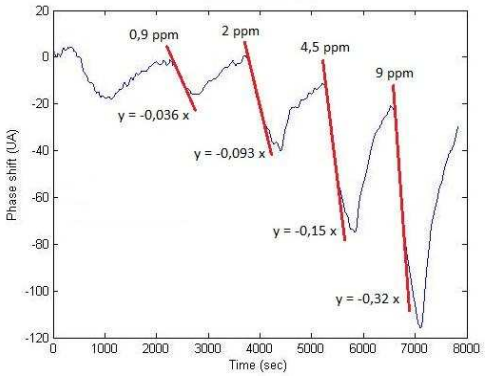

Figure 6. Phase variation due to CO adsorption onto the SAW device surface.

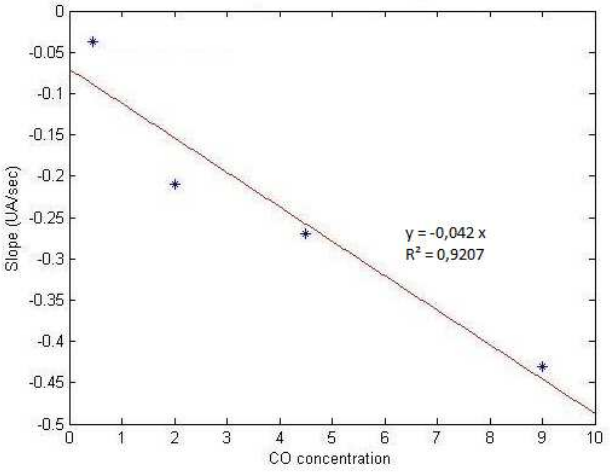

Figure 7. Graphic representation of the phase shift velocity obtained with porphyrine #5 versus CO concentration at atmospheric pressure.

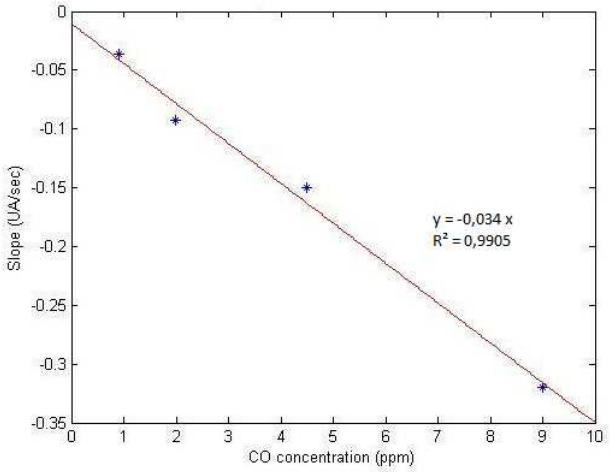

Figure 8. Graphic representation of the phase shift velocity obtained with cobalt corroles versus CO concentration at atmospheric pressure.

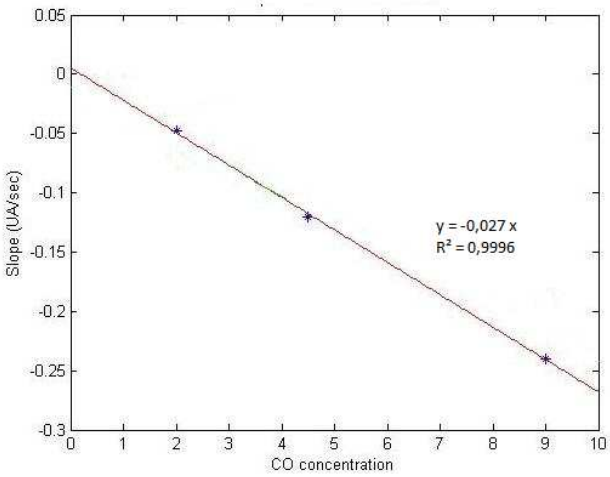

Figure 9. Graphic representation of the phase shift velocity obtained with porphyrine #6 versus CO concentration at atmospheric pressure.

 ISBN: 978-1-61208-145-8

TABLE I. FUNCTIONALIZATIONS PERFORMANCES

	Functionalization type		
	Porphyrine n°5	***Cobalt corroles***	***Porphyrine n°6***
Detection threshold	450 ppb	900 ppb	2ppm
Corresponding phase shift velocity	-0.04 UA/s [a]	-0.05 UA/s [a]	-0.05 UA/s [a]

a. UA: Arbitrary Units

Porphyrine #6 enables us to detect at least a CO concentration of about some ppm. With cobalt corroles, the detection threshold is situated below one ppm. We note that the porphyrine #5 provides a clear detection of a minimum of 450ppb CO concentration [Table I].

We also note that the phase shift velocity induced by the injection of 900ppb with porphyrine #5 is about four times higher than with corroles. This reflects the highest sensitivity of porphyrine #5 with CO.

Since porphyrine #5 induces phase shifts velocity four times larger than what we get with cobalt corroles we can conclude that this compound represents the preferred solution for CO detection at atmospheric pressure.

REFERENCES

[1] V. Blondeau-Patissier, M. Vanotti, J.M. Friedt, R. Paolesse, S. Ballandras, *Detection of carbon monoxide with a metalloporphyrin film on quartz microbalalnce and Love wave device*, Eurosensors, Linz, 2010

[2] J. M. Barbe, G. Canard, S. Brandès, F. Jérome, G. Dubois, and R. Guilard, *Metallocorolles as sensing components for gas sensors: remarkable affinity and selectivity of cobalt(III) corolles for CO vs. O2 et N2*, Dalton, 2004, pp. 1208-1214.

[3] R.Paolesse et al., *Porphyrin Based Chemical Sensors*, Encyclopedia of Nanoscience and Nanotechnology. H. Nalwa Ed. American Science Publishers, 2004, vol 9, pp. 21-43

[4] J.B. Kim, A.A. Adler, and F.R. Longo, *Synthesis of poprhyrin from monopyrroles*, D. Dolphin (Ed.). The Porphyrins, vol. 1, Academic Press, New York, 1978, pp. 85–100.

[5] R. Paolesse, C. Di Natale, A. Macagnano, F. Davide, T. Boschi, and A. D'Amico, *Self-assembled monolayers of mercaptoporphyrins as sensing material for quartz crystal microbalance chemical sensors*, Sens. Actuators B 47, 1998, pp. 70–76.

[6] D. Rabus, J.M. Friedt, S. Ballandras, G. Martin, E. Carry, and V. Blondeau-Patissier, *A High Sensitivity Open Loop Electronics for Gravimetric Acoustic Wave-Based Sensors, EFTF*, 2010

 ISBN: 978-1-61208-145-8

Distributed Chemical Sensor Networks for Environmental Sensing

Fiachra Collins, Dylan Orpen, Damien Maher, John Cleary, Cormac Fay and Dermot Diamond*
CLARITY Centre for Sensor Web Technologies, National Centre for Sensor Research, Dublin City University, Dublin 9, Ireland.

Abstract—**Society is increasingly accustomed to instant access to real-time information, due to the ubiquitous use of the internet and web-based access tools. Intelligent search engines enable huge data repositories to be searched, and highly relevant information returned in real time. These repositories increasingly include environmental information related to the environment, such as distributed air and water quality. However, while this information at present is typically historical, for example, through agency reports, there is increasing demand for real-time environmental data. In this paper, the issues involved in obtaining data from autonomous chemical sensors are discussed, and examples of current deployments presented. Strategies for achieving large-scale deployments are discussed.**

Keywords-environmental monitoring, chemical sensors, air, water, sensor networks.

I. INTRODUCTION

We live in a world wherein people are increasingly accustomed to instant access to a huge and exponentially growing volume of information stored on web-repositories. Through highly efficient search engines, people and organizations expect the internet to provide instant access to repositories spanning entertainment (music, movies, e-books, video clips, TV/radio), news and current affairs, hobbies, Government and Agency reports, financial data, and so on. The recent environmental disaster in Japan again highlights the need for access to real-time sensed information that may provide early warnings of impending events, and rapidly disseminate information to the public to minimize loss of life. This has once again placed the spotlight on how to gather, integrate, analyze and share sensed environmental data. We are particularly interested in how to sense the *chemistry* of our environment, and in particular, how to realize chemical sensors that are reliable, robust, and able to function autonomously for periods of weeks to years. As our ultimate goal is to achieve widely deployed networks of chemical sensors, it follows that the cost of ownership of these devices must be as low as possible.

II. THE ELEMENTS OF SCALABILITY

The basic building block any sensor network is the sensor/communications platform [1]. Our specific interest is to build autonomous chemical sensor platforms that could provide the basis of a widely dispersed sensor network, providing frequent updates about the concentration of specific target species at many locations [2]. When one considers how to deploy and maintain sensor networks that will comprise many thousands of individual devices scattered across a large geographical area, the issue of scalability becomes paramount. The key to scalability is to produce sensor platforms that are not overly expensive to buy and can function autonomously for as long as possible (ideally months, years), while providing a stream of accurate data. For chemical sensing in water bodies, this is a formidable challenge, as chemical sensors are typically subject to drift and loss of sensitivity over time, and require regular calibration in order to maintain accuracy. Biofouling is a particularly difficult issue for environmental water monitoring that can have drastic impact on electrodes and other sensors directly exposed to the sample within a few days or weeks 3].

In this paper we will demonstrate how a microfluidics approach can provide very reproducible sample and reagent handling, enabling reliable data to be generated by autonomous chemical analysers deployed in hostile environments. The small reagent and sample volumes required to perform microfluidic assays means that multiple assays can be performed using relatively small reservoirs, and a small lead-acid cell can provide enough power to sustain the analyzer for a period of up to several months. For example, the typical reagent volume consumed is in the region of 50-100 µL per assay, which translates to 1000 - 2000 assays per 100 mL of reagent. Continuous monitoring at a frequency of 1 measurement per hour means that the platform can operate for 50-100 days per 100 mL of reagent, and provided the reagents are stable, this obviously scales as the volume per assay is reduced, or the reagent volume is increased. In parallel, we have fabricated similar platforms employing IR gas sensors targeting important environmental targets. These can function unattended for many months and yet remain within calibration, as they do not depend on a sensitive sensor surface to generate the analytical signal, or a supply of analytical reagents to function. The gas/air and water analysis platforms follow the same basic analytical approach in that they sense the analyte in the sample, process the analytical signal, store the data locally, and transmit the data to a remote server, for example, using GSM, Wifi or zigbee wireless communications. Both platforms have an integrated power source that can support all operational functions for periods of several months without intervention.

 ISBN: 978-1-61208-145-8

III. NUTRIENT (PHOSPHATE) MONITORING

A. Autonomous Nutrient Analyzer

The autonomous nutrient analyzer is a compact and portable device capable of performing reagent based chemistry in remote locations. The first-generation (GEN1) system originally developed at Dublin City University [4] has been extensively field trialed both at waste water treatment plants [5] and in natural waters [6]. In excess of 10,000 assays have been performed using the platform across 12 separate field trials. Current work is focused on the development of an improved version of the analyzer platform that provides equivalent or better analytical performance for a component cost of less than €200 per unit. Initial field trialing of the second generation (GEN2) system has recently commenced and the results from a three day field trial are reported below along with a description of the analyzer design and operation.

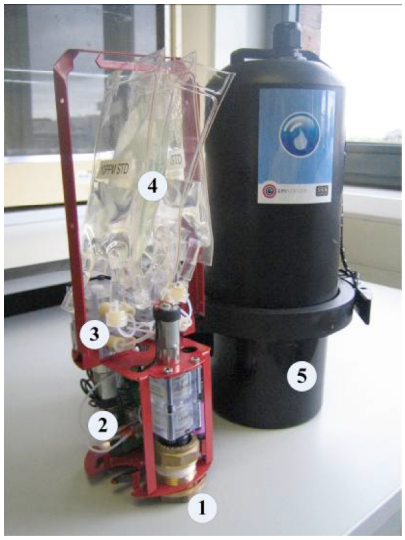

Figure 1: GEN2 Nutrient analyzer design; (1) Sample inlet; (2) Control board and detection system; (3) Dual channel peristaltic pumps; (4) Reagent bags; (5) IP68 enclosure

B. Analyzer Design and Operation

The GEN2 analyzer is a fully integrated system incorporating fluid handling, microfluidic technology, colorimetric chemical detection, and real time wireless communications in a compact and rugged portable device. The major system components are shown in Figure 1.

The sensing system is employs the molybdenum yellow method, a simple colorimetric technique based on the formation of a yellow-colored compound when a reagent is mixed with a phosphate-containing sample. The color of the reacted sample is detected at ca. 380nm using an ultra violet light emitting diode (LED) light source and a photodiode detector. This reagent chemistry is preferred due to its long-term stability even though it is less sensitive than other more commonly employed reagent chemistries.

The sensor implements a two-point calibration protocol using a blank solution (0 mg/L orthophosphate) and a standard orthophosphate solution. The concentration of the standard solution can be varied depending on the range of orthophosphate levels in a particular sample/site. The two-point calibration is carried out for each sample measured. The importance of this procedure lies in its ability to correct for:

- Changes in LED output/photodiode response due to temperature fluctuations;
- Possible drift in response of detection system over time;
- Possible change in sensitivity of detection system over time.

The system communicates using short range ZigBee radio to a remote network gateway, which passes the sensor data via GSM or Wifi to a web-database for remote access by the user. This setup allows the user to not only monitor sensor data in real time but also to remotely change the sensor setup parameters, such as sampling rate.

C. Field Trial

Following an initial laboratory based calibration, the system was placed *in situ* at Broadmeadow Water Estuary, Co. Dublin, Ireland on 04/09/2010. This estuarine water body is know to have elevated nutrient levels due to a combination of inputs from industry, agriculture and a nearby waste water treatment plant. The trial location is shown in Figure 2. The analyzer was initialised to take samples at 30 minute intervals for the duration of the deployment.

Figure 2: Broadmeadow Water site

The sensor output over the 62-hour deployment period is shown in Figure 3. The sensor performed 124 autonomous measurements during the trial, and four manual samples were collected for lab analysis and validation. These

 ISBN: 978-1-61208-145-8

samples were analyzed in the laboratory using a Hach-Lange DR890 Portable Colorimeter. Figure 4 shows the excellent correlation (r = 0.9706) between the sensor output and the manual sample phosphate concentrations. The manual sample collected at 13:35 on 06/09/2010 shows the largest deviation from the sensor value. However, on that day, the river water levels did not allow this sample to be taken close to the sensor sample inlet. All other manual samples were taken at the sensor sample inlet. The daily fluctuations in the phosphate level can be attributed to the tidal nature of the estuary which lead to significant dilution of the outflow of the nearby waste water treatment plant.

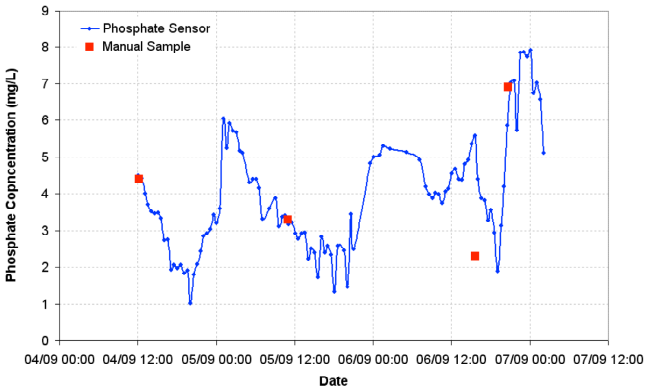

Figure 4: Phosphate concentrations measured during the trial by the phosphate analyzer and by parallel manual samples (red)

IV. AUTONOMOUS GREENHOUSE GAS MONITORING

European directives [7] have driven a growing need for autonomous platforms that can provide real-time monitoring of gases in the environment. Such platforms, along with the accompanying data recording and interface software, provide an attractive alternative to the current norm, which still depends largely on labour intensive manual monitoring [8].

A. Design concept

For the autonomous gas-monitoring platform, components are housed within the same robust casing used for the nutrient analyzer, which we knew to be suitable for long-term outdoor deployment (Figure 5). Our primary goal was to meet a need for a remote autonomous platform for monitoring greenhouse gas levels (CH_4 and CO_2) in landfill site boreholes. This system is designed to fit to borehole wells, which are typically located at the landfill site perimeter, to facilitate monitoring of gas migration [9].

The monitoring operation is controlled via a custom programmed MSP430 microcontroller (1), managing the gas extraction (4), gas sampling (5) and data communication (2). The power supply (3), a 12V 5Ah lead acid battery, currently allows a deployment of 8 weeks at a sampling frequency of four sample cycles per day (approximately 220 separate sample cycles in total). The principal components of landfill gas, carbon dioxide (CO_2) and methane (CH_4) [3], are measured by infrared gas sensors (Dynament Ltd. IRCEL-CO2 and IRCEL-CH4). A SKC Grabair pump (SKC Inc., 222-2301) extracts a sample at 0.6 L/min from a depth of 1 metre in the borehole well. The data are statistically represented and sent in SMS format to a central base-station via GSM communication (Siemens MC35iT). As a backup, all harvested data are stored locally on an onboard flash memory chip. At the central base-station, the communicated data are parsed and placed onto a database, whereupon email alerts are sent to stakeholders. In addition, all present and historical sampled data are accessible to the relevant authorities and site personnel via a web-based visualisation application. This communications and web-portal design is the same as that used with the nutrient analyzer.

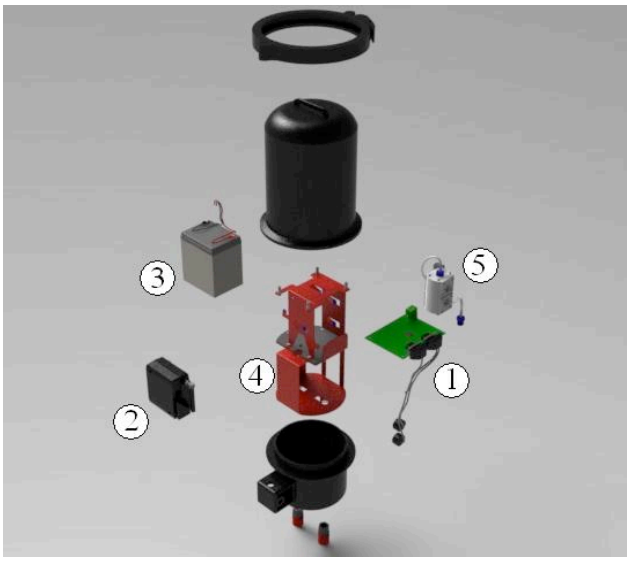

Figure 5: Exploded view of the autonomous landfill gas monitoring platform. (1) Control board, (2) GSM Module, (3) Battery, (4) Extraction pump, (5) Sample chamber and sensors

B. Deployment results

To date, extensive field deployment trials have resulted in gas monitoring platforms achieving continuous deployments in excess of 12 months. For the purpose of this results section and to highlight the benefits of this system, a subset of the data corresponding to June 2009 is displayed in Figure 6 [10]. The CO_2 levels can be seen to fluctuate significantly over this period, and greatly exceeding the threshold limit (1.5 % v/v) for significant periods.

Consultation with the landfill site operators revealed that an increment in soil cover restricted the dissipation of generated gas, resulting in a build-up of CO_2 concentration (events 1 and 2 as annotated in Figure 2). These actions were rectified by increasing in the extraction flow rate by site personnel. However, this remedial work was hindered by a partial blockage in the underground gas extraction pipe (event 3), which was subsequently identified and removed. The diagnosis of events and subsequent monitoring of the effectiveness of remedial measures illustrates the usefulness of this system in landfill site management.

 ISBN: 978-1-61208-145-8

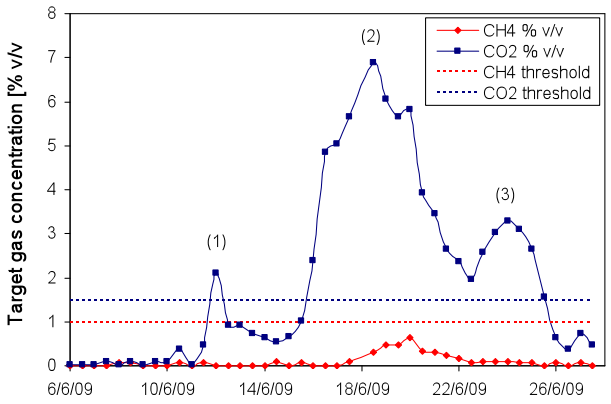

Figure 6: Recorded gas concentration data for June '09 with threshold limits of 1.5% v/v for CO_2 and 1.0 % v/v for CH_4 also indicated [10].

C. *Further system development*

As mentioned in the introduction, a key goal for scalability of deployments has to be the duration of autonomous operation. Currently continuous deployments of the platform in excess of 12 months have been achieved at two locations on an active and dormant landfill site. During this time, the system successfully monitored gas migration, with the batteries being remotely monitored and manually replaced when depleted. The systems uptimes were calculated upon retrieval, and were found to be approximately 83% over the duration of both deployments. The discrepancy from complete autonomy was attributed to the 12V/5Ah battery depleting below its operating threshold (ca. 11.5V) after approximately one month in the field (see original code battery decay in Figure 7). Below this threshold, the GSM unit cannot draw sufficient current to transmit and the data cannot be accessed remotely via the website. While battery replenishment can be achieved reasonably quickly, it is obvious that a reduction in power usage would increase the duration of autonomous operation. This has been achieved through optimization of the microcontroller C-code to refine the device functionality, and in particular introduce sleep modes. Using this optimised code resulted in a three-fold increase in battery lifetime (i.e. ca. 3 months). The battery decay of a unit programmed with both the old (blue series) and new power saving code (red series) can be seen in Figure 7.

In order to further extend deployment lifetime, and potentially realise a fully autonomous field-deployable sensing platform, a solar cell has been assessed as a local energy generation source for the platform. A study was conducted by coupling the system with a charge controller (4Ah, Radionics 706-7934) and photovoltaic module (17.5V, 0.27A, Radionics 194-149). The solar cell was chosen to provide sufficient power to charge the battery even in low lighting conditions. The charge controller serves to regulate the power being delivered to the battery, and to provide protection against battery overload, reverse polarity and feed. For the purpose of this study, one of the systems was retrieved after the 12-month deployment and retro fitted with the charge controller and solar cell (wiring configuration shown in Figure 8). Once the solar cell was fitted, the unit was setup on a test borehole well, sampling as per the normal field setup (with the old inefficient code). The monitored battery level can be seen in Figure 9. The graph also includes the decay of the battery before it was fitted with the solar panel. This shows the graph initially decaying from its full charge until the operating threshold is crossed.

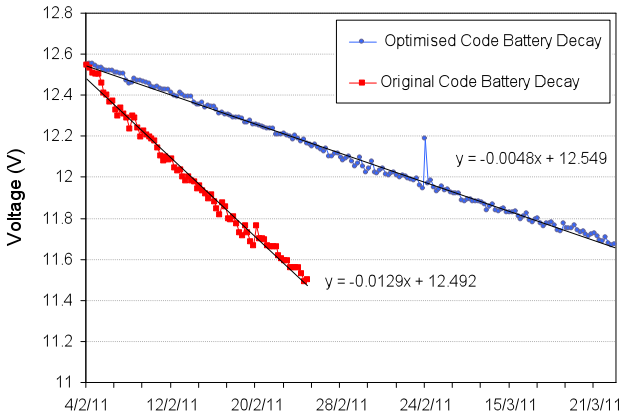

Figure 7: Battery decay curves passing operating threshold with both the original code (red), and the new updated code (blue) which includes sleep routines.

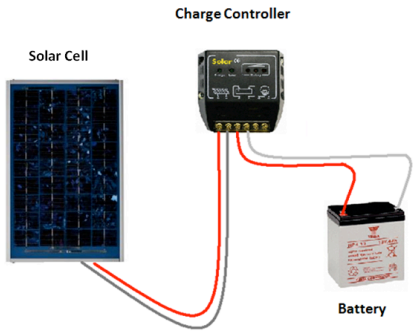

Figure 8: Annotated schematic of the solar charging configuration, demonstrating the wiring configuration

When integrated, the integrated solar cell immediately begins to produce a net positive increase in battery level. Voltage fluctuations, as seen from the repeating pattern reading at a period of 6 hours, are attributed to the changing sunlight conditions. Despite these fluctuations, it is clear that the battery charge is accumulating. Although these are only initial studies (6 days), we are confident that a fully autonomous gas sensing platform will be realised with the

 ISBN: 978-1-61208-145-8

implementation of the these power saving/generation measures.

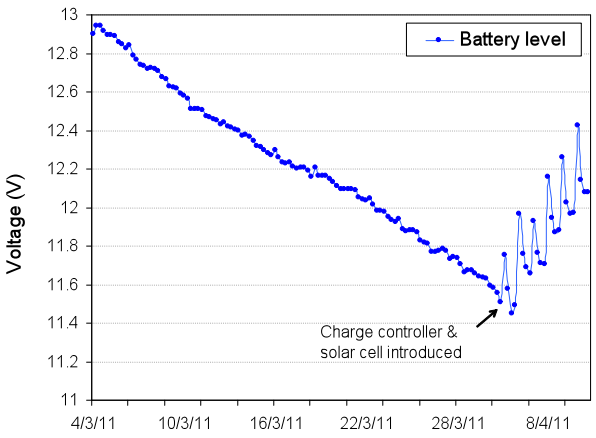

Figure 8: Battery level monitoring showing the initial decay from fully charged to failure threshold (ca. 11.5V) at which point the solar panel is integrated, and the voltage begins to accumulate while the system continues to operate as normal.

V. CONCLUSIONS

The cost of ownership, reliability and duration of autonomous operation of chemical sensing platforms for air and water monitoring will improve dramatically in the coming years, enabling widely distributed networks of these devices to be realized. This in turn will generate new information about our environment, which can be made available to environmental scientists, technical specialists, regulatory agencies, communities and commercial entities. In this way, knowledge of the status of our water and air chemistry will become integrated with other information sources (e.g. satellite based weather and remote sensing data) to provide a much richer picture of the dynamics and inter-relationships that together determine the quality of our environment.

.

ACKNOWLEDGMENTS

We acknowledge support for this research from Science Foundation Ireland through the CLARITY Centre (grant code 07/CE/I1147), Enterprise Ireland (grant codes IP/2008/544 and CFTD/08/111) and the Irish Environmental Protection Agency (grant code 2010-ET-MS-10). We also acknowledge support from Episensor Ltd. in project IP/2008/544.

REFERENCES

[1] D. Diamond, K. T. Lau, S. Brady, and J. Cleary, “Integration of Analytical Measurements and Wireless Communications – Current Issues and Future Strategies”, Talanta vol. 75, pp. 606-612, 2008.

[2] D. Diamond, S. Coyle, S. Scarmagnani, J. Hayes, “Wireless Sensor Networks and Chemo/Bio-Sensing”, Chemical Reviews, vol. 108 Issue: 2, pp 652-679, 2008.

[3] A. Radu, S. Anastasova-Ivanova, B. Paczosa-Bator, J. Bobacka, A. Lewenstam, D. Diamond. “Diagnostic of functionality of polymer membrane–based ion-selective electrodes by impedance spectroscopy”, Analytical Methods, vol 2, issue 10, pp. 1490-1498, 2010.

[4] C. M. McGraw, S. E. Stitzel, J. Cleary, C. Slater, D. Diamond, “Autonomous microfluidic system for phosphate detection”, Talanta, Vol. 71, Issue 3, pp. 1180-1185, 2007.

[5] J. Cleary, C. Slater, C. McGraw, D. Diamond, “An Autonomous Microfluidic Sensor for Phosphate: On-Site Analysis of Treated Wastewater”, Sensors Journal, IEEE , vol.8, no.5, pp. 508-515, 2008.

[6] J. Cleary, D. Maher, C. Slater, D. Diamond, “In situ monitoring of environmental water quality using an autonomous microfluidic sensor”, Sensors Applications Symposium (SAS), Limerick, Ireland, pp. 36-40, 2010.

[7] “Directive 2008/50/EC of 21 May 2008 on ambient air quality and cleaner air for Europe”, European Parliament and Council of the European Union, 2008.

[8] “Landfill Manuals – Landfill Monitoring”, 2nd edition, 2003, Environmental Protection Agency, Ireland.

[9] E. Aitchison, “Methane generation from UK landfill sites and its use as an energy source”, Energy Convers. Manage., vol. 37, issue 6-8, pp. 1111-1116, 1996.

[10] S. Beirne, B. Kiernan, C. Fay, C. Foley, B. Corcoran, A.F. Smeaton, D. Diamond, "Autonomous greenhouse gas measurement system for analysis of gas migration on landfill sites", 2010 IEEE Sensors Applications Symposium, SAS 2010, pp. 143-148, doi : 10.1109/SAS.2010.5439422.

 ISBN: 978-1-61208-145-8

Potentialities of $La_{0.7}Sr_{0.3}MnO_3$ thin films for magnetic and temperature sensors at room temperature

Sheng Wu *†‡§, Dalal Fadil*†‡§, Shuang Liu*†‡§, Ammar Aryan*†‡§, Benoit Renault*†‡
Jean-Marc Routoure*†‡§ , Bruno Guillet*†‡§, Stéphane Flament†‡§, Pierre Langlois*†‡§, and Laurence Méchin *†‡§‖
* *Université de Caen Basse-Normandie, UMR 6072 GREYC, F-14032 Caen, France.*
† *ENSICAEN, UMR 6072 GREYC, F-14050 Caen, France*
‡ *CNRS, UMR 6072 GREYC, F-14032 Caen, France*
§ *email addresses: first-name.name @unicaen.fr*
‖ *corresponding author: laurence.mechin@ensicaen.fr*

***Abstract*—In this paper, the potentialities of the manganese oxide compound $La_{0.7}Sr_{0.3}MnO_3$ (LSMO) for the realization of sensitive room temperature thermometers and magnetic sensors are discussed. For these two applications, the sensor performances are described in terms of signal to noise ratio especially in the 1 Hz-100 kHz frequency range. It is shown that due to the very low 1/f noise level, LSMO based sensors can exhibit competitive performances at room temperature.**

***Keywords*- low frequency noise, magnetoresistance sensors, thermometers**

I. INTRODUCTION

Because of the colossal magnetoresistance effect and the strong spin polarization at the Fermi level, the rare-earth manganese oxides may find important applications in magnetoresistive devices such as magnetic random access memories and magnetic sensors [1]. The large change of their electrical resistance R at the metal-to-insulator transition, which takes place around 300 K makes them potential materials for the fabrication of room temperature thermometers. Ideal materials would indeed present at the desired operating temperature T close to 300 K: i) the highest-temperature coefficient of the resistance (β_T), expressed in K^{-1} and defined as the relative derivative of the resistance versus temperature $\frac{1}{R} \cdot \frac{dR}{dT}$, or β_H, expressed in T^{-1}, the highest relative change of the resistance with the magnetic field $\mu_0 H$ and defined as $\frac{1}{R} \cdot \frac{dR}{d(\mu_0 H)}$ (with μ_0 the vaccum permeability) and ii) the lowest noise level. The limits of the device performances will then be given by the signal to noise ratio.

Temperature coefficient of the resistance values and operating temperatures are important parameters to be considered in the fabrication of high sensitivity room-temperature thermometers or magnetoresistances. However, more attention should be drawn to the low-frequency noise level in these materials since it can vary by several orders of magnitude while β_H or β_T values may only vary by a factor less than 10. Noise is more difficult to optimize since its origin is still not well known [2].

Even if it does not exhibit the highest β_T or β_H values, $La_{0.7}Sr_{0.3}MnO_3$ (LSMO) has been selected among all the possible manganite composition because it has shown the lowest reported low-frequency noise level so far [3]–[9].

In this paper, sample preparation is shown in the next Section. In Section III, the measurement set-up and the measurement protocol and low frequency noise measurements are presented. A discussion about the sensor performances as a function of the geometry, of the bias condition and of the frequency is given in Section IV. The performances in terms of thermometers as well as magnetoresistive sensors are then presented and compared with published values.

II. SAMPLE PREPARATION

The sensors consist in t=100 nm thick LSMO thin films deposited by pulsed laser deposition from a stoichiometric target onto $SrTiO_3$ [001] single crystal substrate. The laser radiation energy density, the target-to-substrate distance, the oxygen pressure and the substrate temperature were 220 mJ, 50 mm, 0.35 mTorr and 720 °C respectively. These parameter values were found optimal for producing single-crystalline films with smooth surface as judged by x-ray diffraction and atomic force microscopy. The x-ray diffraction study indicated a full [001] orientation of the LSMO films. The magnetic moment as a function of the temperature was measured using a superconducting quantum interference device. We thus measured a Curie temperature of about 340 K, typical for good quality films of this composition.

After LSMO deposition, a 200 nm thick gold layer was sputtered on the films in order to make low resistive connections. The LSMO thin films were patterned by UV photolithography and argon ion etching to form lines. As shown in Figure 1, the mask enables the study of lines of four different widths W=20, 50, 100 and 150 μm. For each width, five lengths L could be measured depending on the position of the voltage contacts 50, 100, 150, 200, and 300 μm. tens of samples with different geometries have

 ISBN: 978-1-61208-145-8

been investigated. Typical results for a 100 nm thick sample are reported here.

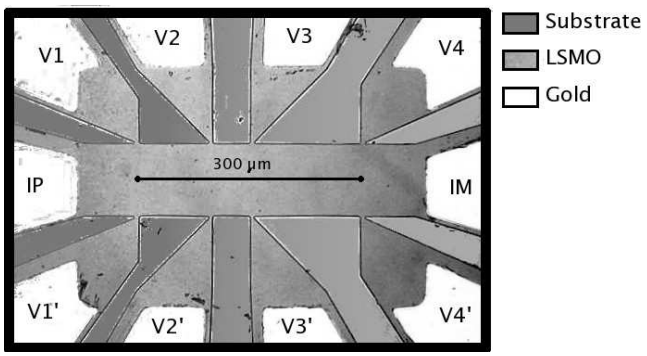

Figure 1. Optical photography of a 100 μm width line with the two current probes IP and IM and 4 voltage probes (V1...V4, V1'...V4') on each side of the line. The line lengths between V1 -V2, V2 - V3 and V3 -V4 are 100 μm, 50 μm and 150 μm respectively.

III. Low frequency noise measurements

A. Measurement set-up and protocol

The experimental set-up mainly consists in one low noise high output impedance DC current source and a dedicated low noise instrumentation amplifier with the following characteristics: a DC output dedicated to resistance measurement with a voltage gain equal to 10 and an AC output dedicated to noise measurements with a voltage gain around one thousand and a 1 Hz-1 MHz bandwidth [10]. The input voltage white noise is around $20 \cdot 10^{-18}$ V^2·Hz^{-1} and its input current noise is negligible. The device is connected at the output of the DC current source using IP and IM pads (defined in Figure 1). The DC voltage as well as the voltage noise are measured using the instrumentation amplifier connected either on IP, IM pads for two probe configuration or on Vi, Vj (i,j=1..4 with i≠j) for four probe configuration. A spectrum analyzer Agilent 89410A calculates the noise spectral density for frequencies in the 1 Hz-1 MHz range.

According to [10], the DC current source is quasi-ideal: its output impedance is infinite and its noise contribution is negligible. It is also assumed that the input impedance of the instrumentation amplifier is very high so that no DC current flows in its inputs. It will be also considered that the noise contribution of the amplifier is known and can be subtracted from the measured noise when a device is connected at its input. The noise of the measurement set-up is deduced from the measurement performed at zero bias. This set-up contribution is then removed for all the measurement points when the current is non zero.

Different noise contributions that both generate white noise and 1/f noise have to be considered in the sensor: the voltage contact noise, the current contact noise and the film noise. Details can be found in [11] and it can be shown that in the two probe configuration, the film and current contact noise contributions are measured. In the four probe configuration, due to the high output impedance of the DC current source, the current contact noise contribution can be completely eliminated. Since no DC current flows into the voltage contact, one would assumed that no 1/f noise exists for the voltage contact sources.

B. Obtained results

Figure 2 shows the noise spectral density measured in the two probe (S_{V2p}) and the four probe configurations (S_{V4p}) for the same DC current I. Two noise contributions were found: a white noise one and a 1/f noise one. The white noise level is clearly due the thermal noise contribution given by $4 \cdot k_B \cdot T \cdot R$ (k_B is the Boltzmann constant equal to $1.38 \cdot 10^{-23}$ J·K^{-1}) and should not depend on the bias. The white noise level is consistent with the expected value deduced from the DC measurement of the sample resistance thus validating the thermal origin of the white noise.

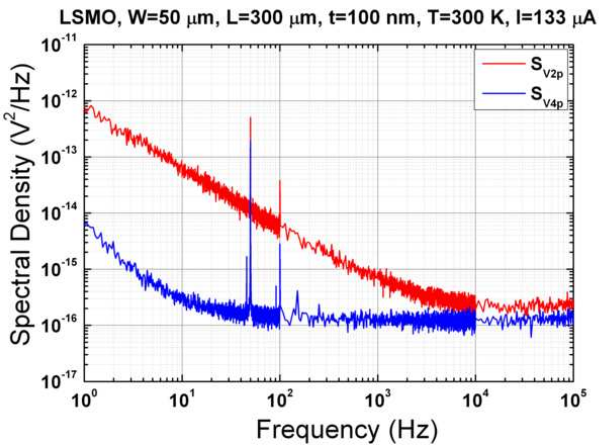

Figure 2. Noise spectral densities in the two probe (S_{V2p}) and the four probe (S_{V4p})configurations for the same DC bias current. With the mask shown in the Figure 1, the current contact noise is non negligible and may have a great impact on sensor performances.

For this sample, the current contact contribution is much higher than the film noise. This results has already been reported by other studies [12]. It can lead to an overestimation of the film noise if the current source used for the measurement does not exhibit a large output impedance (at least 30 times higher if the current contact noise is one thousand time higher than the film noise).

The contact contribution originates from the contact between gold and LSMO and thus presents a great impact for sensor applications. The sensor can not be used with two contact configuration. A four probe configuration must be used to ensure best signal to noise ratio. Moreover, the metallic pads used for the voltage contacts have also to be

 ISBN: 978-1-61208-145-8

placed in a correct manner in order to avoid any possible current path through this metallic contact. As a consequence, metallic voltage pads should not be placed onto the line (like in Transmission Line Measurement (TLM) patterns for instance) but on the side of the line in order to achieve a low frequency noise level sensor.

Figure 3 shows the voltage noise spectral density measured for a typical device (W=50 μm and L=300 μm) in four probe configuration for different values of the bias current I in the device. The inset shows the noise level at 1 Hz versus the DC voltage V across the sample. As expected, the white noise level does not depend on the bias current and 1/f noise level depends on the square of the DC voltage V.

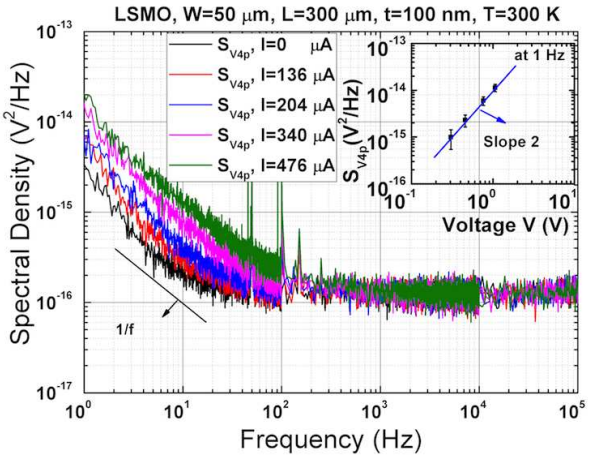

Figure 3. Noise spectral density measured in the four probe configuration at different bias currents. White noise does not depend on the bias point on the contrary of 1/f noise. The inset shows that the 1/f noise at 1 Hz depends on the square of the DC voltage V.

From measurements performed on different geometries, it follows that the 1/f noise level at 1 Hz is in the inverse ratio of the device volume $W \cdot L \cdot t$. Finally, the noise spectral density of the sample in the four probe configuration $S_{V4p}(f)$ can be written as follow:

$$S_{V4p}(f) = \frac{K_{1/f}}{f \cdot W \cdot L \cdot t} V^2 + \frac{4 \cdot k_B \cdot T \cdot \rho \cdot L}{W \cdot t} \quad (1)$$

In equation 1, ρ is the film electrical resistivity (typical value of 2 mΩ·cm for LSMO at 300 K) and $K_{1/f}$ is a material characteristic independent of the geometry that quantify the value of the 1/f noise level. In this sample, $K_{1/f}$ is found around $1 \cdot 10^{-30}$ m^3.

Equation (1) clearly shows length and bias dependency of the noise are completely different in the low frequency and white noise ranges. These discussions are extended in the next Section in the framework of sensor performance analysis.

IV. Sensor performances

In this Section, the performances in terms of signal to noise ratio will be presented and discussed in the case of thermometers and magnetoresistance sensors.

A. Background

To use the devices as sensors, a current source is connected and the voltage across the sensor is measured. A four probe configuration will be used to avoid the current contact noise contribution. Either the temperature T or the magnetic field $\mu_0 H$ are the mesurand. For these theoretical derivations, the mesurand will be noted M and the relative sensitivity β_M, defined in the following equation, will be used:

$$\beta_M = \frac{1}{R} \cdot \left(\frac{dR}{dM} \right)_{M0} \quad (2)$$

$M0$ is the DC value of the mesurand for which the relative sensitivity is estimated. The equivalent input sensor noise $S_M(f)$ is given by the ratio of the voltage noise spectral density of the sensor $S_V(f)$ (given by $S_{V4p}(f)$ in the case of our LSMO samples in the previous sample) over the square of the voltage sensitivity at $M0$ given by $(dV/dM = V \cdot \beta_M)$. Using equation (1), it follows that $S_M(f)$ finally writes:

$$\begin{aligned} S_M(f) &= \frac{S_V(f)}{(dV/dM)^2} \\ &= \frac{1}{\beta_M^2} \left(\frac{K_{1/f}}{f \cdot W \cdot L \cdot t} + \frac{4 \cdot k_B \cdot T \cdot \rho \cdot L}{V^2 \cdot t \cdot W} \right) \end{aligned} \quad (3)$$

In order to obtain the smallest noise sensor, this equation shows that in addition to large sensitivity values, low value of the 1/f noise parameter $K_{1/f}$ and low value of the electrical resistivity are first required. Two geometrical and bias dependencies can then be distinguished:

- in the low frequency part where 1/f noise dominates, the equivalent input sensor noise does not depend on the bias and the sample should have the largest volume $W \cdot L \cdot t$.
- in the white noise range of frequencies, the equivalent input sensor noise decreases with the square of the bias voltage. The geometry should have the smallest ratio value L/W and the sensor should also be as thick as possible.

All these considerations obviously do not take into account other constraints such as frequency bandwidth or cost, which usually leads to opposite conclusions in term of device volume or size. These results are illustrated in the next Sections for thermometers and magnetoresistance sensors for a optimal devices regards 1/f noise (L=300 μm, W=150 μm).

 ISBN: 978-1-61208-145-8

B. Thermometers

LSMO electrical resistivity ρ and relative temperature sensitivity β_T (also called TCR for thermometers) versus temperature T are shown in Figure (4). In this kind of material, a transition from metallic to insulator behavior occurs for temperature close to room temperature as already reported [13]. In this sample, the maximum value of β_T is found for temperature close to 330 K. A typical value is reported in Table I.

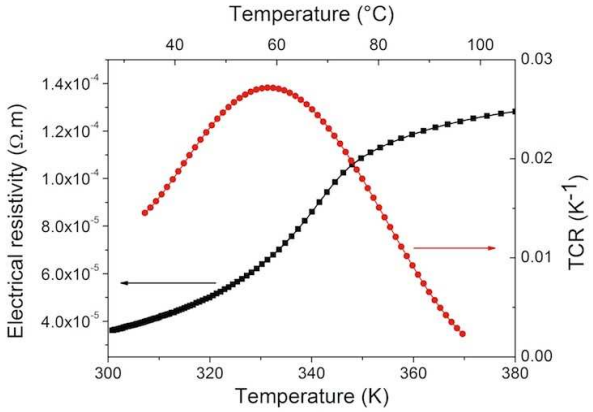

Figure 4. LSMO electrical resistivity ρ(square symbols, left axis) and relative temperature sensitivity β_T (circle symbols, right axis) versus temperature T in the 300-380 K range for a line with W=50 μm and L=300 μm. The maximum sensitivity is found around 330 K where β_T=2.7 $\cdot 10^{-2}$ K^{-1}.

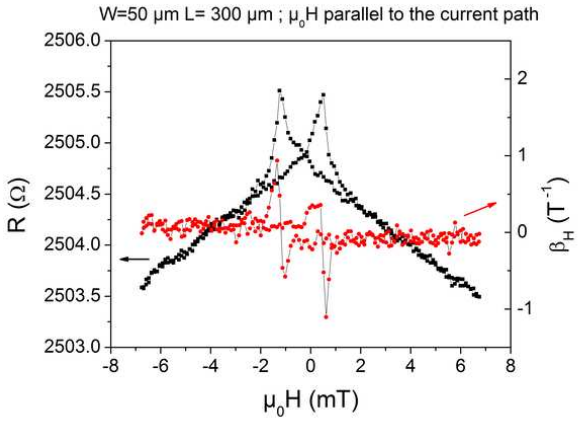

Figure 5. LSMO electrical resistance R (square symbols, left axis) and relative magnetic field sensitivity β_H (circle symbols, right axis) as a function of the magnetic field $\mu_0 \cdot H$ at room temperature for a line with W=50 μm and L=300 μm. Magnetic field is parallel to the current direction. Sensitivity maxima observed at low magnetic field are related to the magnetization reversal in the film.

Parameter	Value
$K_{1/f}$ (m^3) at 300 K	$1 \cdot 10^{-30}$
ρ ($\Omega\cdot$ m) at 300 K, at 330 K	$3.5{\cdot}10^{-5}$, $6.3{\cdot}10^{-5}$
β_T at 330 K (K^{-1})	$2.7{\cdot}10^{-2}$
β_{HMAX} at 300 K (T^{-1})	$\simeq 1$

Table I
TYPICAL ELECTRICAL CHARACTERISTICS AND NOISE PROPERTIES OF THE SAMPLE USED FOR THE ESTIMATIONS OF THE SIGNAL TO NOISE RATIO. FOR THESE VALUES, THE DEVICE LENGTH AND WIDTH ARE RESPECTIVELY 300 μm AND 50 μm.

C. Magnetoresistance sensors

LSMO electrical resistance and relative magnetic field sensitivity β_H as a function of the magnetic field $\mu_0 \cdot H$ are shown in the Figure 5. Due to the ferromagnetic behavior of LSMO at room temperature, a magnetoresistance effect is observed. Two kinds of effect can be distinguished: i) a Colossal MagnetoResistance effect (CMR) for magnetic field values greater than 2 mT [14], [15] and ii) a low magnetoresistance effect for magnetic field values close to 0.5 mT. The first one leads to a small sensitivity with no interesting sensor applications. The second one is related to the magnetization reversal [16]–[18]. It leads to two peaks in the R versus $\mu_0 H$ characteristic and a relatively high value of the relative magnetic field sensitivity (absolute typical values around 1 T^{-1} for an operation point around 1 mT) at room temperature (cf. Table I).

D. Discussions

In this discussion, it will be assumed that the thermometer or the magnetoresistance is connected in four probe configuration and that the device geometry leads to the smallest value of 1/f noise. The noise performances in terms of equivalent input sensor noise values of DC current will be calculated with the data in Table I for three values of the DC current I=100 μA, I=1 mA and I=5 mA.

Table II summarizes the results for a 150 μm wide and 300 μm long thermometer or magnetoresistance at optimal operating point (330 K for the thermometer, 300 K and 0.1 mT for the magnetoresistance). In this Table, the equivalent input sensor noise has been calculated at two frequencies (30 Hz and 10 kHz) to distinguish between the low frequency domain where 1/f noise dominates and the white noise domain.

The equivalent input sensor spectral densities $S_T(f)$ (also called NET Noise Equivalent Temperature) and $S_H(f)$ calculated using equation 3 and data from Table I are shown in Figure 6. As expected, the spectral density at low frequency does not depend on the bias when 1/f noise dominates. On the contrary, at high frequency, the noise level is directly related to the applied bias current. From this Figure, it appears that ultimate performances can be achieved at highest current. This remarks has obviously to be moderated by the fact that self heating effects occur for too high current values so that the noise performances will

 ISBN: 978-1-61208-145-8

Bias current I (mA)	0.1	1	5
$\frac{dV}{d(\mu_0 H)}$ at 300 K (mV/T) (*)	45.5	455	2275
$\sqrt{S_H(f)}$ at 300 K (nT·Hz$^{-0.5}$)			
f=30 Hz	78	8.6	4.4
f=10 kHz	75	7.5	1
$\frac{dV}{dT}$ at 330 K (mV/K) (**)	3.4	34	170
$\sqrt{S_T(f)}$ at 330 K (nK·Hz$^{-0.5}$)			
f=30 Hz	1400	170	100
f=10 kHz	1400	140	30

Table II
SENSOR PERFORMANCES FOR A 150 μm WIDE 300 μm LONG LINE AT DIFFERENT BIAS CURRENT I. (* R=700 Ω AT 300 K, ** R=1260 Ω AT 330 K.)

be discussed in the following for a bias current limited to 100 μA. At low bias current, the 1/f noise contribution is negligible. In this LSMO sample, due to the low value of the 1/f noise level, the noise spectral density mainly consists in white noise even at a bias current of about 300 μA.

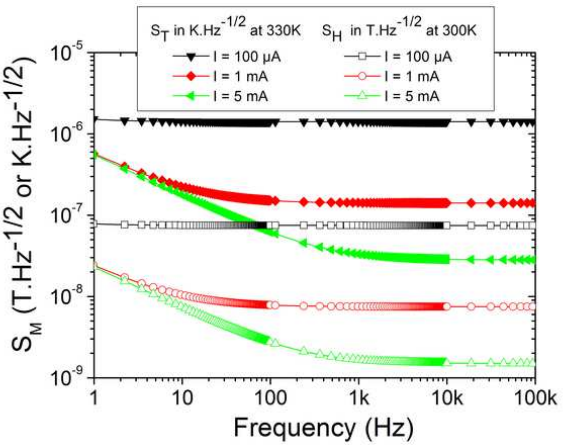

Figure 6. Square root of the estimated equivalent input sensor spectral densities $S_T(f)$ (filled symbols) or $S_H(f)$(open symbols) using equation (3) and the Table I data for three values of the DC current I for a 150 μm width and 300 μm length sensor.

These NET values are lower (at least one magnitude order) than the one of other uncooled thermometers such as amorphous semiconductors, vanadium oxides, etc. or the well-known Pt100 thermometer [8], [9]. This can easily be explained by the lower noise level of epitaxial manganites thin films compared to others. The results show that despite a quite small TCR value and thanks to a very low-noise level, LSMO thin films are real potential material for uncooled thermometry.

According to [19] where equivalent input sensor spectral densities $S_H(f)$ have been compared for various kinds of magnetic sensors, this LSMO magnetoresistance noise performances are better than hall effect sensors. Equivalent input sensor spectral densities is only one order of magnitude higher than commercial honeywell HMC1001 sensors. Same results are also proposed by [19], [20]. These results are promising since the mask used was not optimized for sensor applications so that the sensitivity could be increased by changing the substrate type or the line geometry. Moreover, it has been demonstrated that LSMO can be deposited onto silicon substrate [21] without modifications of the magnetic properties: compatibility with the standard semiconductor used in the microelectronic industry has thus been demonstrated. This is another way to extend to "More than Moore" idea proposed by the International Roadmap for Semiconductor by the integration of manganese oxide.

V. CONCLUSIONS

In this paper, the potentialities of LSMO thin films as magnetic and temperature sensors at room temperature have been reported. It has been shown that a four probe configuration is required to remove the current contact noise that is often several order of magnitude higher than the material noise. In such conditions, It has been shown that the performances of the room thermometers are competitive and that magnetoresistance exhibits noise performances one decade better than classical hall effect sensors.

REFERENCES

[1] T. Venkatesan, M. Rajeswari, Z.-W. Dong, S. B. Ogale, and R. Ramesh, "Manganite-based devices: opportunities, bottlenecks and challenges," *Philos. Trans. R. Soc. London, Ser. A*, vol. 356, no. 1742, pp. 1661–1680, 1998.

[2] M. Rajeswari, A. Goyal, A. Raychaudhuri, M. Robson, G. Xiong, C. Kwon, R. Ramesh, R. Greene, T. Venkatesan, and S. Lakeou, "1/f electrical noise in epitaxial thin films of the manganite oxides $La_{0.67}Ca_{0.33}MnO_3$ and $Pr_{0.67}Sr_{0.33}MnO_3$," *Appl. Phys. Lett.*, vol. 69, no. 6, pp. 851–853, 1996.

[3] B. Raquet, J. Coey, S. Wirth, and S. von Molnár, "1/f noise in the half-metallic oxides CrO_2, Fe_3O_4, and $La_{2/3}Sr_{1/3}MnO_3$," *Phys. Rev. B*, vol. 59, no. 19, pp. 12 435–12 443, 1999.

[4] A. Lisauskas, S. Khartsev, and A. Grishin, "Studies of 1/f Noise in $La_{1-x}M_xMnO_3$ (M= Sr, Pb) Epitaxial Thin Films," *J. Low Temp. Phys.*, vol. 117, no. 5, pp. 1647–1651, 1999.

[5] A. Palanisami, R. Merithew, M. Weissman, M. Warusawithana, F. Hess, and J. Eckstein, "Small conductance fluctuations in a second-order colossal magnetoresistive transition," *Phys. Rev. B*, vol. 66, no. 9, p. 92407, 2002.

[6] L. Méchin, J.-M. Routoure, S. Mercone, F. Yang, S. Flament, and R. Chakalov, "1/f noise in patterned $La_{0.7}Sr_{0.3}MnO_3$ thin films in the 300–400 K range," *J. Appl. Phys*, vol. 103, p. 083709, 2008.

[7] K. Han, Q. Huang, P. Ong, and C. Ong, "Low-frequency noise in $La_{0.7}Sr_{0.3}Mn_{1-x}Fe_xO_3$ thin films," *J. Phys. Condens. Matter*, vol. 14, p. 6619, 2002.

 ISBN: 978-1-61208-145-8

[8] F. Yang, L. Méchin, J.-M. Routoure, B. Guillet, and R. A. Chakalov, "Low-noise $La_{0.7}Sr_{0.3}MnO_3$ thermometers for uncooled bolometric applications," *J. Appl. Phys*, vol. 99, no. 2, p. 024903, Jan 2006.

[9] L. Méchin, J.-M. Routoure, B. Guillet, F. Yang, S. Flament, D. Robbes, and R. Chakalov, "Uncooled bolometer response of a low noise $La_{2/3}Sr_{1/3}MnO_3$ thin film," *Appl. Phys. Lett.*, vol. 87, p. 204103, 2005.

[10] J.-M. Routoure, D. Fadil, S. Flament, and L. Méchin, "A low-noise high output impedance DC current source," in *Proceedings of the 19th International Conference on Noise and Fluctuations; ICNF 2007, AIP Conference Proceedings*, vol. 922, no. 1, 2007, pp. 419–424.

[11] C. Barone, A. Galdi, S. Pagano, O. Quaranta, L. Méchin, J. Routoure, and P. Perna, "Experimental technique for reducing contact and background noise in voltage spectral density measurements," *Rev. Sci. Instrum.*, vol. 78, p. 093905, 2007.

[12] C. Barone, S. Pagano, L. M. echin, J.-M. Routoure, P. Orgiani, and L. Maritato, "Apparent volume dependence of 1/ f noise in thin film structures: Role of contacts," *Rev. Sci. Instrum.*, vol. 79, p. 053908, 2008.

[13] A. Urushibara, Y. Moritomo, T. Arima, A. Asamitsu, G. Kido, and Y. Tokura, "Insulator-metal transition and giant magnetoresistance in $La_{1-x}Sr_xMnO_3$," *Phys. Rev. B*, vol. 51, no. 20, pp. 14 103–14 109, 1995.

[14] J. O'Donnell, M. Onellion, M. Rzchowski, J. Eckstein, and I. Bozovic, "Low-field magnetoresistance in tetragonal $La_{1-x}Ca_xMnO_3$ sfilms," *Phys. Rev. B*, vol. 55, no. 9, p. 5873, 1997.

[15] ——, "Anisotropic properties of molecular beam epitaxy-grown colossal magnetoresistance manganite thin films," *J. Appl. Phys*, vol. 81, p. 4961, 1997.

[16] M. Saïb, M. Belmeguenai, L. Méchin, D. Bloyet, and S. Flament, "Magnetization reversal in patterned $La_{0.67}Sr_{0.33}MnO_3$ thin films by magneto-optical Kerr imaging," *J. Appl. Phys*, vol. 103, no. 11, p. 113905, Jun 2008.

[17] L. Méchin, P. Perna, M. Saïb, M. Belmeguenai, S. Flament, C. Barone, J. Rouroure, and C. Simon, "Structural, 1/f noise and MOKE characterization of vicinal $La_{0.7}Sr_{0.3}MnO_3$ thin films," *Acta Phys. Pol. A*, vol. 111, no. 1, pp. 63–70, 2007.

[18] T. McGuire and R. Potter, "Anisotropic magnetoresistance in ferromagnetic 3d alloys," *IEEE Trans. Magn.*, vol. 11, no. 4, pp. 1018– 1038, 1975.

[19] A. Jander, C. Smith, and R. Schneider, "Magnetoresistive sensors for nondestructive evaluation (Invited Paper)(Proceedings Paper)," in *proceeding of the 10th SPIE International Symposium, Nondestructive Evaluation for Health Monitoring and Diagnostics, Conference 5770*, Jan 2005.

[20] M. Díaz-Michelena, "Small magnetic sensors for space applications," *Sensors*, vol. 9, no. 4, pp. 2271–2288, 2009.

[21] M. Belmeguenai, S. Mercone, C. Adamo, L. Méchin, C. Fur, P. Monod, P. Moch, and D. G. Schlom, "Temperature dependence of magnetic properties of $La_{0.7}Sr_{0.3}MnO_3/SrTiO_3$ thin films on silicon substrates," *Phys. Rev. B*, vol. 81, no. 5, p. 054410, Feb 2010.

 ISBN: 978-1-61208-145-8

MEMS-based Ethanol Sensor Using Zinc Oxide Nanostructured Films

Hardik Jeetendra Pandya, Sudhir Chandra, Anoop Lal Vyas
Indian Institute of Technology Delhi, Hauz Khas
New Delhi, India
hjpele@yahoo.com, schandra@care.iitd.ernet.in, alvyas@iddc.iitd.ac.in

***Abstract*—An ethanol sensor incorporating nanostructured zinc oxide film and silicon micromachining is reported. A salient feature of the sensor is its lower operating temperature which has been achieved due to the use of nanostructured material as sensing layer. A suitably designed nickel microheater has been integrated with the sensor. The optimum temperature of operation for ethanol sensing was found to be 100 °C, though the sensor could operate at temperature as low as 50 °C with reduced sensitivity. The power consumption, at an operating temperature of 100 °C, was 180 mW while at 50 °C, it is only 90 mW. The sensor is capable of giving detectable response for concentrations of ethanol vapor as low as 10 ppm.**

Keywords- Zinc films; Zinc oxide nanocombs; Thermal evaporation; Lithography; Ethanol sensor.

I. INTRODUCTION

Sensors based on metal oxides for detection of volatile organic compounds (VOCs) and gases have been widely investigated because of their small size, low cost and compatibility with semiconductor processing. ZnO has great potential for use in gas sensors because of the high mobility of conduction electrons and good chemical and thermal stability under the operating conditions. The higher operating temperature (approximately 400 °C) and poor sensitivity are some of the major concerns in using ZnO as sensing layer [1]. The use of CMOS (complimentary metal oxide semiconductor) compatible MEMS (micro-electro-mechanical-systems) technologies in sensor fabrication is advantageous on account of miniaturization of the devices, lower power consumption, faster sensor response, batch fabrication at reduced cost and greater sensitivity [2–5].

The use of nano-structured materials for the sensing device is envisaged to further improve the sensitivity of these devices. This is attributed to enormously increased surface to volume ratio compared to their bulk counterpart. It is further envisaged that the use of nanostructured material may leads to lowering of operating temperature of gas sensors based on metal oxide semiconductors [6]. Very few reports have been published on sensors using nano-structured ZnO thin film on micromachined silicon substrate [8, 9]. In most of the publications on sensors incorporating micromachined microheaters, either platinum or polysilicon microheater has been used as the heating element as these materials are particularly suitable for the higher temperature operation (400–700 °C) [10-12]. Furthermore, with a view to reduce the power consumption, the platforms for micromachined gas sensor reported so far are based on a SiO_2-Si_3N_4 composite layer on a thick (~ 400 μm) silicon substrate [13]. A thin Si plug underneath the dielectric membrane can be used for achieving uniform temperature distribution over the active heater area owing to the higher thermal conductivity of Si [14]. Recently, few reports on operating gas sensors at relatively lower temperatures using nanotextured semiconducting oxides have been published [7, 15]. This type of gas sensor operates at relatively lower temperature (150–250 °C) and does not require an expensive Pt or poly-Si microheater [7, 15]. The microheater may be fabricated using a low cost material such as nickel.

The present work is an attempt to address the problems of elevated operating temperature and high power consumption by taking a twin approach namely: (a) reducing the operating temperature through the use of nanostructured metal oxide (ZnO) and (b) reducing the power consumption through the deployment of MEMS structure with a thin silicon membrane. In this paper we report a nanostructured ZnO based sensor using micromachined silicon substrate for efficient detection of ethanol vapors in the range of 200 – 1000 ppm at fairly low operating temperature of 50 °C. For this purpose, a nickel microheater has been designed and monolithically integrated with the sensor to obtain the required heating of the sensing layer. The response of the nanostructured ZnO based sensor having an integrated nickel microheater has been evaluated at different operating temperatures in the range of 30–100 °C, for different concentrations of ethanol vapors.

II. EXPERIMENTAL WORK

A schematic drawing of the sensor structure is shown in Fig. 1 and the corresponding process flowchart is shown in Fig. 2. The starting silicon wafer is 280 μm thick, N-type, having 5-10 Ω-cm resistivity and (100) orientation. A layer of SiO_2 (0.8 μm) was grown by thermal oxidation process. After opening a window in SiO_2 by photolithography technique on the backside of the wafer, bulk micromachining was carried out in 40 % KOH solution at a temperature of 80 °C, to obtain a 100 μm Si membrane.

 ISBN: 978-1-61208-145-8

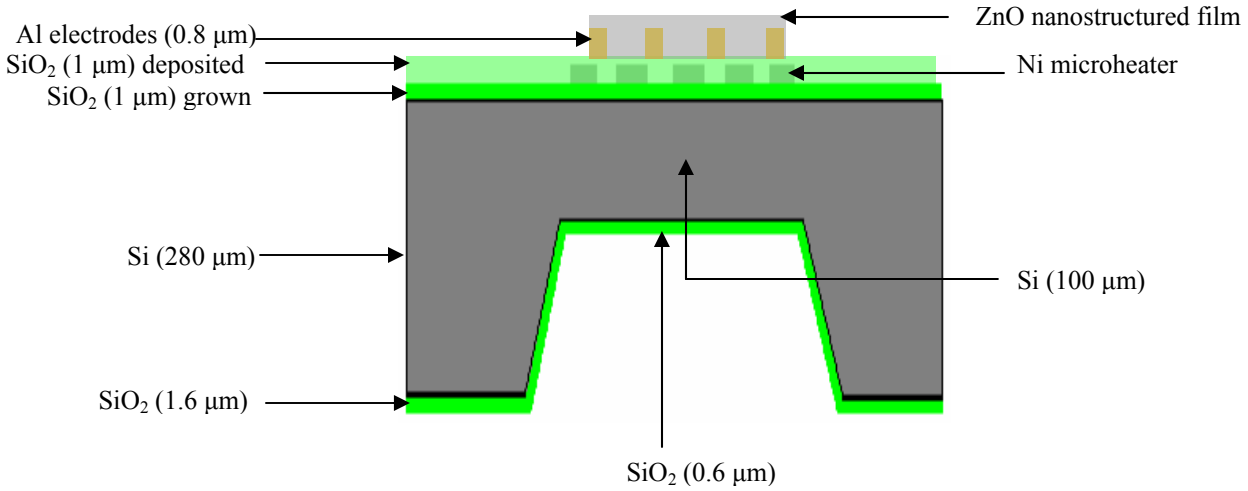

Figure 1. A schematic diagram of the MEMS gas sensor.

A silicon oxide layer (0.8 μm) was then grown in the next step. The purpose of this oxidation is to reduce the thermal losses from the backside of the membrane. A layer of nickel (0.3 μm thickness) was then deposited using RF diode sputtering on the front side of the oxidized wafer. The Ni layer was then patterned using photolithography to form the microheater. The meander shaped Ni microheater has line- width of 100 μm and the gap between the lines was also kept 100 μm. A layer of SiO_2 (0.8 μm) was then sputter deposited on the front side of the wafer. The purpose of this step is to electrically isolate the heater and the aluminum interdigital electrodes (to be formed in the next step). The aluminum layer of 0.8 μm was then deposited by thermal evaporation and patterned to form the sensing interdigital electrodes. A thin film of Zn (0.3 μm) was then deposited by thermal evaporation and patterned using photolithography process. The wafer was then heated to 300 °C in air for 6 h and cooled slowly to room temperature. It was observed that, following the annealing process, the color of the deposited Zn films turned white from the grey color of the as-deposited zinc films. The active area of the sensing layer was 2 mm X 2 mm while the total chip size was 5 mm X 5 mm.

III RESULTS AND DISCUSSION

The SEM image of the backside of the membrane is shown in the Fig. 3. Most of the papers reported so far use a freestanding dielectric layer (SiO_2 or SiO_2–Si_3N_4 composite) for lower power consumption and higher operating temperature at the cost of long-term stability [16-17]. In the present work, a 100 μm Si membrane has been used for better mechanical stability which also provides fairly good temperature uniformity. The SEM image of Ni microheater is shown in Fig. 4. The resistance of the heater was measured to be about 120 Ω. The experimentally measured power consumption versus temperature graph for the Ni microheater is shown in Fig. 5.

It can be observed that the power consumption, at a temperature of 50 °C, was 90 mW and at 100 °C, it was 180 mW. The microheater was driven by 5 V supply. The X-ray diffractograms (XRD) of the as-deposited Zn film and ZnO film (obtained by annealing of Zn film in air at 300 ºC for 6 h) are shown in Fig. 6. The XRD of the annealed film shows the peaks corresponding to ZnO, confirming that the Zn film has been completely oxidized to form ZnO. The SEM image of nanostructured ZnO film is shown in Fig.7. It can be seen that the film consists of nanocombs of ZnO. It is further observed that each comb is composed of stem to which many nanowires are attached. The nanowires have diameter in the range 40-50 nm and length of up to 500 nm.

The sensor was tested for ethanol vapors in a closed chamber. The sensor was heated to different temperatures by applying power to the integrated heater. The ethanol vapors were introduced in the chamber by bubbling N_2 through the ethanol maintained at room temperature (20 °C). The desired concentration of the vapors was obtained in the chamber by controlling the flow rate of N_2 through ethanol and adding pure air through a separate gas line [18]. The flow rates were measured and controlled using precession flow meters. The concentration of ethanol vapors was calculated using the following equation [19].

$$C = \frac{\frac{P^* \times L}{760 - L}}{\frac{P^* \times L}{760 - L} + L + L^*} \times 10^6 \qquad (1)$$

where, L and L* are gas flow rates of N_2 (through the bubbler) and air respectively. P* is the vapor pressure of the ethanol (in mm of Hg) at room temperature (20 ºC).

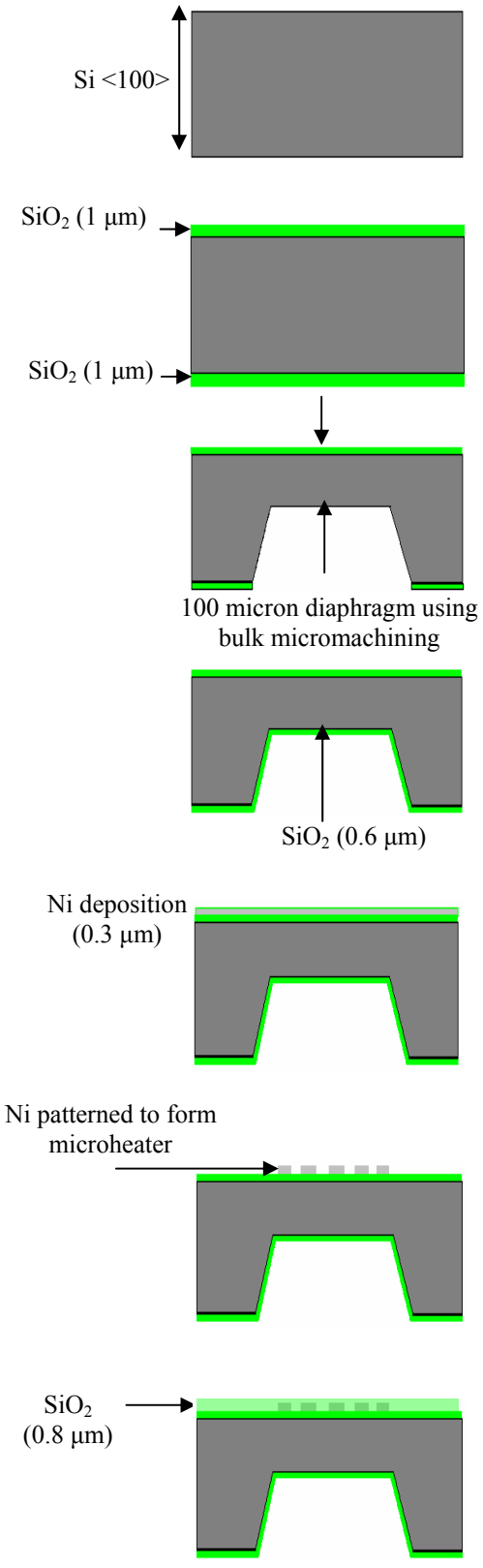

Figure 2. Process flow chart for the fabrication of nanostrucutred ZnO based micromachined ethanol sensor with embedded Ni microheater.

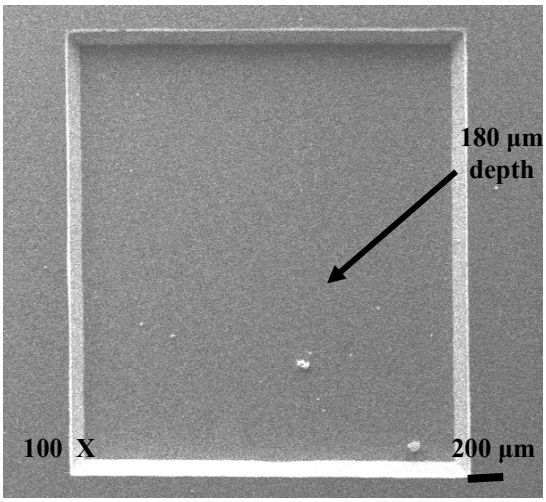

Figure 3. SEM image of micromachined diaphragm from the back side.

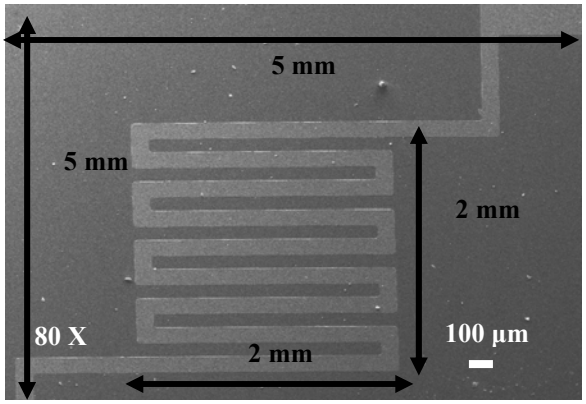

Figure 4. SEM image of nickel microheater

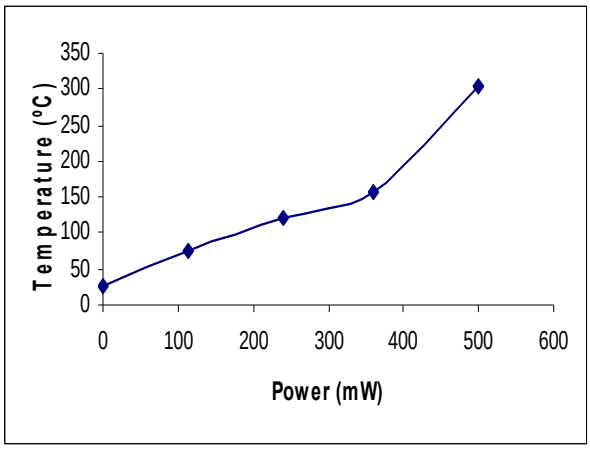

Figure 5. Plot of power versus temperature obtained for Ni microheater

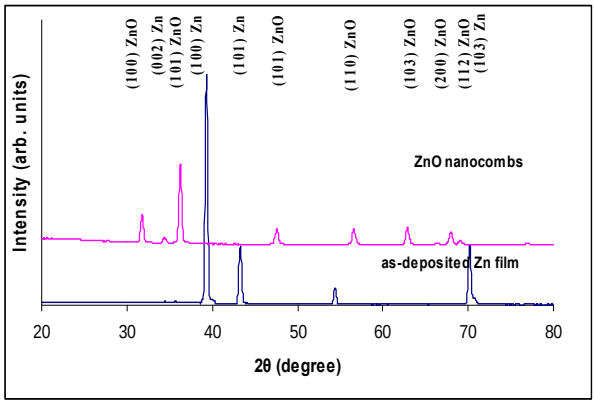

Figure 6. XRD micrographs of as-depsoited Zn film and Zn annealed at 300 °C for 6 h.

Based on this equation, the relationship between the flow rates and the concentration of ethanol in ppm is summarized in Table1. Fig. 8 shows the response (Ra-Rg) / Rg of the

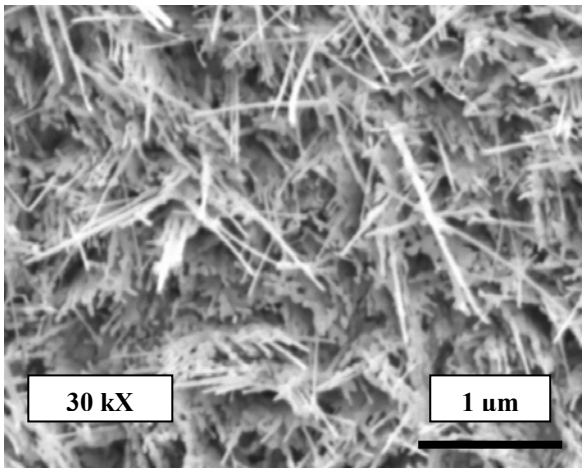

Figure 7. SEM image of ZnO nanocombs obtained after annealing Zn film (300 nm) at 300 °C for 6 h.

sensor for 200 ppm of ethanol vapors as a function of its operating temperature. Here, we define Ra and Rg as the resistance of the sensor in clean air and in the ethanol containing air respectively. From Fig. 8, it can be observed that the maximum sensitivity is achieved at the operating temperature of 100 °C. At the lowest operating temperature of 30 °C, the sensitivity falls significantly, but the sensor is still able to detect the presence of ethanol.

Table I. Relationship between flow rates and ethanol vapor concentrations in the test chamber at 20 °C. The vapor pressure (P*) of ethanol at 20 °C is 67.5 mm of Hg [19, 20].

Flow rate of N_2 through bubbler containing ethanol (ml/min)	Flow rate of air used for diluting ethanol concentration (L/min)	Ethanol concentration (ppm)
10	5	180
20	5	363
20	4	453
30	5	552
40	5	746
50	5	940

At 50 °C, the sensitivity of the sensor improves significantly. It is evident from Fig. 8 that as the operating temperature of the sensor decreases the time to reach the saturation level increases. This is consistent with the operation of gas sensors based on metal oxides [9, 12]. Fig. 9 shows the response of the sensor to successively increasing concentrations of ethanol vapor. This was achieved by increasing the flow rate of N_2 through the bubbler corresponding to the desired concentration levels, as shown in Table 1. As expected, the sensitivity increases for higher concentrations of ethanol. Furthermore, it can be

 ISBN: 978-1-61208-145-8

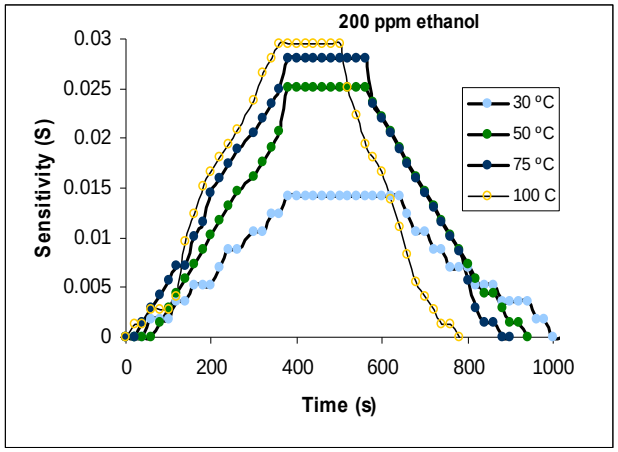

Figure 8. Response of sensor to 200 ppm of ethanol vapors as a function of operating temperature.

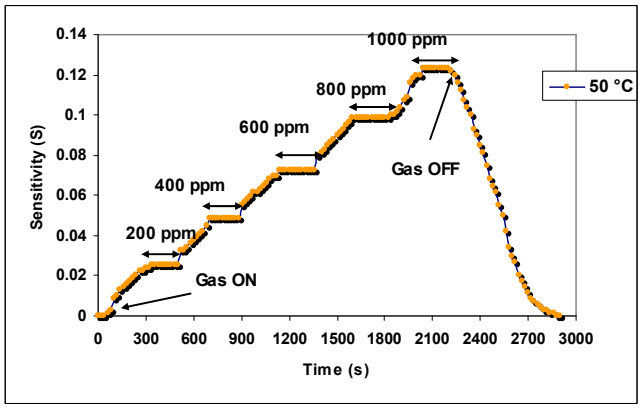

Figure 9. The dynamic response of the sensor for different concentration of ethanol vapors on injection and switching off the N_2 passing through bubbler.

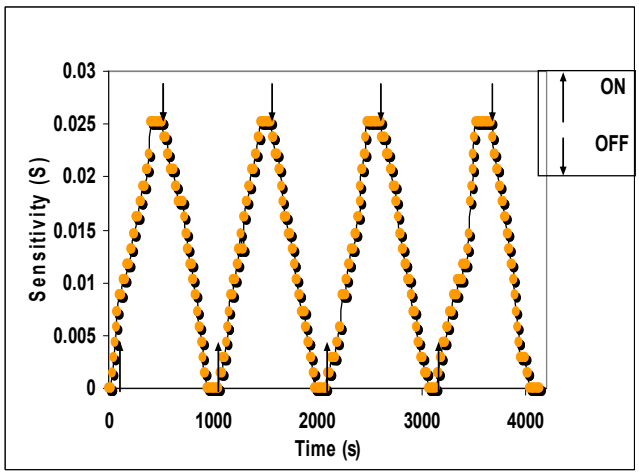

Figure 10. Dynamic response of the sensor for 200 ppm ethanol vapor operating at 50 °C. The arrows indicate the switching ON and OFF of N_2 flowing through the bubbler containing ethanol.

seen that there is varying delay in reaching the saturation value of the sensor resistance, as the ethanol concentration is increased in steps. Since the volume of the test chamber is quite large (14 L) in our test set up, this does not reflect the true response time of the sensor [18]. The dynamic response of the sensor was also evaluated. For this purpose, the N_2 gas (flowing through the bubbler) was turned ON and OFF periodically, as indicated in Fig. 10. Measurements were made at an operating temperature of 50 °C. It is evident that the response of the sensor is reproducible for the selected concentration of ethanol vapors (200 ppm). The response and recovery time of the sensor was almost constant for several cycles which show the good repeatability of the sensor. It was also found that the sensor is sensitive to humidity. Furthermore, if more than one VOC vapors are present then the sensor may give false response.

CONCLUSION

We have successfully synthesized nanostructured ZnO by a low cost process of oxidation of Zn film in air without using any template or catalyst. The integration of the nanostructured ZnO with sensor fabrication process is demonstrated. The sensitivity of the sensor is significantly enhanced and the operating temperature is considerably reduced by using the ZnO nanostructured material. Lowering of the operating temperature of the sensor has significant advantage in terms of power consumption and choice of the heater material. A low cost nickel heater has been successfully integrated with the sensor in the present work. ZnO based MEMS micro-hotplate (with Ni microheater) provides a promising platform for low power sensors for ethanol sensing at a fairly low operating temperature of 50 ºC. Integration of nanostructure ZnO film along with MEMS technology provides a platform for low power low temperature sensor with appreciable sensitivity and response time. It will be interesting to see the sensor behavior in the presence of other VOCs.

REFERENCES

[1] B.L. Zhu, C.S. Xie, W.Y. Wang, K.J. Huang, and J.H. Hu, "Improvement in gas sensitivity of ZnO thick film to volatile organic compounds (VOCs) by adding TiO_2", Mater. Lett. 58, pp. 624-629, 2004.

[2] K.D. Mitzner, J. Strnhagen, and D.N. Glipeau, "Development of micromachined hazardous gas sensor array", Sensors Actuators B, 93, pp. 92–99, 2003.

[3] J.S. Suehle, R.E. Cavicchi, M. Gaitan, and S. Semancik, "Tin oxide gas sensor fabricated using CMOS micro-hotplates and in situ processing", IEEE Electron Dev Lett, 14(3), pp. 118-120, 1993.

[4] J.A. Salcedo, J.L. Juin, Y.M. Afridi, and R.A. Hefner, "On-chip electrostatic discharge protection for CMOS gas sensor systems-on-a-chip (SoC)", Microelectron Reliab,46, pp. 1285–1294, 2006.

 ISBN: 978-1-61208-145-8

[5] X. Lafontan, F. Pressecq, F. Beaudoin, S. Rigo, M. Dardalhon, and J.L. Roux, "The advent of MEMS in space", Microelectron Reliab., 43(7), pp. 1061–1083, 2003.

[6] E. Comini, G. Faglia, G. Sberveglieri, Z. Pan, and Z.L. Wag, "Stable and highly sensitive gas sensors based on semiconducting oxide nanobelts", Appl Phys Lett, 81, pp. 1869–1871, 2002.

[7] P. Bhattacharyya, P.K. Basu, H. Saha, and S. Basu, "Fast response methane sensor using nanocrystalline zinc oxide thin films derived by sol–gel method", Sensors Actuators, B124, pp. 62–67, 2004.

[8] F. Hassani, O. Tigli, S. Ahmadi, C. Korman, and Zaghloul, "Integrated CMOS surface acoustic wave gas sensor: design and characteristics", Proc IEEE Sensors, 2, pp. 1199–1202, 2002.

[9] Q. Wan, Q.H. Li, Y.J. Chen, T.H. Wang, X.L. He, and J. P. Li, "Fabrication and ethanol sensing characteristics of ZnO nanowire gas sensors", Appl Phys Lett, 84, pp. 3654–3656, 2004.

[10] S.M. Lee, D.C. Dyer, and J.W. Gardner, "Design and optimization of a high-temperature silicon micro-hotplate for nanoporous palladium pellistors", Microelectron Journal, 43, pp. 115–1126, 2003.

[11] J. Puigcrobe, D. Vogel, B. Michel, A. Vila, I. GraciaI, and C. Cane, "Thermal and mechanical analysis of micromachined gas sensors", J Micromech Microeng, 13, pp. 548–556, 2003.

[12] W. Chung, C. Shim, S. Choi, and D. Lee, "Tin oxide microsensor for LPG monitoring", Sensors Actuators, B20, pp. 139–43, 1994.

[13] C. Rossi, E. Scheid, and D. Esteve, "Theoretical and experimental study of silicon micromachined microheater with dielectric stacked membranes", Sensors Actuators, A63, pp. 183–189, 1997.

[14] A. Gotz, I. GraciaI, C. Cane, E. Lora-Tamayo, M.C. Horrilo, and J. Getino, "A micromachined solid state integrated gas sensor for the detection of aromatic hydrocarbons", Sensors Actuators, B44, pp. 483–487, 1997.

[15] P. Nunes, E. Fortunato, A. Lopes, and R. Martins, "Influence of the deposition conditions on the gas sensitivity of zinc oxide thin films deposited by spray pyrolysis", Int J Inorg Mater, 3, pp. 1129–1131, 2001.

[16] L.Y. Sheng, Z. Tang, J.P. Wu, C.H. Chan, and J.K.O. Sin, "A low-power CMOS compatible integrated gas sensor using maskless tin oxide sputtering", Sensors Actuators, B49, pp. 81–87, 1998.

[17] C. Rossi, P.T. Boyer, and D. Esteve, "Realization and performance of thin SiO2/Si3Nx membrane for microheater applications", Sensors Actuators, A 64, pp. 241–245, 1998.

[18] H.J. Pandya, Sudhir Chandra, and A.L.Vyas, "Fabrication and characterization of ethanol sensor based on RF sputtered ITO films", Sensors and Transducers, 10, pp. 141-150, 2011.

[19] C.B. Lim, J.B. Yu, D.Y. Kim, H.G. Byun, D.D. Lee, and J.S. Huh, "Sensing characteristics of nano-network structure of polypyrrole for volatile organic compounds (VOCs) gases", IEEE Sensors, pp. 695-698, 2006.

[20] H. Das, "Food Processing Operation Analysis", Asian Books Private Limited, 2005.

 ISBN: 978-1-61208-145-8

Towards Flexible Biocompatible Pressure Sensors: Covering Polymeric Films with a Highly Piezoresistive Organic Molecular Metal

Elena Laukhina
dept. name: NANOMOL
CIBER de Bioingeniería, Biomateriales y Nanomedicina (CIBER-BBN) at ICMAB-CSIC
Bellaterra, Barcelona, Spain
e-mail: laukhina@icmab.es

Vladimir Laukhin
dept. name: NANOMOL
Institució Catalana de Recerca i Estudis Avançats at ICMAB-CSIC, CIBER-BBN
Bellaterra, Barcelona, Spain
e-mail: vladimir@icmab.es

Victor Lebedev, Concepció Rovira, Jaume Veciana
dept. name: NANOMOL
Institut de Ciencia de Materials de Barcelona (ICMAB)-CSIC, CIBER-BBN
Bellaterra, Barcelona, Spain
e-mail: vlebedev@icmab.es; cun@icmab.es; vecianaj@icmab.es

Abstract—**The article reports a promising approach to engineering biocompatible and highly piezoresistive membrane for flexible weightless transparent pressure sensors. The developed membrane is based on a bi layer (BL) film composing a polycarbonate (PC) matrix "self-metallized" with a highly piezoresistive organic molecular metal. The key role of the matrix thickness in the enhancement of the pressure sensitivity of BL film-based membranes was shown. The presented approach permits engineering biocompatible all-organic membranes with pressure sensitivity being of 8 Ω/mmHg. To determine restrictions for BL films applications in biomedical high-tech, the effect of the body temperature on membrane piezoresitive properties was studied. The pressure tests at 26 °C, 33 °C and 40 °C showed that the body temperature does not significantly influence on the membrane pressure sensitivity. Therefore this type of membrane sensors is able to take the place of conventional metal-based strain and pressure gages in monitoring biomedical high-tech.**

Keywords- piezoresistive covering; flexible, biocompatible pressure sensors; organic molecular metal; pressure testing

I. INTRODUCTION

Among the more challenging tasks undertaken in the field of sensors is design and manufacture of reliable, robust pressure sensors for plastic electronics [1-8]. There is also a continuing need to lower the cost of sensors utilized in pressure sensing applications. To lower the cost and raise efficiency of sensors, few components, less expensive materials and fewer manufacturing-processing steps are necessary. For some applications size and weight constraints may be as important as or more than cost. For example, in biomedicine, catheter-based devices must occupy small volume, or they cannot be used at all [1, 6, 8]. In order to achieve these goals pressure sensors could be made of organic materials, along with low cost processing steps. Most of all-organic pressure sensors compose of a polymeric material surfaced with a conducting polymer layer [1, 7] The conducting polymer layers are preferably grown electrochemically [6]. Therefore, making sensitive covering layers based on conductive polymers requires both the use of specific electrochemical equipments and deposition of conventional metallic electrodes on the surface of a polymeric matrix [6, 7]. This method offers many problems that must be worked out: the adhesion between conducting layers, substrates, and electrodes, the growth of conductive polymer should be in a reproducible manner, a limited area between two electrodes applying for electrochemistry etc. Moreover, the conductive polymers tend to degrade rapidly, resulting in sensors having only a relative short lifespan.

In this context surfacing plastics with "soft" organic molecular metals [9] which have been developed in order to replace heavy-weight metals in traditional technologies, is able to overcome the above mentioned problems. Organic molecular metals are attractive for covering polymeric films for many reasons; below we will list four main ones. First, these synthetic metals demonstrate good long term stability. Second, the set of hydrogen bonds presented in the crystal structures of all organic molecular conductors [9] endows their crystallites with high elasticity and, therefore, they are able to withstand large deformation. Third, due to soft crystal structures the conducting bands of organic molecular conductors can be easily deformed and, therefore, the electrical resistance of molecular metals responds strongly to deformation [10, 11]. Fourthly, a simple single- or two-stage covering procedure has been developed to prepare such "metallized" polymeric films [12, 13] The method consists in switching on a redox reaction in the swollen surface of a polymer film that provokes the nucleation of small clusters of a molecular conductor, which are able to growth into a conductive polycrystalline layer. This covering process occurs at room or moderate (33°C) temperature.

It should be noted that the above mentioned approach to covering plastics lived up to expectations. Recently we

 ISBN: 978-1-61208-145-8

reported that polycarbonate films surfaced with polycrystalline layers of organic molecular metals α-, β-$(ET)_2I_3$, were ET=bis(ethylenedithio)tetrathiafulvalene (Fig. 1), revealed a giant tenso-resistance effect [14-16].

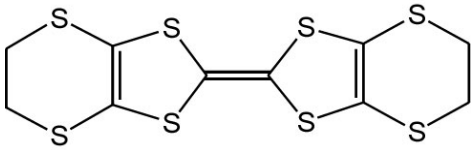

Figure 1. Skeletal formula of bis(ethylenedithio)tetrathiafulvalene (ET).

These bi-layer (BL) films are attracting large attention due to their ability to combine properties such as electrical conductivity, high sensitivity to strain (pressure), lightweight, and flexibility [12-16]. Moreover, it has been shown that BL films can be successfully integrate in textiles [17].

In order that a tenso-resistive BL film can sense pressure changes, it has to be located as a membrane. With this in mind, the first prototype of a contact sensing lens equipped with a membrane pressure sensor based on the above mentioned piezoresistive BL film has been developed for monitoring intraocular pressure (IOP) changes: a 25 μm thick polycarbonate film covered with molecular metal β-$(ET)_2I_3$ was used as a flexible pressure sensor [18]. The tests showed that this BL film-based sensing membrane, being *biocompatible*, is able to control IOP changes with sensitivity of 1,4 Ω/mmHg; the pressure tests were made at room temperature (26 ^oC) [18, 19]. In order to adapt flexible tenso-resistive *biocompatible* BL film-based membranes for pressure monitoring in biomedical high-tech two key questions to be answered are: (1) is it possible to improve membrane sensitivity to pressure? and (2) does the body temperature significantly influence on membrane piezoresistive properties?

The goal of our study was a search for experimental data being able to answer on the above mentioned questions. We suggested that decreasing the thickness of a membrane's plastic component (polycarbonate matrix) on retention of the thickness of a membrane's piezoresistive layer has to enhance the membrane pressure sensitivity. With this in mind, we fabricated the thin membrane based on a 5 μm thick polycarbonate film covered with the polycrystalline layer of piezo-resistive molecular metal β-$(ET)_2I_3$, the sensitive layer being prepared so as to be purely comparable with that of the above mentioned 25 μm thick BL film-based sensing membrane.

Herein we show that an engendering approach based on the foregoing suggestion permitted us to fabricate a BL film-based membrane with sensitivity to pressure being five times higher than that for the previous reported one [14, 18, 19]. We also present data on electromechanical properties of this membrane showing that the body temperature does not significantly influence on membrane pressure sensitivity: pressure tests were carried out at 26^{o}C, 33^{o}C and 40^{o}C.

II. FABRICATING POLYCARBONATE FILM COVERED WITH A HIGHLY PIEZORESISTIVE ORGANIC MOLECULAR METAL

In line with the early reported method [12, 13] we first prepared a 5 μm thick polycarbonate film spiced up with an 8 wt. % of ET that is a precursor for organic molecular metal $(ET)_2I_3$. The film was cast on a glass support at 130 ^oC from a 1,2-dichlorobenzene solution of a 0.5 wt.% of PC and 0.04 wt. % of ET. It should be noted that an 8 wt. % of ET embedded in this thin BL film is able to form the same amount of molecular metal $(ET)_2I_3$ as a 2 wt. % of ET inherent in a 25 μm thick BL film. Therefore, the prepared composite film made possible to form the conductive covering layer of $(ET)_2I_3$ with the thickness being identical to that of the covering $(ET)_2I_3$-based layer formed at the surface of the early developed 25 μm thick BL film [14, 18, 19].

In order to cover the film with a conducting layer of $(ET)_2I_3$, we exposed the film surface to the vapors of a saturated solution of iodine in dichloromethane. The covering mechanism is as follows: the surface of a polycarbonate film easily swells under its exposure to dichloromethane vapors; this swelling facilitates a migration of ET molecules from the film bulk to the swollen film surface where the part of ET molecules are oxidized to radical cations $ET^{+\bullet}$ by iodine, which penetrates in the film surface together with dichloromethane vapors. This redox process induces the rapid nucleation of highly insoluble $[(ET)^0(ET)^{+\bullet}](I_3)^-$ species and a piezoresitive facing layer of molecular metal α-$(ET)_2I_3$ is formed. Electrical resistance of the 25 μm thick BL film with the covering layer of α-$(ET)_2I_3$ responded to strain with a gage factor being 10, whereas the polycarbonate film with the same thickness but surfaced with β-$(ET)_2I_3$ has a gage factor being 20 [15]. The difference in gage factors between α- and β-phases of $(ET)_2I_3$ can be attributable to a variety of the softness of their crystal structure: β-phase has one short C-H…C and three long C-H…I hydrogen bonds whereas α-polymorphous has two short C-H…C and only two long C-H…I bonds [9]. Thanks to a larger number of the long hydrogen bonds, the crystal structure of the β-phase is significantly softer than that of the α-one and, therefore, the conducting band of β-$(ET)_2I_3$ can be easily deformed under load.

The 5 μm thick BL film covered with a highly piezoresistive layer of β-$(ET)_2I_3$ was formed via a thermo-activated α→β phase transition that occurs at T>100 ^oC [9, 13]. For this purpose the BL film covered with the layer of α-$(ET)_2I_3$ was annealed at 150 ^oC during 30 min. The formation of the covering layer of β-$(ET)_2I_3$ was confirmed by its X-ray diffraction pattern (Fig. 2). The figure shows only one line at $2\theta=5.8^o$ and its higher order reflections, that corresponds to "c"-oriented crystallites of organic metal β-$(ET)_2I_3$ [9, 13].

The surface analysis on a micro scale, performed using "Quanta FEI 200 FEG-ESEM" scanning electron microscope (SEM), showed that the crystallites of the covering layer of β-$(ET)_2I_3$ are of submicro size (Fig. 3). It should be noted that the sizes of the crystallites of the reported 25 μm thick BL film were of the same scale. The calculated possible

maximal thickness of the piezoresistive covering layer is around 250 nm.

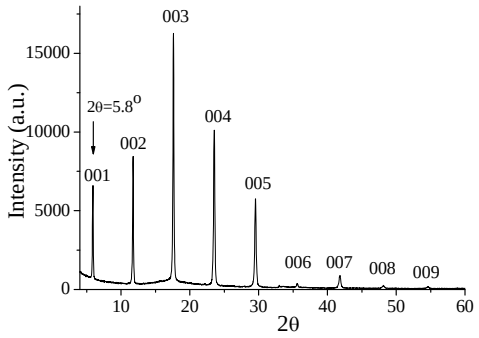

Figure 2. X ray diffraction pattern of the covering layer of the 5 μm thick BL film after its annealing. The film sample with 2.3 cm^2 was attached to a glass support and X-ray diffraction data were recorded on a Rigaku "Rotaflex" RU-200B diffractometer in reflection mode with monochromatic CuKα radiation (λ = 1.540598 Å); the generator was activated at 50 kV and 80 mA.

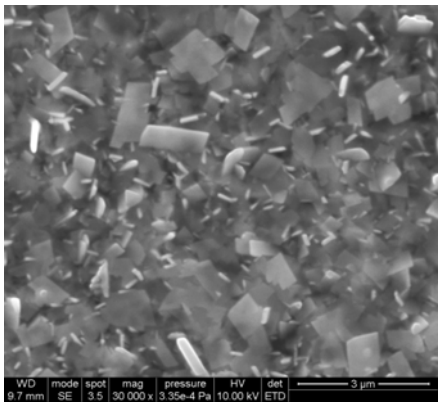

Figure 3. SEM image of the piezoresistive covering layer of β-$(ET)_2I_3$; the SEM image was acquired at 20 kV.

The BL film-based sensing membrane of a round configuration was cut and equipped with two electrical contacts: two 20 μm thick Pt wires were attached to the piezoresistive layer of the membrane using a linear contact configuration (Fig. 4).

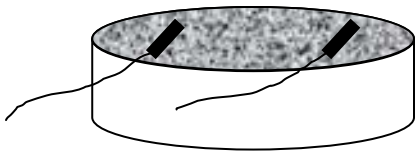

Figure 4. Schematic view of the pressure membrane sensor with two electrical contacts attached using a linear configuration

As a final remark we would like to add that the membrane temperature resistance coefficient (TRC) and membrane gage factor were found as 0.3 %/°C and 20, respectively. These values are in excellent agreement with the data reported for the 25 μm thick BL film [15]. The TRC was calculated as a relative resistance change per grade and gage factor was calculated as the ratio between the relative resistance change and the relative strain value.

The above result demonstrates that both TRC and gage factor of polycarbonate films "self-metallized" with molecular metal β-$(ET)_2I_3$, being independent on the thickness of a polymeric matrix, are governed by the nature of the molecular metal used for covering a polycarbonate film.

III. PRESSURE TESTS

The pressure testing experiments were performed by using a tailor-made water based column manometer that is shown in Fig. 5. To prepare pressure tests under moderated temperature a demountable home made thermostat was designed and fabricated. This mini thermostat is made up of a rigid polyurethane foam-based camera whose interior walls were faced with Cu plates. The thermostat was equipped with two commercial Kapton Flexible Heaters (KHLV - 102/10) that were arranged on the opposite camera walls. The heaters were connected with DC Power Supply E3617A. Temperature was maintained constant with an accuracy of ±0.02°C and controlled by the Pt-thermometer.

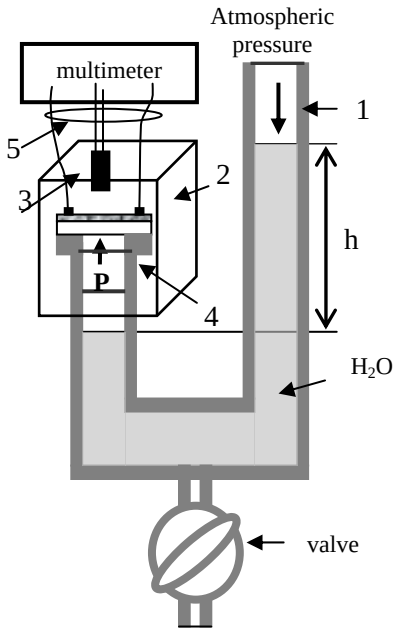

Figure 5. Schematic view of setup developed for pressure tests: 1 - water column U- tube manometer; 2 –home-made thermostat; 3 - Pt thermometer; 4 - glass holder with a BL film-based sensing membrane; 5 – electrical connections.

The pressure tests were curried out when thermostat temperature was stabilised at 26 ±0.02 °C, 33±0.02 °C and 40±0.02°C. Tests were conducted with simultaneously

temperature monitoring; for this purpose the Pt-thermometer was located very close to the tested membrane. The membrane was pasted over a ring-like top of a glass holder as shown in Fig. 6. The holder was designed and tailor-made for connecting the BL film-based membrane with one of the tube of the tailor-made U-shaped tube manometer.

In these experiments the pressure (P) of the gas that is trapped in the end of the tube closed with the tested membrane is greater than atmospheric pressure by the amount of pressure exerted by the column of water of height h. The bottom part of the manometer was equipped with a valve; the valve permits decreasing the water column height that in turn results in gas pressure decrease in the closed end of the tube. Pressure applied to a BL film-based membrane pasted over the holder can be easily measured as h mmH_2O.

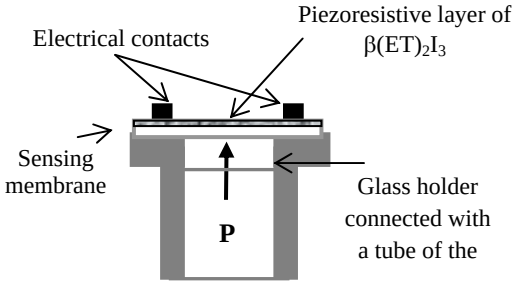

Figure 6. Schematic view of BL film-based membrane located over the tailor-made holder fabricated for pressure tests

The electrical responses of the thin sensing membrane to pressure changes were measured with a multimeter Agilent 34970A. The applied pressure was changes from 0 to 320 mmH_2O (0-32 mbar). The responses of the sensing membrane to applied pressure at 26 °C, 33 °C, and 40 °C are shown in Fig 7, 8 and 9, respectively. The pressure sensitivities (S_P) of the membrane at different temperature were calculated from the R(P) dependences shown in the bottom of the figures and summarised in Table 1.

Figs. 7, 8 and 9 demonstrate that in the studied pressure and temperature ranges the electrical resistance of the membrane linearly and reproducible response to pressure changes with a steep-slope, which has only a weak dependence on the body temperature.

The data presented in Table 1 clearly show that the matrix thickness is a key parameter for engineering highly piezoresistive BL film-based membranes: a fivefold decrease in the thickness of a membrane plastic component on retention of the thickness of the piezoresistive layer resulted in a fivefold increasing of the membrane pressure sensitivity.

TABLE I. RELATIONSHIP BETWEEN THE THICKNESSES OF BL FILMS-BASED MEMBRANE AND ITS ELECTRICAL AND ELECTRO-MECHANICAL PROPERTIES

Membrane thickness µm	TRC, %/°C	Gage Factor	Pressure sensitivity (S_p) Ω/mmHg		
			26°C	33°C	40°C
25 (Ref. 15)	0.26	18±2	1.4	-	-
5	0.25	20.2	8.4	7.54	7.51

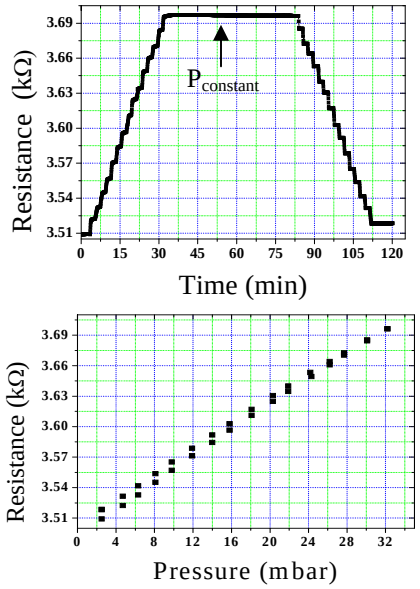

Figure 7. Loading at 26°C; Top: Electrical response of the BL film-based membrane corresponding to a variation of pressure in range 0- 32 mbar (0-320 mmH_2O or mmHg), each step up and down being 2 mbar (20 mmH_2O or 1.5 mmHg); Bottom: R(P) dependence based on data collected for up and down sweeps from the loading graph presented at the top. Constant load of 32 mbar was applied during 65 min

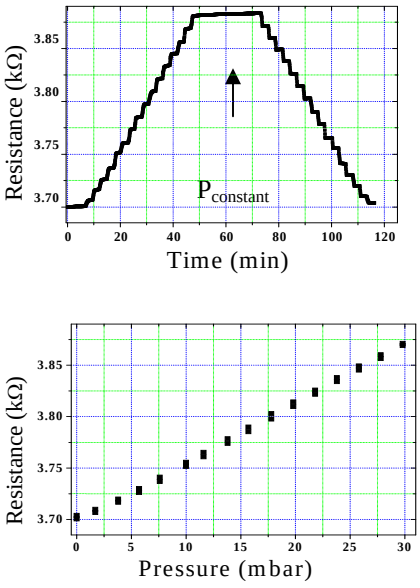

Figure 8. Loading at 33°C; Top: Electrical response of the BL film-based membrane corresponding to a variation of pressure in range 0- 32 mbar (0-320 mmH_2O), each step up and down being 2 mbar (20 mmH_2O or 1.5 mmHg); Bottom: R(P) dependence based on data collected for up and down sweeps from the loading graph presented at the top. Constant load of 32 mbar was applied during 30 min.

Additionally, the pressure tests showed that resistance of the BL film based membrane under constant load of 32 mbar (24 mmHg) is time-independent in the studied temperature

range. Following the above pressure tests the membrane was studied anew by pressure loading at 26 °C (Fig. 10). According to data presented in Fig. 10, the sensitivity of the BL film-based membrane to pressure was found as 8,4 Ω/mmHg that is precisely the same as before it was found from the first loading experiment (Table 1). Therefore, the polycarbonate films covered with organic molecular metal β-$(ET)_2I_3$ are highly piezoresistive materials with a good reproducible electrical response to pressure

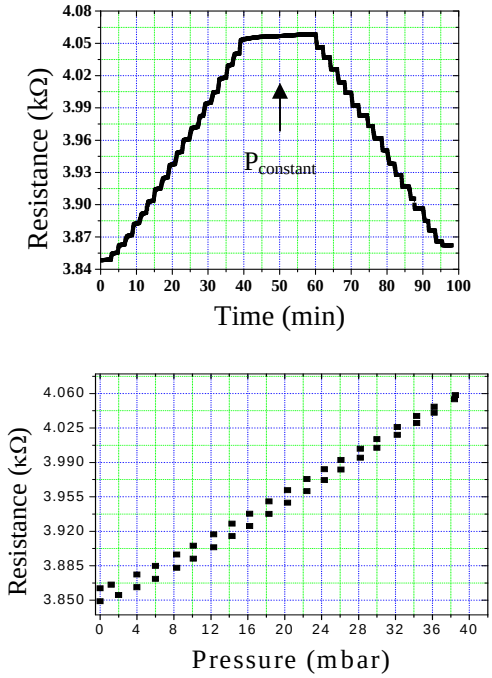

Figure 9. Loading at 40°C; Top: Electrical response of the BL film-based membrane corresponding to a variation of pressure in range 0- 32 mbar (0- 320 mmH_2O or 24 mmHg), each step up and down being 2 mbar (20 mmH_2O or 1.5 mmHg); Bottom: R(P) dependence based on data collected for up and down sweeps from the loading graph presented at the top. Constant load of 32 mbar was applied during 20 min.

IV. SUMMARY

The flexible pressure sensing membranes capable of measuring very small pressure changes have been developed. The pressure tests at different temperature showed that the body temperature does not significantly influence on the membrane pressure sensitivity.

This study also demonstrated the feasibility of a fivefold increase of the sensitivity of BL film-based membranes to pressure changes that is a very important step on the road to the development of flexible weightless miniature pressure sensors.

From the above it might be assumed that BL film-based sensors can be embedded in catheters, contact lenses and textiles for monitoring the body's physiological processes and mechanical movements.

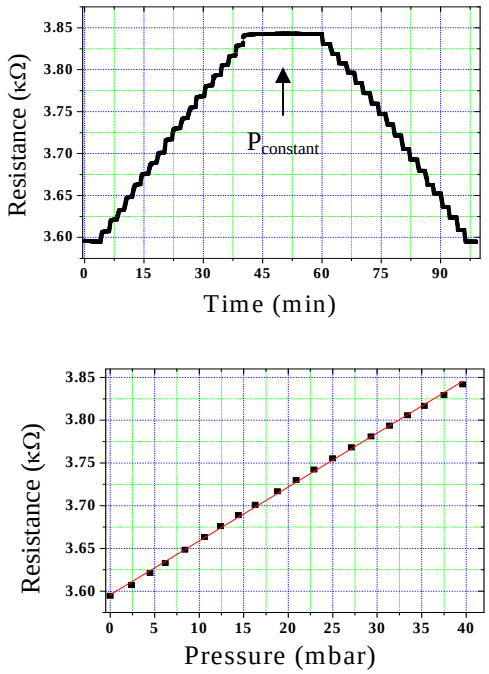

Figure 10. Replicate of loading at 26°C; Top: Electrical response of the BL film-based membrane corresponding to a variation of pressure in range 0- 32 mbar (0- 320 mmH_2O or 24 mmHg), each step up and down being 2 mbar (20 mmH_2O or 1.5 mmHg), Bottom: R(P) dependence based on data collected for up and down sweeps from the top. Constant load of 32 mbar was applied during 20 min.

ACKNOWLEDGMENT

We acknowledge the support from European Community's Seventh Framework Programme (FP7/2007-2013) under grant agreement n° 212311 of the ONE-P project, DGI, Spain (contracts CTQ2006-06333/BQU and CTQ2010-195011/BQU), DGR, Catalunya (grant 2009SGR-00516). Authors thank the CIBER-BBN, an initiative funded by the VI National R&D&i Plan 2008-2011, Iniciativa Ingenio 2010, Consolider Program, CIBER Actions and financed by the Instituto de Salud Carlos III with assistance from the European Regional Development Fund.

REFERENCES

[1] S. Y. Yurish, N. V. Kirinaki, and I. L. Myshkin, "World Sensors and MEMS Markets: Analysis and Trends", Sensors & Traducers Magazine (S&T e-Digest), vol. 62, Issue 12, pp. 456-461, 2005.

[2] J. R. Matsuzaki, A. Todoroki, "Wireless flexible capacitive sensor based on ultra-flexible epoxy resin for strain measurement of automobile tires", Sensors and Actuators A: Physical, vol. 140, Issue 1, pp. 32-42, October 2007.

[3] C. Maxwell, R. Igreja, and C.J. Dias, "Dielectric response of interdigital chemocapacitors: the role of the sensitive layer thickness", Sens. Actuators B, 115, pp. 69–78, 2006.

[4] Y. Yorozu, B.E. Boser, and K.W. Markus, "Design of integrated MEMs, designing low power digital systems, emerging technologies", IEEE, 1996, pp. 207–232.

[5] S. Tung, S. R. Witherspoon, L. A. Roe, A. Silano, D. P. Maynard, and N. Ferraro, "MEMS-based flexible sensor and

actuator system for space inflatable structures", Smart Mater. Struct. 10, pp. 1230–1239, 2001.

[6] W. P. Eaton, J. H. Smith, "Micromachined pressure sensors: review and recent developments", Smart Mater. Struct., vol. 6, pp. 530-539, 1997.

[7] B. Adhikari, S. Majumdar, "Polymers in sensor applications", Progress in Polymer Science, vol. 29, pp. 699-766, 2004.

[8] F. Axisa, P. M. Schmitt, C. Gehin, G. Delhomme, E. McAdams and A. Dittmar, "Flexible technologies and smart clothing for citizen medicine, home healthcare and disease prevention", IEEE Transactions on Information Technology in Biomedicine, vol. 9, No. 3, pp. 325-336, 2005.

[9] R. Shibaeva, E. Yagubskii, "Molecular Conductors and Superconductors Based on Trihalides of BEDT-TTF and Some of Its Analogues", vol. 104, pp. 5347-5378, 2004.

[10] R. Kondo, M. Higa, S. Kagoshima, H. Hoshino, T. Mori, and H. Mori, "Electrical and Structural Properties of θ-type BEDT-TTF Organic Conductors under Uniaxial Strain", J. Phys. Soc. Jpn., vol. 75, pp. 044716-7, 2006.

[11] H. Karimov, V. Laukhin, H. Ahmedov, and E. Laukhina, patent: "Pressure sensor", SU 1668855 A1, USSR, 1989.

[12] E. Laukhina, C. Rovira, and J. Ulanski, "Organic metals as active components in surface conducting semitransparent films", Synth. Met., N. 21, pp. 1407-1408, 2001.

[13] E. E. Laukhina, V. A. Merzhanov, S. I. Pesotskii, A. G. Khomenko, E. B. Yagubskii, J. Ulanski, M. Krysezewski, J. and K. Jeszke, "Superconductivity in reticulate doped polycarbonate films containing $(BEDT\text{-}TTF)_2I_3$", Synth. Met., N. 70, pp. 797-800, 1995.

[14] E. Laukhina, V. Laukhin, M. Mas-Torrent, C. M. Creely, D.V. Petrov, J. Veciana, and C. Rovira, "High piezoresistive organic film for plastic pressure sensors", Proc. IEEE, Cat. Number 07TH8933 ISBM, vol. 2, pp. 2247-2249, 2007.

[15] E. Laukhina, R. Pfattner, L. R. Ferreras, S. Galli, M. Mas-Torrent, N. Masciocchi, V. Laukhin, C. Rovira, and J. Veciana, "Ultrasensitive Piezoresistive All-Organic Flexible Thin films", Adv. Mater., vol. 22, pp. 977-991, 2010.

[16] E. Laukhina, R. Pfattner, M. Mas-Torrent, C. Rovira, J. Veciana, Vladimir Laukhin, "Film-based Sensors with Piezoresistive Molecular Conductors as Active Components: Strain Damage and Thermal Regeneration", Sensors & Transducers Journal, , vol. 10, Special Issue, February, pp. 1-12, 2011.

[17] L. R. Ferreras, R. Pfattner, M. Mas-Torrent, E. Laukhina, L. López, V. Laukhin, C. Rovira, J. Veciana *J.* "Highly piezoresistive textiles based on a soft conducting charge transfer salt", Mater. Chem**.**, **21**, pp. 637- 641, 2011

[18] V. Laukhin, C. Rovira, E. Laukhina, J. Veciana, M. Mas-Torrent, A. Quimera Brunet, J. Aguiló Llobet, R. Villa Sanz, J. C. Pastor, and F. Ussa, "Truncated contact lens for use in telemetry system, has truncation plane provided parallel to base of lens, and centrally placed polymer nanocomposite material joined to perimeter of truncated zone", Patent: ES2330405-A1; WO2009147277-A1.

[19] V. Laukhin, I. Sánchez, A. Moya, E. Laukhina, R. Martin, F. Ussa, C. Rovira, A. Guimera, R. Villa, J. Aguiló, J.-C. Pastor, J. Veciana, "Prototype for Noninvasive IOP Monitoring with a Nanostructured Polymeric Sensor Embeded in a Contact Lens", Sensors and Actuaters A: Physical, 2011, accepted.

 ISBN: 978-1-61208-145-8

Development and Application of Nanoscale Polymeric Platforms for Advanced Protein Sensors

Sheng Song and Jong-in Hahm
Department of Chemistry, Georgetown University
Washington, DC USA
jh583@georgetown.edu

***Abstract*—This article discusses recent progress of surface-bound proteins in facilitating solid-phase sensing applications, particularly focusing on nanoscale polymeric supports that can be used as advanced solid state biosensors. Recent approaches involving nanoscale self-assembly of proteins are highlighted. Current challenges in the applications of surface-bound proteins are identified, specifically in the production and development areas of nanoscale polymeric surfaces for next-generation protein arrays. These efforts are of paramount importance, especially in high-density and high-throughput biotechnological applications such as gene chips, protein arrays, and lab-on-a-chip sensors.**

Keywords-protein array; protein sensor; array fabrication; polymer nanodomain; nanomaterial assembly

I. INTRODUCTION

Current demands for highly miniaturized, small-volume detection platforms in basic biological research and clinical diagnosis underscore the importance of examining proteins on surfaces. In comparison to liquid-phase protein assays, solid-phase sensors involving proteins on array or plate surfaces can be carried out using only a very small amount of assay agents. Solid-phase approaches also enable rapid and simultaneous detection involving a large number of samples. The use of surface-bound proteins in the form of microtiter plates, protein chips, and microwell plates for optical detection is routinely observed both in laboratory and clinical settings. Material choice for these solid surfaces includes glass, nitrocellulose paper, gold, silicon, and polymer. A large number of these protein assays, however, involves polymer-based platforms due to the wide range of polymeric materials that are available and also as a result of the flexibility in which their surface chemistry can be easily tailored for the immobilization of proteins.

II. PARALLEL AND SERIAL METHODS FOR PROTEIN ASSEMBLY

Methods used to deliver and localize proteins on polymeric surfaces include manual and robotic delivery [1], microcontact printing [2-6], imprint- and nano-lithography [7-9], microfluidic channel networks [10-12], focused-ion-beam patterning [13, 14], inkjet deposition [15, 16], dip-pen lithography and related scanning probe microscopies [2, 17-19]. In a laboratory setting, simultaneous protein delivery is frequently carried out either manually by using commercially available multichannel pipettes or automatically by employing robotic protein spotters mounted with capillary print heads.

In recent years, advances in the area of microfabriaction and nanofabrication have influenced protein delivery to surfaces. Methods based on robotic printing, ink-jet printing, soft lithography, and microfluidic channel networks are used to produce micron-size protein patterns on surfaces. These parallel approaches have the benefit of producing a large number of patterns simultaneously on surfaces and are applied as model systems to guide the study of biological systems. However, the micrometer-scale resolution, typically achieved by these parallel approaches can often limit address density of proteins.

Although microscale patterns of proteins are of great interest and application, the nanoscale size and structure of most proteins can be most aptly investigated through a nanoscale assembly of proteins. Nanoscale protein patterns can be beneficial to the further miniaturization of detection platforms. Dip-pen lithography and related scanning probe tip-based protein printing have been exploited to place proteins into nanometer scale areas on surfaces. Such serial approaches, in which proteins are written line-by-line onto solid surfaces via probe tips, permit a nanoscale positional control and provide smaller feature sizes for proteins compared to the parallel methods such as microcontact printing and microchannel networks. Despite the advantage, the practical application of these serial methods at large scales can be hampered by their low speed and time-consuming production.

Nanoscale assembly of proteins is also achieved by physical or chemical patterning of surfaces. In the former method, substrate surfaces are modified to inscribe topological patterns for subsequent protein binding. In the latter approach, selective sites of surfaces are chemically activated for subsequent protein attachment. Methods such as laser ablation [20, 21], reactive ion etching [22], and sputtering [23, 24] have been used for the physical alterations of the solid surfaces. Chemical patterning of substrates for protein adsorption has also been accomplished by the use of self-assembled monolayers [2, 25-29]. Despite these numerous efforts, significant challenges still exist in producing high-density, biologically active, surface-bound proteins rapidly at a large scale.

 ISBN: 978-1-61208-145-8

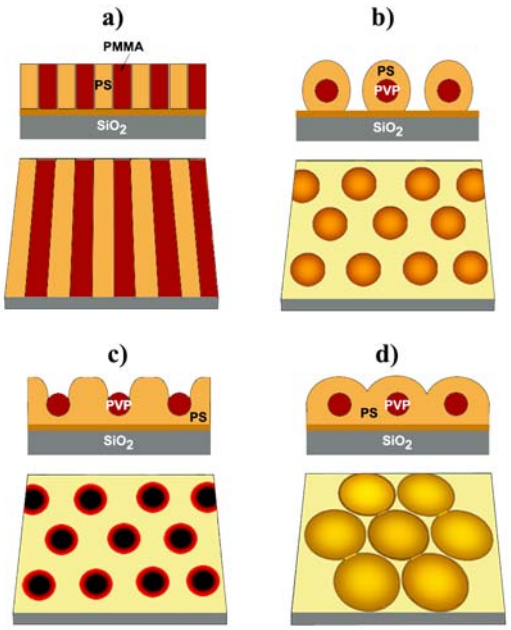

Fig.1 Nanoscale surface geometry of self organizing polymeric domains of (a) stripes in half cylinder-forming diblock copolymers and (b, c, and d) spheres in micelle-forming diblock copolymers. Adapted with permission from [30]. Copyright American Chemical Society.

III. ALTERNATIVE METHOD FOR PROTEIN SENSOR FABRICATION: NANOSCALE SELF ASSEMBLY

Distinct from the protein assembly methods described above, a bottom-up approach has also been proven to be successful in creating surface-bound proteins at a large scale in a straightforward and convenient manner. Self-assembly has been recently exploited to organize effectively proteins on nanoscale polymeric surfaces [30-34]. In these recent studies, both the underlying polymeric substrates as well as the proteins themselves are positioned via self-assembly where highly periodic and aligned patterns of proteins are instantaneously produced over a large area of substrates.

A class of polymeric materials called diblock copolymers is known to provide chemically heterogeneous, self-assembling surface structures through microphase separation. Diblock copolymers are formed by covalently joining two, chemically-immiscible, polymer blocks end-to-end. Due to the immiscibility and differential wetting properties associated with the two components of these materials, microphase separation occurs in diblock copolymer thin films in directions both perpendicular and parallel to the underlying support substrate [35-38]. The unique microphase separation behavior of a block copolymer, polystyrene-block-polymethylmethacrylate (PS-b-PMMA), has previously been shown to expose both block components to the air/polymer interface under carefully balanced thermodynamic conditions [39]. This phenomenon generates spatially periodic, self-assembled, nanoscale polymeric domains consisting of the different chemical constituents of the two polymeric components, whose scale and geometry reflect the chemical and physical properties of the polymer [40-42]. Their phase diagram dictates the packing nature and orientation of the resulting polymer chains where their microphase separation behavior is predictable based on a mean field theory [35, 37]. Therefore, the repeat spacing and surface geometry of the diblock copolymer can be controlled by changing the molecular weight and compositions of the two blocks. These chemically alternating and self-assembling polymeric domains can serve as convenient self-constructed templates for nanoscale arrangement of the desired biocomponents. Fig. 1 demonstrates some examples of such phase separating diblock copolymers which provide nanometer scale domains in their ultrathin films.

Recently, preferential interaction of several model proteins with PS and their selective segregation on the PS regions were monitored on the surface of phase-separated, PS-b-PMMA diblock copolymer ultrathin films [31]. No proteins were found on the neighboring PMMA areas. Proteins showing this behavior include bovine immunoglobulin G (IgG), fluorescein isothiocyanate (FITC) conjugated anti-bovine IgG, and protein G. When the protein loading condition was increased to a monolayer-forming concentration, the proteins exhibited close-packing behavior where they self-assembled themselves in a closely packed configuration on the PS domain in order to avoid the neighboring PMMA domain. In a follow-up study, protein adsorption experiments were carried out on both chemically homogeneous and heterogeneous supports, leading to the observation that protein density on the chemically heterogeneous PS-b-PMMA is larger than that on the chemically homogeneous, homopolymer surfaces of PS and PMMA by several fold [33]. They noted that more proteins adsorb on the diblock copolymer than on the PS or PMMA homopolymer, although approximately half of the exposed surface on the diblock copolymer consists of the non-preferred PMMA domains. The study concluded that the nanoscale chemical heterogeneity provided by the underlying PS-b-PMMA promotes protein adsorption more effectively than chemically homogeneous, homopolymer templates.

In addition to these methods for arranging proteins into periodic, one-dimensional stripes, mimicking the spot layout of conventional protein arrays via two-dimensional protein assembly was accomplished by using micelle-forming diblock copolymers. Amphiphilic polymeric systems such as polystyrene-*b*-polyacrylic acid, poly(ethylene-propylene)-b-polyethylene oxide, polystyrene-*b*-poly(2-vinylpyridine) and polystyrene-*b*-poly(4-vinylpyridine) were extensively studied to understand their fascinating micellar properties and dependence on diblock copolymer characteristics [43-46]. Micellar assembly, above a critical polymer concentration, is a well known behavior of such amphiphilic diblock copolymers. The exact structures and configurations of the resulting micelles or aggregates are length of each polymer segment, the polarity of the solvent,

 ISBN: 978-1-61208-145-8

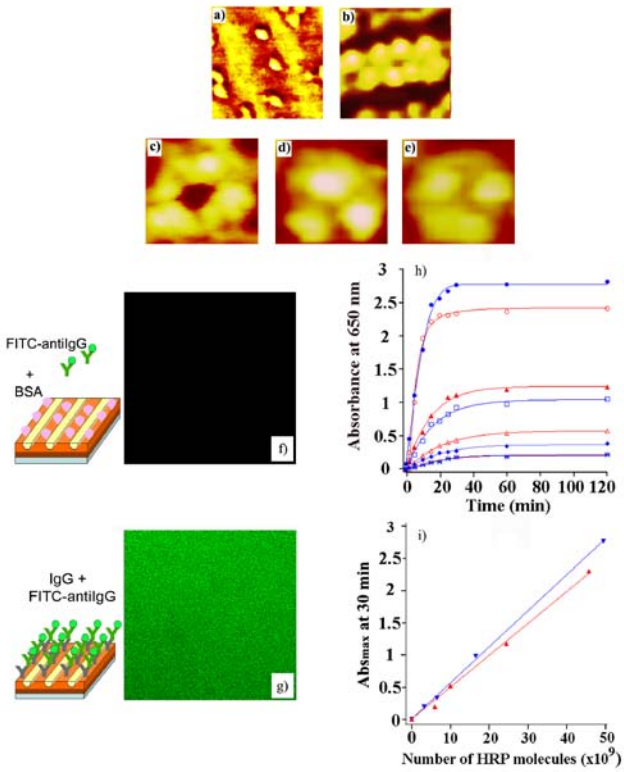

Figure 2. Atomic force microscope images of individual proteins of immunoglobulin G and mushroom tyrosinase that are self-assembled on nanodomains of PS-b-PMMA and PS-b-PVP diblock copolymer ultrathin films. (a) 150 by 150 nm phase, (b) 100 by 100 nm topography, and (c through e) 60 x 60 nm topography. Qualitative and quantitative activity measurements on proteins bound on PS-b-PMMA. Confocal fluorescence data are displayed for (f) the pair of fluorescein isothiocyanate conjugated anti-bovine IgG (FITC-antiIgG) and bovine serum albumin-incubated PS-b-PMMA, and (g) the pair of IgG and FITC-antiIgG on PS-b-PMMA. The two graphs of (h) and (i) display the quantitative results of horse radish peroxidase (HRP) activity difference measured between their free state (blue data) and PS-b-PMMA bound state (red data). When the enzymatic activity of the same number of HRP molecules in free- versus bound-state was compared, bound-state HRP retained approximately 85 % of its free-state activity. Adapted with permission from [30, 31] [32] and [34]. Copyright American Chemical Society.

and the relative solubility of each polymer block in the solvent.

These amphiphilic diblock copolymers can serve as extremely useful guides in organizing biomolecules into two-dimensional arrays since they exhibit a rich spectrum of morphologies and their repeat spacings are tunable in two dimensions. The advantages of amphiphilic diblock copolymers have been exploited to achieve rapid and large-scale self-assembly of two-dimensionally controlled protein arrays with periodic repeat spacing in nanoscopic dimensions [30]. The study demonstrated that polystyrene-*b*-poly(4-vinylpyridine) (PS-b-PVP) can be effectively used for the self-assembly of surface-bound, two-dimensional, nanoscale protein arrays. The study also established a straightforward method to produce protein patterns of different geometries and sizes by successfully manipulating topological structures of the underlying PS-b-PVP templates via various chemical treatments. Fig. 2 displays some examples of protein molecules arranged via self-assembly onto half cylinder- and micelle-forming diblock copolymer surfaces.

IV. CURRENT CHALLENGES

Ideal protein arrays for practical and clinically meaningful biosensing applications should be prepared for quantifiable, parallel, small-volume sensors that can be readily applied to large numbers of samples. They should also feature a reliable placement of protein molecules in a well-defined, highly dense pattern, while fully retaining their native functionality. Current challenges associated with the application of proteins printed on surfaces lie in the precise control over protein density, spot density, protein orientation, spotting uniformity, array standardization, array stability, surface fouling, and protein activity. Quantification of conventional assays, in which the exact number of biologically functional biomolecules participating in reactions can be easily and meaningfully compared between sensors, is also important but hard to achieve through conventional methods.

To date, easy fabrication of regularly-spaced protein platforms displaying high areal density and natural protein conformation is still extremely challenging. In addition to these general difficulties, inherent problems associated with manipulating small individual protein molecules on nanoscopic surfaces have restricted both the study and application of nanoscale protein arrays. Therefore, concerted research efforts are highly warranted in the future to facilitate high density protein assembly and to promote a high level of protein activity on solid surfaces. Improvements are also needed in conventionally available methods of sample delivery and optical signal detection. The development of an automated sample handling system and novel detection techniques, capable of processing a picoliter (or smaller) reaction volume and overcoming the optical diffraction limit, is also warranted. These advances will be particularly helpful to the application of the diblock copolymer-based nanoscale protein arrays in which the nanoscopic dimension of each spot in the sensor can be addressable as an independent detection unit.

V. OUTLOOK AND SUMMARY

Recent research efforts made in the areas of assembly, and applications of polymeric surface-bound proteins that are important both in sensor applications are considered in this article. Various methods to assemble proteins on polymeric surfaces both at macro/micro- and nano-scale are discussed and compared to one another. Current challenges and areas of further study are identified for the application of surface-bound proteins in the next-generation, solid-phase detection.

The presence of an underlying polymeric surface in solid-phase protein platforms adds an additional degree of

 ISBN: 978-1-61208-145-8

complexity which necessitates more comprehensive, thorough, and systematic investigation in the identified areas of further study. The significance of the polymeric surface-bound proteins in many important applications as gene chips, protein array sensors, and lab-on-a-chip devices warrants such future investigation. Therefore, such efforts will be extremely beneficial to developing highly miniaturized, high density biosensors that also permit quantitative sensing of bioanalytes in a cost effective and straight forward manner.

ACKNOWLEDGMENT

J. H. acknowledges support on this work by the National Science Foundation under Grant Number CBET-1042735 from the Division of Chemical, Bioengineering, Environmental, and Transport Systems under the Directorate for Engineering.

REFERENCES

[1] L. G. Mendoza, et al., "High-throughput microarray-based enzyme-linked immunosorbent assay (ELISA)," Biotechniques vol 27, 1999, pp 778.

[2] K. Wadu-Mesthrige, S. Xu, N. A. Amro and G. Y. Liu, "Fabrication and imaging of nanometer-sized protein patterns," Langmuir vol 15, 1999, pp 8580-8583.

[3] S. A. Brooks, et al., "Segregation of micrometer-dimension biosensor elements on a variety of substrate surfaces," Anal. Chem. vol 72, 2000, pp 3253-3259.

[4] R. S. Kane, S. Takayama, E. Ostuni, D. E. Ingber and G. M. Whitesides, "Patterning proteins and cells using soft lithography," Biomaterials vol 20, 1999, pp 2363-2376.

[5] J. F. Mooney, et al., "Patterning of functional antibodies and other proteins by photolithography of silane monolayers," PNAS vol 93, 1996, pp 12287-12291.

[6] E. Blinka, et al., "Enhanced microcontact printing of proteins on nanoporous silica surface," Nanotechnology vol 21, 2010, pp 415302.

[7] J. Clemmens, et al., "Mechanisms of microtubule guiding on microfabricated kinesin-coated surfaces: Chemical and topographic surface patterns," Langmuir vol 19, 2003, pp 10967-10974.

[8] D. Falconnet, et al., "A novel approach to produce protein nanopatterns by combining nanoimprint lithography and molecular self-assembly," Nano Lett. vol 4, 2004, pp 1909-1914.

[9] J. Hyun and A. Chilkoti, "Micropatterning biological molecules on a polymer surface using elastomeric microwells," JACS vol 123, 2001, pp 6943-6944.

[10] D. T. Chiu, et al., "Patterned deposition of cells and proteins onto surfaces by using three-dimensional microfluidic systems," PNAS vol 97, 2000, pp 2408-2413.

[11] E. Delamarche, A. Bernard, H. Schmid, B. Michel and H. Biebuyck, "Patterned delivery of immunoglobulins to surfaces using microfluidic networks," Science vol 276, 1997, pp 779-781.

[12] N. Patel, et al., "Atomic force microscopic analysis of highly defined protein patterns formed by microfluidic networks," Langmuir vol 15, 1999, pp 7252-7257.

[13] A. A. Bergman, et al., "Nanometer-scale arrangement of human serum albumin by adsorption on defect arrays created with a finely focused ion beam," Langmuir vol 14, 1998, pp 6785-6788.

[14] J. Jiang, X. Li, W. C. Mak and D. Trau, "Integrated direct DNA/protein patterning and microfabrication by focused ion beam milling," Adv. Mater. vol 20, 2008, pp 1636-1643.

[15] G. M. Nishioka, A. A. Markey and C. K. Holloway, "Protein damage in drop-on-demand printers," JACS vol 126, 2004, pp 16320-16321.

[16] J. Sumerel, et al., "Piezoelectric ink jet processing of materials for medicaland biological applications," Biotechnol. J. vol 1, 2006, pp 976-987.

[17] J. R. Kenseth, J. A. Harnisch, V. W. Jones and M. D. Porter, "Investigation of approaches for the fabrication of protein patterns by scanning probe lithography," Langmuir vol 17, 2001, pp 4105-4112.

[18] K. B. Lee, J. H. Lim and C. A. Mirkin, "Protein nanostructures formed via direct-write dip-pen nanolithography," JACS vol 125, 2003, pp 5588-5589.

[19] K. B. Lee, S. J. Park, C. A. Mirkin, J. C. Smith and M. Mrksich, "Protein nanoarrays generated by dip-pen nanolithography," Science vol 295, 2002, pp 1702-1705.

[20] A. M. Douvas, et al., "157-nm Laser ablation of polymeric layers for fabrication of biomolecule microarrays.," Anal. Bioanaly. Chem. vol 381, 2005, pp 1027-1032.

[21] E. P. Ivanova, et al., "Polymer microstructures fabricated via laser ablation used for multianalyte protein microassay," Langmuir vol 18, 2002, pp 9539-9546.

[22] V. C. Rucker, et al., "Functional antibody immobilization on 3-dimensional polymeric surfaces generated by reactive ion etching," Langmuir vol 21, 2005, pp 7621-7625.

[23] Z.-Y. Huang, M. Chen, S.-R. Pan and D.-H. Chen, "Effect of surface microstructure and wettability on plasma protein adsorption to ZnO thin films prepared at different RF powers," Biomed. Mater. vol 5, 2010, pp 054116.

[24] N. Aggarwal, K. Lawson, M. Kershaw, R. Horvath and J. Ramsden, "Protein adsorption on heterogeneous surfaces," Appl. Phys. Lett. vol 94, 2009, pp 083110.

[25] M. Mrksich and G. M. Whitesides, "Using self-assembled monolayers to understand the interactions of man made surfaces with proteins," Ann. Rev. Biophys. Biomol. Struct. vol 25, 1996, pp 55-78.

[26] M. Mrksich, G. B. Sigal and G. M. Whitesides, "Surface-plasmon resonance permits in-situ measurement of protein adsorption on selfassembled monolayers of alkanthiolates on gold. ," Langmuir vol 11, 1995, pp 4383-4385.

[27] K. L. Prime and G. M. Whitesides, " Adsorption of proteins onto surfaces containing end-attached oligo(ethylene oxide): A model system using self-assembled monolayers. ," J. Am. Chem. Soc. vol 115, 1993, pp 10714-10721.

[28] T. Wink, S. J. van Zuilen, A. Bult and W. P. van Bennekom, "Self-assembled monolayers for biosensors.," Analyst vol 122, 1997, pp 43R-50R.

[29] K. Wadu-Mesthrige, N. A. Amro and G. Liu, "Immobilization of Proteins on Self-Assembled Monolayers," Scanning vol 22, 2000, pp 380-388.

[30] N. Kumar, O. Parajuli and J. Hahm, "Two-dimensionally self-arranged protein nanoarrays on diblock copolymer templates," *J. Phys. Chem. B* vol 111, 2007, pp 4581-4587.

[31] N. Kumar and J. Hahm, "Nanoscale protein patterning using self-assembled diblock copolymers," Langmuir vol 21, 2005, pp 6652-6655.

[32] N. Kumar, O. Parajuli, A. Dorfman, D. Kipp and J. Hahm, "Activity study of self-assembled proteins on nanoscale diblock copolymer templates," Langmuir vol 23, 2007, pp 7416-7422.

[33] N. Kumar, O. Parajuli, A. Gupta and J. Hahm, "Elucidation of protein adsorption behavior on polymeric surfaces: Towards high density, high payload, protein templates," Langmuir vol 24, 2008, pp 2688-2694.

[34] O. Parajuli, A. Gupta, N. Kumar and J. Hahm, "Evaluation of enzymatic activity on nanoscale PS-b-PMMA diblock copolymer domains," *J. Phys. Chem. B* vol 111, 2007, pp 14022-14027.

 ISBN: 978-1-61208-145-8

[35] F. S. Bates and G. H. Fredrickson, "Block copolymer thermodynamics - Theory and experiment," Annu. Rev. Phys. Chem. vol 41, 1990, pp 525-557.

[36] B. L. Carvalho and E. L. Thomas, "Morphology of steps in terraced block-copolymer films," Phys. Rev. Lett. vol 73, 1994, pp 3321-3324.

[37] K. R. Shull, "Mean-field theory of block copolymers: bulk melts, surfaces, and thin films," Macromolecules vol 25, 1992, pp 2122-2133.

[38] R. Nagarajan and K. Ganesh, "Block copolymer self-assembly in selective solvents: Spherical micelles with segregated cores," J. Chem. Phys. vol 90, 1989, pp 5843-5856.

[39] T. L. Morkved, W. A. Lopes, J. Hahm, S. J. Sibener and H. M. Jaeger, "Silicon nitride membrane substrates for the investigations of local structures in polymer thin films," Polymer vol 39, 1998, pp 3871.

[40] J. Hahm, W. A. Lopes, H. M. Jaeger and S. J. Sibener, "Defect evolution in ultrathin films of polystyrene-block-polymethylmethacrylate diblock copolymers observed by atomic force microscopy," J. Chem. Phys. vol 109, 1998, pp 10111-10114.

[41] J. Hahm and S. J. Sibener, "Cylinder alignment in annular structures of microphase-separated polystyrene-b-poly(methyl methacrylate)," Langmuir vol 16, 2000, pp 4766-4769.

[42] J. Hahm and S. J. Sibener, "Time-resolved atomic force microscopy imaging studies of asymmetric PS-b-PMMA ultrathin films: Dislocation and disclination transformations, defect mobility, and evolution of nanoscale morphology," J. Chem. Phys. vol 114, 2001, pp 4730-4740.

[43] A. Choucair and A. Eisenberg, "Control of amphiphilic block copolymer morphologies using solution conditions," Eur. Phys. J. E. vol 10, 2003, pp 37-44.

[44] A. Choucair, C. Lavigueur and A. Eisenberg, "Polystyrene-b-poly(acrylic acid) vesicle size control using solution properties and hydrophilic block length," Langmuir vol 20, 2004, pp 3894-3900.

[45] S. N. Sidorov, et al., "Influence of metalation on the morphologies of poly(ethylene oxide)-block-poly(4-vinylpyridine) block copolymer micelles," Langmuir vol 20, 2004, pp 3543-3550.

[46] L. Zhang, K. Yu and A. Eisenberg, "Ion-induced morphological changes in ``crew-cut'' aggregates of amphiphilic block copolymers," Science vol 272, 1996, pp 1777-1779.

 ISBN: 978-1-61208-145-8

A Rapid Modeling and Prototyping Technique for Piezoelectric Energy Harvesting Systems

Aldo Romani, Enrico Sangiorgi, Marco Tartagni
Advanced Research Center on Electronic Systems
University of Bologna – Cesena Campus
Cesena, Italy
{aldo.romani, e.sangiorgi, marco.tartagni}@unibo.it

Rudi P. Paganelli
IEIIT-CNR
National Research Council (CNR)
Bologna, Italy
rudipaolo.paganelli@cnr.it

***Abstract*—This paper describes a reliable modeling technique for piezoelectric transducers and a procedure for identifying model parameters with few simple measurements and standard laboratory equipment. Direct measurements were taken on commercial Q220-A4-303YB piezoelectric transducers from Piezo Systems in a cantilever configuration with tip masses between 6 g and 18 g. For validation purposes, the behavior of the equivalent electromechanical circuits was simulated and compared to direct observations in real operating conditions. The model showed to predict with a high degree of accuracy both the response of the transducers to vibrations and a set of second order effects associated to the presence of a non-linear power converter and usually ignored by conventional models presented in literature.**

Keywords: piezoelectric devices, energy harvesting, model identification, equivalent electromechanical circuit

I. INTRODUCTION

Piezoelectric transducers are widely used in energy harvesting applications. Small-sized oscillating structures with seismic masses attached are often used (Fig. 1a). Several types of electronic interfaces have also been proposed up to now for collecting electrical charge from the transducers [1].

The behavior of this kind of systems depends on many factors such as the input vibrations, the shape of the transducer, the seismic mass attached to the transducer and the electronic interface. During the design phase a rapid and reliable quantitative estimate of the behavior of transducers and circuits is highly desirable for optimizing the system as a whole. In this task two main difficulties coexist: (a) in piezoelectric transducers electrical and mechanical quantities are strictly coupled; (b) conversion circuits are usually non-linear and include power transistors, diodes and digital control. Currently, especially during the design phase, there is still need of reliable methods for rapid prototyping and predicting the behavior of such complex systems.

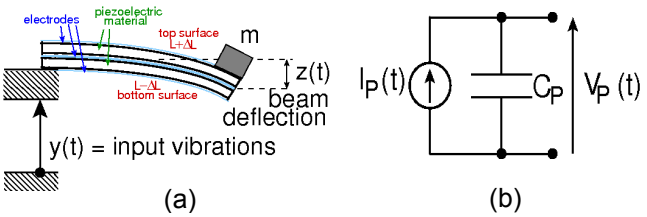

Figure 1. (a) Structure of a piezoelectric cantilever beam with a tip mass harvesting energy from vibrations; (b) a simplified equivalent circuit of a piezoelectric transducer.

An analytical approach [2] can accurately model the behavior of the piezoelectric transducer itself, but such models cannot be used in circuit simulations. In [3] a modeling approach based on an equivalent electro-mechanical circuit with lumped parameters provided reliable results. This type of approach is also suitable for joint simulations with non linear (e.g. switching) power converter circuits. However, in practical cases not all the required electrical, mechanical and geometrical parameters are known. Nonetheless, an accurate modeling is essential for carrying out system design efficiently. In fact, the way charge is extracted and transferred away from the transducer might significantly affect the response to vibrations of the transducer itself. Recent works on non-linear power conversion circuits [1][4][5] made use of assumptions such as weak electromechanical couplings, forced displacements or purely capacitive transducers (Fig. 1b) which are not valid in many practical cases, especially when the transducers operate near resonance.

This paper presents a new technique for a fast and reliable identification of the parameters of the equivalent electromechanical circuit of a generic piezoelectric transducer. The proposed approach is general and the technique can be applied to any type of transducer. For validation purposes, the equivalent circuits of a set of commercial piezoelectric transducers will be identified and a series of experimental measurements in both frequency and time domain will be compared to simulations. The results will show that the modeling technique produces reliable results in predicting the behavior of the transducers.

II. EQUIVALENT ELECTROMECHANICAL CIRCUIT OF A PIEZOELECTRIC TRANSDUCER

As shown in Fig. 1, in energy harvesting applications piezoelectric transducers are usually coupled with a seismic mass in order to build up a mechanical oscillator. Because of formal analogies between Newton's laws and Kirchoff's laws, as discussed in [3], an equivalent electromechanical circuit such as the one shown in Fig. 2a can model the behavior of a piezoelectric transducer .

The mechanical part may be described in terms of forces (F) and velocities ($\dot{z}$), where z is the deflection of the cantilever.

 ISBN: 978-1-61208-145-8

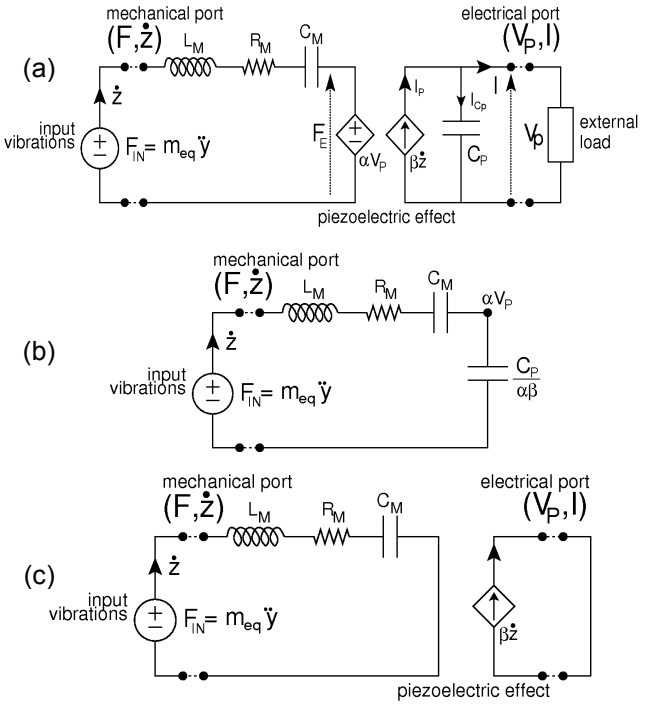

Figure 2. (a) generic equivalent electromechanical circuit of a piezoelectric transducer modeled as a two-port network; (b) equivalent oscillator circuit of a piezoelectric transducer in open circuit configuration; (c) equivalent oscillator circuit of a piezoelectric transducer in a short circuit configuration

In general, according to the laws of dynamics it holds that $F_{IN} = m_{eq}\ddot{y}$, where F_{IN} is the force acting on the transducer (e.g. expressed in N), $\ddot{y}$ is the amplitude of input vibrations (e.g. in m/s^2) and m_{eq} the equivalent mass of the oscillating system (e.g. in kg) which is related to the inertial mass and to the geometries of the transducer. In this paper, without losing generality, all the forces acting on the system will be expressed in scaled units by assuming a unity equivalent mass m_{eq}. This notation implies that the input force F_{IN} is considered numerically equal to the amplitude of input vibrations $\ddot{y}$, which can be directly measured. On the contrary, an exact value of the equivalent mass m_{eq} cannot be easily determined with direct measurements.

Each lumped element of the equivalent circuit takes into account different physical quantities: L_M, R_M, C_M are respectively related through $(F, \dot{z})$ to kinetic energy, mechanical losses and elastic energy of the system; C_P is the electrical capacitance measured between the surface electrodes of the piezoelectric element; the coefficients α, β respectively model the inverse and the direct piezoelectric effects. Additional vibration modes can be taken into account by including additional mechanical resonators.

An equivalent circuit approach, provided that a reliable estimate of its parameters is provided, allows to perform accurate simulations of the transducer connected to any power conversion circuit or external load. In next section a parameter identification technique based on the observation of few significant quantities will be presented.

III. IDENTIFICATION OF MODEL PARAMETERS

In general, as shown in Fig. 2b, the piezoelectric transducer in an open circuit configuration basically behaves as an oscillator with a resonance frequency f_0:

$$f_0 = \sqrt{\frac{1}{L_M C_{EQ}} - \frac{1}{\tau_M^2}}, \tag{1}$$

where $C_{EQ} = C_M C_P / (C_P + \alpha\beta C_M)$ and τ_M is the exponential damping time constant defined below.

When the terminals of the transducer are shorted ($V_P = 0$), as shown in Fig. 2c, a pure mechanical oscillator is built up with time constant τ_M and resonance frequency f_M:

$$\tau_M = \frac{2L_M}{R_M}, \quad \mathrm{f_M} = \sqrt{\frac{1}{L_M C_M} - \frac{1}{\tau_M^2}}. \tag{2}$$

It can be demonstrated that the transducer can be considered shorted whenever we connect to its terminals a resistor R_L whose value is low enough to drain almost all the current $\beta\dot{z}$ coming from the controlled current source, so that the effect of the αV_P voltage generator on the mechanical part is cancelled. When $R_L \cong 0$ the following relations can be determined by solving circuit equations:

$$\beta = \frac{V_P(f_M)}{R_L \cdot \pi f_M \cdot \Delta z_M} \tag{3}$$

$$L_M = \frac{F_{IN}(f_M)}{\Delta z_M} 2\tau_M^2 \sqrt{\frac{1}{1+16(\pi f_M)^2 \tau_M^2}} \tag{4}$$

$$\frac{1}{C_M} = L_M\left[(2\pi f_M)^2 + 1/\tau_M^2\right] \tag{5}$$

where Δz_M is the peak-to-peak displacement of the shorted transducer at the mechanical resonance f_M.

Conversely, when the transducer is in open circuit configuration the following equation holds:

$$\alpha = \frac{1}{\beta}\frac{C_P}{C_M}\left\{L_M C_M\left[(2\pi f_0)^2 + 1/\tau_M^2\right] - 1\right\} \tag{6}$$

IV. EXPERIMENTAL SETUP AND RESULTS

This section describes the experimental setup used for the identification of model parameters. The measurements were performed on a set of Q220-A4-303YB piezoelectric transducers from Piezo Systems with tip masses respectively of 6 g, 10 g, 12 g, 18 g. The transducers were mounted on a

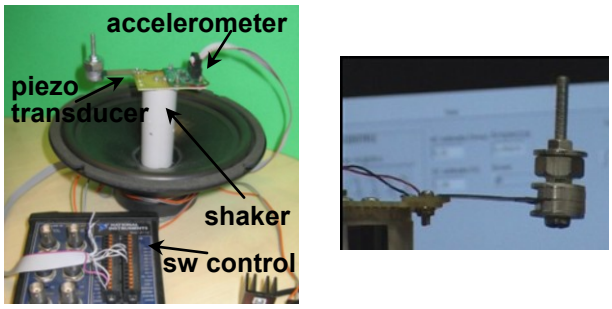

Figure 3. The cost effective shaker system composed of a standard woofer and a digital accelerometer operated under software control in a Labview environment and a detailed view of the piezoelectric transducers used in this work.

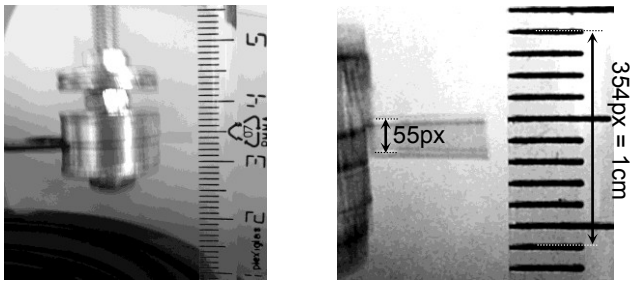

Figure 4. The peak to peak displacement can be directly measured by setting the shaker oscillating frequency and by taking a shot with 1" exposure time with a standard digital camera. Pixel resolution allows to measure the displacement with satisfactory accuracy. As an examples, some measurements are reported on the right.

cost-effective custom shaker system based on a Ciare CW200Z woofer (Fig. 3). A Kionix KXP-84 accelerometer was also mounted on the shaker for measuring the actual input acceleration. The shaker was used for generating sinusoidal vibrations of given frequency and amplitude or other test signals. An Agilent 34401A digital multimeter and a sampling oscilloscope were used for measuring the voltages produced by the transducers. A resistor $R_L = 98\ \Omega$ was used for emulating the shorted devices, as discussed in previous section.

The identification procedure is herein summarized. First, a series of measurements is performed on the mechanical oscillator, with R_L connected as a load.

1. The shaker produces very short mechanical pulses, so that damped voltage oscillations can be observed with an oscilloscope. The damping time constant τ_M can be easily obtained (e.g. from the screen coordinates (t_1, V_1) and (t_2, V_2) of two subsequent maxima with the expression: $\tau_M = (t_2\text{-}t_1) / \ln(V_1/V_2)$.
2. The shaker generates sinusoidal accelerations at different frequencies at which the output voltage $V_P(f)$ and the input acceleration $\ddot{y}(f)$ are measured. The frequency at which $V_P(f)/\ddot{y}(f)$ is maximum is identified as f_M.
3. The peak to peak displacement Δz_M at f_M is measured with a common digital camera. A ruler is positioned next to the transducer and a 1" exposure shot is taken (Fig. 4). The bitmap image then is analyzed at pixel level for measuring the displacement.

Then, additional measurements are performed on the transducer in an open circuit configuration:

4. Step 2 is repeated with no load resistor in order to identify f_0;
5. The electrical capacitance C_P of the transducer is measured with an Agilent 4284A LCR-meter, at a 10 kHz frequency well above the mechanical cut-off frequency, so as to neglect all mechanical effects.

Finally, all the parameters of the equivalent circuit are computed with equations (3)-(6) with the measured quantities. In (4), $F_{IN}(f_M)$ is expressed in scaled units (by a factor m_{eq}) so that it is numerically equal to $\ddot{y}(f_M)$. The values obtained for the considered transducers are reported in Table I.

TABLE I. IDENTIFIED MODEL PARAMETERS

mass [g]	L_M [kg]	C_M [m/N]	R_M [N·s/m]	α [N/V]	β [A·s/m]	C_P [nF]
6	$5.82\cdot10^{-2}$	$2.44\cdot10^{-4}$	1.16	$12.2\cdot10^{-3}$	$2.10\cdot10^{-3}$	52
10	$5.32\cdot10^{-2}$	$4.37\cdot10^{-4}$	0.96	$4.32\cdot10^{-3}$	$3.40\cdot10^{-3}$	52
12	$5.85\cdot10^{-2}$	$4.80\cdot10^{-4}$	1.06	$3.78\cdot10^{-3}$	$2.90\cdot10^{-3}$	52
18	$7.54\cdot10^{-2}$	$5.27\cdot10^{-4}$	1.26	$4.90\cdot10^{-3}$	$2.10\cdot10^{-3}$	52

In order to prove the effectiveness and the degree of reliability of the proposed approach, after identifying their model parameters, Spice simulations of the four previously identified piezoelectric transducers have been compared to direct measurements in different operating conditions.

Fig. 5 shows a comparison between the predicted and the observed behavior of the four transducers in frequency domain. The identified models accurately predict the response of the piezoelectric transducers to vibrations.

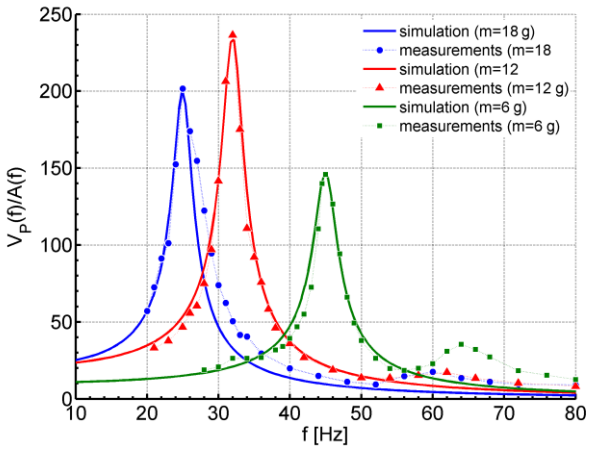

Figure 5. Comparison in frequency domain between measured (dots) and simulated data (continuous lines) for the Q220-A3-303YB transducer with different tip masses of 6g, 12g, 18g in open circuit configuration. VP(f) is the output voltage of the transducer, A(f) is the input acceleration ($\ddot{y}$).

 ISBN: 978-1-61208-145-8

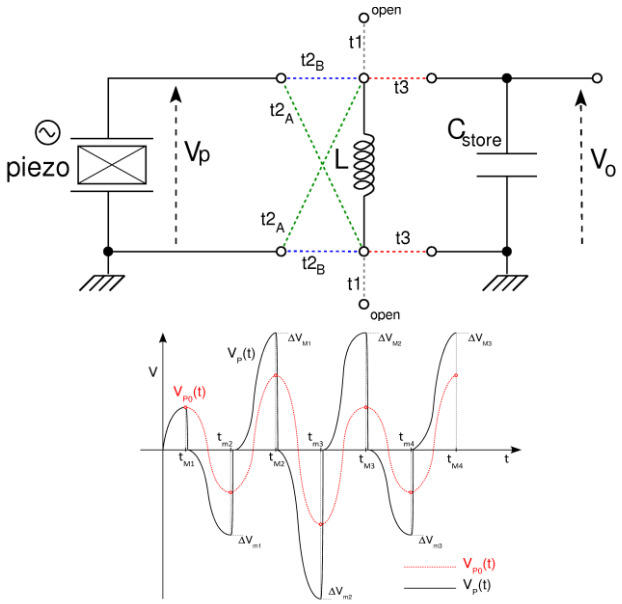

Figure 6. Schematic of the power converter performing synchronous charge extraction (top). Qualitative representation of waveforms when the converter is active and inactive (bottom). Synchronous conversion introduces at each activation a voltage offset, which is expected to increase the peak-to-peak voltage on the transducer.

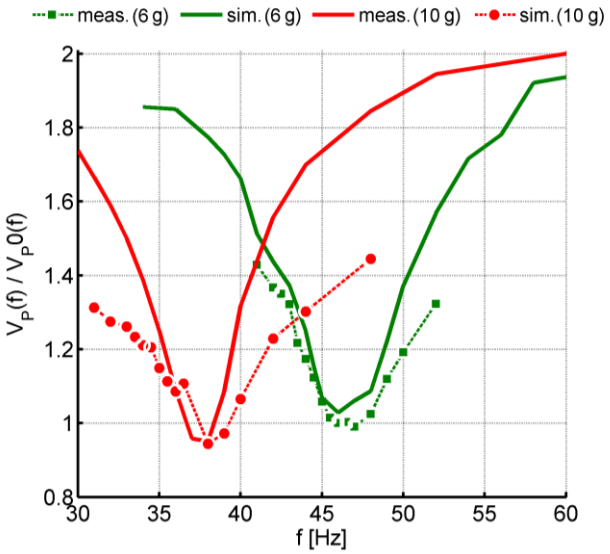

Figure 7. Sinusoidal accelerations of known frequency and amplitude were applied to the Q220-A4-303YB transducer with tip masses of 6g and 10g. The voltage on the terminals of the transducer was measured in an open circuit configuration (V_{P0}) and when the power converter performing synchronous charge extraction is connected (V_P). The plot compares the measured ratioes of the two voltage with values obtained from simulations.

As an additional proof, another measurement and simulation campaign was performed for verifying the capability of the model of predicting the effects of a non linear power converter on the performance of the transducer. In this setup, the piezoelectric transducers were connected to a switching converter circuit performing synchronous charge extraction. A schematic representation of the power converter is shown in Fig. 6.

Each time that the transducer reaches a local maximum or minimum of voltage it is connected to an inductor for a short time interval until his electric charge (and, consequently, its electrostatic energy) is fully removed. This technique was described in [1] and [5] where weakly coupled transducers with simplified capacitive models (Fig. 1b) were considered. These models predict, in case of sinusoidal vibrations, that the peak-to-peak voltage across the transducer doubles. However, with respect to those analyses, in a general case a lower energy harvesting performance should be expected: in fact, in case of sinusoidal vibrations, a synchronized converter actually applies a periodic series of current pulses to the electrical port of the piezoelectric transducer for removing charge. At resonance this effect cannot be neglected and the overall result is a force opposing to input vibrations. As a consequence, the actual output voltage of the transducer is lower than predicted with a capacitive model with weak electro-mechanical coupling.

A series of time domain simulations was performed on the four transducers and compared to direct measurements: sinusoidal vibrations at different frequencies were generated and the amplitude V_{P0} of the open circuit voltage was compared to the actual amplitude V_P observed when the synchronized converter is activated. Fig. 7 shows the V_P/V_{P0} ratio as a function of vibration frequency. Measurements show that near the resonance the power converter produces a significant and undesired damping effect. However, once again circuit simulations with the identified parameters accurately predict the effective behavior and allow taking it into account in the design phase. On the contrary, the hypothesis of weak electromechanical coupling (i.e. a transducer model such as that in Fig. 1b) would predict a constant ratio $V_P/V_{P0} = 2$ [1] and thus lead to a significant overestimate of harvester performance.

An accurate identification of model parameters is extremely useful in energy harvesting applications. The available accelerations can be easily measured with cost effective accelerometers and provided as input to the equivalent electro-mechanical circuits of piezoelectric transducers. At the same time, actual power conversion circuits can be jointly simulated. Different topologies or control algorithms of the power converter, such as for example synchronous charge extraction, can be easily characterized. Moreover, their impact on the actual performance of the transducer is determined. The proposed modeling technique allows to choose the most suitable power converter for maximizing the output power depending on the effectively available accelerations.

 ISBN: 978-1-61208-145-8

V. CONCLUSION

This paper presented a technique for a rapid and reliable identification of model parameters of piezoelectric transducers, with a special focus on energy harvesting applications. All the necessary measurements are carried out with common laboratory instrumentation and cheap equipment. Parameter identification allows performing reliable joint simulations of transducer and electronic circuits. This is of great help during the design phase of piezoelectric energy harvesting systems since it allows better performance estimates even during early design phases.

As a proof of concept it was shown that this technique provides reliable results both in frequency domain and in a transient analysis with a non-linear power converter. In the latter case the proposed model was able to predict undesired side effects at resonance and to overcome the limitations imposed by simplified assumptions or limitative hypotheses commonly taken in literature.

ACKNOWLEDGMENT

The research leading to these results has received funding from the European Community's Seventh Framework Programme (FP7/2007-2013) under grant agreement NANOFUNCTION no. 257375 and from the ENIAC Joint Undertaking under grant agreement END no. 120214. The authors thank Mattia Tassinari of University of Bologna for his valuable contributions to the experimental measurements and Fondazione Cassa dei Risparmi di Forlì for financial support.

REFERENCES

[1] E. Lefeuvre, A. Badel, C. Richard, L. Petit, D. Guyomar, “A comparison between several vibration-powered piezoelectric generators for standalone systems,” *Sensors and Actuators A: Physical*, vol. 126, Feb. 2006, pp. 405-416.

[2] A. Erturk, D.J. Inman, “An experimentally validated bimorph cantilever model for piezoelectric energy harvesting from base excitations,” *Smart Materials and Structures*, vol. 18, no. 025009, Feb. 2009, pp. 1-18

[3] R. P. Paganelli, A. Romani, A. Golfarelli, M. Magi, E. Sangiorgi, M. Tartagni, “Modeling and characterization of piezoelectric transducers by means of scattering parameters. Part I: Theory,” *Sensors and Actuators A: Physical*, vol. 160, Mar. 2010, pp. 9-18.

[4] M. Lallart, L. Garbuio, L. Petit, C. Richard, D. Guyomar, “Double synchronized switch harvesting (DSSH): a new energy harvesting scheme for efficient energy extraction.,” *IEEE transactions on ultrasonics, ferroelectrics, and frequency control*, vol. 55, Oct. 2008, pp. 2119-30.

[5] A. Romani, M. Tartagni, and E. Sangiorgi, “An Energy Autonomous Switching Converter for Harvesting Power from Multiple Piezoelectric Transducers,” *Sensors, 2010 IEEE*, Nov. 2010, pp. 1173-1176

 ISBN: 978-1-61208-145-8

Standard VHDL Modeling and Top-Simulation for the Development of an Integrated Smart-Bolometer

M. Denoual
GREYC-ENSICAEN
University of Caen Basse Normandie
Caen, France
mdenoual@greyc.ensicaen.fr

P. Attia
NXP Semiconductors
Colombelles, France
patrick.attia@nxp.com

***Abstract*—An event-driven modeling technique in standard VHDL is presented in this paper for the high level simulation of a resistive bolometer operating in closed-loop mode and implementing smart functions. The closed-loop mode operation is achieved by the capacitively coupled electrical substitution technique. The event-driven VHDL modeling technique is successfully applied to behavioral modeling and simulation of such a multiphysics system involving optical, thermal and electronics mechanisms. The modeling technique allows the high level simulations for the test of the smart functions algorithms of the future integrated smart-device.**

Keywords- top simulation, standard VHDL, smart sensor, bolometer

I. INTRODUCTION

Smart sensors defined according to the IEEE 1451.2 as sensors "that provide functions those necessary for generating a correct representation of a sensed or controlled quantity" [1] are more and more common on the market. These devices integrate on a single chip or in a single package the sensor, its analogous conditioning electronics, some digital electronics for control and data transmission, feedback means, and possibly RF means [2]. The development of such devices combining analogous, digital electronics and physical transducers implies the availability of tools for the design and the validation. Especially, high-level simulation tools are required for the validation of the algorithms implementing the smart functions. Smart functions are for instance self-calibration, identification, or self-test.

From the sensor side, multiphysics design and simulation softwares exist that allow this type of simulation. From the electronics or algorithm side, modeling using VHDL-AMS, Verilog-AMS has been proposed [3]. As far as top validation is concerned, *i.e.* test of embedded algorithms in their operating context, these modeling techniques exhibit huge simulation times that are not compatible with the tuning and optimization of the algorithms and usually suffer from convergence issues. For complex mixed analogous-digital electronics circuits, some designers have an unusual use of the standard VHDL language combined with mathematical packages to model such mixed systems, and proceed to event-driven simulation. Such simulations prevent the convergence issues and drastically reduce the simulation time [4, 5].

In this work, for the first time to our knowledge, we use the standard VHDL modeling and event-driven purely digital simulations during the design and development of a smart-bolometer for the validation of algorithms implementing smart functions. This work takes place at the beginning of the design and the development of integrated smart-bolometers. The smart-sensors considered consist in uncooled resistive bolometers and the implementation of the capacitively coupled electrical substitution [6, 7] that enables the closed loop operation of the bolometers and the implementation of smart functions.

Uncooled resistive bolometers are one kind of infrared sensors. Among the thermal detectors, resistive bolometers are the most commonly met due to the simplicity of their fabrication process, compatible with the semiconductor industry. Uncooled bolometers represent more than 95% of the market of infrared imaging systems in 2010 and the sales volume is expected to triple by 2015 [8]. In that context, our work is to develop bolometers with self-test, self-calibration and identification function, *i.e.* smart-bolometers.

The paper is organized as follows. The first section describes the detection principle of a resistive bolometer and the capacitively coupled electrical substitution for the feedback. The second section presents the standard VHDL modeling of the system. The result section exhibits some simulation results that illustrate the potential of the standard VHDL modeling technique to validate the functional behavior of multi-domain systems. The results also show that this modeling technique answers the need for high level simulation tools to test the algorithms implementing smart functions. The purpose of such simulations is to validate the functionality of the device not the performances; that is why neither noise nor linearity have been modeled in this work but both could be added if necessary in the future.

II. DESCRIPTION OF THE SYSTEM

The device is a closed-loop system composed of a resistive bolometer, its conditioning electronics and the capacitively coupled electrical substitution feedback part.

A. Uncooled Resistive Bolometer

The operating principle of an uncooled resistive bolometer is illustrated in Fig.1. An uncooled resistive bolometer converts absorbed infrared (IR) radiation into heat, which in turn changes the resistance of a sensing resistor. The sensing resistor is current biased. A bolometer

 ISBN: 978-1-61208-145-8

can be modeled as an IR-sensitive element of thermal mass C_{th} linked *via* a thermal conductance G_{th} to a substrate acting as a heat sink. The performance of the bolometer is characterized by figures of merit such as the temperature coefficient of resistance (TCR or α) of the temperature sensing resistor, its responsivity (R), its specific detectivity (D^*) and its effective time constant ($\tau_{eff}=C_{th}/G_{eff}$, G_{eff} is the effective thermal conductance and depends on G_{th}) [9]. The responsivity describes the variations of the output voltage signal ($v_{Tbolometer}$) depending on the IR input radiation ($p_{radiation}(\omega)$) and it is expressed by the transfer function of the bolometer as follows

$$R(\omega)[V/W] = \frac{v_{T_{bolometer}}(\omega)}{p_{radiation}(\omega)} = \frac{\alpha \eta I_{BIAS} R_B}{G_{eff} + j\omega C_{th}} \quad (1)$$

where η is the absorption coefficient of the absorption layer of the device, I_{BIAS} is the bias current, R_B is the bolometer resistance (sensing resistor). The design of a resistive bolometer results from a tradeoff between responsivity and time constant, under fabrication constraints. Improved responsivity is obtained with small thermal conductance, but this negatively impacts the time constant.

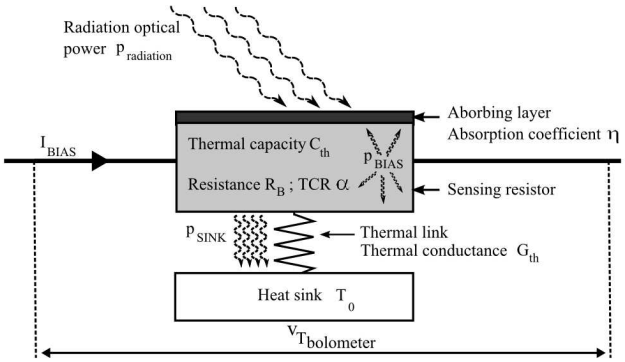

Figure 1. Schematic of a resistive bolometer. The incident IR power is absorbed and converted into heat. The heat rises the temperature of a temperature sensitive resistor thermally coupled to a heat sink at T_0. The resistance change of the sensing resistor is measured.

B. Feedback technique

A way to overcome this trade-off is to operate the bolometer in closed-loop mode. In that case, usually Joule heat is used as feedback means and technique is referred to as electrical substitution [10, 11]. Three techniques of implementation exist for the closed-loop operation:
(i) Direct feedback [12, 13] suffering from stability issues,
(ii) Feedback using an extra heating source [10, 11],
(iii) Capacitively coupled feedback on the sensing resistor [6, 7] that combines the advantages of the two previous solutions. The digital implementation of the capacitively coupled feedback technique, used in this work, is illustrated in Fig.2 and described in details in [6, 7].

The principle is to dissociate the electrical and thermal working points according to a frequency basis. It consists in the use of a high frequency modulated signal for the heat feedback voltage applied to the sensing resistor. This implementation can be applied to any kind of uncooled resistive bolometer. The digital implementation, involving pulse width modulation (PWM) or Sigma-Delta modulation, enables the linearization of the feedback path as well as a direct digital output power reading [7].

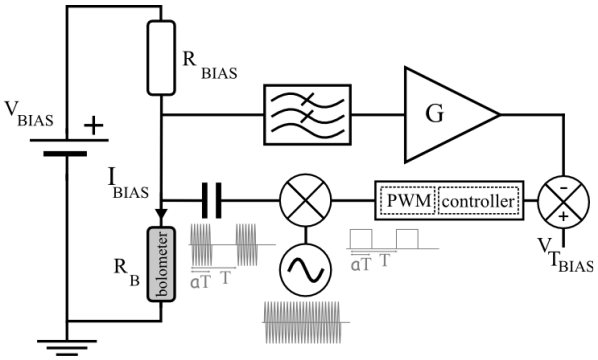

Figure 2. Digital implementation of the capacitively coupled electrical substitution feedback. R_B represents the sensing resistor. The feedback is a PWM signal of duty cycle α, translated at high frequency.

C. Smart functions

In addition to the benefits of the operation in closed-loop mode (*e.g.* reduction of the time constant, operation at a defined working point, improvement of the measurement dynamics), the feedback path enables smart functions. This has been extensively studied for in the case of accelerometer or pressure sensor [14]. The basic smart functions of a smart sensor are self-test, self-calibration or autorange. Identification in open and closed-loop is another smart function that enables the monitoring of the aging of the sensor. It consequently allows the update of the feedback controller. Those smart functions correspond to algorithms implemented in the digital part of the smart sensor. The main objective of the standard VHDL modeling is to dynamically test and validate algorithms in their operating context, *i.e.* the mixed analogous-digital and multi-domain high level context.

III. MODELING TECHNIQUE

Advantages of the presented modeling technique come from: (i) the event-driven nature of the simulation using purely digital environment and (ii) the properties of the standard VHDL language. The event-driven nature of the simulation results in drastically shorter simulation times compared to time-driven simulation using for instance Spice or Matlab-Simulink [15]. Using existing digital simulation software (ModelSim, NCSim,…), this modeling technique does not suffer from the convergence issues usually observed with other techniques. The standard VHDL syntax with user's defined types enables implicit connectivity check between the parts of the designed system as in VHDL two connected signals must have the same type.

The basic principle of this modeling technique is the digitalization of the analogous parts of the design. The appropriate modeling of the analogous parts of the design enables to overcome the problematic induced by different time scales. It is the case in this work involving low frequency thermal phenomena (< kHz), and high frequency

 ISBN: 978-1-61208-145-8

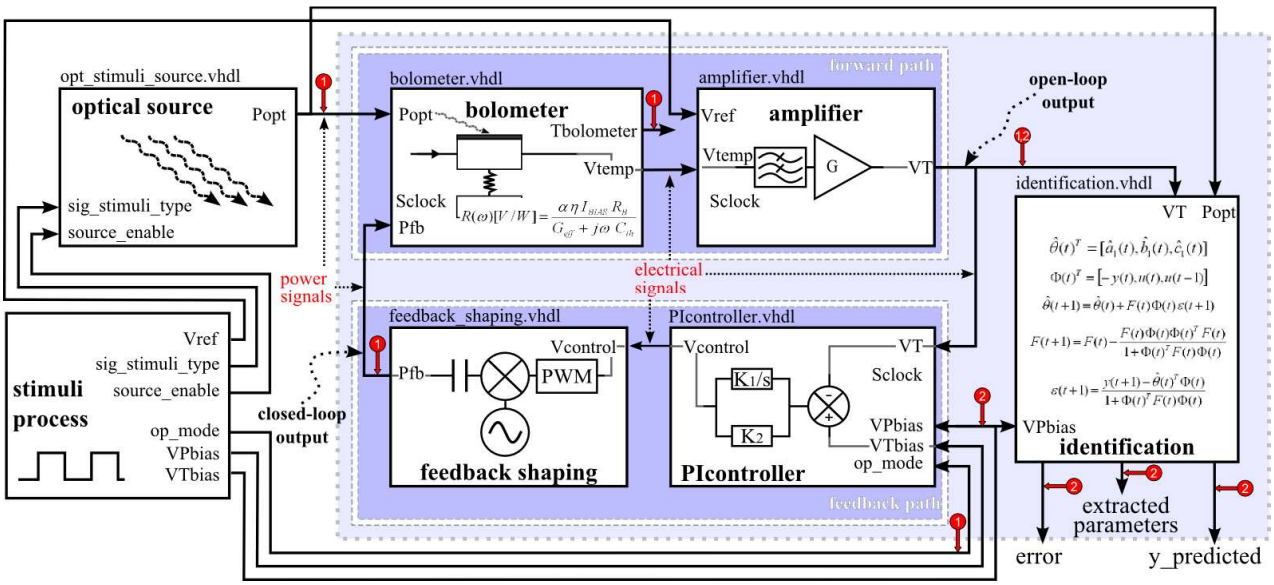

Figure 3. : Block diagram of the complete testbench. The filled box with dotted border represents the smart-bolometer to be integrated, *i.e.*: the sensor itself, the conditioning electronics, the heat feedback and here, as an example of smart function, an open-loop identification function. The circle marked arrows indicate the signals observed in the simulations 1 and 2 presented in the figure Fig.5. All the boxes correspond to standard VHDL files. Sclock is the sampling signal at frequency f_S.

electronics signals due to the modulated feedback signal of the capacitively coupled electrical substitution (MHz range). Those frequency ranges are represented in Fig.4. In the model developed, the phenomena are treated differently depending on their frequency range. Low frequency phenomena such as power/temperature variations or voltage variations due to the temperature variations are considered as signals. On the contrary, high frequency phenomena, essentially the modulated feedback voltage, are not treated as signals. That means no signals at those high frequencies are generated. The model only takes into account the effective feedback power generated by this high frequency modulated signal, which in case of PWM modulation is proportional to the duty cycle [7]. The effective feedback power applied to the sensing resistor varies in the low frequency range related to the thermal phenomena (system bandwidth in Fig. 4). This modeling enables drastic simulation time reduction. In practice the simulation time step corresponds to the digital sampling period of the system ($T_S=1/f_S$). This sampling period is chosen as a tenth of the closed-loop time constant. Consequently, it allows a one-thousand reduction of the simulation time compared to a simulation that would take into account the high frequency feedback signal.

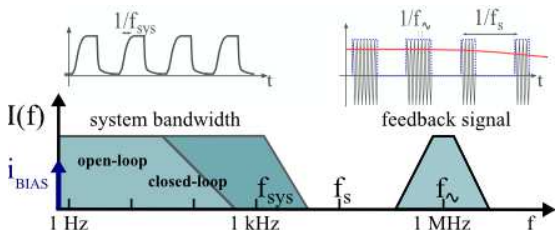

Figure 4. : Frequency domains

All the elements of the system are modeled using standard VHDL. Those elements are schematically presented in the figure Fig.3 corresponding to the testbench. The testbench also includes the optical power stimuli and the stimuli process. In this example, the smart function simulated is open-loop identification.

The model for the bolometer corresponds to the VHDL transcription of the digitalized transfer function (1). The digitalization is achieved using the bilinear transformation. The conversion process is divided into two consecutive steps: (i) the thermal process dealing with power inputs and temperature, (ii) the electrical process corresponding to the temperature measurement. This structure would enable to take into account the electrothermal feedback phenomenon [9] of the bolometer itself if needed in the simulation. At the present time, this phenomenon is taken into account through the use of the effective thermal conductance (G_{eff}) rather than the physical thermal conduction (G_{th}).

The model for the filter and amplifier block only consists in a gain since the bolometer voltage output signal is in the bandpass range of the filter.

The model of the controller in this case implements the equations of a digital proportional integral (PI) controller. The op_mode input enables to choose the operation mode of the controller (open/closed loop).

The model for the feedback shaping block consists in a gain and saturations corresponding to the PWM modulation. As mentioned earlier, the high frequency carrier that translates the feedback bandwidth is not taken into account. Only the feedback duty cycle is considered.

The identification block implements a least-mean-square adaptative fitting algorithm which role is to extract parameters in order to optimize the feedback controller and/or to monitor the aging of the device.

The optical source generates stimuli with parameterized frequency, amplitude and shape.

IV. EXAMPLE OF SIMULATION RESULTS

This section illustrates the type of simulation that can be done with this modeling technique. The simulations were performed using the ModelSim Altera 6.3 Quartus II 8.1

 ISBN: 978-1-61208-145-8

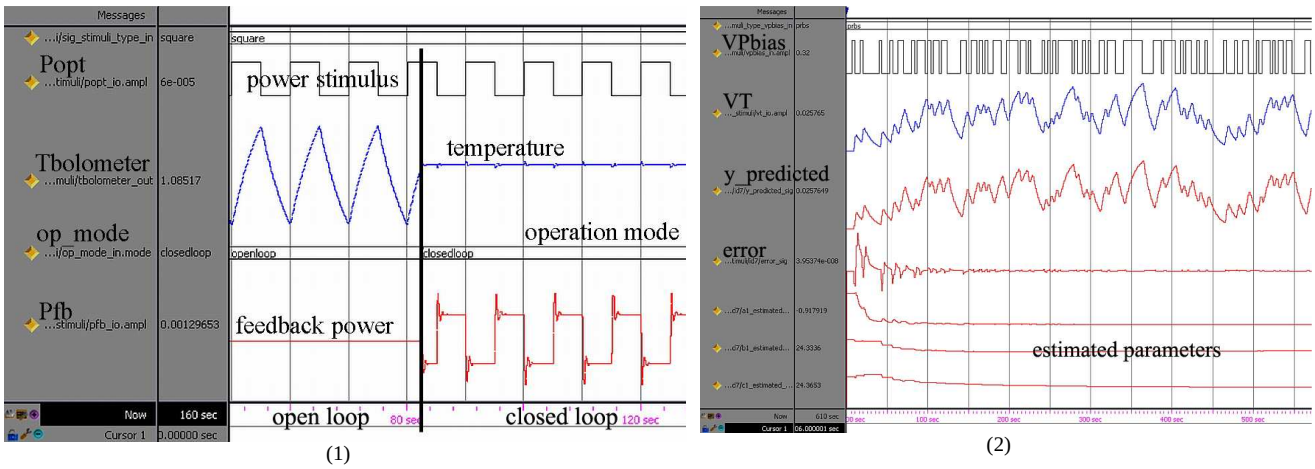

(1) (2)

Figure 5. : Examples of digital simulations of the VHDL modelized system.
(1) Open/closed-loop simulation. The simulation begins in open-loop. The square applied optical stimuli (Popt) induces temperature changes in the bolometer (Tbolometer) which is the open-loop ouput. In closed-loop mode, the temperature is regulated as the feedback power (Pfb) compensates the incoming optical power. The closed-loop operation of the bolometer enables a direct power reading of the incoming power through the variations of Pfb.
(2) Open-loop identification process. A least-mean square adaptative algorithm is implemented for the extraction of parameters in order to identify the bolometer characteristics. The predicted output is evaluated with the estimated parameters and the electrical stimuli (VPbias) converted into power stimuli by the feedback path. The prediction error corresponds to the difference between this predicted ouput and the open-loop ouput signal (VT). According to the error the estimated parameters are adjusted. The stimuli is a pseudo random binary sequence (PRBS) in order to optimize the identification process.

software. Parameters for the sensor and the electronics were taken from [7] and correspond to a macro-scale device.

The figure Fig.5 shows two simulation results. Fig.5(1) corresponds to open and closed-loop simulation of the system. The results are in good agreement with experimental results previously obtained [7]. Simulations in either open or closed-loop are performed without convergence issues within a few seconds. This enables fast parameter optimization for the control through series of simulations.

Fig.5(2) corresponds to simulation of a smart function: the identification of the system. An adaptative least-mean-square algorithm is implemented using standard VHDL to extract the characteristic parameters of the bolometer while stimuli are applied. This simulation underlines the ability of the modeling technique to validate algorithm supporting smart functions in their operating context by top simulation.

V. CONCLUSION

An event-driven modeling technique in standard VHDL is presented for the high level simulation of a resistive bolometer operating in closed-loop mode and implementing smart functions. This behavioral modeling technique is successfully applied to the simulation of such a multi-domain system. It enables fast simulations without any convergence issues. The modeling technique allows the test and validation of algorithms supporting smart functions. It is therefore a useful tool for the development of integrated smart sensors.

REFERENCES

[1] R. Frank, Understanding smart sensors: control techniques Artech House publisher, 2000, ch. 7, pp. 149-171.

[2] K.D. Wise, Integrated sensors, MEMS, and microsystems: Reflections on a fantastic voyage, Sens. & Act. A, 2007, vol. 136, pp. 39-50.

[3] Y-A. Chapuis, L. Zhou, H. Fujita, Y. Hervé Multi-domain simulation using VHDL-AMS for distributed MEMS in functional environment: Case of a 2D air-jet micro-manipulator, Sens. & Act. A, 2008, vol. 148, pp. 224-238.

[4] M. Schubert, Mixed-Sginal Event-Driven Simulation of a Phase-Locked Loop, BMAS, 1999.

[5] R.B. Staszewski, C. Fernando, P.T. Balsara, Event-Driven Simulation and modeling of phase noise of an RF oscillator, IEEE Trans. Circ. and Syst., 2005, vol. 52(4), pp 723-733.

[6] M. Denoual, G. Allègre, S. Delaunay, D. Robbes, Capacitively coupled electrical substitution for resistive bolometer enhancement, Meas. Sci. Technol., 2009, vol. 20, doi: 015105.

[7] M. Denoual , S. Lebargy, G. Allègre, Digital implementation of the capacitively coupled electrical substitution for resistive bolometers, Meas. Sci. Technol., 2010, vol. 21, doi: 015205.

[8] Yole Développement, Uncooled IR Cameras & Detectors for Thermography and Vision, Tech. & Market Report, 2010.

[9] P. L. Richards, Bolometers for infrared and millimeter waves, J. Appl. Phys., vol. 76, 1994, pp. 1–24

[10] J. P. Rice, S. R. Lorentz, R. U. Datla, et al., Active cavity absolute radiometer based on high-Tc superconductors, Metrologia, 1998, vol. 35(289).

[11] M. Galeazzi, An external electronic feedback system applied to a cryogenic micro-calorimeter, Rev. Sci. Instr., 1998, vol. 69(5), pp. 2017-2023.

[12] C. D. H. Williams, An appraisal of the noise performance of constant temperature bolometric detector systems, Meas. Sci. Technol., 1990, vol. 1(322).

[13] R. C. S. Freire, S. Y. C. Catunda, B. A. Luciano, Applications of Thermoresistive Sensors Using the Electric Equivalence Principle, IEEE Trans. Instr. Meas., 2009, vol. 58(6), pp. 1823-1830.

[14] L. Zimmermann, J. Ebersohl, F. Le Hung, et al., Airbag application: a microsystem including a silicon capacitive accelerometer, CMOS switched capacitor electronics and true self-test capability, Sens. & Act. A, 1995, 46-47 pp. 190-195.

[15] J. Zhuang, Q. Du, T. Kwaniewski, Event-Driven Modeling and Simulation of a Digital PLL, BMAS, 2006, pp. 67-72

 ISBN: 978-1-61208-145-8

Real-time Detection of Infrared Radiation by Position-sensitive Superconducting Bolometer

Francesco Laviano, Roberto Gerbaldo, Gianluca Ghigo, Laura Gozzelino, Enrica Mezzetti
dept. Physics
Politecnico di Torino and INFN Sezione Torino
Torino, Italy
Email: francesco.laviano, roberto.gerbaldo, gianluca.ghigo, laura.gozzelino, enrica.mezzetti@polito.it

Luca Mesin
dept. Electronics
Politecnico di Torino
Torino, Italy
Email: luca.mesin@polito.it

Alberto Rovelli
Istituto Nazionale Fisica Nucleare
Laboratori Nazionali del Sud
Catania, Italy
Email: rovelli@lns.infn.it

***Abstract*—Infrared sensors are fundamental building blocks of strategic applications such as atmospheric gas monitoring, thermal imaging and telecommunications. While single frequency applications can employ resonant devices that have high resolution and high sensitivity, broad-band infrared detection relies on bolometric sensors. In this paper, we present a high-temperature superconducting sensor whose structural and electrical properties are locally modified by heavy-ion irradiation, in order to obtain position-sensitive broad band infrared detection. The bolometer, biased with constant current, responds to infrared radiation (from near to far-infrared spectra), with a dissipative voltage signal that can be monitored in real-time with a standard voltmeter. The digitized signal is processed with artificial neural networks (ANN) in order to correct for thermal and electronic noise contributions. Once trained, the ANN can be applied to new detected data and process them in real-time. In this way, real-time, position-sensitive detection of broad-band infrared radiation is achieved.**

***Index Terms*—Real-time sampling, superconducting devices, superconducting films, THz detector, neural networks.**

I. INTRODUCTION

Detection of infrared radiation is a fundamental task for many strategic applications in biomedical, environment monitoring, space science and military fields [1]. Since the very beginning of the research in these fields [2], much attention was paid to the low-frequency part of the infrared spectrum, the far-infrared (FIR), because many molecular absorption spectra are centered in this frequency range. However, the FIR radiation slightly interacts with solid state devices and therefore development of high responsivity devices is still a crucial task for many applications. Resonant devices [3] have high sensitivity for selected frequency ranges and operate at room temperature, making them the best choice for single frequency applications. On the other hand, wide band bolometric detection is commonly achieved with bolometers operated at liquid Helium temperature or below [1], making them expensive solutions (both for what concerns cost of instrumentation and size), sometimes limiting the operation time due to the cryogenic requirements, e.g., in satellite application. After the discovery of high temperature superconductors (HTSC) [4], promising applications of HTSC bolometers were envisaged, because they can be used above the liquid nitrogen temperature. In particular, several solutions have been already proposed for HTSC $YBa_2Cu_3O_{7-x}$ (YBCO) based bolometers that have been demonstrated to respond to the infrared radiation [5]. Since responsivity is corresponding to the resistance versus temperature slope, the maximum responsivity is achieved at the mid-point of the transition to the superconducting state. Optimally doped YBCO bolometers, whose critical temperature (Tc) is around 90 K, display the highest responsivity [6]. For what concerns high speed operation, thermal modeling suggested that thin membranes or suitable substrates should be used. In order to obtain a high responsivity and position-sensitive YBCO bolometer with controlled Tc, we employed irradiation with micro-collimated high energy heavy ion (HEHI) beams. In this way, Tc can be finely tuned (reduced), while the resistance versus temperature slope is totally preserved. Another chief result of this process is to confine the sensitive area to the irradiated part, therefore a position-sensitive detector is obtained. Detection of broad-band infrared radiation can be performed with standard four probe techniques used for resistance measurement, therefore real-time monitoring of infrared signals is achieved. Since the device is sensitive to the full infrared spectrum, thermal fluctuation is an important noise source along with Johnson noise. In order to correct for these major noise sources, we applied an artificial neural network (ANN) signal processing. The ANN processing eliminates the thermal background fluctuation and renormalizes the signal intensity due to the change in responsivity. In this way, real-time monitoring of infrared signals is achieved with a position sensitive detector that can be housed in a light weight, liquid nitrogen temperature dewar.

 ISBN: 978-1-61208-145-8

II. METHODS

A. Device design and construction

YBCO films are deposited by thermal co-evaporation on MgO substrates [7]. YBCO film thickness is 250 nm, in order to obtain high critical current density, Jc, in the as-grown material [8]. Tc of as-grown samples is about 89 K, at the transition onset, and the transition width, ΔTc, is less than one kelvin. Sample patterning is obtained by standard UV photolithography and wet-etching in HCl/H_2O solution. The device layout consists of two meander structures, which are connected in series. One of them is uniformly irradiated with a suitable ion fluence, in order to obtain localized dissipation. The other meander serves as control signal for the background temperature monitoring [9]. The irradiation was performed at INFN laboratories [10], employing 114 MeV ^{197}Au ions for the controlled reduction of YBCO Tc. With a fluence of 4.84 $\cdot$ 10^{11} cm^{-2}, the zero resistance temperature is lowered by about 5 K.

B. Photoresponse measurements

Broad-band, continuous-wave infrared radiation is produced by a high pressure Hg arc lamp (OSRAM HBO 100W) [2]. The wavelength range is selected by proper filtering. In particular, high-resistivity n-type Si (flat transmittance above 50%), enables the transmission of the mid and far infrared (MIR-FIR) spectra (wavelength range 1-100 μm). The electrical measurements were performed by 4-probe method for each meander following the scheme reported in Figure 1 . The contacts were made by direct soldering Au wires (diameter of 50 μm for voltage pads and 125μm for current leads), on the YBCO pads with a low-temperature alloy (In-Sn-Bi). The electrical current was kept constant during the measurement (current source Keithley model 224) and the voltage signals were recorded in real-time (integration time 100 ms) by a dual channel nano-voltmeter (Keithley model 2182A). A custom Labview software was used for controlling the instruments (through GPIB interface) and for collecting the raw data on a PC.

C. Features selection and neural model

The output of the sensor is affected by thermal and electronic noise. In particular, thermal noise induces a nonlinear bias which increases as the sensor warms during the measurement. In order to compensate for the effect of noise, a nonlinear, real time signal processing technique was developed, based on ANN. ANNs are biologically inspired models consisting of a network of interconnections between neurons, which are the basic computational units. A single neuron processes multiple inputs and produces an output which is the result of the application of an activation function (usually nonlinear) to a linear combination of the inputs

$$y_i = \phi_i \left(\sum_{j=1}^{N} w_{ij} x_j + b_i \right) \qquad (1)$$

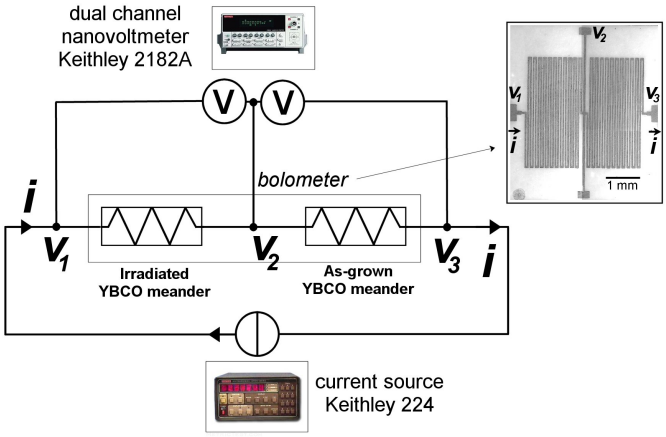

Fig. 1. Scheme of electrical measurement method. In the inset, a photo of the actual bolometer is shown.

where y_i is the output of the i^{th} neuron, ϕ_i is the activation function, w_{ij} is the weight between the j^{th} input x_j and the i^{th} neuron and b_i is a bias. The weights and the bias are free parameters that can be adaptively chosen in order to estimate an input-output map associating the input measurements to the desired output, provided by a set of training data.

The selection of optimal features that are going to be used as the input of the ANN is of great importance, in order to reduce the measurement and storage requirements, to counteract the difficulties of facing a problem with large dimension, to reduce noise content and to improve performance. We used a method based on the selection of the input data providing maximal information on the output. In order to avoid redundancy between input features, we used the algorithm proposed in [11] which determines the interdependencies between candidate variables computing the Partial Mutual Information (PMI). This technique found applications in feature selection for system identification in meteo forecast and in air pollution distribution prediction [12]. PMI represents the information between a considered variable and the output that is not contained in the already selected features. Variables with maximal PMI with the output are iteratively selected from the set of candidates.

The considered candidate variables were the values of the output of the sensor at the present instant and its delayed versions, with a time delay up to 5 samples. The desired output was the power of the source. Using PMI selection method, the candidate variables were ordered, starting from the one with maximum mutual information with the output and continuing with the input features in decreasing order of PMI with the output. Then, to map the input to the desired output, a set of multilayer perceptrons (MLP) was used. Different MLPs were obtained using a different number of inputs, a single hidden layer with number of neurons in the range $1 - 10$ (with sigmoidal activation function) and a single output neuron (with linear activation function). Different MLP topologies were trained by modifying iteratively the weights and the bias in order to reduce the error in fitting the desired output, using

 ISBN: 978-1-61208-145-8

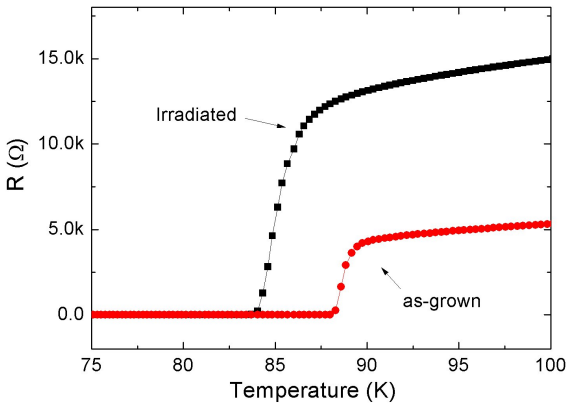

Fig. 2. Resistance versus temperature behavior of irradiated and as-grown YBCO (bias current 10 μA). The Tc difference is around 5 K (114 MeV ^{197}Au 4.84 $\cdot$ 10^{11} ion cm^{-2}). Note that the resistance versus temperature slope is preserved.

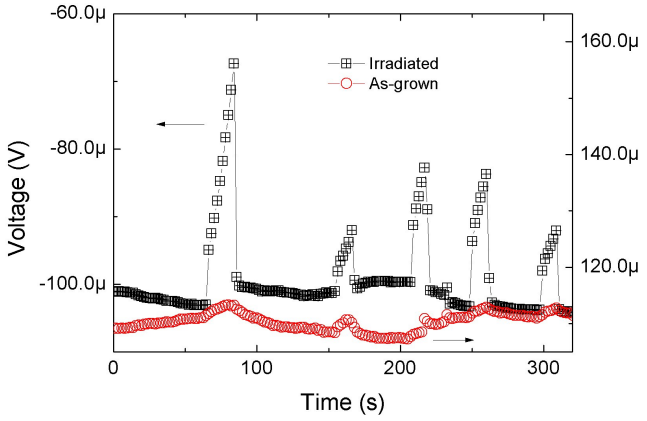

Fig. 3. Sample signals of both irradiated and as-grown meanders. The infrared beam is coming from a black-body source which is turned on and off by means of an electro-mechanical shutter. The irradiated meander responds with sharp jumps to the infrared beam, while the as-grown meander displays a signal whose evolution is determined by the background temperature.

the quasi-Newton algorithm with a number of iterations in the range $10 - 50$.

Data included 5 radiation events with constant power. Each ANN was trained with a portion of signal including 4 of the 5 events and tested on a portion of signal including the remaining one (test set). All root mean squared (RMS) errors on the test data were computed and the ANN with minimum average error across the 5 trials was selected as that with best generalization performance.

III. Results

The resistance versus temperature characteristics of the device are shown in Figure 2. The irradiated meander displays increased resistivity and lowered Tc with respect to the as-grown structure, as expected. The working point for the device is around the onset of dissipation of the irradiated meander (around T = 81.5 K with a bias current of 1 mA [9]).

If the device is exposed to infrared radiation, the local temperature will raise and only the irradiated meander displays dissipative signals, as shown in Figure 3.

The voltage picked up on the as-grown meander is due to the thermoelectric signal spreading from the irradiated YBCO and therefore it is indicating the variation of the substrate temperature. On the other hand, the temperature fluctuations due to the infrared radiation to be detected and to the environment are changing the responsivity of the bolometer: the voltage is continuously increasing when the infrared beam hits the detector. In order to correct for these problems due to the thermal backgroung, we applied an ANN signal processing as described above. For each of the five training experiments, PMI selected the present measurement as the feature with maximal mutual information with the radiated power and the one step delayed measure as the feature with maximal partial mutual information with the desired output, once selected the present measure. The selected optimal ANN, with best

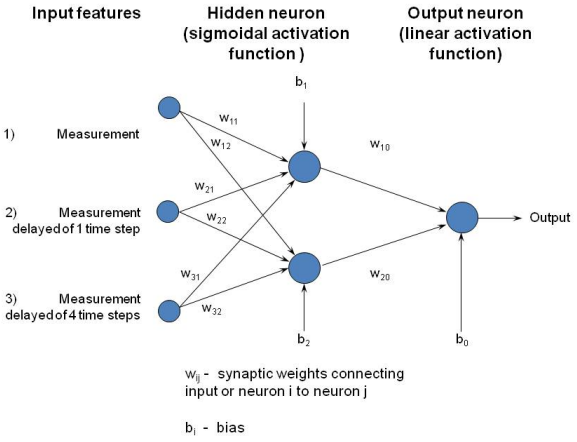

Fig. 4. Topology of the ANN with best generalization performances.

generalization to the test set (average generalization error about 2.5%), has three inputs and two hidden neurons (see Figure 4) and was trained for 30 iterations. Figure 5 shows the raw data and the infrared radiation estimated by the optimal ANN for one choice of the training and the test sets. Good performances (average generalization error about 10%) were obtained also using two input features (the present measure and the 1 step delayed measure) and a single hidden neuron.

IV. Conclusion

We have tested a high-temperature superconducting bolometer for monitoring infrared signals in real-time. High responsivity is obtained for temperature just above the liquid nitrogen temperature thanks to the local irradiation with HEHI which reduces in a controlled way the critical temperature but retains the resistance versus temperature slope. Since the

 ISBN: 978-1-61208-145-8

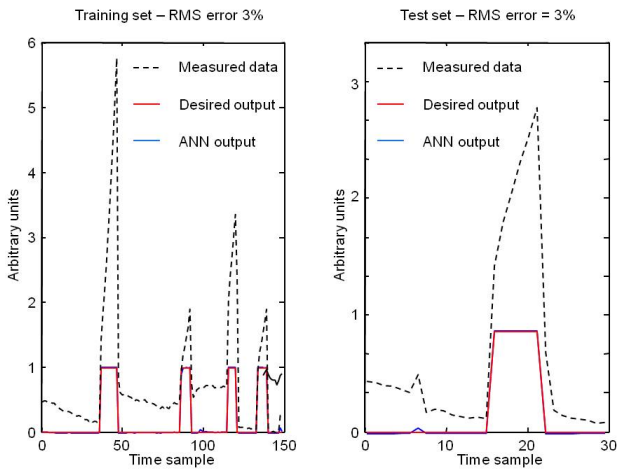

Fig. 5. Raw data, desired output and ANN estimated output for an example of training set and test set.

infrared radiation to be detected is coupled with a noisy thermal background, we implemented an ANN approach in order to obtain the subtraction of the thermal background and the renormalization of the output intensity in dependence on such background. Once trained and validated on experimental signals, the ANN can filter new detected data in real-time.

Different MLPs were tested. Optimal performances were achieved using MLPs with simple topology. Good performances were obtained using only the actual measure and the 1 step delayed one. This selection of inputs indicates that the measurement and its time derivative are sufficient to estimate the required output. In that case, only one neuron in the hidden layer was required. This is due to the binary desired output. The optimal MLPs was a bit more complicated, as a further delayed version of the measure was selected and one more neuron was placed in the hidden layer. This choice improved the stability of the estimates to noise, improving slightly the performances. It is worth noticing that to detect the presence of a constant radiation, the output neuron could also have a sigmoidal activation function. Future investigation will be devoted to the estimation of an arbitrary profile of thermal radiation. In such a case, a linear activation function for the output neuron is preferred. Moreover, a more complex topology of the network is expected to be able to optimally adapt to the data.

This study demonstrates the possibility to develop high responsivity infrared bolometers based on superconducting oxides which are working at temperature above the liquid nitrogen. The suitably engineered detector in a portable, light-weight cryostat is desired for molecular spectroscopy, thermal imaging and telecommunications.

V. Acknowledgment

This work was partially supported by INFN-MONADE and INFN-TERASPARC projects and by the national project AWIS (Airport Winter Information System), funded by Piedmont Authority, Italy.

References

[1] P. H. Siegel, *Terahertz Technology,* IEEE Trans. on Microwave Theory and Techniques, vol. 50, no. 3, pp. 910-928, 2002.

[2] M.F. Kimmitt, *Restrahlen to T-Rays - 100 Years of Terahertz Radiation,* Journal of Biological Physics, vol. 29, pp. 77-85, 2003.

[3] W. Knap, F. Teppe, Y. Meziani, N. Dyakonova, J. Lusakowski, F. Boeuf, T. Skotnicki, D. Maude, S. Rumyantsev and M. S. Shur, *Plasma wave detection of sub-terahertz and terahertz radiation by silicon field-effect transistors,* Appl. Phys. Lett. vol. 85, pp. 675-677, 2004.

[4] J. G. Bednorz and K. A. Mller, *Possible high Tc superconductivity in the Ba-La-Cu-O system,* Zeitschrift fr Physik B Condensed Matter 64, pp. 189-193, 1986.

[5] A.J. Kreisler and A. Gaugue, *Recent progress in high-temperature superconductor bolometric detectors: from the mid-infrared to the far-infrared (THz) range,* Supercond. Sci. Technol. 13 pp. 1235-1245, 2000

[6] A. Jukna and R. Sobolewski, *Time-resolved photoresponse in the resistive flux-flow state in YBaCuO superconducting microbridges,* Supercond. Sci. Technol., vol. 16 pp. 911-915, July 2003

[7] B. Utz, R. Semerad, M. Bauer, W. Prusseit, P. Berberich, and H. Kinder, *Deposition of YBCO and NBCO films on areas of 9 inches in diameter,* IEEE Trans. Appl. Supercond., vol. 7, no. 2, pp. 1272-1277, 1997.

[8] F. Laviano, D. Botta, R. Gerbaldo, G. Ghigo, L. Gozzelino, L. Gianni, S. Zannella, and E. Mezzetti, *Thickness dependance of the current density distribution in superconducting films,* Physica C, vol. 404, pp. 220-225, 2004.

[9] F. Laviano, R. Gerbaldo, G. Ghigo , L. Gozzelino, B. Minetti, A. Rovelli, and E. Mezzetti, *THz detection above 77K in YBCO films patterned by heavy-ion lithography,* IEEE Sensors Journal, vol. 10, pp. 863-868, 2010.

[10] A. Rovelli, A. Amato, D. Botta, A. Chiodoni, R. Gerbaldo, G. Ghigo, L. Gozzelino, F. Laviano, B. Minetti, and E. Mezzetti, *A new apparatus for deep patterning of beam sensitive target by means of high energy ion beam,* Nucl. Instrum. Methods Phys. Res. B, vol. 240, no. 4, pp. 842-849, 2005.

[11] A. Sharma, *Seasonal to interannual rainfall probabilistic forecasts for improved water supply management: 1 - A strategy for system predictor identification,* Journal of Hydrology, vol. 239, pp. 232-239, 2000.

[12] L. Mesin, F. Orione, R. Taormina, E. Pasero, *A feature selection method for air quality forecasting,* Proceedings of the 20th International Conference on Artificial Neural Networks (ICANN), Thessaloniki, Greece, September 15-18, 2010.

 ISBN: 978-1-61208-145-8

PIR Sensor Array for Hand Motion Recognition

Piotr Wojtczuk*, Alistair Armitage†, T. David Binnie*, and Tim Chamberlain‡
*School of Engineering and the Built Environment, Edinburgh Napier University, Edinburgh, UK
†School of Computing, Edinburgh Napier University, Edinburgh, UK
‡Pyreos Ltd., Edinburgh, UK
Email: p.wojtczuk@napier.ac.uk, a.armitage@napier.ac.uk, td.binnie@napier.ac.uk, tim.chamberlain@pyreos.com

***Abstract*—In this paper we present our work towards a hand gesture recognition system realised with a passive thermal infrared sensor array. In contrast with the majority of recent research activities into gesture recognition, which focus on the complex analysis of video sequences, our approach shows that the functionality of a simple pyroelectric movement sensor can be expanded to detect differing hand gestures at short range. We show that blob detection from a hand waving over a 16 element passive infrared sensor array provides sufficient information to discriminate four directions of hand stroke. This sensor system is unique and lends itself to low cost, low profile and low power applications.**

***Keywords*-touchless input device; dynamic hand gesture; infrared motion sensor; infrared sensor array; pyroelectricity;**

I. INTRODUCTION

Non-contact operation of electrical appliances is becoming increasingly desirable. This is particularly the case in public areas where hygiene is important. Public washrooms increasingly have taps, cisterns, soap dispensers, hand dryers and doors activated by simple hand proximity/movement detectors. The advantages of removing physical contact from the activation and control of devices range from limiting the chance of infections transmitted through touch and better energy efficiency to simple convenience. In other environments such as medical facilities and food processing areas, strict hygiene rules are essential and direct hand contact with appliances is best avoided if at all possible [1]. These environments present a wide spectrum of opportunities for non-contact control, as reducing the number of touched surfaces positively suppresses risk of cross contamination and infection. There are often cases, where operators' hands may contaminate surfaces, e.g., in a kitchen or a workshop. Strict rules apply in operating rooms, where doctors' hands must remain sterile throughout a procedure [2]. There are other, rarer cases where a cultural or individual preference may be not to make physical contact with an appliance. In all these circumstances touch-free control is beneficial.

Existing non-contact hand proximity/motion switches provide the binary "on/off" operation. They are commonly based on single or dual cell pyroelectric infrared sensors with a simple lens system [3], although capacitive sensing can also be used [4]. Thus the degree of human control over the electrical appliance is severely limited.

In this paper details are given of a pyroelectric array device that detects simple hand movement gestures, thereby allowing greater non-contact control capability with little increase in size, cost or power consumption. This paper gives an overview of existing methods of gestures detection. Further, the problem of hand gesture recognition is discussed and our implementation is explained.

II. RELATED WORK

Gesture recognition systems can be categorized into three broad groups [5]: those that use a handheld pointing device, those that require wearable sensors and those with no user-held devices but operating using the analysis of 2D images (external sensing). For general application of gesture recognition sensors, it is important that the system requires no user held or worn devices.

Research into gesture feature extraction from image sequences is the most active. Most common implementation uses a video camera to capture a wide scene, from which hands are extracted and tracked, for example [6] and [7]. Such approach gives great flexibility in terms of detection distance and detection precision and scope. Commercially, systems operating on a video processing basis have been developed by GestureTek [8], EyeSight [9] and Edge 3 Technologies [10]. However, it is not practical to implement such systems ubiquitously, for example as switches, due to size, cost and, in many cases, energy consumption.

Byung-Woo Min et al. [11] classify hand gestures into static (hand posture) and dynamic (hand movement). Dynamic gestures are generally more intuitive for the user, as the direction of motion or its shape can reflect the resulting action, e.g., up/down hand stroke for increasing/decreasing brightness in a room. Moreover, it is easier to capture this type of gesture with a low resolution and low cost imager.

Sensor based touchless solutions become more popular after the recent success of touch screen interfaces. Mechaless [12] provide a hardware solution. They use an active near infrared (NIR) arrangement with multiple IR LEDs and a sensor that is used to calculate the distance of an object from each LED by timing pulse to reception interval. They propose use of their touchless interface in wall-mounted gesture switches (increase / decrease a control by up / down

 ISBN: 978-1-61208-145-8

hand movement) or in a remote control with a touchless 'joystick'.

One of many NIR proximity array systems is being developed by Dongseok et al. [13]. A 3-dimensional map of the scene is created by analyzing reflections of emitted near infrared light captured by an infrared array. Each pixel can read range, as with simple infrared range-finders. Interestingly, the research group develops a near-field touchless, free air touchpad-like device, where position of a finger in front of the sensor is tracked precisely and analysed.

An ultrasonic realization of a touchless pointing interface is proposed by Chiu et al. [14]. In this case an array of ultrasonic receivers creates an image-like output based on reflections received from a pointing object.

The related concept of interactive shop windows is introduced by Krumm [15]. Interactive or immersive advertising reacts to people passing by, trying to engage them by showing dynamic content accordingly.

Active arrangements, comprising an emitter and a receiver, usually have the advantage of providing absolute measurements of distance and position. However the presence of the emitter results in higher energy needs than for a passive measurement. For dynamic hand gestures such precision is not necessary and detection can be realised by passively sensing thermal infrared radiation change only.

We believe that our solution is very well suited to the task of near distance, dynamic hand gesture recognition application and provides an alternative to existing propositions, that is more cost and energy efficient due to reduction in number of components or their complexity.

III. PIR Array Based Hand Motion Recognition

The set of basic hand movements in front of a sensor is limited, e.g., horizontal, vertical and diagonal swipes across the field of view, circular motion and in and out movements. At this stage, only linear motion across the field of view is considered. Four directions of swipe were chosen as easy to describe and reproduce: up / down, left / right.

A. Design Principle - PIR Array

As identified in the introduction to this paper, a simple, low cost and low energy consumption device to extend the concept of a touchless interface is desirable in many environments.

A PIR Array is an interesting potential solution: the technology has been widely proven in settings such as burglar alarms and automatic light switches. However, only now has it become financially viable for ubiquitous application in the form of an array (previously mostly used a single or dual element occupancy sensor).

Passive detector does not require additional light sources for illumination of the scene, as the human body is naturally a good thermal infrared emitter [16]. Scenes at a temperature above 0 K may be dark in visible spectrum, while still full of thermal energy [17].

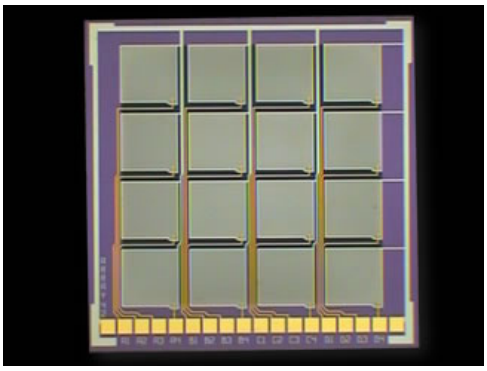

Figure 1. 4x4 PIR Sensor Array ([18], with permission).

A limitation common to all passive infrared detectors exists. The minimum detectable temperature difference creates a band of target temperature relative to the background temperature resulting in low signal to noise ratio. When the temperature of the detected object is higher than that of the background, the response of the infrared elements will be positive. While when temperature of the object is lower, the response is inverted. Increase in the temperature of the environment and hence that of the sensor can reduce responsivity of such passive device.

B. Research Questions

The primary aim of this study is to investigate whether it is feasible to use a passive infrared array for hand gesture recognition, and if so, under what conditions, and what range of gestures can be recognized. The secondary aim is to compare the cost effectiveness and power efficiency of the passive infrared system with existing solutions using active infrared or visible cameras.

IV. Implementation

We propose a system to realize the task of simple dynamic hand gesture recognition at short distances.

A. Prototype

The implementation described in this paper is a proof-of-concept prototype. Existing signal conditioning integrated circuit and PC interface board and software provided by the sensor manufacturer are used for signal capture. Signals are processed using the computer for ease of development. In future developments a migration to an embedded system is anticipated in order to provide a low footprint, low power solution.

B. Capture Device

A thin-film, passive infrared sensor, 4 pixel x 4 pixel array, pictured in Figure 1, is enclosed in a package with a broadband infrared filter.

 ISBN: 978-1-61208-145-8

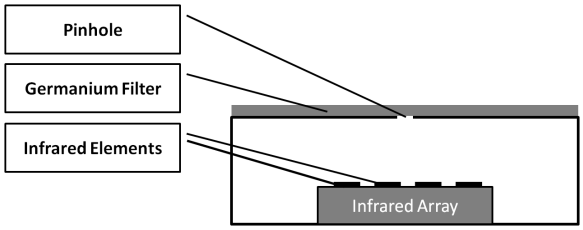

Figure 2. Optical Arrangement.

This thin-film sensor is manufactured using standard, high throughput wafer processing techniques. The sensor die is a customisable MEMS structure with pixels patterned on a silicon membrane. Such approach provides an integrated, robust array with consistent physical properties.

Thin-film infrared elements have low thermal mass compared with bulk PZT elements. The result is higher optimal frequency of operation, well suited for tasks such as gesture recognition, where detected object moves quickly across the field of view.

An infrared-blocking film is mounted on the underside of the filter, with a pinhole centred above the array, as seen in Figure 2. This optical arrangement produces a low resolution infrared image of the scene in front of the sensor within a field of view of 60° up to 20 cm away from the sensor.

Electrical signals from the infrared array are amplified, low pass filtered and digitised. The images are captured using a dedicated interface board. The digitized frames are sent to a computer and pre-processed to provide a stable and uniform output. This involves per-pixel low pass filtering and normalisation of signals across the array.

C. PIR Sensor Array

The PZT infrared array sensing elements transform thermal radiation into electrical charge based on the pyroelectric principle.

The transducer operates in the same manner as standard security PIR motion detectors, where the change in incident flux arises from the motion of a thermal infrared source across the field of view. This has an advantage in that the background subtraction is inherent in the transducer itself: stationary infrared emitters do not cause a change in incident flux, and therefore are not detected. However, it also becomes a limitation in that an object that moves into the field of view and then becomes stationary will soon become invisible. This is not a problem in a system designed to recognize simple 'swipe' type gestures where motion, and the direction of the motion, are the dynamic features that are to be recognized.

In a fully passive arrangement, where there is no additional modulated illumination nor is the incoming infrared radiation modulated, effectively only active motion can be reliably detected.

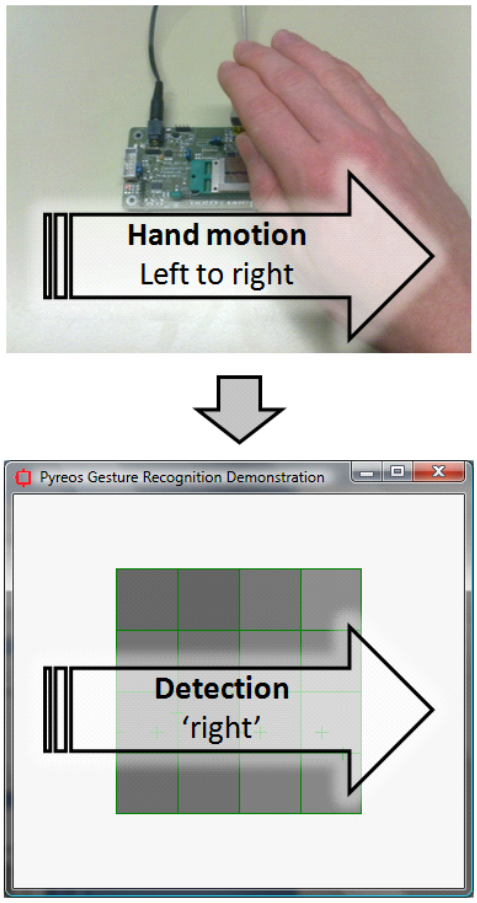

Figure 3. Hand motion and tracker response [21].

D. Signal Processing

A tracking algorithm is applied to the frame sequence. Blob detection technique is derived from the Automatic Centroid Extractor [19], also used for people counting application [20]. Adaptation of the algorithm involved increased processing rate and adjustment for larger object size.

Hotspots are localized and tracked in the image. Analysis of the trail of a detected and tracked object allows the determination of direction of motion. The length of the track is used to determine if it was a valid detection, while the x and y difference between starting and finishing point is evaluated to provide direction information.

V. Initial Evaluation

Functionality of the system was tested in four main directions of hand swipe across the sensor. Five participants were asked to perform a set of 100 hand movements each (25 per direction). Detection rate and accuracy of system response (correct direction detected) were recorded.

Figure 3 demonstrates the test arrangement and correct detection: a sample hand motion from left to right results in a correct 'right' detection.

 ISBN: 978-1-61208-145-8

Table I
INITIAL EVALUATION RESULTS

Direction	Detection Rate (%)	Accuracy (%)
Up	72.8	93.6
Down	86.4	93.6
Left	88.0	93.6
Right	78.4	89.6
Average	**81.4**	**92.6**

Detection in the distance range of up to 20 cm from the sensor was accurate 92.6% of time overall. 81.4% of gestures were detected at the first attempt. When considering only horizontal swipes (left to right and right to left), it can be seen that the detection rate (87.2%) and accuracy (93.6%) were higher than overall. This is attributed to the test arrangement, where it was more difficult to accurately present clean vertical swipes to the system then it was to produce horizontal ones.

VI. APPLICATION

As an example application of the system, the output of the prototype was used to emulate arrow key strokes on the host computer. This simple test demonstrates the suitability of the system for performing certain tasks on the computer. As an example, the gesture recognizer was used to change slides during a multimedia presentation.

VII. CONCLUSION AND FUTURE WORK

With our prototype system we have demonstrated that it is feasible to recognize hand motion direction with a pyroelectric passive thermal infrared array. Our approach shows that the functionality of a simple pyroelectric movement sensor can be expanded to detect differing hand gestures at short range. We show that blob detection from a hand waving over a 16 element passive infrared sensor array provides sufficient information to discriminate four directions of hand stroke.

Operation under different ambient conditions still needs to be determined: detection relies on there being a perceptible temperature difference between the hand and the background scene.

Future work on the software algorithms will focus on improving detection reliability, working towards an increase in angular resolution for more gestures to be recognised. Optimization towards embedded system application is required to achieve a low power system suitable for real application. With the development of a dedicated array for this type of recognition, further optimisation of the system is possible.

VIII. ACKNOWLEDGEMENT

This work is supported by the UK Engineering and Physical Sciences Research Council and Pyreos Ltd. under EPSRC CASE Award EP/I50137/1. The authors thank C. Giebeler at Pyreos Ltd. Scotland, UK for his direction and support.

REFERENCES

[1] WHO. (2009). *WHO guidelines on hand hygiene in health care* [Online]. Available: www.who.int/rpc/guidelines/9789241597906/en/ [May, 2011].

[2] J. P. Wachs, H. I. Stern, Y. Edan, M. Gillam, J. Handler, C. Feied, and M. Smith, "A gesture-based tool for sterile browsing of radiology images," *Journal of the American Medical Informatics Association*, vol. 15, no. 3, pp. 321–323.

[3] T. R. Winings and R. Samson, "Automated dispenser for disinfectant with proximity sensor," U.S. Patent 5 695 091, Dec 9, 1997.

[4] D. K. Lambert, "Capacitive proximity sensor," U.S. Patent 6,724,324, Apr 20, 2004.

[5] M. Ishikawa and H. Matsumura, "Recognition of a hand-gesture based on self-organization using a DataGlove," in *Neural Information Processing, 1999. Proceedings. ICONIP '99. 6th International Conference on*, vol. 2, 1999, pp. 739–745 vol.2.

[6] C. Hsieh, D. Liou, and D. Lee, "A real time hand gesture recognition system using motion history image," in *Signal Processing Systems (ICSPS), 2010 2nd International Conference on*, vol. 2, 2010, pp. V2–394–V2–398.

[7] L. Yun and Z. Peng, "An automatic hand gesture recognition system based on Viola-Jones method and SVMs," in *Computer Science and Engineering, 2009. WCSE '09. Second International Workshop on*, vol. 2, 2009, pp. 72–76.

[8] GestureTek Technologies. "Company Website." Internet: www.gesturetek.com [May, 2011].

[9] EyeSight Mobile Technologies. "Company Website." Internet: www.eyesight-tech.com [May, 2011].

[10] Edge 3 Technologies. "Company website." Internet: www.edge3technologies.com [May, 2011].

[11] B. Min, H. Yoon, J. Soh, Y. Yang, and T. Ejima, "Hand gesture recognition using hidden markov models," in *Systems, Man, and Cybernetics*, 1997, vol. 5, 1997, pp. 4232–4235.

[12] Mechaless Systems GmbH. "Company Website." Internet: www.mechaless.com [May, 2011].

[13] D. Ryu, D. Um, P. Tanofsky, D. H. Koh, Y. S. Ryu, and S. Kang, "T-less : A novel touchless human-machine interface based on infrared proximity sensing," in *Intelligent Robots and Systems (IROS), 2010 IEEE/RSJ International Conference on*, 2010, pp. 5220–5225.

[14] T. Chiu, H. Deng, S. Chang, and S. Luo, "Implementation of ultrasonic touchless interactive panel using the polymer-based CMUT array," in *Sensors, 2009 IEEE*, 2009, pp. 625–630.

[15] J. Krumm, "Ubiquitous advertising: The killer application for the 21st century," *Pervasive Computing, IEEE*, vol. 10, no. 1, pp. 66–73, 2011.

[16] C. M. Payne, *Principles of naval weapon systems*. Naval Inst Pr, 2006.

[17] R. Siegel and J. R. Howell, *Thermal radiation heat transfer*. Taylor & Francis Group, 2002.

[18] Pyreos Ltd. "Company Website." Internet: www.pyreos.com [May, 2011].

[19] T. S. Axelrod and T. F. Tassinari, "A VLSI centroid extractor for real-time target tracking applications," Lawrence Livermore National Lab., CA (USA), Tech. Rep., 1989.

[20] T. Chamberlain. (2008). *People counting demonstration using a pyreos IR detector array* [Online]. Available: www.pyreos.com [May, 2011].

[21] Pyreos Ltd. (2011). *Pyreos: Gesture control - low power, smal size* [Online]. Available: www.youtube.com/watch?v=0YpI3J2lThA [May, 2011].

 ISBN: 978-1-61208-145-8

Group IV Photonic Slot Structures for Highly Efficient Gas Sensing in mid-IR

Vittorio M. N. Passaro, Benedetto Troia
Photonics Research Group, DEE
Politecnico di Bari
Via E. Orabona n. 4, 70125 Bari, Italy
e-mail: passaro@deemail.poliba.it
e-mail: ing.b.troja@gmail.com

Francesco De Leonardis
Photonics Research Group, DIASS
Politecnico di Bari
Viale del Turismo n. 8, 74100 Taranto, Italy
e-mail: f.deleonardis@poliba.it

***Abstract*—In this paper, novel high-performance group IV photonic structures for very efficient gas sensing are presented. Various combinations of group IV materials and alloys based on silicon (Si), germanium (Ge), tin (Sn) and carbon (C), have been studied in CMOS-compatible technology for design of optical slot waveguides for homogeneous optical sensors in mid-IR (3.39 µm). An analysis of fabrication tolerances is presented and a comparison among different photonic sensing structures is also given. Theoretical investigation demonstrates very efficient optical field concentrations in the sensing area, as well as ultra high sensitivity of gas sensing for environmental applications.**

Keywords- Silicon-on-Insulator; Photonic Sensors; Gas Sensing; Slot Waveguides; Group IV materials.

I. INTRODUCTION

Nowadays, increasing interest is devoted to photonic label-free integrated sensors and biosensors, which represent the state of the art in a number of application fields, including environmental monitoring, biomedical, healthcare, pharmaceuticals, homeland security, to name a few. Gas sensing is a crucial application field for environment monitoring and health. Usually, spectroscopic-based sensing techniques are used, but with high costs. Both miniaturization, integration and low cost should be possible by photonic structures. However, the integration of photonic devices for gas sensing in sophisticated architectures like Mach-Zehnder interferometers, photonic crystals [1] and ring resonators [2] is not yet developed as for chemical and biochemical sensors [3] [4].

Slot waveguides implemented in Si/SiO_2 material system (Silicon-on-Insulator, SOI) constitute an intriguing photonic sensing approach, which potentially enables high sensitivity (S) and ultra-low limit of detection (LOD) [5]. Optimized SOI slot waveguides designed at λ = 1.55 µm, have been presented in literature [6], demonstrating a homogeneous sensitivity S_h > 1. In order to detect the exact gas concentration, different research groups have proposed some test methods, including spectroscopic absorption, photo-acoustics and electrochemistry. Despite this potential, early mid-IR sensing applications were limited to specific applications due to the involved instrumentation sizes and limited availability of appropriately compact mid-IR optical components, such as light sources, detectors, waveguides and spectrometers. On the other hand, reasons that encourage research efforts in mid-IR gas sensing are mainly related to increasing attention to harmful gases like carbon dioxide (CO_2), carbon monoxide (CO), methane (CH_4) and sulfure dioxide (SO_2), to name a few, all having refractive indices around 1. Moreover, these gases are characterized by absorption spectra in mid-IR, specifically in the range 2-8 µm. Thus, ingenious design techniques are needed to extend group IV photonics from near-IR to mid-IR wavelength range, exploiting the advantages of photonic architectures in terms of high compactness, high sensitivity and low LOD. In this context, this paper presents some significant results for design of efficient group IV photonic sensors working in mid-IR. In particular, several alloys characterized by precise compositional space configurations have been considered in order to ensure optical transparency and prevent photon absorption at λ = 3.39 µm. In addition, optical properties of alloys as SiGeSn, SiGe, SiGeC, GeC and GeSn, have been evaluated by using Sellmeier dispersion equations, in order to predict their refractive indices (RIs) as a function of optical wavelength. In this paper, novel vertical slot waveguides are investigated at 3.39 µm, by using full-vectorial 2D Finite Element Method (FEM) approach [7]. In FEM mesh generation for effective index and modal profile calculation, triangular vector-elements have been adopted with about 35,000 elements and a domain region area of 9 μm^2, using Dirichlet boundary condition. Changing from a perfect electric to a perfect magnetic conductor, influence on simulation results appears to be negligible. In all simulations, the buried oxide layer is assumed 1 µm thick. The influence of slot waveguide geometrical parameters (gap region g, slot height and width of lateral wires w) is analyzed in order to optimize both field confinement in the slot region and homogeneous sensitivity. A detailed optimization to achieve the best alloys of group IV materials enabling ultra-high gas sensing is given. Finally, an analysis of fabrication tolerances is presented.

II. HOMOGENEOUS AND SURFACE SENSING IN OPTICAL SLOT WAVEGUIDES

Slot waveguides represent a very interesting and promising architecture for photonic sensing. In fact, using

 ISBN: 978-1-61208-145-8

such structures it is possible to confine an extremely high optical field in a low RI region called "slot region". In Figure 1, schematic cross-sectional view of a typical slot waveguide is shown. The structure consists of a thin low-index (n_L) slot embedded between two high-index (n_H) regions (Si-wires), separated to each other by a slot region gap g. Due to the large index contrast at the interfaces, the normal electric field undergoes a large discontinuity, which results in a field enhancement in the low-index region [8]:

$$|E_L| = \left(\frac{n_H}{n_L}\right)^2 |E_H| \qquad (1)$$

In Eq. (1) E_L is the E-field in the slot region, while E_H is the E-field in high index regions (Si-wires). Thus, the larger the refractive index contrast ($\Delta n = n_H - n_L$) between slot region and Si-wires, the higher the field confinement in slot region. For instance, an optimized SOI waveguide has been designed at 1.55 µm with $n_{Si} = 3.45$, $n_{SiO2} = 1.45$, and $\Delta n = 2$ [4].

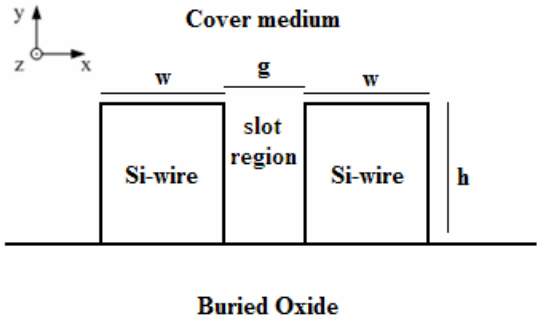

Figure 1. Cross-section of a typical SOI single-slot waveguide.

In vertical slot waveguides, the main E-Field component undergoing discontinuities is that along x-direction, the only one subjected to a refractive index change in the slot region. For this reason, the only fundamental eigenmode considered in this paper is quasi-TE, as shown in Figure 2 for air cover.

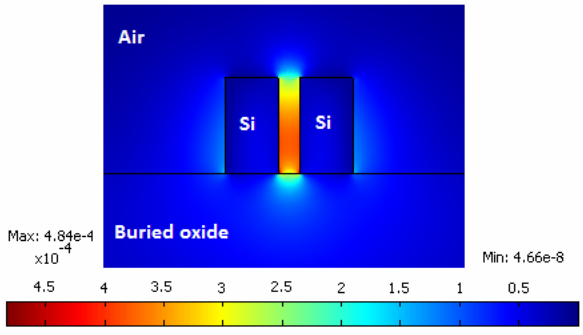

Figure 2. E_x-Field intensity of quasi-TE mode distribution (w = 180 nm, h = 324 nm, g = 70 nm, λ = 1.55 µm, air cover).

Thus, in the design of novel photonic slot waveguides working in mid-IR, high index contrast is needed in order to ensure high E_x-Field confinement. This constitutes a fundamental requirement for both homogeneous and surface sensing. In fact, in both approaches the concentration change of an analyte (gas) to be sensed affects the propagating mode effective index to be monitored in different ways, i.e., reflection, transmission, absorption and so on, according with sensor architecture. In general, this effective index change can be produced either by a change of cover medium refractive index (*homogeneous sensing*) or by a change of thickness of an ultra-thin layer of receptor molecules, immobilized on the waveguide surface (*surface sensing*), as sketched in Figure 3. The ultra-thin adlayer directly influences the mode effective index. As a consequence, it is possible to define two different waveguide sensitivities, one for homogeneous sensing (S_h) and the other for surface sensing (S_s), as follows:

$$S_h = \frac{\partial n_{eff}}{\partial n_c} \qquad S_s = \frac{\partial n_{eff}}{\partial \rho} \qquad (2)$$

where n_{eff} is the propagating mode effective index, n_c is the cover medium RI, and ρ is the molecular adlayer thickness.

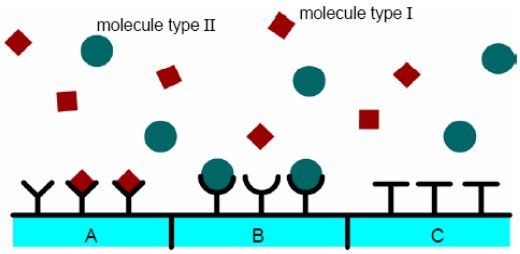

Figure 3. Selective surface sensing of two different types of molecules.

Now, our approach to photonic gas sensing can be classified as homogeneous sensing. In fact, when a particular gas (e.g., CO_2, CO, CO_4, SO_2) covers the device, the cover medium RI will change with respect to air RI as evaluated at the same wavelength. By this way, the index contrast $\Delta n = n_H - n_L$ at the interface between wires and cover medium (gas) will change and, consequently, the optical field distribution in the slot region will be modified according to Eq. 1. Then, its sensitivity S_h can be evaluated as follows [6]:

$$S_h = \left.\frac{\partial n_{eff}}{\partial n_c}\right|_{n_c = n_c^0} = \frac{2 \cdot n_c^0}{\eta_0 \cdot P} \iint_C \left|\vec{E}(x,y)\right|^2 dxdy = \frac{2 \cdot n_c^0 \cdot \Gamma_c}{\eta_0 \cdot P} \iint_\infty \left|\vec{E}(x,y)\right|^2 dxdy \qquad (3)$$

$$P = \iint_\infty \left[\left(\vec{E} \times \vec{H}^* + \vec{E}^* \times \vec{H}\right) \cdot \hat{z}\right] dxdy$$

where n_c^0 is the unperturbed value of n_c, η_0 is the free space impedance (377 Ω), z the unit vector of the propagation direction, and $\vec{E}, \vec{H}$ the electric and magnetic field vectors, respectively. Moreover, optical power confinement factors are defined as the fractions of power confined and guided in the regions of interest, i.e., cover medium including slot (Γ_C) or only slot region (Γ_S), as follows:

 ISBN: 978-1-61208-145-8

$$\Gamma_C = \frac{\iint_C |E(x,y)|^2 \, dxdy}{\iint_\infty |E(x,y)|^2 \, dxdy} \quad (4)$$

$$\Gamma_S = \frac{\iint_S |E(x,y)|^2 \, dxdy}{\iint_\infty |E(x,y)|^2 \, dxdy} \quad (5)$$

where the integrals are calculated in the regions of interest, cover *C* and slot *S*, respectively.

Slot wires are characterized by different combinations of group IV material systems, which have been chosen on the basis of their electronic and optical properties, as well as their technological compatibility.

III. OPTIMIZED GROUP IV OPTICAL SLOT WAVEGUIDES

The first step needed for optimization of these novel group IV photonic sensors is the definition of their alloys and material systems for slot wires. In Table I all group IV materials and alloys employed in this paper are summarized with their refractive indices calculated at 3.39 μm.

TABLE I. GROUP IV ALLOYS AND MATERIALS AND RELEVANT RI

Group IV materials and alloys	RI @ 3.39 μm
Si	3.429
Ge	4.035
SiO_2	1.488
$Si_{0.15}Ge_{0.85}$	3.9441
$Si_{0.08}Ge_{0.91}C_{0.01}$	3.97
$Ge_{0.97}C_{0.03}$	3.9854
$Ge_{0.91}Sn_{0.09}$	4.2340
$Ge_{0.78}Si_{0.08}Sn_{0.14}$	4.2960

At mid-IR wavelengths, it is very important to analyze and ensure very low propagation losses. In fact, the longer the wavelength, the greater the spatial distribution of the E-Field in the guided region and, possibly, the relevant losses. However, it is clear that a percentage of the total confined optical field will interact and be distributed into the buried oxide layer. A lot of investigations have been carried out in order to predict propagation losses of different well known technologies, e.g., SOI, silicon-on-sapphire (SOS) [9]. In particular, using linear interpolation and assuming that a significant fraction (30%) of the guided-mode power is found in the buried insulator layer, the estimated wavelength region with propagation losses less than 2 dB/cm ranges from 1.2 μm to 3.6 μm for SOI (apart from a 2.6÷2.8 μm spike), and from 1.2 μm to 4.3 μm for SOS. Obviously, in order to prevent high propagation losses, it is needed to confine a high percentage of E_x-Field in the slot region instead of dispersing it in the buried oxide.

Additional criteria have been followed for choice of material systems used in this work. In fact, Ge-on-Si exhibits infrared wavelength ranges of operation (1.9 ÷ 16.8 μm and 140 ÷ 200 μm) at 300 K, where the fundamental mode propagation loss is less than 2 dB/cm. The other material system SiGe-on-Si exhibits operative wavelength ranges 1.6 ÷ 12 μm and 100 ÷ 200 μm. Finally, the material system GeSn-on-Si has propagation losses lower than 2 dB/cm in the range 2.2 ÷ 19 μm. Therefore, the principal operative limitation is represented by SiO_2 buried cladding layer, since this layer presents significant propagation losses in a shorter wavelength range.

The optimization procedure proposed in this paper consists in a numerical iterative method allowing to achieve the optimal geometrical configuration giving maximum sensitivity and low losses. This procedure has been applied to each proposed photonic structure, characterized by a different group IV material combination. In Figure 4 cross sectional views of all investigated photonic slot waveguides are sketched. The photonic structures proposed in this paper include Ge-on-Si material system (Figure 4a), SiGe alloy directly grown on SiO_2 (Figure 4b), binary alloy SiGe grown on Si (Figure 4c), SiGeC ternary alloy directly grown on SiO_2 (Figure 4d) and SiGeC-on-Si material system (Figure 4e). Moreover, the last two structures are characterized by slot wires with three different layers, based on SiGeSn-on-GeSn-on-Si (Figure 4f) and SiGeSn-on-GeC-on-Si material system (Figure 4g), respectively.

In Table II all waveguide configurations are named with a letter from (a) to (g) as in Figure 4, in order to simplify the notation. In particular, all alloys and material systems in Figure 4 and Table II are characterized by different percentages of single group IV materials, according with data in Table I. Moreover, optimized parameters are given in Table II, with the only exception of the slot region width *g,* which is considered as a variable for parametric sweep analysis, since it critically influences sensing performance such as sensitivity and confinement factors.

TABLE II. OPTIMIZED GEOMETRICAL STRUCTURES AT λ = 3.39 μm.

	Geometrical parameters [nm]			
Structure	*w*	*h*	*t*	*s*
Type (a)	410	660	40	0
Type (b)	400	690	0	0
Type (c)	400	680	50	0
Type (d)	400	710	0	0
Type (e)	400	690	30	0
Type (f)	380	520	20	50
Type (g)	390	560	20	50

IV. SENSING PERFORMANCE

As stated before, performance parameters, in particular sensitivity S_h and confinement factors Γ_C and Γ_S, have been investigated as a function of the slot region width *g* in each optimized slot waveguide reported in Table II.

In Figure 5 it is possible to note the high value of sensitivity evaluated, being $S_h > 1$ in every structure with $g < 110$ nm. A value $S_h > 1$ clearly implies that an effective index change $\Delta n_{eff} > \Delta n_C$ is induced by a cover index shift Δn_C. The waveguides previously indicated with letters (f) and (b) are the best suitable, because their sensitivities are very high still remain stable over a large range, $g < 140$ nm.

 ISBN: 978-1-61208-145-8

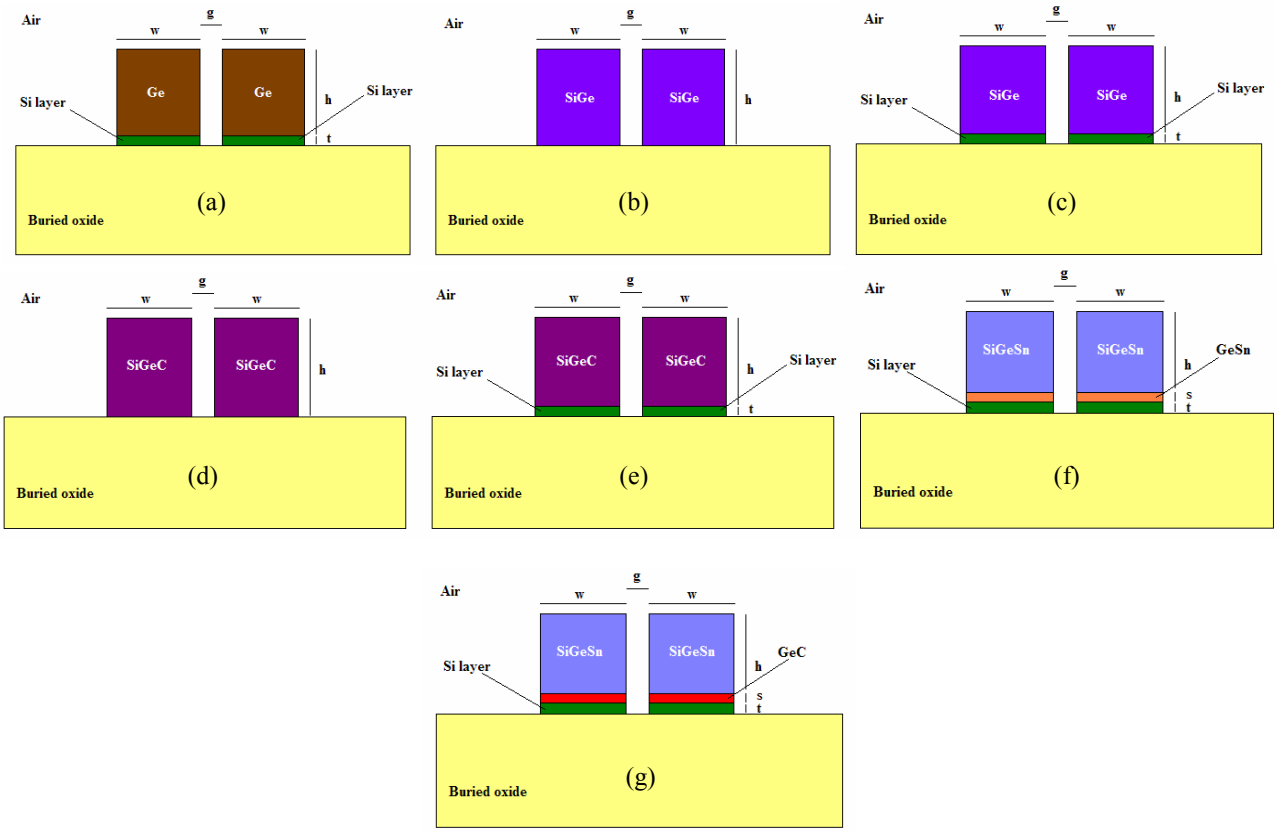

Figure 4. Novel slot optical waveguides based on group IV alloys and material systems, designed at λ = 3.39 µm.

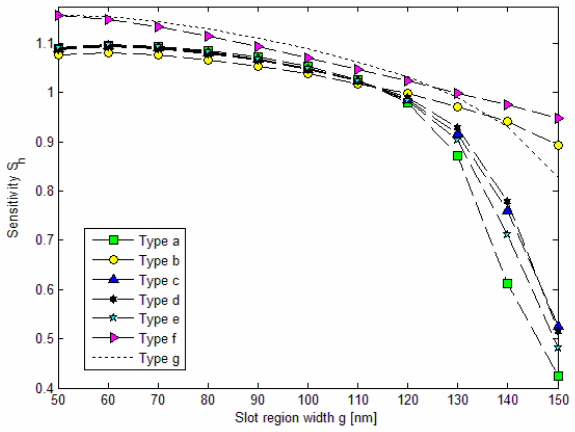

Figure 5. Sensitivity of optimized waveguides designed at 3.39 µm (quasi-TE slot mode).

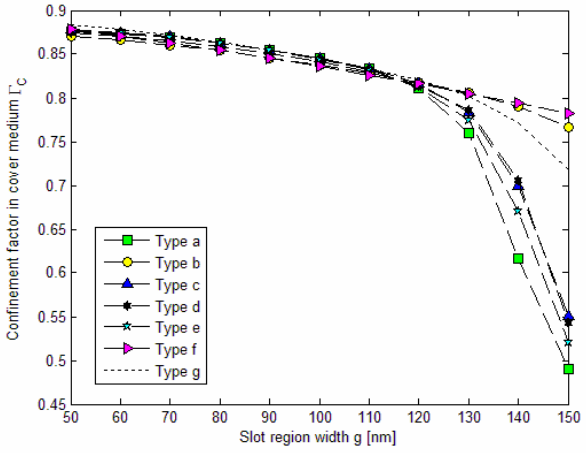

Figure 6. Confinement factor in the cover medium of optimized slot waveguides.

This means to have more relaxed sizes, without any critical technological limitation as lithographic resolution. The parametric analysis has allowed the waveguide geometrical sizes to be optimized by setting a precise value of g, simultaneously achieving very high sensitivity, large confinement factors as well as low losses. Generally, the trend of the sensitivity function can be well supported by the analysis of relevant confinement factors, as shown in Figures 6 and 7.

In fact, the waveguides exhibiting the highest Γ_C and Γ_S are still those previously indicated as (f) and (b). In both photonic devices, the percentage of the optical field in the slot region is higher than 60% for g < 140 nm. All other optimized photonic devices are characterized by a strong dependence on the slot region width. In fact for g > 140 nm, all sensitivities rapidly drop to 0.5 and 0.4. Analogous considerations can be derived for confinement factors.

 ISBN: 978-1-61208-145-8

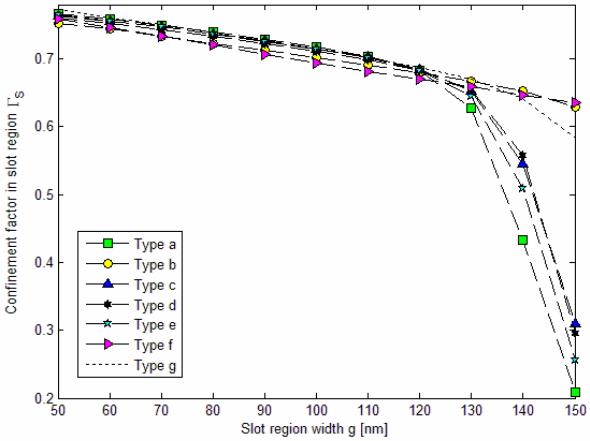

Figure 7. Confinement factor in the slot region of optimized waveguides.

V. FABRICATION TOLERANCES

All above investigated photonic structures represent an ideal case of realistic optical slot devices. In fact, vertical sidewalls characterizing slot waveguide wires are very difficult to be obtained by state of the art etching processes, for example inductively coupled plasma (ICP) etching. Thus, deviations from ideal case have to be considered and the most important parameter quantifying this effect is the tilting angle θ, as sketched in Figure 8. Thus, it is possible to distinguish between ideal and real structures, having vertical (θ = 0°) or non vertical sidewalls ($\theta \neq$ 0°), respectively.

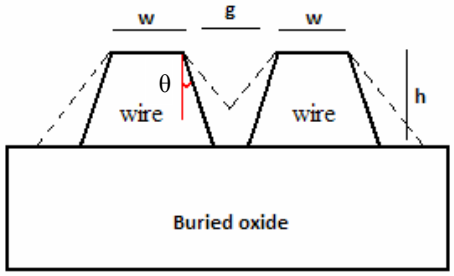

Figure 8. Schematic view of real slot waveguide.

Therefore, an analysis of real photonic structures, corrupted by fabrication characteristics, has been carried out, again in terms of homogeneous sensitivity, by choosing a specific value for the slot region width, g = 100 nm. Figure 9 shows the influence of etching tilting angle on sensitivity. All values at θ = 0° are referred to optimized ideal waveguides, whose geometrical parameters are summarized in Table II, and are also shown in Figure 5 for g = 100 nm.

Therefore, it is possible to define a critical range for the tilting angle θ, extended from 4° to 6°. In particular, a large negative slope of all sensitivity functions can be recognized in Figure 9 for these values.

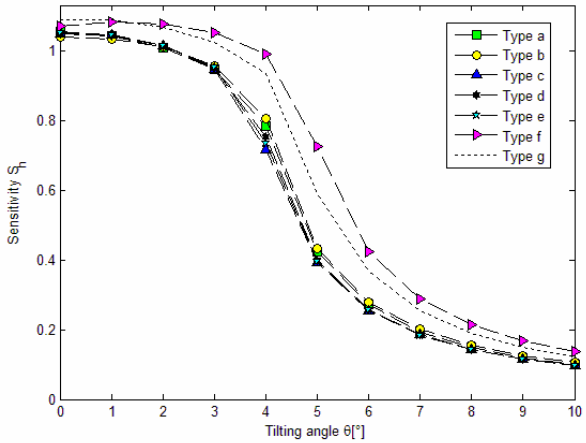

Figure 9. Sensitivity of optimized slot waveguides as a function of the tilting angle for g = 100 nm (λ = 3.39 μm).

In fact, sensitivities rapidly drop to very low values, e.g., S_h = 0.2. It is clear how this performance cannot be suitable for gas sensing because only 20 % of cover refractive index change should be detected in this case. Obviously, the smaller the parameter g, the poorer the fabrication tolerances. In addition, the thicker the slot wires, the stronger the effect of the sidewalls inclination.

The theoretical investigation on fabrication tolerances has been also carried out for calculation of confinement factors in the same way, where Γ_C and Γ_S are characterized by similar trends as a function of tilting angle θ. In conclusion, it is not possible to fabricate real photonic sensors with g = 50 nm, i.e., the lowest slot gap width allowing highest sensitivity (see Figure 5), while etching tilting angle must be limited within 4° or 5°, to avoid any corruption of sensor performance. Thus, the solution to this technological problem is strictly related with optimization of etching process for a given combination of material systems. However, standard etching processes can assure tilting angles within 1°-2°, not critical for our structures.

Moreover, these novel photonic structures are also characterized by another very important feature, i.e., the presence of a second order quasi-TE slot mode. In Figure 10 the sensitivity evaluated for the second order slot mode in all optimized structures presented in Table II, is shown as a function of g. All curves, obtained by FEM, exhibit a peak value (around 1) of sensitivity, commonly placed at g = 160 nm. For g > 160 nm, all sensitivities drop to 0.6. For values of g < 160 nm, a steep negative peak characterizes all trends, S_h quickly dropping to about 0.55. In conclusion, the presence of the second order slot-mode in optimized waveguides represents an additional technological degree of freedom in the design of these novel photonic sensors working in mid-IR. Thus, the solution to fabrication tolerance problems can be found by selecting the parameter g greater than the optimal one, in order to prevent a reduction of the slot region width due to non vertical sidewalls generated by etching process.

 ISBN: 978-1-61208-145-8

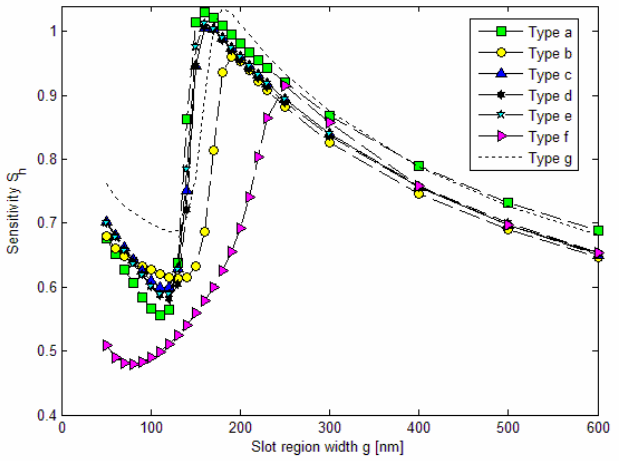

Figure 10. Sensitivity of optimized SOI slot waveguides as a function of g (second order slot-mode, λ = 3.39 μm).

In addition, confinement factors are both characterized by analytical trends similar to those of sensitivity functions. In conclusion, the choice of g = 100 nm appears to be the best suitable for both first order and second order slot-mode, simultaneously improving the fabrication tolerances. Then, relaxed dimensions of optimized waveguides will allow the fabrication of high performance multi-mode photonic devices for gas sensing applications.

In summary, novel photonic sensors proposed in this paper exhibit intriguing performances (S_h > 1). In particular, their integration in sophisticated photonic architectures, such as ring resonators, is expected to show very interesting performance in terms of wavelength shift per refractive index unit (RIU). This possibility has been also simulated and some values of wavelength sensitivity (WS) $\Delta\lambda/n_c$ are summarized in Table III for optimized structures with g = 100 nm.

TABLE III. OPTIMAL STRUCTURE WAVELENGTH SENSITIVITY IN RING RESONATOR ARCHITECTURES (g = 100 nm).

Optimal structures	WS [nm/RIU]	LOD [RIU]
Photonic crystal [1]	80	1×10^{-4}
Ring resonator [2]	140	8×10^{-5}
SOI at 1.55 μm [6]	~ 1000	8×10^{-5}
Type (a)	2050	3.90×10^{-5}
Type (b)	2126	3.76×10^{-5}
Type (c)	2126	3.76×10^{-5}
Type (d)	2111	3.79×10^{-5}
Type (e)	2115	3.78×10^{-5}
Type (f)	2194	3.64×10^{-5}
Type (g)	2128	3.76×10^{-5}

A comparison with some results in literature, both experimental and theoretical, can be observed. Thus, huge wavelength shifts as large as 2200 nm/RIU, which cannot be achieved by other photonic architectures, could be exploited in ring resonators based on these optimized photonic slot structures, realized with an appropriate combination of group IV materials and alloys. Since a wavelength resolution as low as 80 pm is practical in ordinary optical spectrum analyzers, a limit of detection as low as 3.6×10^{-5} RIU could be obtained in these powerful photonic structures, able to detect very small volumes of gas traces in mid-IR, of the order of 1 μm^3.

VI. CONCLUSION AND FUTURE WORK

In this paper, intriguing novel photonic sensors have been investigated in detail by a FEM approach. In particular, unconventional group IV alloys and material systems have been adopted for design of ultra-high performance photonic gas sensors working in mid-IR. Appropriate combinations of group IV compounds have been chosen on the basis of their technological compatibility and low losses in mid-IR wavelength range. Optimized photonic slot structures are characterized by relaxed dimensions allowing large margins of fabrication tolerances. In addition, the presence of a second order slot-mode has been also demonstrated, giving further flexibility in design. In conclusion, optimized slot waveguides for efficient sensing in mid-IR exhibit much higher performance with respect to SOI slot devices designed at near-IR (1.55 μm), with an improvement of more than 110%. Further work on this topic will be devoted to detailed model and design of slot-based ring resonators constituted by several combinations of group IV materials and alloys, with the aim to further improve the performance of photonic sensors in mid-IR and their use in several application fields.

REFERENCES

[1] T. Sunner, T. Stichel S.-H. Kwon, T. W. Schlereth, S. Holfing, M. Kamp, A. Forchel "Photonic crystal cavity based gas sensor," Appl. Phys. Lett., Vol. 92, n. 26, 2008, art. 261112.

[2] V. M. N. Passaro, F. Dell'Olio, and F. De Leonardis, "Ammonia Optical Sensing by Microring Resonators," Sensors, Vol. 7, n. 11, 2007, pp. 2741-2749.

[3] X. Fan, I. M. White, S. I. Shopova, H. Zhu, J. D. Suter, Y. Sun, "Sensitive optical biosensors for unlabeled targets: A review," Analytica Chimica Acta, Vol. 620, 2008, pp. 8-26.

[4] V. M. N. Passaro, F. Dell'Olio, C. Ciminelli, and M. N. Armenise, "Efficient Chemical Sensing by Coupled Slot SOI Waveguides," Sensors, Vol. 9, n. 2, 2009, pp. 1012-1032.

[5] P. Bienstman, K. De Vos, T. Claes, P. Debackere, R. Baets, J. Girones, E. Schacht, "Biosensors in Silicon on Insulator," Proc. SPIE on Silicon Photonics IV, Vol. 7220, 2009, art. 72200N.

[6] F. Dell'Olio, and V. M. N. Passaro, "Optical sensing by optimized silicon slot waveguides," Opt. Express, Vol. 15, n. 8, 2007, pp. 4977-4993.

[7] Comsol Multiphysics by COMSOL, Stockholm, ver. 3.2, single license, 2005.

[8] M. Iqbal, Z. Zheng, and J. S. Liu, "Light confinement in multiple slot structures investigated," Proc. IEEE Int. Conf. on Microwave and Millimiter Wave Technol. (ICMMT), 2008, pp. 878-891.

[9] R. Soref, S. J Emelett, and W. R Buchwald, "Silicon waveguided components for the long-wave infrared region," J. Opt. A: Pure Appl. Opt., Vol. 8, 2006, pp. 840-848.

 ISBN: 978-1-61208-145-8

Statistical Analysis of Dark Current in Silicon Photomultipliers

Giuseppina Valvo, Alfio Russo, Delfo Sanfilippo,
Giovanni Condorelli, Clarice Di Martino,
Beatrice Carbone, PierGiorgio Fallica
IMS-R&D STMicroelectronics, stradale Primosole, 50
95121 Catania, ITALY
giusy.valvo@st.com

Roberto Pagano, Sebania Libertino,
Salvatore Lombardo
CNR-IMM, Ottava Strada Zona Industriale, 5, 95121
Catania, ITALY
salvatore.lombardo@imm.cnr.it

***Abstract*—The aim of this paper is to investigate on a statistical basis at the wafer level the relationship existing among the dark currents of the single pixel compared to the whole Silicon Photomultiplier array. This is the first time to our knowledge that such a comparison is made, crucial to pass this new technology to the semiconductor manufacturing standards. In particular, emission microscopy measurements and current measurements allowed us to conclude that optical trenches strongly improve the device performances.**

Keywords - silicon photomultipliers; dark current; wafer level.

I. INTRODUCTION

Silicon-based single photon detectors [1-11] have been widely investigated since their appearance thanks to their interesting features: reduced dimensions, low weight, low fabrication costs, insensitivity to magnetic fields, and low operation voltage. Starting from single diode devices, progress in the field has driven the microelectronic industry to go towards designing and fabricating arrays of such devices, that is, avalanche detectors with an integrated quenching resistor connected in parallel and operating in Geiger mode, referred to as Si Photomultipliers (SiPMs), to cover areas up to ≈10 mm^2 per device. The principle of operation of each single avalanche detector consists in a p-n junction biased above the breakdown voltage (BV). Thanks to the high quality substrate and fabrication technology (low defect concentration), it can remain quiescent above the BV until a photon is absorbed in the depletion volume. Once the photon is absorbed, the electron-hole (e-h) pair generated triggers a self-sustaining avalanche breakdown. The avalanche is switched off through an opportunely designed quenching resistance that reduces the voltage below breakdown as soon as the current flows through the diode. The operation of the whole SiPM array is the parallel sum of the currents produced by each single pixel.

Aim of this paper is to investigate on a statistical basis at the wafer level the relationship existing among the dark currents of the single pixel compared to the whole SiPM array. This is the first time to our knowledge that such a comparison is made, crucial to pass this new technology to the semiconductor manufacturing standards.

II. EXPERIMENTAL

Single cells and arrays of 64x64 cells were fabricated in B doped Si wafers An enrichment region was obtained through B implantation, to define both the device active area and the BV. The cathode was fabricated through diffusion from a heavily doped polysilicon layer [12]. The quenching resistor was integrated on the cathode of the cell itself and fabricated using low-doped polysilicon. Finally, optical trenches surround the pixel active area in order to reduce electro-optical coupling effects (crosstalk) between adjacent microcells. A schematic cross-section of the final structure of the single cell is shown in Figure 1.

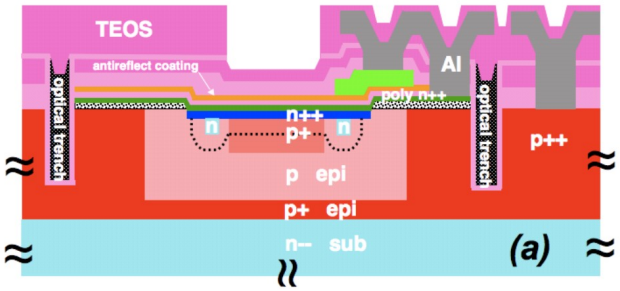

Figure 1. Schematic cross section of the SiPM single pixel, showing the central active area with the cathode (indicated as "n++"), the enriched anode ("p+"), the sub-anode ("p epi"), the anode contact region ("p+ epi"), the substrate ("n-- sub"), and the optical trenches.

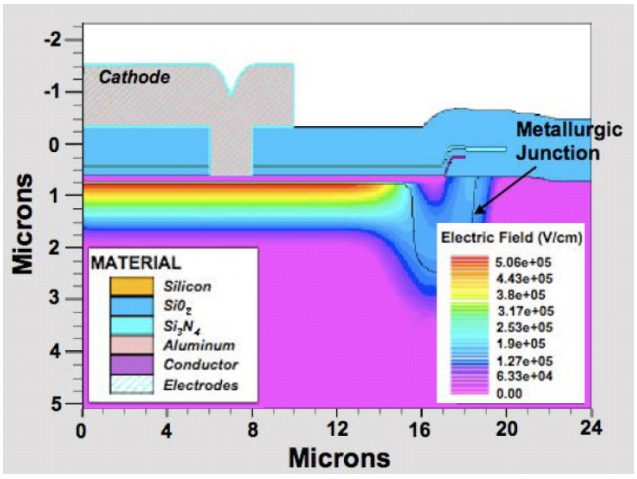

Figure 2. 2D TCAD simulation of the electric profile performed at a bias polarization of -30 V in the structure sketched in Fig. 1.

 ISBN: 978-1-61208-145-8

Figure 2 shows the 2D simulation of the electric profile performed at a bias polarization of -30 V. The electric field at the lateral border is well below its maximum value for junction breakdown and is negligible with respect to the maximum value in the active region, in which, on the contrary, the field is above the critical field for avalanche breakdown.

Devices basic electrical characterization provided a breakdown voltage in agreement with that predicted by TCAD simulation, and equal to about -28.0V at room temperature.

Emission microscopy (Em.Mi) measurements were carried out at 25°C using an overvoltage (*i.e.*, voltages above the junction breakdown voltage, ΔV) of 3V.

III. RESULTS AND DISCUSSION

One of the major issues to solve is the minimization of the cross-talk effect among close pixels. An improper isolation scheme results in an avalanche correlation effect which trigger avalanches in close pixels (Fig. 3(a)). The avalanches in close pixels are likely triggered either by photons or by minority carriers produced by the avalanche of a primary pixel which migrates to close pixels causing new avalanches. The use of a proper electro / optical isolation trench scheme dramatically improves the situation (Fig. 3(b)), rendering negligible the cross-talk effect among neighbor pixels, and strongly reducing the dark current (from 300 to 10 μA).

The relationship among the dark currents in single pixels and in complete SiPM arrays is investigated in Fig. 4. We model the dark current of a single pixel as [13]:

$$I_D = q\left(\frac{N_{Def}}{\tau} + \frac{A_{Pixel}}{\tau_i}\right)G \qquad (1)$$

where q is the elementary charge, N_{Def} the number of carrier generating defects per pixel in the active volume, τ the average time for carrier generation event by one defect, A_{Pixel} the single pixel active area, τ_i the average time per unit area for the intrinsic carrier generation due to diffusion from the quasi neutral regions to the active volume, and G the gain, *i.e.*, the total number of carriers generated in a single avalanche, from the avalanche buildup to the avalance quenching and pixel recharge. We find that the I_D of the overall SiPM devices is simply the sum of the currents of single pixels as above modeled, with no contribution of extrinsic defects providing high leakage paths. In particular Fig. 4 shows frequency histograms comparing the dark currents measured at room temperature of single pixels and SiPM arrays for a total of 952 devices at overvoltages (*i.e.,* voltages above the junction breakdown voltage) of 2, 3, and 4 V. The SiPM device contains 4096 pixel, so the respective currents of SiPM to single pixel should stay in ratio of about 4,000, as actually found.

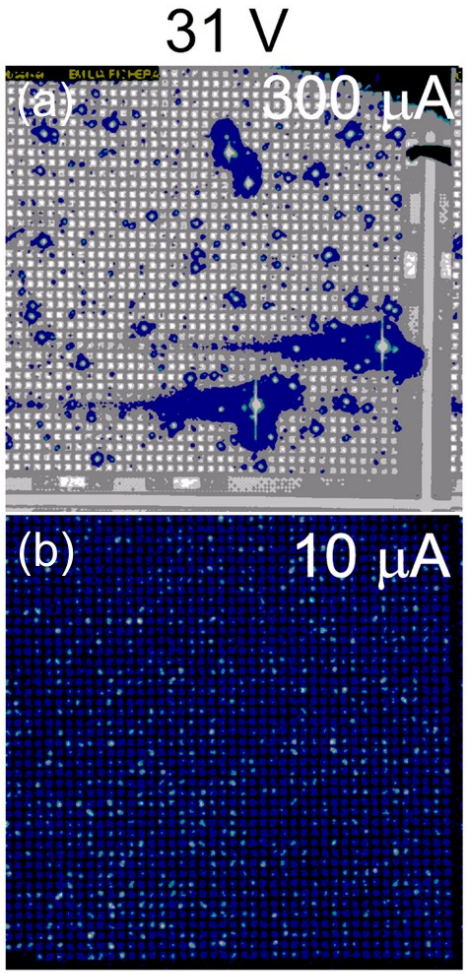

Figure 3. Emission Microscopy measurements on SiPM arrays (a) without and (b) with optical trenches.

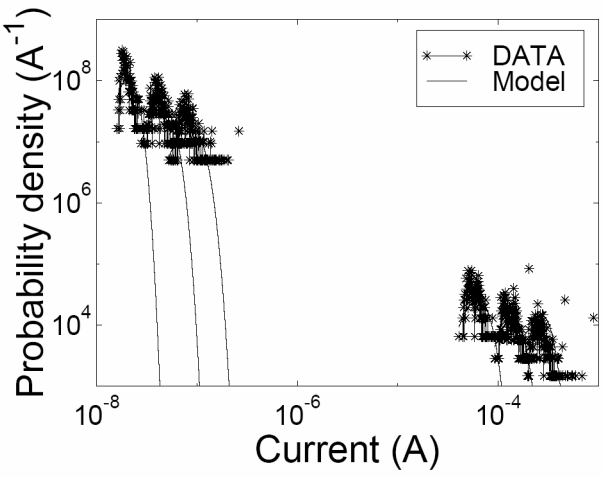

Figure 4. Probability density as a function of the output current at overvoltages of 2V, 3V and 4V, for both single pixels and arrays (having 4096 cells). The solid red lines are the model results.

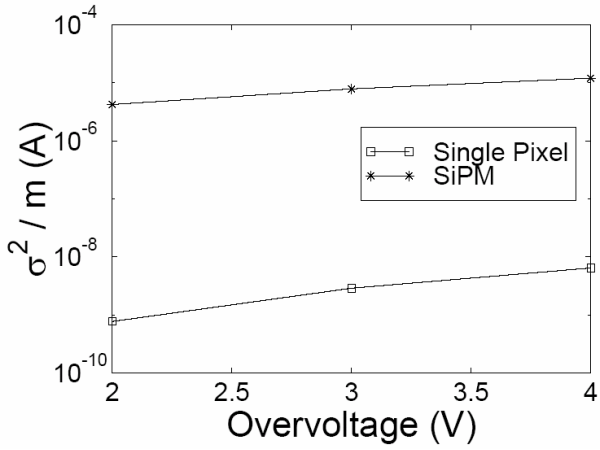

Figure 5. Experimental values of the variance divided by average device current as a function of the device overvoltage for the single pixel (in blue) and the SiPM (in red)

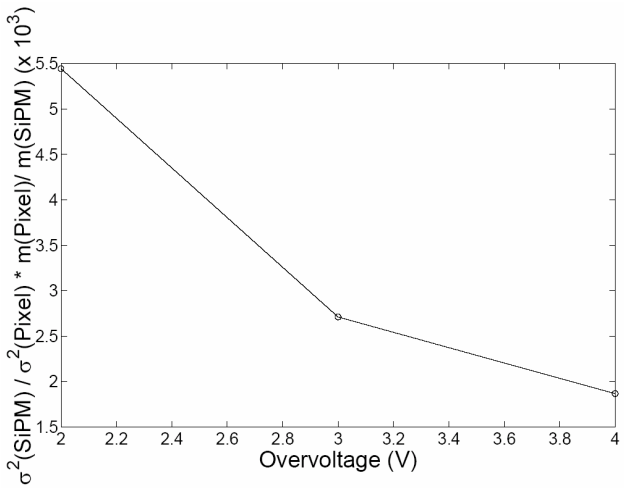

Figure 6. Experimental values of the ratio of the variance divided by the average device current between SiPMs and single pixels as a function of the overvoltage. The model, in good agreement with the experimental results, predicts that the ratio should be equal to the number of pixels in the SiPM device, equal to 4,096.

To model I_D in the present devices, we note that at room temperature the term $\frac{N_{Def}}{\tau}$ dominates, so the I_D statistics should essentially coicide with the N_{Def} statistics. The prevalence of the $\frac{N_{Def}}{\tau}$ term has been demonstrated through the temperature dependence of the leakage current, as reported in ref. [14]. For the N_{Def} statistics we assume the Poisson statistics so we find that the probability dP of having a dark count between I_D and I_D+dI_D is:

$$\frac{dP}{dI_D} = N \exp\left[\frac{m_{I_D}}{\sigma^2_{I_D}}\left(I_D \log(m_{I_D}/I_D) + (I_D - m_{I_D})\right)\right] \quad (2)$$

where N is a normalization constant, m_{I_D} is the statistical average of the dark current and $\sigma^2_{I_D}$ is the variance. In the case of the SiPM arrays the same expression holds. Fig. 4 reports also the model curves, which show a good match with the experimental data. The model predicts that the combination of statistical parameters $\frac{\sigma^2_{I_D}}{m_{I_D}}$ should be equal to $\frac{q}{\tau}G$ or $4096 \times \frac{q}{\tau}G$, for the single pixel and the SiPM array, respectively. Fig. 5 reports the experimental values of $\frac{\sigma^2_{I_D}}{m_{I_D}}$ as a function of the device overvoltage. As the overvoltage increases, $\frac{\sigma^2_{I_D}}{m_{I_D}}$ grows, due to the G increment. Morevover the ratio of $\frac{\sigma^2_{I_D}}{m_{I_D}}$ between SiPM and single pixel results of the order of 4,000 (Fig. 6), as predicted by the model. More details will be shown in the presentation.

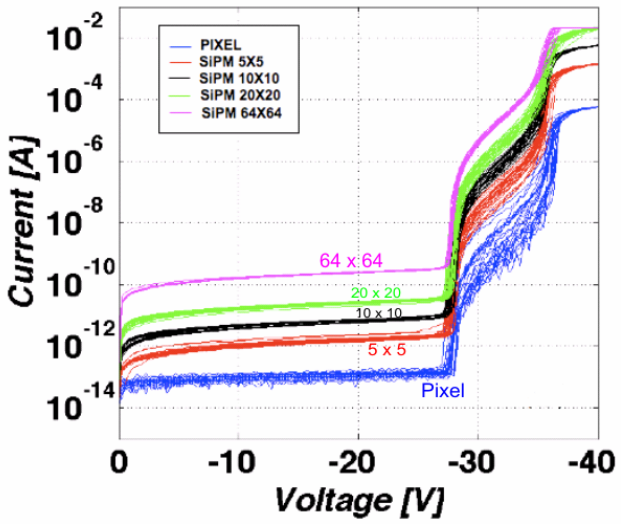

Figure 7. Reverse current for single pixels and arrays from 25 up to 4096 cells.

Further developments are ongoing and will be reported at the conference. In particular we would like to mention that an improved version of our SiPM technology shows a further reduced dark current leakage (Fig. 7). This is

 ISBN: 978-1-61208-145-8

attributed to an improved minority carrier lifetime (larger τ_i in Eq. (1)), obtained through a better device architecture [14].

ACKNOWLEDGMENTS

CNR authors gratefully acknowledge ST support for research funding.

REFERENCES

[1] R.H. Haitz, "Model for the electrical behavior of a microplasma", J. Appl. Phys., 35 (1964), p. 1370.

[2] R. H. Haitz, "Mechanisms contributing to the noise pulse rate of avalanche diodes," J. Appl. Phys., 36, (1965), pp. 3123–3131

[3] R. J. McIntyre, "The distribution of gains in uniformly multiplying avalanche photodiodes: Theory," IEEE Trans. Electron Devices, 19, 6, (1972), pp. 703–713.

[4] "SPCM-AQR Data Sheet", Perkin Elmer Optoelectronics, available online http://www.htds.fr/doc/optronique/scientifiqueBiomedical/SPCM-AQR.pdf

[5] S. Cova et al., "Active-quenching and gating circuits for single-photon avalanche diodes (SPADs)", IEEE Trans. Nucl. Sci., 29, 1, (1982), pp. 599–601.

[6] F. Zappa et al., "Fully-integrated active-quenching circuit for single-photon detection", Proc. of the 28th European Solid-State Circuits Conference, ESSCIRC 2002, p. 355.

[7] S. Vasile et al., "High gain avalanche photodiode arrays for DIRC applications", IEEE Trans. Nucl. Sci. 46 (1999) p. 848.

[8] P. P. Antich, "Avalanche photo diode with local negative feedback sensitive to UV, blue and green light", Nucl. Instrum. Meth. A, 389 (1997) pp. 491-498.

[9] G. Bondarenko, "Limited Geiger-mode microcell silicon photodiode: new results", Nucl. Instrum. Meth. A, 442 (2000) pp. 187-192.

[10] V. Golovin, Avalanche Photodetector, Russian Agency for Patents and Trademarks, Patent No. RU 2142175 (1998).

[11] Z. Sadygov, Avalanche Detector, Russian Agency for Patents and Trademarks, Patent No. RU 2102820 (1998).

[12] E. Sciacca et al., "Silicon Planar Technology for Single-Photon Optical Detector", IEEE Trans. Electr. Dev.,50, 4 (2003) pp. 918-925.

[13] R. Pagano, S. Lombardo, S. Libertino, G.Valvo, G. Condorelli, B. Carbone, D. N. Sanfilippo, and G. Fallica, "Understanding dark current in pixels of silicon photomultipliers", IEEE, Proc. Of 40th European Solid State Device Research Conference, pp. 265-268 (2010)

[14] R. Pagano, S. Libertino, D. Corso, G. Valvo, D. Sanfilippo, G. Fallica, and S. Lombardo, "Dark current in SiPM pixels: data and model", article in preparation.

 ISBN: 978-1-61208-145-8

Nanoparticles with Conductive Polymer as Photosensing Applications

Si-Han Zeng[a], Shin-Hung Tsai[b] and Guo-Dung J. Su[c]
Graduate Institute of Photonics and Optoelectronics, National Taiwan University
Taipei, Taiwan
E-mail: r98941035@ntu.edu.tw[a], r98941081@ntu.edu.tw[b], gdjsu@cc.ee.ntu.edu.tw[c]

***Abstract* —In this study, we observed that the electric property of PEDOT:PSS was affected by LSPR effect. LSPR effect was generated by nano gold particles that embedded in PEDOT:PSS films. The high-intensity electric field of LSPR enhances the mobility of carriers. In order to observe this phenomenon, we made some devices. The devices under measurement were composed of ITO glass, thin PEDOT:PSS film, nano gold particles and an Al electrode. In our study, the effect of the devices that were doped with different density of gold nano particles was measured. The higher density of gold nano particles made the lower total resistance of device. The different wavelengths of incident light also made the total resistance of device different. Through those experiments, we validated that the change of electric property of PEDOT:PSS was caused by the LSPR effect from nano gold particles.**

Keywords-PEDOT: PSS; gold nano particles; LSPR (Localized Surface Plasmon Resonance).

I. INTRODUCTION

PEDOT:PSS (Poly-3-4-ethyleneoxythiophene/poly-4-sytrensulfonate) is an electro-chemically stable conjugated polymer that is commonly used as the buffer layer and a hole transport layer of organic solar cells and OLED (Organic Light-Emitting Diode), or with the ITO (Indium Tin Oxide) as the anode material. PEDOT:PSS has good light transmission, good conductivity, and can be deposited by either spin coating or ink-jet printing process as a more simpler way to make thin-films. A PEDOT:PSS can be coated on many different substrates, like flexible polymers or ITO glass substrates. These features also show that the PEDOT:PSS can reduce the cost of fabrication [1-3].

A thin film of PEDOT:PSS is a buffer layer of organic solar cells or OLED between the active layer and ITO glass because the surface ITO glass usually has some defects and it is difficult to form a good thin-film active layer on the substrate. The buffer layer of PEDOT:PSS film can modify the surface of ITO glass and can make the film better. A PEDOT:PSS film can also reduce the generation of leakage current [4]. Adding an extra layer in the structure could increase the series resistance of solar cell inevitably. Those extra resistances would reduce the efficiency of components. In this study, the resistance of sample was decreased by LSPR (Localized Surface Plasmon Resonance). The localized surface plasmon resonance was generated by the gold nanoparticles deposited between ITO glass substrate and the PEDOT:PSS film.

The idea of spreading gold nanoparticles between the substrate ITO glass and PEDOT:PSS film was inspired by the organic solar cell. Lots of studies have validated that the surface plasma induced by metallic nano particles can increase the efficiency of organic solar cell [5].

LSPR effect has already been widely applied to biotechnology, such as surface enhanced Raman scattering (SERS) [6-7]. Those works usually made use of the different incident wavelength to measure the dielectric constant, so that the material type can be inferred then. In this study, we aimed for using the reaction of LSPR effect of the different incident wavelength with conductive polymer as a photo sensor.

PEDOT:PSS is an important material in many photonic devices. In order to prove that the difference of the device resistance was caused by LSPR, DDSCAT was used to simulate the localized surface plasmon resonance spectrum of gold particles [8-10].

In the following paragraphs, simulation methods and the sample preparation are described and explained. After that, experiment result and simulation result are discussed.

II. SIMULATION OF SURFACE PLASMON

Surface plasmon is a phenomenon that surface electromagnetic waves propagate on the interface between metal and dielectric material. Surface plasmon mode is confined near the metal surface to form a highly enhanced near-field. Surface plasmon between the metal and the dielectric material is divided into two types, SPP (surface plamon polariton) and the LSPR (localized surface plasmon resonance). SPP refers to the surface plasmon on the metal surface in the form of surface wave propagating in the interface of metal and dielectric material. LSPR refers to the highly localized, high intensity electric field resonance that is generated on the surface of metal particle. The electric field resonance would be calculated by Maxwell's equations and boundary condition under Quasi-static approximation [11].

$$\begin{aligned} \Phi_{in}(r,\theta) &= Ar\cos\theta & (r<a) \\ \Phi_{out}(r,\theta) &= -E_0 r\cos\theta + \frac{B}{r^2}\cos\theta & (r>a) \end{aligned} \quad (1)$$

In these two equations, 'a' is the radius of the metal particle. Those equations and boundary condition (equation 2 below) could be used to simulate the LSPR effect on a single particle. With the boundary condition, *A* and *B* in equation 1 can be solved accordingly.

 ISBN: 978-1-61208-145-8

$$\Phi_{out}(a,\theta) = \Phi_{in}(a,\theta)$$
$$\varepsilon E_{out}\hat{n} = \varepsilon_m E_{in}\hat{n} \quad (2)$$

Then assuming an ideal dipole that can be described as $\vec{P} = \varepsilon\alpha\, E_0 e^{-i\omega t}\hat{Z}$. The electric field of incident electromagnetic wave is $\vec{E}_{inc} = E_0 e^{-i(kx-\omega t)}\hat{Z}$.

We can use the above equations to calculate the extinction cross section (C_{ext}) and scattering cross section (C_{sca}).

TABLE I. THE SIGNIFICANCE OF VARIABLES

variables	significance
ϕ	Electric Potential
ε	Dielectric constant
A, B	Constant
E_0	Electric field magnitude
$\vec{P}$	Dipole moment
α	Polarizability

But, to simulate a metal particle array just with those equations would be very difficult [12]. For this purpose, DDSCAT is used to simulate the effect that LSPR is generated on the surface of gold nanoparticles. DDSCAT, a FORTRAN code for calculating scattering and absorption of light by irregular particles, has been jointly developed by Bruce T. Draine and Piotr J. Flatau [8-10].

Based on the discrete-dipole approximation, DDSCAT simulated the electric field around the particles by Maxwell's equations. The discrete-dipole approximation (DDA) is a flexible approach for calculating scattering and absorption properties of arbitrary continuum targets, usually a finite geometry of polarizable points. The local electric field induces dipole moments that could be acquired by the points. The dipoles influence each other through their electric fields as well. Therefore the DDA is sometimes called discrete dipole approximation.

DDSCAT is well-developed simulation software. There can get the source code of DDSCAT on the internet [10]. After compiling the source code, we have an executable file. There are other two files, ddscat.par and diel.tab, that are used to control the executable file.

For building the boundary condition to process DDACAT, it would be crucial to enter the dielectric constant of gold nano particles and the dielectric material (PEDOT:PSS and ITO glass) to the file (i.e., diel.tab) of DDSCAT. The particle radius and other boundary condition were entered into another file (i.e., ddscat.par). We could then simulate the scattering and absorption of incident light by different wavelengths on gold nano particles. In this study, DDSCAT was used to simulate the absorption of the incident light between 300 nm and 800 nm and gold nano particles with 20nm diameter. The data of simulation would be compared with the experiment results in the following section.

III. SAMPLE PREPARATION

Samples were fabricated with PEDOT:PSS (Baytron P VP Al 4083), gold nano particles (gold colloid SI-G1652) and ITO glass substrates (15 ohm/square). The patterned ITO glass substrates were placed into the ultrasonic cleaners for removing the surface dirt. Then the ITO glass substrates were washed by oxygen plasma for 20 minutes in order to make the PEDOT:PSS easy to form on substrates. After being cleaned by oxygen plasma, the surface of ITO glass would be changed to hydrophilic. We took PEDOT:PSS out from the refrigerator and put it aside until it returned to room temperature. After that, filtering PEDOT:PSS twice by target syringe filters with pore size of 0.45um.

After finishing the preparation of PEDOT:PSS, we mixed the solution of gold nanoparticles and ethylene glycol at one to one and one to two ratio (The concentration of gold nanoparticles is 3.9 * 10 ^ -5g/ml and 2.6 * 10 ^ -5g/ml). Next, we coated the solution that contained gold nano particles on the ITO glass substrates by 1000 rpm for 10 seconds and 2000 rpm for 20 seconds. We baked the samples after coating at 180 ℃ for 3 minutes to dry those residue of ethylene glycol. Then, those nano gold particles spread on the ITO glass substrate. The distance from particle to particle was about 100 nm. We then coated PEDOT:PSS on the ITO substrate with and without gold nano particles by 3000 rpm for 30 seconds. Baking those prepared sample at 180 ℃ for 5 minutes [13]. PEDOT:PSS covered gold nano particles and formed a 30nm film. The thickness of PEDOT:PSS films were 30nm with and without gold nano particles. Finally, we deposited 120 nm of aluminum on the sample as the electrode by thermal evaporator. The samples are illustrated in Figure 1.

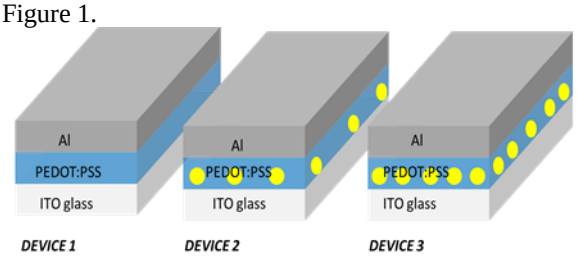

Figure 1. The structure of device 1 without add PEDOT:PSS, device 2 with gold nanoparticles 2.6 * 10 ^ -5g/ml, device3 with gold nanoparticles 3.9 * 10 ^ -5g/ml.

The measurement was performed by using Keithley 2400 to record the IV curve. PL-2100 COOL LIGHT SOURCE was light source, and we measured the current density of devices with bias voltage 1V under illuminating of different wavelength incident light from QE-III (Enlitech). The measurement setup is shown in Figure 2.

 ISBN: 978-1-61208-145-8

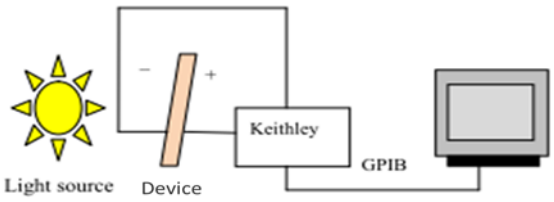

Figure 2. The measurement setup diagram

IV. EXPERIMENTAL RESULTS

Figure 1 shows the sample structure. The top aluminum is the cathode and the bottom of the ITO is the anode. Light source was incident from the side of ITO, and we used Keithley 2400 to record the current value from 0V to 1.5V. Figure 3 is the comparison of the two samples with and without gold nanoparticles. In Figure 3, it shows that the current density of the sample with gold nano particles was higher than the sample without gold nano particle at the same bias voltage. We also observed that if the density of gold nano particles was higher, the current density was higher too. In other words, the sample with gold nanoparticles has lower total resistance than the sample without gold nanoparticles when those sample are exposed to incident light irradiation [14- 15].

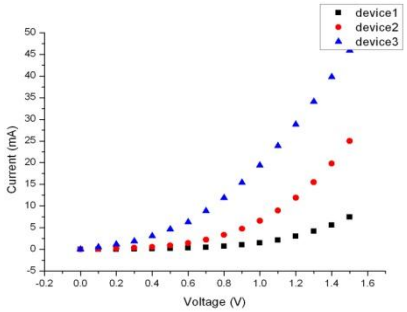

Figure 3. The sample current varies with voltage, device 1 (black square), device 2 (red circle), device3 (blue triangle).

Although the performance of device 3 is the best, the low repeatability and stability of device 3 is the reason that we focus our discussion on device 2 and device1. Figure 4 shows the IV-curve of device 2 (with gold nanoparticles between ITO glass and PEDOT:PSS film) that was under illumination and not under illumination. In this figure, it can be found that when the bias voltage was the same, the current value of device 2 under illumination was increased significantly than device 2 without being exposed to incident lights. When the bias voltage was 1.5 volts, the current density of device2 under illumination was increased from 15 mA to 25 mA. But if there were no bias voltage, the current density would be the same no matter the sample was under illumination or not. Therefore, this result can prove that the increase of current density was not caused by the excess carrier generation. We believe the overall resistance was decreased because of the incident light.

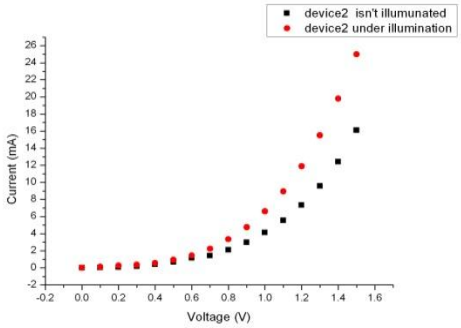

Figure 4. The device2 current density varies with voltage that is illuminated and isn't illuminated.

In order to confirm that the effect of resistance decrease was caused by gold nano particles, we compared the current increases under illumination between device 1 (the sample with only PEDOT: PSS) and device 2 (the sample with gold nano particles) in Figure 5.

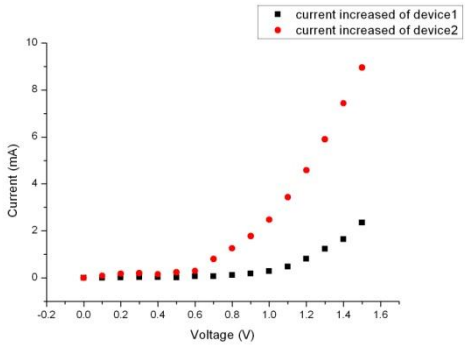

Figure 5. The increase of current density while device2 (red square) and device 1 (blue diamond) were exposed to incident light

Even though the current density of device 1 also increased while the sample was illuminated, the value of increased current density was far less than that of device2. Therefore, it can be claimed that the phenomenon of the resistance reduce was due to the gold nano particles within the sample irradiated by light.

The reason of that is considered that the LSPR generated by gold nanoparticles reduces the resistance of the junction of PEDOT:PSS films and ITO glass substrate

The highly localize, and high-intensity electric field resonance of LSPR in the junction causes the transmission of those carriers (holes) easily, as shown in Figure 6. Due to the existence of the gold nano particles, the gold nanoparticles is in the dashed area. This increase the electric field gives electric holes an attractive force and make the mobility of electric holes be increased.

 ISBN: 978-1-61208-145-8

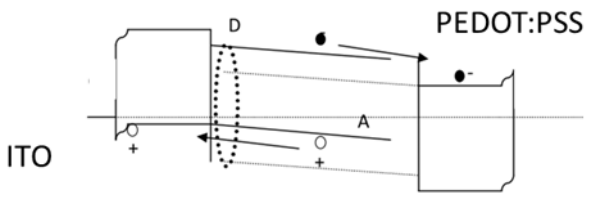

Figure 6. Schematic drawing of device with nano goldparticles, where A is acceptor, and D is the donor. The dashed area is gold metal cluster surface plasmon resonance.

To further confirm the relationship between resistance and LSPR, the device 2 was exposed to visible light irradiation with the wavelength from 350 nm to 750 nm. We measured the current density with bias voltage, as shown in Figure 7. We used DDSCAT to simulate the absorption spectra of gold nano particles, 20nm diameter, from 300 nm to 800 nm, and compare it with experimental results. The simulation results are shown in Figure 8.

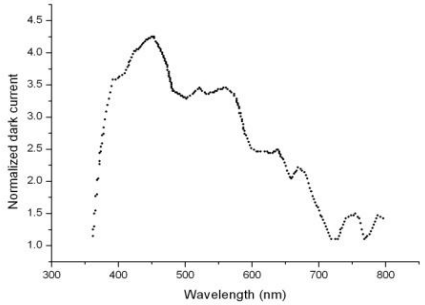

Figure 7. Current density (device 2) versus the wavelength of incident lights, normalized with the dark current density.

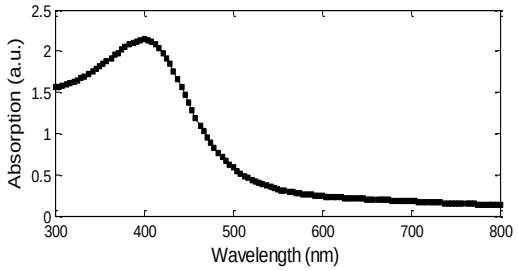

Figure 8. The absorption rate of 20nm gold particles versus incident wavelength by DDSCAT simulation.

Comparing Figure 7 and Figure 8, it can be observed that the shape of those curve are very consistent with each another. Although the curve of experiment result was 20-30nm shift to longer wavelength, we believed that reason of red shift is that not all the diameter of gold nano particles is actually 20nm. In our simulation the diameter is set to be 20nm, since the average diameter of the gold nano particles used in the experiment is 20nm. However, those gold nano particles with diameter larger than 20nm may affect the waveform. But it was still within measurement tolerance. This result still directly proved that the effect of LSPR was the main cause of sample's resistance decrease.

As shows in Fig. 7, the device with gold nano particles are measured different current density while the wavelength of incident light is changed. We can use device 2 to recognize the wavelength of incident light by the measurement setup as shown in Fig. 2. This feature makes the device as a wavelength sensor.

V. DISCUSSIONS

According to the experiment and simulation, we get the following two results. First, the resistance of devices is reduced by gold nanoparticles. Besides, this effect is strong when gold nanoparticles are illuminated. Second, the magnitude of absorption of gold nanoparticles is consistent with the current density of device.

From the two results, it is validated that LSPR from gold nano particles is the reason why the current density of device is increased.

ACKNOWLEDGMENT

The project was financially supported by National Science Council of Taiwan under contract number NSC 99-2221-E-002 -206 -MY3.

REFERENCES

[1] G. Greczynski, Th. Kugler, and W. R. Salaneck**, "**Characterization of the PEDOT-PSS system by means of X-ray and ultraviolet photoelectron spectroscopy "Thin Solid Films 354, pp. 129-135 (1999)

[2] J. Luo and W. Tang, "Influence of PEDOT with Different Conductivity on the Performance of Polymer Photovoltaic Cells", Journal of Guangdong University of Technology Vol. 25 No. 3, pp. 6-9, (2008)

[3] Nurdan D. Sankir, "Selective deposition of PEDOT/PSS on to flexible substrates and tailoring the electrical resistivity by post treatment" , Circuit World Vol. 34 · Number 4, ·pp.32–37(2008) ·.

[4] J. Ouyang, C.-W. Chu, F.-C. Chen, Q. Xu, and Y. Yang, "High-conductivity poly (3, 4-ethylenedioxythiophene): poly (styrene sulfonate) film and its application in polymer optoelectronic devices", Advanced Functional Materials Vol. 15, Issue 2, pp. 203–208, (2005)

[5] S.-S. Kim, S.-I. Na, J. Jo, D.-Y. Kim, and Y.-Ch. Nah, Plasmon, "Plasmon enhanced performance of organic solar cells using electrodeposited Ag nanoparticles", APPLIED PHYSICS LETTERS 93,pp. 073307-073309 (2008)

[6] Jeffrey M. McMahon, Anne-Isabelle Henry, Kristin L. Wustholz, Michael J. Natan, R. Griffith Freeman, Richard P. Van Duyne ,and George C. Schatz, "Gold nanoparticle dimer plasmonics: finite element method calculations of the electromagnetic enhancement to surface-enhanced Raman spectroscopy" , Vol. 394, Number 7, pp.1819-1825 (2009)

[7] Qiuming Yu and Greg Golden, "Probing the Protein Orientation on Charged Self-Assembled Monolayers on Gold Nanohole Arrays by SERS", Langmuir, 23 (17), pp 8659–8662 (2007)

[8] Draine, B.T. and Flatau, P.J., "Discrete dipole approximation for scattering calculations", J. Opt. Soc. Am. A, 11, pp.1491-1499 (1994)

 ISBN: 978-1-61208-145-8

[9] Draine, B.T. and Flatau, P.J., "User Guide to the Discrete Dipole Approximation Code DDSCAT 7.1", http://arXiv.org/abs/1002.1505v1 (2010)

[10] Draine, B.T. and Flatau, P.J., "Discrete-dipole approximation for periodic targets: theory and tests", J. Opt. Soc. Am. A, 25, pp.2593-2703 (2008)

[11] Stefan A. Maier, " Plasmonics: fundamentals and applications" , Springer Verlag, pp.65-75 (2007)

[12] N. W. Ashcroft, and N. D. Mermin, "Solid State Physics",Harcount(2000)

[13] Vishal Shrotriya, Gang Li, Yan Yao, Tom Moriarty, Keith Emery, and Yang Yang, Accurate Measurement and Characterization of Organic Solar Cells, Adv. Funct. Mater., 16, pp2016–2023(2006)

[14] Y.H. Zhou, F.L. Zhang, K. Tvingstedt, Sophie Barrau, F.H. Li, W.J. Tian, and Olle Inganäs, "Investigation on polymer anode design for flexible polymer solar cells", APPLIED PHYSICS LETTERS 92, pp.233308-233310 (2008)

[15] S.W. Tong, C.F. Zhang, C.Y. Jiang, G. Liu, Q.D. Ling, E.T. Kang, D.S.H. Chan, and Chunxiang Zhu, "Improvement in the hole collection of polymer solar cells by utilizing gold nanoparticle buffer layer", Chemical Physics Letters 453, pp.73–76 (2008)

 ISBN: 978-1-61208-145-8

Effect of the Optical Bias on the a-Si:H Optical Demultiplexer Device

Miguel Fernandes, Manuela Vieira, Manuel A. Vieira, Paula Louro
Electronics Telecommunications and Computer Department
ISEL
Lisbon, Portugal
mfernandes@deetc.isel.ipl.pt

Miguel Fernandes, Manuela Vieira, Manuel A. Vieira, Paula Louro
CTS
UNINOVA
Caparica, Portugal

***Abstract*—This paper presents results on the use of multilayered a-SiC:H heterostructures as a device for wavelength-division demultiplexing of optical signals. The devices presented enable the simplification of the optical front end system by using their intrinsic color selectivity to avoid the need of external optical filters. The device is composed of two stacked p-i-n photodiodes, each optimized for the absorption of a part of the optical spectrum. Band gap engineering was used to adjust the photogeneration and recombination rates profiles of the intrinsic absorber regions of each photodiode to short and long wavelength absorption and carrier collection in the visible spectrum. The photocurrent signal using different input optical channels (wavelengths) was analyzed at reverse and forward bias and under steady state illumination. A demultiplexing algorithm based on the voltage controlled selectivity of the device is proposed and tested. The operation frequency of the device was analyzed under different optical bias conditions. An electrical model of the WDM device is presented and supported by the solution of the respective circuit equations. The main application of these devices is in the field of optical communications that use the wavelength division multiplexing technique to encode multiple signals into the same transmission medium. Other possible applications of the device in optical communication systems are also proposed.**

Keywords-WDM; Optical sensor; a-Si:H

I. INTRODUCTION

Wavelength division multiplexing (WDM) devices are used when different optical signals are combined on the same optical transmission medium, in order to enhance the transmission capacity and the application flexibility of optical communication and sensor systems. The use of WDM technologies not only provides high speed optical communication links, but also offers advantages such as higher data rates and self-routing. The commercially available WDM devices usually include prisms, interference filters or diffraction gratings in order to separate the different channels. Currently modern optical networks use Arrayed Waveguide Grating (AWG) as optical wavelength (de)multiplexers [1] that use multiple waveguides to carry the optical signals. In this paper we report the use of a monolithic WDM device based on an a-Si:H/a-SiC:H multilayered semiconductor heterostructure. The device makes use of the fact that the optical absorption of the different wavelengths can be tuned by means of electrical bias changes or optical bias variations. This capability is obtained using adequate engineering design of the multiple layers thickness, absorption coefficient and dark conductivities [2, 3].

II. EXPERIMENTAL DETAILS

The device described herein operates in the 400 to 700 nm range which makes it suitable for operation at visible wavelengths in optical communication applications. The device is a multilayered heterostructure based on a-Si:H and a-SiC:H. The device is quite simple, consisting in a stack of two p-i-n structures sandwiched between two transparent electrical contacts (Fig. 1). Both front and back structures behave as optical filters confining, respectively, the absorption of the short and the long wavelength optical carriers, while the intermediate wavelengths are absorbed across both [4, 5]. The device was operated within the visible range using as optical signals three modulated light beams (with variable modulation frequency and intensity) supplied by red, green and blue LED's with wavelengths of 470 nm, 524 nm and 626 nm, respectively. An electrical model of the WDM device is presented and supported by the solution of the respective circuit equations. Other possible applications of the device in optical communication systems are also proposed.

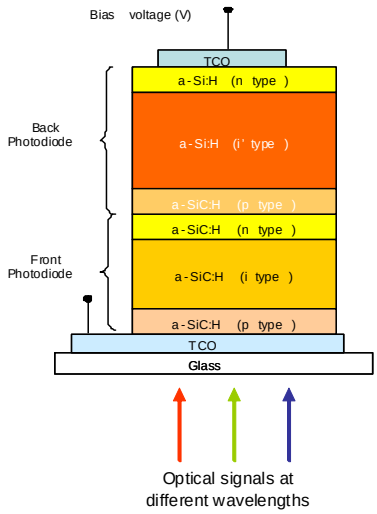

Figure 1. WDM device configuration.

 ISBN: 978-1-61208-145-8

The semiconductor layers were produced by Plasma Enhanced Chemical Deposition (PECVD) technique and optimized for specific wavelength sensitivity. The active device consists of a p-i'(a-SiC:H)-n/p-i(a-Si:H)-n heterostructure with low conductivity doped layers. The thicknesses and optical gap of the thin i'- (200nm; 2.1 eV) and thick i- (1000nm; 1.8 eV) layers are optimized for light absorption in the blue and red ranges, respectively. Transparent contacts have been deposited on front and back surfaces to allow the light to enter and leave from both sides (see Fig. 1).

To test the sensitivity of the device under different applied voltage and optical bias three modulated monochromatic lights beams: red (R: 626 nm; 51μW/cm^2), green (G: 524 nm; 73μW/cm^2) and blue (B: 470 nm; 115μW/cm^2) and their polychromatic combinations (multiplexed signal) illuminated separately the device and the generated photocurrent was measured under positive and negative voltages (+1V<V<-10V), under or without steady state green optical bias (G: 524 nm; 73μW/cm^2). The modulation frequency of each channel was chosen to be a multiple of the others in order to ensure a synchronous relation of ON-OFF states along each cycle and the optical powers were adjusted to give different signal magnitudes at -8V bias.

Fig. 2 displays the measured spectral photocurrent under reverse and forward bias. Results show that in the long wavelengths range (> 600 nm) the spectral response is independent on the applied bias while in the short wavelength the collection strongly increases with the reverse bias. As expected from Fig. 2, the red signal remains constant while the blue and the green ones decrease as the voltage changes from negative to positive. The output multiplexed electrical signal, obtained with the combination of the three optical sources, depends on both the applied voltage and on the ON-OFF state of each input optical channel. Under negative bias, there are eight separate levels while under positive bias they were reduced by half. The highest level appears when all the channels are ON and the lowest if they are OFF. Furthermore, the levels ascribed to the mixture of three or two input channels are higher than the ones due to the presence of only one (R, G, B).

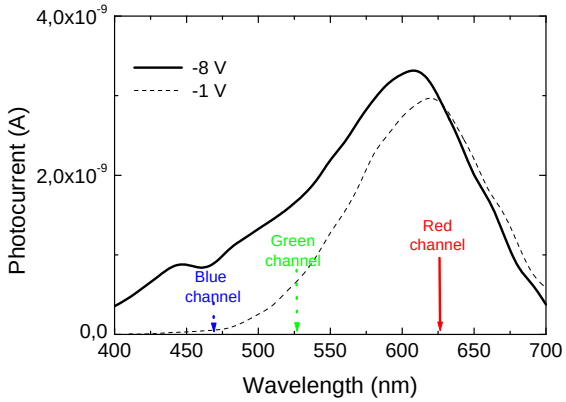

Figure 2. Spectral photocurrent under reverse and forward bias.

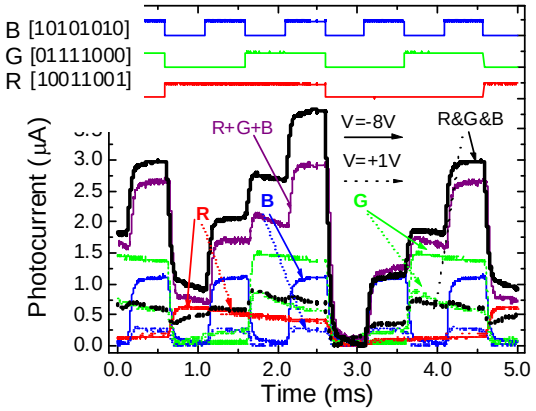

Figure 3. Single and multiplexed signals under negative (-8V) and positive (+1V) electrical bias.

An optical nonlinearity was detected; the sum of the input channels (R+B+G) is lower than the correspondent multiplexed signals (R&G&B). This optical amplification, mainly on the ON-ON states, suggests capacitive effects due to the time-varying nature of the incident lights. Under positive bias the levels are reduced by half since and the blue component of the combined spectra falls into the dark level, the red remains constant and the green one decreases.

To recover the transmitted information (8 bit per wavelength channel) the multiplexed signal, during a complete cycle, was divided into eight time slots, each corresponding to one bit where each independent optical signals can be ON (1) or OFF (0).

Under positive bias, the device has no sensitivity to the blue channel (Fig. 1-2), so the red and green transmitted information can be extracted. The highest level corresponds to both channels ON (R&G: R=1, G=1), and the lowest to the OFF-OFF stage (R=0; G=0). The two levels in-between are related with the presence of only one channel ON, the red (R=1, G=0) or the green (R=0, G=1). To distinguish between these two situations and to decode the blue channel, the correspondent sub-levels, under reverse bias, have to be analyzed. The highest increase at -8V corresponds to the blue channel ON (B=1), the lowest to the ON stage of the red channel (R=1) and the intermediate one to the ON stage of the green (G=1). Using this simple key algorithm the independent red, green and blue bit sequences can be decoded as: R[01111000], G[10011001] and B[10101010], as shown on the top of Fig. 2, which are in agreement with the signals used for the independent channels.

III. INFLUENCE OF THE STEADY STATE OPTICAL BIAS

Fig. 4 shows the time dependent photocurrent signal measured under reverse (-8V, symbols) and forward (+1V, dotted lines) bias using different input optical signals without and with (λ_L) red, green and blue steady state additional optical bias. Both optical signals and steady state bias were incident on the device by the side of the a-SiC:H

 ISBN: 978-1-61208-145-8

thin structure. The optical signals were obtained modulation of the LED driving current and the optical power intensity of the red, green and blue channels adjusted to 51, 90, 150 $\mu W/cm^2$, respectively. The steady state light was generated by LED's driven at a constant current value (R: 290 $\mu W/cm^2$, G: 150 $\mu W/cm^2$, B: 390 $\mu W/cm^2$).

Results show that the blue steady state optical bias increases the signals carried out by the red (Fig. 4a) and the green channels (Fig. 4b) and reduces the signal of the blue channel (Fig. 4c). Red steady state optical bias has an opposite behavior, reinforcing the blue channel and decreasing the blue and the green channels. The green optical bias mainly affects the green channel, as the output signal is reduced while the signals of the red and blue channels show negligible changes.

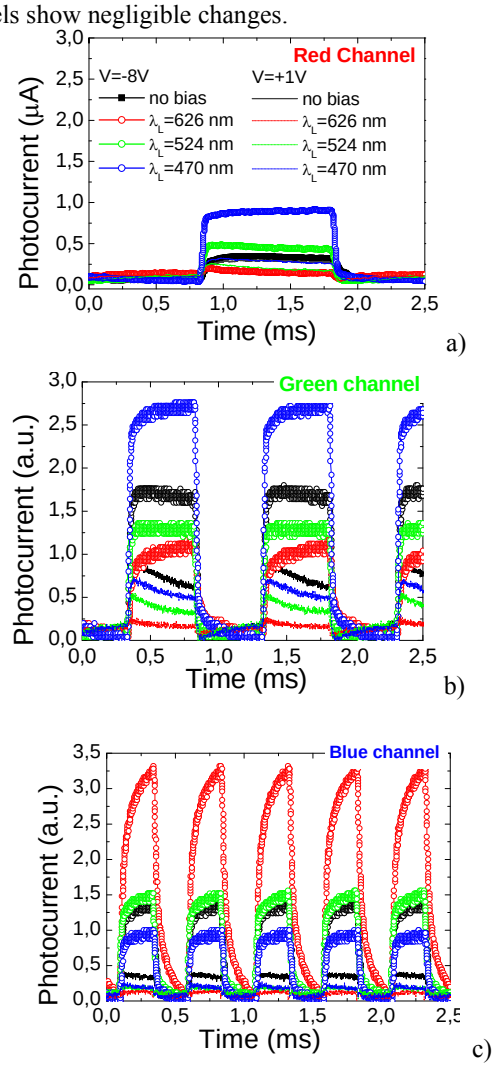

Figure 4. Red (a), green (b) and blue (b) channels under reverse and forward voltages without and with (λ_L) red, green and blue steady state bias.

The behavior of the device under steady state optical bias can be explained attending to the dependence of the internal electric field distribution. When an optical bias is applied it mainly enhances the field distribution within the less photo excited sub-cell: the back under blue irradiation and the front under red steady bias. Therefore, the reinforcement of the electric field under blue irradiation and negative bias increases the collection.

The study of the modulation frequency influence on the device performance was analyzed through the spectral response of the device without and with steady state optical bias. Results are displayed in Fig. 5. Data from Fig. 5 show that without background light the curves measured under different modulation frequencies exhibit the same trend with two peaks located at 500 nm and 600 nm. The signal is reduced with the increase of the frequency. Under blue steady state illumination (Fig. 5b) the spectral response exhibits a different trend with a single peak located at 600 nm.

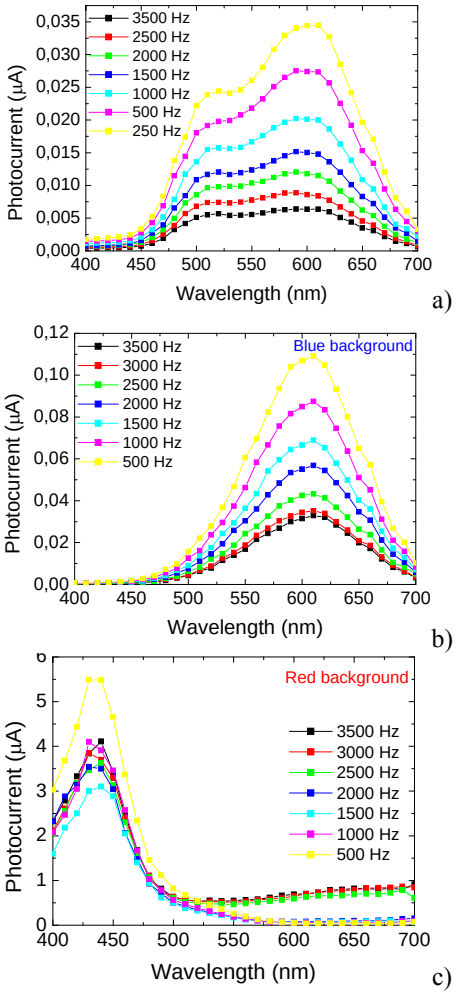

Figure 5. Photocurrent variation with the wavelength for different modulation frequencies at -8 V obtained: a) without, b) with blue, and d) with red background.

 ISBN: 978-1-61208-145-8

This is due to the strong attenuation of the short wavelengths (Fig. 4c). The red steady state illumination (Fig. 5c) has the opposite effect with a single peak at 500 nm. Under green background the spectral response shows two different regimes depending on the operation frequency. In the low frequency range the signal is similar to the trends obtained under red steady state light, while at higher frequencies it follows the behavior obtained without background light.

In Fig. 6 it is displayed the ratio of the signal measured under steady light and without it at different frequencies. Results show that at all frequencies of the analyzed range, under blue steady state illumination, the long wavelengths are amplified while shorter wavelengths (< 530 nm) are reduced. A similar result is observed for the red steady state illumination. Here the reinforcement of the signal level occurs for shorter wavelengths, while in the longer ones it is reduced.

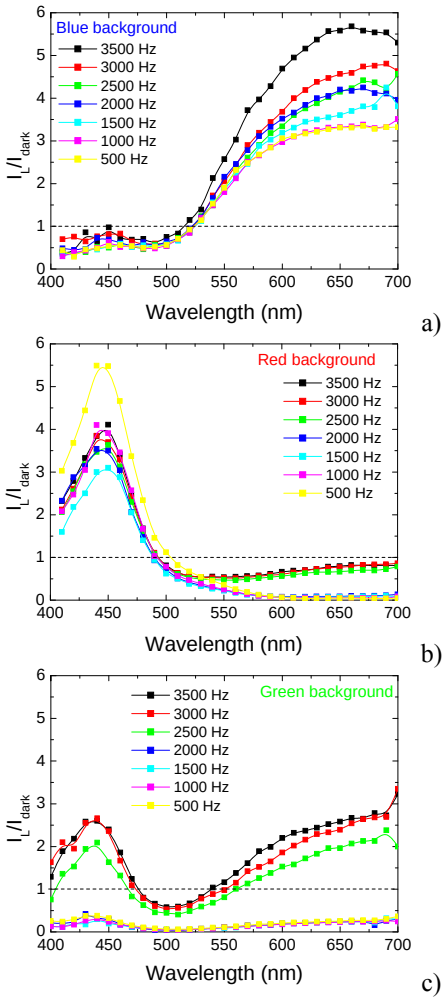

Figure 6. Ratio between the photocurrents under a) blue, b) red and c) green steady state illumination and without it (dark) at -8 V under different frequencies.

For the green background light the ratio between the photocurrents shows two different trends. At low frequencies the presence of the steady state light reduces the photocurrent, while for higher frequencies this reduction is only observed in a narrow range of the spectrum (from 470 nm up to 480 nm). In the remaining ranges the signal is enhanced. The maximum value observed for the amplification factor is around 3.

IV. Optical Bias Controlled Wavelength Discrimination

In Fig. 7, the input and the multiplexed channels, without or with green optical bias, are displayed at -8V. The bit sequence is shown at the top of the figure to guide the eyes. Results show that the presence of the optical bias reduces significantly the amplitude of green channel while a slightly increase is observed for the others two. The sum of the input channels (R+G+B) shows that when the green channel is ON no amplification occurs. This suggests that the green channel can be tuned by making the difference between the multiplexed signal without and with green irradiation (symbols).

This nonlinearity is due to the asymmetrical light penetration of the input channels and on the optical selectivity properties of the device. When an external optical bias is applied, it mainly influences the field distribution within the less photo excited sub-cell.

Under green light irradiation the electric field decreases on both sub-cells. So, some of the carriers generated by the green channel, also in both sub-cells, recombine and the collection decreases. When the red or blue channels are ON, the generation occurs only in one sub-cell. The electrical field, in the presence of the red and blue channels, lowers, respectively, in the back and front photodiodes (most absorbing cells), while the correspondent front and back photodiodes (less absorbing cells) reacts by assuming a reverse bias configuration compensating the effect of the green optical bias [7]. This self bias effect explains the slightly increase on the red and blue collection under green optical bias.

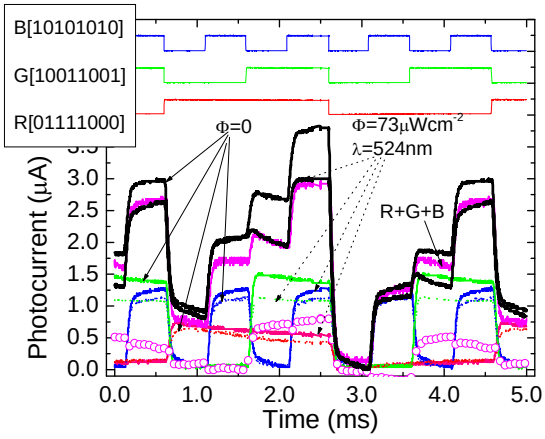

Figure 7. Single and combined signals @-8V; without (solid arrows) and with (dotted arrows) green optical bias.

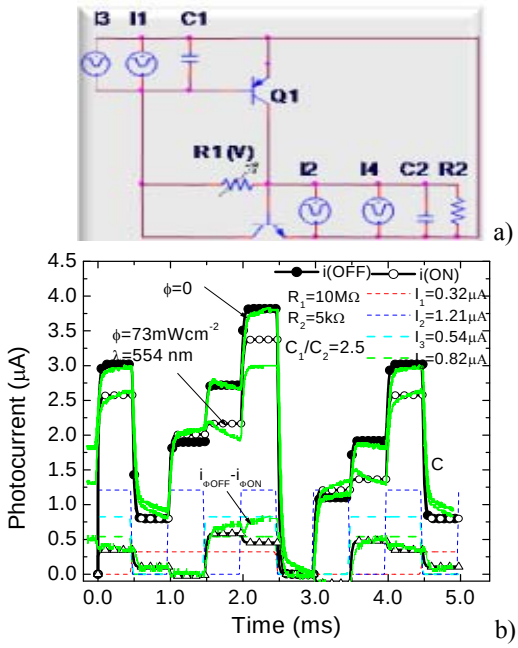

Figure 8. a) Electrical model, b)Simulated (symbols), current sources (dash lines) and experimental (solid lines) under +1V dc bias.

V. ELECTRIAL SIMULATION

The silicon-carbon pi'npin device can be considered as a monolithic double pin photodiode structure with two red and blue optical connections for light triggering. Based on the experimental results and device configuration an electrical model was developed [6]. Operation is explained in terms of the compound connected phototransistor equivalent model displayed as an inset in Fig. 8.

In Fig. 8 the currents under negative bias, with and without optical green bias, are compared. To simulate the green background, current sources intensities were multiplied by the on/off ratio between the input channels with and without optical bias (Fig. 6). The same bit sequence of Fig. 3 was used in both figures. To validate the model the experimental multiplexed signals are also shown (solid lines). Good agreement between experimental and simulated data was observed. The eight expected levels, under reversed bias, and their reduction under green irradiation are clearly seen.

When the pi'npin device is reverse-biased, the base emitter junctions of both transistors are inversely polarized and conceived as phototransistors, taking, so, advantage of the amplifier action of neighboring collector junctions which are polarized directly. This results in a charging current gain proportional to the ratio between both collector currents (C_1/C_2). Under positive bias the internal junction becomes always reverse-biased. If not triggered ON it is nonconducting, when turned ON by light it conducts like a photodiode, for one polarity of current.

Green irradiation moves asymmetrically voltages at the Q_1 and Q_2 bases toward their emitter values, resulting in lower values of I_3 and I_4 when compared without optical bias (Fig. 7). I_1 and I_2 slightly increase due to the increased carrier generation on the less absorbing phototransistors. Under negative bias and during the duration of the red and blue pulses (I_1 or I_2 ON), as without optical bias, the internal junction remains forward biased and the transferred charge between C_1 and C_2 reaches the output terminal as a capacitive charging current. During the green pulse (I_3 and I_4 ON) only residual charges are transferred between C_1 and C_2. So, only the charges generated in the base of Q_2 (I_4) reaches the output terminal as can be confirmed by the good fitting between simulate and experimental differences of both multiplexed signals without and with optical bias.

VI. CONCLUSIONS

A double pi'n/pin a-SiC:H heterostructure with two optical sensitive regions sensitive to different spectral regions was presented. Multiple monochromatic communication channels, in the visible range, were transmitted together, each one with a specific bit sequence, and detected by the device. The combined optical signal was analyzed by reading out, under positive and negative voltages and optical green bias, the generated photocurrent across the device. Results show that the output multiplexed signal has a strong nonlinear dependence on the light absorption profile, i.e. on the incident light wavelength, bit rate, intensity and optical bias due to the self biasing of the junctions under unbalanced light generation profiles. By switching between positive and negative voltages the input channels can be recovered or removed.

The influence of the operation frequency was analyzed under different optical bias conditions. Further works on this topic is necessary for better understanding and further optimize the device operation.

ACKNOWLEDGMENT

This work was supported by FCT (CTS multi annual funding) through the PIDDAC Program funds and PTDC/EEA-ELC/115577/2009

REFERENCES

[1] M. Bas, Fiber Optics Handbook, Fiber, Dev.and Syst. for Opt. Comm., Chap, 13, Mc Graw-Hill, 2002.

[2] P. Louro, M. Vieira, Yu. Vygranenko, A. Fantoni, M. Fernandes, G. Lavareda, and N. Carvalho Mat. Res. Soc. Symp. Proc., 989 (2007) A12.04.

[3] M. Vieira, M. Fernandes, P. Louro, A. Fantoni, Y. Vygranenko, G. Lavareda, and C. Nunes de Carvalho, Mat. Res. Soc. Symp. Proc., Vol. 862 (2005) A13.4.

[4] P. Louro, M. Vieira, M.A. Vieira, M. Fernandes, A. Fantoni, C. Francisco, and M. Barata, Physica E: Low-dimensional Systems and Nanostructures, 41 (2009) 1082-1085.

[5] P. Louro, M. Vieira, M. Fernandes, J. Costa, M. A. Vieira, J. Caeiro, N. Neves, and M. Barata, Phys. Status Solidi C 7, No. 3–4, 1188– 1191 (2010).

[6] M. A. Vieira, M. Vieira, M. Fernandes, A. Fantoni, P. Louro, and M. Barata, Amorphous and Polycrystalline Thin-Film Silicon Science and Technology 2009, MRS Proceedings Vol. 1153, A08-0.

[7] M. Vieira, A. Fantoni, P. Louro, M. Fernandes, R. Schwarz, G. Lavareda, and C. N. Carvalho, Vacuum, Vol. 82, Issue 12, 8 August (2008), pp: 1512-1516.

 ISBN: 978-1-61208-145-8

Acoustic Emission Sensing of Structures

Irinela Chilibon
National Institute of Research and Development for Optoelectronics, INOE-2000, 409 Atomistilor Str., P.O. MG-5, 77125, Bucharest-Magurele, Romania
e-mail: qilib@yahoo.com

Marian Mogildea and George Mogildea
Institute of Space Science, ISS
Bucharest-Magurele, Romania
e-mails: marian_mogildea@yahoo.com
georgemogildea@yahoo.com

Abstract—**This paper presents some experimental results concerning the acoustic emission (AE) of different material structures, submissive at mechanical tests. Acoustic emission signals were prevailed by AE sensor, fixed on the material surface by an electroacoustic material. The AE piezoelectric sensor realizes the mechanical to electrical energy conversion, and the output signal is displayed on the memory digital oscilloscope. By signal analysis in time and frequency one can get the attenuation coefficients, delaminating, voids, defects, into material, revealing important information about the material structure behavior at mechanical stresses. Also, we can determine the moments when the material could be cracked or irreversibly deteriorated. Therefore, one can detect the maximum acoustic emissions and predict the material failure. Experimental works provided information concerning the AE response of different type of materials (aluminum, brass and concrete) under mechanical strengths, in order to predict their behavior at maximum strengths. The information could be applied for complex construction structures, in order to prevent their breaking risks.**

Keywords-acoustic emission; AE; sensor.

I. INTRODUCTION

A critical issue in practical structural strength state monitoring is related to the capability of proper sensing systems integrated within the host structures to detect, identify, and localize damage generation, such as cracks and potential problem areas in metal pressure boundary applications while other types of Nondestructive techniques are used to provide acceptance or rejection criteria [1]. To this aim, many techniques have been proposed involving dynamic measurements such as: modal analysis, acoustic emission, and ultrasonics [2].

Acoustic Emission techniques have been used in the field for the testing of metal and composite pressure vessels and piping. Nondestructive techniques were not accepted long time for the testing of bridges, and other components of the infrastructure because of two primary reasons: the difficulty in separating valid signals from extraneous noise and the inability of the AE technique to determine the size of the crack [1].

It results in the need for the development of advanced and effective inspection techniques. Thus, AE techniques draw a great attention to diagnostic applications and in material testing.

Acoustic Emission inspection is a powerful aid to materials testing and the study of deformation, fracture and corrosion. It gives an immediate indication of the response and behavior of materials under stress, intimately connected with strength, damage, fracture and failure [3].

Acoustic emissions (AEs) are the stress waves produced by the sudden internal stress redistribution of the materials caused by the changes in the internal structure. Possible causes of the internal-structure changes are crack initiation and growth, crack opening and closure, dislocation movement, twinning, and phase transformation in monolithic materials and fiber breakage and fiber-matrix debonding in composites. Most of the sources of AEs are damage-related, the detection of these emissions are commonly used to predict material failure. The Acoustic Emission method can be successfully applied for monitor the integrity of piping systems, and to aid in maintenance planning.

AE technology involves the use of ultrasonic transducers (20 kHz - 1 MHz) to listen for the sounds of failure occurring in materials and structures. Crack growth due to fatigue, hydrogen embrittlement, stress corrosion, and creep can be detected and located by the use of AE technology. In addition high pressure leaks can also be detected and located. AE technology is also finding wide application in the nondestructive testing for structural integrity of composite materials and structures made from composite materials. Fiber breakage, matrix cracking, and delaminating are three mechanisms that can produce AE signals when stress is applied to the material or structure.

AE sensors typically consist of a piezoelectric element on a ceramic plate inside a metal case with an electrical contact on top, insulated by epoxy. The shape, dimensions and mass of most commercial AE sensors make them unsuitable for integration into composites. In spite of extensive work with thin PVDF films (e.g. [4], [5], and [6]) there are to the best of our knowledge no commercial PVDF AE sensors available. AFCs present a number of advantages

 ISBN: 978-1-61208-145-8

in comparison with conventional AE sensors: (1) light weight, (2) flexibility (adaptable to curved surfaces), (3) anisotropic sensitivity, and (4) potential for integration into composites due to their low thickness (about 300 µm) and compatibility with polymer-matrix laminate and related manufacturing processes. Ultrasound wave propagation in materials is presented in [7].

II. USUAL AE APPLIED TECHNIQUES

Acoustic Emission (AE) techniques have been studied in civil engineering for a long time. The techniques are recently going to be more and more applied to practical applications and to be standardized in the codes. This is because the increase of aging structures and disastrous damages due to recent earthquakes urgently demand for maintenance and retrofit of civil structures in service for example.

Crack initiation can be determined by the appearance of the AE signal at low stretch stress levels. After the crack advent, the AE signals around the zero stress were thought to be caused by crack-face grinding when the cracks were closed.

2.1 Wireless Monitoring Techniques Based on MEMS

Existing monitoring systems use traditional wired sensor technologies and several other devices that are time consuming to install and relatively expensive (compared to the value of the structure). Typically they are using a large number of sensors (i. e. more than ten) which are connected through long cables and will therefore be installed only on a few structures. A wireless monitoring system with MEMS (Micro-Electro-Mechanical-Systems) could reduce these costs significantly [8]. MEMS are small integrated devices or systems combining electrical and mechanical components that could be produced. The principle of such a system is shown in the scheme given in Figure 1.

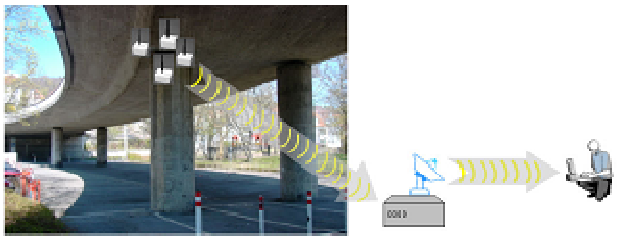

Figure 1. Scheme for wireless sensing of structures using radio frequency transmission techniques and MEMS [8].

2.2 Motes

Monitoring systems equipped with MEMS sensors and wireless communication can reduce the costs to a small percentage of conventional monitoring systems, and will increase its field of application. For instance, due to the detailed information of the structural behavior of bridges obtained from the monitoring system, maintenance costs could also be reduced, since inspection methods can be applied more efficiently [9].

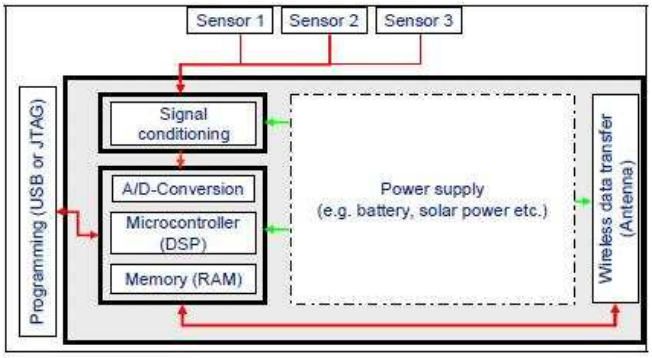

Figure 2. Principle of MEMS based *mote*; Concept of the sensor and processing board [9].

III. AE SIGNALS DURING TENSILE TESTING

Acoustic-emission activities have been shown to relate to different stages of tensile tests of materials Figure 1 presents the cumulative AE count, AE count rate, and stress versus strain relationship during a tensile test [10]. The cumulative AE count is the sum of the count of all AE events. The AE count rate is the time derivative of the AE cumulative count. The beginning portion of the linear elastic region is very quiet (i.e., low count rates and cumulative counts) or is associated with an incubation stage. The AE activity reaches its peak in the second stage right before yielding occurs. After the material yields, the AE activity decreases, but is still detectable until the material fails.

3D-Localization of acoustic emission events is a powerful tool in quantitative AE techniques. It is the basis of advanced signal interpretation and the discrimination between signal and noise. Signal-based procedures, such as: accurate 3D localization of damage sources, solutions for fault plane orientation, and moment tensor inversion, are described with respect to applications in civil engineering. More quantitative analysis of the signals is based on a 3D localization of AE sources (hypocenters) and the recordings obtained from a sensor network. For instance, using moment tensor inversion methods, the radiation pattern of acoustic emission sources and the seismic moment (as an equivalent to the emitted energy), as well as the type (Mode I, Mode II, and mixed modes) and orientation of the cracks, can be determined [11].

Fatigue tests are usually long-term experiments. A great amount of signals, including the noises from the load-chain, are detected by the sensitive AE sensors during fatigue testing. According to the time sequence for the guard and main sensors to receive the signals, the signals originating from outside the test section can be detected and discarded. Crack initiation was determined by the first appearance of the AE signal at low stress levels. This stage has a steady-state dislocation motion that will eventually result in microvoids and initiate microcracks. The third stage is an AE-active stage. In this stage, cracks start to grow and propagate. Many of the AE signals in the third stage can come from the crack-tip plastic deformation, fracture of hard inclusions, microcrack coalescence, transgranular cleavage, and fracture along grain boundaries.

 ISBN: 978-1-61208-145-8

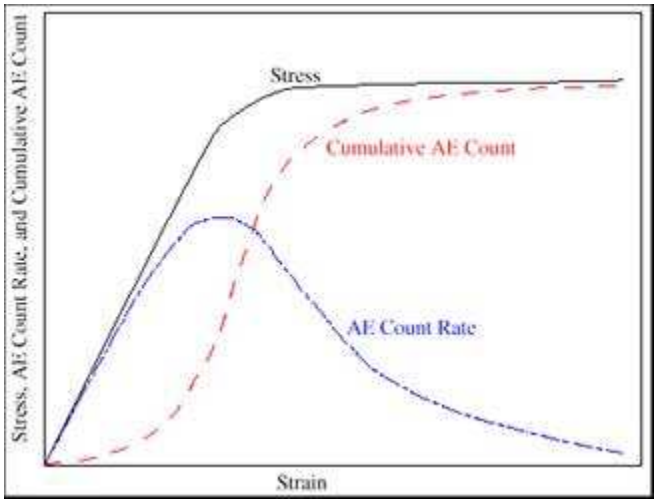

Figure 3. A tensile stress-strain curve and AE signals [10].

As example [10], the maximum stress was 644.8 MPa with a ratio of 0.05, where:

$$R = \frac{\sigma_{\min}}{\sigma_{\max}} \quad (1)$$

σ_{min} and σ_{max} are the applied minimum and maximum stresses, respectively. The frequency was 5 Hz initially to study crack-initiation behavior.

Tabel 1 presents the main mechanical and thermal properties of some construction materials.

TABLE I. MECHANICAL AND THERMAL PROPERTIES OF DIFFRENT CONSTRUCTION MATERIALS

Material	*Longitudinal elasticity module, E, daN/cm²*	*Transversal elasticity module G, daN/cm²*	*Poisson Coefficient μ*	*Thermal Dilatation Coefficient α_t*
Soft steel	$(2.0\text{-}2.15)\cdot10^6$	$(7.8\text{-}8.5)\cdot10^5$	0.24-0.28	$12\cdot10^{-6}$
Hard steel	$(2.0\text{-}2.2)\cdot10^6$	$8.5\cdot10^5$	0.25-0.29	$11.7\cdot10^{-6}$
White wrought iron	$(1.0\text{-}0.6)\cdot10^6$	$4.5\cdot10^5$	0.23-0.27	$10\cdot10^{-6}$
Tin	$0.2\cdot10^6$	$0.7\cdot10^5$	0.42	$26.7\cdot10^{-6}$
Copper	$(1.1\text{-}1.3)\cdot10^6$	$4.9\cdot10^5$	-	$16.5\cdot10^{-6}$
Bronze	$1.1\cdot10^6$	-	-	$17.5\cdot10^{-6}$
Brass	$(0.8\text{-}1.0)\cdot10^6$	$(3.5\text{-}3.7)\cdot10^5$	0.32-0.42	$18.4\cdot10^{-6}$
Brick	$(0.027\text{-}0.03)\cdot10^6$	-	-	-
Concrete strength 100-200 daN/cm²	$(0.15\text{-}0.23)\cdot10^6$	-	0.16-0.18	$(8.8\text{-}0.4)\cdot10^{-6}$
Concrete	$(0.18\text{-}0.43)\cdot10^6$	-	-	$10\cdot10^{-6}$

IV. THEORY

The acoustic emission (AE) signal can be divided into successive type signal and sporadic type signal. This type of AE signals are analyzed through the signal processor in the form of variables such as the existence of a signal generation or the shape of signal etc. excepting the signal of special case. Therefore, in the signal processor, the critical voltage is set up for the signal processing, and the acoustic emission would be regarded to be generated if it exceeds the critical voltage.

As shown in Figure 4, the displacement of one point x in the external domain by the surface traction or the body force (volume stress) at the micro area is expressed as follows using the Green function [12].

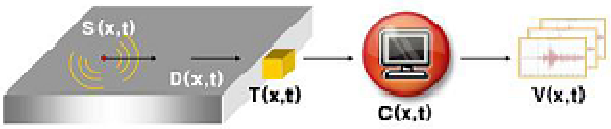

Figure 4. Transfer function [12].

$$u_i(x,t) = \int dx' \int G_{ij,k'}(x,x',t-t')\Delta\sigma_{jk}(x',t')dt' - \int dS'_{k'} \int G_{ij,k'}(x,x',t-t')\Delta t_{jk}(x',t')dt' \quad (2)$$

It is usually called transfer function. This function consists of many sub transfer functions as follows.

$$G(x,t) = D(x,t) * T(x,t) * C(x,t) \quad (3)$$

It can express as the convolution integral of each transfer functions by the mold (D), the converter (T) and computer (C).

On the other hand, the output V (x, t) that is to be visibly recognized is expressed as a function of G and S as follows.

$$V(x,t) = G(x,t) * S(x,t) \quad (4)$$

As remark, the direction of force is applied vertical to the surface of the test piece.

V. EXPERIMENTAL WORK

The experimental works were made by an original set-up, composed by: FPZ 10 Universal Testing Machine, Fritz Heckert, Germany (Figure 5), an AE piezoelectric sensor (200 kHz bandwidth), and TDS 3034B, Tektronix memory digital oscilloscope for the sensor output displaying.

The metallic samples (aluminum and brass pipes) were fasten into the mechanical testing machine at both ends, the piezoelectric sensor was fixed on the sample surface by mediation of Vaseline medium for a maximum electroacoustic coupling between the sensor and sample.

 ISBN: 978-1-61208-145-8

The metallic samples were precisely stretched by the mechanical testing machine till their breaking. The AE signals from the sensor output were continuous displayed and memorized on the oscilloscope.

Figure 5. FPZ 10 Universal mechanical testing machine.

Figure 6 presents the AE sensor catch on the sample surface. The AE piezoelectric sensor realizes the mechanical - electrical conversion, revealing the AE signals from the metallic samples, submissive at mechanical stretches by the testing machine.

Figure 6. AE sensor is fixed with a spring instead of the dead weight used for the tests.

The main technical characteristics of some AE piezoelectric sensors are presented into the Table 2

TABLE II. PROPERTIES OF SOME AE PIEZOELECTRIC SENSORS

Properties	*AE sensor characteristics*
Outer dimension	Diameter: 20.5 mm x 14 mm
Effective sensing area	Around 230 mm^2
Total mass (g)	12
Piezoelectric mass (g)	5 – 6
Capacitance (pF)	350
Piezoelectric charge coefficient d_{31} (10^{-12} m/V)	-150
Frequency range (kHz)	100 - 450

Figure 7 presents the aluminum pipe structure after its breaking produced by the stretch procedure.

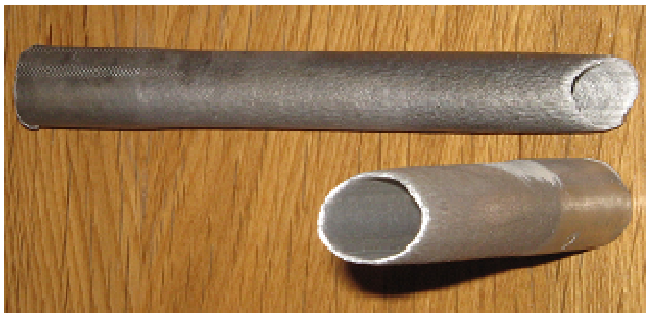

Figure 7. Broken aluminum pipe after stretching.

Figure 8 presents the prevailed AE signals from the sensor output in the breaking moment of aluminum pipe at the maximum stretch.

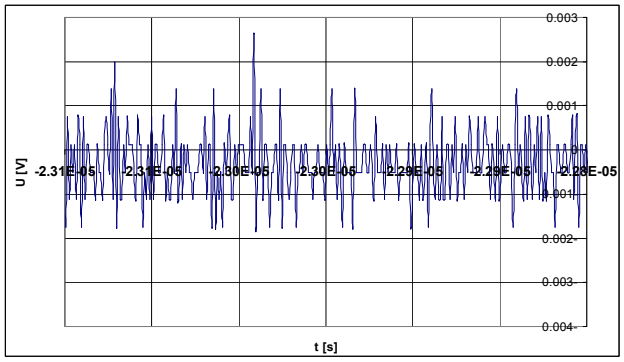

Figure 8. AE time spectra for aluminum pipe (ϕ 20x150 mm, and thickness 1mm).

Figure 9 presents a brass pipe structure after its breaking produced by the stretch procedure.

Figure 9. Brass pipe after stretch cracking (ϕ10x150 mm and 0.5 mm thickness).

Figures 10 and 11 present prevailed AE signals by the sensor in the breaking moment of the brass pipe at the maximum stretch. Therefore, one can detect these emissions and predict the material failure.

 ISBN: 978-1-61208-145-8

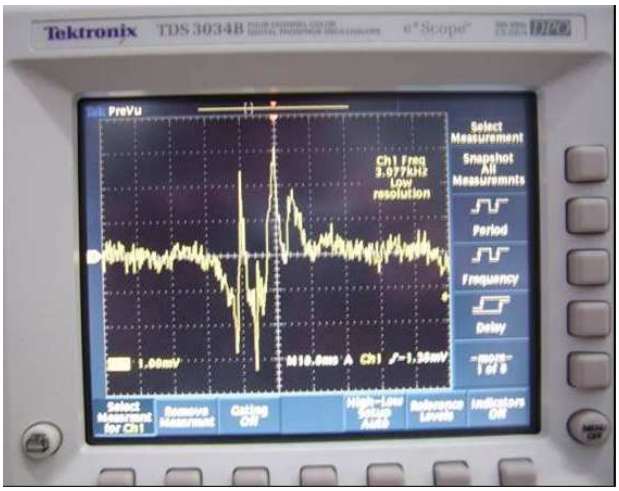

Figure 10. AE time spectra for brass pipe at mechanical stretch, at the oscilloscope display.

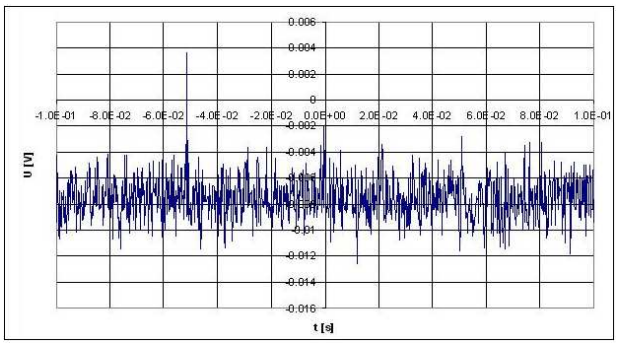

Figure 11. Detailed AE time spectra for brass pipe at mechanical stretch.

Figure 12 presents the AE signals prevailed by the sensor in the breaking moment of concrete sample at the maximum stretch. Therefore, one can detect these acoustic emissions and predict the material failure.

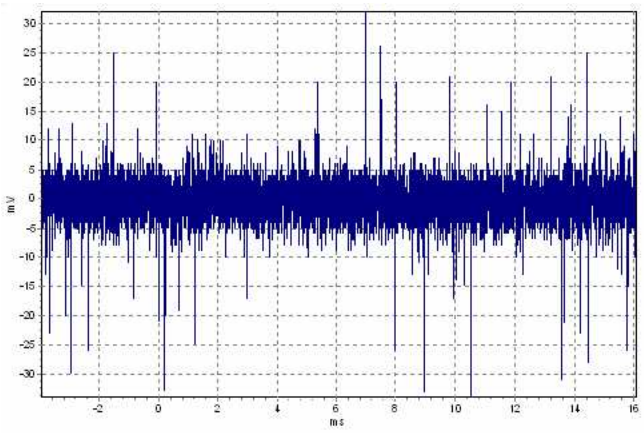

Figure 12. AE signals from a concrete sample at breaking point at mechanical stretch.

Crack initiation was determined by the appearance of the AE signal at low stretch stress levels. After the crack initiated, the AE signals around the zero stress were thought to be caused by crack-face grinding when the cracks were closed.

Further, the AE signals cached by the sensor could be stocked on the digital memory oscilloscope and then analyzed in time and frequency, in order to determine the relevant material structure characteristics, such as: the attenuation coefficients, delaminating, voids, defects, etc.

Also, by signal graphic representation analysis in time and frequency can be determined the attenuation coefficient of the pulse into material. In the literature we can find specific tables with experimental material parameter values for different type of metallic samples and structures.

By studding the AE signals, one can detect the acoustic emissions and predict the material failure. Each material type, structure and geometry has particular AE impress. As result, specific base data could be made and applied for complex structures, and architectures such as: metallic beams, crossbeam, bridges, buildings, etc.

VI. CONCLUSION

By these experimental works one can determine practical information concerning the AE response of different type of materials (aluminum, brass and concrete) at mechanical strength and predict their behavior and maximum strengths.

The AE signals prevailed by the sensor in the breaking moment of samples at the maximum stretch, could offer important data, in order to detect the AE emissions, predict the material failure and cracks initiation into material.

In the future research it is provided to realize a large data base, concerning the various materials samples behavior at mechanical stretches and their AE signals analysis (shape, amplitude, frequency, bandwidth, etc.). So, it can obtain practical information about AE of monitories complex construction structures, such as: bridges, containers fulfilled with liquids, etc., in order to prevent the possible risks and catastrophes, their breaking due to hostile environmental (shocks, long time vibrations, bending, temperature differences, etc.).

ACKNOWLEDGMENT

This work was supported in part by the National Authority for Scientific Research (ANCS), the Executive Agency for Higher Education and RDI Funding (UEFISCDI) and the Romanian National Centre of Programs Management (CNMP).

REFERENCES

[1] H.L. Dunegan, The use of plate wave analysis in acoustic emission testing to detect and measure crack growth in noisy environments, 1996 Structural Materials Technology NDE Conference, San Diego, CA February 1996.

[2] A. Cusano, P. Capoluongo, S. Campopiano, A. Cutolo, M. Giordano, F. Felli, A. Paolozzi, M. Caponero, “Experimental modal analysis of an aircraft model wing by embedded fiber Bragg grating sensors”, Sensors Journal, IEEE, Vol. 6 Issue 1, pp. 67 – 77, Feb. 2006.

 ISBN: 978-1-61208-145-8

[3] C. U. Grosse and M. Ohtsu, Acoustic Emission Testing Basics for Research - Applications in Civil Engineering, (Eds.), X, 406 p. 270 illus., Hardcover, 2008.

[4] I. Grabec, M. Platte, "A comparison of high-performance acoustic emission transducers", Sens. Actuators A: Phys, Vol. 5, No. 4, pp. 275–284, 1984.

[5] H.I. Schlaberg and J.S. Duffy, "Piezoelectric polymer composite arrays for ultrasonic medical imaging applications", Sens. Actuators A: Phys., Vol. 44, No. 2, pp. 111–117, 1994.

[6] R. Stiffler and E.G. Henneke, "The application of polyvinylidene fluoride as an acoustic emission transducer for fibrous composite materials", Mater. Evaluat., Vol. 41, No. 8, pp. 956–960, 1983.

[7] I. Chilibon and S. Velizar, "Ultrasound propagation in asphalt", B.H.V. Topping and M. Papadrakakis, (Editors), Civil-Comp Press, Stirlingshire, Scotland, paper 91, Reference CST91, 10 pages, 2008.

[8] C.U Grosse, F. Finck, J.H. Kurz, H.W. Reinhardt, "Monitoring techniques based on wireless AE sensors for large structures in civil engineering", in Proc. EWGAE 2004 symposium in Berlin, BB90, 2004, pp. 843-856.

[9] C. Grosse, S.D. Glaser, M. Krüger, "Wireless acoustic emission sensor networks for structural health monitoring in civil engineering", Proc. European Conf. on Non-Destructive Testing (ECNDT), DGZfP BB-103-CD, Berlin, Tu.1.7.3, Sept. 2006, pp. 1-8. http://www.ndt.net/article/ecndt2006/doc/Tu.1.7.3.pdf

[10] D. Fang and A. Berkovits, "Fatigue Design Model Based on Damage Mechanisms Revealed by Acoustic Emission Measurements", Trans. of ASME, 117, 1995, pp. 200–208.

[11] C.U. Grosse, H.W. Reinhardt, and F. Finck, Signal-Based Acoustic Emission Techniques in Civil Engineering, Mat. in Civ. Engrg. , Vol. 15, 274, 2003.

[12] D.H. Kim, W.K. Lee, S. W. Kim, ,"Analysis of Acoustic Emission Signal for the Detection of Defective Manufactures in Press Process", World Academy of Science, Engineering and Technology, Vol. 53, pp. 1301-1305, 2009. http://www.waset.org/journals/waset/v53/v53-210.pdf

 ISBN: 978-1-61208-145-8

Investigations on aluminum nitride thin film properties and design considerations for smart high frequency ultrasound sensors

Susan Walter, Thomas Herzog, Henning Heuer,
Fraunhofer Institute for Non-Destructive Testing,
IZFP Dresden Branch,
Dresden, Germany
Thomas.Herzog@izfp-d.fraunhofer.de

***Abstract*— Basic investigations were carried out on the usability of aluminum nitride thin films for the manufacturing of ultrasound transducers. Some design considerations were performed for different sensor designs, electrode sizes and substrate materials in this work. It could be shown that the electrode size can be smaller than 1 mm square for use as high frequency sensors. Different substrate materials are principle usable, like e.g. silicone, aluminum oxide or quartz. Additional tests showed that these sensors can also be used for high temperature application up to 200 °C. The reason is the very good temperature resistance of the AlN thin films. The sensor design was varied for these investigations and simulations based on a MASON model assisted the material considerations.**

Keywords: ultrasonic high frequency sensor; Aluminium nitride thin film;

I. INTRODUCTION

Ultrasonic microscopes are frequently used for the non-destructive evaluation of micro-technical components and structures; because of their versatility and efficiency. The frequency of an ultrasonic test system defines the attainable resolution and the penetration depth into a material. The higher the frequency is, the better is the resolution and the smaller is the penetration depth. The efficiency of conventional microscopes can be enhanced by a combination with high frequency phased array (PA) techniques. With the use of segmented transducers (~ into pixels divided sensors), it is possible to evaluate the whole volumes of specimen in 3 dimensions. The advantage is that the ultrasonic transducer does not need to be manipulated mechanically by a scanner. The shape and the sound beam direction can be controlled on a large scale since each of the array elements can be pulsed with appropriate time delays. At present PA ultrasonic sensors with working frequencies up to 20 MHz are available, but frequencies above 50 MHz are necessary for the applications that require a high resolution. Therefore new high frequency PA sensors need to be developed.

A promising alternative piezoelectric material is aluminum nitride (AlN). Aluminum nitride is a piezoelectric but not ferroelectric material with a Wurtzite crystal structure. Compared to the widely used ferroelectric materials like PZT, AlN can not be electrically poled. Therefore piezoelectric activity can only be achieved with single crystals or with a polycrystalline structure with a strong crystal orientation. To achieve a thickness vibration of the sensor, a crystalline orientation in (001) direction is necessary (c-axis of the AlN crystalline structure being oriented perpendicular to the substrate surface). AlN in this condition exhibits several attractive properties that were verified in various publications (e.g. [1]) and in our own experimental work:

- Piezoelectric coupling coefficient of 20 %
- Piezoelectric constant d_{33} of about 8 pm/V
- Piezoelectric constant g_{33} of about 100 mVm/N
- High sound velocity for longitudinal waves 10700 m/s
- High dielectric strength of up to 20 MV/cm
- Low dielectric constant of 8,6
- High electrical resistivity of more than 10^{11} Ωcm
- High temperature stability (up to 1000°C)

Additionally the AlN thin film technology is compatible to CMOS technology and therefore interesting in MEMS (Microelectromechnical Systems) and MOEMS (Microoptomechanical Systems) fabrication. Recent publications show, that for these applications very thin films (below 1µm, e.g. [2]) were deposited with deposition rates between 5 nm/min [3] and 100 nm/min [4]. But until now AlN is seldom used for ultrasonic transducers, only a few groups are working on single element ultrasonic transducers for low frequencies based on membrane vibration [5] or based on thickness vibration to reach a high resonance frequency of 100 MHz [6]. Further investigation on the behaviour of thin film AlN piezoelectric sensors and design consideration need to be performed.

II. TEST SETUP AND MEASUREMENT METHODS

A simple layout was used for optimization of deposition process in previous investigations [7]. Here additionally sensor investigations were carried out for high temperature storage; and design considerations performed for different substrate materials with the same test layout. An electrode structure with 10 mm diameter was deposited on an isolated silicon wafer. An aluminium nitride film in a circle structure with a diameter of 13 mm was deposited, followed by a second aluminium electrode to fabricate the sensor and the interconnection pad on the top side as shown in Fig. 1. The aluminum electrodes all have a thickness of 150 nm. These deposition processes were carried out at Fraunhofer Institute for Electron Beam and Plasma Technology - FEP in Dresden.

 ISBN: 978-1-61208-145-8

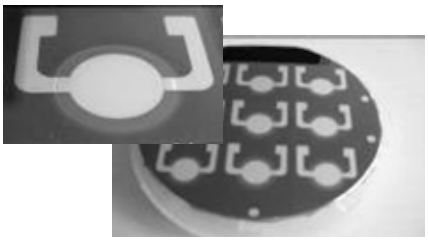

Figure 1. Ultrasonic sensors on silicon wafer

Additionally design considerations were carried out with different electrode sizes. The layer thicknesses and sequence are same as we used in the first experiments. Only the layout was changed as can be seen in fig. 2. The bottom electrode is a square shaped aluminum electrode with a large ground area around for a better electromagnetic shielding. On top of the bottom electrode a square shaped AlN Layer with a thickness of 10 µm and an edge length of 5 mm follows. The top electrode is also square shaped with the same edge length as the bottom electrode and a short track for the connection of the measurement tips. Sensors with edge lengths of 5 mm, 1 mm, 0.5 mm and 0.3 mm were manufactured with the optimized sputtering parameter sets on a 6" silicon wafer. The bottom electrode for the smallest electrode size of 0.3 mm was 0.5 mm to reduce effects caused by a misalignment of the masks. The optimized unipolar and bipolar deposition parameters were used for the deposition of 6" isolated silicon wafers with 17 pieces of the same geometry on each substrate.

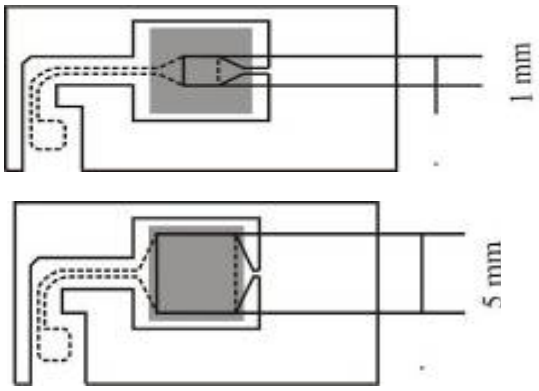

Figure 2. Layout for electrode size variation experiments with coaxial bottom electrode (full line), AlN layer (grey) and top electrode (dashed line), exemplarily for 1 mm² (left) and 25 mm² (right).

A. *Pulse Echo Measurements*

The sensor tests were performed with the pulse echo measurements too [7]. The AlN sensor served as an acoustic transmitter and receiver. The pulser and receiver DPR 500 (JSR Ultrasonics) was used to excite an acoustic sound wave. The ultrasound wave propagates through the substrate, is reflected at the interface substrate-air and travels back to the AlN layer. There the ultrasound wave excites a voltage signal which can be measured and evaluated.

The maximum amplitude of the received voltage signal was used to evaluate the AlN film quality depending on the deposition parameters. The measured voltage values were calculated to absolute voltage values without gain for a better comparability. The fig. 3 shows a typical time response with multiple back wall echoes. To avoid an influence of the sending signal, we did not evaluate the first back wall echo but the fourth.

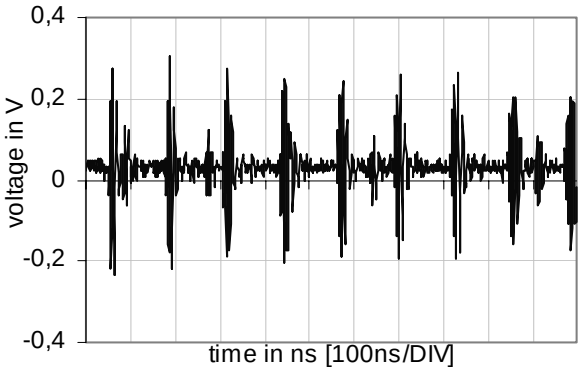

Figure 3. Echo pulse signal from silicon back wall reflection

B. *Measurements of piezoelectric constant d_{33}*

The piezoelectric charge constant d_{33} was determined with a conventional Berlincourt-Meter (Piezotest PM300). The samples were clamped and loaded with an alternating force. The generated electric charge was compared to the value of a reference sample to obtain the piezoelectric charge constant. The measurements were carried out by applying an alternating force of 0.25 N and a frequency of 110 Hz; see [7]. Additional test specimen with new substrate materials were created after the optimization of the AlN thin film deposition process. Different substrate materials, like aluminium oxide, glass, quartz and aluminium were investigated. This is important for the sensor design considerations, because different substrate materials have different mechanical and acoustic properties, which have an influence on the thin film ultrasonic transducers. The mechanical clamping of the thin film to the substrate plays an important role as well as the geometry dimensions. The relative big thin film sensor area in versus to the thin film thickness has a second influence on the d_{33} measurement with this method. This takes effect as a second clamping.

C. *Modelling of sensor design for single element transducer*

The basis for the simulation of different thin film sensor designs and substrate materials was a MASON model. This model was created by electrical engineering values for the piezo-effect. The Model in these investigations was build in PSpice and consists of a transmission line driven by an ideal transformer (fig. 4). The single element transducer in this

 ISBN: 978-1-61208-145-8

transmission line was described by modelling of all layer materials, and therefore the material properties needed to be known.

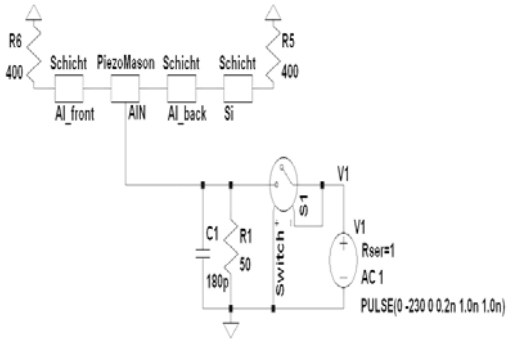

Figure 4. PSpice-Model of a AlN single element transducer

D. Measurements of warping with Laser vibrometer

The warping vibration of the sensor thin films of the single transducer was determined with an ultra high frequency Laser vibrometer UHF-120. The investigation took part at Polytec laboratories. This measurement system is able to detect mechanical vibration up to 1.2 GHz. Other conventional Laser vibrometers are only working in the frequency range of 20 MHz and couldn't be used here.

A sinusoidal voltage with an amplitude of +/- 3 V was applied to the single element transducers to realize a continuously excitation and vibration. The mechanical warping of the thin film elements was measured in z-direction in a range of some 10 pm. Afterwards the exciting frequency was raised continuously to detect the resonance frequencies of the thin film sensors. Additionally the laser worked in a scanning mode to evaluate the vibration pattern of the complete sensor surface.

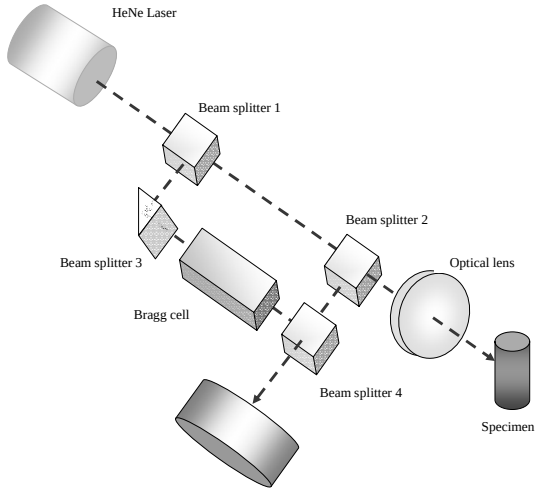

Figure 5. Principle of Laser vibrometer

III. EXPERIMENTS AND RESULTS

A. Substrate variation and temperature storage

An acceptable piezoelectric activity could be proofed on a variety of substrate materials, which are common in electronics manufacturing, using sputtering parameter sets found in earlier investigations [7]. The d_{33}-meter can be used for a very fast estimation of the thin film quality for AlN sensors with the same substrate material and film thickness (see Fig.).

The measured value d_{33} is not the actual d_{33} value. This follows from the mentioned clamping of the thin film transducer on the substrate. During the testing with the d_{33}-meter the sample should only be loaded by the force head with a stress in thickness direction, which means parallel to the crystal orientation to obtain an unaffected d_{33} value.

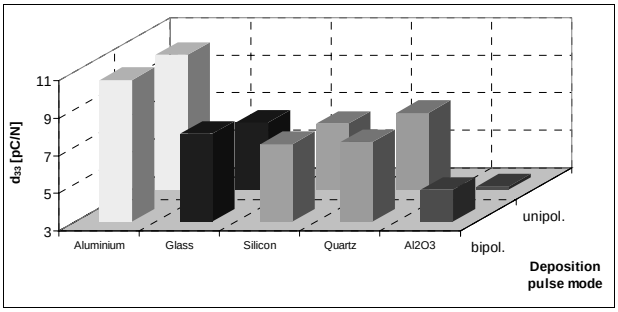

Figure 6. Results of d_{33} constants for AlN sensors deposited on different substrates

In this case an additional stress in planar direction is induced, because of the clamping of the thin film on the substrate and because of the very low ratio of film thickness to diameter. Therefore the measured d_{33} value is lower than the true value and depends on the Poisson ratio of the substrate material. The lower the Poison ratio of the substrate is, the lower is the measured d_{33} value. The rather hard materials which have a lower Poisson ratio and a lower elongation coefficient (e.g. 2.0 for silicon and 23.0 for aluminium α in [10^{-6}/K]), show also lower d_{33} measurement results. This relationship can be seen in fig.6. These results are similar for both deposition processes.

Additionally the sensors were stored at high temperatures to evaluate the influence on the piezoelectric properties of the AlN and the substrate. The maximum signal voltages of the pulse echo measurements of all sensors were obtained, but a direct comparison was not possible because of the different substrate thicknesses and acoustical damping coefficients. Monocrystalline silicon has a much lower damping coefficient compared to the other substrate materials and therefore the maximum voltage received is much higher. For all materials it is obvious, that the temperature storage at 200°C had no significant influence.

 ISBN: 978-1-61208-145-8

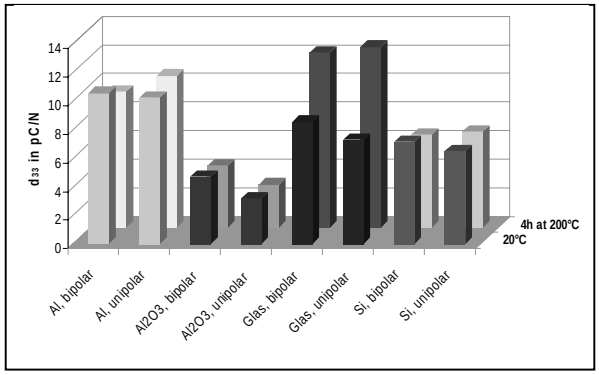

Figure 7. Piezoelectric charge constant of AlN thin film before and after temperature storage

For aluminium, aluminium oxide and silicon no change in the d$_{33}$ value could be observed, but the d$_{33}$ value of glass seemed to be much higher. Due to the fact, that there was no change in the measured back wall echo amplitude, it can be assumed that this effect is not caused by a change of the AlN properties, but by a change of the glass structure.

B. *Laser vibration measurements*

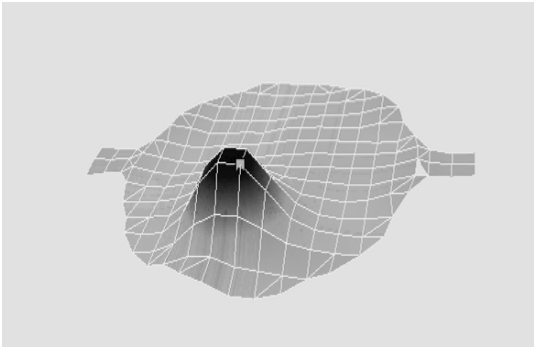

Figure 8. Vibration style of a thin film sensor at 128 MHz with max. z-warping of 11 pm

The figure 8 shows an example of the resonance behaviour of a thin film sensor at 128 MHz, which is nearly the lambda/4 vibration. A mechanical z-warping of the AlN thin film sensors by exciting with an electrical voltage could be detected with these Laser measurements.

The result shows a small displacement of the centre of warping vibrations from the sensor midpoint. The reason of this behaviour can be explained by the sensor geometry and the additional warping of the silicon substrate. This was an excellent test for investigating different sensor electrode designs and substrate materials in the future.

C. *Simulation results*

The influence of typical materials parameters can be calculated and the results compared to the pulse-echo measurements with the simulation of thin film layers by the MASON model. Therefore it is necessary to use the exact geometries, density, acoustic wave velocity and piezoelectric charge constants, e.g. to compare the real measurements with the simulation results. In the fig. below can be seen a simulated back wall echo signal with a silicon substrate of 500 micron thickness and a transducer geometry like mentioned above.

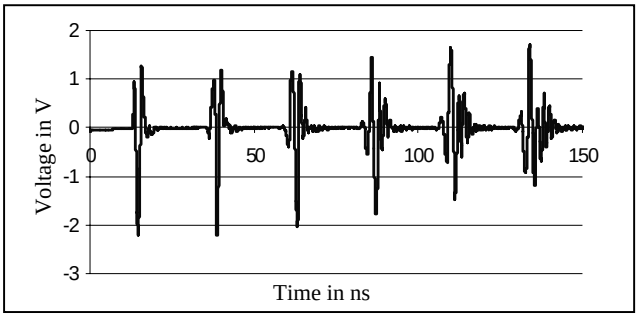

Figure 9. Simulated back wall echo from silicon substrate

D. *Electrode Size Variation*

The variation showed a detectable reflected ultrasound wave for all electrode sizes. Sensors with the smallest electrode size and deposited with the bipolar mode could not be used for measurements. For these sensors a misalignment of the masks caused short circuits between top electrode and ground layer.

The overview of the measured maximum signal amplitudes is shown in fig. 10. For both parameter sets the electrodes with 1 mm² showed the highest signal amplitude. All measurements were done with a conventional pulser-receiver with an input impedance of 50 Ω without additional impedance matching of the sensors. The impedance of the sensors with an electrode area of 1 mm² fits best to the characteristic impedance of the measurement cables used and the input impedance of the hardware. The reflection coefficient for these sensors is much lower than for the sensors with other geometries. The matching of the electric impedances, the sensor size and the film properties influence the maximum signal amplitude. Therefore there is no direct dependency visible between the maximum signal amplitude and the electrode area. But we could prove that it is possible to send and receive ultrasound waves with very small electrodes, which is important for an application of these films in phased array ultrasound transducers.

 ISBN: 978-1-61208-145-8

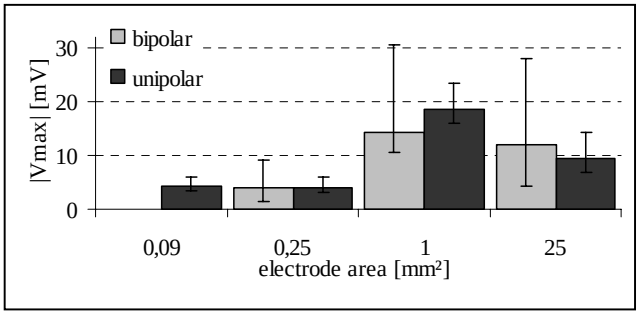

Figure 10. Maximum amplitude |Vmax| of the 4th back wall echo without additional gain for square shaped electrodes with edge lengths of 0.3mm, 0.5 mm, 1 mm and 5 mm.

The variation of the mean values for the unipolar mode is between 7.5 % for the 1 mm² electrodes and 15.6 % for the 25 mm² electrodes. The variation of the values for the bipolar mode is higher. It varies between 15.7 % for the 0.25 mm² electrodes and 21.5 % for the 25 mm² electrodes.

Fig. 11 shows the single values for the measured maximum amplitude of the different sensors for both deposition parameter sets. A dependency between maximum amplitude and sensor position on the substrate could not be found. Therefore a misalignment of the masks (e.g. offset or rotation) could not be the main reason for the higher scattering with the bipolar deposition mode.

Further there was no connection between a low amplitude and the position of the sensor that was similar on all substrates. Thus a systematic variation of the film properties or crystal structure caused by the deposition process could be excluded.

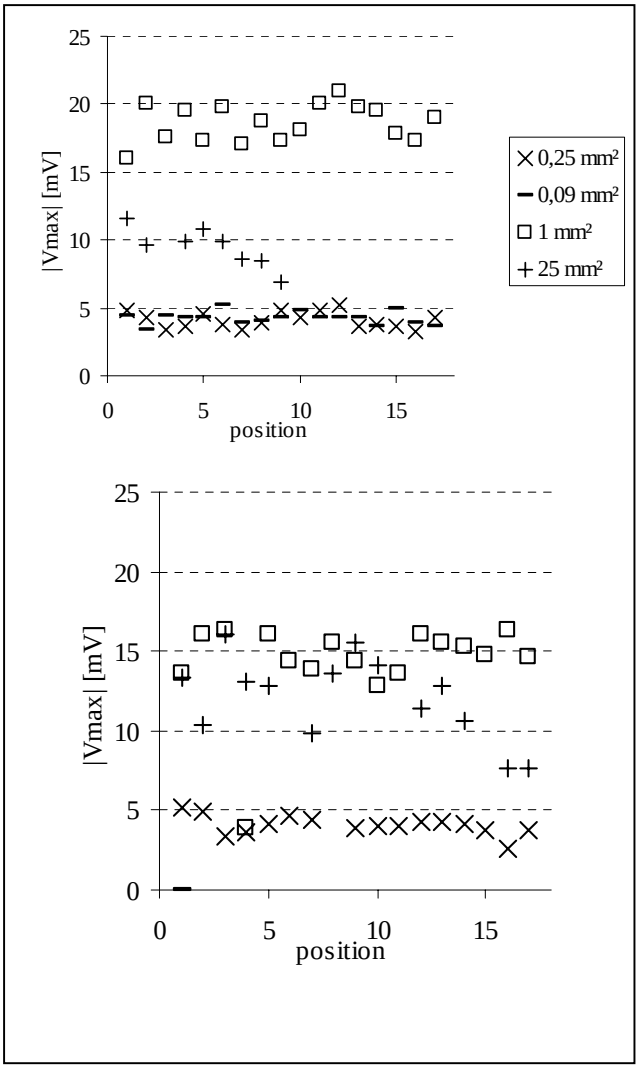

Figure 11. Maximum amplitude |Vmax| of the 4th back wall echo without additional gain for square shaped electrodes against sensor position on the silicon substrate. Each electrode area was sputtered with unipolar (top) and bipolar (bottom) deposition mode.

IV. CONCLUSION AND VISION

Basic investigations were carried out for different ultrasonic thin film AlN sensor designs, electrode sizes and substrate materials. It could be shown that the electrode size can be smaller than 1 mm square for use as high frequency sensors. Additionally test of different substrate materials have shown, that this sensor substrates can also be use in higher temperature application up to 200 °C. The reason is the very good temperature resistance of the AlN thin film transducers. The sensor design was varied for these investigations and simulations of layer thicknesses based on a MASON model have assisted the material considerations. Different substrate materials are principle usable, like e.g. silicone, aluminum oxide or quartz.

 ISBN: 978-1-61208-145-8

The development of thin film based ultrasonic sensors should enhance the application range of ultrasonic microscopes. Especially the non-destructive evaluation becomes more and more important for micro-technical components, heterogeneous structures, new materials like reinforced carbon fiber composites and thin film components in the flat screens or solar cells. Today these components were investigated with the ultrasonic microscope and mechanical scanning of single transducer during the components are placed in a liquid bath. The ultrasonic microscope is therefore very sensitive in case of delaminations, flaws, pores, cracks and gives important information about the consistence and quality of a product. The evaluations were carried out with single element transducer and frequencies from 5 MHz up to 200 MHz. The measurement time is relative long caused by the necessary mechanical scanning and the lateral resolution limited by the scanner precision. For the scanning in z-direction also a parallel use of 2 to 4 single transducers focusing in different depth are necessary. With the use of phased array sensors working in higher frequency range then today available, this technique will become more effective. The vision of the project idea is the development and demonstration of a new ultrasonic sensor test system with high frequency phased array transducer for the evaluation of complex three-dimensional components, structures or medical Applications. Therefore a new phased array sensor has to be developed on the basis of piezoelectric thin films. A demonstrator working in a frequency range above 50 MHz in phased array technique with multi-channel electronic will be created in further investigations.

ACKNOWLEDGEMENTS

This work has been partially supported by a Grant-in-Aid for Technology Funding by the European Regional Development Fund (ERDF) 2007-2013 and the State of Saxony as well as by Fraunhofer-Gesellschaft. Many thanks also to Fraunhofer Institute for Electron Beam and Plasma Technology FEP in Dresden for the deposition processes and micro analyses by SEM and XRD, also to Polytec GmbH for the Laser vibrometer measurements.

REFERENCES

[1] Patel, N.D., Nicholson, P.S., “High Frequency, High Temperature Ultrasonic Transducers”, NDT International, Volume 23, Number 5, 262-266 (1990)

[2] Conrad, H., Schmid, J. U., Pufe, W., Zimmer, F., Sandner, T., Schenk, H., Lakner H., “Aluminum Nitride – A promising and Full CMOS Compatible Piezoelectric Material for MOEMS Applications”, Smart Sensors and Actuators, Proc. of SPIE, Vol. 7362, (2009)

[3] Akiyama, M., Nagao, K., Ueno, N., Tateyama, H., Yamada, T., “Influence of Metal Electrodes on Crystal Orientation of Aluminum Nitride Thin Films”, Vacuum, Vol. 47, 699-708 (2004)

[4] Iborra, E., Clement, M., Olivares, J., González-Castilla, S., Sangrador, J., Rimmer, N., Rastogi, A., Ivira, B., Reinhardt, A., “BAW Resonators Based on AlN with Ir Electrodes for Digital Wireless Transmissions”, 2008 IEEE International Ultrasonics Symposium Proceedings, 2189-2192 (2008)

[5] Valbin, L., Sevely, L., “Piezoelectric Aluminum Nitride Thin Film for Ultrasonic Transducers”, MEMS Components and Applications for Industry, Automobiles, Aerospace and Communication, Proceedings of SPIE, Vol. 4559, 95-102 (2001)

[6] Martin, P..M., Good, M.S., Johnston, J.W., Posakony, G.J., Bond, L.J., Crawford, S.L., “Piezoelectric Films for 100MHz Ultrasonic Transducers”, Thin Solid Films, Vol. 379, 253-258 (2000)

[7] Bartzsch, H, Gittner, M., Gloess, D., Frach, P., Herzog, T., Walter, S., Heuer, H., “Properties of piezoelectric AlN layers deposited by reactive pulse magnetron sputtering”, Proceedings of the 2011 Technical Conference of the Society of Vacuum Coaters, 16-31 April 2011 (to be published)

 ISBN: 978-1-61208-145-8

Reactive pulse magnetron sputtering for deposition of piezoelectric AlN layers

D. Glöß, H. Bartzsch, M. Gittner, P. Frach
Fraunhofer-Institute for Electron Beam and Plasma Technology (FEP),
Winterbergstr. 28, 01277 Dresden, Germany

e-mail: Daniel.Gloess@fep.fraunhofer.de

T. Herzog, S. Walter, H. Heuer
Fraunhofer Institute for Non-Destructive Testing, Dresden Branch (IZFP-D),
Maria-Reiche-Straße 2, 01109 Dresden, Germany

e-mail: Thomas.Herzog@izfp-d.fraunhofer.de

Reactive pulse magnetron sputtering of Al targets in a gas mixture of Argon and Nitrogen allows the deposition of AlN layers at high deposition rates of up to 200 nm/min. In the reported experiments films were deposited AlN onto unheated substrates with a thickness of typically 10 µm. Deposited films have been characterized for a variety of layer properties using e.g. XRD, SEM, profilometry, weighting and piezoelectric measurements regarding crystalline structure and orientation, surface morphology, density, film stress and piezoelectric coefficient d_{33}. The characterized AlN films can be classified into 2 groups. The first group shows a nearly pure 001 orientation of the crystalline structure, an undisturbed surface morphology, a high density and a very high piezoelectric coefficient d_{33} of up to 7.2 pm/V on silicon substrate. The second group exhibits a dominating but not pure 001 orientation, disturbances in the surface morphology, a slightly lower density and a piezoelectric coefficient close to zero. The range of the process parameters pulse mode, pressure, sputtering power and reactive working point to achieve the layers of the first group is very narrow. Surprisingly films with high piezoelectric constant can be obtained both by strong and moderate particle bombardment during deposition using adapted parameter sets. The suitability for the intended application in high frequency ultrasonic phased array sensors systems is investigated using pulse echo measurements.

Keywords: Reactive pulse magnetron sputtering, AlN, Piezoelectric layers, Ultrasound

I. INTRODUCTION

New 3-dimensional integrated electronic devices, next generations of textured materials like carbon fiber reinforces polymers (CFRP) and complex multilayered devices like solar cells require new approaches for non destructive evaluation techniques. One area of research and development are high frequency ultrasonic phased array sensors systems that combine the performance of phased array methods with the resolution of a scanning acoustic microscope. The very high frequencies in phased array sensors require a very thin transducer thickness and cannot be realized with traditional piezoelectric materials like PZT ceramics, piezoelectric 1-3 composites or polymers like polyvinylidenfluoride (PVDF). A promising alternative piezoelectric material is aluminum nitride (AlN).

Aluminum nitride is a piezoelectric but not ferroelectric material with a Wurtzite crystal structure. Compared to the widely used ferroelectric materials like PZT, AlN cannot be electrically polarized. Therefore piezoelectric activity can only be observed in single crystals or in a polycrystalline structure with a strong crystal orientation. To achieve a thickness vibration of the sensor, a crystalline orientation in (001) direction is necessary (c-axis of the AlN crystalline structure being oriented perpendicular to the substrate surface).

In this paper, piezoelectric AlN films with a thickness of up to 10 µm were investigated. The reactive pulse magnetron sputtering process was optimized for high rate deposition of AlN thin films with strong piezoelectric properties.

II. EXPERIMENTAL

Coatings were carried out in cluster type sputter equipment using the Double Ring Magnetron DRM 400 developed at Fraunhofer FEP. This type of magnetron combines two concentric discharges allowing uniform coating of substrates with a diameter up to 200 mm [1]. Figure 1 shows the schematic of the deposition set up. Pulse powering at 50 kHz in unipolar or bipolar pulse mode was applied using the pulse unit UBS-C2 of Fraunhofer FEP and standard DC power supplies. Pure metallic aluminum targets were sputtered in a mixture of argon and oxygen as reactive gas. A closed loop control of the reactive gas inlet allowed stabilizing the process in the so-called transition mode, where stoichiometric films are deposited at high deposition rates.

Using the DRM 400, the pulse mode of the pulse magnetron sputtering process can be changed between unipolar and bipolar. In the unipolar pulse mode, a pulsed dc is applied between each of the two targets and the separate hidden anode. In the bipolar pulse mode, a voltage with alternating polarity is applied between the two targets. For the two pulse modes, the plasma properties are completely different (Table I). Thus, variation of the pulse mode allows new degree of freedom to optimize deposition process. On one hand, the unipolar pulse mode shows low thermal substrate load and it allows e.g. coating of very temperature sensitive substrates. On the other hand, in the bipolar pulse

 ISBN: 978-1-61208-145-8

mode a very intense energetic ion bombardment occurs that allows deposition of very dense films.

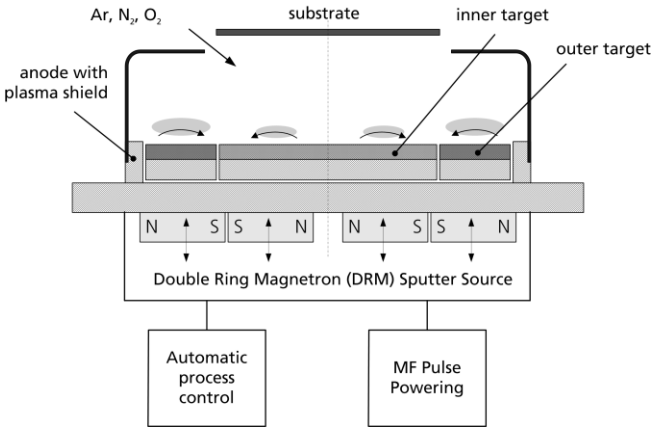

Figure 1. Deposition setup for sputter deposition

TABLE I. RESULTS OF LANGMUIR PROBE AND TEMPERATURE MEASUREMENTS, SiO_2 SPUTTERING AT 7.5KW

Pulse mode		unipolar	bipolar
Plasma density	[1/cm^3]	$1.8 \cdot 10^{10}$	$11.0 \cdot 10^{10}$
Electron temperature	[eV]	10	6
Thermal substrate load	[W/cm^2]	0.15	0.75

From literature it is known, that the sputter parameters strongly influence the piezoelectric behavior [2]. Thus, for each of the two pulse modes the power and voltage applied to the sputter target as well the pressure was varied to find optimal process parameters for the deposition of AlN layers with highest piezoelectric properties. In Table II, deposition parameters are summarized.

TABLE II. RANGE OF ALN DEPOSITION PARAMETERS

Sample		AlN-UP	AlN-BP
Pulse mode		unipolar	bipolar
Preheating		room temperature	room temperature
Power	[kW]	6…13	6…13
Pressure	[Pa]	0.15…2	0.15…2
Deposition rate	[nm/min]	100...200	80...160

For the evaluation of piezoelectric properties, a simple ultrasound transducer test layout was used. An electrode structure with 10 mm diameter was deposited on an isolated silicon wafer. An AlN film in a circle structure with a diameter of 13 mm was deposited, followed by a second aluminum electrode to fabricate the sensor and the interconnection pad on the top side. The structures were realized by using laser cutted aluminum oxide ceramic masks with a high stiffness to prevent bending when being reused. The area of the deposited sensor layer needs to be larger than the electrodes themselves, because there occur edge effects during the deposition process, which influence the piezoelectric behavior of the sensor.

III. STRUCTURAL, ELECTRICAL AND MECHANICAL PROPERTIES

The characterized AlN films can be classified into 2 groups. The first group shows a nearly pure 001 orientation of the crystalline structure, an undisturbed surface morphology, a high density and a very high piezoelectric coefficient d_{33} of up to 8 pm/V. The second group exhibits a dominating but not pure 001 orientation, disturbances in the surface morphology, a slightly lower density and a piezoelectric coefficient close to zero. The range of the process parameters pulse mode, pressure, sputtering power and reactive working point to achieve the layers of the first group is very narrow. Surprisingly films belonging to the first group with high piezoelectric constant can be obtained both by moderate and strong particle bombardment during deposition in unipolar and bipolar pulse mode respectively.

Figure 2 shows the XRD diagrams of films with nearly pure 001 orientations (002 and 004 peaks) deposited in unipolar and bipolar mode. Figure 3 shows the results of SEM investigations on these samples. The fracture in the SEM micrograph exhibits in both cases a dense microstructure. Surface morphology is rather coarse in bipolar compared to unipolar pulse mode. In Table III, most important layer properties for the two layers with highest piezoelectric properties are summarized. Films deposited in bipolar mode exhibit slightly higher values of piezoelectric coefficient, density, resistivity and breakdown field strength, but show significantly stronger compressive stress.

TABLE III. DEPOSITION PARAMETERS AND LAYER PROPERTIES FOR PIEZOELECTRIC ALN LAYERS

Sample		AlN-UP	AlN-BP
Pulse mode		Unipolar	Bipolar
Crystalline orientation (fraction)		002 (99.9%)	002 (99.9%)
Density	[g/cm3]	3.16	3.20
Break down field strength	[MV/cm]	2.3	3.1
Resistivity	[Ωcm]	$5.3 \cdot 10^{12}$	$1.2 \cdot 10^{13}$
piezoelectric charge constant d33	[pm/V]	6.5	7.2
Mechanical stress	[GPa]	-1	-2

 ISBN: 978-1-61208-145-8

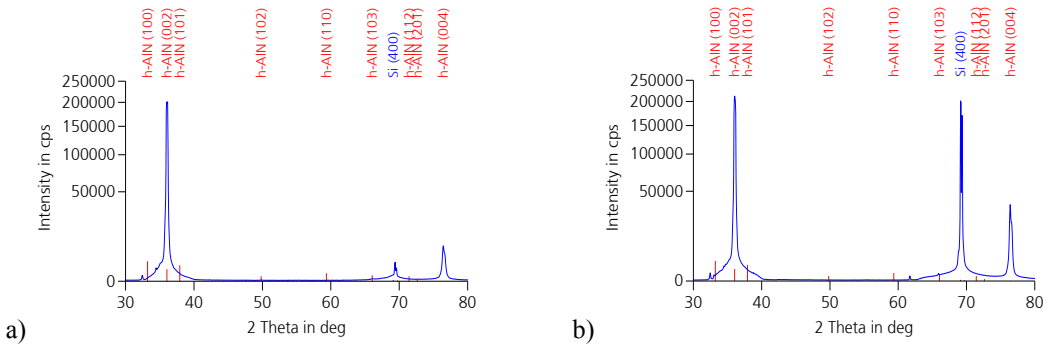

Figure 2. XRD diagrams (a: unipolar pulse mode, b: bipolar pulse mode)

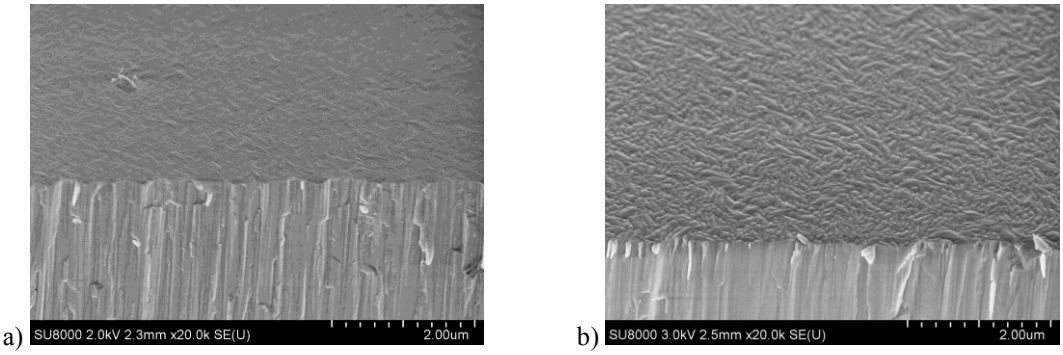

Figure 3. SEM-micrographs of AlN films, thickness 10µm (a: unipolar pulse mode, b: bipolar pulse mode)

IV. CHARACTERIZATION OF PIEZOELECTRIC PROPERTIES

The AlN thin films were used already for SAW filters, microwave filter or resonator and ultrasound transducers [3-5]. One possible new application is as sensor thin films in special phased array ultrasound transducers. For this application, the transformation of electrical energy in acoustical energy and vice versa has to be verified and quantified. Acoustical measurement in pulse echo mode were carried for each sensor to characterize the vibration behavior and the maximum signal voltage. Afterwards the electrical properties and piezoelectric charge constants were measured with a Berlincourt-Meter.

A. Pulse Echo Mode

In the pulse echo measurements the AlN sensor serves as an acoustic transmitter and receiver. The pulser and receiver DPR 500 (JSR Ultrasonics) was used to excite an acoustic sound wave. The ultrasound wave propagates through the silicon substrate, is reflected at the interface silicon-air and travels back to the AlN layer. The aluminum metal electrode with 150 nm thickness has only a very small influence and can be neglected. The mechanical vibration pulse gets transformed to an electrical signal, which can be measured.

The illustration in Figure 4 shows the schematic setup of the pulse echo measurements. All AlN sensors were connected to the pulse generator and were excited with a needle pulse at high amplitude (-143 V) and very short pulse time (~1.4 ns). The receiver was set to a gain of 36 dB and a high frequency pass filter between 30 MHz and 500 MHz was used.

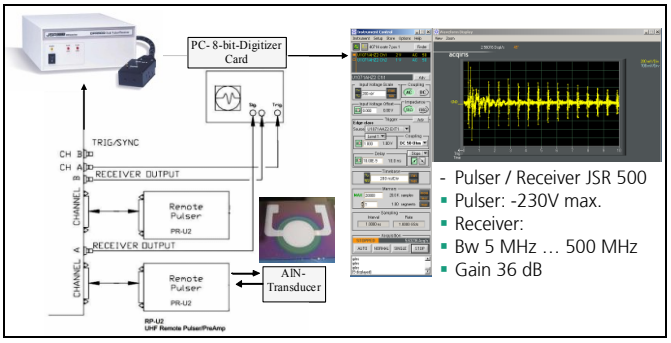

Figure 4. Measurement setup with Pulser/Receiver and PC Digitizer Card.

In the first tests the receiver output was connected to an oscilloscope, but during the evaluation of all AlN sensors the receiver signals where transmitted to a PC Digitizer Card (Aquiris U1071 A, Agilent Technologies). This hardware has an real-time sampling rate up to 2 GS/s and the amplifier response are optimized to ensure that high-frequency measurements can be made with a bandwidth (-3 dB) of maximum 1 GHz. The sending pulse after excitation could be observed, followed by multiple reflections from the silicon back wall. The distance between the multiple echoes equals the time the ultrasound longitudinal wave needs to

pass through the silicon and return back. Because of the small damping behavior of silicon, the echo pulse signal is relatively long. The evaluated sensors were deposited on silicon substrates with the same thickness and were excited with the same electrical pulse. Therefore the amplitudes of the received signals could be used to compare the sending-receiving efficiency of the different AlN transmitters indirectly.

In the right handed diagram of Figure 4, a typical time response with multiple back wall echoes is shown. To avoid an influence of the sending signal, the first back wall echo was not evaluated, but the fourth. In Figure 5, the fourth back wall echoes are shown for the optimized layers deposited in the unipolar and bipolar pulse mode as well as for a not optimized layer. Strong differences in the transmitting and receiving properties of AlN based sensor could be verified as result from the different sputtering and deposition parameters.

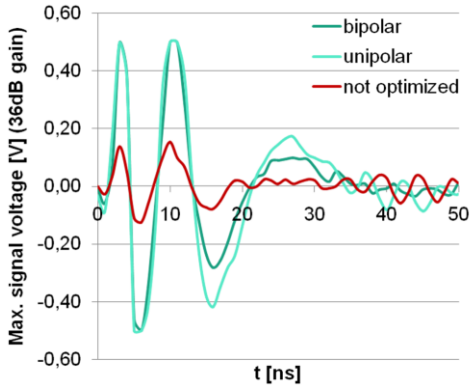

Figure 5. Examples of signal amplitudes of one back wall echo depending on the deposition parameter set.

B. *Berlincourt-Meter*

Additionally the piezoelectric charge constant (d_{33}) was measured with a Berlincourt piezometer PM 300 (PiezoTest). The samples were clamped and loaded with an alternating force. The generated electric charge was compared to the value of a reference sample to obtain the piezoelectric charge constant. The measurements were carried out by applying an alternating force of 0.25 N and a frequency of 110 Hz. Quasi-static measurements of the dissipation factor tan δ and the electric capacity of the AlN sensor layers was performed at a frequency of 1 kHz.

Measured Samples piezoelectric charge constant $d_{33}$for AlN thin films was between below 1 pC/N and 7.2 pC/N in maximum. The reasons for these differences is the different microstructure and c-axis orientation of the AlN thin films. Figure 6 shows, that the d_{33} value can be correlated to the maximum signal voltage obtained in the pulse echo measurements. Therefore the Piezometer can be used for a very fast estimation of the thin film quality for AlN sensors with the same substrate material and film thickness.

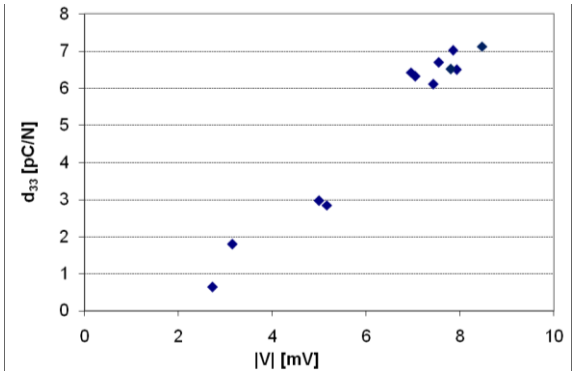

Figure 6. Correlation of maximum pulse amplitude and piezoelectric charge constants.

V. CONCLUSIONS

In this paper, the piezoelectric behavior of ultrasound sensors based on the AlN thin films was investigated. The process parameters like pulse mode during sputtering, power and process pressure strongly influenced the crystalline growth and the orientation of the thin films. As result, sensor samples with excellent c-axis orientation were obtained, that were investigated regarding their structural, electrical and mechanical properties. The electro acoustic measurements and the evaluation of the piezoelectric charge constants have shown good piezoelectric activity. But, the piezoelectric activity is depending strongly on the deposition parameters. For AlN thin films on silicon substrates, d_{33} was about 7.2 pC/N in maximum for films with nearly perfect c-axis orientation and it was below 1.0 pC/N for films with weak c-axis orientation. Also in pulse echo measurements, the AlN sensors with good c-axis orientation showed a much higher echo amplitude.

ACKNOWLEDGMENT

This work has been partially supported by a Grant-in-Aid for Technology Funding by the European Regional Development Fund (ERDF) 2007-2013 and the State of Saxony.

REFERENCES

[1] P. Frach, Chr. Gottfried, H. Bartzsch, K. Goedicke, “The double ring process module-a tool for stationary deposition of metals, insulators and reactive sputtered compounds”, Surf. Coat. Technol. 90, 1997, 75-81.

[2] E. Iborra, A. Sanz-Hervás, M. Clement, L. Vergara, J. Olivares, and J. Sangrador, “Assessment of the piezoelectric response of sputtered AlN films by X-ray diffraction”, Proc. of the IEEE Ultrasonics Symposium , 2005, pp. 1808.

[3] M.-A. Dubois, P. Muralt, “Properties of aluminum nitride thin films for piezoelectric transducers and microwave filter applications”, Appl. Phys. Lett., Vol. 74, No. 2, 17 May 1999, pp.3032.

[4] L. Valbin, L. Sevely, “Piezoelectric aluminum nitride thin film for ultrasonic transducers”, Proc. of SPIE , Vol. 4559, 2001.

[5] P.M. Martin, M.S. Good, J.W. Johnston, G.J. Posakony, L.J. Bond, S.L. Crawford, ”Piezoelectric films for 100-MHz ultrasonic transducers”, Thin Solid Films 379, 2000, p 253-258.

 ISBN: 978-1-61208-145-8

New Ultrasonic Sensor for a Simultaneous Mechanical and Electrical Characterization for the Contact Quality of a Mechanically Loaded Interface

Naima Alaoui-Ismaili, Franck Augereau, Gilles Despaux
Institut d'Electronique du Sud (IES)
Université de Montpellier 2, UMR CNRS 5214
Place Eugene Bataillon (cc082)
F-34095 Montpellier, France
e-mail: franck.augereau@univ-montp2.fr, Naima.Alaoui-ismaili@ies.univ-montp2.fr, gilles.despaux@univ-montp2.fr

***Abstract*— This ultrasonic sensor made of a copper delay line operates in dry coupling configuration to detect modifications of the contact quality between two materials under compressive stress by measuring the acoustic energy reflected on the air volumes trapped at the interface. Frequency domain analysis of the first delay line round trip echo is useful to operate with harmonics for different selectivities to the interface properties but, pressed on a unpolished copper plate, the sensitivity of acoustic reflection to contact quality vanishes for high roughness level. To overpass this limitation, measurement with the sixth delay line echo has been successfully performed to investigate the stress dependence of the contact quality between a copper plane surface and rugged industrial materials such as amorphous carbon and carbon-carbon composite. This acoustic method, associated with an electric contact resistance measure, has given a direct insight of the deformability of the interface depending on the roughness and the mechanical properties of the two materials involved in the connection. Plasticity, anelasticty effects are observed. Acoustic waves and electromagnetic ones are also not perturbed in the same way by the gas interface modification versus mechanical loading.**

Keywords - Dry coupling; contact area; contact resistance; carbon composite; acoustic reflection coefficient.

I. INTRODUCTION

The interface between two mechanically tied materials in service is generally difficult to access in a non destructive way. Yet, evaluation of the contact area can be a reliable parameter to detect the wear level of the connection and to predict its tribological behavior. For instance, in some industrial applications, electric contacts are obtained by maintaining a given mechanical load on the two materials in contact. At this interface, the electric contact resistance is controlled by current constriction effect and by the insulating properties of pollution layer. From a mechanical point of view, contact surface roughness and material elasticity are predominant factors. Echography measurement performed in dry coupling configuration may give access to these parameters [1][2]. For all these reasons, we developed a specific ultrasonic sensor to detect in a non destructive way the variations of the contact quality from the reflection fraction of ultrasounds on the gas volumes trapped within two contact surfaces as function of the applied mechanical load [3]. When the two sides of the contact are conductive ones, the electric contact resistance can be also simultaneously measured [4].

II. SENSOR PRINCIPLE AND EXPERIMENTAL CONFIGURATION

By definition, a contact is the association of two materials. The concept of our device is to use, as our sensor delay line, one of these two materials and to press it against the second one lately called "the sample". In our demonstrator, a piezoelectric cell is placed in a cavity within a metallic rod mounted on a load cell. This piezo-ceramic emits the acoustic pulse and detects the reflection at the end of the rod acting as a delay line. For simultaneous electric contact resistance measurement, a source meter is used in a 4 wires configuration: current injection and voltage measurement are done with screwed contacts on the metallic rod and clamped ones for the sample (cf. Fig 1).

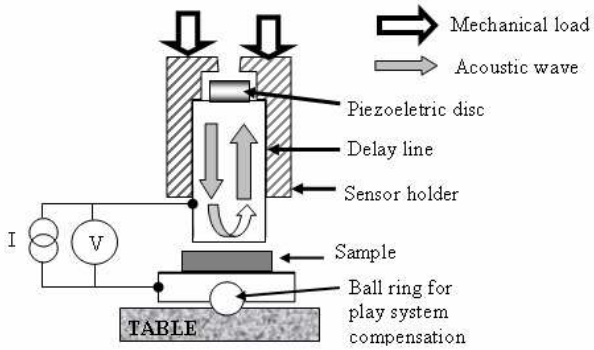

Figure 1. Sensor and experimental setup descriptions

To measure the acoustic reflection at the interface, we calculate the ratio of the reflected pulse energy to its value when the sensor is in air, since reflection coefficient between solid and gas is almost unity. This measurement is done from the first round trip echo digitized with a scope. This signal is recorded simultaneously with the corresponding value of the applied load reached during the mechanical test. To investigate the behavior of the contact interface versus mechanical stress, we chose to perform three successive loading and unloading cycles up to a compression strength of

 ISBN: 978-1-61208-145-8

4500 N. The cross-head displacement speed is maintained down to a sufficiently low level in order to deal with the time response of our different equipments. Fast Fourier Transform analysis is used to get the reflection coefficient for various frequencies using the harmonic modes of the piezoelectric cell. For our demonstrator, we used a PIC155 type piezoceramic disc with a diameter of 16 mm and a thickness of 2 mm. The outer diameter of the sensor is 30 mm defining the geometrical size of its contact area. This last dimension gives only the apparent size of the sensor contact area. Nevertheless, the real contact area may be far smaller and not accurately known especially at the interface with rough surfaces. For this reason, we chose to present on figures the applied load and not the supposed stress values.

III. APPLICATION TO CONTACT EVALUATION FOR COPPER/COPPER INTERFACE

Copper is a material commonly used for electric connections and, for some applications, this is achieved by mechanically loading or tightening two plane surfaces. To investigate this kind of connection, our sensor has been made of a copper rod pressed against a thick copper plate in order to prevent time superposition of the successive round trip echoes in this plate with the multiple delay line echoes.

In Figure 2, we present the variation of the reflection coefficient at the interface with a mirror polished sample.

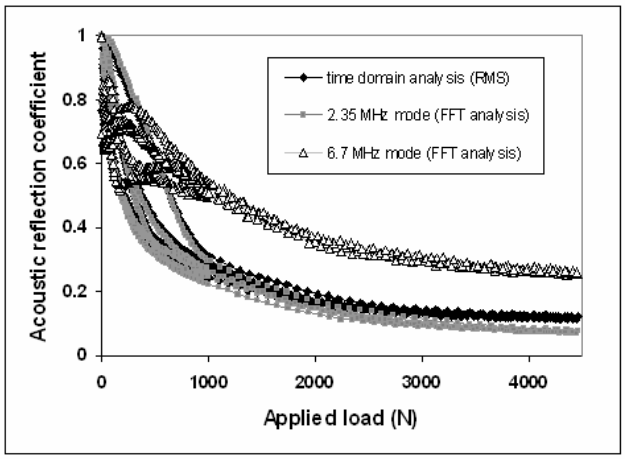

Figure 2. Evolution versus applied load of the acoustic reflection amplitude measured from time or frequency analysis for a copper mirror polished samle

For this test, the energy of the first delay line echo is measured versus applied strength. Two calculation methods are presented: the peak to peak amplitude or equivalently the RMS value of the acoustic echo and a second approach using the amplitudes of the modes (fundamental and harmonics) obtained from FFT analysis. This figure shows that the contact quality increases rapidly for mechanical load smaller than 1000 N and then reaches slowly an optimum value around 4000 N. Indeed, as strength increases, the air volumes trapped within the vicinity of the two surfaces decrease due to the compressive strain of the surface asperities and this decreases the reflection of the incident acoustic pulse. Compared to time domain analysis (RMS), information contained by FFT for the fundamental mode (2.35 MHz) is slightly more sensitive to the acoustic reflection evolution. For a given load, the acoustic reflection value measured using the first harmonic mode (6.7 MHz) is systematically higher compared to fundamental mode analysis. This is explained by wavelength consideration : the smaller the wavelength is compared to the interface defects, the worst wave propagation through the interface is.

Next, we compare the interface behavior between the previous mirror polished copper sample and the same material unpolished with a 120 grade sandpaper (cf. Figure 3). It can be noticed on the curve for the mirror polished surface that the reflection coefficient evolution is different for the first compression loading compared to the rest of the mechanical test due to surface plasticity.

For the unpolished surface, ultrasounds remain almost completely reflected because the interface is too much filled with air even for a 4500 N mechanical load.

This test demonstrates the sensitivity of this method to measure the mechanical contact quality and the roughness level detectable range.

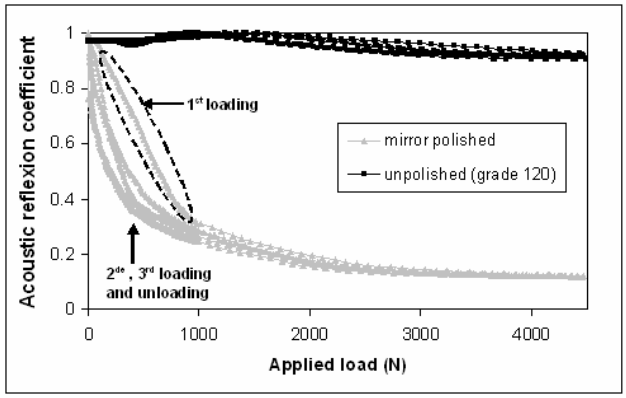

Figure 3. Effect of roughness on the evolution of the interfacial acoustic reflection for a plane copper to copper contact

With our experimental set-up, the electric contact resistance is measured simultaneously with acoustic reflection in order to give a further insight of the quality contact between the two copper surfaces. Electric contact resistance is known to depend on an electric field constriction effect due to the contact area delimited by the air volume trapped in the residual roughness. Surface pollution can also create an insulating layer strained by the mechanical load. Copper oxide has generally to be taken into account but we assumed that, using later samples with rough surfaces, their asperities should be large enough to sufficiently indent this insulating layer limiting its effect on electric measure. Despite the surface roughness created with the 120 grade sandpaper, the Figure 4 shows a fast decrease of the contact resistance down to only few fractions of milli-ohms as expected for a copper made contact. Secondly, its value is already smaller than few milli-ohms for a mechanical load of only few Newtons.

 ISBN: 978-1-61208-145-8

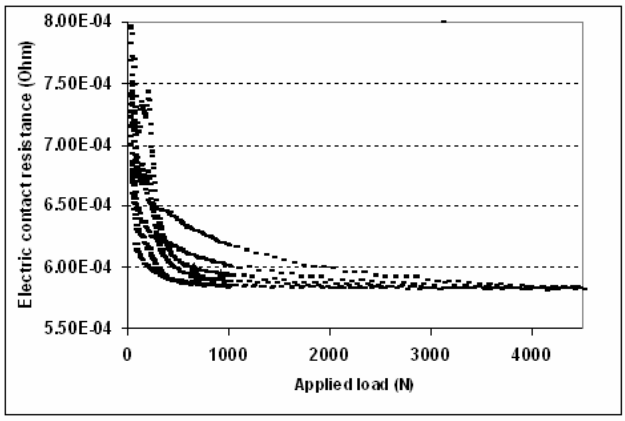

Figure 4. Evolution of the electric contact resistance versus applied load for the unpolished copper sample

For the unpolished sample, comparison of Figures 3 and 4 shows that the correct contact resistance level is achieved at very low mechanical load whereas the mechanical contact area detected by Acoustics is very poor due to the large amount of air trapped at the interface. Indeed, for electric fields, few contact spots are enough to enable a good current flow. At the opposite, ultrasonic waves can not travel through air filled surfaces and are totally reflected. So, to extend the application range of our sensor to rougher surfaces such most of industrial materials have, we have increased its sensitivity using higher order reflection coefficient measurement.

IV. ACOUSITC REFLECTION METHOD DEDICATED TO ROUGH INTERFACE CONTATC QUALITY EVALUATION

The aim of the following tests is to succeed in detecting the evolution of the contact between a plane copper surface and materials with a large roughness.

A. Samples description

For these tests, we used 30 mm wide cubes of amorphous carbon materials and plates of woven carbon-carbon composites (25 mm x 25 mm x 10 mm). These two carbon made materials have different surface states due to their fabrication process (cf. Fig. 5 a) and b)). Both materials have a large roughness with faults as deep as 200µm from topography maps obtained with a Scanning Acoustic Microscope using a 100 MHz acoustic focused lens (cf. Fig. 5 c)).

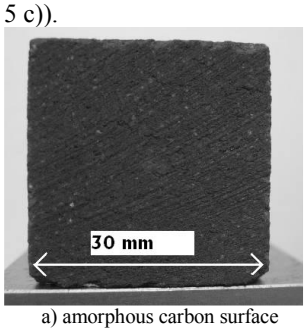

a) amorphous carbon surface

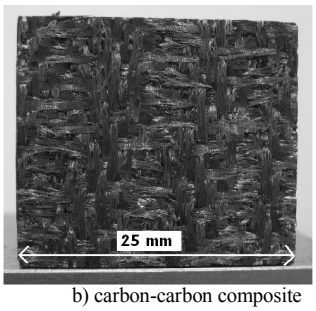

b) carbon-carbon composite

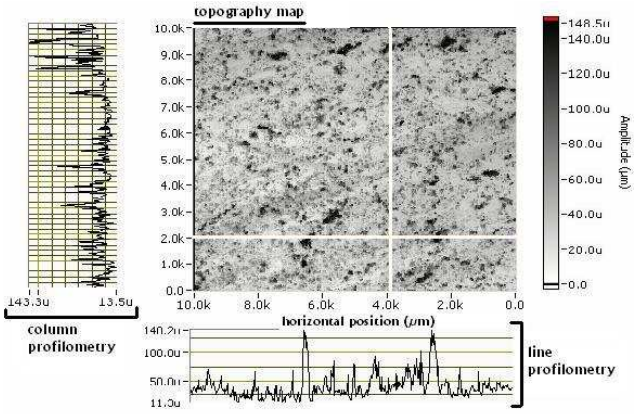

c) topography map of the amorphous carbon surface (100 MHz SAM)

Figure 5. Caracterisation and comparison of the samples topography

B. Optimisation of the sensivity to the contact quality

Thanks to material elasticity or deformability, roughness tends to decrease under compressive stress but this effect will be quite small for our carbon samples due to the large size of their faults. So, to amplify the variation of acoustic reflectance at the copper/carbon interface, we used the sixth delay line round trip echo. Its energy is measured and normalised with sensor in air configuration but this "acoustic reflected energy" is not the interface reflection coefficient.

With this method, variation of contact quality has been successfully detected for amorphous carbon and carbon-carbon composite (cf. Fig. 6), showing a better deformability of this second material. On these curves, hysteresis loops are visible. For each material, the upper parts correspond to mechanical loadings and the lower ones to unloadings. This effect is associated to anelasticity.

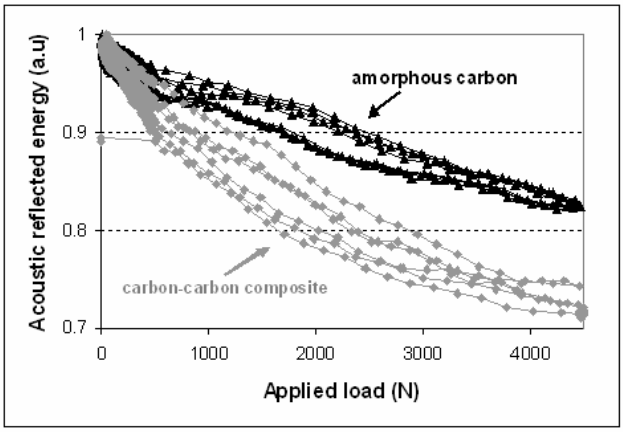

Figure 6. Detection of quality contact evolution for industrial carbon samples pressed against a mirror polished copper surface using the sixth round trip delay line echo

On these materials, contact resistance measurement reveals that the carbon-carbon composite provides the best electric contact (cf. Fig. 7). Compared to amorphous carbon, its contact resistance is smaller and is also decreasing faster.

 ISBN: 978-1-61208-145-8

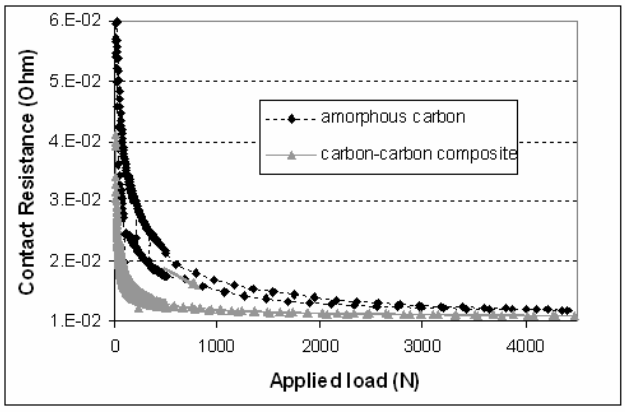

Figure 7. Electric caracterisation of the contact quality at the interface between carbon materials and a polished copper plane surface

This information could be helpful to determine for example the optimum torque to use in order to avoid cracks generation due to over loading when screw-binding is used.

C. Surface rougnhess otpimisation for amorphous carbon material

In an attempt to find the best contact conditions, we modified the roughness of the sensor by gradually unpolishing its copper surface. The figure 8 shows that unpolishing decreases the contact quality. The use of grade 800 sandpaper seems to increase the anelastic behaviour of this interface with a larger hysteresis loops. Large plasticity occurs for the first loading cycle when the copper surface is unpolished with grade 120 sandpaper. Indeed, sandpaper unpolishing creates sharp asperities where the mechanical load exceeds locally the material yield stress limit.

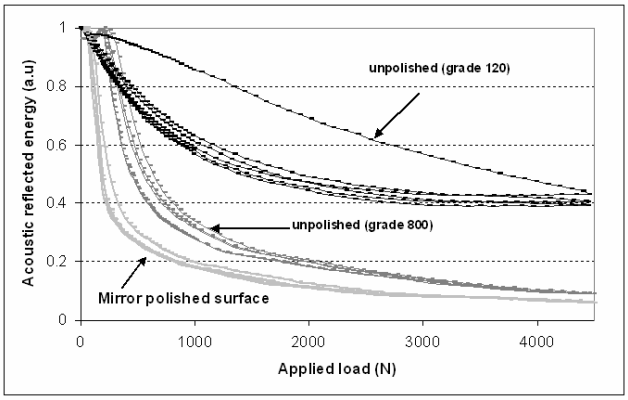

Figure 8. Effect of the copper surface roughness for the the contact quality with the amorphous carbon sample

V. CONCLUSION

This ultrasonic sensor is a new approach to characterize simultaneously the mechanical and electrical quality of the contact made by a compressive stress between two plane conductive materials. As demonstrated in this work, this technique is a non destructive means to optimize the materials roughness, the tightening torque and potentially surface treatments. This measurement could be performed for various temperatures too. Moreover, the contact quality sensitivity of this ultrasonic sensor can be improved to deal with high roughness level by using high order delay line round trip echo. As function of the materials properties and contact size, ultrasounds frequency could be further adapted to any given interface: small frequency yielding to large diameter sensors but larger wavelength giving easier propagation conditions through rough interface.

REFERENCES

[1] J.Krolikowski, J. Szczepek, and Z. Witczak, "Ultrasonic investigation of contact between solids under high hydrostatic pressure", Ultrasonics vol. 27 (1989) pp. 45-49

[2] B. Drinkwatter, R.S. Dwyer-Joyce, and P. Cawley, "A study of the interaction between ultrasound and a partially contacting solid-solid interface", Proc. R. Soc (London) A, vol. 452 (1996) pp. 2613-2628.

[3] J. Duwattez, F. Augereau, E. Caplain, and J.M. Saurel, "Dry coupling ultrasonic high frequency (10-100MHz) sensors for detetcion of surface and tribological properties at a submicrometric scale", Journal of Nondestructive evaluation, vol. 22 (2004) pp. 79-92.

[4] F. Augereau, M. El Hadachi, G. Despaux, and L. Crétinon, “Characterizaion of copper surface alterations using a soft ultrsonic indenter and comparison witch contact resistance measurement”, Proc. 24th International Conference on Electrical Contacts (2008) pp. 456-460.

 ISBN: 978-1-61208-145-8

A Microelectrode-Cell Sensor Model for Real Time Monitoring

Alberto Yúfera, Daniel Cañete
Seville Microelectronics Institute (IMSE)
Microelectronic National Centre (CNM), Seville Uni
Av. Americo Vespucio, sn, 41092, Seville, Spain
yufera@imse-cnm.csic.es

Paula Daza
Dpt. Cell Biology
Biology Faculty, Seville University
Av. Reina Mercedes sn, 41012, Seville, Spain
pdaza@us.es

***Abstract*-- In this paper the application of a cell-microelectrode model to cell biometry experiments is proposed, using the cell-electrode area overlap as main parameter. The model can be applied to cell size identification, cell count, and their extension to cell growth and dosimetry protocols. Experimental results using AA8 cell line are presented, obtaining promising results.**

Keywords- Microelectrode; ECIS; bio-impedance; impedance sensor; cell culture; dosimetry.

I. INTRODUCTION

Many biological parameters and processes can be sensed and monitored using its impedance as marker [1-5], with the advantage of being a non-invasive and relatively cheap technique. Cell growth and activity, changes in cell composition and shape, or in cell location are examples of how processes can be detected with microelectrode-cell impedance sensors [6-9]. Among Impedance Spectroscopy (IS) techniques, Electrical Cell-substrate Impedance Spectroscopy (ECIS) [7,8], based on two-electrode setups, allows the measure of cell-culture impedances and the definition of the biological nature (material, internal activity, motility and size) of a kind of cell and its relationship with the environment [11]. One of the drawbacks of ECIS technique is the need of efficient models to decode the full system electrical performance composed by the electrodes, medium and cells. Several works have been developped in this field. In [8], magnitude and phase impedance are deduced from electric field equation solution at the cell-electrode interface, giving a three parameter based model. h, the cell-electrode distance, R_b, cell-to-cell barrier resistance and r_{cell}, cell radius. In [9,10], finite element simulation (FEM) are executed to solve electrical field considering the whole structure. This method gives one parameter model (R_{gap}) to describe the gap or cell-electrode region resistance. In both, the model considers cells are in confluent phase [7] or a fixed area over the electrode [9]. The latest was extended in [10] to several cell sizes, allowing to define the cell-electrode covered area as the main model parameter. In this work is considered a model extension of R_{gap} based model, to incorporate the variable cell-microelectrode area overlap [10]. Impedance sensor sensitivity curves based on the cell size and density will be presented and applied to measure the growth-tax in cell-cultures and to describe cell toxicity experiments.

In this paper, section II resumes the electrode solution model for cell-electrode characterization. The process to extract practical models is included at section III, illustrating the simulations on a simplified system leading to cell size detection. Section IV relies on real time cell culture monitoring and its applicarion to dosimetry experiments. Conclusions will be highlighted at section V.

II. ELECTRODE-ELECTROLYTE MODEL

The impedance of electrodes in ionic liquids has been rather extensively investigated. An excellent review can be found at [6]. The main componets describing the electrical performance of an electrode metal inside a solution are four: the double layer capacitance, C_I, the current flowing through the electrified interface will encounter a resistance R_{ct} caused by the electron transfer at the electrode surface and Warburg impedance Z_W due to limited mass diffusion from the electrode surface to the solution. The electron transfer resistance R_{ct} is in series with the mass diffusion limited impedance Z_W. As the current spreads out to the bulk solution, the electrode has a solution conductivity determined by series resistance, represented as spreading resistance R_S in the equivalent circuit. These four parameters depends on technology, medium and geometry.

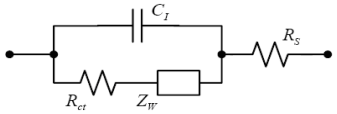

Figure 1. Equivalent circuit of electrode-solution interface. C_I is the double layer capacitance. Faradic impedance includes Z_w, the Warburg impedance and R_{ct}, the charge-transfer resistance. R_s is the spreading resistance.

III. CELL-ELECTRODE MODEL

The Fig. 2 illustrates a two-electrode impedance sensor useful for ECIS technique: e_1 is the sensing electrode and e_2 the reference one. Electrodes can be manufactured in CMOS process with metal layers [9] or using post-processing steps [13]. The cell location and size on e_1 top must be detected.

The model in Fig. 3 considers the sensing surface of e_1 could be total or partially filled by cells. For the two-electrode sensor in Fig. 2, e_1 is the sensing area A, $Z(\omega)$ is the impedance by unit area of the empty electrode (without cells on top). When e_1 is partially covered by cells in a surface A_c, $Z(\omega)/(A-A_c)$ is the electrode impedance associated to non-covered area by cells, and $Z(\omega)/A_c$ the impedance of the covered area. R_{gap} models the current flowing laterally in the electrode-cell interface, which depends on the electrode-cell distance at the interface (in the range of 15-150nm). R_s is the spreading resistance through the conductive solution. For an empty electrode, the impedance model $Z(\omega)$ is represented by the circuit in Fig. 1. It has been considered for e_2 the model in Fig 3a, not covered by cells. The e_2 electrode is commonly large

 ISBN: 978-1-61208-145-8

and ground connected, being its resistance small enough to be rejected. Figure 4 represents the impedance magnitude, Z_c, for the sensor system in Fig. 2, considering that e_1 could be either empty, partially or totally covered by cells. The parameter *ff*, called *fill factor*, can be zero for A_c=0 (e_1 electrode empty), and 1 for A_c=A (e_1 electrode full). It is defined Z_c (*ff*=0)=Z_{nc} as the impedance magnitude of the sensor without cells.

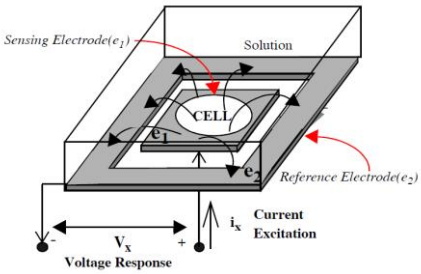

Figure 2. Two electrodes for ECIS: e_1 (sensing) and e_2 (reference). AC current i_x is injected between e_1-e_2, and voltage response V_x is measured.

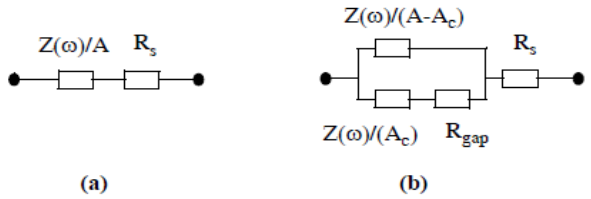

Figure 3. Proposed model for the an electrode-solution-cell model with area A, uncovered with cells (a) and covered and area A_c (b).

The relative changes at impedance magnitude, defined as,

$$r = \frac{Z_c - Z_{nc}}{Z_{nc}} \quad (1)$$

inform more accurate from these variations, being r the change of impedance magnitude for the two-electrode with cells (Z_c) with respect to the system without them (Z_{nc}). The graphics of r versus frequency is plotted in Fig. 5, for a cell-to-electrode coverage ff from 0.1 to 0.9 in steps of 0.1, using a R_{gap}=90 kΩ. The size of the electrode is 32x32 μm^2 [9,10]. It can be identified again the frequency range where the sensitivity to cells is high at 100kHz, represented by r increments. For a given frequency, each normalized impedance value of r can be linked with its ff, being possible the cell detection and estimation of the covered area A_c. Even more, area covered can be intrepreted as consequence than two o more cells, allowing cell count for a given cell size.

From Fig. 5, it can be deduced that models of electrode-cell electrical performance can be used to derive the overlapping area in cell-electrode systems, useful for biological studies. It can be observed how the curve fits well with the frequency range, placing the maximum r value around 100 kHz, as predicts the FEM simulations [9, 10]. A value of R_{gap}= 90kΩ was selected for this curve, representing a maximum value of the r curve with ff=0.69, which represents the ratio (A_c/A), for a cell size of 30μm diameter represented at figure obtained using FEM simulations [10]. Impedance sensor curves at figures 4 and 5 were obtained using SpectreHDL [15] mixed-mode simulator, with Analog Hardware Description Language (AHDL) for circuits in Fig. 3. An advantage of using AHDL models is the possibility of including non-linear performance of circuit elements, in our case, the frequency squared-root function at the Warburg impedance.

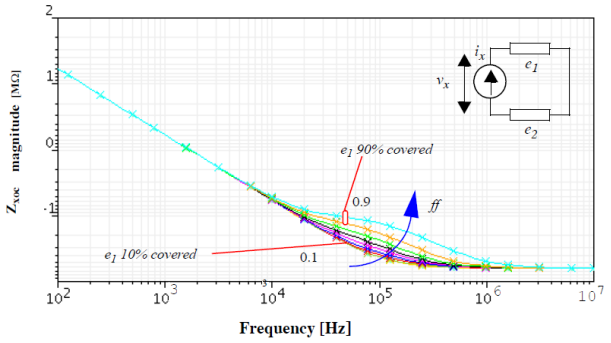

Figure 4. Impedance evolution when fill factor increases 32 x 32 μm^2.

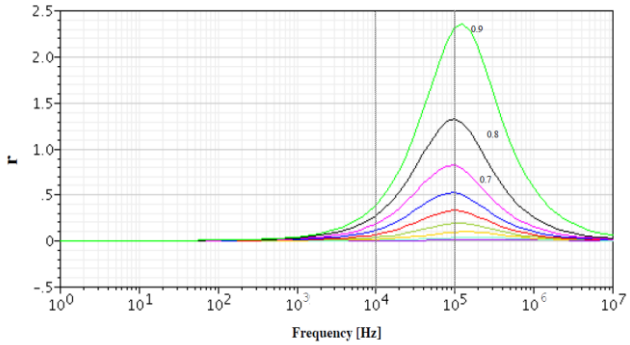

Figure 5. Normalized impedance r versus frequency derived from Fig. 4. Curves correspond to ff in the range of 0.1 (near empty) to 0.9 (near full).

IV. CELL CULTURE APPLICATIONS

A: Electrode Model

The proposed model based in Fig 3 has three main parameters: the electrode area (A), the fill-factor (ff), and the resistance of the gap region (R_{gap}). Technology data were included and simulation results obtained to model a commercial electrode: 8W10E, from Applied Biophysics [12]. It is composed by eight wells; each one contains ten circular gold microelectrodes, with 250μm diameter. Ten sensing electrodes, in paralell, were used for e_1 and only one common reference electrode, much larger than sensing ones. Figure 6 represents the normalized impedance r expected for these electrodes, for R_{gap}=22kΩ, if fill factor changes from electrodes without cell on top (ff=0.1) to near those fully covered (ff=0.9). Values of R_{gap} can be used to match the models to observed performance. In Fig. 7, R_{gap} values were changed for ff=0.9, observing large r changes. Finally, it was also modifyed the electrode area for R_{gap}=22kΩ and ff=0.9, showing the results at Fig. 8. It can be observed that optimal working frequency is near the proposed by the electrode factory (around 4 kHz), and that electrode area covered by cells can be approximated by using the fill factor parameters. The performance curves obtained before can be used to fit experimental results to proposed model and find relevant biometric characteristics.

 ISBN: 978-1-61208-145-8

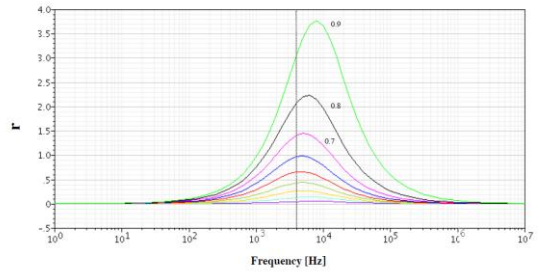

Figure 6. Obtained curves for r vs frequency, for ff ∈ [0.1,0.9] and R_{gap} = 22kΩ, using 8W10E electrodes.

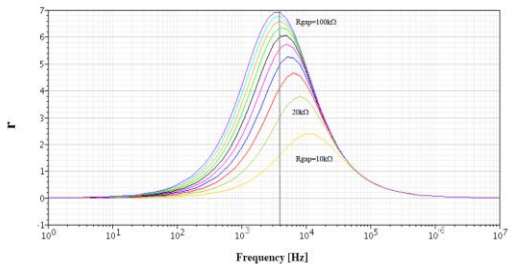

Figure 7. Obtained curves for r vs frequency, for $R_{gap} \in$ [10kΩ,100kΩ] in steps of 10kΩ, for ff=0.9, using 8W10E electrodes.

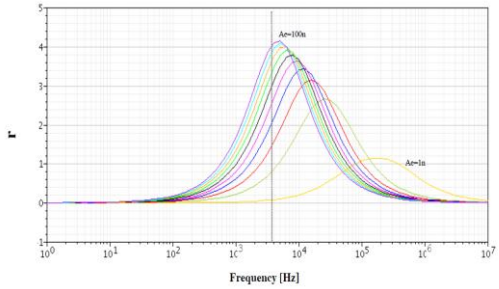

Figure 8. Obtained curves for the r vs frequency, for R_{gap}=22kΩ and ff=0.9, for differents electrode areas (1n to 100n). 49n ($49.10^{-9}m^2$) corresponds to a circular electrode with a 250μm diameter.

B: Cell growth

In Fig. 9a it is shown the growth curve obtained by us during seven days using 8W10E sensors with a similar setup in [8]. AA8 cells for chinese hamster were seeded initially, in an approximated number of 5000. The impedance range is around 1220Ω (380Ω–1600Ω). Considering an initial cell number of 5000 very low, we take the initial impedance as due to no-cell impedance value (Z_{nc}). At t=6000 min, the medium was changed, and the confluent phase was achieved at t = 8500 min approximately. The maximum experimental value given from eq. (1) is around r = 3.1, as illustrates Fig. 9b. We consider in our model that the electrodes are aproximatelly fully covered by cells for ff=0.9, the value of R_{gap} that better fits is 22kΩ. System response corresponds to r-values illustrated in Fig. 6. From these curves, it can be obtained the fill factor at different times. Table I summarized the relative normalized impedance values r at several times. Using Fig. 6 for the sensor response, fill factor is calculated at every instant. For a well area of 0.8 cm^2, the maximum cell number goes from $0.8x10^6$ to $1.6x10^6$. Number of cells, n_{cell}, in Table I, is obtained from $0.8x10^6$ expected final cell number. A value of Z_{nc}=380Ω for r calculus in eq. (1) was considered.

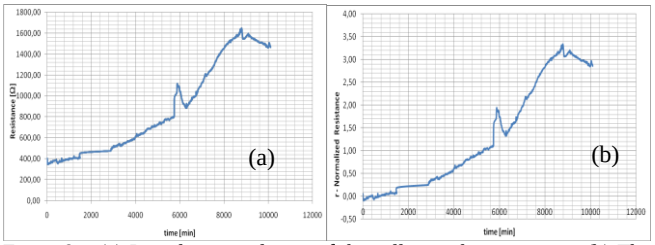

Figure 9. (a) Impedance evolution of the cell growth experiment. (b) The normalised impedance r evolution obtained.

TABLE ME: CELL NUMBER (n_{cell}) OBTAINED FROM IMPEDANCE Z_C MEASURE IN Fig. 9, AND USING THE r CURVES PROPOSED FOR 8W10E SENSORS.

t (min)	r	ff	n_{cell}
0	0	-	5000
500	0.024	0.020	18000
1000	0.050	0.050	44000
1500	0.072	0.070	63000
2000	n.a.	n.a.	n.a.
2500	n.a.	n.a.	n.a.
3000	0.374	0.362	322000
3500	0.437	0.395	351000
4000	0.615	0.475	422000
4500	0.777	0.530	471000
5000	0.903	0.581	516000
5500	1.033	0.602	535000
6000	1.074	0.620	551000
6500	1.507	0.710	631000
7000	1,970	0.775	689000
7500	2,353	0.810	720000
8000	2,837	0.860	764000
8500	3.113	0.890	791000
9000	3.134	0.900	800000
9500	3.010	0.875	778000
10000	2,857	0.864	768000

C: Dosimetry

Experiments to characterize the influence of some drugs in cell growth were done. The objective is to proof that proposed model allows counting cell number at different dosis. It was considered the AA8 cell line and as drug, six different doses of MG132 for growth inhibition (from 0.2μM to 50μM). After 72 hours normal cell growth, the medium was changed and the drug added at different doses: 0.2, 0.5, 1, 5, 10 and 50μM for wells 3 to 8 respectively. Well 2 is the control.

Measured impedances for the 8 wells are at Fig. 10, for 4kHz working frequency. At the end of the experiment can be observed that impedance decreases as drug dosis increases. Control (W2) is full of cells with the maximum impedance, while maximum dosis (W8) has the lowest resistance, at the botton. The black line (W1) represents the electrode-solution impedance. After the medium change (t=4000min), it is observed a decreasing impedance below the initial baseline level (400Ω) that we cannot explain. Final impedance values at 8000min, Z_c, were considered, at Table II. From Z_{nc} and Z_c, r values are calculated in third colunm. Using curves for r versus frequency in Fig. 6, ff estimated values from proposed model are obtained. The cell number at the end of the experiment was also count and shown at the last column for each well. Considering ff_{max}=0.9 for a measured cell number of $8.06x10^5$, the expected values for ff are calculated.

The same data are summarized at Table III for 2, 4 and 10kHz frequencies respectively. The better agreement it is obtained at 4kHz in fill factor (ff). It is observed that the impedance baseline, Z_{nc}, for r calculus decreases with frequency due probably to electrode impedance dependence.

 ISBN: 978-1-61208-145-8

For medium resistance (W1) and high drug concentrations wells (W6-W8), the resistance measured is below to Z_{nc}, so eq. (1) can no be applied for r calculation.

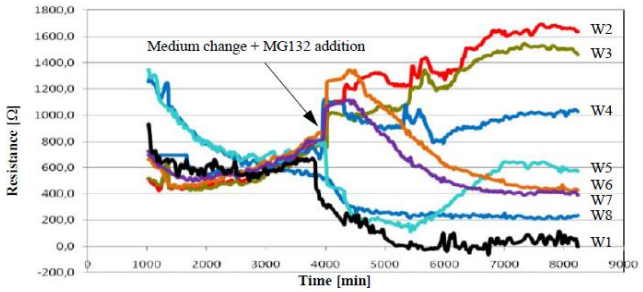

Figure 10. Impedance measure in dosimetry at 8 wells for 4kHz frequency. W1: Medium. W2: Control. W3: 0.2μM. W4: 0.5 μM. W5: 1 μM. W6: 5 μM. W7: 10 μM and W8: 50 μM.

TABLE II: EXPERIMENTAL VALUES FOR RELATIVE IMPEDANCE (r) AND FILL-FACTOR (ff) FOR Z_{nc} = 400 Ω. FREQUENCY = 4 KHZ.

Well	Z_c t=8000min	r Z_c ,Z_{nc}	ff estimated	ff expected	n_{cell} measured
1	259.2	-	-	-	Medium
2	1631.7	3.1	0.90	0.900	$8.06x10^5$
3	1454.7	2.6	0.85	0.690	$6.13x10^5$
4	1030.6	1.5	0.72	0.610	$5.41x10^5$
5	625.8	0.5	0.44	0.410	$3.60x10^5$
6	417.4	0.05	0.037	0.036	$3.20x10^4$
7	406.8	0.015	0.016	0.024	$2.10x10^4$
8	99.6	< 0	-	0.005	$4.00x10^3$

TABLE III: EXPERIMENTAL VALUES FOR RELATIVE IMPEDANCE (r) AND FILL FACTOR (ff) AT VARIOUS FREQUENCIES. Z_{NC} = 480Ω, 400Ω, AND 315Ω FOR 2, 4 AND 10 KHZ WORKING FREQUENCY RESPECTIVELY.

	r (from Z_c and Z_{nc})			ff (from model)			
Well	2kHz	4kHz	10kHz	2kHz	4kHz	10kHz	ff expect.
1	-	-	-	-	-	-	Medium
2	2.43	3.1	3.76	0.98	0.90	0.90	0.900
3	2.18	2.6	3.24	0.94	0.85	0.88	0.690
4	1.17	1.5	2.21	0.82	0.72	0.82	0.610
5	0.21	0.5	0.84	0.32	0.44	0.44	0.410
6	-	0.05	-	-	0.037	-	0.036
7	-	0.015	-	-	0.016	-	0.024
8	-	-	-	-	-	-	0.005

V. DISCUSSION AND CONCLUSIONS

This work describes an area dependent model for cell-electrode systems and its application to measure and identify cells during cell culture protocols. A practical circuit for electrode-solution-cell simulation was employed, using an AHDL description for commercial electrodes, obtaining a good matching. Optimal measurement frequency was identified near 4 kHz. It was proposed the cell growth evolution study based on 8W10E electrode models. Curves obtained experimentally, allows the real time growth monitoring by fitting the R_{gap} parameter. An estimation of the number of cells was obtained by using sensor curves calculated from electrical model proposed. Dosimetry experiments reproduce similar conditions than cell growth, but in this case, it is added a growth inhibitor at different dosis. There is observed a decreasing impedance, below the baseline expected (Z_{nc}) that we can not explain. However, for the control and small drug dosis, impedance curves are perfectly aligned. It was fitted a proposed model with R_{gap}=22kΩ to explain experiemental data. Deviations from data are over 10-20% in fill factor, more accurate for 4 kHz.

The deviations in fill factors measured are not small, being required to analize the influence of error sources to increase the system performance. First, Signal-to-Noise Ratio (SNR) should be increased at the setup. Second, proposed model has the advantage that need only one parameter (R_{gap}), versus other reported model using three parameters [8]. One parameter model makes easy to fit experimental data, but can introduce inaccuracy. The possibility to add more parameters to the model should be considered in the future.

ACKNOWLEDGEMENTS

Part of this work was done thanks the financial help from the project: Auto-calibración y auto-test en circuitos analógicos, mixtos y de radio frecuencia: Andalusian Government project P0-TIC-5386, co-financed with FEDER program. Also, we thanks to Citoquimica Ultraestructural Group (BIO132) of Cell Biology Department, Biology Faculty, Seville University, for its help at the lab to develop the cell culture experiments.

REFERENCES

[1] S. Grimnes and O. Martinsen, "Bio-impedance and Bioelectricity Basics," Second edition. Academic Press, Elsevier. 2008.

[2] R. D. Beach et al., "Towards a Miniature In Vivo Telemetry Monitoring System Dynamically Configurable as a Potentiostat or Galvanostat for Two- and Three- Electrode Biosensors," IEEE transaction on Instrumentation and Measurement, vol 54, nº1, pp:61-72. 2005.

[3] A. Yúfera et al., "A Tissue Impedance Measurement Chip for Myocardial Ischemia Detection," IEEE transaction on Circuits and Systems: Part I. vol.52, nº:12 pp:2620-2628. 2005.

[4] S. Radke et al., "Design and Fabrication of a Microimpedance Biosensor for Bacterial Detection," IEEE Sensor J. vol 4,nº 4,434-440. 2004.

[5] A. Yúfera et al., "A Method for Bioimpedance Measure With Four- and Two-Electrode Sensor Systems," 30th Annual International IEEE EMBS Conference, pp: 2318-2321. 2008.

[6] D. A. Borkholder. Cell-Based Biosensors Using Microelectrodes. PhD Thesis, Stanford University. 1998.

[7] I. Giaever, et al., "Use of Electric Fields to Monitor the Dynamical Aspect of Cell Behaviour in Tissue Cultures," IEEE Transaction on Biomedical Engineering, vol. BME-33, No. 2, pp. 242-247. 1986.

[8] I. Giaever and C. R. Keese, "Micromotion of mammalian cells measured electrically," Proc. Nail. Acad. Sci. USA. Cell Biology, vol. 88, pp: 7896-7900, Sep. 1991.

[9] X. Huang et al., "Simulation of Microelectrode Impedance Changes Due to Cell Growth," IEEE Sensors J., vol.4, nº5, pp: 576-583. 2004.

[10] A. Olmo et al., "Computer Simulation of Microelectrode Based Bio-Impedance Measurements With COMSOL," BIODEVICES 2010. pp: 178-182. Valencia (Spain), 20-23, Jan. 2010.

[11] P. Wang and Q. Liu, editors. Cell-Based Biosensors: Principles and Applications, Artech House Series. 2010.

[12] Applied Biophysics. Http://www.biophysics.com/.

[13] A. Manickam, A. Chevalier, M. McDermott, A. D. Ellington, and A. Hassibi, "A CMOS Electrochemical Impedance Spectroscopy (EIS) Biosensor Array," IEEE Transactions on Biomedical Circuits and Systems, vol 4, nº 6. pp: 379-390. 2010.

[14] A. Yúfera and A. Rueda, "A Real-Time Cell Culture Monitoring CMOS System Based on Bio-impedance Measurements," Kluwer Academic P.. Analog Integrated Circuits and Signal Processing. 2011. (accepted)

[15] A. Yúfera A. and E. Gallego, "Generation of HDL Models for Bioimpedance Sensor Simulation Based on Microelectrodes," Sensors and Transducers Journal, pp: 160-170. vol. 10. Feb. 2011.

 ISBN: 978-1-61208-145-8

Cell Chip to Analyze Cell lines and Cell Cycle Stages Based on Electrochemical Method

Md. Abdul Kafi[1], Tae-Hyung Kim[2] and Jeong-Woo Choi[1,2*]
[1]Interdisciplinary Program of Integrated Biotechnology and [2]Department of Chemical & Biomolecular Engineering,
Sogang University,
#1 Shinsu-dong Mapo-gu, Seoul 121-742, Republic of Korea
*E-mail: jwchoi@sogang.ac.kr

***Abstract*— Cell chip was fabricated to analyze different cell lines and cell cycle-stages based on the electrochemical tools. Cell-based biochips are becoming promising tools in the various kinds of biotechnology field such as early diagnosis, cell therapy and drug screening. In this study, cells were immobilized on collagen coated gold surface and subjected to voltammetric methods including cyclic voltammetry and differential pulse voltammetry. The distinct redox phenomena were detected at the cell-electrode interface which varies with different kinds of cell lines. Moreover, the redox peaks were found to be different from same cell line but in different cell cycle stages. A typical sigmoid curve was achieved between the electrochemical signals and cell concentrations that proved the reproducibility of electrochemical signals. Hence, our developed cell chip based on the electrochemical tool can be applied for the differentiation of metastatic cancer cells from unknown origin, as well as for the assessment of cell cycle-dependent effects of drugs or toxins.**

Keywords: Cyclic voltammetry; Differential pulse voltammetry; Cell cycle progression; Cell chip

I. INTRODUCTION

Cell analysis plays an important role in many research areas such as early diagnosis of diseases, disease treatment and drug screening. Among the analytical tool for the living cells, cell-based sensor arrays have been proved as potentially useful method for studying the effects of drugs and cellular responses induced by external stimuli [1]. Recently, cell chip based on electrochemical method is becoming a popular method due to its simplicity, ease of use and the huge potential as a label-free biosensor with high sensitivity. Several amperometric or electrochemical impedance techniques have been tried to detect cell viability and cellular functions by discovering the electrochemical dynamics at cell-electrode interface [2-4]. However, amperometric method was found to be suitable for the specific materials which have well-known redox properties such as the dopamine or ascorbic acid. Impedance-based method is another common electrochemical tool that focuses on the changes of impedance induced by the cell attachment on the working electrode surface. This method is not sensitive to the redox properties of target materials; however, the impedance values are the only one indicator of cells and are not proper for achieving valuable information from cells which can be useful for the intensive cellular research such as the differentiation of different kinds of cell lines or different cellular response.

We have previously reported a cell chip that utilized electrochemical tool to detect redox properties of target cells. Unlike the other method that employed voltammetric method for the characterization of living cells, cells can be directly attached on the electrode surface by the modification of extracellular matrix protein on the working electrode that contributed to the increase of cell attachment, as well as the enhancement of electrochemical signals. The fabricated cell chip was found to be very effective for detecting the effects of different kinds of anticancer drugs or environmental toxins by analyzing and quantifying the electrochemical signals [5,6]. Later, we also extend our work to detect cell cycle-dependant characteristics based on cell chip technology [6]. The cell cycle progress through the defined sequence of events was detected where several specific nuclear and cytosolic changes occurred in each of the events. It is well-known that double thymidine or thymidine/nocodazole treatment can block the cell cycle progression at the synthetic phase or mitotic phase, respectively [7]. These two different phages have the different cellular composition and induce the changes of redox behavior of cells which can be detected by proper electrochemical tools. Therefore, cells from different origin and cells in different stage of cell cycle can be easily differentiated by our cell chip technology that is essential for the practical use of cell chip.

Therefore, in the present study, a cell chip composed of collagen modified Au surface was fabricated for the cell immobilization and cell cycle synchronization. Cyclic voltammetry (CV) and differential pulse voltammetry (DPV) were performed to compare signals from neuronal (PC12) and non-neuronal (HeLa) cells. Finally, DPV was carried out to detect the electrochemical characteristics of PC12 cells synchronized at synthetic and mitotic stages.

II. MATERIALS AND METHOD

A. Electode modification

A 50 nm thick titanium (Ti) layer was established on the silicon substrate and then a 150 nm thick gold (Au) layer was deposited by DC magnetron sputtering. The Au surface was cleaned with piranha solution as previously described. The cleaned Au surface was further polished carefully by the sonication in absolute alcohol and double-distilled water for 5 min, respectively. Finally, the electrode was electrochemically cleaned by 0.5M H_2SO_4 until a stable cyclic voltammogram was obtained. To develop an oligopeptide layer on the Au surface, 0.1 mg/ml of collagen

 ISBN: 978-1-61208-145-8

solution diluted with distilled water was added on a freshly cleaned Au substrate and incubated for 30 min. Finally, the substrate was washed with deionized distilled water and dried under N_2 gas. All the chemicals used are of analytical grade.

B. Cell chip chamber design and cell immobilization

The cell chip chamber (Lab-Tek®, Thermo fisher scientific, USA) of 2 cm × 2 cm × 0.5 cm (width × length × height) dimensions was created on freshly prepared Au working electrodes with an area of 3 cm^2. This created approximately a 2.6 mm^2 exposure area for cell attachment. Polydimethylesyloxane (PDMS) was used to affix substrate to the chamber. Then, cells were seeded on the chip surface at a known cell density. PC12 cells in passage 3 were used for each electrochemical investigation. After 48 hour of incubation, the chips were ready for electrochemical analysis. All experiments were performed in triplicate using freshly prepared chip.

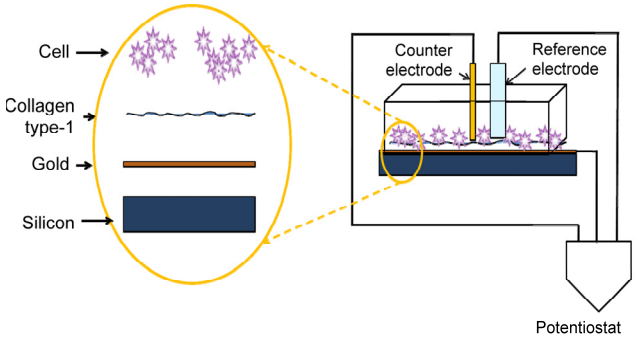

Figure 1. Schematics of cell-chip. The circle shows the steps of fabrication: establishment of 150 nm Au on silicon base, collagen coating and cell seeding.

C. Cell cycle synchronization

Cell on the chip surface was treated with 2mM thymidine diluted with a culture medium (RPMI 1640) for 18h, followed by 8h of release (replaced by fresh medium) and again 2mM thymidine for 18h to block cell at synthetic phase. Similarly, another cell was treated initially with 2mM thymidine for 18 h, followed by a 4h release with thymidine-free medium and then, 100 ng/ml nocodazole was treated for 10h to block cell at mitosis phase. Finally, the cell chip was prepared for the measurement of electrochemical signal of the cells at the different phases of its growth cycle. A cell chip with the same number of unsynchronized cells served as control group.

D. Electrochemical measurements

The Electrochemical measurements were carried out using CHI660C Potentiostat (CH Instruments). The common three-electrode configuration was employed for the electrochemical measurements, while standard Ag/AgCl electrode and platinum wire were used as the reference and counter electrode, respectively. Prior to the electrochemical measurement, living cells on chip surface was washed twice with a 10mM phosphate buffered saline (PBS) buffer (pH 7.4) containing NaCl- 0.138M and KCl -0.0027M. Finally, electrochemical measurements were performed using 2 ml of PBS working as the electrolyte. Before the measurement, the buffer solution was bubbled thoroughly with high-purity nitrogen for 30 min. All the measurements were repeated at least three times, and the error bars have been shown in the figures.

E. Statistical analysis

Quantitative data was written as the mean ± SD. The intensities of reduction peaks in cyclic voltammogram were used for all the quantitative measurements.

III. RESULTS AND DISCUSSION

Figure 1 shows the electrochemical system based on cell chip technology. To achieve the accurate cellular responses, cells should be maintained on the chip surface as in vivo-like condition. It was found that polysaccharides, extracellular matrix (ECM) proteins or its components significantly enhances the cell attachment on the artificial surface and also help the establishment of cell-friendly environment [9,10]. Collagen, which is the main constituent of connective tissue and a member of ECM proteins, was used to increase cell binding affinity to the artificial electrode surface, as well as to detect the electro-physiological characteristics of target cells sensitively.

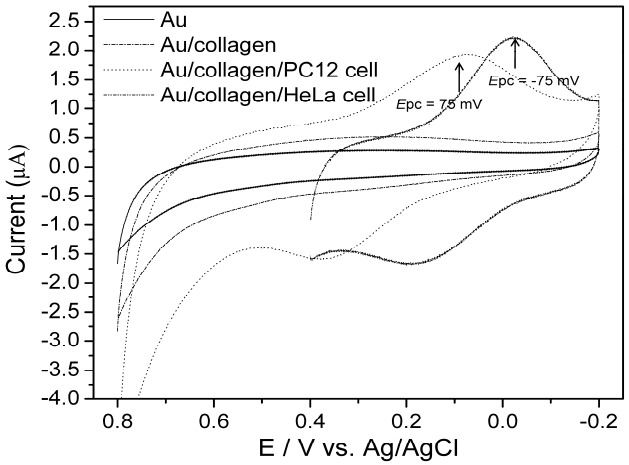

Figure 2. Redox behavior of PC12 and HeLa cell on collagen modified Au surface. CV was measured using phosphate buffered salilne (PBS) (0.01 M, pH 7.4) as electrolyte at a scan rate of 100 mVs^{-1}. All the experiment was conducted at 27 ± 1°C. The experiment was repeated three times with maintaining identical condition.

A. Comparative electrochemical analysis of neuronal (PC12) and non-neuronal (HeLa) cells

Cell is the basic structural and functional unit of a tissue that possesses unique functionality according to the organs which they derived. Therefore, cells derived from different organ will have different electrochemical characteristics which can be easily detected by our cell chip technology. Gold electrode was chosen as working electrode due to the fast electron transfer characteristics over the semiconductor or

 ISBN: 978-1-61208-145-8

non-metal. PC12 cells derived from rat pheochromocytoma and HeLa cells derived from human cervical cancer were analyzed by cell chip and showed quasi-reversible redox behavior when subjected to cyclic voltammetric tool. The potential window was determined as -0.2 V to 0.8 V and the scan rate was 100 mVs^{-1}. A distinct anodic peak and cathodic peak from PC12 cells were detect at 75 mV and 350 mV, respectively. HeLa cells also gave specific anodic and cathodic peak at -75 mV, 150 mV which was different from PC12 cells [Figure 2]. This indicates the distinguishable differences of redox behavior of two kinds of cell due to the differences of their origin. The difference between the potential peaks $|E_{pc}-E_{pa}|$ exceeded 100 mV and the peak current ratio $I_{pa}/I_{pc} \geq 1$, indicating the distinct quasi-reversible properties of cells [11].

The cell line specific CV signal was further confirmed by another sensitive electrochemical method, differential pulse voltammetry (DPV). Considering the potential of anodic peak obtained from CV technique, a potential window was determined as -0.2 to 0.4 V. Well defined DPV signals were measured from both PC12 and HeLa cells as shown in figure 3. Cathodic peaks were detected at 75 mV and -75 mV for PC12 and HeLa cells which were exactly same as the potential obtained from CV. Redox peaks were not achieved form bare Au surface indicating that cathodic peaks were fully originated from the cells on the Au/collagen electrode surfaces. Hence, the developed cell chip was proved as efficient tool for the differentiation of different kind of cancer cell lines.

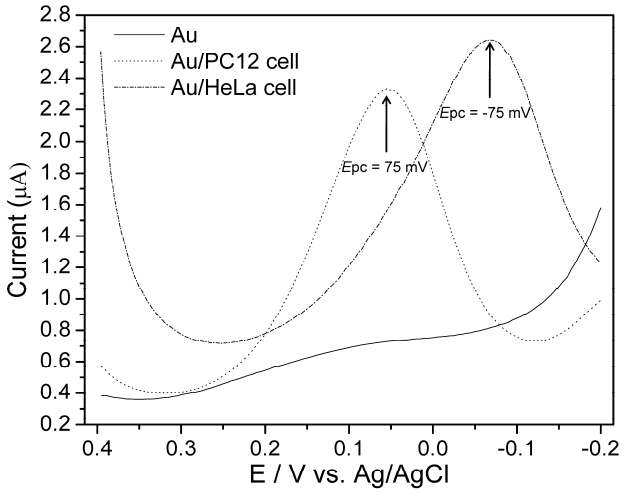

Figure 3. Differential Pulse voltammogram of PC12 and HeLa cell on collagen modified Au surface. DPV was measured using PBS (0.01 M, pH 7.4) as an electrolyte at a scan rate of 100 mVs^{-1}. Pulse amplitude and pulse width were 50 mV and 50 ms, respectively.

B. Comparative study of electrochemical signal from PC12 cells in different cell cycle stages

Considering the cell line-specific electrochemical signals, we hypothesized that same cell line but in different stages of growth cycle may have different redox properties. Cells generally pass through a number of complex processes during its growth cycles including prophase, prometaphase, metaphase, anaphase and telophase that lead to the several changes in the physiological and morphological aspects [6]. These cytological changes may affect the various kinds of redox proteins in cell cytosol and contribute to the alterations of electrochemical behavior of the cell. To prove our hypothesis, PC12 cells on the chip surface were synchronized at the synthetic and mitotic phase by chemical treatment and were subjected to DPV method. A sharp electrochemical signal appeared at +50 mV from the cells at synthetic phage and another peak was observed at +150 mV from the same PC12 cells at mitotic stage which were significantly different from unsynchronized cells (Figure 4). Generally, detection of cells in the different phages depends on the fluorescence activated cell sorting (FACS) or western blotting method which is expensive and time-consuming. Since our cell chip based on electrochemical tool proved the potential for the determination of cell cycle stages, this method can be useful for the detection of cell cycle-dependent effects of various kinds of drugs or toxins on target cells.

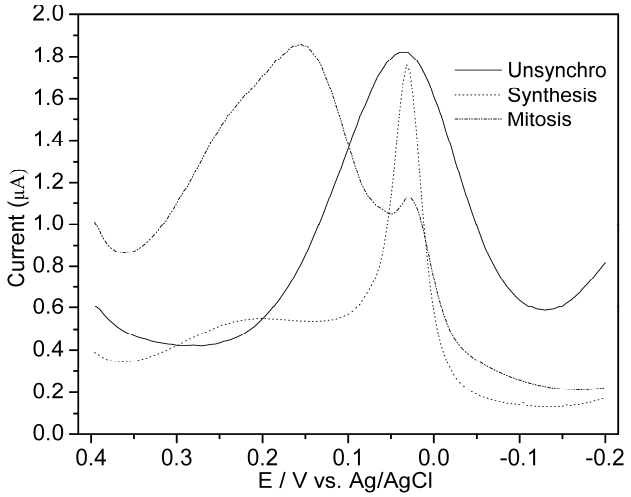

Figure 4. Differential Pulse voltammogram of PC12 cell synchronized at synthesis and mitosis phase as compared with unsyncronized (control). All the experimental condition was maintained as mensioned before.

C. Rreproducibility of electrochemical tool

The reproducibility of electrochemical signals achieved from cell-based chip was determined by varying the concentrations of cells synchronized at synthetic phage. Various concentrations of cells from 0.25×10^5 cells/ml to 1.75×10^5 cells/ml were seeded on the chip surface and synchronized at synthetic stage. The synchronized cells were further subjected to the electrochemical measurements and showed the increase of current peak with increasing cell concentrations (Figure 5a). A concentration-dependent sigmoid curve ($r^2 = 0.989$) was obtained between the current intensities and cell numbers (Figure 5b). The concentrations of cells from 0.25×10^5 cells/ml to 1.25×10^5 cells/ml showed the exponential increases of signals, whereas steady state signals were observed after the concentration of $1.25 \times$

 ISBN: 978-1-61208-145-8

10^5 cells/ml due to the limitation of the chip surface. Therefore, a concentration of 1.25×10^5 cell/ml was determined to be the optimum concentration for on-chip electrochemical monitoring. The relative standard deviation of the DPV peak for seven different concentrations of cells (n=3) was 5.6%, indicating that the electrochemical cell chip possess high sensitivity and reproducibility. Therefore, the fabricated chips was proved to be a potential tool for characterizing cells of different origin as well as different stages of cell cycle electrochemically.

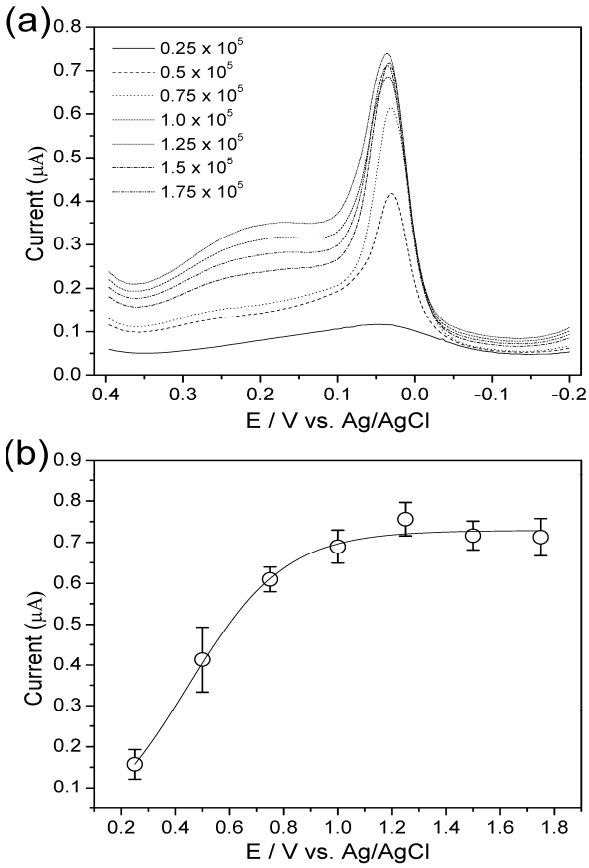

Figure 5. (a) Changes in DPV peak intensities corresponding to the various concentrations of PC12 cells on the chip surface (from 0.5×10^5 cells/ml to1.75×10^5 cells/ml), (b) a typical sigmoid curve indicates the linear increases in current peaks (I_{pc}) in a concentration-dependent manner ($R^2 = 0.989$). Data are the mean ± standard deviation of three different experiments.

IV. CONCLUSION

A cell-based chip was fabricated to determine cell line- and cell cycle-specific electrochemical signals. Living cells immobilized on the collagen modified chip surface gave different signals according to the origin of the cell line, as well as the stage of cell cycle. PC12 and HeLa cells were found to give voltammetric peak at 75 mV and -75 mV, respectively. Moreover, two kinds of completely different voltammetric signals were obtained from PC12 cells synchronized at synthetic and mitotic phases. These results suggest that electrochemical signals not only differ from different cell lines but also from the different cell cycle stages. Finally, various concentrations of cells synchronized at synthetic stage were subjected to DPV method and found to give electrochemical signals which showed a concentration-dependent sigmoid curve ($r^2 = 0.989$) between the current intensities and cell numbers. The optimal concentration of cells on chip surface was 1.25×10^5 cell/ml based on the obtained sigmoid curve. Hence, our developed cell chip based on the electrochemical tool can be usefully applied for the analysis of metastatic cancer cells from unknown origin, as well as for the assessment of cell cycle-dependent effects of drugs or toxins.

ACKNOWLEDGMENT

This work was supported by the National Research Foundation of Korea (NRF) grant funded by the Korea government (MEST) (2011-0000384) and by the Nano/Bio Science & Technology Program (M10536090001-05N3609-00110) of the Ministry of Education, Science and Technology (MEST), and by the Graduate School of Specialization for Biotechnology Program of the Ministry of Knowledge Economy (MKE).

REFERENCES

[1] C. H. Yea, J. Min, and J. W. Choi, “The fabrication of cell chip for use as bio-sensors”, Biochip J., vol. 1, 2007, pp. 219-227.

[2] J. W. Choi, Y. S. Nam, and M. Fujihira, “Nanoscale fabrication of biomolecular layer and its application to biodevices”, Biotechnol. Bioprocess Eng. vol. 9, 2004, pp. 76–85.

[3] B. S. Kim and J. W. Choi, "Polyelectrolyte multilayer microcapsules : self assembly and toward biomedical applications." Biotechnol. Bioprocess. Eng. vol. 12, 2007, pp. 323-332.

[4] M. N. Bery and M. B. Grivrll, “Bioelectrochemistry of Cells and Tissues”, Birkhauser, Basel, Verlag, pp. 134, 1995.

[5] W. A. El-Said, C. -H.. Yea, I. -K. Kwon and J. -W. Choi, “Fabrication of electrical cell chip for the detection of anticancer drugs and environmental toxicants effect”, Biochip J. vol. 3, 2009, pp. 105-112.

[6] L. H. Hartwell and T. A., Weinert, “Checkpoints: controls that ensure the order of cell cycle events”, Science vol. 246, 1989, pp. 629-634.

[7] G. P. Reddy, “Cell cycle: regulatory events in Gl-S transition of mammalian cells”, J. Cell Biochem. vol. 54, 1994, pp. 379-386.

[8] G. J. Gutierrez, T. Tsuj, J. V. Cross, R. J. Davis, D. J. Templeton, W. Jiang and Z. A. Ronai, “JNK-mediated Phosphorylation of Cdc25C Regulates Cell Cycle Entry and G2/M DNA Damage Checkpoint”, J. Biol. Chem. vol. 285, 19, 2010, pp. 14217–14228.

[9] C. H. Streuli and M. J Bissel, “Expression of extra cellular matrix components is regulated by substratum”, J. Cell Biol., vol. 110, 1990, pp. 1405–1415.

[10] C. Ploetz, E. I. Zycband and D. E. Birk. “Collagen fibril assembly and deposition in the developing dermis: segmental deposition in extracellular compartments” J. Struct. Biol., vol. 106, 1991, pp. 73-81.

[11] M. A. Kafi, T. -H. Kim, C. -H. Yea, H. Kim, and J. -W. Choi, “Effects of nanopatterned RGD peptide layer on electrochemical detection of neural cell chip”, Biosens. Bioelectron. vol. 26, 2010, pp. 1359-1365.

 ISBN: 978-1-61208-145-8

Flexible All-organic Highly Tenzo-resistive bi Layer Films as Weightless Strain and Pressure Sensors for Medical Devices

Vladimir Laukhin
dept. name: NANOMOL
Institució Catalana de Recerca i Estudis Avançats,
ICMAB-CSIC, CIBER-BBN
Bellaterra, Barcelona, Spain
e-mail: vladimir@icmab.es

Elena Laukhina
dept. name: NANOMOL
CIBER de Bioingeniería, Biomateriales y Nanomedicina
(CIBER-BBN) at ICMAB-CSIC
Bellaterra, Barcelona, Spain
e-mail: laukhina@icmab.es

Victor Lebedev, Raphael Pfattner, Concepció Rovira, Jaume Veciana
dept. name: NANOMOL
Institut de Ciencia de Materials de Barcelona (ICMAB) -CSIC, CIBER-BBN
Bellaterra, Barcelona, Spain
e-mail: vlebedev@icmab.es; rpfattner@icmab.es, cun@icmab.es; vecianaj@icmab.es

Abstract—**The article is addressed to the development of flexible lightweight strain and pressure sensors capable of monitoring blood pulsing, breathing, and body movements. The prototypes of body sensing devices equipped with sensors based on all-organic highly tenzo-resistive bi layer films are described. The electrical resistance of the flexible sensors linearly and reversibly depends on deformation resulted from body movements. Sensors electrical responses suffice to measure very small pressure changes as well as delicate elongations in a wide deformation range.**

Keywords- piezoresistive covering; flexible, biocompatible pressure and strain sensors; organic molecular metal

I. INTRODUCTION

The development of flexible, lightweight, conducting materials, whose electrical transport properties strongly respond to delicate strain, brings great opportunities in the field of strain, pressure or bending sensors for their applications in intelligent textiles, robotic interfaces and body sensing devices [1-3]. Recently, we reported ultra-sensitive tenzo-resistive bi layer (BL) films composed of a polycarbonate (PC) matrix surfaced with crystallites of organic molecular metal β-$(ET)_2I_3$, were ET=bis(ethylene-dithio)tetrathiafulvalene (Fig. 1) [4, 5]. These BL films show ability to sense the uniaxial deformations given by the minimum value of a 10^{-3} % of relative strain that is well below those of many conventional strain gages [4]. The processing characteristics of polycarbonate films, "self-metallized" with the highly tenzo-resistive β-$(ET)_2I_3$-based layer, make them potentially useful for electronic applications where conductivity, lightweight, large or small area coverage and flexibility are required [4]. Moreover, it has been shown that BL films can be successfully integrate in textiles [6]. The BL film-based strain gages can be engineered with gage factors (S) up to 20 and different temperature resistance coefficients [4, 5]. The tests have shown that BL film-based pressure sensors, being *biocompatible*, are able to control intraocular pressure changes [7]. The contact IOP sensing lens with a membrane pressure sensor based on the above mentioned BL film is already under development [7, 8].

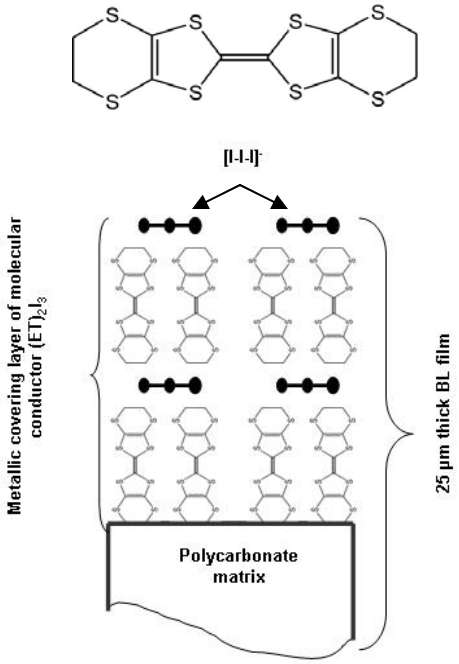

Figure 1. Top: Skeletal formula of bis(ethylenedithio)tetrathiafulvalene (ET); bottom: schematic view of the orientation of $(ET)^{+0.5}$ radical cations and $[I\text{-}I\text{-}I]^-$ anions in a metallic covering layer of β-$(ET)_2I_3$ formed at the surface of a polycarbonate film.

 ISBN: 978-1-61208-145-8

In order that a tenso-resistive BL film can sense pressure changes, it should be located in devices as a membrane. In this case the electrical resistance of a BL film will respond to its bending deformation resulted from a pressure change. We used this engineering approach to fabricating the set of medical sensing prototypes.

Here we report a promising approach to engineering biocompatible and highly tenzo -resistive membranes for their applications to monitoring medical parameters. The prototypes of medical devices capable of controlling the body movements are presented

II. FABRICATING FLEXIBLE SENSING MEMBRANES

In line with the early reported method [9] we first prepared a 25 μm thick polycarbonate film spiced up with an 2 wt. % of ET that is a precursor for organic molecular metal $(ET)_2I_3$. The film was cast on a glass support at 130 ^oC from a 1,2-dichlorobenzene solution of PC and ET. In order to cover the film with a layer of $(ET)_2I_3$, we exposed the film surface to the vapors of a saturated solution of iodine in dichloromethane. The covering mechanism is following: the surface of a polycarbonate film easily swells under its exposure to dichloromethane vapors; this swelling facilitates a migration of ET molecules from the film bulk to the swollen film surface where the part of ET molecules are oxidized to radical cations $ET^{+\bullet}$ by iodine, which penetrates in the film surface together with dichloromethane vapors. This redox process induces the rapid nucleation of highly insoluble $[(ET)^0(ET)^{+\bullet}](I_3)^-$ species and a facing layer of molecular metal α-$(ET)_2I_3$ is formed. Electrical resistance of the 25 μm thick BL film with the covering layer of α-$(ET)_2I_3$ responded to strain with a gage factor being 10, whereas the polycarbonate film with the same thickness but surfaced with β-$(ET)_2I_3$ has a gage factor being 20 [4]. The BL film covered with a highly piezoresistive layer of β-$(ET)_2I_3$ was formed via a thermo-activated $\alpha \rightarrow \beta$ phase transition that occurs at T>100 ^oC [9]. For this purpose the BL film covered with the layer of α-$(ET)_2I_3$ was annealed at 150^oC during 30 min. The formation of the covering layer of β-$(ET)_2I_3$ was confirmed by its X-ray diffraction pattern that shows only one line at $2\theta=5.8^o$ and its higher order reflections, that corresponds to "c"-oriented crystallites of organic metal β-$(ET)_2I_3$ (Fig. 1, bottom) [9]. The surface analysis on a micro scale, performed using "Quanta FEI 200 FEG-ESEM" scanning electron microscope (SEM), showed that the crystallites of the covering layer of β-$(ET)_2I_3$ are of nano or submicro sizes (Fig. 2). The calculated possible maximal thickness of the piezoresistive covering layer is around 250 nm.

As a final remark to this part we would like to add that the BL film temperature resistance coefficient (TRC) and its gage factor were found as 0.3 %/^oC and 20, respectively. These values are in excellent agreement with the early reported data [4]. The TRC was calculated as a relative resistance change per grade and gage factor was calculated as the ratio between the relative resistance change and the relative strain value.

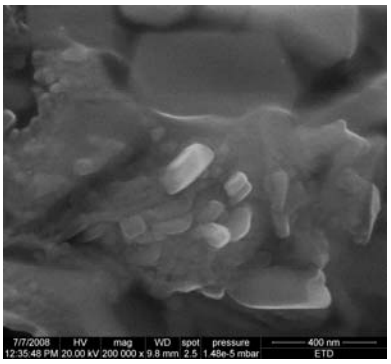

Figure 2. SEM image of the piezoresistive covering layer of β-$(ET)_2I_3$;

III. PROTOTYPES OF BODY SENSING DEVICES

The simple sensing prototype devices for monitoring the body movements breathing rhythms [4] blood pulse, intraocular pressure [7, 8] finger movement are already under development. Below we present some of them.

Blood pulse sensor (Fig. 3). The BL film-based membrane with sensing layer of β-$(ET)_2I_3$ was equipped with electrical contacts and fixed between two rigid plastic rings. To measure pulse the device was fixed on the carpus of a volunteer (Fig. 3 bottom). The resistance response of the sensor to strain provoked by pulse movement was measured by a four probes dc method. Data were gathered for different persons and time periods. As seen in the Fig. 4, the pulse movement resulted in an oscillated resistance curve that can be easily recorded and analyzed.

Figure 3. Photo images of the blood-pulse sensor (Top) and sensor location on the carpus of a volunteer under pulse testing (Bottom).

 ISBN: 978-1-61208-145-8

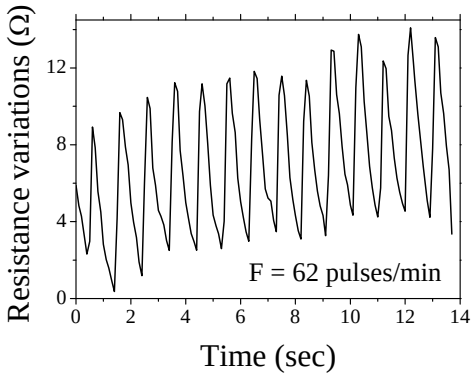

Figure 4. Resistance response to the blood-pulse movement.

Breathing sensor. This prototype contains the BL film as a tenzo-resistive diaphragm on springy plastic U-shape plate, which was attached to an elastic-textile belt (Fig. 5). The resistance response of sensors to strain provoked by the breathing was measured by a four probes dc method. Data were gathered for a different persons and time periods. As seen in the Fig. 6 the breathing movement resulted in an oscillated resistance curve that can be easily recorded and analysed. A relatively long time periods between the oscillations, observed in Fig. 6, correspond to holding up breathing.

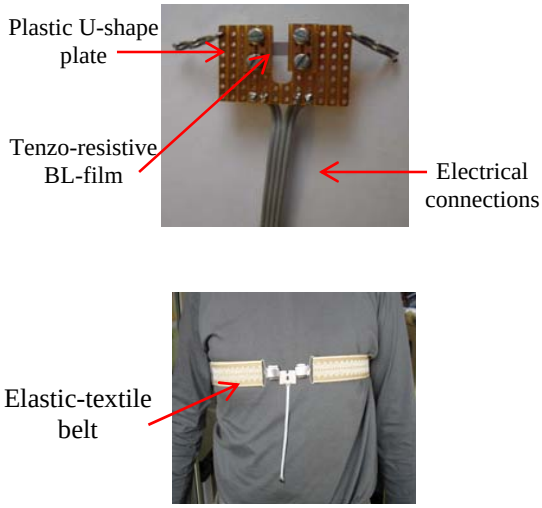

Figure 5. Photo images of the breathing sensor (Top) and sensor location on the breast of a volunteer for monitoring his breathing (Bottom).

Devices for monitoring finger movement. The first prototype of such type of medical devices is now under development. The prototype uses the BL-film as a tenzo-resistive diaphragm. The fabricated prototype is capable of measuring a very delicate finger movement as an easily controlled electrical signal. Its design also permits tracking of the large-scale finger movement.

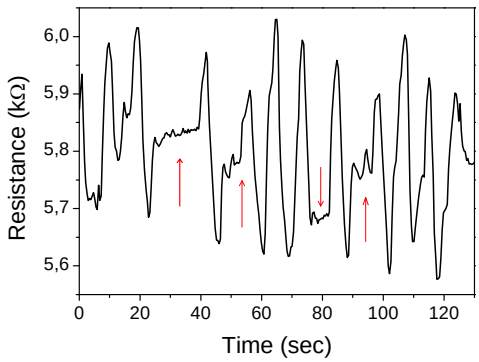

Figure 6. *Resistance response to the breathing of* a volunteer*; red arrows correspond to holding up breathing.*

IV. SUMMARY

It was shown that electrical resistance of flexible sensors with the active layer of tenzo-resistive organic metal $(ET)_2I_3$ linearly and reversibly depends on deformation resulted from the body movements.

The preliminary data display that the polycarbonate films metallized with β-$(ET)_2I_3$ show considerable promise as flexible strain/pressure gages for use in detecting body movements. Therefore this type of lightweight sensors is able to take the place of conventional metal-based strain and pressure gages in monitoring biomedical high-tech.

ACKNOWLEDGMENT

We acknowledge the support from European Community's Seventh Framework Programme (FP7/2007-2013) under grant agreement n° 212311 of the ONE-P project, DGI, Spain (contracts CTQ2006-06333/BQU and CTQ2010-195011/BQU), DGR, Catalunya (grant 2009SGR-00516). Authors thank the CIBER-BBN, an initiative funded by the VI National R&D&i Plan 2008-2011, Iniciativa Ingenio 2010, Consolider Program, CIBER Actions and financed by the Instituto de Salud Carlos III with assistance from the European Regional Development Fund.

REFERENCES

[1] S. Y. Yurish, N. V. Kirinaki, and I. L. Myshkin, “World Sensors and MEMS Markets: Analysis and Trends”, Sensors & Traducers Magazine (S&T e-Digest), vol. 62, Issue 12, pp. 456-461, 2005.

[2] F. Axisa, P. M. Schmitt, C. Gehin, G. Delhomme, E. McAdams and A. Dittmar, “Flexible technologies and smart clothing for citizen medicine, home healthcare and disease prevention”, IEEE Transactions on Information Technology in Biomedicine, vol. 9, No. 3, pp. 325-336, 2005.

[3] B. Adhikari, S. Majumdar, “Polymers in sensor applications”, Progress in Polymer Science, vol. 29, pp. 699-766, 2004.

[4] E. Laukhina, R. Pfattner, L. R. Ferreras, S. Galli, M. Mas-Torrent, N. Masciocchi, V. Laukhin, C. Rovira, and J. Veciana, “Ultrasensitive Piezoresistive All-Organic Flexible Thin films”, Adv. Mater., vol. 22, pp. 977-991, 2010.

[5] E. Laukhina, R. Pfattner, M. Mas-Torrent, C. Rovira, J. Veciana, Vladimir Laukhin, “Film-based Sensors with

Piezoresistive Molecular Conductors as Active Components: Strain Damage and Thermal Regeneration", Sensors & Transducers Journal, , vol. 10, Special Issue, February, pp. 1-12, 2011.

[6] L. R. Ferreras, R. Pfattner, M. Mas-Torrent, E. Laukhina, L. López, V. Laukhin, C. Rovira, J. Veciana *J.* "Highly piezoresistive textiles based on a soft conducting charge transfer salt", Mater. Chem**.**, vol. 21, pp. 637- 641, 2011.

[7] V. Laukhin, I. Sánchez, A. Moya, E. Laukhina, R. Martin, F. Ussa, C. Rovira, A. Guimera, R. Villa, J. Aguiló, J.-C. Pastor, J. Veciana, "Prototype for Noninvasive IOP Monitoring with a Nanostructured Polymeric Sensor Embeded in a Contact Lens", Transducers & Sensors, 2010, to be published.

[8] V. Laukhin, C. Rovira, E. Laukhina, J. Veciana, M. Mas-Torrent, A. Quimera Brunet, J. Aguiló Llobet, R. Villa Sanz, J. C. Pastor, and F. Ussa, Truncated contact lens for use in telemetry system, has truncation plane provided parallel to base of lens, and centrally placed polymer nanocomposite material joined to perimeter of truncated zone, Patent: ES2330405-A1; WO2009147277-A1.

[9] E. E. Laukhina, V. A. Merzhanov, S. I. Pesotskii, A. G. Khomenko, E. B. Yagubskii, J. Ulanski, M. Krysezewski, J. and K. Jeszke, "Superconductivity in reticulate doped polycarbonate films containing $(BEDT\text{-}TTF)_2I_3$", Synth. Met., vol 70, pp. 797-800, 1995.

 ISBN: 978-1-61208-145-8

Building a Prototype for a Magnetic Nanoparticle Bead Based Biosensing Device

Wen Yaw Chung, Kimberly Jane Uy, Yi Ying Yeh, Ting Ya Yang, Hao Chun Yang, and Hsi Wen Li
Department of Electronic Engineering
Chung Yuan Christian University
Chung-Li, Taiwan, R.O.C.
eldanny@cycu.edu.tw, kimuy_1984@yahoo.com, polnna25@hotmail.com, tingya0112@gmail.com,
derry2010@hotmail.com, fea7777777@gmail.com

***Abstract*—In the modern day society with its modern way of life, there is a growing problem with regard to the health of the people. One of the major concerns right now is the increasing number of overweight and obese people in the world. A way to determine whether the person has this problem is by detecting Adiponectin. The aim of the work is to make use of magnetic beads for future detection of the adiponectin, which is the target analyte of the work. This work will discuss the theoretical background of the target system as well as results for experiments using the prototype of the system implemented using commercially available components. The work shows a working prototype for a biosensing device that will be developed in the microscale level in the future.**

***Index Terms*—Magnetic Beads, Point of Care Testing (POCT), Hall Sensor, Adiponectin, Enzyme-Linked Immunosorbent Assay (ELISA)**

I. INTRODUCTION

The need for Point of Care Testing (POCT) has been growing for the past couple of years. It is a tool that may be used in diagnostics which plays an important part in the modern day. They can be separated into four different categories which include clinical diagnostics, veterinary diagnostics, environmental monitoring and food testing. Clinical diagnostics does not only involve detection of disease but also in its prevention and health care

This work will address the growing problem of obesity in the world. In order to deal with obesity, we must understand the physiology of an obese person. Obesity is defined as a medical condition wherein there is an excessive accumulation of body fat and has already reached a point where the person's health problem has increased and the life expectancy has decreased

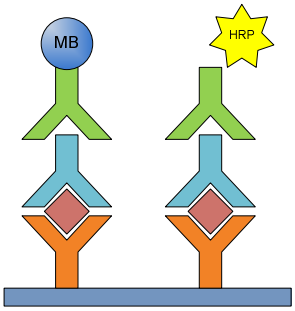

Figure 1. Capture of sample using sandwich ELISA. Illustration shows two ways of detection of sample presence; (left) magnetic bead, (right) HRP used in conventional ELISA

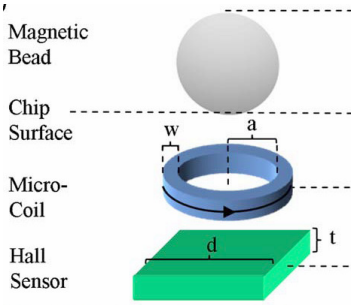

Figure 2. Magnetic Bead Sensing System [3]. The system make use of inductor as a source of polarization.

[1]. Therefore we must understand what is body fat. Body fat or fat is referred to as the adipose tissue in histology. It is a loose connective tissue that is composed of adipocytes or fat cells. Its main role in our body is to store energy in the form of fat. It also provides the body with cushion and insulation. It is made of several types of hormones, of which, have different effects on the body. One of the hormones that have been studied and are found to be a promising therapeutic tool in treating obesity and other human diseases is the adiponectin. There are a hundred ways to detect adiponectin, which from here on will also be referred to as the target analyte, but the most commonly used way is the enzyme-link immunosorbent assay (ELISA) protocol [2].

The work aims to develop in the future a portable POCT device that would utilize the characteristics of the magnetic beads to detect the concentration of the adiponectin protein hormone. Magnetic beads are ideal for such kind of bioassay application due to the following reasons: (a) cells exhibit few magnetic properties, (b) signals from magnetic beads are stable with time, (c) results from magnetic detection is independent of the color and clarity of the sample, and (d) magnetic labeling has functionalities that may be used to improve bioassay performance such as magnetic filtration and manipulation [3].

As a proof of concept for the microscale device, this work will present a working prototype developed using commercially available components. For the prototype, 2mm steel balls will be used in place of the magnetic beads that are superparamagnetic. Superparamagnetic behavior is an important property of magnetic beads used for detection since it prevents the beads from clustering at the absence of magnetization [4]. The components used to build the prototype are also discussed. There are several types of devices that can be used in the detection of magnetic field. Of which include

 ISBN: 978-1-61208-010-9

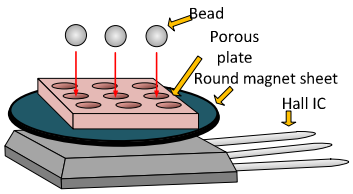

Figure 3 Circuit model of the sensing system. This includes steel balls, magnetic sheet and commercially available hall sensor IC.

superconducting quantum interference devices (SQUIDs), Giant Magnetoresistive (GMR) Sensors, spin valve sensor, Tunneling Magnetoresistive (TMR) sensors, and Anistropic Magnetoresistive (AMR) sensors. However, such devices are not ideal for dense arrays due to the presence of magnetic field caused by applied bias conditions [4]. For this work, a commercially available hall sensor, WSH 136, was used in the system and is characterized in the following article. The said device is ideal for such application since it is designed to track extremely small change in the magnetic flux density [5].

The work will give a theoretical background of the concepts of which the work is based on. Such discussion will include description of adiponectin, the ELISA protocol, the magnetic beads, and the sensor system. After which, a detailed discussion of the implementation of the circuit model will be given. This is then followed by the discussion of the experimental data and results，conclusion and future work.

II. THEORETICAL BACKGROUND

A. *Adiponectin*

Adiponectin is a protein hormone that is secreted exclusively by the adipose tissue into the bloodstream. It is relatively abundant in plasma as compared other hormones. Its function includes modulation of a number of metabolic processes. These processes include glucose regulation and fatty acid catabolism. Study shows that the higher the level of adiponectin, the lower is the production of insulin. Our blood sugar is also better controlled. The increased number of adiponectin will reduce the risk of diabetes and heart disease. Furthermore, people with plenty of adiponectin will have a better controlled weight. Although the adiponectin is produced from body fat, it is found that the plasma level of adiponectin is inversely proportional to the body fat. Therefore, as adiponectin level is lowered, the weight of the person further increased. Some studies have shown that the adiponectin production is increased when a person does exercise.

B. *Enzyme-Linked Immunosorbent Assay (ELISA)*

Enzyme-Linked Immunosorbent Assay (ELISA) is a protocol dominantly used for medical diagnostics. The work will make use of its basic principle for the detection of the target analyte, which refers to the substance being to be analyzed by the procedure. The protocol will consist of three different antibodies. The first antibody will be the capture antibody that will be placed on the surface of the micro plate and is

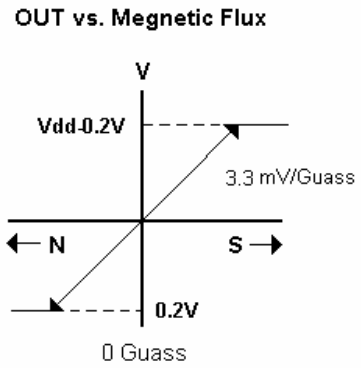

Figure 4. Characteristic curve of the WSH 136 commercial hall sensor IC. [5] The figure illustrates the output voltage of the component with regard to the sensed magnetic field

responsible for capturing the target analyte from the sample. The second antibody will attach itself to the target analyte captured. The third antibody is the detection antibody which will have horseradish peroxidase (HRP) attached to it and will bind to the second antibody. Figure 1 illustrates the architecture of the said antibodies and analyte. In general ELISA protocol, the concentration of the sample will be calculated based on the optical density measured from the result of the experiment. Optical density can be described as the amount of light absorbed by the target sample. HRP is used to increase the detectability of the target analyte. The number of detection antibody that will remain on the sample will be proportional to the concentration of the target analyte. The reaction between the HRP attached on the detection antibody and a substrate will change the opacity of the sample giving it a much denser color. The optical density of the solution is then measured and is presumed to be the concentration level of the target analyte in the sample. A low value of optical density will mean a higher concentration of the target analyte present in the sample. For this work, the ELISA protocol will slightly be altered. The detection antibody will be attached to magnetic beads instead of HRP. There will no longer be a need for a substrate to react with sample. The number of magnetic beads left in the sample will determine the level magnetic field detected by the sensing system. Figure 1 illustrates the difference between the typical ELISA protocol and the proposed structure with the magnetic beads. This process is often referred to as magnetic assays.

C. *Magnetic Beads*

Magnetic beads are made from $\gamma - Fe_2O_3$ or Fe_3O_4 nanometer crystals that are dispersed in a polymer matrix [4]. Their superparamagnetic behavior is an important property when used for biomedical detection. When the beads are coated with specific chemical substance they are able to bind to specific biological material. They can be used in POCT devices that use bioassays for detections and measurements. The super paramagnetic characteristics of these beads are ideal for such applications since they have little or no intrinsic magnetization. This means that there will be no clustering of magnetic beads at the absence of magnetic field.

 ISBN: 978-1-61208-010-9

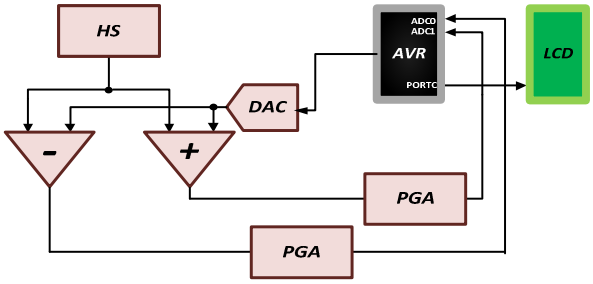

Figure 5. Illustration of the readout circuit diagram for the implementation of the large scale model. The system also includes a microcontroller that would process the data to human understandable number.

D. Sensing System

Figure 2 illustrates a sample magnetic beads sensing system [3]. The sensing system is composed of a hall sensor and a micro-coil. The system is implemented using the complementary metal oxide semiconductor (CMOS) technology. In order for the hall sensor to detect the magnetic beads, it needs to have a flux generator to induce magnetic field onto the super paramagnetic beads. A micro-coil is, therefore, placed on top of the hall sensor to serve such purpose. This, at the same time, will serve as a calibration mechanism for the system. Since there is a magnetic field source specific for the system, the environmental magnetic fields are negligible. The hall sensor would then be connected to a source that will provide an electrical signal running on a uniform direction. And another distinct electrical signal will be measured. An example of such electric signal is having a constant current fed through your hall sensor. And for the measured electrical signal; the voltage across the hall sensor shall be taken. At the presence of additional magnetic field which will come from the super paramagnetic beads, at constant supply current, the value of the measured voltage will change in proportion to the number of magnetic particles present in the system.

III. Circuit Model Implementation

A. Sensing System

For this work, the magnetic beads are replaced with steel ball with a 2mm diameter. The steel balls are ideal for this work since they are unpolarized and get magnetized when placed near a magnetic field which is similar to the characteristic of magnetic beads. The downside, though, is that they will not automatically demagnetize when taken away from a magnetic field. Therefore, this work also made use of a demagnetizer circuit to demagnetize the steel balls after each use. The system was made such that the system would be able to test up to a quantity of nine steel balls. A porous plate was made to hold the steel balls in place. In place of the micro-coil, a round magnetic sheet is placed for polarization of the steel balls. On the bottom is the commercially available hall sensor integrated circuit (IC). The hall sensor already have amplifier that would preprocess the reading from the hall sensor. The illustration of the described sensing system is shown in Figure 3.

Table I. List of Components Used in Implementation of the Large Scale System

Component	Model
Shift Register	74LS164
Digital to Analog Converter (DAC)	DAC0808
Operational Amplifier (OPA)	LMC6484
Microcontroller	ATmega8535
Hall Sensor	WSH 136

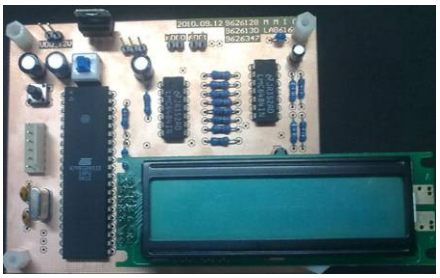

Figure 6. A picture of the whole large scale system implemented on a custom made PCB board.

B. Characteristic of the Hall Sensor IC

The work made use of a commercially available hall sensor IC made by Winson. The model used in this work is the WSH 136. Integrated into this component is a hall sensing element, linear amplifier, sensitivity controller, and emitter follower output stage [5]. The component operates in a voltage range of 3.0V to 12V. It has a sensitivity of 3.3mV/Gauss. Figure 4 illustrates the operating curve of the sensor IC at a given range of magnetic field.

C. Circuit Implementation

The circuit for readout circuit is illustrated in Figure 5. The system includes the following components: shift register, digital to analog converter (DAC), operation amplifier (OPA), microcontroller, and the hall sensor IC. The system consists of an adder and a subtractor. These components are used to compute the analog signal from the hall sensor. The system simultaneously adds and subtracts the output the DAC from hall sensor IC.

Figure 7. LCD display output of the whole sensor system.

 ISBN: 978-1-61208-010-9

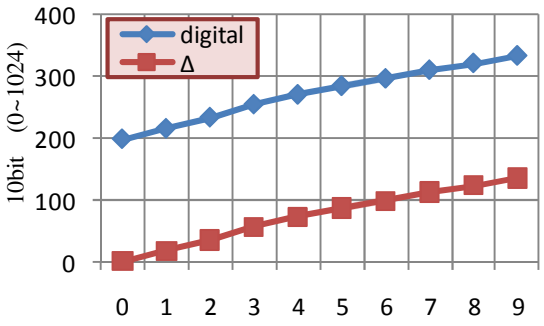

Figure 8. Digital output value for the system generated from 0 to 9 numbers of steel balls placed on the sensor system.

Their output is then fed into a programmable gain amplifier that is designed using OPAs. Since they are of the same potential and current we are able to derive equations (1) and (2). Although the adder and the subtractor work simultaneously, only one path will be used for the measurement of the result. This will be done by the microcontroller.

The system will perform an Auto Zero calibration or AZC which is performed when no steel ball is placed on the system. This is done to eliminate the magnetization coming from the surrounding. This will be done every time the device is turned on and is used to account for the offset given by the magnetic field from the surrounding. Then when the steel balls are placed, the computation of the magnetization measurement will start. The output from the adder and the subtractor will be fed into the microcontroller wherein the internal analog to digital converter (ADC) will be used to convert the analog signal to a digital value that could be processed by the microcontroller. The two values are then averaged and compared to the values from the adder and subtractor through the use of an XOR operation until the desired value is reached.

$$HS - DAC = V- \quad (1)$$

$$HS + DAC = V+ \quad (2)$$

The implemented system is illustrated in Figure 6. And the list of commercially available components used in the building of this system is listed in table 1.

D. Data Display

Figure 7 shows a picture of the LCD display for the reading of the system. Table 2 shows the description of each value in the LCD display. “AZC” stands for the Auto Zero Calibration which is the initial reading value of the system. The initial value is the reading when there is no steel ball placed on the system. The “initial reading” will account for the magnetic field surrounding the system. The magnetic field from the surrounding will be the offset value of the system. This value will change at different locations. Therefore, auto zero calibration will be time each time the device is used. This also means that the “initial value” will vary each time the device is used. The “corrected value” stands for the value of the reading when a certain number of steel balls are placed on the system.

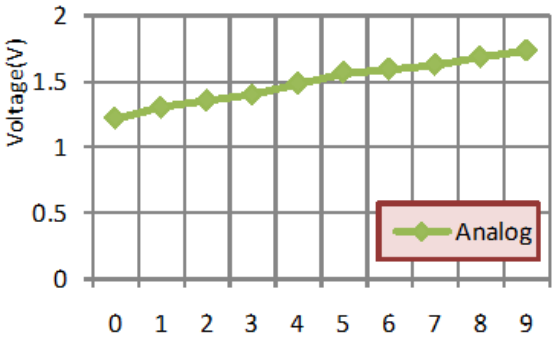

Figure 9. Analog output value for the system generated from 0 to 9 numbers of steel balls placed on the sensor system.

And “MAG” will stand for the magnitude of the readout. The “measured value” will have the same value as that of the corrected value. The “variation” will stand for the change in the output value between the first reading and the second reading.

IV. Data and Results

Figure 8 shows the digital output value of the system while Figure 9 shows the analog output value of the system. The digital output shows a linearity of 0.98. And the delta in the figure represents the difference between the initial value and each count of steel balls present in the sensor system ranging from 1 to 9. This result also shows a linearity of 0.98. The analog output of the system also shows a linearity of 0.98 same as that of the digital output. The output voltage range, as shown in Figure 8 is ranging from 1.217V to 1.728. This shows a system sensitivity of 56.77mV for each steel ball.

V. Conclusion and Future Work

A circuit model was implemented with components having the same function as that of their counterparts on the submicron technology scale to be implemented. The steel balls were used in place of the magnetic beads, the round magnetic sheet were used in place of the micro-coil and the hall sensor IC with internal preprocessing circuit was used in place of the CMOS based hall sensor. The results show that the quantity of steel balls present on the sensor will affect the output voltage of the system. The result also shows high linearity for the results. From this we can conclude that the system is able to give an accurate result for sensing the quantity of beads present on the system. For the future work, the system shall be implemented on a submicron CMOS technology for its intended application.

From the results shown in this work, the number of magnetic beads captured by the sensor using magnetic assay should

Table II. Description of the displayed values of the LCD display panel.

AZC	initial value	corrected value
MAG	measured values	variation

 ISBN: 978-1-61208-010-9

reflect the concentration of the target antigen. The sensor will use BioMEMS technology for implementation. This will provide the sensor to have greater binding capabilities to biological materials. And it will also provide a smaller distance between sensor and magnetic beads due to its post process etching capability, thereby increasing the sensitivity of the sensor. The post data processing of the said device would be done using an 8051 microcontroller. The data gathered from the device would be converted to a value that is understandable by the user. The signal quality of the system will be taken into consideration. Additional filters will be applied to the system as deemed needed to reduce noise levels during the development of the micro-scale system. The said device shall not be limited to the testing of a specific analyte. The device may be altered to the need of the user. This is simply done with the change antibodies used for the reactions.

ACKNOWLEDGMENT

This work would like to acknowledge the National Science Counsel, Taiwan, R.O.C. for funding this project (NSC 99-2221-E-033-064) and Hall sensors donated by Winson Semiconductor Corp, Taiwan.

REFERENCES

[1] Y. Arita, S. Kihara, N. Ouchi, M. Takahashi, K. Maeda, J. Miyagawa, K. Hotta, I. Shimomura, T. Nakamura, and K. Miyaoka, “Paradoxical decrease of an adipose-specific protein, adiponectin, in obesity,” Biochemical and Biophysical Research Communications, 1999. **257**(1): pp. 79-83.

[2] R. S. Yalow and S. A. Berson, “Immunoassay of Endogenous Plasma Insulin in Man”, J Clin Invest. 1960 Jul; 39:1157–1175, 1960.

[3] O. Florescu, M. Mattmann, and B. Boser, “Fully integrated detection of single magnetic beads in complementary metal-oxide-semiconductor,” Journal of Applied Physics, 2008.

[4] F. Colle, “Hallsensor based detection of magnetic particles for lab-on-a-chip,” 2007, s.n.

[5] Winson Semiconductor Corp., “Linear Hall Effect Sensor IC – WSH136,” Data sheet.

[6] T. Aytur, P. R. Beatty, and B. Boser, "An immunoassay platform based on CMOS hall sensors," *Proc. Solid-State Sensor, Actuator and Microsystems Workshop*, pp. 126 - 129, 2002.

[7] H. H. Tsai, C. F. Lin, Y. Z. Juang, I. Wang, and Y. C. Lin, “Multiple type biosensors fabricated using the CMOS BioMEMS platform,” Sensors and Actuators B: Chemical. **144**(2): pp. 407-412.

[8] Wang, H. and S.A. Hajimiri, “A Frequency-Shift CMOS Magnetic Biosensor Arraywith Single-Bead Sensitivity and No External Magnet,” California Institute of Technology, Pasadena, CA.

[9] P. A. Besse, G. Boero, M. Demierre, V. Pott and R. Popovic, “Detection of a single magnetic microbead using a miniaturized silicon Hall sensor,” Applied physics letters, 2002. **80**(22): pp. 4199-4201.

[10] L. Brown, "Beyond the Ivory Tower: Disease detection on a chip," Berkeley Science Review, issue 6, pp. 32, Spring 2004.

[11] T. S. Aytur, T. Ishikawa, and B. E. Boser, “A 2.2-mm CMOS Bioassay Chip and Wireless Interface,” 2004: IEEE.

[12] R. Elliott, “Flux Meter,” Page Created 28 November 2008. Access Date 15 July 2011. http://sound.westhost.com/clocks/fluxmeter.html.

[13] Y. J. Chang, C. Y. Hu, L. T. Yin, C. H. Chang, and H. J. Su, “Dividable Membrane with Multi-Reaction Wells for Microarray Biochips,” J. of Bioscience and Bioengineering, Vol. 106, No.1, pp. 59-64, 2008.

[14] S. M. Grundy, H. B. Brewer, Jr, J. I. Cleeman, S. C. Smith, Jr, and C. Lenfant., “Definition of Metabolic Syndrome,” Circulation, No. 109, pp. 433-438, 2004.

 ISBN: 978-1-61208-010-9

An Automatic System for Bilayer Lipid Membrane Formation and Monitoring

Michele Rossi, Federico Thei, and Marco Tartagni
ARCES – Advanced Research Center on Electronic Systems
Second School of Engineering, University of Bologna - Via Venezia 52, 47521 – Cesena (FC), Italy
mrossi@arces.unibo.it, fthei@arces.unibo.it, mtartagni@arces.unibo.it

***Abstract*— Ion channels are natural nanometric pores formed by proteins across cell membranes. They are responsible of part of cell signaling and a large part of pharmaceutical compounds are interacting with them. Therefore, single ion channel screening is being proposed as a fundamental technique for investigating the function of cell membrane proteins with pharmaceutical compounds. The technique consisting in embedding ion channels in artificial bilayer lipid membranes (BLM) is gaining attention over patch clamp approach due to its characteristics of performing parallel tests over selected classes of channels. However, no valid procedures for automatic formation and real time monitoring of BLM arrays have been presented so far. More specifically, since BLM is based on a manual and time-consuming technique, there is a strong need of automatic systems for forming BLMs in a fully parallel fashion for testing compounds in high throughput screening (HTS) fashion. In this paper, an automatic liquid dispensing system for BLM formation is presented using commercial 3+1 axes movement stepper machine together with a multi-sensor technique for monitoring BLM formation in real time. As proof of this concept, the automatic dispensing system is interfaced with an 8 channel electronic interface where low noise amplifiers are able to automatically sense BLM formations by means of current sensing.**

Keywords - Bilayer lipid membrane, automatic dispensing system, ion channels, high thoughput screening.

I. INTRODUCTION

Bilayer lipid membranes are artificial biological substrates composed of phospholipid mixtures suspended into different organic solvents that self assemble to form bilayers under specific conditions [1]. BLMs are used to host ion channel proteins since they well approximates the natural behavior of cell membranes. Ion channels are natural nanopores that regulates the ions exchange from intra and extra-cellular solution, and they are involved into all the cellular life process [2]. Because of their key role in the physiologic process, ion channels behavior can be altered or compromised from several diseases [3]. For these reasons, simple and versatile systems that allow to verify and screening drugs interaction with ion channels are required to reduce time consuming in the drugs discovery and validation processes [4].

The integration of biological nanopores, such as ion channels with electronics is also a promising approach for the development of novel biosensors that are able to detect low concentrations of target molecules [5], or even identify differences between different DNA bases [6].

BLMs can be used instead of natural cell membrane without significant information loss using channel proteins incorporation techniques [5]. BLMs can be formed by means of different techniques using microfluidic chambers and systems to mechanically support the bilayer.

Various techniques to form BLMs are reported in literature: one of the first developed is the painting method, consisting in applying a small quantity of lipid-solution dissolved in an organic solvent using a borosilicate rod over an aperture immersed in water. The orfice, in the range of tens to hundreds micrometers, is created in a hydrophobic material foil such as Teflon or Delrin [1]. At the lipid-aqueous interface, a lipid monolayer will be constituted thanks to the amphiphilic properties of lipids. The lipid-solvent solution wets the hydrophobic walls of the aperture, resulting in a thinning of the solvent solution in the center of the aperture, until a completely fusion of the two monolayers into a single bilayer. A small quantity of solvent remains at the aperture perimeter (the annulus), increasing the BLM stability and acting as connection between the thick Teflon sheet and the final thickness of the BLM, typically in the nanometric range [1].

Following different approaches, other techniques were developed: some are based on droplets of water inside lipid solution [8], others using solvent evaporation and resulting thinning of the bilayer [9], or based on the liquid insertion through a microfluidic chip which spreads lipids over a small Teflon apertures [10]. These techniques allow the BLMs formation, but they are not suitable to be automated. In contrast, the Montal-Muller approach presents some characteristic procedures so as to to be automated [11]. As illustrated in Figure 1, the Montal-Muller technique consists of the formation of two lipid monolayers above the aqueous surface of two separated chambers by applying a lipid solution in a volatile solvent, such as hexane or chloroform. The chambers are separated by a thin septum where a micro aperture is drilled and, during the monolayer formation, it is kept out from the aqueous surface. After the evaporation time, the micro aperture of the septum is lowered and the two monolayers formed into the chambers aqueous surfaces are folded down against each other, forming a bilayer across the aperture [11].

This paper present first example of a fully automatic system for parallel BLM formation inspired on the Montal Muller approach employing disposable bilayer chambers [12] and an array of sensing amplifiers to continuously

 ISBN: 978-1-61208-145-8

monitor BLM formation. The system allows testing and optimizing different protocols, offering a large flexibility and a fast characterization of membranes.

Section II will show the system architecture and working principle. Section III will present the implementation of the mechanical control. Section IV will show a real experiment where BLM are formed in parallel fashion and monitored in real time by embedded amplifiers. Finally, Section V will present an application of the apparatus for recording single ion-channel signals.

II. SYSTEM STRUCTURE AND CALIBRATION

The proposed automatic liquid handling system (Figure 2) is composed of: i) Sutter Instrument MP-285: 3-axis micromanipulator for pipette automatic movements in the 3D space; ii) Newport NSA12: single-axis micromanipulator for multipipette flux control; iii) Anachem Ltd 8-Channel Pipette (20-200 µL); iv) LabVIEW™ control panel.

Sutter Instruments MP-285 micromanipulator offers a range of movement of 25 mm in the 3 directions. It allows also selecting between two submicron movement resolutions of 0.2 mm (coarse range) and of 40 nm (fine range). Newport NSA12 provides a motorized, linear plunger, whose position can be controlled with sub-micron (0.1 µm-µSTEP) resolution over 11 mm of travel, with a minimum incremental motion of 0.3 µm (3 µSTEPs). Each µSTEP is 1/64 of the full-step (FS) of 6.4 µm. The NSA is mounted in a fixed aluminum bracket (screwed in the MP-285 vertical plate) that provides both a rigid coupling between NSA12 plunger and the pipette plunger along the vertical axis and the rigid coupling between the MP-285 and the multipipette. In order to have the maximum pipette volume range, when the NSA12 plunger is fully retracted, the pipette plunger is fully extended and vice-versa. The mechanical interface is compatible with any kind of pipettes.

Calibration is done using a precision balance (±0.1mg resolution) knowing these experimental relationships, which are dependent on the particular pipette tips used:

$$8100\,\mu STEPS = 100\,\mu L \Rightarrow 810\,\frac{\mu STEPS}{\mu L} = 12.66\,\frac{FS}{\mu L} \quad (1)$$

$$1\cdot\frac{mm}{s} = 156.25\cdot\frac{FS}{s}\cdot\frac{\mu L}{12.66\,FS} = 12.35\,\frac{\mu L}{s} \Rightarrow 12.34\,\frac{\mu L}{mm} \quad (2)$$

Using these two relationships, it has been possible to relate the volume with the linear movement of the NSA12 plunger as in equation (1) and its velocity with the infusion/withdrawal flow rate as in equation (2) in order to have a control with a precision of ±1µL.

Both micromanipulator are connected to a PC using RS-232 interface and are controlled by LabVIEW™. Elementary operations are implemented in LabVIEW™ executable in order to obtain modular software, very versatile for different applications as described below.

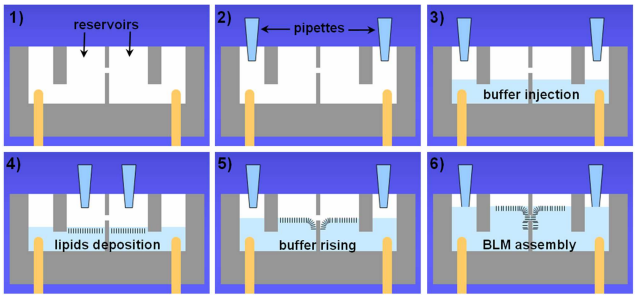

Figure 1. Montal Muller technique for BLM formation on a small hole on a Teflon or Delrin septum separating two chambers. 1) device empty; 2) pipette positioning on the inlet channels; 3) injection of buffer solution; 4) deposition of lipids for monolayer assembly on the two solution surfaces; 5) rising solution level 6) final bilayer assembly.

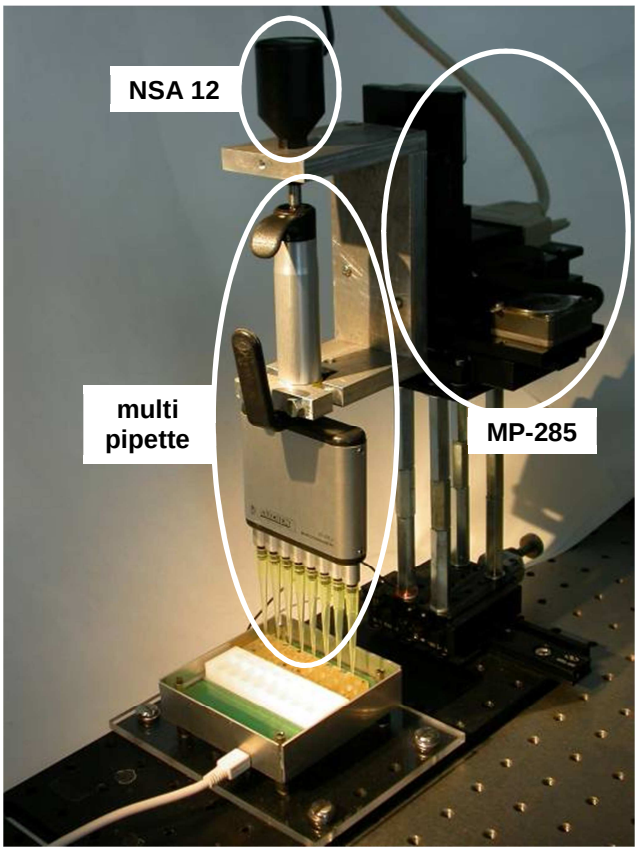

Figure 2. Details of the micromanipulators and multipipette composing the compact automatic liquid handling system.

III. IMPLEMENTATION OF THE CONTROL

The described system has been designed with the particular aim to create a compact automatic liquid handling robot for BLM formation able to be interfaced with an array platform [13]. The system is controlled by an implemented user-friendly control panel (Figure 3). This has been

 ISBN: 978-1-61208-145-8

designed following a modular and reusable design, starting from elementary operations, implemented in different subroutines and associated to single independent controls.

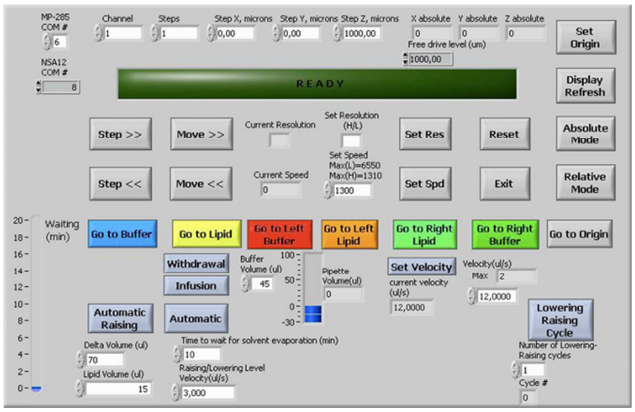

Figure 3. LabVIEW™ Control Panel interface for automatic liquid handling.

The operations are referred to the reference system fixed to the array platform [13]. Elementary operations are available to the user, more specifically: 1) to move the multipipette to buffer reservoir; 2) to move the multipipette to lipid reservoir; 3) to shift left/right the multipipette on the bottom of left/right chamber; 4) to move the multipipette on the bottom of left/right chamber at the air-buffer interface level where lipids are deposited; 5) to return to origin: move the multipipette to the reference system origin; 6) to withdraw a fixed amount of buffer selected by the user (µL); 7) to inject a fixed amount of buffer selected by the user (µL). Furthermore, several important parameters for BLM formation can be set, in order to test different BLM protocols, in particular: a) volume of buffer/lipids injected/withdrawed (µL); b) infusion/withdrawal flow rate (µL/s); c) number of lowering/raising buffer level cycles in both chambers; d) waiting time for lipid solvent evaporation (minutes). Finally, stacking and synchronizing the different elementary operations, two automatic BLM formation protocols (both using the Montal-Müller method) have been implemented.

IV. MEASUREMENTS ON PARALLEL BLM FORMING BY REAL-TIME MONITORING

As proof of concept, two protocols for automatic BLM formation have been implemented, following the Montal Muller technique [11]. They are called “Automatic Raising” and “Automatic”. I) Automatic raising. The system withdraws a quantity of buffer from the reservoir and then fills the two chambers beneath the microhole (buffer volume ≤ 70µl). Then, a selected quantity of lipids is injected in the two chambers and, after a waiting time for solvent evaporation, the buffer level in the two chambers is raised by a fixed quantity at a fixed velocity. At the end the pipette is moved to the reference system origin. II) Automatic. This sequence is illustrated in Figure 5. The system withdraws a quantity of buffer (1) from the reservoir it fills the two chambers above the microhole (2) (3), in order to allow to use the offset correction (4) functionality implemented in the readout interface. Then a selected quantity (5) of lipid is infused (6) (7) in the two chambers and, after a waiting time for solvent evaporation, the buffer level in the two chambers is lowered and immediately raised (8) (9) by a selected quantity of buffer.

For a better lipid spreading over the microhole, the “lowering/raising cycle” functionality has been implemented. This procedure automatically move alternatively the pipette to both chambers, withdraws and then injects a selected quantity of buffer from the two chambers using a fixed pipette flow rate (selected in “raising/lowering level velocity” option). In order to better distribute the lipid at the air-buffer interface, the user can set several automatic cycles.

To monitor the membrane formation, following a known technique [1], a triangular wave of 80 mV_{pp}@6Hz is applied by the electronic system and the current signals coming from the parallel fluidic bilayer chambers are visualized and recorded by means of a PC-based custom graphical user interface (GUI). As shown, in Figure 4, if the lipid bilayer is not formed, the microhole acts as an electrical resistor. Hence, the current follows the same shape as the voltage stimulus. When a BLM is formed, the equivalent circuit element could be modelled as a capacitor and the current is given by the derivative of voltage stimulus, resulting in a square current waveform proportional to the membrane capacitance. This method allows to known the dimensions of the bilayer since different BLM have different square wave amplitudes (Figure 5).

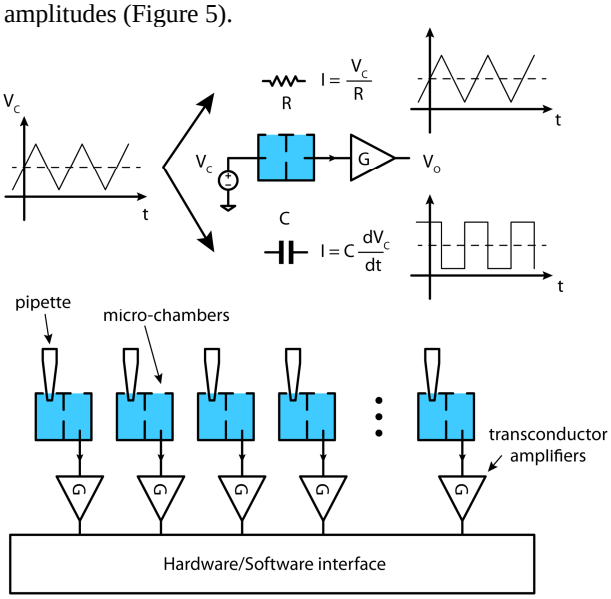

Figure 4. Equivalent electrical circuit of the septum (above). If BLM is not present, the microhole can be represented by a resistor. In the presence of a lipid membrane it can be modeled by a capacitor. The difference is sensed by a low-noise transconductance amplifier placed on each spot of the array (below).

The typical measured current is about 300 pA_{pp}, equivalent to a membrane capacitance of about 156 pF,

much higher of the septum strain capacitance (8–10 pF range), which can be neglected.

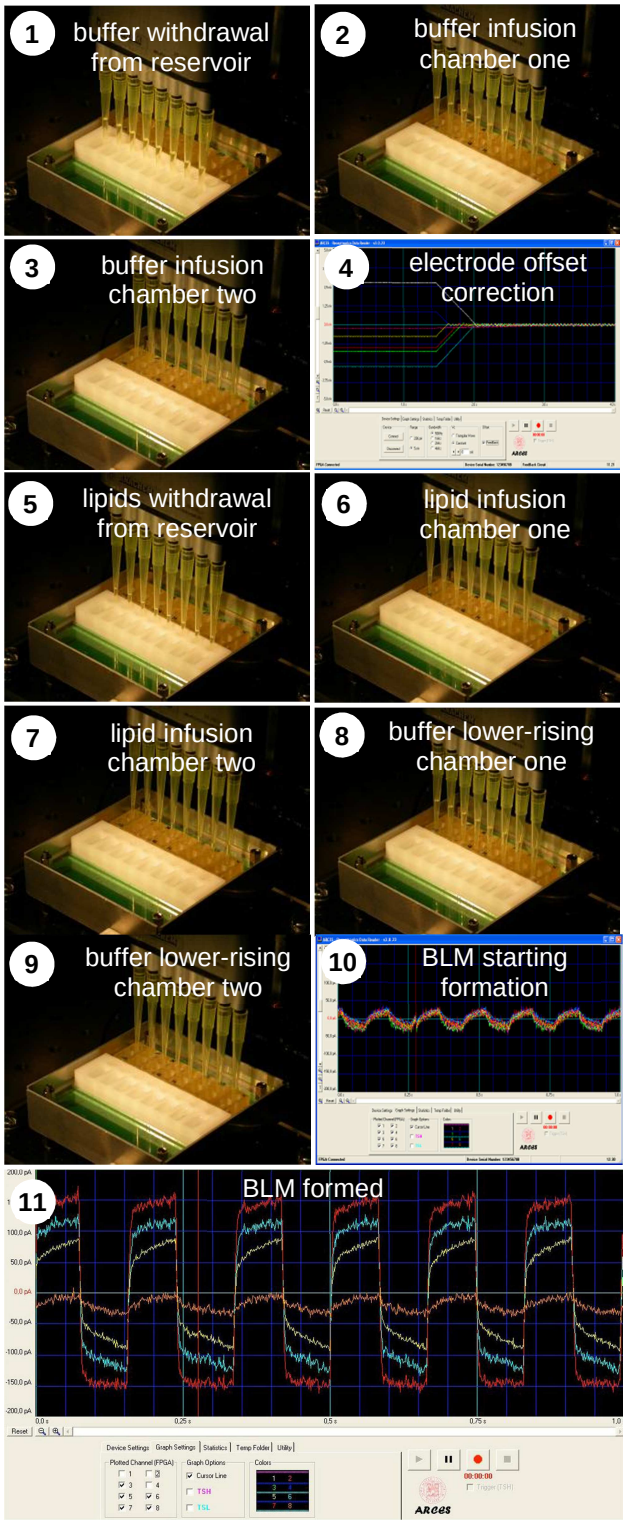

Figure 5. Example of automatic operations sequence implemented in the "automatic" procedure. Steps 4-10-11 are screenshots of the GUI interface. The three square-wave signals (red, cyan and yellow) in step 11 demonstates the concurrent formation of three independent BLMs of different dimensions on different microholes, while brown wave indicates the early stages of membrane formation where a lipid agglomerate is present and acts as a very small capacitance between the two chambers.

V. APPLICATION TO SINGLE CHANNEL RECORDINGS

As a working proof of formation of artificial lipid bilayer resulting from the proposed approach, a typical single channel recording using artificial lipid bilayer membrane will be shown. In the trans-chamber an α-haemolysin (αHL) protein is embedded with the BLM with a final concentration of 5ng/mL. αHL is an exotoxin secreted by the bacterium *staphylococcus aureus* that forms pores allowing ions and molecules to pass through the BLM.

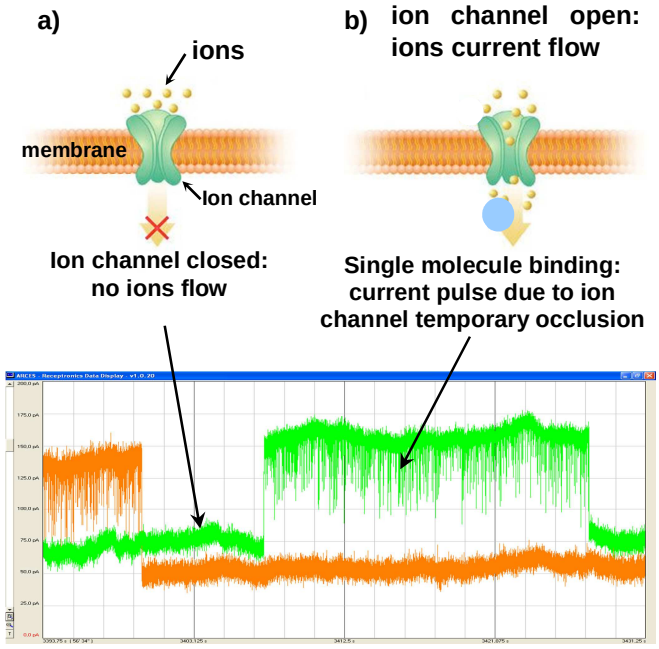

Figure 6. Example of single molecule binding activity over two differents BLM.

When no ion channel is embedded into BLM, no passage of current occurs, due to the high electrical resistance (several Gigaohms) of the membrane with respect to ions. After insertion of a αHL pore into BLM a constant current is detected through the membrane. When a transmembrane potential of -80mV, is applied a current of about -80pA is observed. Finally, we have also introduced β-cyclodextrin (βCD), which binds the α-haemolysin protein and significantly reduces the ionic channel conductance, and thus the measured current. This molecule is able to get into the lumen of the pore from the stem side and to bind to it, partially blocking the channel and causing stochastic current spikes. Figure 6 is illustrating this experiment where current pulses are readout using the same low-noise transconductance amplifiers used for monitoring BLM formation.

 ISBN: 978-1-61208-145-8

VI. CONCLUSION

A compact parallel liquid handling system for automatic BLMs formation procedure and real time monitoring is presented. The apparatus shows for the first time a complete automatic setup for parallel BLM formation. A user-friendly interface controlling the micromanipulators has been implemented in order to automatically create BLMs regardless of the user's ability with a high yield rate. As proof of concept, a complete sequence for parallel BLM formation is reported together with single channel recording using the same transconductance amplifiers used to monitor BLM formation.

ACKNOWLEDGMENT

This work was supported by the 6th Framework Programme of the European Commission under the contract NMP4-CT-2005-017114 "RECEPTRONICS". We are also grateful to the "Fondazione Cassa dei Risparmi di Forlì" for its support.

REFERENCES

[1] H.T. Tien, "Bilayer lipid membranes (BLM), Theory and practice", Ed. Marcel Dekker Inc., New York, 1974.

[2] B. Hille, "Ion Channels of Excitable Membranes", Sinauer Associates Inc. 2001.

[3] J.P. Overington, B. Al-Lazikani, and A.L. Hopkins, "How many drug targets are there?", Nature Review Drug Discovery 5, pp. 993-6, 2006.

[4] J.J. Clare, "Targeting Ion Channels for Drug Discovery", Discovery Medicine, 9(46):253-260, 2010.

[5] H. Bayley, and P.S. Cremer, "Stochastic sensors inspired by biology", Nature 413, pp. 226–230, 2001.

[6] J. Clarke, H. C. Wu, L. Jayasinghe, A. Patel, S. Reid, and H. Bayley, "Continuous base identification for single-molecule nanopore DNA sequencing.", Nature Nanotechnology, 4, pp. 265-270, 2009.

[7] D.J. Estes, S. Memarsadeghi, S.K. Lundy, F. Marti, D.D. Mikol, D.A. Fox, and M. Mayer, "High-throughput profiling of ion channel activity in primary human lymphocytes", Anal. Chem. 80, pp. 3728–3735, 2008.

[8] M. Zagnoni, M.E. Sandison, H. Morgan, "Microfluidic array platform for simultaneous lipid bilayer membrane formation", Biosens. Bioelectron., 24, pp. 1235-1240, 2009.

[9] M.E. Sandison, M. Zagnoni, and H. Morgan, "Air-Exposure Technique for Formation of Artificial Lipid Bilayers in Microsystems", Langmuir, 23, pp. 8277-8284, 2007.

[10] V.C. Stimberg, I. Uitert, S. Le Gac, A. Berg, "BLM Experimentation and Opto-Electrical Characterization on Microchips. Towards an Integrated Platform for Drug Screening on Membrane Proteins", MicroTAS conference, Groningen (NL), pp. 830-832, 2010.

[11] M. Montal, and P. Mueller, "Formation of Bimolecular Membranes from Lipid Monolayers and a Study of Their Electrical Properties", Proceedings of the National Academy of Sciences of the United States of America, 69, pp. 3561-3566, 1972.

[12] F. Thei, M. Rossi, M. Bennati, M. Crescentini, F. Lodesani, H. Morgan, and M. Tartagni, "Parallel Recording of Single Ion Channels: A Heterogeneous System Approach", IEEE Transaction on Nanotechnology, 1536-125X, pp. 295-302, 2010.

[13] M. Rossi, F. Thei, H. Morgan, and M. Tartagni, "A Disposable Microfluidic Array Platform for Automatic Ion Channel Recording", MicroTAS, Groningen, pp. 1913-1915, 2010.

[14] F. Thei, M. Rossi, M. Bennati, M. Crescentini, and M. Tartagni, "An Automatic Offset Correction Platform for High-Throughput Ion-Channel Electrophysiology", Eurosensors XXIV, Linz, pp. 816-819, 2010.

 ISBN: 978-1-61208-145-8

Smart Sensor Magnetometer Based Virtual Gyroscope

Baptiste Delporte, Laurent Perroton, Thierry Grandpierre
Université Paris Est, ESIEE Engineering,
Marne-la-vallée, France
Email: {delportb,perrotol,grandpit}@esiee.fr

Jacques Trichet
Freescale Semiconductor, Inc.
Toulouse, France
Email: jacques.trichet@freescale.com

***Abstract*—In this paper, we propose two methods based on quaternions for computing the angles of inclination and the angular velocity with 6 degrees of freedom using the measurements of a 3-axis accelerometer and a 3-axis magnetometer. Each method has singularities which occur during the computation of the orientation of the device in the 3-dimensional space. We propose solutions to avoid these singularities. Experimental results are given to compare our model with a real gyroscope.**

***Keywords*-smart sensor; sensor fusion; accelerometer; magnetometer; angular velocity; gyroscope**

I. INTRODUCTION

The computation of the angles of inclination of a device and its angular velocity has many applications for aeronautics, transportation systems, human motion tracking, games and virtual reality. Classical methods use accelerometers, magnetometers and gyroscopes. For some particular angles, there are singularities for which it is impossible to compute neither the orientation of the device in the 3-dimensional space nor its angular velocity [1, page 407].

Our goal is to design a smart sensor magnetometer based virtual gyroscope, i.e. a method for computing the angular velocity based on the measurements of a 3-axis accelerometer and a 3-axis magnetometer, without any gyroscope, and with 6 degrees of freedom: 3 degrees of freedom are provided by the accelerometer and the others are provided by the magnetometer. It is easier to implement, less expensive and has a lower power consumption than the classical gyroscope solutions. Our target is small motion tracking with embedded devices like cellular phones, with application fields like virtual or augmented reality. Moreover, it is possible to create a virtual gyroscope using a magnetometer and an accelerometer, whereas it is not possible to create a virtual magnetometer nor a virtual accelerometer using a gyroscope only. Methods with accelerometers only have been already proposed in [2], [3], [4], [5].

A well-known method for computing a strapdown gyroscope output simply consists in differentiating the angles of inclination of the device, but we want to compute the total angular velocity, which is the addition of the angular velocities about the three axes of the fixed frame.

Two methods with two different approaches have been developed. They are proposed in this paper. The method that uses the angles of inclination of the device have been implemented. The method that uses the rotation matrix will be implemented and the two methods will be compared in order to find the method which offers the best precision on the target architecture. This work is a collaboration project between Freescale and ESIEE Engineering school which started in June 2010.

In Section II, we introduce the platform and the sensors. In Section III, a first method for computing the angular velocity using the absolute angles of inclination is presented. In Section IV, a second method for computing the angular velocity using the rotation matrix is presented. In Section V, experimental results are given.

II. HARDWARE AND SMART SENSORS

We use the new Freescale MMA9550L smart sensor. This motion sensing platform can manage multiple sensor inputs. It includes a 3-axis accelerometer and a ColdFire V1 32-bit microprocessor with an integrated Multiply and ACcumulate module (MAC module) for DSP-like operations. An additional Honeywell HMC5843 3-axis magnetometer is mounted on the MMA9550L board so that the two sensors are strictly parallel and their frames are aligned.

This paper focuses on the mathematical model which provides the angular velocity and the angles of inclination of the device in the 3-dimensional space. The algorithms have been implemented in the form of MATLAB scripts for testing purposes and the curves show the results of these implementations. In the future, the algorithms will be directly implemented on the MMA9550L, since it includes its own microprocessor.

III. VIRTUAL GYROSCOPE BASED ON THE ANGLES OF INCLINATION OF THE DEVICE

In this section, the angles of inclination and the angular velocity are computed from the accelerometer and the magnetometer measurements using Tait-Bryan angles and quaternions.

A. Parametrization of Rotations with Tait-Bryan Angles

In order to describe the orientation of the device in the 3-dimensional space, 2 right-handed Cartesian coordinate systems are used: a fixed reference frame with X_r = North,

 ISBN: 978-1-61208-145-8

Y_r = East and Z_r = Down (NED convention), and denoted by the subscript r, and a moving frame attached to a mobile device, denoted by the subscript d. The reference frame and the device frame are aligned when the device is flat and aligned with the X_d axis pointed to magnetic North. Rotation angles are positive when clockwise viewed along the relevant axis vector in the positive direction.

The orientation of the device in the reference frame can be described by Tait-Bryan angles: ϕ, θ and ψ. ψ is the angle of rotation about the Z_r axis (yaw). θ is the angle of rotation about the Y_r axis (pitch). ϕ is the angle of rotation about the X_r axis (roll). Any rotation of the device can be expressed as a composition of these three rotations in the reference frame, as shown in Fig. 1.

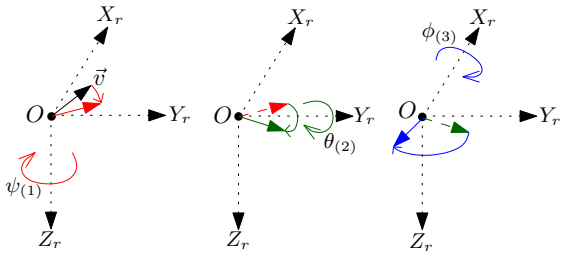

Figure 1. Angles ϕ, θ, ψ, and Composition of the 3 Rotations about Z_r, Y_r and X_r Axes

A rotation about the Z_r axis, the Y_r axis or the X_r axis can be respectively described by a rotation matrix $R_z(\psi)$, $R_y(\theta)$ or $R_x(\phi)$:

$$R_z(\psi)=\begin{bmatrix}\cos(\psi) & \sin(\psi) & 0\\ -\sin(\psi) & \cos(\psi) & 0\\ 0 & 0 & 1\end{bmatrix} \quad R_y(\theta)=\begin{bmatrix}\cos(\theta) & 0 & -\sin(\theta)\\ 0 & 1 & 0\\ \sin(\theta) & 0 & \cos(\theta)\end{bmatrix}$$

$$R_x(\phi)=\begin{bmatrix}1 & 0 & 0\\ 0 & \cos(\phi) & \sin(\phi)\\ 0 & -\sin(\phi) & \cos(\phi)\end{bmatrix}$$

The composition of the 3 rotations about the Z_r axis, then the Y_r axis and finally the X_r axis, is described by the rotation matrix $R(\phi,\theta,\psi) = R_x(\phi)\cdot R_y(\theta)\cdot R_z(\psi)$.

It is possible to compute ϕ, θ, ψ and the angular velocity $\vec{\omega_r}$ from the Earth's magnetic field $\vec{B_d}$, expressed in the device frame, and the Earth's gravitational field $\vec{g_d}$, expressed in the device frame. The magnetic field is measured by the magnetometer. On the other hand, the accelerometer measures the total acceleration including the gravitational field, the acceleration provided by the user and the acceleration due to the Coriolis force. Consequently, an extraction of the gravitational field $\vec{g_d}$ needs to be performed with a filter.

The expression of the Earth's magnetic field in the reference frame is given by $\vec{B_r} = \begin{pmatrix}B\cdot\cos(\delta) & 0 & B\cdot\sin(\delta)\end{pmatrix}^T$ where B denotes the strength of the magnetic field (in Teslas), δ denotes the angle of inclination of the magnetic field, which depends on the location on the Earth, and $(.)^T$ denotes the transpose of $(.)$.

The expression of the Earth's gravitational field in the reference frame is given by $\vec{g_r} = \begin{pmatrix}0 & 0 & g\end{pmatrix}^T$ where g denotes the strength of the gravitational field, i.e. the acceleration (in Newtons).

The computation process is shown in Fig. 2.

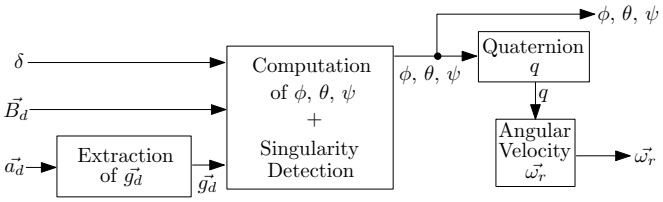

Figure 2. Computation Process 1

B. Extraction of $\vec{g_d}$

Since $\vec{g_d}$ is a constant offset in the measurement of $\vec{a}$, it can be extracted with a low-pass filter. The resulting vector $\vec{g_e}$ contains sensor medium frequencies and spurious noise. In order to keep only $\vec{g_d}$, a sliding median filter and a sliding average filter are used, as shown in Fig. 3. The same delay is applied to $\vec{B_d}$ to make sure they are in phase.

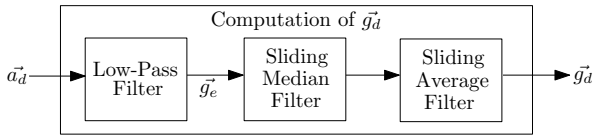

Figure 3. Computation of $\vec{g_d}$

1) Low-Pass Filter: The frequency of $\vec{g_d}$ equals 0. Consequently, the gravitational field can be extracted with a first-order Butterworth low-pass filter. The Z-transform transfer function of the filter is given by:

$$\frac{\vec{g_e}(z)}{\vec{a_d}(z)} = \frac{b_0 + b_1\cdot z^{-1}}{1 + a_1\cdot z^{-1}}$$

The default coefficients have been computed with MATLAB by synthetizing a low-pass filter with an experimentally determined cut-off frequency $F_c = 0.02\cdot F_e$, where F_e denotes the sampling frequency. They are given by $[b_0, b_1, a_1] = [0.0305, 0.0305, -0.9391]$. If a variation of the norm $\|\vec{g_d}\|$ exceeds a threshold, the cut-off frequency of the Butterworth filter increases of $0.05\cdot F_e$ and the coefficients $[b_0, b_1, a_1]$ are computed again. If the cut-off frequency reaches $F_c = 0.4\cdot F_e$, the filter waits for the norm $\|\vec{g_d}\|$ to stabilize. Then, F_c decreases of $0.05\cdot F_e$ until it reaches $0.02\cdot F_e$. Then, F_c is kept, until the norm $\|\vec{g_d}\|$ exceeds again the threshold. A threshold of $\Delta_{gd} = \frac{1}{100}\cdot\|\vec{g_d}\|$ has been experimentally determined.

 ISBN: 978-1-61208-145-8

2) Sliding Median Filter: A sliding median filter is used in order to eliminate the highest frequencies sensor spurious noise, which creates variations of the norm of $\vec{g_d}$. Since this norm should be constant, we need to eliminate the samples that have an erroneous norm. As we will see in section III-C, $\vec{g_d}$ directly impacts the accuray of the entire computation process, hence the need to get $\vec{g_d}$ with the least error. The sliding median filter uses a sliding window of n norms. At the beginning, the window contains the first n norms of the first n samples. Then, the norms of the window are sorted. Finally, the median value of the window is extracted, and the sample whose norm is the median value is output from the filter, as shown in Fig. 4.

Let $\vec{g} = (g_x \ g_y \ g_z)^T$ be the input vector, $\vec{g_f} = (g_{fx} \ g_{fy} \ g_{fz})^T$ the filtered vector and i the index of the sample. The expression of the filter is given by:

$$\vec{g_f}(i) = \vec{g}(k) \text{ such that } \|\vec{g}(k)\| = median(\|\vec{g}(i-n+1..i)\|)$$

Then, the window slides to the right and the norms of $\vec{g}(i-n+2..i+1)$ are extracted. A sliding median filter creates a delay of $n-1$ samples.

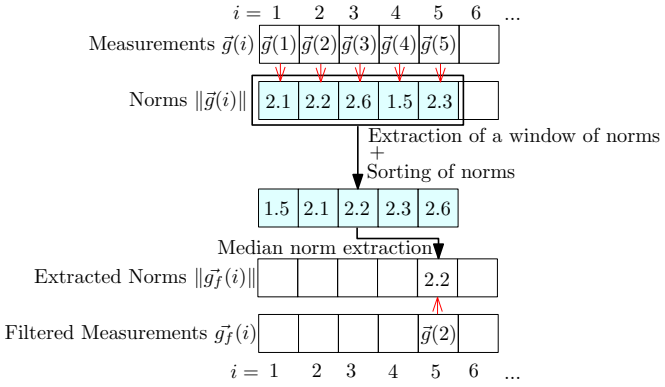

Figure 4. Sliding Median Filter

The gravitational field filtered with the sliding median filter still has variations, a sliding average filter is used to smooth it.

3) Sliding Average Filter: The sliding average filter uses a sliding window of n samples. At the beginning, the window contains the first n samples. Then, the average value of the window is extracted and output from the filter.

Let $\vec{g} = \begin{pmatrix} g_x & g_y & g_z \end{pmatrix}^T$ be the input vector, $\vec{g_f} = \begin{pmatrix} g_{fx} & g_{fy} & g_{fz} \end{pmatrix}^T$ the filtered vector and i the index of the sample. The expression of the filter is given by:

$$\vec{g_f}(i) = \frac{1}{n} \cdot \sum_{k=i-n+1}^{i} \vec{g}(k)$$

Then, the window slides to the right and filters the values $\vec{g}(i-n+2..i+1)$. A sliding average filter creates a delay of $n-1$ samples.

C. Computation of the Angles of Inclination

The Earth's magnetic field $\vec{B_d}$, expressed in the device frame, results from the rotation of the magnetic field $\vec{B_r}$, expressed in the reference frame.

$$\vec{B_d} = R_x(\phi) \cdot R_y(\theta) \cdot R_z(\psi) \cdot \vec{B_r} \quad (1)$$

The Earth's gravitational field $\vec{g_d}$, expressed in the device frame, results from the rotation of the gravitational field $\vec{g_r}$, expressed in the reference frame. Since $\vec{g_r}$ remains unchanged after a rotation about the Z_r axis, $R_z(\psi) \cdot \vec{g_r} = \vec{g_r}$. It follows:

$$\vec{g_d} = R_x(\phi) \cdot R_y(\theta) \cdot \vec{g_r} \quad (2)$$

It is possible to compute the roll angle ϕ from the gravitational field by developing Eq. 2:

$$\phi_g = \arctan2\left(\frac{g_{dy}}{g_{dz}}\right) \quad (3)$$

arctan2 denotes the arctangent on the domain $[-\pi, \pi]$.

Once ϕ is known, it is possible to compute θ:

$$\theta = \arctan\left(\frac{-g_{dx}}{g_{dy} \cdot \sin(\phi) + g_{dz} \cdot \cos(\phi)}\right) \quad (4)$$

arctan denotes the arctangent on the domain $[-\frac{\pi}{2}, \frac{\pi}{2}]$.

If $\vec{g_d}$ is aligned with the X_d axis, the denominator in Eq. 4 becomes 0. Please see Tab. I for the detection of this singularity.

Once ϕ and θ are known, it is possible to compute ψ by developing Eq. 1:

$$\psi = \arctan2\left(\frac{B_{dz} \cdot \sin(\phi) - B_{dy} \cdot \cos(\phi)}{B_{dx} \cdot \cos(\theta) + B_{dy} \cdot \sin(\phi) \cdot \sin(\theta) + B_{dz} \cdot \cos(\phi) \cdot \sin(\theta)}\right)$$

D. Singularity Detection

A table of the singularities is given in Tab. I. The normalized gravitational and magnetic field in the device frame are denoted respectively by $\vec{g_{dN}} = (g_{dNx}, g_{dNy}, g_{dNz}) = \frac{\vec{g_d}}{\|\vec{g_d}\|}$ and $\vec{B_{dN}} = (B_{dNx}, B_{dNy}, B_{dNz}) = \frac{\vec{B_d}}{\|\vec{B_d}\|}$. If a singularity is detected, several compositions of rotations give the same result. Consequently, there are two methods. The first method consists in keeping the previous values of ϕ, θ and ψ. The second method consists in finding the appropriate case that allows the accurate determination of ϕ, θ and ψ.

E. Parametrization of Rotations with Quaternions

The quaternions are hypercomplex numbers, i.e. 4-dimensional mathematical objects, used to describe rotations in the 3-dimensional space [6].

1) Definition and Properties of a Quaternion: A quaternion q has 4 coordinates in a 4-dimensional vector space and is denoted by $q = \begin{pmatrix} q_1 & q_2 & q_3 & q_4 \end{pmatrix}^T$ with $(q_1, q_2, q_3, q_4) \in \mathbb{R}^4$. It consists of a vector part $q_v = \begin{pmatrix} q_1 & q_2 & q_3 \end{pmatrix}^T$ and a scalar part $q_s = q_4$. It can be expressed in the following form:

$$q = q_1 \cdot i + q_2 \cdot j + q_3 \cdot j + q_4 \quad (5)$$

g_{dNx}	g_{dNy}	B_{dNx}	B_{dNy}	ϕ	θ	ψ
1	0	$\sin(\delta)$	$\cos(\delta)$	$-\pi/2$	$-\pi/2$	0
				0	$-\pi/2$	$-\pi/2$
				$\pi/2$	$-\pi/2$	π
				π	$-\pi/2$	$\pi/2$
1	0	$\sin(\delta)$	$-\cos(\delta)$	$-\pi/2$	$-\pi/2$	π
				0	$-\pi/2$	$\pi/2$
				$\pi/2$	$-\pi/2$	0
				π	$-\pi/2$	$-\pi/2$
0	-1	$\cos(\delta)$	$-\sin(\delta)$	$-\pi/2$	0	0
				$\pi/2$	π	π
0	-1	$-\cos(\delta)$	$-\sin(\delta)$	$-\pi/2$	0	π
				$\pi/2$	π	0
-1	0	$-\sin(\delta)$	$-\cos(\delta)$	$-\pi/2$	$\pi/2$	0
				0	$\pi/2$	$\pi/2$
				$\pi/2$	$\pi/2$	π
				π	$\pi/2$	$-\pi/2$
-1	0	$-\sin(\delta)$	$\cos(\delta)$	$-\pi/2$	$\pi/2$	π
				0	$\pi/2$	$-\pi/2$
				$\pi/2$	$\pi/2$	0
				π	$\pi/2$	$\pi/2$
0	1	$-\cos(\delta)$	$\sin(\delta)$	$-\pi/2$	π	0
				$\pi/2$	0	π
0	1	$\cos(\delta)$	$\sin(\delta)$	$-\pi/2$	π	π
				$\pi/2$	0	0

Table I
TABLE OF SINGULARITIES

In Eq. 5, i, j and k are imaginary numbers: $i^2 = j^2 = k^2 = -1$, and $i \cdot j = -j \cdot i = k$, $j \cdot k = -k \cdot j = i$, $k \cdot i = -i \cdot k = j$. Therefore, it is possible to compute the product of two quaternions $q = \begin{pmatrix} q_1 & q_2 & q_3 & q_4 \end{pmatrix}^T$ and $q' = \begin{pmatrix} q'_1 & q'_2 & q'_3 & q'_4 \end{pmatrix}^T$, denoted by $q \cdot q'$, using the properties of the hypercomplex numbers. It can be noticed that the product between 2 quaternions is not commutative: $q \cdot q' \neq q' \cdot q$.

The inverse of a quaternion $q = \begin{pmatrix} q_1 & q_2 & q_3 & q_4 \end{pmatrix}^T$ is denoted by $q^{-1} = \begin{pmatrix} -q_1 & -q_2 & -q_3 & q_4 \end{pmatrix}^T$.

2) Euler-Rodrigues Parameters: A quaternion $q = \begin{pmatrix} q_1 & q_2 & q_3 & q_4 \end{pmatrix}^T$ can be used to describe a rotation by an angle α about a unit vector $\vec{a} = \begin{pmatrix} a & b & c \end{pmatrix}^T$ that is the axis. $\vec{a}$ is a unit vector, so $\|\vec{a}\| = 1$. The Euler-Rodrigues parameters corresponding to the rotation are given by:

$$q_1 = a \cdot \sin(\tfrac{\alpha}{2}) \quad q_2 = b \cdot \sin(\tfrac{\alpha}{2}) \quad q_3 = c \cdot \sin(\tfrac{\alpha}{2})$$
$$q_4 = \cos(\tfrac{\alpha}{2})$$

3) Rotation: Let $\vec{v} = \begin{pmatrix} x & y & z \end{pmatrix}^T$ be a vector. The quaternion q transforms $\vec{v}$ into another vector $\vec{v_f} = \begin{pmatrix} x_f & y_f & z_f \end{pmatrix}^T$ by rotating it by angle α about an $\vec{a}$ axis. A 4^{th} null coordinate is added to $\vec{v}$, so it becomes $\vec{v_q} = \begin{pmatrix} x & y & z & 0 \end{pmatrix}^T$. The rotated vector $\vec{v_f}$ corresponds to the vector part of $\vec{v_{fq}}$ given by:

$$\vec{v_{fq}} = q \cdot \vec{v_q} \cdot q^{-1} \tag{6}$$

The scalar part of $\vec{v_{fq}}$ is 0, since $\vec{v_{fq}}$ is a pure vector in the 3-dimensional space.

4) Composition of Two Rotations: Let q_α be a quaternion describing a rotation by an angle α about an $\vec{a}$ axis and q_β a quaternion describing a rotation by an angle β about a $\vec{b}$ axis. The composition of the rotations about the $\vec{b}$ axis, then the $\vec{a}$ axis, is given by the quaternion $q_{\alpha,\beta} = q_\alpha \cdot q_\beta$. Let $\vec{v} = \begin{pmatrix} x & y & z \end{pmatrix}^T$ be a vector. The quaternion $q_{\alpha,\beta}$ transforms $\vec{v}$ into another vector $\vec{v_f} = \begin{pmatrix} x_f & y_f & z_f \end{pmatrix}^T$ by rotating it by angle β about a $\vec{b}$ axis, then by angle α about an $\vec{a}$ axis. With $\vec{v_q} = \begin{pmatrix} x & y & z & 0 \end{pmatrix}^T$, the expression of Eq. 6 becomes $\vec{v_{fq}} = (q_\alpha \cdot q_\beta) \cdot \vec{v_q} \cdot (q_\beta^{-1} \cdot q_\alpha^{-1})$. The rotated vector $\vec{v_f}$ corresponds to the vector part of $\vec{v_{fq}}$. The scalar part of $\vec{v_{fq}}$ is 0, since $\vec{v_{fq}}$ is a pure vector in the 3-dimensional space.

5) Computation of the Angular Velocity: The instantaneous angular velocity $\vec{\omega_r}(t)$ of the device at the instant t, expressed in the reference frame, corresponds to the vector part of $\vec{\omega_{rq}}(t)$ given by [7]:

$$\vec{\omega_{rq}}(t) = 2 \cdot q^{-1}(t) \cdot \frac{dq(t)}{dt}$$

The scalar part of $\vec{\omega_{rq}}(t)$ is 0, since $\vec{\omega_{rq}}(t)$ is a pure vector in the 3-dimensional space, which finally gives:

$$\vec{\omega_r}(t) = \begin{pmatrix} \cos(\theta) \cdot \cos(\psi) \cdot \dot{\phi} + \sin(\psi) \cdot \dot{\theta} \\ -\cos(\theta) \cdot \sin(\psi) \cdot \dot{\phi} + \cos(\psi) \cdot \dot{\theta} \\ \sin(\theta) \cdot \dot{\phi} + \dot{\psi} \end{pmatrix}$$

F. Computation of the Quaternion q From the Angles of Inclination

A rotation by angle ψ about the Z_r axis, by angle θ about the Y_r axis or by angle ϕ about the X_r axis can be respectively described by the quaternion $q_\psi = (0 \ 0 \ \sin(\frac{\psi}{2}) \ \cos(\frac{\psi}{2}))^T$, $q_\theta = (0 \ \sin(\frac{\theta}{2}) \ 0 \ \cos(\frac{\theta}{2}))^T$ or $q_\phi = (\sin(\frac{\phi}{2}) \ 0 \ 0 \ \cos(\frac{\phi}{2}))^T$.

The quaternion describing the composition of the rotations about the Z_r axis, then the Y_r axis, and finally the X_r axis, is given by $q = q_\phi \cdot q_\theta \cdot q_\psi$.

The method described above has 8 singularities. Consequently, the computation of the angles ϕ, θ and ψ cannot be accurate if the detection of singularities is not efficient enough.

IV. VIRTUAL GYROSCOPE BASED ON THE ROTATION MATRIX

In this section, the angles of inclination of the device and the angular velocity are computed from the accelerometer and the magnetometer measurements using the rotation matrix and quaternions. Although its computation cost is higher, the major advantage of this method is that it reduces the number of singularities to only 2. Furthermore, this method does not require the explicit computation of the angles. The computation process is shown in Fig. 5.

 ISBN: 978-1-61208-145-8

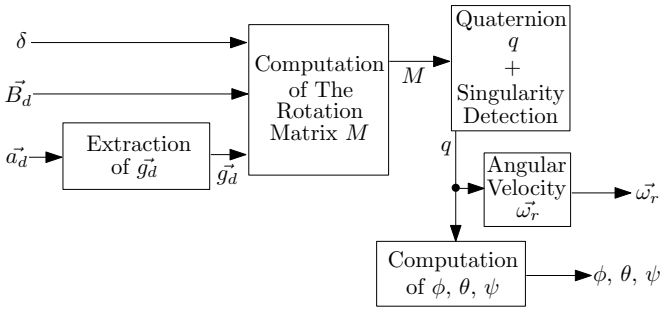

Figure 5. Computation Process 2

A. Computation of the Rotation Matrix M

Let $\vec{v} = \begin{pmatrix} x & y & z \end{pmatrix}^T$ be a vector. The rotation matrix M transforms $\vec{v}$ into another vector $\vec{v_f} = \begin{pmatrix} x_f & y_f & z_f \end{pmatrix}^T$ by rotating it by an unknown angle α about an unknown $\vec{a}$ axis. The coordinates of the resulting $\vec{v_f}$ are given by:

$$\vec{v_f} = M \cdot \vec{v} \tag{7}$$

Once $\vec{v}$ and $\vec{v_f}$ are known, it is possible to compute M. Consequently, we will be able to deduce α and $\vec{a}$.

Let $\vec{g_{dN}} = \frac{\vec{g_d}}{\|\vec{g_d}\|}$ be the normalized gravitational field in the device frame, $\vec{B_{dN}} = \frac{\vec{B_d}}{\|\vec{B_d}\|}$ the normalized magnetic field in the device frame, $\vec{C_d} = \vec{g_d} \times \vec{B_d}$ the cross product between the gravitational field and the magnetic field in the device frame, $\vec{C_{dN}} = \frac{\vec{C_d}}{\|\vec{C_d}\|}$, $\vec{T_{Bd}} = \vec{B_{dN}} \times \vec{C_{dN}}$ and $\vec{T_{gd}} = \vec{g_{dN}} \times \vec{C_{dN}}$.

On the other hand, let $\vec{g_{rN}} = \frac{\vec{g_r}}{\|\vec{g_r}\|}$ be the normalized gravitational field in the reference frame, $\vec{B_{rN}} = \frac{\vec{B_r}}{\|\vec{B_r}\|}$ the normalized magnetic field in the reference frame, $\vec{C_r} = \vec{g_r} \times \vec{B_r}$ the cross product between the gravitational field and the magnetic field in the reference frame, $\vec{C_{rN}} = \frac{\vec{C_r}}{\|\vec{C_r}\|}$, $\vec{T_{Br}} = \vec{B_{rN}} \times \vec{C_{rN}}$ and $\vec{T_{gr}} = \vec{g_{rN}} \times \vec{C_{rN}}$.

The expressions of $\vec{g_{rN}}$ and $\vec{B_{rN}}$ are respectively given by $\vec{g_{rN}} = \begin{pmatrix} 0 & 0 & 1 \end{pmatrix}^T$ and $\vec{B_{rN}} = \begin{pmatrix} \cos(\delta) & 0 & \sin(\delta) \end{pmatrix}^T$. Consequently, $\vec{C_r} = \begin{pmatrix} 0 & g \cdot B \cdot \cos(\delta) & 0 \end{pmatrix}^T$, $\vec{C_{rN}} = \begin{pmatrix} 0 & 1 & 0 \end{pmatrix}^T$, $\vec{T_{Br}} = \begin{pmatrix} -\sin(\delta) & 0 & \cos(\delta) \end{pmatrix}^T$ and $\vec{T_{gr}} = \begin{pmatrix} -1 & 0 & 0 \end{pmatrix}^T$.

The general expression of the matrix M is given by:

$$M = \begin{bmatrix} M_{11} & M_{12} & M_{13} \\ M_{21} & M_{22} & M_{23} \\ M_{31} & M_{32} & M_{33} \end{bmatrix}$$

Since $\vec{T_{gd}} = M \cdot \vec{T_{gr}}$, $\vec{C_{dN}} = M \cdot \vec{C_{rN}}$ and $\vec{g_{dN}} = M \cdot \vec{g_{rN}}$, the matrix M can be deduced from $\vec{T_{gd}}$, $\vec{C_{dN}}$ and $\vec{g_{dN}}$:

$$M = \begin{bmatrix} -T_{gdx} & C_{dNx} & g_{dNx} \\ -T_{gdy} & C_{dNy} & g_{dNy} \\ -T_{gdz} & C_{dNz} & g_{dNz} \end{bmatrix}$$

Since $\vec{T_{Bd}} = M \cdot \vec{T_{Br}}$ and $\vec{B_{dN}} = M \cdot \vec{B_{rN}}$, there is another method, which is to deduce the matrix M from $\vec{T_{Bd}}$, $\vec{C_{dN}}$ and $\vec{B_{dN}}$:

$$M = \begin{bmatrix} B_{dNx} \cdot \cos(\delta) - T_{Bdx} \cdot \sin(\delta) & C_{dNx} & B_{dNx} \cdot \sin(\delta) + T_{Bdx} \cdot \cos(\delta) \\ B_{dNy} \cdot \cos(\delta) - T_{Bdy} \cdot \sin(\delta) & C_{dNy} & B_{dNy} \cdot \sin(\delta) + T_{Bdy} \cdot \cos(\delta) \\ B_{dNz} \cdot \cos(\delta) - T_{Bdz} \cdot \sin(\delta) & C_{dNz} & B_{dNz} \cdot \sin(\delta) + T_{Bdz} \cdot \cos(\delta) \end{bmatrix}$$

B. Computation of the Quaternion q

Once the matrix M is known, it becomes possible to compute q. The four possible cases are given in Tab. II [8, page 15]. The comparison of M_{11}, M_{22} and M_{33} gives the appropriate case that allows the computation of q.

$M_{22} < -M_{33}$ $M_{11} > M_{22}$ $M_{11} > M_{33}$	$q = \frac{1}{2} \cdot \begin{pmatrix} \sqrt{1+M_{11}-M_{22}-M_{33}} \\ (M_{12}+M_{21})/\sqrt{1+M_{11}-M_{22}-M_{33}} \\ (M_{31}+M_{13})/\sqrt{1+M_{11}-M_{22}-M_{33}} \\ (M_{23}-M_{32})/\sqrt{1+M_{11}-M_{22}-M_{33}} \end{pmatrix}$
$M_{22} > M_{33}$ $M_{11} < -M_{22}$ $M_{11} < -M_{33}$	$q = \frac{1}{2} \cdot \begin{pmatrix} (M_{12}+M_{21})/\sqrt{1-M_{11}+M_{22}-M_{33}} \\ \sqrt{1-M_{11}+M_{22}-M_{33}} \\ (M_{23}+M_{32})/\sqrt{1-M_{11}+M_{22}-M_{33}} \\ (M_{31}-M_{13})/\sqrt{1-M_{11}+M_{22}-M_{33}} \end{pmatrix}$
$M_{22} < M_{33}$ $M_{11} < -M_{22}$ $M_{11} > M_{33}$	$q = \frac{1}{2} \cdot \begin{pmatrix} (M_{31}+M_{13})/\sqrt{1-M_{11}-M_{22}+M_{33}} \\ (M_{23}+M_{32})/\sqrt{1-M_{11}-M_{22}+M_{33}} \\ \sqrt{1-M_{11}-M_{22}+M_{33}} \\ (M_{12}-M_{21})/\sqrt{1-M_{11}-M_{22}+M_{33}} \end{pmatrix}$
$M_{22} > -M_{33}$ $M_{11} > -M_{22}$ $M_{11} > -M_{33}$	$q = \frac{1}{2} \cdot \begin{pmatrix} (M_{23}-M_{32})/\sqrt{1+M_{11}+M_{22}+M_{33}} \\ (M_{31}-M_{13})/\sqrt{1+M_{11}+M_{22}+M_{33}} \\ (M_{12}-M_{21})/\sqrt{1+M_{11}+M_{22}+M_{33}} \\ \sqrt{1+M_{11}+M_{22}+M_{33}} \end{pmatrix}$

Table II
COMPUTATION OF q FROM M

C. Computation of the Angles of Inclination

Once q is known, ϕ, θ and ψ can be computed:

$$\phi = \arctan2\left(\frac{2 \cdot (q_1 \cdot q_4 + q_2 \cdot q_3)}{1 - 2 \cdot (q_1^2 + q_2^2)}\right)$$

$$\theta = \arcsin\left(2 \cdot (q_2 \cdot q_4 - q_3 \cdot q_1)\right)$$

$$\psi = \arctan2\left(\frac{2 \cdot (q_3 \cdot q_4 + q_1 \cdot q_2)}{1 - 2 \cdot (q_2^2 + q_3^2)}\right)$$

With this method, there are only 2 singularities left: $\theta = \pm\frac{\pi}{2}$. They are known as *the gimbal lock*. If such a singularity is detected, the previous value of θ is kept.

V. EXPERIMENTAL RESULTS

A. Extraction of $\vec{g_d}$

The Fig. 6 shows the results of the computation of $\vec{g_d}$. First, the X_d axis has been aligned with the Z_r axis, then the device has been shaken by the user, who created accelerations of about $2g$. Then, the Y_d axis has been aligned with the Z_r axis and, finally, the Z_d axis has been aligned with the Z_r axis.

We can notice that the norm of the extracted gravitational field equals $1g$ and that the highest frequencies due to the fast shakes of the user have been eliminated.

 ISBN: 978-1-61208-145-8

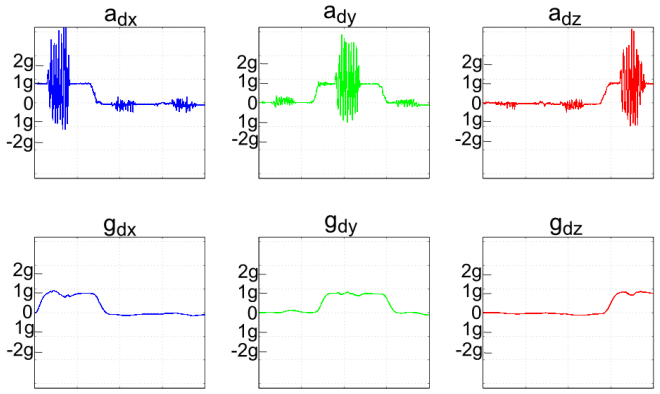

Figure 6. Extraction of $\vec{g_d}$

B. Angular Velocity

Experimental results of the angular velocity computed with our first method virtual gyroscope (top) compared to the one from a real gyroscope (bottom) are given in Fig. 7. The real gyroscope is tied to the accelerometer and the magnetometer and their frames are aligned to get a 9 degree of freedom system. The similarity of the two measures confirms the accuracy of our model.

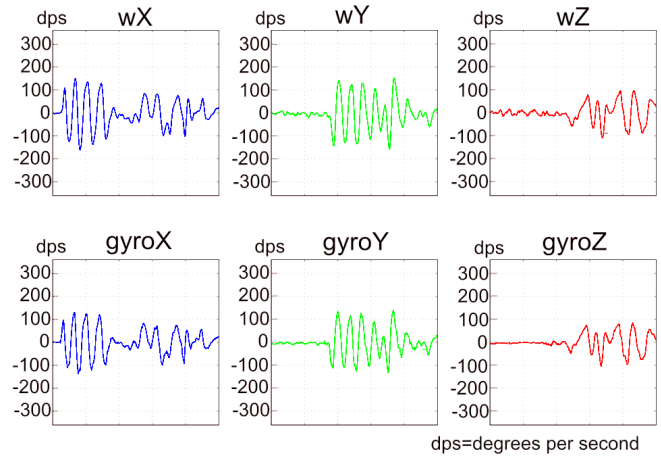

Figure 7. Angular Velocity Computed With our Virtual Gyroscope (top) vs. a Real one (bottom)

VI. Conclusion and Future Works

In this paper, we have presented two methods to implement a virtual gyroscope that only uses the measurements of an accelerometer and a magnetometer, with 6 degrees of freedom.

The two methods have their own advantages and drawbacks. The method which uses the angles of inclination is easier to implement, but there are 8 singularities, which need to be solved. Moreover, the computation of ψ depends on the computation of θ, which in turns depends on ϕ. If there is a singularity on ϕ, the computation of the angles is not possible. On the other hand, the method with the rotation matrix has only two singularities but its computation cost is higher. The second method has not been completely implemented and validated yet; this is our current work.

The precision of both methods and their limitations must be investigated and will be our main future work.

Finally, we plan to optimize the implementation of both methods on the MMA9550L. This will allow us to provide the angular velocity and the angles of inclination of the device and use them for several applications, like a 3-dimensional mouse, a virtual joystick, a human motion tracker. The MMA9550L board can communicate with the PC with a Bluetooth connection. Consequently, the board can become a portable device with its own power supply.

Acknowledgment

The authors would like to thank Freescale for their support, the platform, and Mr. Mark Pedley whose work is the base of this project.

References

[1] J. R. Wertz, *Spacecraft Attitude Determination and Control*, J. R. Wertz, Ed. D. Reidel Publishing Company, Dordrecht, Holland, 1978.

[2] T. Liu, G.-R. Zhao, and S. Pan, "New calculating method of angular velocity in gyroscope-free strapdown inertial navigation systems," *Systems Engineering and Electronics*, vol. 32, no. 1, pp. 162–165, January 2010.

[3] P. Schopp, L. Klingbeil, C. Peters, A. Buhmann, and Y. Manoli, "Sensor fusion algorithm and calibration for a gyroscope-free imu," in *Proceedings of the Eurosensors 23rd Conference*, vol. 1, no. 1, 2009, pp. 1323–1326.

[4] C. Wang, J.-X. Dong, S.-H. Y., and X.-W. Kong, "Hybrid algorithm for angular velocity calculation in a gyroscope-free strapdown inertial navigation system," *Journal of Chinese Inertial Technology*, vol. 18, no. 4, pp. 401–404, 2010.

[5] X.-N. Wang, S.-Z. Wang, and H.-B. Zhu, "Study on models of gyroscope-free strap-down inertial navigation system," *Bing-gong Xuebao/Acta Armamentarii*, vol. 27, no. 2, pp. 288–292, 2006.

[6] D. Stahlke. (2007) Quaternions in classical mechanics. [Online]. Available: http://www.stahlke.org/dan/phys-papers/quaternion-paper.pdf

[7] A. L. Schwab. (2002) Quaternions, finite rotation and Euler parameters. [Online]. Available: http://audiophile.tam.cornell.edu/~als93/Publications/quaternion.pdf

[8] J. Diebel, "Representing attitude: Euler angles, unit quaternions, and rotation vectors," Stanford University, California 94301-9010, Tech. Rep., october 2006. [Online]. Available: http://www.astro.rug.nl/software/kapteyn-beta/_downloads/attitude.pdf

 ISBN: 978-1-61208-145-8

Consistency and Distributed Sensor Data Processing

Laurent-Frédéric Ducreux, Suzanne Lesecq, François Pacull, Stéphanie Riché
CEA-LETI MINATEC Campus
17 rue des Martyrs, 38000 Grenoble, France
Email: surname.name@cea.fr

***Abstract*—This paper proposes a framework dedicated to the management of data processing within a geographically distributed system made of heterogeneous software and hardware components. The integration and coordination of these different components is easily performed thanks to a uniform abstraction level proposed here. The resource-oriented approach combined with a rule-based system allowing transactional manipulation of these resources provides a unified view of the distributed system. An example will show the powerfulness of the proposed middleware.**

***Keywords*-Middleware; rule-based language.**

I. INTRODUCTION

When dealing with distributed sensors data processing, from co-located sensors to sensors spread over different continents, the problem to solve at the application level always remains the same:

- to share data;
- to synchronize "entities";
- to manage concurrent accesses;
- to define conditions, and
- to ensure consistency on the system "global state".

Until now, each level was defining its own way to solve (or sometimes not!) its own issues, with different specific points of view and mechanisms.

The proposition in this paper is to provide a uniform abstraction layer that eases the integration and coordination of the different components (software and hardware) that compose the network of sensors and actuators. It is based on a resource-oriented approach combined with a rule-based system allowing transactional manipulation of these resources. This results in a unified view of the system, whatever its size and its geographical distribution.

Chaski is rooted in previous projects conducted at XRCE (Xerox Research Centre Europe), in particular the Coordination Language Facilities (CLF) project [1], [2] and STITCH [3] developed from 1995 to 2003. Chaski may be seen as a natural evolution, based on the lessons learned and the will to reduce the middleware footprint in order to better fit with a large number of small devices and appliances.

Chaski, is the combination of three paradigms, namely *associative memory*, *distributed transaction* and *production rules* presented in Section 2. Put together they offer a powerful framework to address distributed (sensor) data processing with properties that are up to our knowledge novel in this field. Section 3 presents the Chaski rule-based language, an intermediate coordination layer that can be used by application programmers or automatically generated from *Domain Specific Languages* or graphical user interfaces. This rule-based language offers in addition the possibility to dynamically modify the application to adapt not only to changes induced by the user, but also changes due to the self adaptation of the system to the context (both for planned modifications and failures). Section 4 demonstrates the Chaski expressiveness through an application.

II. PARADIGMS

A. Associative Memory

An abstraction layer is highly desirable to unify the view of the various components usually involved in distributed sensor processing: the sensors, the sensed data, the actuators, the software components responsible for the data fusion, the software components used to interact with the system either for application or monitoring purpose, etc.

The option chosen is to consider these entities as "resources" managed in an *associative memory*. The associative memory is implemented with a tuple-space, following the concept introduced by Linda in the 80s [4] and resurrected several times since in the middleware field [5], [6]. An associative memory provides a repository of tuples that can be concurrently accessed by a set of software components that may either insert resources (data) as tuples in the space or retrieve or consume resources from the space according to a matching given pattern. This tuple-space may be seen as a distributed shared memory.

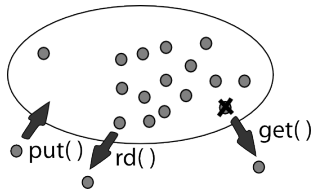

Figure 1. Associative memory and basic operations

From original Linda, only 3 operations are retained (see Figure 1) to manipulate tuples: `rd()` which verifies the presence of a tuple matching a given pattern, `get()` which consumes a tuple, and `put()` which inserts a tuple (the

 ISBN: 978-1-61208-145-8

original Linda operations `in()` and `out()` have been renamed to make their semantic less ambiguous).

In Chaski, the associative memory is split into distinct units called *bags*. Unlike in the original Linda, bags may be distributed over different hosts, offering a fully distributed associative memory. Moreover, the bags are typed. Distinct types introduce specific differentiations in the semantic and operation of the `rd()`, `get()` and `put()` methods. For instance, the bag may be a *set*, or a *multiset* with an impact on the `put()` operation. When a resource is `put()` in a bag already containing an identical resource, then it is inserted when the bag is a *multiset* but inserted if it is a *set*.

The abstraction of bags completely hide the data distribution thus it matches the first problem that is how *to share data*. It is also well suited to encapsulate sensors and actuators. Actually, a sensor is a "virtual" bag in which the resources are the different sensed information that can be accessed one by one through the `rd()` and `get()` operations. An actuator is a "virtual" bag where each inserted resource through the `put()` may trigger actions.

B. Distributed transactions

A distributed transaction is a set of operations in which at least 2 geographically distributed clients are involved. Transactions usually ensure the so-called Atomicity, Consistency, Isolation, Durability (ACID) properties. In Chaski, only atomicity is managed, to ensure all-or-nothing outcomes for each unit of work (operations set). The atomicity is implemented using a two-phase commit protocol (2PC) [7] to ensure that each participant in the transaction agrees on whether the transaction should be committed or not. In the first phase, the participants involved in the transaction are queried. In the second phase, when all participants replied they are ready, the coordinator formalizes the transaction.

In order to allow transactional manipulation at the resources level, the `rd()`, `get()` and `put()` basic operations are divided into 2 phases. The first one prepares the operation and locks the resources. The second phase performs the operation if the transaction has to be committed or it unlocks the resources otherwise. Distributed transactions tackle two problems raised in the introduction, i.e. *"entities" synchronization* and *concurrent accesses management*.

C. Production rule system

A production rule consists in 2 parts: a precondition part and a performance/action part. If a precondition matches the current system state, then the action is performed. A production system can be seen as a mechanism that executes productions in order to achieve some goals. An example of production rule system is, e.g. OPS5 [8].

The production rules in Chaski use only the 3 basic operations defined on top of the associative memory. The system state is kept and managed through the associative memory (tuple-space). So, `rd()` operations are naturally used to access and evaluate this state. The precondition of a rule is a set of `rd()` operations. The distinct `rd()` operations required to evaluate the precondition are performed sequentially, with a right propagation following logic programming approach [9]. This will be developed in details in Section III. The performance phase of a rule is a set of `rd()`, `get()` and `put()` operations embedded in one or more transactions. Broadly speaking:

- `rd()` operations are used to ensure that the conditions which triggered the rule are still valid when the rule is actually executed. If the conditions are no longer valid, then the transaction is aborted. This ensures that a rule cannot be performed when conditions were fulfilled at some point in the past, but this is no longer the case;
- `get()` operations are used to validate the resources existence (e.g. resources involved in the definition of the precondition) but, in addition, to ensure the resources will be consumed when the transaction is committed. Therefore, if different transactions depend on the same resource availability, only one is committed;
- `put()` operations are used to insert new resources in the associative memory, as combinations of resources returned by `rd()` operations of the precondition phase.

When a performance phase contains multiple transactions, they are executed in sequential order. Then, if the distinct transactions perform a `get()` over the same "token" resource, it is very easy to formalize alternative treatments for a given precondition with the insurance that only the first possible treatment will be performed. This provides a natural and very elegant way to solve various difficult problems (e.g. graceful degradation, redundancy or dispatching) that arise in a distributed environment. The full picture of this mechanism is described in Section III.

The Chaski production rule system answers the two last problems, that is how *to verify distributed conditions* and *to ensure consistency on the "global state" of the "system"*.

III. RULE-BASED LANGUAGES

One of the key features of Chaski relies on its coordination language which is an evolution of the STITCH language. In this section, the basis of the Chaski language are introduced.

A. Writing of Chaski rules

In a Chaski rule, the precondition and a performance parts are separated by the symbol "::".

The associative memory is split into bags. These bags may be grouped into objects according to the application design. For instance, bags may be grouped for location reasons (hosted by the same machine) or for semantic reasons (all the bags used to manage a given sensor network are grouped in the same object).

A bag is uniquely defined among the overall system with syntax `[<objectname>,<bagname>]` where `<objectname>` and `<bagname>` respectively define the

 ISBN: 978-1-61208-145-8

names by which the object and the bag are known within the system. As an example, `"Zigbee"` and `"Sensors"` could uniquely define the bag containing tuples built as `(<sensorid>, <value>)` and corresponding to all the measurements done by the sensors currently connected to the system through the zigbee protocol.

Then, applying an operation on this bag (e.g. `rd()`) is noted `["Zigbee","Sensors"].rd(id,value)`. A `["Zigbee","Sensors"].rd(id,value)` operation in the precondition returns one by one the tuples matching the given pattern `(id,value)`, that is, in the present example, all the sensed informations collected by the system through the zigbee protocol. When the last corresponding tuple is returned, the `rd()` is blocked until a new matching tuple becomes available.

This mechanism is similar to the one a software program that is reading a file on which one or several other software programs are appending data. The read operation blocks when the pointer reaches the current end of the file and is automatically unblocked when new data become available, as the result of append operations performed by the other software programs. If one or several fields (e.g. `id`) are set with the identity of a specific sensor (e.g. `"Zig001"`) then `["Zigbee","Sensors"].rd("Zig001",value)` only returns the current value associated to this particular sensor. As soon as the sensor reads a new measurement, the corresponding new tuple is added to the bag and then will be returned by the pending `rd("Zig001",value)`.

In the precondition part, several *read*s can be sequentially invoked and the related instantiated variables are instantly right propagated, as it would be done in a classical logic programming approach. For instance, the following precondition will be true each time a new temperature is read by any of the temperature sensors in the system.

```
["Directory","SensorNetworks"].rd(network) &
[network,"Type"].rd(id, "temperature") &
[network,"Sensors"].rd(id, value)
```

The first `rd()` returns all the wireless sensor networks known by the system. Obviously, if a new wireless network is integrated in the system, and if the resource defining its availability is inserted in the bag `"SensorNetworks"`, then it will be automatically taken into account in the evaluation of the precondition. Each returned value will be instantly propagated in order to define the variable `network` used to designate the object name in which the `"Sensors"` and `"Type"` bags have to be queried. The second `rd()` gets the `id` of all the temperature sensors while the last `rd()` gets, for each of them, their mesured `value`. As a result, we obtain the search tree of Figure 2. Here, the computation item is seen as a ”virtual bag” that, each time a `rd()` is done, takes the first field of the tuple as input parameter, computes the `consign = compute_consign(value)` function, and then returns a tuple containing the result in the updated second field.

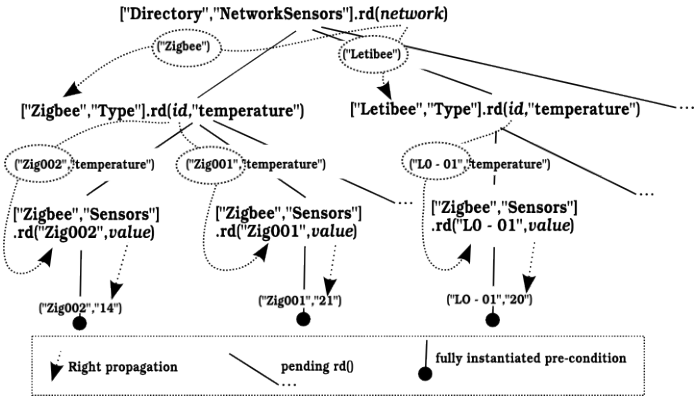

Figure 2. Evaluation tree

From the system side, it is seen exactly as any other bag. In the same way, it is possible to map *assertions*:

```
ASSERT: lib.lowerthan(value,threshold)
```

Here too, a virtual bag generates the expected resource if the condition is true. If the condition is not met, no resource is generated and the `rd()` is blocked.

The last facility allows to define of *temporization* in seconds:

```
TIMEOUT: 30
```

Here, the virtual bag waits the given delay before returning a tuple allowing the evaluation of the rest of the precondition.

For instance, if supplemented with an assert condition, the rule explained above will only consider the sensors with readings lower than 16°:

```
["Directory","SensorNetworks"].rd(network) &
[network,"Type"].rd(id, "temperature") &
[network,"Sensors"].rd(id, value) &
ASSERT lib.lowerthan(value,"16") &
COMPUTE lib.compute_consign(value,consign) &
[network,"Location"].rd(id, location) &
```

In addition, the reference that has to be transmitted to the heater according to the measured temperature is computed. Finally, the location of the temperature sensor related to the heater that has to receive this reference is retrieved. For the tree in figure 2 that contains 3 sensors, only the first one will actually trigger the performance phase.

The last point is to control the frequency of the precondition evaluation. Currently, each time a new measure is performed by a temperature sensor, the precondition is evaluated. This is obviously not suitable. Thus, at the beginning of the precondition, a `rd()` is added to a bag called `Ticket` that regularly generates resources used as tickets for triggering time-dependent actions. For instance, suppose that the `Ticket` bag generates a `("heating","ticket")` resource each 10 mn. Then, the precondition presented above is evaluated each 10 mn. If such a sensor exists, its location and the reference to apply to the related heater is computed. The full rule with its performance part can now be written:

 ISBN: 978-1-61208-145-8

```
["Clock","Ticket"].rd("heating","ticket") &
["Directory","SensorNetworks"].rd(network) &
[network,"Type"].rd(id, "temperature") &
[network,"Sensors"].rd(id, value) &
ASSERT lib.lowerthan(value,"16") &
COMPUTE lib.compute_consign(value,consign) &
[network,"Location"].rd(id, location) &
::
{
["Clock","Ticket"].get("heating","ticket") ;
[network,"Sensors"].rd(id, value) ;
["Heating","Actuators"].(location,consign)
}{
["Clock","Ticket"].get("heating","ticket") ;
[network,"Sensors"].rd(id, value) ;
["Alarm","SMS"].("06778899","heating problem")
}.
```

The performance part is made of 2 distinct transactions, basically corresponding to 3 different cases:

1) in the first phase of the first transaction, we check if the ticket (`"heating","ticket"`) is still available, if the temperature is the same as the one measured in the precondition, and if the heating system is manageable. If it is true, the second phase is performed: the ticket is consumed and the resource defining the consign for the heater is inserted in the bag controlling the heating system. Since, the resource corresponding to the temperature value might be shared by some other rules we do not consume it: a `rd()` is used instead of a `get()`; The second transaction has no chance to be performed as the ticket resource disappeared.
2) the temperature measurement has not been modified but, for some reason, in the first phase, the system has not been able to communicate with the heating system. In this case, the first transaction aborts, the ticket remains and the second transaction is tried. This second transaction sends an alarm via SMS to the user to warn her of the heating system problem;
3) if the temperature measurement has changed, then none of the 2 transactions are performed because the resource corresponding to the temperature of the precondition disappeared. In this case, the resource ticket is preserved in the system, enabling the precondition to be re-evaluated with the new temperature resource.

B. Other extensions

Two other mechanisms are provided to refine the evaluation mechanism of the precondition. Their goal is mainly to reduce the size of the search tree and to cut off earlier branches. These mechanisms are exemplified hereafter:

```
{*,!}["Clock","Ticket"].rd("heating","ticket") &
{*,!}["Directory","SensorNetworks"].rd(network) &
{*,600}[network,"Type"].rd(id, "temperature") &
{*,!}[network,"Sensors"].rd(id, value) &
ASSERT lib.lowerthan(value,"16") &
COMPUTE lib.compute_consign(value,consign) &
{1,!}[network,"Location"].rd(id, location) &
```

The first field into the curly brackets defines the number of awaited replies. It has already seen that `rd()` opens a stream of replies. With this new field, the system knows that after receiving the required number of values, the stream can be closed. For instance, a sensor is known to stay in a single location (a single location resource exists in the bag for the given sensor). The second field indicates how long (in s) to wait for resources while the `rd()` is pending. Here, for instance, the waiting for a temperature measurement will be no longer than 10 mn (i.e. 600 s), as a new ticket is issued every 10 minutes. Then, even if the temperature would finally be read after 10 mn, it would not anyway be validated in the precondition re-evaluation. Then, it is not useful to keep the stream waiting for this `rd()` open.

To be complete, it is worth to say that opened streams are automatically closed by the system when the resource on which depends the `rd()` stream gets consumed.

IV. Application

In this section, we illustrate the high level of expressiveness of the Chaski coordination language through the following application. Several seniors are living autonomously in their own habitation. Nevertheless, they need a daily checking. A pool of health professional has to check that the elderly people are fine.

Two organizations of these daily meetings can be proposed. The first one consists in fixing in advance the appointment between one elderly people and one health professional. Obviously, this way will not take into account the different unforeseen events:

- an elderly person is late at the appointment because involved in daily activities;
- a health professional is late because previous check-up lasted more than expected;
- emergency has to be taken into account;
- if a check-up is shorter than planned, the remaining time is just lost even if another check-up would be possible;
- the load is not balanced among the pool of health professionals, some are idle, some are overwhelmed.

The second way is to let to the application organizing the scheduling in real time by relying on the Chaski framework and its rules to capture information from different type of sensors and to synchronize distributed actions.

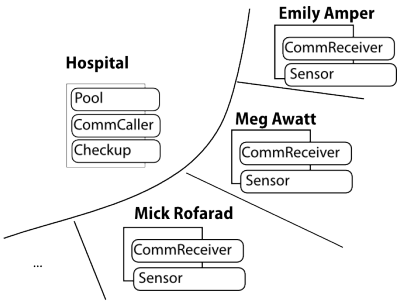

Figure 3. Overview of the distributed application

Figure 3 gives an overview of the distributed application with the decomposition in Objects/Bags:

`["Hospital","Checkup"]` is a bag containing information about the people to be contacted during a day;

`["Hospital"."Pool"]` manages the available doctors who can make the daily checking;

name
Emily Amper
Eloi de Moure
Mani Kor
Meg Awatt
Mick Rofarad
Kyle Hobbit

doctorname	status
”Dr. Home”	”idle”
”Dr. Whatelse”	”idle”

Table I
EXAMPLE OF RESOURCES CONTAINED IN CHECKUP AND POOL BAGS

`[ ?? ,"Sensor"]` encapsulates a presence sensor at the location of each elderly person;

`["Hospital","CommCaller"]` is a bag encapsulating the video conference equipment of the hospital;

`[ ?? ,"CommReceiver"]` is a bag encapsulating the video conference equipment at elderly person location;

The main rule is:

```
["Hospital","Checkup"].rd(senior) &
["Hospital","Pool"].rd(doctor,"idle") &
[senior,"Sensor"].rd("present")
::
{
["Hospital","Checkup"].get(senior) ;
["Hospital","Pool"].get(doctor,"idle") ;
[senior,"Sensor"].rd("present") ;
["Hospital","CommCaller"].put(doctor,"call",senior) ;
[senior,"CommReceiver"].put("accept",doctor)
}.
```

The bag `[senior,"Sensor"]` encapsulates a presence sensor that insert in the bag the information about the presence or not of the person. For instance, it can be a simple presence sensor put on top of a computer/laptop/pad screen. The bags `["Hospital","CommCaller"]` and `[senior,"CommReceiver"]` just encapsulate the video conference software module used by the system. It can use for instance the command line interface of skype.

The behavior of the rule is as follows. The first token returns all the people that are waiting for a checkup. The second token returns all the available Health professional. The third token corresponds to a presence sensor on the location of each of the elderly people. When one of them is detected as ”present” then the precondition of the rule is verified and the performance part may be triggered.

Assume that the precondition becomes true with `"Mani Kor"` as `senior` and `doctor` is `"Dr Home"`. Then the performance part is:

```
{
["Hospital","Pool"].get("Dr Home","idle") ;
["Mani Kor","Sensor"].rd("present") ;
["Hospital","Checkup"].get("Mani Kor") ;
["Hospital","CommCaller"].put("Dr Home","call","Mani Kor") ;
["Mani Kor","CommReceiver"].put("accept","Dr Home")
}.
```

When the performance part is triggered, the initial situation responsible for the precondition could have changed and then it is required to verify that the condition is still true. This is done either using the `rd()` or the `get()` operations. Both verify that the required resource is still available but the second in addition will consume the resource in the second phase of the transaction. The different cases concerning the performance are discussed hereafter.

If the 3 resources `("Mani Kor")`, `("present")` and `("Dr Home","idle")` are still available then they are locked and the 2 last tokens verify that the video conference is technically possible (e.g. equipment ”on” at both sides). If everything is fine then resources `("Dr Home","idle")` and `("Mani Kor")` are consumed and the video conference is launched. The consumption of resources `("Dr Home","idle")` and `("Mani Kor")` prevents the two people (doctor and senior) to be involved in another video conference because all the rules that require one of these resources will fail in the performance phase. When the check-up is finished, the doctor has just to notify the system that he is available again. As a consequence the resource `("Dr Home","idle")` is inserted in the bag `["Hospital","Pool"]`. This will reactivate all the rules waiting for a resource in this bag.

The transaction may cancel because:

- the doctor could have received an emergency. In this case, the corresponding resource is removed from `["Hospital","Pool"]`. This could be done automatically by removing the resource when the doctor id card used for authentication and tracing is removed from the reader associated to the computer;
- the doctor could be involved in another check-up if 2 check-ups were possible at the same time. Only one triggers the video conference and the other fails due to the absence of the resource `("Dr Home","idle")`;
- `"Mani Kor"` could already be with another doctor;
- `"Mani Kor"` could have left the room equipped with video conference system for some reason and then the resource `("present")` is no longer available;
- video conference equipment failed at one of the sides.

If the transaction fails then no resources are consumed. Thus, the precondition of the rule may become again true if the doctor or the senior becomes again available.

Concerning the faulty equipment, another transaction can be added after the first one and then triggered in sequence.

```
{
["Hospital","Pool"].get("Dr Home","idle") ;
["Mani Kor","Sensor"].rd("present") ;
["Hospital","checkup"].get("Mani Kor") ;
["Hospital","Support"].put("Pb","Dr Home","Mani Kor");
}
```

If the resources awaited by the 3 first token are available, this means that the previous transaction failed. Otherwise `("Mani Kor")` would have disappeared. Then this transaction is executed only if the first one fails. In this case

 ISBN: 978-1-61208-145-8

a resource `("Problem","Dr Home","Mani Kor")` is inserted allowing another rule waiting for it to manage the problem and to warn the support team for instance.

V. DISCUSSION

The simple example given in the previous section shows the expressiveness of the Chaski language may simplify the design of distributed applications which need to put together data coming from different distributed locations.

ECA rules

This language goes beyond what is possible to do with Event-Condition-Action (ECA) rules [10] on different points. First, it unifies the event and the condition because they are seen in the same way by the system: an event and value condition are resources contained in the bags. This allows to have much more refined way to trigger the rules. Second, the event and the condition evaluation concern distributed data with no restriction about the distribution. Third, the verification of the condition is embedded in a transaction including also the actions to be performed. This guaranties the same logical time.

STITCH coordination language

As Chaski rules are an improvement of the STITCH coordination language, we discuss here the differences.

First, STITCH does not allow to consider alternative transactions in the same rule. This means that fall-back treatment is less natural and requires additional bags and explicit extra rules that makes the design of the application more complex. In addition, in STITCH, the insertion (put) is not embedded in the transaction but handled by a separate mechanism ensuring that the resource is eventually inserted. It obviously ensures the insertion but does not allow any treatment if the insertion cannot be done at the transaction time. This makes the system less flexible. For instance, this could not ensure the correct setting of the video conference in our example. Another difference is that, in STITCH, the exact same resource of the precondition is used in the transaction. Then, if the sensor reads many times the presence of a person and inserts each time a new identical `("present")` resource, this would cause the transaction to abort and to be retried with another resource with the same value. This generates much more work. The last difference that is not highlighted in the present example concerns the extension introduced in Section III-B that allows respectively to define the number of replies awaited and the maximum time to be blocked when pending.

VI. CONCLUSION

In this paper, a new abstraction layer is proposed. It provides a uniform view of the components - sensors, actuators and services - that are encountered in (wireless) sensors and actuators networks. Thanks to this abstraction layer, integration of geographically distributed software and hardware components is easier. Morever, to enforce the whole system consistency, sensing and actuation are embedded in transactions. Prototyping is accelerated thanks to the rule-based coordination language. The powerfulness of this middleware is exemplified on a realistic application.

ACKNOWLEDGMENT

This research has been sponsored in part by the European Project OUTSMART (PN 285038) under the 7th Framework Programme FP7-2011-ICT-FI.

REFERENCES

[1] J.-M. Andreoli, F. Pacull, D. Pagani, and R. Pareschi, "Multiparty negotiation of dynamic distributed object services," *Journal of Science of Computer Programming*, vol. 31, pp. 179–203, 1998.

[2] D. Arregui, F. Pacull, and M. Riviere, "Heterogeneous component coordination: the clf approach," in *In Proc. of EDOC'2000, Makuhari*, 2000, pp. 194 – 203.

[3] J.-M. Andreoli, D. Arregui, F. Pacull, and J. Willamowski, "Resource-based scripting to stitch distributed components," in *in Proc. of EDICS'02*, 2002, pp. 429–443.

[4] N. Carriero and D. Gelernter, "Linda in context," *Commun. ACM*, vol. 32, pp. 444–458, April 1989.

[5] E. Freeman, K. Arnold, and S. Hupfer, *JavaSpaces Principles, Patterns, and Practice*, 1st ed. Essex, UK, UK: Addison-Wesley Longman Ltd., 1999.

[6] S. W. McLaughry and P. Wycko, "T spaces: The next wave," in *Proceedings of the Thirty-second Annual Hawaii International Conference on System Sciences-Volume 8 - Volume 8*, ser. HICSS '99. Washington, DC, USA: IEEE Computer Society, 1999, pp. 8037–.

[7] P. A. Bernstein, V. Hadzilacos, and N. Goodman, *Concurrency control and recovery in database systems*. Boston, MA, USA: Addison-Wesley Longman Publishing Co., Inc., 1987.

[8] "Book review: Rule based programming with ops5 by thomas a. cooper and nancy wogrin (morgan kaufmann pubtishers)," *SIGART Bull.*, pp. 14–15, July 1989, reviewer-Trowbridge, Timothy L.

[9] R. A. Kowalski, "The early years of logic programming," *Commun. ACM*, vol. 31, pp. 38–43, January 1988.

[10] U. Dayal, A. P. Buchmann, and D. R. McCarthy, "Rules are objects too: A knowledge model for an active, object-oriented databasesystem," in *Lecture notes in computer science on Advances in object-oriented database systems*. New York, NY, USA: Springer-Verlag New York, Inc., 1988, pp. 129–143.

 ISBN: 978-1-61208-145-8